

BULGARIAN CHEMICAL COMMUNICATIONS

2015 Volume 47 / Special Issue D

*Journal of the Chemical Institutes
of the Bulgarian Academy of Sciences
and of the Union of Chemists in Bulgaria*

Coarsening behaviour of Pb particles in a Al-5wt%Pb nanocomposite alloy produced by mechanical alloying

Wu Zhi-fang, Liu Chao, Wu Runong

Key Laboratory for Ferrous Metallurgy and Resources Utilization of Ministry of Education, Wuhan University of Science and Technology, Wuhan 430081, China

Received June 26, 2015; Revised September 10, 2015

Abstract: The coarsening behavior of Pb particles in a Al-5wt%Pb nanocomposite alloy produced by mechanical alloying has been studied by X-ray diffraction, scanning electron microscopy and transmission electron microscopy. Result shows that the cube of the average particle radius of Pb phase grows proportional with the annealing time even though the size of the constituent phase was in nanometer range. The activation energy for coarsening of Pb particles closes to the activation energy of grain boundary self-diffusion of solvent matrix (Al). In the nanocomposite alloys, the solute atoms diffuse along the grain boundaries of the solvent matrix.

Keywords: Nanocomposite alloy, Mechanical alloying, Secondary phase, Coarsening

INTRODUCTION

Nanocomposite alloys, which consist of at least two phases in nanometer size, have potential application in the fields of magnetic materials [1], hydrogen storage materials [2], hard metals [3], bearing alloys [4], and so on. The unique nanocomposite structure makes those materials exhibit properties much superior to those with conventional phase size. The size of the secondary phase particles has a direct influence on the properties of nanocomposite alloys. In this case the structure stability of nanocomposite alloys is very important because their significant high fraction of grain boundary provides a strong driving force for coarsening and results in change of properties. Thus, to clarify the coarsening behaviour of secondary phase in nanocomposite alloys is of great importance.

For the conventional grain sized composite alloys with constant volume fraction ratio, as it is well known, the coarsening, or called as Ostwald ripening, of the small fraction component was formulated by Lifshitz, Slyozov and Wagner, and is widely referred to as the LSW theory [5, 6]. The LSW theory predicts that the cube of the average particle radius grows proportionally with the annealing time if the mass transport is governed by a diffusion mechanism. However, the LSW theory is valid only in the physically unrealistic limit of zero volume fraction of secondary phase. Effort has been made to modify LSW theory and extend to high volume fraction of dispersed phases using both analytic and numerical method. The results show

that the cubic law can be used for embedded phase of high volume fraction, with the coarsening rate being dependent on volume fraction [7, 8].

For the nanocomposite alloys, the results show that the coarsening of secondary phase still follows the LSW theory and the activation energy for coarsening of secondary phase is different from that of conventional grain sized alloys [9, 10]. Actually, the LSW coarsening theory assumes zero volume fractions of secondary phases, which is obviously not suitable for the case of nanocomposite alloys due to their high volume fractions of secondary phases (26.6-50.88%). In addition, the interparticle diffusion interactions are more remarkable when the size of the constituent phase is in nanometer range. Therefore, it's necessary to take into account the effect of volume fraction to investigate the coarsening kinetics of secondary phase with nonzero volume fraction in the nanocomposite alloys.

In this study, the coarsening behavior of Pb phase with very small volume fraction has been studied. This is because of Al-Pb is a typical immiscible system and the Al-Pb nanocomposite alloys fabricated by MA exhibit super wear resistance which is very much dependent on the grain size (and/or phase size) [11]. Therefore, a study of the coarsening behavior of Pb phase with very small volume fraction in Al-Pb nanocomposite alloy is significant to both the fundamental research of nanocomposite alloys and their application in engineering.

EXPERIMENTAL

Al and Pb powders of 99.9% purity with the average particle size of 70~80 micron were used as raw materials. An alloy with composition of Al-5wt%Pb was selected, in which the volume fraction of Al and Pb phase is 99.32% and 0.68%, respectively, and Al and Pb are hence regarded as matrix phase and secondary phase with very small volume fraction, respectively. The powder mixtures were sealed in stainless steel vials together with hardened steel balls. The weight ratio of the powder to ball was 1 to 10. The handling of powders was performed inside a glove box filled with pure argon. The milling process was performed in a QM-3SP2 planetary ball mill. The milled powders were uni-axially cold pressed under a pressure of 440 MPa to get bulk samples. The as-compacted bulk samples were then heated at different temperatures for different times under the protection of pure argon atmosphere. Then the samples were characterized by X-ray diffraction (Philips X'Pert MPD with Cu-K α radiation), scanning electron microscopy (SEM, FEI-Navo Nano SEM 400) and transmission electron microscopy (TEM, JEM-2100).

RESULTS AND DISCUSSION

The X-ray diffractograms of Al-5wt%Pb powders after milling for different times are presented in Fig. 1. It can be observed that there are only diffraction peaks of Al and Pb phase and they have no obvious shift. That means that only pure Al and Pb phase existed in the milled powder and no supersaturated solid solution formed. It is obvious that the diffraction peaks of both Al and Pb phases broaden gradually with increased of milling time, which reveals the remarkable grain refinement of Al and Pb phases after ball milling. The grain size of Al and Pb phase were estimated from broadening of different peak using the Vogit method [12], and the results are shown in Fig. 2. It shows that the grain sizes of Al and Pb reduce sharply in the initial stage (1-10 h) and then tend to level off with increase of milling time, and they reach 77 and 7 nm, respectively after 30 h of milling.

Figure 3 shows a bright field image of Al-5wt%Pb sample milled for 30 h. It can be seen that Pb particles with nanometer sizes are single crystal particles. Therefore, it is assumed that the Pb particles embedded in Al matrix are generally single crystal and the grain size of Pb phase estimated from XRD analysis represents the size of Pb particles. The average grain size is about 10 nm, which is in good agreement with the XRD result.

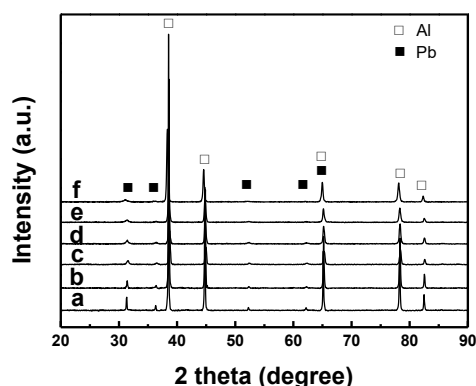


Fig. 1. X-ray diffractograms of Al-5wt%Pb alloy powder after milling for different times: (a) 1 h; (b) 2 h; (c) 5 h; (d) 10 h; (e) 20 h; and (f) 30 h.

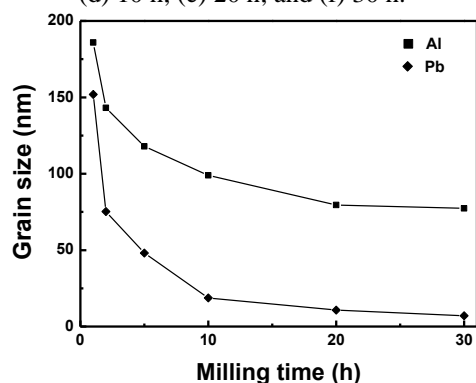


Fig. 2. Dependence of grain sizes of Al and Pb in Al-5wt%Pb powders on milling time.

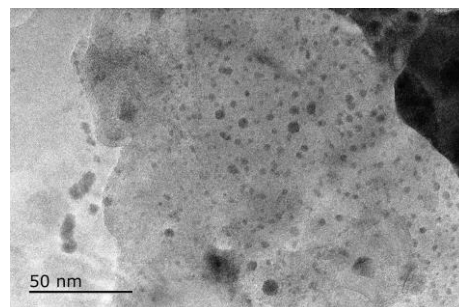


Fig. 3. TEM bright field image of Al-5wt%Pb alloy powder milled for 30 h.

Fig. 4 gives the XRD patterns of Al-5wt%Pb samples after 30 h milling and then heating for 1 h at different temperatures (573, 623, 673 and 723 K). It is obvious that diffraction peaks of Al and Pb phase become sharper with increase of heating temperature which indicates that Al and Pb phases grew gradually during heating. As shown in Fig. 5, the grain size of Pb phase increases with the increasing of heating temperature.

Fig. 6 shows SEM images of Al-5wt%Pb alloy compacted from the milled powder and heated at different temperatures for 1 h. For the as-compacted Al-5wt%Pb alloy, as shown in Fig. 6(a), the bright Pb particles are very fine and uniformly distributed in the dark Al matrix. It is obvious that the size of Pb particles increase with increase of

heating temperature and the particles of Pb phase are also homogeneously distributed in the Al matrix of as-heated Al-Pb sample.

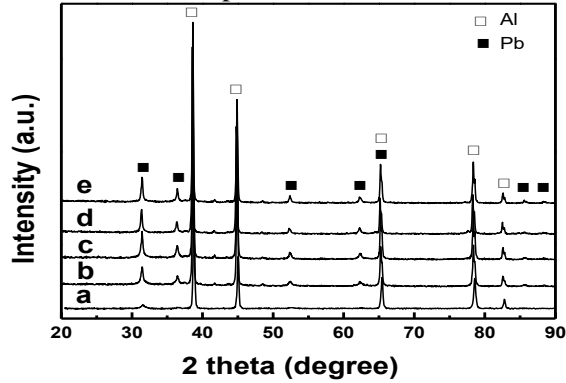


Fig. 4. X-ray diffractograms of Al-5wt%Pb alloy samples after 30 h milling and then heating at different temperatures for 1 h: (a) as-milled; (b) 573 K; (c) 623 K; (d) 673 K; and (e) 723 K.

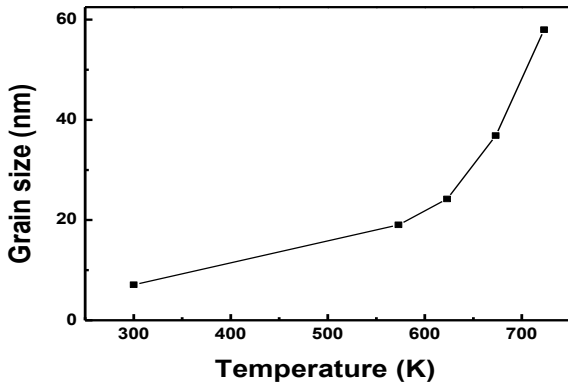


Fig. 5. Temperature dependence of the size of Pb phase in MA Al-5wt%Pb (dwelling time: 1 hour)

In order to clarify the coarsening kinetics of Pb phase, the dependence of Pb particle size, which was deduced from X-ray diffraction analysis, on heating dwelling time was determined and illustrated in Fig. 7. It is clear that there exists an excellent linear correlation between the cubic of particle size (r) and dwelling time (t) in the particle size range in this work. Here, r_0 is the average radius of the phase in the as-milled condition. This suggests that the coarsening of Pb phase follows the standard cube kinetics of diffusion-controlled particle growth. The excellent linear relationship between the cubic of r and t means the coarsening of Pb phase in Al-5wt%Pb nanocomposite alloys is controlled by diffusion even though the size of the constituent phase is in the nanometer range. The slope of each line in Fig. 7 is the particle coarsening rate constant $K(\phi)$.

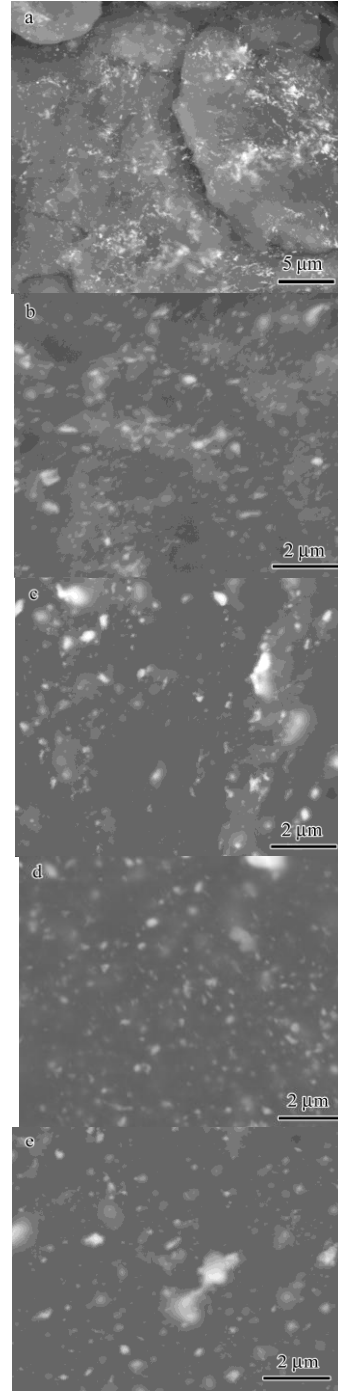


Fig. 6. SEM images of MA Al-5wt%Pb alloys: (a) as-compacted, heated at (b) 623 K, (c) 673 K, (d) 723 K and (e) 773 K for 1 h. The bright phase is Pb and the dark matrix is Al.

According to the modern Ostwald ripening theories, the coarsening rate constant $K(\phi)$ determined by $K(\phi) = \frac{A(\phi) C_e \Omega^2 \gamma D}{RT}$. When the diffusion coefficient D is given by $D = D_0 \exp(-\frac{Q}{RT})$, the constant $K(\phi)$ can be formulated as follows:

$$K(\phi) = \frac{A(\phi) C_e \Omega^2 \gamma D_0}{RT} e^{-\frac{Q}{RT}}, \quad (1)$$

where $A(\phi)$ is a dimensionless constant depending on the volume fraction (ϕ) of secondary phase and $A(0) = 8/9$; thus, the theories reduce to the LSW theory in the limit of zero volume fraction. C_e is the equilibrium solute content of the matrix, Ω is the molar volume of the particle, γ is the particles-matrix interfacial energy per unit area, D_0 is a frequency factor, R is the universal gas constant (8.31 J/mol/K) and T is the absolute temperature, Q is the activation energy for Pb particles coarsening. The relationship (1) is reformulated as follows:

$$\ln \left[\frac{K(\phi)T}{C_e} \right] = \text{constant} - \frac{Q}{RT} \quad (2)$$

In order to estimate the Q in the Al-5wt%Pb nanocomposite alloy, we calculated the solubility of Pb in Al solid-solution at different temperatures (573, 623, 673 and 723 K) according to the Ref. [13]. Therefore, the coarsening activation energy can be determined from the slope of the plot of $\ln \left[\frac{K(\phi)T}{C_e} \right] \sim \frac{1}{T}$. The coarsening rate constants

$K(\phi)$ at different heating temperatures are shown as the plot of $\ln \left[\frac{K(\phi)T}{C_e} \right]$ versus $\frac{1}{T}$ in Fig. 8. The

activation energy Q for Pb particles coarsening is determined to be 79.64 kJ/mol. For comparison, the diffusion activation energy of Pb in Al of different diffusion mechanisms is given in Table 1. It shows that the value obtained in this work is much smaller than that of lattice diffusion mechanism of Pb in Al and lattice self-diffusion of Al but very close to that of boundary self-diffusion of Al. This indicates that the coarsening mechanism in the nanocomposite alloys is different from that in conventional grain sized composite alloys. The observation of the cubic law for the coarsening of secondary phase in nanocomposite alloys reveals that the coarsening process is controlled by the three-dimensional long distance diffusion of solute atoms. However, the agreement of the activation energy to that of grain boundary self-diffusion of matrix indicates that the diffusion mechanism in the nanocomposite alloys is basically grain boundary diffusion. This is because the grain sizes of matrix phase and secondary phase are in nanometer range. Thus, the solute atoms should diffuse more easily along nanograin

boundary than in conventional grain sized composite alloys.

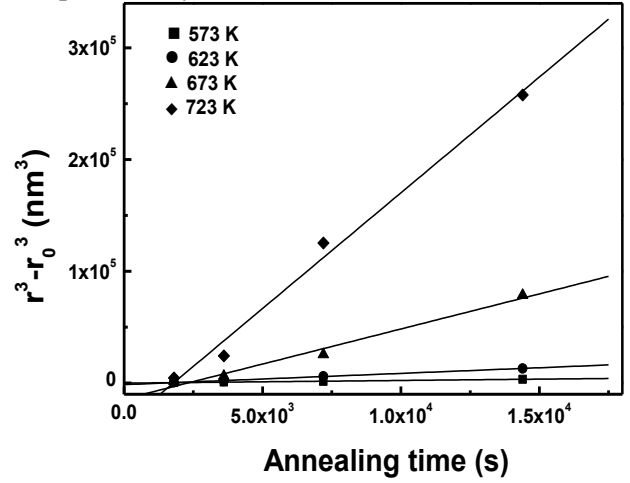


Fig. 7. Dependence of the cubic of Pb particle radius on heating time for Al-5wt%Pb alloy heated at different temperatures (573, 623, 673 and 723 K) after 30 h of milling.

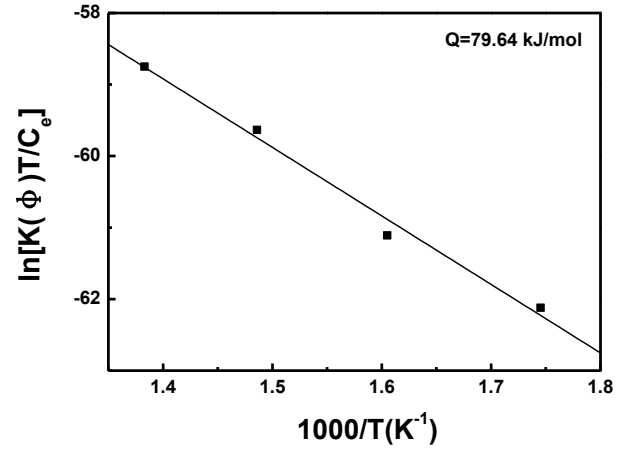


Fig. 8. Determination of the activation energy (Q) for coarsening of Pb phase in a Al-5wt%Pb nanocomposite alloy.

CONCLUSIONS

In the present work, the coarsening behaviour of Pb particles in a Al-5wt%Pb nanocomposite alloy prepared by mechanical alloying has been investigated. The main conclusions obtained from the present work are as follows:

(1) The cube of the average particle radius of Pb phase grows proportional with the annealing time even though the size of the constituent phase was in nanometer range.

(2) The activation energy for coarsening of Pb particles closes to the activation energy of grain boundary self-diffusion of solvent matrix (Al). In the nanocomposite alloys, the solute atoms diffuse along the grain boundaries of the solvent matrix.

Table 1. Activation energy in kJ/mol of experiment and theory in Al-Pb system

Activation energy of our result	Activation energy of lattice diffusion [14]	Activation energy of lattice (self-) diffusion [14]	Activation energy of grain boundary (self-) diffusion [14]
79.64	Pb in Al: 145.6(777-876 K)	Pb: 107.4 (473-596 K) Al: 142.4 (723-923 K) 144.4 (573-923 K) 123.5 (298-581 K) 126.4 (358-482 K)	Pb: 66 (487-533 K) Al: 90 (623-753 K)

ACKNOWLEDGEMENT: The financial support of the National Natural Science Foundation of China under grant No. 51201118, Key Laboratory of Clean Energy Materials of Guangdong Higher Education Institute under grant No. KLB11003 and the National College Students' innovation and Entrepreneurship Training Program under grant No. 201210488023 are greatly acknowledged.

REFERENCES

1. J. I. Betancourt, H. A. Davies, *J. Magn. Magn. Mater.*, **246**, 6 (2002).
2. M. Zhu, H. Wang, L. Z. Ouyang, M. Q. Zeng, *Int. J. Hydrogen Energy*, **31**, 251 (2006).
3. S. I. Cha, S. H. Hong, G. H. Ha, B. K. Kim, *Scripta Mater.*, **44**, 1535 (2001).
4. X. Liu, M. Q. Zeng, Y. Ma, M. Zhu, *Wear*, **265**, 1857 (2008).
5. I. M. Lifshitz, V. V. Slyozov, *J. Phys. Chem. Solids*, **19**, 35 (1961).
6. C. Wagner, *Ber. Bunsen-Ges. Phys. Chem.*, **65**, 581 (1961).
7. A. Baldan, *J. Mater. Sci.*, **37**, 2171 (2002).
8. A. Baldan, *J. Mater. Sci.*, **37**, 2379 (2002).
9. J. H. Yu, T. H. Kim, J. S. Lee, *NanoStruct. Mater.*, **9**, 229 (1997).
10. M. Zhu, Z. F. Wu, M. Q. Zeng, L. Z. Ouyang, Y. Gao, *J. Mater. Sci.*, **43**, 3259 (2008).
11. M. Zhu, Y. Gao, C. Y. Chung, Z. X. Che, K. C. Luo, B. L. Li, *Wear*, **242**, 47 (2000).
12. J. I. Langford, *J. Appl. Cryst.*, **11**, 10 (1978).
13. E. Ma, J. H. He, P. J. Schilling, *Phys. Rev. B*, **55**, 5542 (1997).
14. W. E. Gale, T. C. Totemeier, *Smithells materials reference book[M]*, 8th ed. Elsevier, Butterworth-Heinemann, 2004, pp:13-11, 13-17.

Effect of calcination and chromium doping on the structural characteristics of titanate nanotubes

A. H. Shahbazi Kootenaeei, S. Maghsoodi

Department of Chemical Engineering, Mahshahr Branch, Islamic Azad University, Mahshahr, Iran.

Received June 26, 2015; Revised September 10, 2015

Titanate nanotubes were synthesized by alkaline hydrothermal method using TiO₂ P25 at 140°C. In the present study the effects of calcination and chromium doping was investigated. At various chromium concentrations some phase changes occurred. The BET specific surface area altered from 404 m²g⁻¹ to lesser values by chromium loading augmentation. Calcination process accelerated the phase transformation from hydrogen titanate to anatase polymorph of TiO₂ along with specific surface area deterioration. In the range of the studied parameters, the emergence of rutile phase was not confirmed. Calcination of 1 wt% and 2 wt% chromium doped titanate sample induced the chromium oxide phase development. Calcination process brought about nanotubular structure deterioration along with nanoparticles evolution.

Keywords: Titanate nanotubes; Chromium; Doping; Anatase; Calcination.

INTRODUCTION

Kasuga et al. [1] recently announced the synthesis of TiO₂-derived nanotubular structures by hydrothermal treatment of titania powder in a concentrated NaOH aqueous solution. The aforementioned method is a template-free one producing elongated nanotubes with diameters of ca. 10 nm. These rather novel nanostructures are characterized by a high specific surface area [2].

Affecting from many parameters such as synthesis and calcination temperatures, dopants, and etc., the abovementioned hydrothermal method offers a simple, cost-effective, and environmentally friendly technology with the potential of high-yield titanate nanotube production [3-6].

These novel structures can be modified by grafting [7], ion-exchange [8], calcination, and treatment with chemical agents [9, 2].

Metal ion incorporation into titanate nanotubes will definitely alter the properties, however, as a consequence of metal ion insertion, the structure of nanotubes can be greatly affected as well.

Wang et al. [10] synthesized titanate nanotubes doped with magnetic ions (Fe, Ni, and Mn) that were synthesized by hydrothermal method as the ions were added to the nanostructure during the formation process of nanotubes. The as-prepared nanotubes transformed into the anatase polymorph of titania when the calcined temperature surpassed

350K, and further transformed into the mixture of anatase and rutile phases in consort with temperature rise.

Kulish et al. [11] found that the structure of (Fe, Mn, Zn, Cd, and Ni) doped nanotubes is analogous to Na₂Ti₂O₄(OH)₂ structure. Also, they suggested that the structure of Cd doped nanotubes may be a mixture of anatase and rutile polymorph of titania. Their results led to the conclusion that the examined metals did not form a solid solution of metal with titania. Besides, they asserted that the ions adsorption occurred on external and internal surfaces of the nanotubes.

In this contribution, calcined/uncalcined titanate nanotubes with/ without doping with chromium were examined for phase transformation behavior as well as specific surface area alteration using XRD and BET techniques. A morphology study was performed on the calcined chromium-containing sample by HRTEM technique in order to probe the morphology change.

EXPERIMENTAL

Preparation of Cr doped titanate nanotubes

For preparation of titanate nanotubes, 1.7 g of TiO₂ powder (Degussa P25) along with various amounts of chromium nitrate was added to aqueous solution of NaOH (10M) with constant stirring for 30 min. A Teflon-lined stainless steel autoclave with a capacity of 180 mL was filled with the resulting mixture up to about 80% of its total volume. The autoclave was sealed and heated at 140°C for 24 h. After the reaction was completed,

To whom all correspondence should be sent:
E-mail: kootena@gmail.com

the autoclave was allowed to cool to room temperature naturally. Then, the resulting material subjected to centrifugation and washing with a diluted 0.1M HNO₃ acid solution. The washing process continued until the pH of the rinsing solution reached about 1. The precipitates then washed with deionized water until the pH of washing solution achieved about 7. The acid-treated sample was oven-dried at 110°C overnight.

In TNT-x (x=0.2, 0.5, 1, and 2), “x” represents weight percent of chromium oxide in Final uncalcined samples. In the sample names, “C” represent calcination of samples at 500°C.

All chemical materials were purchased from Merck Company.

Material Characterization

X-ray diffraction (XRD) patterns of the samples were obtained with a Philips PW1800 diffractometer using Cu K α radiation. The intensities were determined over an angular range of $5^\circ < 2\theta < 70^\circ$ for all the prepared samples with a step-size $\Delta(2\theta)$ of 0.03° and a count time of 2 seconds per step. The diffraction spectra have been indexed by comparison with the JCPDS files (joint committee on powder diffraction standards).

Sample morphology was investigated by "JEOL" JEM-2100 (200 kV) high resolution transmission electron microscope (HRTEM). For HRTEM measurements the sample was grounded, suspended in isopropanol at room temperature and dispersed by ultrasonic agitation. Then, an aliquot of the prepared solution was dropped on a 3mm diameter lacey carbon copper grid.

The specific surface areas (S_{BET}) of the samples were determined at the liquid nitrogen (N₂) temperature from the adsorption and desorption isotherms of nitrogen by a Quantachrome CHEMBET-3000 apparatus using single-point method. Prior to BET surface area measurement samples were degassed by flow of nitrogen at 200°C for 2h.

RESULT AND DISCUSSION

HRTEM analysis

The HRTEM analysis performed on the CTNT-2 for the sake of investigating possible morphology alteration stemmed from chromium addition (Fig. 1). As can be noted, the nanotube morphology along with other nanostructures such as nanorod and nanoparticles is observed. Nanowire are estimated possessing diameters about 20 nm. Calcination exerted detrimental effects on nanotubular structure of pristine chromium doped

titanate nanotubes. As will be noted in section 3.2, doping with chromium led to specific area loss. Therefore, phase transformation from nanotubular structure into other morphologies such as nanoparticles as well as chromium oxide development (see next section) may be responsible for this observation. It has been reported that metal incorporation in nanotubular titanates altered the phase transformation in the acceleration or deceleration of the tubular phase deterioration can be observed [2, 12-14].

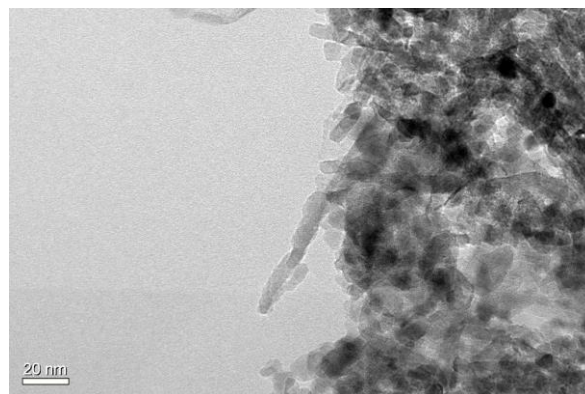


Fig. 1. HRTEM micrograph of CTNT-2.

XRD and BET analysis

The X-ray diffraction patterns acquired from uncalcined samples of undoped titanate nanotubes and chromium doped titanate nanotubes are shown in Fig. 2. The structure of undoped pristine nanostructures proposed to be H₂Ti₂O₅.H₂O in our previous work [2].

According to the XRD analysis, TNT-0.2 (Fig. 2b) differs slightly as compared to pristine undoped titanate nanotube (TNT) (Fig 2a). Hence, 0.2 wt% chromium loading hardly affected the crystalline structure of titanate nanotube. In the other hand, BET specific surface area dropped about 10% for this sample. This may be ascribable to the slight morphology change of TNT. The characteristic peak intensities of titanate nanotubes lowered for TNT-0.5 (Fig. 2c) as compared to the ones for TNT, which is ascribable to the crystal growth and emergence of new phase. It is noteworthy to claim that no characteristic peak assignable to the crystalline chromium oxide was observed. Chromium species may occurred in undetectable sizes beyond the capacity of XRD apparatus [15, 16]. The corresponding XRD patterns of TNT-1 is depicted in Fig. 2d. A noticeable shift in the peak located originally at $2\theta=10^\circ$ for pristine undoped titanate nanotube was observed, for TNT-1 sample. The alteration in the roll distances is reported to be responsible for this observation. Besides, BET

specific surface area decline was also reported to be accompanied with this phenomena [10, 11].

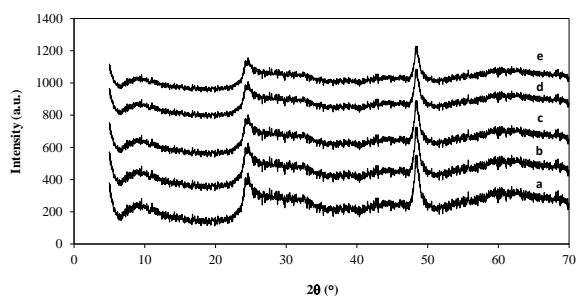


Fig. 2. XRD patterns of (a) uncalcined acid-treated titanate nanotubes [2], (b) TNT-0.2, (c) TNT-0.5, (d) TNT-1, and (e) TNT-2.

No characteristic peaks of the typical polymorph of titanate dioxide naming anatase, rutile and/or brookite were distinguishable.

It has been reported that some titanate phase may convert to titanium oxide with anatase phase. Generally, the greater the metal oxide doping, the higher the possibility of metal oxide crystalline phase development [15, 17]. Like the other analyzed samples, we could not find the characteristic peaks associable to the presence of the crystalline phase of chromium oxide in the TNT-2 (Fig. 2d) with the highest metal oxide loading. No characteristic peaks of anatase and/or other polymorphs of TiO_2 was present in this sample.

XRD analysis was performed on the CTNT-x samples calcined at 500°C (Fig. 3). As can be noted from Table 1, BET specific surface area of pristine undoped titanate nanotube lowered from $404 \text{ m}^2\text{g}^{-1}$ (TNT) to $186 \text{ m}^2\text{g}^{-1}$ (CTNT). Similar reports support this observation. Gao et al. [18] investigated the phase transformations of titanate nanotubes by in situ XRD. In their report, dehydration and recrystallization claimed to be the main causes of anatase phase emergence in calcination temperatures above 300°C which is accompanied by specific area loss. Water molecules along with the protons present loosely between the layer that are mobile and exchangeable by external ions. Poudel et al. [19] reported that titanate nanotubes are prone to transform into anatase phase of titanium oxide through calcination in air at rather

elevated temperatures. This process is a function of calcination temperature, impurities (intentional or unintentional), atmosphere, and etc. [20, 21]. However, this is a controversial research topic and the issues are under debates. As can be seen in the acquired XRD patterns shown in Fig. 3, the phase transformation from hydrogen titanate to anatase is obvious. In all of the calcined samples, XRD patterns hints that rutile phase may not coexist with anatase phase in the heat treated chromium doped titanate nanotubes.

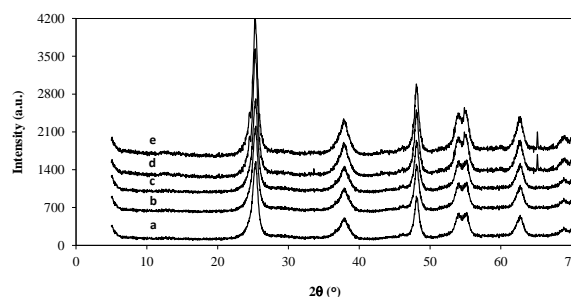


Fig. 3. XRD patterns of (a) calcined titanate nanotubes, (b) CTNT-0.2, (c) CTNT-0.5, (d) CTNT-1, and (e) CTNT-2.

BET specific surface area of CTNT-0.2 dropped to $164 \text{ m}^2\text{g}^{-1}$ due to calcination. We could not find any peaks that can be ascribable to the presence of chromium oxide phase. This may be due to the fact that XRD apparatus has limited detection capacity which for lower than a certain particle sizes no characteristic peak of the crystalline phase is demonstrated in the obtained patterns. BET specific surface area of CTNT-0.5 lowered to $150 \text{ m}^2\text{g}^{-1}$. As can be noted, increasing the chromium content led to surface area loss. The XRD patterns of CTNT-1 is shown in Fig. 3d. This sample possess a specific surface area of $98 \text{ m}^2\text{g}^{-1}$. The characteristic peaks ascribable to the presence of chromium oxide phase can be observed clearly. The characteristic peaks of this phase demonstrate at $2\theta=24.49^\circ$, 33.59° , 36.19° , 41.47° , 50.21° , 63.44° , and 65.10° (JCPDS 38-1479). The specific surface area was measured to be $66 \text{ m}^2\text{g}^{-1}$. The characteristic peaks of chromium oxide phase were measured with higher intensity that may be due to the superior population of the phase with large particles.

Table 1. BET specific surface area of the synthesized samples.

Sample	BET specific surface area m^2g^{-1}	Sample	BET specific surface area m^2g^{-1}
P25	52	CTNT	186
TNT	404	CTNT-0.2	164
TNT-0.2	362	CTNT-0.5	150
TNT-0.5	328	CTNT-1	98
TNT-1	203	CTNT-2	66
TNT-2	157		

CONCLUSION

The phase change behaviors of acid-washed titanate nanotube samples were examined by varying the chromium content as well as calcining in air. The higher the chromium loading was the lower the BET specific surface area. Also, calcination in 500°C caused a surface area loss along with the apparent new phase development for higher chromium containing samples. Chromium oxide was detected at loadings higher than 1 wt.%. The calcined samples morphology transformed from elongated nanotubular structure to truncated tubes as well as nanoparticles. No indication revealing the occurrence of rutile phase was noticed after calcination for all chromium concentrations.

Acknowledgements: Financial support for research project granted by Islamic Azad University of Mahshahr is highly appreciated.

REFERENCES

1. T. Kasuga, M. Hiramatsu, A. Hoson, T. Sekino, K. Niihara, *Langmuir*, **14**, 3160 (1998).
2. A.H. Shahbazi Kootenaeei, J. Towfighi, A. Khodadadi, Y. Mortazavi, *Appl. Surface Sci.*, **298**, 26 (2014).
3. A. Oszko, G. Potari, A. Erdo'helyi, A. Kukovecz, Z. Konya, I. Kiricsi, J. Kiss, *Vacuum*, **85**, 1114 (2011).
4. A. Kukovecz, G. Potari, A. Oszko, Z. Konya, A. Erdo'helyi, J. Kiss, *Surface Sci.*, **605**, 1048 (2011).
5. G. Potari, D. Madarasz, L. Nagy, B. Laszlo, A. Sapi, A. Oszko, A. Kukovecz, A. Erdo'helyi, Z. Konya, and J. Kiss, *Langmuir*, **29**, 3061 (2013).
6. J. Liu, Y. Fu, Q. Sun, J. Shen, *Micropor. Mesopor. Mater.*, **116**, 614 (2008).
7. L. Wang, W. Liu, T. Wang, J. Ni, *Chem. Eng. J.*, **225**, 153 (2013).
8. T. Kasuga, *Thin Solid Films*, **496**, 141 (2006).
9. R. Doong, C. Tsai, C. Liao, *Separ. Purif. Technol.*, **91**, 81 (2012).
10. M. Wang, G. Song, J. Li, L. Miao, B. Zhang, *J. Univ. Sci. Technol. Beijing, Mineral, Metallurgy, Material*, **15**, 644 (2008).
11. M.R. Kulish, V.L. Struzhko, V.P. Bryksa, A.V. Murashko, V.G. Il'in, *Semicond. Physics, Quantum Electronics & Optoelectronics*, **14**, 21 (2011).
12. K. Takashi, S. Keijiro, O. Takamasa, Yamasaki Yuki, N. Atsushi, *Mater. Trans.*, **50**, 1054 (2009).
13. J.S. Jang, D.H. Kim, S.H. Choi, J.W. Jang, H.G. Kim, J.S. Lee, *Int. J. Hydrogen Energy*, **37**, 11081 (2012).
14. A. Rónavári, B. Buchholz, Á. Kukovecz, Z. Kónya, *J. Molec. Struct.*, **1044**, 104 (2013).
15. A.A. Lemonidou, L. Nalbandian, I.A. Vasalos, *Catalysis Today*, **61**, 333 (2000).
16. V.L. Volkov, E.I. Andreikov, G.S. Zakharova, V.Y. Gavrilov, V.V. Kaichev, V.I. Bukhtiyarov, *Kinetics and Catalysis*, **49**, 446 (2008).
17. B. Grzybowska-Swierkosz, *Appl. Catalysis A: General*, **157**, 263 (1997).
18. T. Gao, H. Fjeld, H. Fjellvåg, T. Norby, P. Norby, *Energy & Environ. Sci.*, **2**, 517 (2009).
19. B. Poudel, W.Z. Wang, C. Dames, J.Y. Huang, S. Kunwar, D.Z. Wang, D. Banerjee, G. Chen, Z.F. Ren, *Nanotechnology*, **16**, 1935 (2005).
20. R. Yoshida, Y. Suzuki, S. Yoshikawa, *Mater. Chem. Physics*, **91**, 409 (2005).
21. C.C. Tsai, H. Teng, *Chem. Mater.*, **16**, 4352 (2004).

Parameters effecting on photocatalytic degradation of the phenol from aqueous solutions in the presence of ZnO nanocatalyst under irradiation of UV-C light

Davood Jalili Naghan¹, Ali Azari¹, Nezam Mirzaei^{2,1}, Azad Velayati³, Fahim Amini Tapouk⁴, Shervin Adabi⁵, Meghdad Pirsaeheb⁶, Kiomars Sharafi^{6, 1*}

¹Department of Environmental Health Engineering, School of Public Health, Tehran University of Medical Sciences, Tehran, Iran

² Social Determinants in Health Promotion Research Center, Hormozgan University of Medical Sciences, Bandar Abbas, Iran.

³Student Research Committee, Sabzevar University of Medical Sciences, Sabzevar, Iran.

⁴Department of Environmental Health Engineering, school of Public Health, International Campus, Tehran University of Medical Sciences (IC-TUMS), Tehran, Iran.

⁵Environmental Health Research Center, Kurdistan University of Medical Sciences, Sanandaj, Iran.

⁶Department of Environmental Health Engineering, School of Public Health, Kermanshah University of Medical Sciences, Kermanshah, Iran.

Received June 26, 2015, Revised September 10, 2015

Phenol or hydroxyl-benzene is one of the toxic hydrocarbons that grouped as a priority pollutant by EPA. It is one common compound that exists in industrial wastewaters including petroleum refining and petrochemistry, pesticide, oils and painting, organic chemicals, plastics, resins etc. that leads to environment pollution especially water resources. The aim of this study was evaluation of phenol degradation by use of nano-photocatalytic UV/ZnO process in a pilot. In the study, a 125 Watt UV lamp was used. Phenol measurement carried out using spectrophotometer. Results showed that there is reverse relationship between removal efficiency of phenol with increasing of pH in the case of nano-photocatalytic UV/ZnO process. Optimum conditions in nano- photocatalytic UV/ZnO process obtained in 10 mg/l phenol, contact time 30 min at pH=5. Results indicate that nano-photocatalytic UV/ZnO process can be used as an effective method for phenol removal from aqueous solutions.

Keywords: phenol, industrial wastewaters, UV, ZnO.

INTRODUCTION

Nowadays, conventional water and wastewater treatment processes are inadequate and sometimes disabling in treatment of toxic and resistant materials in water, because the production of toxic and complex substances. Hence, considering the performance technologies in this field is required to ensure the provide public health and environmental protection. The chemical compounds in industrial wastewater, especially petroleum compounds, phenol and its derivatives are very inclusive [1]. Phenol is the aromatic alcohol with C_6H_5OH formula and main component of coal tar that its compounds are the most important aromatic compounds. Phenol has another name, including benzenol, phenolic acid, phenol alcohol, phenic acid, hydroxy benzene, carboic acid and phenyl hydroxide [2-4]. Beside the artificial way, Phenol can entrance to water resources in natural ways, and because the physical structure can be found in most chemical compounds. Phenol, even exist in the urban wastewater and is taken into consideration due to

environmental stability, solubility in water and health problems [1]. Chlorination of drinking water containing phenol can produce the chlorophenolic compounds that lead to the stench and the protest by consumers. Therefore, phenol is classified as priority hazardous pollutants introduced by EPA's list [5, 6]. Most water quality standards are recommended that the phenolic compounds concentration in drinking water resources to be $\mu\text{g/L}$, and maximum concentrations in effluent discharged to the environment less than 1 mg/L [7-9]. In general, the phenol removal and control methods can be divided into two groups [10]:

1. Recycling methods of phenol compounds such as adsorption, ion exchange, solvent extraction, steam and hot gas removal.

2. Decomposition and destruction of methods for convert phenolic compounds into safe materials, including the use of oxidizing agents such as hydrogen peroxide, potassium permanganate, sulfur dioxide and ozone, biological methods, aeration and advanced oxidation. Physico-chemical processes for the purification of phenol including [11]:

1. Adsorption

2. Extraction by chemical solvents

To whom all correspondence should be sent:
E-mail: kio.sharafi@gmail.com

3. Water steam
4. Freezing & Crystallization
5. Chemical oxidation
6. Wet oxidation
7. Advanced Oxidation Processes

Many researches are still ongoing for reach the more appropriate methods. For this aim, advanced oxidation processes (AOP) and oxidation photocatalytic are used more than other methods. UV/ZnO photocatalytic is one of the common methods that used to degradation of water contaminants. In photocatalytic degradation of pollutants under the influence of ultraviolet radiation (UV) and in the presence of catalyst particles of metal oxides such as TiO₂ and ZnO [12]. Nanoparticles are essential element nanoscience that considered due to its applications in various fields. ZnO is II-VI family as a semiconductor important material due to direct energy gap and excitation binding energy at room temperature and its high bond length (3.37eV in room temperature) and has especially optical and electrical properties that can have many applications. ZnO, due to its sustainable properties of photonic and chemical corrosion similar TiO₂, is a semiconductor material potential in solar energy conversion. Size and morphology are two important parameters to measure and identify physical and physical chemistry properties of ZnO nanoparticles. There are two commercial methods for ZnO nanoparticles producing: The French and American methods. In both methods, the oxidation of zinc metal vapor is used both need a lot of heat, which also demands a lot of energy [13]. Considering the use of various materials nanoparticles are highly regarded for the removal of contaminants from water and sewage, therefore, in this study ZnO nanoparticles were used for photocatalytic degradation of phenol, and the effect of initial concentration, nanoparticle dosage, pH and contact time factors were studied.

MATERIAL AND METHODS

Initially, phenol stock solution was prepared according to the solution provided in the standard of the examination of water and wastewater method [14]. as follows: 1.5g pure phenol solution to 1L of DI-water. Then 2mL of concentrated sulfuric acid were added to enhance stability. Subsequently 10, 40 and 90 mg/L concentration of phenol were provided. A ZnO nanoparticle manufactured by Spadana Company was used as nanocatalyst. In order to activation of ZnO, nanoparticle catalyst was placed in the oven at a temperature 500 ± 50 C° for 2 - 2.5

hours and then cooled in the desiccator and powdered.

Experiments were carried out in a cylindrical glass reactor with a 2 liters volume. UV lamp (W125) at 254 nm wavelength by following features: length 25 cm, which protected in quartz sleeve with 30 and 5 cm highest, and diameter respectively, manufacturing engineering Shekoofan Tawseh exclusive agency agreement of Arda Company France was used as irradiation source. For better irradiation of sample, the lamp was immersed in solution at center of reactor. Overall the system was wrapped with aluminum foil to prevent the leak irradiation. Reactor designs is shown in Fig. 1. Phenol photocatalytic process carried out at pH (7, 11), contact time (5, 10, 20 and 30 min), nanoparticles dosage (0.15 and 0.3 mg/L) and the initial concentration of phenol (10, 40 and 90 mg/L). then, 10, 40, 90 mg/L concentrations of phenol in a cylindrical container prepared in 2 L, then added the nanoparticles in certain dosage to obtain the optimum nanoparticles dosage. Then container placed on the magnetic stirrer in a completely dark environment for 30 minutes to reach the balance of nanoparticle emissions created in attraction and repulsion. Stirring was constantly to prevent the nanoparticle sedimentation and mix thoroughly in all parts of the solution to be created. Then UV lamp was turn on and sampling carried out according considering contact time. The samples volume was selected 10 mL to prevent the noticeable change of solution volume. Subsequently samples were centrifuged for 10 minutes at a speed of 6000 to deposit the particles.

Phenol concentration was measured based on standard method [14]. The direct method photometry (that part of the book is given 5530D). Firstly, 5 mL of sample picked up and reached to 100 mL of volume with DI- water and 2.5 mL ammonium hydroxide added and pH of solution was reached to 7.9 ± 0.1 with phosphate buffer. Then, 4 mL amino anti-Pyridin -added and well stirred, also, 1 mL potassium Ferro cyanide was added to solution. Similarly these steps were conducted for control sample. Adding the Ferro cyanide reagent to sample leads to create the yellow to dark red hat is depending on the concentration of phenol in the solution. Then, the absorption value was measured after 15 min at 500 nm with spectrophotometer (model UV-1650-Shimadzu. Japan). Moreover, standard curve was prepared in 5 concentrations of phenol 1, 2, 3, 4, and 5 mg/L [15]. The multiple regression analysis method were used to determine the effect of pH, contact time, ZnO dosage, initial

concentration of phenol and UV variables on efficiency removal of phenol.

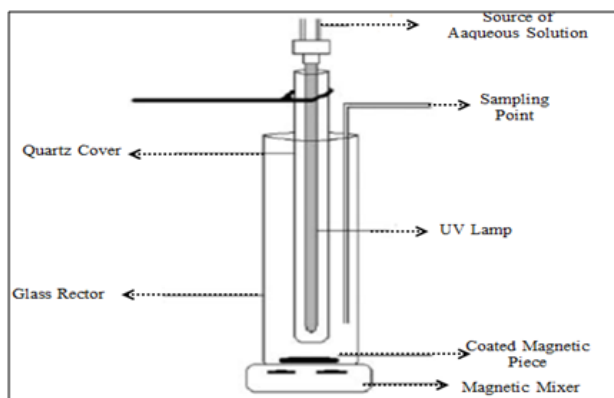


Fig. 1. Schematic of photocatalytic reactor.

RESULTS AND DISCUSSION

Effect of pH

The effect of pH on phenol removal was studied in nano-photocatalytic process (UV/ZnO). Results indicated that pH is an important variable in this process, and plays important role in acid-base balance in that affected on material concentration of degraded or not degraded compounds. Result indicated that with increasing of pH, the phenol removal was decreased (Fig. 2). This revealed that pH has negative effect on nano-photocatalytic process (UV/ZnO). So that the trend of phenol removal was as fallow acidic >neutral > basic condition.

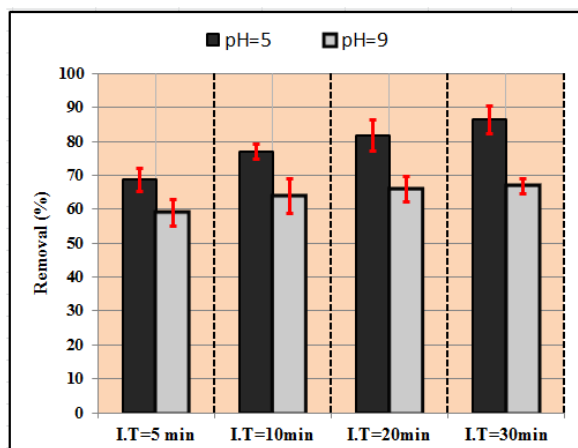


Fig. 2. The phenol removal in the presence of UV (W 125) in the both acidic and basic pH, $C_0=15$ mg/L.

The most phenol degradation in acidic condition can attributed to the presence of proton (H^+) that leads to formation of H^0 radicals [5, 16]. Beside the above reason, the positive charge of ZnO in acidic condition can increased the phenol degradation, however, there are not evidence document about positive charge of ZnO in acidic condition [17, 18].

Therefore, the electrostatic attraction between positive charges of ZnO and phenoxic anions caused the more removal of phenol in acidic condition. The results of Kashif et al. [19] and Akbal et al [20] correspond with our study.

Effect of ZnO dosage

Results showed the use of nanoparticles leads to the increasing removal efficiency of phenol due to the increasing concentration of generated radicals. Also, the number of photons absorbed will also increase [19], Resulting the availability and accessibility of active sites has also increased that leads to increasing of the adsorbed phenol molecules [19, 21].

Fig. 3 showed with constant the other conditions (phenol concentration and pH), increased the nanoparticle dosage at 0.15 to 0.3 g/L caused the decrease of kinetic reaction. Because catalyst makes reducing the UV penetration in solution and increased dispersion of irradiation on nanoparticles surfaces, therefore, leads to reduce the amount of nanoparticles activated by photon [17, 19, 21, 22]. Similarly, Guo et al. reported this result [16]. So, 0.15 g/L dosage of ZnO was determined as the optimum value for the experiments.

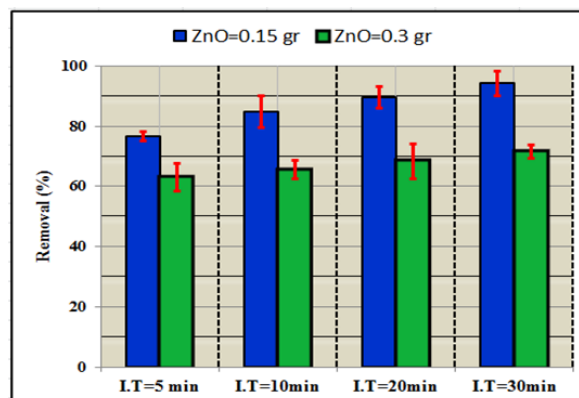


Fig.3. The percentage removal of phenol at various ZnO dosage in UV/ZnO process: pH=5, $C_0=15$ mg/L.

Effect of initial concentration of phenol

Results showed efficiency removal of phenol was decreased with increased of initial concentration (Fig.4), so that in constant condition (nanoparticle dosage and pH), the kinetic reaction was decreased with increasing of phenol concentration from 10 to 90 mg/L. The percentage removal of phenol at acidic pH (pH =5), the nanoparticle 0.15 g/L and 30 minutes obtained 94.24%, while, 74 and 45.88% removal obtained at 40 and 90 mg/L concentration respectively. This can due to the concentration of radicals produced in all the solutions are same, so at low concentration of phenol with the same amount of

hydroxyl radical, the degradation value will be more than high phenol concentration.

Another possible reason, production the more reactive intermediate of phenol that reacts with free present radicals. Considering the competition between phenol and intermediate products, by increasing the initial concentration of phenol and increase the accumulation and concentration of intermediate products on one hand and reducing the amount of phenol concentration in the solution, so leads to significant amount of radical formation used to intermediate products degradation. In this regard, the study of Malaki et al [5] also revealed that phenol degradation rate decreases with increasing initial concentration because it would produce more reactive intermediate products of phenol which react with free present radicals [5]. The study of Sobczyński&Duczmal [22] showed that the degradation rate decreased at the high concentration of phenol, and attributed to made polymeric compounds such as biphenol that are insoluble in water and may stick on the catalyst surface and caused reduce photocatalytic performance in high concentrations of phenol. Kashif & Ouyang proposed that the UV absorption of phenol is more than catalyst, therefore, the absorbed photon hasn't effect for degradation [19].

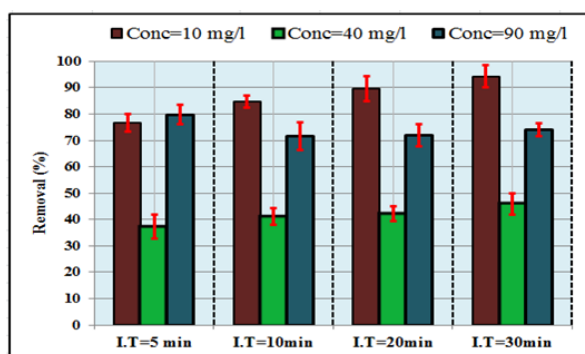


Fig. 4. The effect of initial concentration of phenol on its removal trend in UV/ZnO process: pH=5, ZnO=0.15 g/L.

Effect of irradiation time

The irradiation effect was studied at 4 times (5, 10, 20 and 30 minutes). Results indicated efficiency removal of phenol was increased with increasing of irradiation time. So that the maximum removal obtained at 30 min. (Fig. 2, 3 and 4) [23].

CONCLUSION

Results revealed that the phenol degradation rate increased in the nano-photocatalytic UV / ZnO process. Many factors affect edoxidation rate

including pH, initial concentration of phenol, irradiation time and ZnO dosage. The efficiency removal of phenol increased with increasing of radiation time and efficiency decreased with increasing of pH, ZnO dosage and initial concentration.

Acknowledgement: The authors acknowledge all non-financial supports provided by Tehran University of Medical Sciences and Kermanshah University of Medical Sciences. The authors declare that there is no conflict of interest.

REFERENCES

1. W. Kujawski, A. Warszawski, W. Ratajczak, T. Porebski, W. Capała, I. Ostrowska, *Desalination*, **163**(1), 287(2004)
2. K. Sharafi, K. Karimi, H. Arfainia, R. Rezaie Kalantari, Z. Hosienie, H. Sharafi, M. Moradi, *The Int. Res. J. Appl. Basic Sci.*, **9**, 1789(2015).
3. V. C. Srivastava, M. M. Swamy, I. D. Mall, B. Prasad, I. M. Mishra, *Colloids and Surfaces A: Physicochemical and Engineering Aspects*, **272**, 89(2006).
4. D. N. Jadhav, A. K. Vanjara, *Ind. J. Chem. Technol.*, **11**, 35(2004).
5. M. Moradi, A. M. Mansouri, N. Azizi, J. Amini, K. Karimi, K. Sharafi, *Desalination & Water Treatment*, **57**(11), 1(2015).
6. M. Moyo, E. Mutare, F. Chigondo, B. C. Nyamunda, *Int J Res Rev Appl Sci.*, **11**, 486 (2012).
7. J. Bevilacqua, M. Cammarota, D. Freire, Jr. S. Anna, *Braz. J. Chem. Eng.*, **19**, 151 (2002).
8. L. D. Claxton, V. S. Houk, T. J. Hughes, *Mutation Research/Reviews in Mutation Research*, **410**, 237(1998)
9. W. Hoeben, E. Van Veldhuizen, W. Rutgers, C. Cramers, G. Kroesen, *Plasma Sources Sci. Technol.*, **9**, 361 (2000).
10. M. A. Berry, D. A. Rondinelli, *The Academy of Management Executive*, **12**, 38(1998).
11. T. A. Özbelge, Ö. H. Özbelge, S. Z. Başkaya, *Chem. Eng. Process.: Process Intensification*, **41**, 719(2002).
12. A. Rahmani, M. A. Enayati, *J. Water Wastewater*, **17**(2), 32(2006).
13. X. Hu, T. An, M. Zhang, G. Sheng, J. Fu, *Research J. Chem. Environ.*, **11**, 13 (2007).
14. K. Slinkard, V. L. Singleton, *Am. J. Enol. Viticulture*, **28**, 49(1977).
15. Y. J. Xing, Z. H. Xi, X. D. Zhang, J. H. Song, R. M. Wang, J. Xu, Z. Q. Xue, D. P. Yu, *Solid State Commun.*, **129**, 671(2004).
16. Z. Guo, R. Ma, G. Li, *Chem. Eng. J.*, **119**, 55 (2006).
17. K. Byrappa, A. Subramani, S. Ananda, K. L. Rai, R. Dinesh, M. Yoshimura, *Bulletin of Materials Science*, **29**(5), 433 (2006).
18. Y. Paz, *Comptes Rendus Chimie*, **9**(5), 774 (2006).
19. N. Kashif, F. Ouyang, *Journal of Environmental Sciences*, **21**(4), 527 (2009).
20. F. Akbal, A. N. Onar, *Environmental monitoring and assessment*, **83**(3), 295 (2003).

21. A. Mahvi, M. Ghanbarian, S. Nasser, A. Khairi, *Desalination*, **239**(1), 309 (2009).
22. A. Sobczyński, Ł. Duczmal, *Reaction Kinetics and Catalysis Letters*, **82**(2), 213 (2004).
23. R. Shokouhi, L. Ebrahimzadeh, A.R. Rahmani, S. Ebrahimi, M.R. Samarghandi, *Journal of Water and Wastewater*, **20**(4),30(2010).

Influence of CaCO₃ micro- and nano-particles on the structure and properties of Nylon-66

Aboutaleb Ghadami, Jadval Ghadam

Faculty of Engineering, Departments of Chemical & Petroleum Engineering, Yasouj Branch, Islamic Azad University, Yasouj, I.R. IRAN

Received June 26, 2015; Revised September 10, 2015

Polyamide-66 (PA66)/CaCO₃ micro- and nano-composites were successfully prepared by polymer solution method. The material was characterized by XRD, SEM, FTIR, UV-VIS, DSC, Viscometry technique and UTM. The XRD results of composites have suggested that the α -crystalline form is thermodynamically more stable and has a higher modulus than the γ -crystalline forms. Uniform dispersion of particles in polymer was shown through SEM. The results showed that incorporation of CaCO₃ particles increased the modulus and tensile strength of neat PA66 however decreased its elongation at yield and break. Nanosized CaCO₃ was superior to micro-sized CaCO₃ in that it caused higher modulus and strength.

Keywords: Polyamide-66, CaCO₃ nanoparticles, nano-composites, optical properties, thermal properties, mechanical properties.

INTRODUCTION

Polymer composites represent an important class of engineering materials. Although, polymers possess less stability and low module in comparison to metals and ceramics, one of the best ways for modification of their mechanical characteristics is the use of fillers [1, 2]. The incorporation of inorganic fillers into thermoplastics has been widely practiced in industry to extend them and to improve certain properties. Fillers have been used extensively in the past many years to improve properties of polymeric materials. Besides the increment obtained in stiffness, hardness, abrasion resistance, and reduced cost, addition of filler to the polymer also modifies their flow behaviour and consequently its process-ability [3, 4]. One of the most important mineral fillers occupying an important role as particle reinforcing agent in the thermoplastics industry is Calcium Carbonate (CaCO₃) [5]. In fact, CaCO₃ in most cases is cheaper than other fillers like talc and therefore takes an overwhelming proportion of the filler market in plastics [6]. The production of composites by various methods has become a usual affair since last few years [7]. Nano-composites are a relatively new class of materials with ultrafine phase dimensions, typically of the order of a few nanometres. The objectives for preparation of enhanced performance nano-materials are to obtain

a homogeneous distribution of the nano-particles within the polymer matrix, and to promote a strong interfacial adhesion between the matrix and the nano-filler. Uniform dispersion of the nanometre particles offers a major specific surface area enhancement, compared to conventional reinforcements of micrometre size. As a result, addition of small amount of filler, compared to conventional composites, can induce dramatic changes in host matrix properties [8]. While micron-sized fillers were historically used to lower the cost of relatively expensive polymer resins [9], it is well-understood that incorporation of surface modified inorganic nano-scale fillers (1–100 nm) within a polymer matrix enhances the properties of the polymer dramatically, and the phenomenon has been described as the “nano-effect” [10]. As a consequence, the nano-composite properties are strongly influenced by the nature of the interface between inorganic and polymer matrices. A strong interfacial interaction between the inorganic nano-particles and the polymer matrix can give rise to some unusual properties in these materials [11]. In recent years, demands have increased in using polyamide (PA) to replace certain metals and thermosets in the automotive vehicle and power train systems, and lawn or garden tools with addition of different fillers like fibres, talc and CaCO₃ [12]. Nylon is one of the first commercialized polymers and polyamide-66 having the distinction of highest production [13]. Polyamide-66 (PA66) is a semi-crystalline material that has a combination of strength, flexibility,

To whom all correspondence should be sent:
E-mail: aghadami80@gmail.com; ghadami@iauyasooj.ac.ir

toughness, and abrasion resistance. It is also known for its dye-ability, low coefficient of friction (self-lubricating), low creep, and resistance to solvents, oils, bases, fungi, and body fluids. The applications of polyamide-66 range from textile fibers, membranes, tapes, food packaging to electronics, medical and automotive parts [14].

In this study, the micro-particles (procured in the lab) and nano-particles of CaCO₃ (synthesized using microemulsion method) were used as filler to prepare polyamide-66/CaCO₃ micro- and nano-composites through polymer solution method. The characteristics and properties of the two composites (micro- and nano-) have been compared. The structural and morphological properties of composites were characterized by XRD and SEM. The optical properties of the sample was investigated by FTIR and UV-VIS spectrophotometer. Thermal properties of composites were studied using DSC. The viscosity average molecular weights of polyamide-66 and its micro- and nano-composites were determined using an Ubbelohde viscometer. Universal Testing Machine (UTM) was used to measure mechanical properties (tensile tests) of composites at room temperature according to ASTM-D882.

EXPERIMENTAL

Materials

CaCO₃ nano-particles with an average size of 33 nm were synthesized via microemulsion route [15]. Micro-CaCO₃ (Merck Company, Germany) particles, procured in the lab with an average size of 2 μm, Dimethyl Sulfoxide (DMSO), 99%, and formic acid (90%) were supplied by Merck Company, Germany. Injection moulding grade polyamide-66 from SRF Limited, India was used to produce micro- and nano-composites.

Synthesis of micro- and nano-composites

Polymer solution method was used for the synthesis of micro- and nano-composites. Effect of the quantity of micro- and nano-particles of CaCO₃ on the synthesized composites was studied for 0, 1, 2 and 3 wt.%. In the following paragraph, the preparation method of polyamide-66/CaCO₃ composites is explained.

Polyamide-66 (PA66), micro- and nano-calcium carbonate particles were first heated in a vacuum oven for 12 hrs at 100°C until any possible residual moisture was removed. Then, polyamide-66 was dissolved in DMSO until a homogeneous solution was obtained. Different amounts of CaCO₃ particles were carefully added to this PA66 solution

under vigorous stirring with a magnetic stirrer bar at room temperature (27°C). The stirring was carried out for 24 hrs under ambient condition of 27°C to get the feed proportion of 1, 2, and 3 wt.% of nano-sized CaCO₃ based on the amount of PA66. Subsequently, the resulting solution was poured onto clean glass plates with side tapes around the glass plates (acting as thin trays) and dried until tack-free in a low-humidity chamber at room temperature. Then, the resultant films were vacuum dried for 24 hrs at 60°C until all the solvent was removed by evaporation delivering polymer nano-composite. All films were prepared for the same time and ambient conditions. Pure PA66 films were prepared in the same manner which also showed opaqueness and milk-white color upon drying of solvent. Conventional composite films were also prepared in the same procedure containing 1, 2, and 3 wt.% of micro-sized CaCO₃.

Filler dispersion analysis

The synthesized nano-calcium carbonate powders [15] were dispersed in isopropyl alcohol (IPA) and placed in an ultrasonic bath to ensure fine dispersion. Two to three drops were then placed on a filter paper and the CaCO₃ nano-particles were observed under a Transmission Electron Microscope, TEM, (JEOL JEM-2100F, Japan) at 120 KV. The average primary particle size of the nano-particles was then determined from the TEM photomicrograph. The phase morphology of the nylon-66/calcium carbonate nano-composites was examined using a Scanning Electron Microscope (SEM) that is expressed in the next section.

Characterization of the synthesized composites

X-ray diffraction (XRD) Analysis: the influence of micro- and nano-CaCO₃ particles on the crystal structure of polyamide-66 was studied using a Rigaku X-ray Powder Diffractometer with Cu anode (Cu K α radiation, $\lambda=1.54186 \text{ \AA}$) in the range of $5^\circ \leq 2\theta \leq 30^\circ$ and at 30 kV and at a scanning rate of 4°/min.

Scanning Electron Microscopy (SEM) Analysis: Scanning Electron Microscope (SEM-EDS, Carl Zeiss: EVO40) at 20 kV was used to characterize the dispersion and agglomeration of micro- and nano-CaCO₃ particles inside the polyamide-66 matrix. The samples were sputter-coated (Sputter Coater: POLARON-SC7640) with a thin layer (10–20 nm) of gold palladium. The coating was carried out by placing the specimen in a high vacuum evaporator and vaporizing the metal held in a heated tungsten basket. In addition, energy-

dispersive X-ray spectroscopy (EDS) was also used to reveal the relative quantities of the different elements present in the compounds.

Fourier Transform Infrared Spectroscopy (FTIR) Analysis: FTIR spectroscopy is used for the identification of polymers and additives, study of coupling effects, conformational studies, crystallinity and end group analysis. FT-IR spectra were recorded with an Interspec-2020 (SPECTROLAB, UK) Spectrophotometer using KBr pellets in order to make small tablets; the analyses were conducted between 400 a 4000 cm⁻¹.

Optical Absorption Analysis: a direct and simple method for probing the band structure of composite materials is to measure the absorption spectrum. The optical absorbance A(v) spectra for the composites were measured using a Ultraviolet-Visible (UV-VIS) Double Beam Spectrophotometer (Perkin Elmer Precisely: Lambda-35) at room temperature in the wavelength range 200-800 nm. The absorption coefficient α(v) was calculated from the absorbance A(v). After correction for reflection, α(v) was calculated using the relation (equation-1):

$$I = I_0 \exp(-\alpha x), \quad (1)$$

Hence,

$$\alpha(v) = \frac{2.303}{x} \log\left(\frac{I_0}{I}\right) = \frac{2.303}{x} A(v), \quad (2)$$

Where, I₀ and I are the incident and transmitted intensity, and x is the thickness of the cuvette. The relationship between fundamental absorption and optical energy gap is given by equation-3:

$$E_{opt} = \frac{hc}{\lambda}, \quad (3)$$

Here, c is the velocity of light. At high absorption coefficient levels for non-crystalline materials, it can be related to the energy of the incident photon by the following relation, equation-4:

$$\alpha(v) = \beta(h\nu - E_{opt})^n, \quad (4)$$

Where, β is a constant and the exponent, n can assume values of 0.5, 1, 2, 3, and 3/2. For allowed indirect transition, the exponent takes the values 1, 2, and 3 [16]. At low absorption levels (in the range of 1–10⁻⁴ cm⁻¹), the absorption coefficient α(v) is described by the Urbach formula [17], equation-5:

$$\alpha(v) = \alpha_0 \exp\left(\frac{h\nu}{E_U}\right), \quad (5)$$

Where α₀ is a constant and E_U is an energy term which is interpreted as the width of the tail of localized state of the mobility gap (forbidden band).

Differential Scanning Calorimetry (DSC): The degree of crystallinity of polyamide-66 and its micro- and nano-composites were determined using

a Thermal Analysis Apparatus (DSC-60 Shimadzu, Japan). The heating scans were recorded in the temperature range 20-300°C at a heating rate of 10°C/min under nitrogen atmosphere. The degree of crystallinity (X_c) of polyamide-66 and its composites was calculated from the heat of fusion (ΔH_m) of the specimen using equation-6:

$$X_c = \frac{\Delta H_m}{\Delta H_m^0(1-W_f)} \times 100 \quad (6)$$

Where W_f is the weight fraction of filler and ΔH_m⁰ is the heat of fusion for virgin (100% pure) crystalline PA66 and its value is reported to be 196 J.g⁻¹ [13].

Determination of Molecular Weight: The viscosity average molecular weights of sample were determined using an Ubbelohde viscometer. Relative viscosity (defined as the ratio of the viscosity of a polymer solution to that of the solvent) was calculated by the ratio of torque values. Intrinsic viscosity was calculated from relative viscosities, equations 7, 8 & 9 [18].

$$\eta_{specific} = \eta_{relative}^{-1}, \quad (7)$$

$$\eta_{reduced} = \frac{\eta_{specific}}{C}, \quad (8)$$

$$\eta_{intinsic} = \lim(\eta_{reduced})^c \rightarrow 0, \quad (9)$$

The intrinsic viscosity [η], dl/g, was measured in formic acid at 25°C and the viscometric average molecular weight (M_v), g/mol, was calculated from the intrinsic viscosity using the Mark–Houwink relation, a relation between viscosity and molecular weight given by equation 10.

$$[\eta] = KM_v^\alpha, \quad (10)$$

Where K and α are constants relating to structure of the solvent, and M_v is the viscosity average molecular weight. The constants K and α used for the polyamide-66/formic acid system at 25°C are 35.3 × 10⁻⁵ dl/g and 0.786, respectively [19].

Mechanical Properties (Tensile Tests): Tensile strength, Young's modulus and percent elongation at yield and break were measured at room temperature according to ASTM-D882 [20] on Zwick 1445 Universal Testing Machine (UTM). The test specimen (film) dimension was 7×0.8×0.09 cm³ (Length × Width × Thickness). For each composite type, seven specimens were used and the average value of three replicated tests was taken for each composition. Subsequently, the mean values and their standard deviations were calculated. The test specimen gauge length was 5.1

cm and crosshead speed for the film testing was 0.10 cm/min.

RESULTS AND DISCUSSION

The used micro- and nano-particles in the Nylon-66 matrix

Fig. 1 shows the TEM photomicrograph of the nano-filler used in this study. The average primary particle size the stearic acid coated nano-CaCO₃ filler was measured to be about 33 nm. This image reveals that most of the coated CaCO₃ nano-particles are quasi-spherical and have rough surface. The nano-particles have a strong tendency to form agglomerates due to their high surface energy which is a result of the small particle size [15].

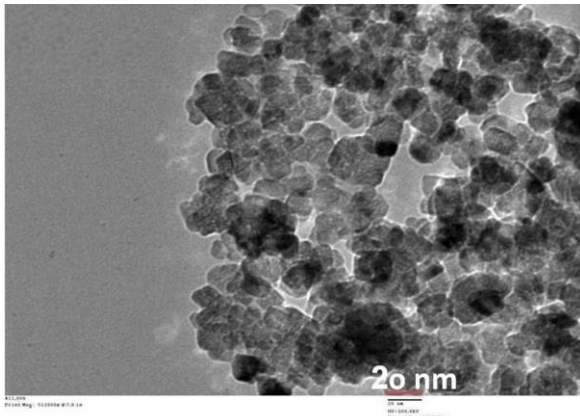


Fig. 1. TEM photomicrograph of the nano-CaCO₃ particles used in this study [15].

XRD analysis

Polyamide-66 (PA66) is a polycrystalline polymer in which triclinic α -crystalline and pseudo-hexagonal γ -crystalline are the most important phases. The triclinic α -phase structure at room temperature transforms into γ -phase structure at elevated temperatures [21]. Liu, et al. (2007) have reported that even though, the stable crystalline form of PA66 at room temperature is in the α -crystalline, γ -crystalline forms can also co-exist along with the α -crystalline form depending on processing conditions [22]. XRD measurements were used to investigate the influence of CaCO₃ particles on the crystal structure of polyamide-66. The XRD patterns of PA66 and PA66/CaCO₃ micro- and nano-composites are shown in Fig. 2.

It is well documented that the crystalline structure of a semi-crystalline thermoplastic has significant effect on the thermal and mechanical properties. Furthermore, XRD results of composites have suggested that CaCO₃ particles are found in the amorphous phase of the semi-crystalline thermoplastic. It has been found that the α -

crystalline form is thermodynamically more stable than the γ -crystalline forms at room temperature [22, 23]. As shown in **Fig. 2**, the XRD pattern of neat PA66 (PA66 with 0 wt.% CaCO₃) displays two strong diffraction peaks at $2\theta=19.232$ and 23.280° corresponding to the (100) and (010) (110) doublet of the α -crystalline structure. Furthermore, a small peak at 12.634° is associated with the (002) plane of the γ -crystalline structure. It can be seen from **Fig. 2** that with increasing the content of CaCO₃ particles within polyamide-66 matrix, the γ crystalline form tends to disappear. Thus, it may be said that calcium carbonate particles form a PA66 crystal thermodynamically more stable with the reduction of the metastable γ crystalline phase within the polymeric matrix and forming only an α crystalline structure. The d-spacing between the planes in the atomic lattice was calculated using Bragg's law [24, 25]:

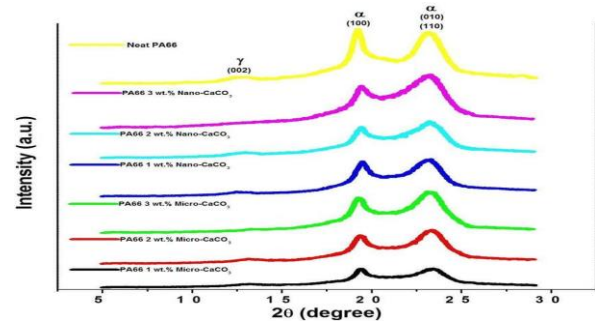


Fig. 2. XRD patterns of neat PA66 and PA66/micro- and nano-CaCO₃ composites: 1, 2 and 3 wt. % CaCO₃ micro- and nano-particles.

It has been obtained that the presence of CaCO₃ particles does not influence the d-spacing of the α - and γ -crystalline forms of polyamide-66. The d-spacings of α (100), α (010) (110) and γ (002) for all nano-composites are 0.46, 0.38 and 0.69 nm, respectively. This may be interpreted as follows: each set of miller planes with a unique d-spacing can give rise to a distinct diffraction peak in the x-ray diffraction pattern. When two or more sets of miller planes have the same d-spacing, the diffraction peaks fall at the same position (angle) in the diffraction pattern. This point is supported by Yasmin and Daniel, 2004 [26]. Thus, the non-variation of the d-spacings of the α -crystalline forms demonstrates that CaCO₃ particles may be found in the free volume of PA66. The incorporation of surface modified CaCO₃ filler in the polymer chains causes the increase of the amorphous region and the particles can have larger surface area in contact with the polymer, especially the nano-particles that have very small size scale and immense surface area per unit volume. This

means that there are more sites available for filler–filler and matrix–filler interactions and adhesions.

Scanning electron microscopy (SEM) analysis

The dispersion of the particles inside the bulk PA66 was investigated using SEM. It is known that the dispersion of filler in the polymer matrix can have significant effect on the mechanical properties of the composites. However, the dispersion of inorganic filler in a thermoplastic is not an easy process. The process becomes more intricate when nano-particles are used as filler, because they have strong tendency to agglomerate. It is reported that a good dispersion can be achieved by surface modification of the filler particles [27]. It is pertinent to state that in this study, it was tried to take those images of samples through SEM that show the cavities on the surface of the polymer. The aggregation of polyamide-66 particles seen in these images is attributed to the size of applied magnifications. Referring to the figure cited in the inset, Fig. 3(b), the normal situation of the presence of the micro-particles in the polymer chains may be observed through different resolution (resolution of 5µm). Fig. 3(a) shows the SEM micrograph of neat PA66. The uniform dispersion of 1, 2, and 3 wt. % surface modified micro- and nano-CaCO₃ within PA66 are evidenced from SEM images as shown in Figs. 3(b)-(g). The Energy dispersive spectrometer (EDS) analysis, Fig. 3(h), shows the presence of CaCO₃ particles in the polymer composites. The weight percentage of constituents of polymer composites may also be found. Figs. 3(d) and (g) indicate the SEM micrograph of well-distributed 3 wt.% of surface modified micro- and nano-CaCO₃ particles within PA66, respectively. A similar degree of the CaCO₃ distribution is also observed for lower weight fraction of CaCO₃ (e.g., 1 and 2 wt. %).

It is clearly noticed from these figures that both types of surface modified, micro- and nano-particles are covered to the PA66 matrix. Moreover, nano-fillers appear homogeneously dispersed into polymer. Referring to Fig. 3(a), cavities can be found on the surface of the neat PA66. Some of these cavities which are occupied by micro-CaCO₃ particles are shown in Figs. 3(b) - (d).

Cavitations are also found on the surface of PA66/micro-CaCO₃ composites, as cited in Figs. 3(b)-(d). However, since no cavity is observed on the surface of PA66/nano-CaCO₃ composites, as noticed in Figs. 3(e) - (g), the presence of nano-particles must be more responsible than micro-particles for the cavitations. The figures cited in the inset, Figs. 3(e)-(g), also show uniform dispersion

of CaCO₃ nano-particles in PA66 matrix through different resolution (resolution of 5µm). In the nano-composites containing CaCO₃, Figs. 3(e) - (g), the particles are found better covered to the PA66 matrix and have larger surface area in contact with the polymer matrix compared to micro-CaCO₃ particles. In addition, cavities are present at the interface, suggesting that the coating of CaCO₃ promotes adhesion between the particles and PA66 matrix thus improving the compatibility between the phases.

Fourier transform infrared spectroscopy (FTIR) analysis

FTIR can be used to detect amorphous or crystalline CaCO₃ on PA66 surfaces. FTIR spectra taken for neat PA66, PA66/CaCO₃ micro- and nano-composites are shown in Figs. 4 to 10. The band assignments for PA66 are well documented in the literature [28]. Fourier-transform IR confirmed the chemical structure of the PA66, Fig. 4, showing absorptions for all required chemical groups: N-H stretch at 3305.52 cm⁻¹, C-H stretch at 2865.02-2936.45 cm⁻¹, Amide-I at 1638.76 cm⁻¹, and Amide-II at 1539.55 cm⁻¹. The band at N-H stretching and C=O stretching strongly depend on hydrogen bonding interaction between the PA66 chains, these results are supported by the reported literature [29]. CaCO₃ forms a complex with C-H groups in polyamides and break the hydrogen bonds between PA66 chains, as can be inferred from Figs. 5 to 10. Therefore it is expected to see a shift in the vibrational bands associated with C-H stretching vibration. For instance, the fundamental bands and probable assignments for neat PA66 and PA66/Nano-CaCO₃ composite consisting 3 wt.% CaCO₃ nano-particles are given in Tables 1 and 2 respectively.

Structural changes were observed in the FTIR spectra after the addition of filler in PA66. There were some significant changes observed in the IR absorption of the C-H region at 1478.87 cm⁻¹ (Strongest peak relating to CaCO₃ nano-particles) between the filled and unfilled PA66. Changes in the peaks proved that the addition of filler in the matrix affects the transmittance of that polymer. It means that the interfacial effect would be a dominant factor where there is direct binding of the polymer and the filler. These results are in good agreement with reported results by Basilia, et al. (2007) [30]. The exposed thick PA66 sample has an absorbance peak at 877 cm⁻¹. This peak is due to the absorbance of the CO₃ group and indicates the presence of CaCO₃; this point is supported by Suel, et al. (2004) [31]. If N-H bonds shift to higher

frequency the red shift will be caused by these bonds but in the reverse case the blue shift is caused by them due to the reduction in bond order. The primary motivation for determining the molecular structure of a polymer using FTIR spectroscopy is to relate the structures to the

performance properties of the polymer in end use. If the polymer chains are completely characterized and the structural basis of its properties are known, the polymerization reaction can be optimized and controlled to produce the optimum properties from the particular chemical system [32].

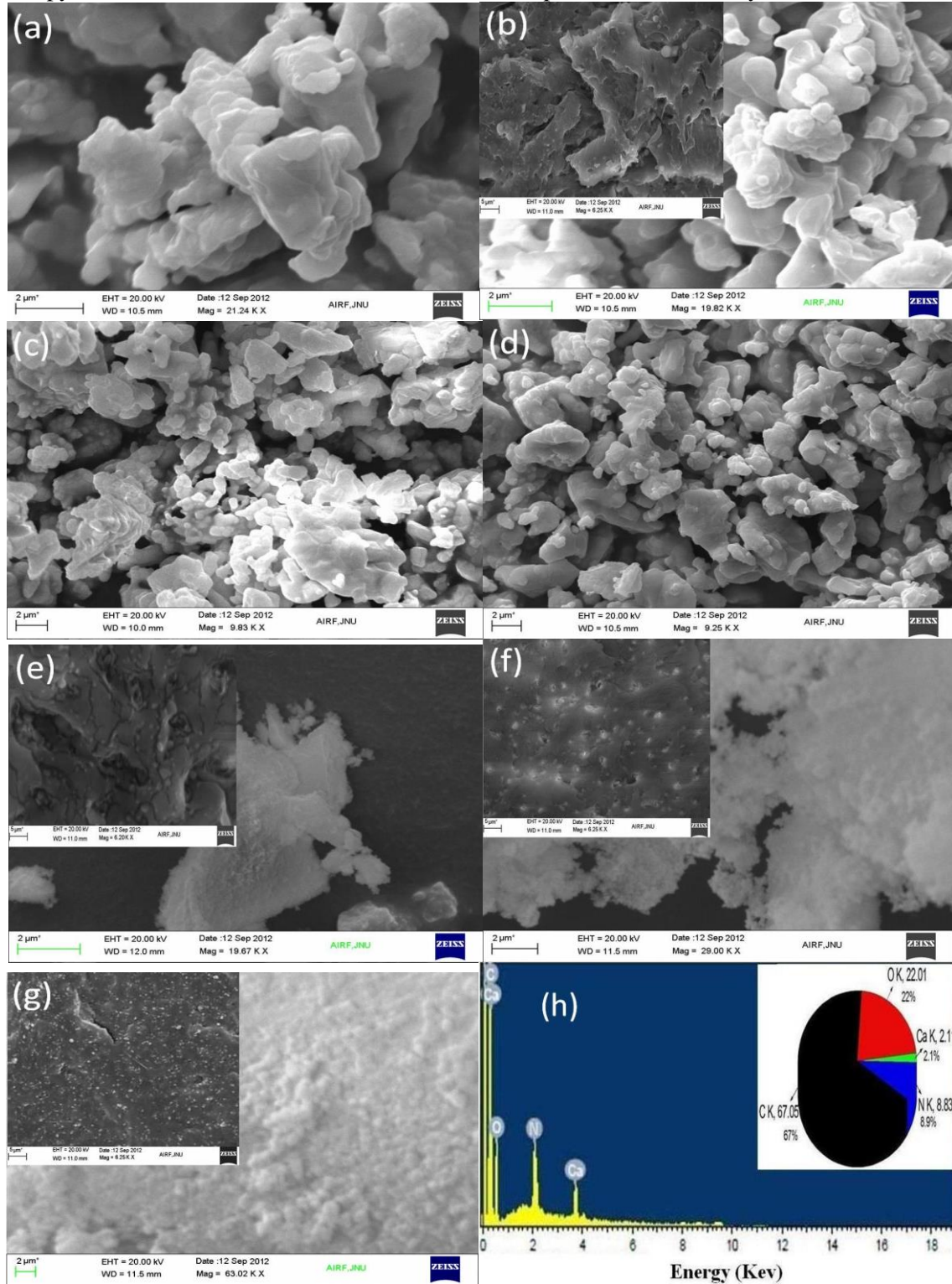


Fig. 3. SEM images of (a): neat polyamide-66 (PA66); PA66/micro- CaCO_3 composite (b): 1 wt. % micro- CaCO_3 (c): 2 wt. % micro- CaCO_3 (d): 3 wt. % micro- CaCO_3 ; PA66/nano- CaCO_3 composite (e): 1 wt. % nano- CaCO_3 (f): 2 wt. % nano- CaCO_3 (g): 3 wt. % nano- CaCO_3 (h): Energy-dispersive x-ray (EDS) spectra of PA66/ CaCO_3 composites; (insets show resolution of 5 μm)

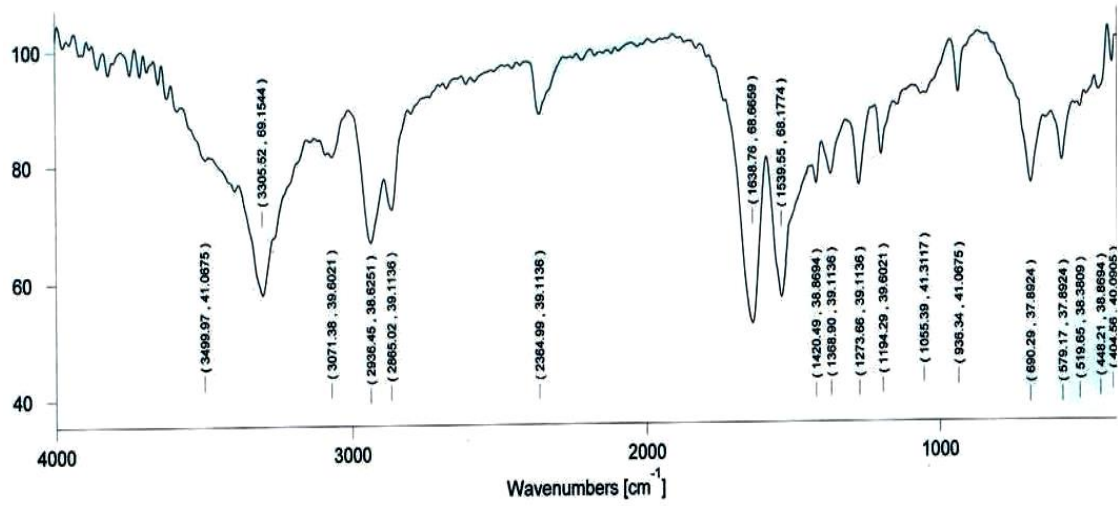


Fig. 4. FT-IR spectrum of neat nylon-66 (PA66).

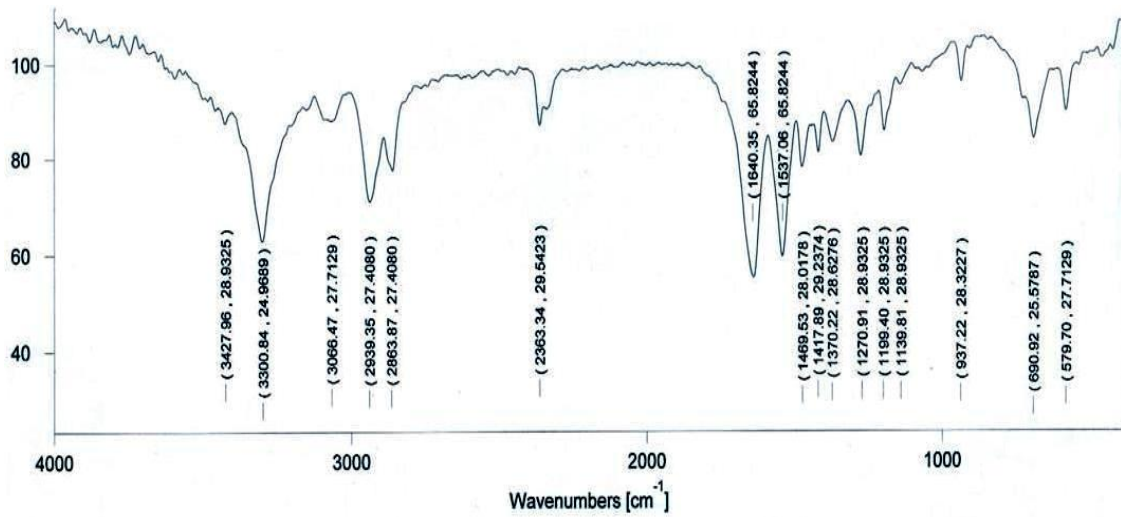


Fig. 5. FT-IR spectrum of PA66/Micro- CaCO_3 composite: 1 wt.% micro- CaCO_3 particles.

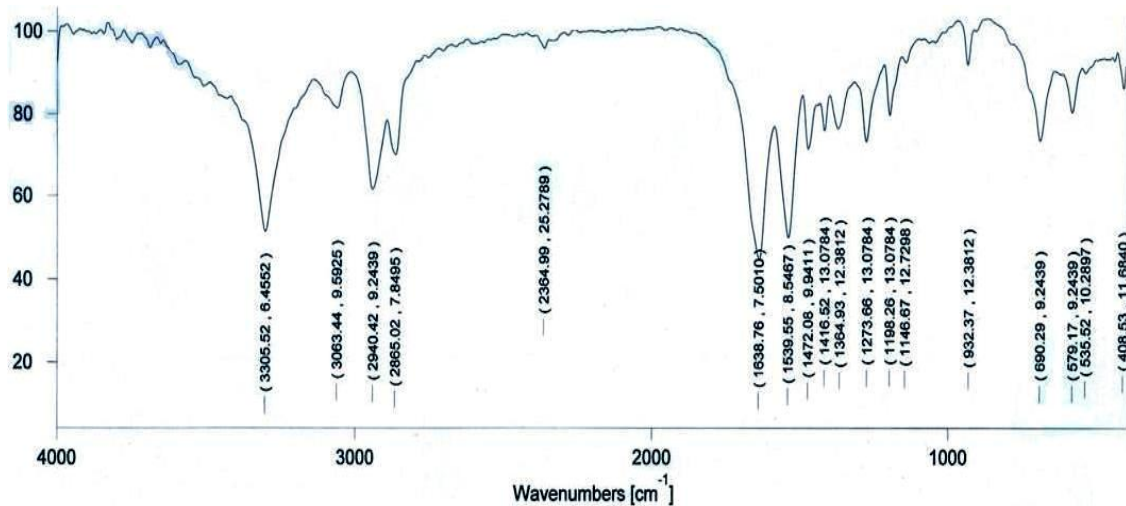


Fig. 6. FT-IR spectrum of PA66/Micro- CaCO_3 composite: 2 wt.% micro- CaCO_3 particles.

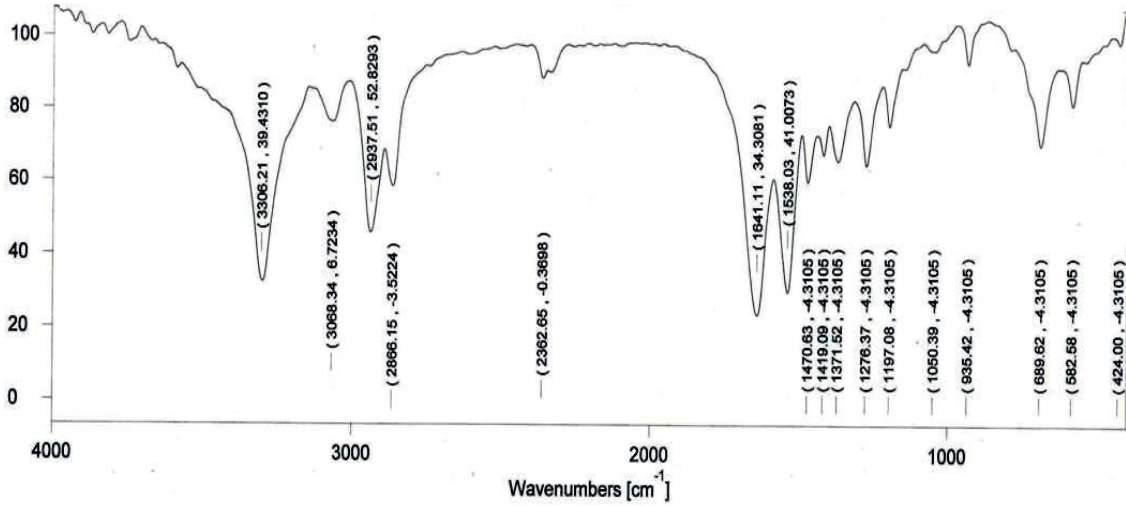


Fig. 7. FT-IR spectrum of PA66/Micro-CaCO₃ composite: 3 wt.% micro-CaCO₃ particles.

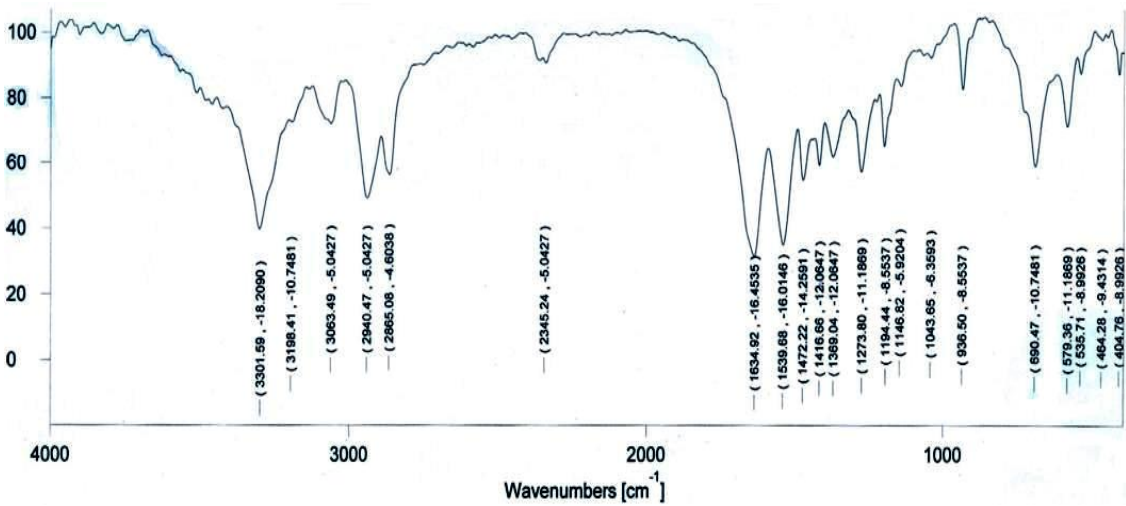


Fig. 8. FT-IR spectrum of PA66/Nano-CaCO₃ composite: 1 wt. % nano-CaCO₃ particles.

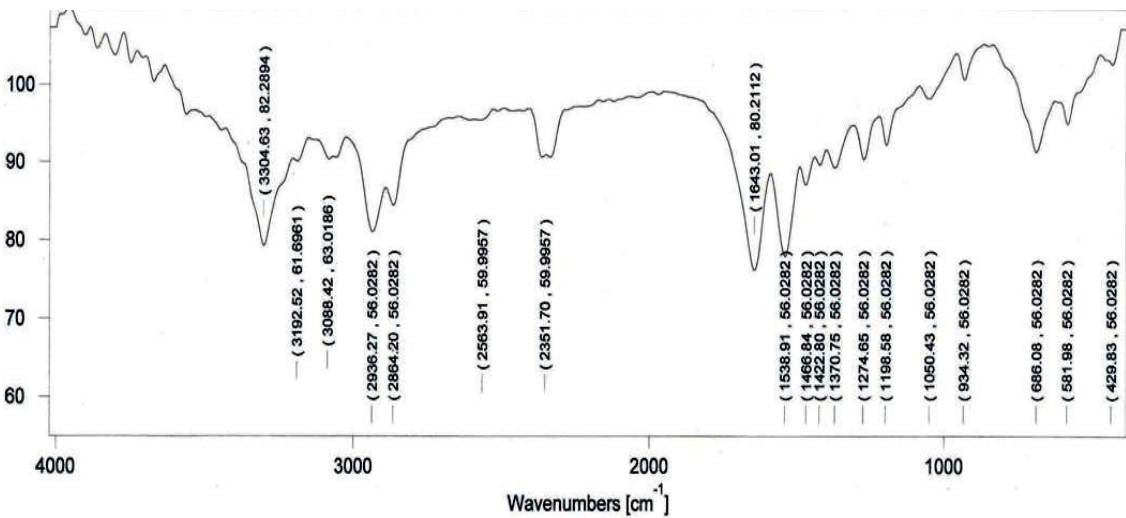


Fig. 9. FT-IR spectrum of PA66/Nano-CaCO₃ composite: 2 wt.% nano-CaCO₃ particles.

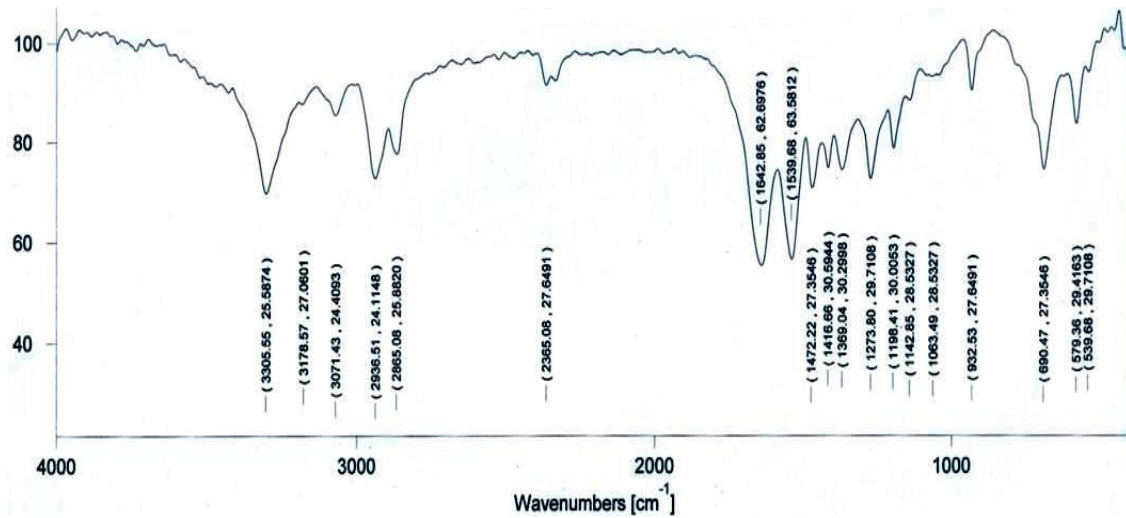


Fig. 10. FT-IR spectrum of PA66/Nano-CaCO₃ composite: 3 wt.% nano-CaCO₃ particles.

Table 1. FT-IR spectra and assignment of PA66.

Wavenumbers (cm ⁻¹)	Assignment
3305.52	N-H stretching
3080.11	C-H asymmetric stretching
3071.38	C-H symmetric stretching
2936.45	CH ₂ asymmetric stretching
2865.02	CH ₂ symmetric stretching
1745.03	C=O stretching
1638.76	Amide I band
1539.55	Amide II band/CH ₂ asymmetric deformation
1420.49	N-H deformation/CH ₂ scissoring
1368.90	Amide III band/CH ₂ wagging
1149.29	CCH symmetric bending/CH ₂ twisting
1128.20	CCH symmetric bending
936.34	C-C stretching
690.29	N-H wagging/CH ₂ rocking
606.23	C-C bending
579.17	O=C-N bending

Table 2. FT-IR spectra and assignment of PA66/CaCO₃ nano-composite: 3 wt. % nano-CaCO₃ particles.

Wavenumbers (cm ⁻¹)	Assignment
3305.55	N-H stretching
3178.57	C-H asymmetric stretching
3091.43	C-H symmetric stretching
2936.51	CH ₂ asymmetric stretching
2865.08	CH ₂ symmetric stretching
1745.23	C=O stretching
1642.85	Amide I band
1539.68	Amide II band/CH ₂ asymmetric deformation
1472.22	N-H deformation/CH ₂ scissoring
1369.04	Amide III band/CH ₂ wagging
1142.85	CCH symmetric bending/CH ₂ twisting
1128.10	CCH symmetric bending
932.53	C-C stretching
690.47	N-H wagging/CH ₂ rocking
606.23	C-C bending
579.36	O=C-N bending

Optical absorption analysis

Optical absorption occurs by transition of electrons and holes between electronic states (bands, tail and gap states) and the energy-band gap is the energy needed to break a bond in the crystal. When a band is broken, the electron has enough energy to leave the valence band and jump to conduction band. The width of the band gap determines the type of material (conductor, semiconductor and insulator). Optical absorption studies on neat PA66 and PA66/CaCO₃ micro- and nano-composites recorded at room temperature and presented in Fig. 11 were carried out to obtain energy-band gaps of the samples.

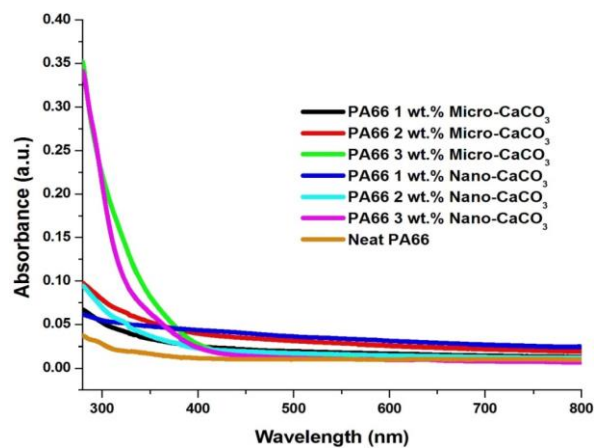


Fig. 11. The optical absorption spectra for neat PA66 and PA66/CaCO₃ micro- and nano-composites.

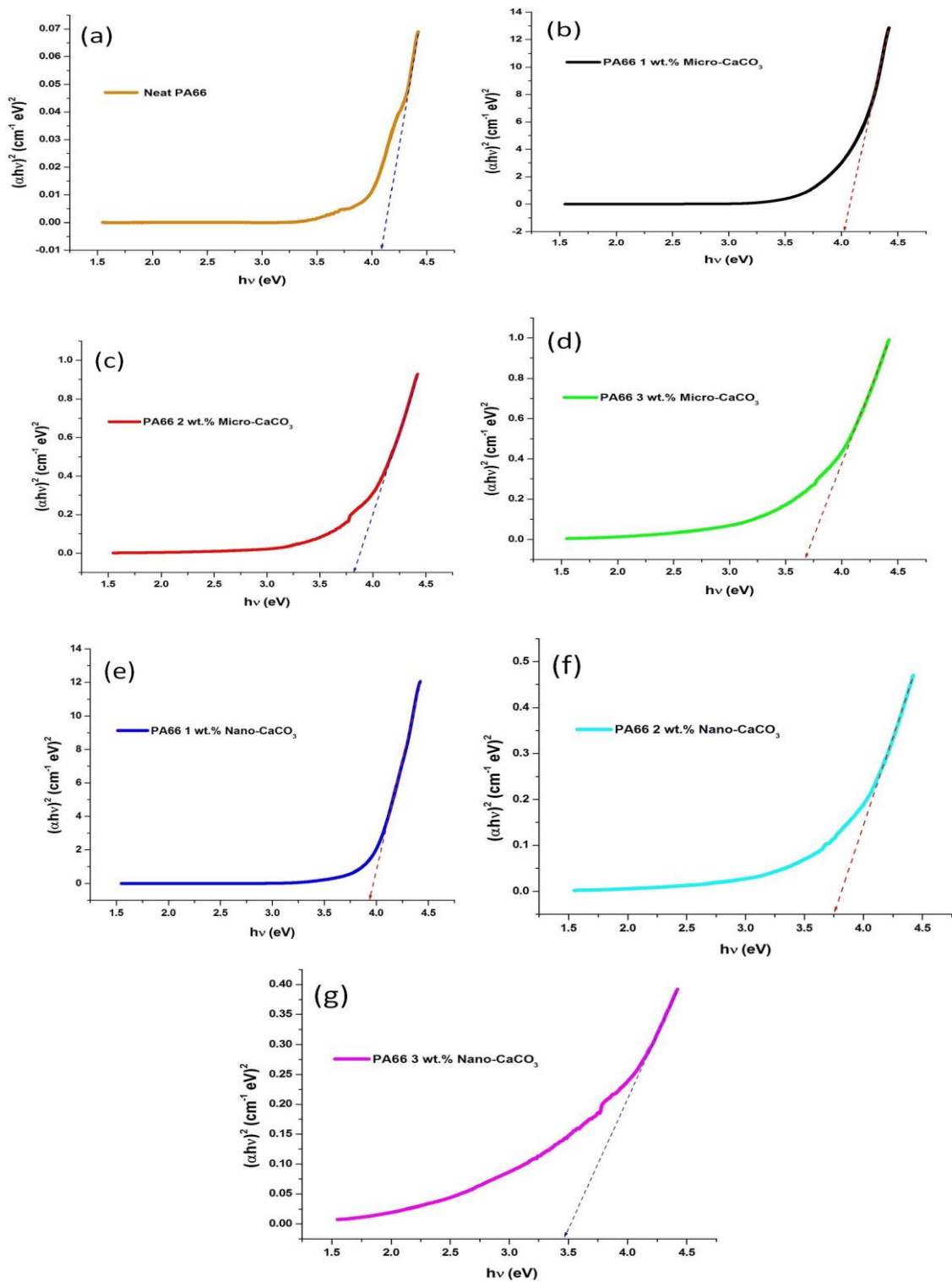


Fig. 12. Evaluations of E_{opt} from optical absorption spectra of (a): neat polyamide-66 (PA66); PA66/micro- CaCO_3 composite (b): 1 wt. % micro- CaCO_3 (c): 2 wt. % micro- CaCO_3 (d): 3 wt. % micro- CaCO_3 ; PA66/nano- CaCO_3 composite (e): 1 wt. % nano- CaCO_3 (f): 2 wt. % nano- CaCO_3 (g): 3 wt. % nano- CaCO_3 .

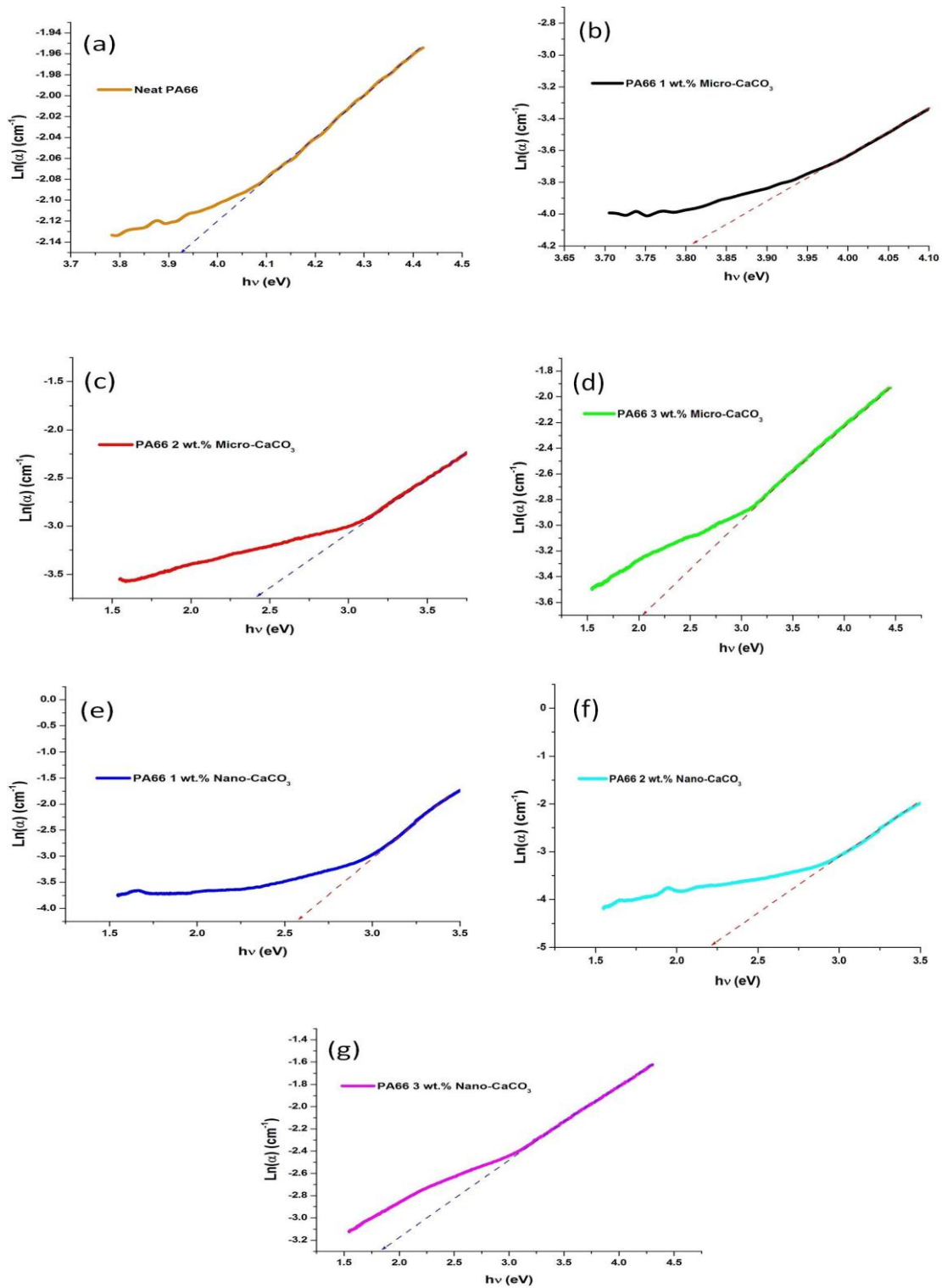


Fig. 13. The linear dependence of $\ln\alpha$ on $h\nu$ and estimation of Urbach's energy for (a): neat polyamide-66 (PA66); PA66/micro- CaCO_3 composite (b): 1 wt. % micro- CaCO_3 (c): 2 wt. % micro- CaCO_3 (d): 3 wt. % micro- CaCO_3 ; PA66/nano- CaCO_3 composite (e): 1 wt. % nano- CaCO_3 (f): 2 wt. % nano- CaCO_3 (g): 3 wt. % nano- CaCO_3 .

Table 3. The estimated optical data of neat PA66 and PA66/CaCO₃ composites.

Material	Wavelength (nm)	Absorbance (arb units)	E_{opt} (eV)	E_U (eV)
Neat PA66	280	0.029	4.10	0.25
PA66/1 wt. % micro CaCO ₃	280	0.067	4.03	0.26
PA66/2 wt. % micro CaCO ₃	280	0.098	3.82	0.41
PA66/3 wt. % micro CaCO ₃	280	0.354	3.68	0.49
PA66/1 wt. % nano CaCO ₃	280	0.061	3.93	0.39
PA66/2 wt. % nano CaCO ₃	280	0.095	3.76	0.45
PA66/3 wt. % nano CaCO ₃	280	0.343	3.47	0.55

Table 4. Summary of DSC heat scan results of neat PA66 and PA66/CaCO₃ micro- and nano-composites.

Sample	Wt. % of loading	T_m (°C)	ΔH_m (J/g)	Crystallinity (%)
Neat PA66	0	262.14	85.14	44.78
PA66/Micro-CaCO ₃ composite	1	260.90	84.05	44.21
	2	254.80	81.46	42.41
	3	246.90	73.13	41.38
PA66/Nano-CaCO ₃ composite	1	259.40	82.59	42.99
	2	247.30	75.47	41.75
	3	242.70	70.77	39.54

It may be deduced from the curves in this figure that the addition of CaCO₃ particles in polyamide-66 increases the absorbance of the composites. In order to evaluate the energy band gaps for the composites, plots of $(\alpha h\nu)^2$ versus photon energy $(h\nu)$ were obtained and are shown in Figs. 12-(a) - (g). The best fit to the absorption spectra were obtained when the value of n used was equal to 0.5, suggesting that the electron transition allowed direct transition for these nano-composite samples. It can be seen that the plots are linear in the region of strong absorption near the fundamental absorption edge. Thus, the absorption takes place through direct transition. The band gap obtained by extrapolating the linear part to zero of the ordinate are also indicated in the figures. This lead to the evaluation of the band gaps, E_{opt} , while slope gives the value of constant β . The factor β depends on the transition probability and can be assumed to be constant within the optical frequency range [33]. Adding CaCO₃ in PA66 matrix may cause the localised states of different colour centres to overlap and extend in the mobility gap. This overlap may give an evidence for decreasing energy gap when adding CaCO₃ in the polymer matrix.

The Urbach formula was used to calculate the width of the Urbach's tail of the localised states due to the defect levels in the transition gap, as suggested by Davis and Mott, 1970 [16]. The Urbach's tail is generally attributed to the disorder in the material that leads to another tail in the valence and conduction bands [34]. It was reported that Urbach's tail is often observed in crystalline and amorphous materials [35]; therefore the Urbach energy (E_U) can be used as a parameter to

determine the optimum growth conditions of these materials. The origin of E_U is considered as thermal vibrations in the lattice, as reported by Zaki, 2008 [33]. The logarithm of the absorption coefficient ($\ln\alpha$) was plotted as a function of the photon energy $(h\nu)$ for composites as presented in Figs. 13-(a) to (g). The reciprocal of the slopes of the curves yields the magnitude of width of the band tail, E_U . The values of energy band gaps, E_{opt} and Urbach's energy, E_U for the pure PA66 and PA66/CaCO₃ composites obtained from the cited figures above are summarised in Table 3. A glance at the data presented in the table reveals that addition of CaCO₃ particles in PA66, results in the decrease of energy-band gaps of the composites; the values being less than that for neat PA66. Highest reduction of energy-band gap was related to PA66/nano-CaCO₃ with 3 wt. % CaCO₃ nanoparticles. It was also observed that the Urbach's tail for pure PA66 is less than that for PA66/CaCO₃ composites. The decrease in the Urbach's energy in case of PA66 may be due to the decrease in the crystalline nature of the polymer.

Differential Scanning Calorimetry (DSC)

The influence of the micro- and nano-CaCO₃ in the composites on the crystallization mechanism of the PA66 matrix was studied through differential scanning calorimetry. DSC studies for neat PA66 and PA66/CaCO₃ micro- and nano-composites upon heating provided the glass transition temperature (T_g), melting temperature (T_m) and degree of crystallinity (X_c) and the endotherms are presented in Fig. 14.

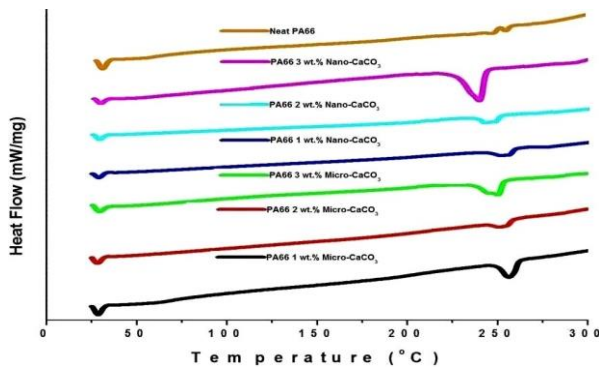


Fig. 14. Composite figure showing DSC melting endotherms during the heating scans of neat PA66 and PA66/micro- and nano-CaCO₃ composites.

The DSC scans of the neat PA66 and PA66/CaCO₃ complexes showed a single relaxation temperature (T_g) at $\square\square 30^\circ\text{C}$. The heat of fusion and melting temperatures obtained from the endotherms are summarised in Table 4. There is an interesting observation in DSC melting endotherm, Fig. 14. Neat PA66 gives two endothermic peaks during the heating ramp, one around 258°C and the other one at 262°C, the first melting peak corresponds to the α -crystalline phase and a small shoulder peak before the main endothermic peak (α -crystalline phase) corresponding to γ -crystalline phase of neat PA66, as noticed by other researchers [36, 37]. This observation is also supported by the XRD analysis of the neat PA66 where both α - and γ -crystalline forms were noticed, Fig. 2 and an explanation given thereof. The percent crystallinity of the PA66 samples was calculated as the ratio of the heat of fusion (ΔH_m) of the sample to the heat of fusion of the pure crystalline at the weight fraction of composite form equation-1. The heat of fusion of pure polyamide is taken as 196 J.g⁻¹ [13]. It can be observed in Table 4 that the crystallinity of pure PA66 is 44.78% and the addition of CaCO₃ causes decrease in crystallinity and these observations are in accordance with the results obtained from the UV-VIS spectrophotometry.

As a result, heat of fusion decreases when inorganic filler was added. It seems that the modified surface of the CaCO₃ filler increases the amorphous region of polymer chains and is in good agreement with the results reported earlier by Basilia, et al., 2007 [30]. However, the DSC data indicate that incorporation of CaCO₃ results in simultaneous decrease of melting point especially at the higher nano-CaCO₃ content. The incorporation of nano-CaCO₃ into polyamide composites shows lower degree of crystallinity than that of micro-CaCO₃ filled polyamide composite. Analytical results for polymer composites obtained independently DSC studies show that incorporation

of CaCO₃ particles in the polymer matrix improves the thermal stability of the micro- and nano-composites, more so for the latter.

Characterization of molecular weight

In a capillary viscometer, the ratio (t/t_0) of the flow time, t of a polymer solution of concentration c to the t_0 of the pure solvent is proportional to the ratio of their viscosity (η/η_0) if temperature is kept constant and the density does not change with polymer concentration in solution [18]. In this study, molecular weights of the pure and synthesised samples were calculated using intrinsic viscosity values which were determined by the solution viscosity method. The experiments for determining the intrinsic viscosity of polyamide-66 were conducted as follows. Polyamide-66 (1 g) was dissolved in formic acid (50 ml) to form a stock solution (2 g/dl). Other samples of varying concentration were prepared by serial dilution of the stock solution. The samples were poured into the viscometer maintained at 25°C. The time taken for the solution to flow between two points (efflux time) on the viscometer was recorded (efflux time was replicated in triplicate to get an average value). The concentration of the polymer solution and the corresponding efflux time was used to calculate various viscosity values. The reduced viscosity (η_{reduced}) values so obtained for each sample were plotted against concentration (c), and the best fit through the data provided the intrinsic viscosity. All the concentrations used in this study were in the range of 1.54 – 2.0 g/dl. Finally, the Mark–Houwink formula was used to determine the viscosity-average molecular weight (M_v) of samples from the intrinsic viscosity measurements, resulting in a $M_v \sim 18,000$ g/mol. Therefore, it may be concluded that the presence of CaCO₃ particles is not able to change the structure and molecular weight of PA66.

Tensile properties of composites

Tensile properties of the seven pieces of each composite sample were examined using Zwick 1445 Universal Testing Machine (UTM). For each piece of all the micro- and nano-composite samples, the stress-strain (σ - ϵ) data was plotted in terms of elongation. For each sample, 2-3 stress-strain (σ - ϵ) curves which had significant differences with the others were rejected and the calculation for the tensile properties was done only on the remaining, and the average results were considered as the property of each sample. The calculated values of the Young's modulus of neat PA66 and PA66/CaCO₃ micro- and nano-composites are

plotted in Fig. 15 showing the effect of content of micro- and nano-sized CaCO₃ particles on the modulus of PA66/CaCO₃ composites. It has been widely accepted that doping of the fillers into polymer matrix would improve the mechanical properties of the resulting composites [38, 39]. The addition of the CaCO₃ leads to improvement in stiffness for both the micro-composites and nano-composites. The results shown in Fig. 15 reveal that the Young's modulus of filled polyamide nano-composites is higher than that of micro-CaCO₃-filled composites. Further, incorporation of CaCO₃ leads to increase in the Young's modulus of polyamide-66 composites in proportion to the increase content of the filler and this observation is attributed to the higher reinforcing effect of nano-particles compared to micro particles. Enhancement of the tensile modulus with increased filler content can be interpreted as follows. In general, adding filler to polymer matrix reduces the mobility of polymer chains which in effect causes more stiffness or higher value of tensile modulus of the polymer composite and also this effect can be raised by increasing the amount of filler.

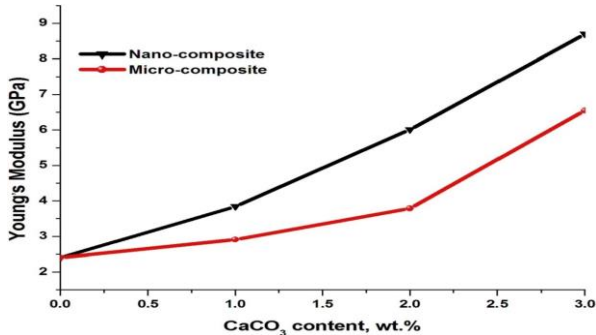


Fig. 15. Effect of filler loading on the Young's modulus of micro- and nano- Polymer composites.

The relationship between weight percentage of filler loading (micro- and nano-CaCO₃) and strength at yield and break for PA66/CaCO₃ micro- and nano-composites are shown in Figs. 16 and 17. The tensile strength of nano-CaCO₃ filled polyamide composites is recorded higher than that of micro-CaCO₃ filled polyamide composites; the highest loading of the filler (in the range studied) shows the highest tensile strengths of composites and nano-fillers provide higher tensile strength compared to micro-CaCO₃. This increment in tensile strength is due to uniform dispersion of nano-filler throughout the matrix. The uniform dispersion of nano-CaCO₃ is confirmed from the SEM images shown in Figs. 3(e)-(g). The reason for higher tensile strength of nano-composites is that the nano-sized CaCO₃ particles have larger surface area in contact with the polymer matrix. As

such, the overall bonding strength between the particles and matrix is higher. Thus, it is to be expected that nano-composites could stand higher loading under external forces, as suggested by Zhu, et al., 2006 [40]. When the content of CaCO₃ is low, the micro- and nano-sized CaCO₃ cannot well disperse in the polyamide matrix and agglomerate to form a big cluster and cause a decrease in tensile strength.

Elongation percent of composite samples under stress can be calculated from the relation (equation-11), where L_o is the initial length of the test specimen, and L is the final length of sample after applying the stretching force.

$$\text{Elongation Percent} = \frac{L - L_o}{L_o} \times 100, \quad (11)$$

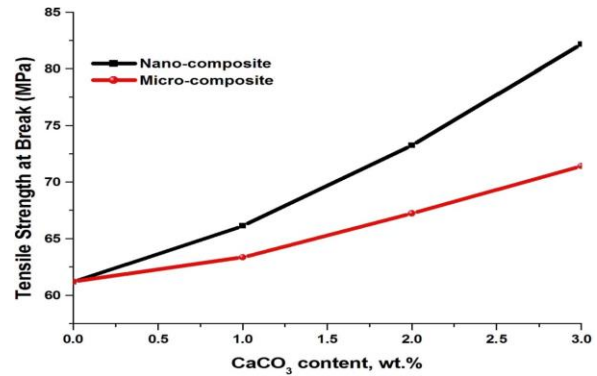


Fig. 16. Variation of tensile strength of micro- and nano-composites with filler loading at break.

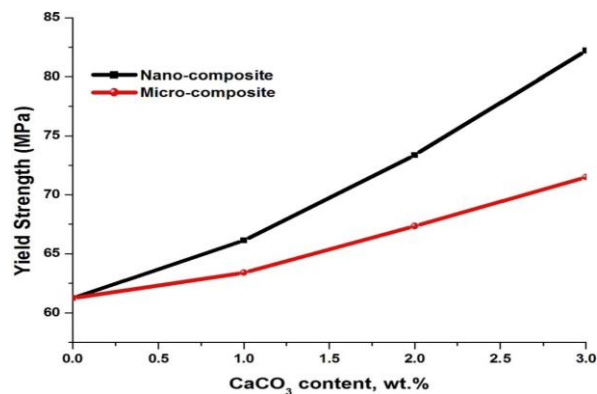


Fig. 17. Variation of tensile strength of micro- and nano-composites with filler loading at yield.

Figs. 18 and 19 show the dependence of elongation at yield and break points, respectively. The incorporation of rigid fillers to polymer matrix reduces the elongation at yield and break. This is a common observation reported by earlier researchers. The results show that with increase in weight percentage of filler loading, elongation at yield and break for micro- and nano-composites

decreases. This might be due to the hard nature of polyamide as well as nano-inorganic filler. Addition of filler decreases the elongation at yield and break of composites. This is due to the increment in numbers of spherulites formation with reduction in size and increase in percentage of filler. This may be attributed to the fact that CaCO₃ particles included into the PA66 matrix restrict the movement of polyamide chains. In other words, with the enhancement in rigidity the ductility of composites decreases; consequently the composites break at lower elongation as explained by Zhu, et al., in 2006 [37].

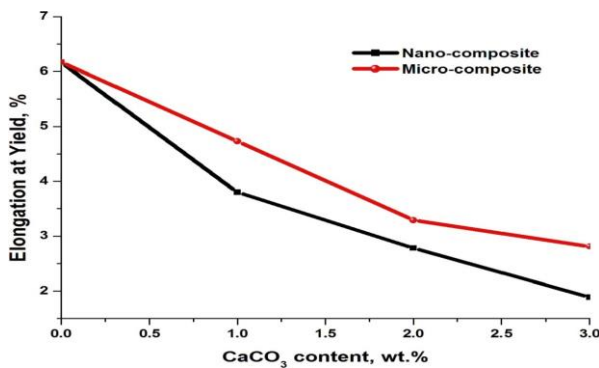


Fig. 18. Variation of elongation of micro- and nano-composites with filler loading at yield.

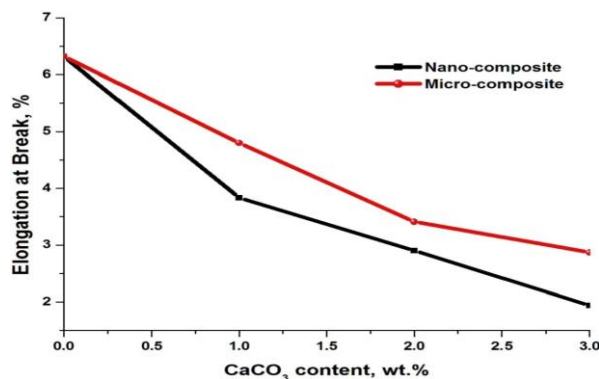


Fig. 19. Variation of elongation of micro and nano-composites with filler loading at break.

CONCLUSIONS

The major findings of this study are summarized as follows:

PA66/CaCO₃ micro- and nano-composites with loading of 0, 1, 2 and 3 wt. % of the micro-particles (~2 μm) and nano-particles (~33 nm) were successfully prepared using polymer solution method. The XRD results of composites have suggested that CaCO₃ particles can form a PA66 crystal thermodynamically more stable with the reduction of the metastable γ-crystalline phase within the polymeric matrix and forming only an α-crystalline structure. SEM results also showed that

both types of surface modified, micro- and nano-particles are covered and quite welded to the PA66 matrix. Moreover, nano-fillers appear homogeneously dispersed into polymer. Fourier-transform infra-red (FT-IR) confirmed the chemical structure of the PA66 showing absorptions for all required chemical groups: N-H stretch at 3305.52 cm⁻¹, C-H stretch at 2865.02-2936.45 cm⁻¹, Amide-I at 1638.76 cm⁻¹, and Amide-II at 1539.55 cm⁻¹. There were some significant changes observed in the IR absorption of the C-H region at 1478.87 cm⁻¹ between the filled and unfilled PA66. Changes in the peaks proved that the addition of filler in the matrix affects the transmittance of that polymer. UV-VIS data proved that addition of CaCO₃ particles in PA66, results in the decrease of energy-band gaps of the composites, and the values are less than that for neat PA66. It was also observed that the Urbach's tail for pure PA66 is less than that for PA66/CaCO₃ composites. DSC data indicated that incorporation of CaCO₃ causes the decrease in crystallinity of composites and also results in simultaneous increase of melting point. Viscometric measurements demonstrated that the presence of CaCO₃ particles is not able to change the structure and molecular weight of PA66. In addition, the results showed that adding CaCO₃ micro- and nano-particles increased the modulus and tensile strength of neat PA66 but decreased its elongation at yield and break. As a result, the nano-CaCO₃ particles cause more effective reinforcement and therefore a stiffer composite.

Acknowledgements: This scientific product was extracted through a research project implemented from funding of research projects of Yasouj Branch, Islamic Azad University.

REFERENCES

1. C.R. Tseng, J.Y. Wu, H.Y. Lee, F.C. Chang, *J. Appl. Polym. Sci.*, **85**, 1370 (2002).
2. J.K. Lim, A. Eggeman, F. Lanni, R.D. Tilton, S.A. Majetich, *Adv. Mater.*, **20**, 1721 (2008).
3. W.C.J. Zuiderduin, C. Westzaan, J. Huetink, R.J. Gaymans, *Polymer*, **44**, 261 (2003).
4. P. Supaphol, P. Thanomkiat, J. Junkasem, R. Dangtungee, *Polymer Test.*, **26**, 20 (2007).
5. M.S.F. Samsudin, Z.A. Mohd Ishak, S.S. Jikan, Z.M. Ariff, *Journal of Applied Polymer Science*, **102**, 5421 (2006).
6. H. Zhang, X. Zeng, Y. Gao, F. Shi, P. Zhang, J.F. Chen, *Ind. Eng. Chem. Res.*, **50**, 3089 (2011).
7. J.K. Pandey, K.R. Reddy, A.P. Kumar, R.P. Singh, *Polymer Degradation and Stability*, **88**, 234 (2005).
8. M. Avella, S. Cosco, M.L. Lorenzo, E.D. Pace, E.M. Errico, *J. Thermal Anal. Calorimetry*, **80**, 131 (2005).

9. D. Wu, X. Wang, Y. Song, R. Jin, *Journal of Applied Polymer Science*, **92**, 2714 (2004).
10. A.J. Crosby, J.Y. Lee, *Polymer Rev.*, **47**, 217 (2007).
11. X. Qiang, Z. Chunfang Y. JianZun, C.S. Yuan, *J. Appl. Polym. Sci.*, **91**, 2739 (2004).
12. S.S. Sonawane, S. Mishra, N.G. Shimpi, *Polymer-Plastics Technology and Engineering*, **49**, 38 (2010).
13. J. Brandrup, E.H. Immergut, *Polymer handbook*, 2nd Edition, J. Wiley Sons, New York, 1989.
14. X. Jia, M. Herrera-Alonso, T.J. Mc-Carthy, *Polymer*, **47**, 4916 (2006).
15. J.G.A. Ghadami, M. Idrees, *Iranian Journal of Chemistry and Chemical Engineering*, **32**, 27 (2013).
16. E.A. Davis, N. Mott, *Phil. Mag.*, **22**, 903 (1970).
17. F. Urbach, *Phys. Rev.*, **92**, 1324 (1953).
18. R.B. Seymour, C.E. Carraher, *Polymer Chemistry: An Introduction*, 4th Edition, New York, 1996.
19. J. Brandrup, E.H. Immergut, *Polymer Hand book*, Wiley, New York, 1975.
20. R. Brendan, in 'Annual Book of ASTM Standards' 1, ASTM International Publisher, Philadelphia, 2002, , p. 160.
21. K. Hedicke, H. Wittich, C. Mehler, F. Gruber, V. Altstadt, *Composites Science and Technology*, **66**, 571 (2006).
22. Y. Liu, L. Cui, F. Guan, Y. Gao, N.E. Hedin, L. Zhu, H. Fong, *Macromolecules*, **40**, 6283 (2007).
23. Z. Xiang, L. Yu-Bao, Z. Yi, L. Guo-Yu, M. Yuan-hua, L. Hong, *Compos Part A Appl Sci Manuf.*, **38**, 843 (2007).
24. H.P. Klugg, L.E. Alexander, *X-ray diffraction procedures*, John Wiley & Sons, New York, 1974.
25. D. Moore, R.J. Reynolds, *X-ray diffraction and identification and analysis of clay minerals of clay minerals*, 2nd Ed., Oxford University Press, U. K, 1997.
26. A. Yasmin, I.M. Daniel, *Polymer*, **45**, 8211 (2004).
27. C.M. Chan, J. Wu, J.X. Li, Y.K. Cheung, *Polymer*, **43**, 2981 (2002).
28. H. Arimoto, *J. Polym Sci, Part A*, **2**, 2283 (1964).
29. M. I. Kohan 'Nylon Plastics', John Wiley & Sons, New York, 1973.
30. B.A. Basilia, M.E.G. Panganiban, A.A.V. Collado, M.O.D. Pesigan, P.A. De Yro, *Journal of Solid Mechanics and Materials Engineering*, **1**, 564 (2007).
31. S. D. Suel, S. R. Lee, Y. H. Kim, 'Journal of Polymer Science; Part A: Polymer Chemistry', **42**, 4063 (2004).
32. J. Charles, G. R. Ramkumaar S. Azhagiri, S. Gunasekaran, *E-Journal of Chemistry*, **1**, 23 (2009).
33. M.F. Zaki, *Brazilian Journal of Physics*, **38**, 558 (2008).
34. C.W. Greeff, H.R. Glyde, *Physical Reviewer B.*, **51**, 1778 (1995).
35. L. Bai, C. Xu, P.G. Schunemann, K. Nagashio, R.S. Feigelson, N.C. Giles, *J. Phys.: Condens. Matter*, **17**, 549 (2005).
36. C. Ramesh, A. Keller, S. Eltink, *Polymer*, **35**, 2483 (1994).
37. G.Z. Zhang, T. Watanabe, H. Yoshida, H. Kawai, *Polymer Journal*, **35**, 173 (2003).
38. J. Cayer-Barrioz, D. Ferry, K. Frihi, R. Cavalier G.V. Seguela, *Journal of Applied Polymer Science*, **100**, 989 (2006).
39. H. Hanim, R. Zarina, M.Y.F. Ahmad, Z.A. Mohd, A. Hassan, *Malaysian Polymer Journal*, **3**, 38 (2008).
40. B.K., Zhu, S.H. Xie, Z.K. Xu, Y.Y. Xu, *Compos. Sci. Technol.*, **66**, 548 (2006).

Nichols stability analysis in multiwall carbon nanotube based interconnects

Somayeh Fotoohi^{1*}, Saeed Haji-Nasiri²

¹Department of Electrical Engineering, Islamshahr Branch, Islamic Azad University, Tehran, Iran

²Department of Electrical, Biomedical, and Mechatronics Engineering, Qazvin Branch, Islamic Azad University, Qazvin 3419915195, Iran

Received June 26, 2015, Revised September 10, 2015

We present Nichols stability analysis based on transmission line modeling for multiwall carbon nanotube (MWCNT) interconnects. This is the first instance that such an analysis has been presented for MWCNT so far. In this analysis, dependence of the degree of relative Nichols stability for MWCNT interconnects on the geometry of each tube has been acquired. It is shown that with increasing the length and the diameter of each tube, MWCNT interconnects become more stable.

Keywords: Multiwall carbon nanotube, interconnects, Nichols stability, phase and gain margin.

BACKGROUND

Quoting the International Technology Roadmap for Semiconductors (ITRS) report: “traditional interconnect scaling will no longer satisfy performance requirements.

Defining and finding solutions beyond copper will require material innovation, combined with accelerated design, packaging and unconventional interconnect.” The main challenges in scaling Cu interconnects are given by the poor current density allowed and the steep increase of the resistivity. Furthermore, the current density required for such technologies will rise to values well beyond the maximum allowed for copper. For these reasons, metallic CNTs have been suggested to replace copper in nano-interconnects [1].

CNTs have long mean free paths (MFPs) on the order of several micrometers (as compared to 40 nm for Cu at room temperature), which provide low resistivity and possible ballistic transport in short-length interconnects. More importantly, an isolated CNT can carry current densities in excess of 1010 A/cm² without any signs of damage even at an elevated temperature of 250°C, thereby eliminating electromigration reliability concerns that plague nanoscale Cu interconnects [2].

While CNTs have desirable material properties, individual nanotubes suffer from an intrinsic ballistic resistance of approximately 6.5 k that is not dependent on the length of the nanotube. To reduce the impact of the resistance of individual nanotubes, bundles of CNTs in parallel, which have

been proposed as a medium for, interconnect in very large scale integration (VLSI) applications [3]. Fig. 1 illustrates a schematic representation of a typical RLC model for a MWCNT interconnect made of N CNTs of the same lengths l and out-diameters D . In this figure, R_C , R_Q , and R_S represent the equivalent resistances introduced by the imperfect contacts, the quantum effect, and the carriers' scatterings, respectively. One can approximate the quantum contact resistance as $R_Q \approx h \{2e^2 N_{ch} N\}^{-1}$ [4], wherein h , e , and N_{ch} are the Plank's constant, electron charge, and number of conducting channels in each CNT. When the length of each CNT is greater than its carriers' mean free path (λ), the equivalent distributed ohmic resistance (per unit length) introduced by carriers scatterings with defects, substrate-induced disorders, and phonons can be written as $R_S \equiv R_Q / \lambda$ [4]. Also shown in Fig. 1 $C_E \approx 2\pi\epsilon / (N \times \ln(y/D))$ [5] in which ϵ is the dielectric permittivity, y is distance of MWCNT from ground plane, and D is diameter of each tube. $C_Q \approx \{R_Q v_F\}^{-1}$ is the per unit length values of the equivalent capacitances induced by the electrostatic and quantum effects, respectively, in which v_F is the Fermi velocity in graphite.

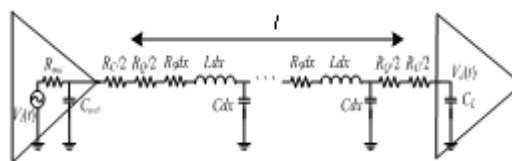


Fig. 1. Simple RLC schematic of transmission line circuit model for a driver- MWCNT interconnect-load configuration.

*To whom all correspondence should be sent:
E-mail: somayehfotoohi@yahoo.com

Since the separation between any two CNT is much smaller than y , the effect of the electrostatic capacitances between any two CNT in the bundle is negligible. Furthermore, $L_K=R_Q/v_F$ and $L_M \approx \mu \times \ln(y/D)/(2\pi N)$ [5] represent the per unit length values of the kinetic and the magnetic inductances, in presence of the ground plane, wherein μ is the CNT permeability. In a practical case $L_M \ll L_K$ [4].

In order to obtain the number of conducting channels in each CNT, one can add up contributions from all electrons in all n_C conduction sub-bands and all holes in all n_V valence sub-bands [6]:

$$N_{ch} = \sum_{i=1}^{n_C} \left[e^{(E_i - E_F)/kT} + 1 \right]^{-1} + \sum_{i=1}^{n_V} \left[e^{(E_i + E_F)/kT} + 1 \right]^{-1}, \quad (1)$$

where $i(=1, 2, 3, \dots)$ is a positive integer, E_F , k , and T are the Fermi energy, the Boltzmann constant, and temperature, respectively, and E_i represents the quantized energy that corresponds to the i -th conduction or valence sub-band. This quantization is due to diameter confinement, introduced by the tube's finite diameter.

In spite of the valuable properties there are several prospect that must be investigated to practical use of carbon nanotube interconnects. Stability analysis in driver-carbon nanotube interconnect-load system is an important viewpoint in performance evaluation of this system. In this paper we have used Nichols analysis as a criterion to compare the relative stability by changing the geometry of the CNTs. Before the frequency response analysis using Nichols chart, we need to ask the following questions:

What is the difference between Nichols chart and any other analysis method like bode and Nyquist plot? What is the advantage of using it?

A Nichol plot is similar to a Nyquist plot but shows gain on a logarithmic scale (dB) vs. phase on a linear scale (degrees), with an axis origin at the point (0dB, -180°). The advantage of Nichol's chart is the ease by which gain and phase margins can be determined graphically. The gain margin (GM) is the vertical distance in dB measured from the phase crossover to the critical point (the phase crossover frequency is where the locus intersects the -180 axis). The phase margin (PM) is the horizontal distance measured in degrees from the gain crossover to the critical point (the gain crossover frequency is where the locus intersects the 0 dB). The system becomes more stable if the GM and PM increase [7].

MATRIX FORMULATION

In the configuration illustrated in Fig. 1, a MWCNT interconnect of length l that is represented by a series of distributed resistances (R_s), inductances (L), and capacitances (C) (all in per length units), is driven by a driver with an output resistance R_{out} and an output capacitance C_{out} . The MWCNT interconnects is also connected to a load of capacitance C_L .

In order to calculate the input-output transfer function of the configuration in Fig. 1, total transmission parameter matrix should be derived. For this purpose ABCD transmission parameter matrix are used for a uniform RLC transmission line of length l that contains N_B distributed blocks. Accordingly, total ABCD transmission parameter matrix is defined as:

$$T_{total} = \begin{bmatrix} A_T & B_T \\ C_T & D_T \end{bmatrix} \equiv \begin{bmatrix} 1 & R_{out} \\ 0 & 1 \end{bmatrix} \begin{bmatrix} 1 & 0 \\ sC_{out} & 1 \end{bmatrix} \begin{bmatrix} 1 & R_{in} \\ 0 & 1 \end{bmatrix} \times \left[\begin{array}{cc} 1 + (R_s dx + L dx s) s C dx & (R_s dx + L dx s) \\ s C dx & 1 \end{array} \right]^{N_B} \times \begin{bmatrix} 1 & R_{in} \\ 0 & 1 \end{bmatrix}, \quad (2)$$

Where $R_{ex}=(R_C+R_Q)/2$, $L=L_K+L_M$, $C=C_E C_Q/(C_E+C_Q)$, $dx=l/N_B$, and $s=j\omega$ is the complex frequency. We obtain the linear parametric equivalent for the transfer function of as:

$$H(s) = \frac{V_o(s)}{V_i(s)} = \frac{1}{A_T + s C_T B_T}, \quad (3)$$

Nichols stability analysis

By varying the nanotubes' dimensions, ($2 \mu m \leq l \leq 10 \mu m$ and $2 \text{ nm} \leq D \leq 10 \text{ nm}$) and generating various Nichols diagrams, we have studied the effect of MWCNT geometry on the relative stability of the configuration given in Fig. 1. All geometrical and physical parameters are according to the 22-nm technology node, extracted from ITRS2009 [8]. Both local interconnects are assumed to have ideal contact (i.e., $R_C=0$) [8]. The driver size is set to be 100 times the minimum sized gate for the 22-nm technology node, given in [8]. The bundle width is 22 nm and its thickness is 44 nm. The space between two adjacent CNTs is assumed as 0.34 nm and E_F as 0.3 eV. All individual CNTs are metallic.

Nichols diagrams are shown in Fig. 2 for the configuration of Fig. 1 regarding $l=2, 6, \text{ and } 10 \mu m$.

The diameter of each tube is assumed to be 2 nm. As shown in Fig. 2, by increasing the length of CNTs to 2, 6, 10 μm , the curves in the critical point shift to the down and right, consequently the gain margin of interconnect increases as 0.54, 2.34 and 4.13, and the phase margin of interconnect increases as -4.64, 44 and 133 respectively.

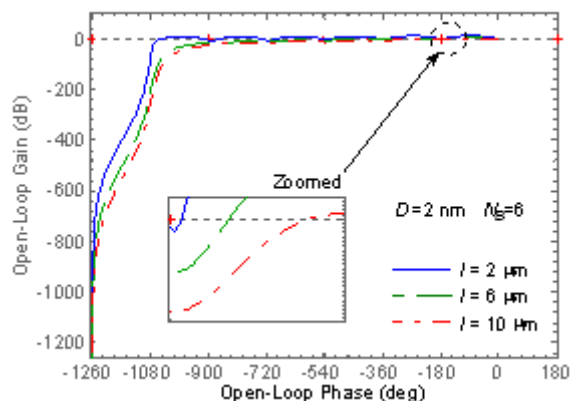


Fig. 2. The Nichols diagrams for driver-MWCNT interconnect-load configuration of Fig. 1 for $D=2 \text{ nm}$ and $2 \mu\text{m} \leq l \leq 10 \mu\text{m}$.

Thus, with an increase in the length of CNT bundle, the system becomes more stable. This is because by increasing the length of tubes, the equivalence impedance of the interconnect increases so that the step response of the system go to more damping and the system tend to be more stable.

Nichols diagrams for $D = 2, 6,$ and 10 nm are illustrated in Fig. 3. The length of each tube is assumed to be $2 \mu\text{m}$. As shown in Fig. 3, by increasing the diameter of CNT to 2, 6 and 10 nm , the curves in the critical point shift to the down and right, consequently the gain margin of interconnect increases as 0.54, 1.02 and 1.46, and the phase margin of interconnect increases as -4.64, 13.3 and 27 respectively. Therefore, with an increase in the diameter of CNT bundle, the system approaches to more stability. This is because by increasing the tube diameters the bundle becomes less dense and its conductivity decreases so that its step response tends to be more damping.

The present general analysis whose transfer function is of the order of 14, provides much more accurate and realistic numerical results than those that could be obtained by similar analyses presented in [9] with order of four and [10] with the order of six both for CNT-bundle interconnects, and in [11] with the order of four for multi layer graphene nanoribbon (MLG NR) interconnects.

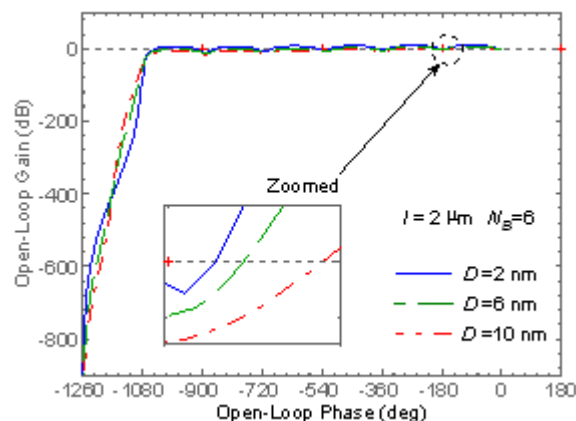


Fig. 3. The Nichols diagrams for driver-MWCNT interconnect-load configuration of Fig. 1 for $l=2 \mu\text{m}$ and $2 \text{ nm} \leq D \leq 10 \text{ nm}$.

CONCLUSION

Using transmission line modeling along with Nichols stability diagrams, relative stability for MWCNT interconnects has been studied. We have shown that with increasing either the length or diameter of each tube, the relative stability increases and hence the system becomes more stable. This is because an increase in either parameter gives rise to switching delay and hence, its step response tends to damp faster and as a result, the system becomes more stable.

REFERENCES

1. A. Maffucci, G. Miano, F. Villone, *IEEE T. Advanced Packaging*, **21**, 692 (2008).
2. H. Li, W.Y. Yin, K. Banerjee, J.F. Mao, *IEEE Electron Device Lett.*, **55**, 1328 (2008).
3. A. Nieuwoudt, Y. Massoud, *IEEE T. Nanotechnology*, **5**, 758 (2006).
4. N. Srivastava, K. Banerjee, *IEEE ICCAD*, **23**, 38 (2005).
5. H. Hayt, A. Buck, *Engineering Electromagnetics*, McGraw-Hill, New York, 2005.
6. A. Naemi, D. Meindl, *IEEE Electron Device Lett.*, **27**, 338 (2006)
7. R. Dorf, R. Bishop, *Modern Control System*, Englewood Cliffs, NJ, Prentice-Hall, 2008.
8. International Technology Roadmap for Semiconductors (ITRS),
9. <http://www.itrs.net/Links/2010ITRS/Home2010.htm>.
10. D. Fathi, B. Forouzandeh, *IEEE Electron Device Lett.*, **30**, 475 (2009).
11. D. Fathi, B. Forouzandeh, S. Mohajerzadeh, R. Sarvari, *Micro & Nano letters*, **4**, 116 (2009).
12. S. Haji-Nasiri, M. K. Moravvej-Farshi, R. Faez, *IEEE Electron Device Lett.*, **31**, 1458 (2010).

Multi-objective multivariable optimization of agglomerated cathode catalyst layer of a proton exchange membrane fuel cell

B. Kazeminasab^{1*}, S. Rowshanzamir^{2,3}, H. Ghadamian⁴

¹Department of Energy Engineering, Graduate College of Environment and Energy, Science and Research Branch, Islamic Azad University, Tehran, Iran. b.kazeminasab@srbiau.ac.ir

²School of Chemical Engineering, Iran University of Science and Technology. rowshanzamir@iust.ac.ir

³Fuel Cell Laboratory, Green Research Center, Iran University of Science and Technology.

⁴Department of Energy, Materials and Energy Research Center (MERC), Tehran, Iran. h.ghadamian@merc.ac.ir

Received June 26, 2015, Revised September 10, 2015

Since the optimization objectives of the cathode catalyst layer (CCL) of a PEM fuel cell affect each other, thinking of them separately, would not be realistic and accurate; so they must be solved simultaneously. In this study, a multi-objective multivariable optimization based on an agglomerate model, is performed and objective functions like current density and the cost of CCL are optimized under different variables. Decision variables include important or measurable parameters, namely platinum loading, ionomer volume fraction, agglomerate radius and porosity, and water saturation. Comparing these results with those of optimizations whose objectives are combined as a single-objective, found the optimization results have a good overlap at low current densities, however when increasing the current the results diverge. This deviation occurs as a result of interaction between objectives. The sensitivity analysis shows that the best range of platinum loading is 0.1 and 0.4 mg cm⁻². The Pareto curve at the voltage of 0.6 V indicates that the best trade-off between the cost and the performance of the CCL is achieved, when the current density increases in the range of 5 % to 12 %, where the optimization objectives are met simultaneously.

Keywords: Agglomerate model, Cathode catalyst layer, Multi-objective optimization, Pareto curve, Trade-off.

INTRODUCTION:

Cathode catalyst layer (CCL) is an important component in proton exchange membrane (PEM) fuel cells. In this layer, the proton current and oxygen molecules are electrochemically converted into an electron current [1]. The losses resulting from this conversion; include the limitation in the transportation of reactants and products, and poor oxygen reduction reaction (ORR) kinetics, which can reduce the efficiency of the fuel cells.

Modelling of the cathode catalyst layer is performed to attain a better discernment of the conditions, structure, transport properties and electrochemical reactions and also to evaluate the effect of variables on the performance. In general, there are three models to describe the CCL: (i) ultra-thin layer, (ii) pseudo-homogeneous and (iii) agglomerate models. Usually, the agglomerate model has the better representation of the catalyst layer (CL) compared to other models [2]. Thus, the overall accuracy of these models depends strongly on the description of the CL [3]. Therefore an agglomerate model has been considered in order to simulate the CCL.

Then, the optimization of CL is performed to improve the performance and reduce the expenses of the fuel cells. Since improving the performance and reducing the cost of CL simultaneously are crucial precondition for the commercialization of fuel cell, this research has been conducted to study multi-objective optimization (MOO) of the CCL. Many real problems require multi-objective evaluation [4] because their optimization objectives affect each other. Moreover, the inherent conflicting of the goals causes more difficulty during the calculation of the optimum solution. Hence, for the optimization study, a MOO coupled to above model is applied.

In the literature, several studies were presented for optimizing the PEM fuel cell or its CLs. Some of these studies are discussed below in brief and then the overall conclusions are also drawn at the end of this section. In order to obtain optimum distributions of catalyst loading and ionomer across the CCL of the PEM fuel cell, Song et al. [5] showed that the optimum distributions are linear when the optimization is performed using a single-variable, while the optimum distribution of ionomer remains linear, but that of catalyst loading becomes convex when the optimization is behaved as a two-variable problem. According to their results, the interaction of variables is significant and should not be ignored. Madhusudana and Rengaswamy [6] studied the

To whom all correspondence should be sent:
E-mail: b.kazeminasab@srbiau.ac.ir

optimization of the agglomerate CCL, in order to minimize the total amount of platinum and to maximize the current density, separately.

For the first time, Na and Gou [7] proposed a MOO technique with two objective functions of performance and expense to optimize fuel cell systems. They demonstrated a more cost-effective fuel cell system with a high-performance level will be obtained. Then Ang et al. [8] suggested a MOO technique for a general PEM fuel cell system, using the weighted-sum method. They showed that, a more efficient system was bigger, and vice versa. Overall, their results indicated that, to reach the most of the size-efficiency trade-off, the system must be operated at efficiency between 40 % and 47 %. Ang et al. [9] in another work, reviewed the methods and strategies of fuel cell system optimization, and then categorized the MOO into a bi-objective and a tri-objective optimal design. Secanell et al. [10] considered fuel cell Membrane-Electrode-Assembly for MOO. The objective was to simultaneously maximize the efficiency and minimize its production expenses. The results showed the expense - efficiency compromises, and they illustrated that considerable yields in the efficiency and cut in expenses were possible.

Srinivasarao et al. [11] individually considered some objective functions in order to optimize the CL. The optimized parameters of CL are vigorously influenced by the constraints and the objective functions. Khajeh-Hosseini et al. [12] improved a 1D agglomerate model for the CCL of a PEMFC to study the effects of catalyst layer variables on the activation loss. Additionally, the harmony search algorithm was utilized to get the optimal values of variables to minimize the activation overpotential of CL.

Tahmasbi et al. [13] applied a novel approximate to the MOO technique in the fuel cell system based on simultaneous power maximization and cost minimization by a genetic algorithm. Power maximization results at the peak power (1.95 kW), the unit expense of energy is \$0.64. On the contrary, the expense minimization decreased the unit expense of energy to \$0.33, while, output power was decreased to 0.93 kW. It means the optimization of fuel cell system is strangely influenced by the weighting factors of the objective functions. Mert and Özçelik [14] implemented MOO of a direct methanol fuel cell with three objective functions of power, energy and exergy efficiencies, and then calculated the optimal values of objective functions separately and simultaneously. According to these results, the best results drawn for the objectives, when considered separately, are larger than those

when all the objectives are considered simultaneously. At last Feali and Fathipour [15] determined the trade-off curve between fuel utilization and output power density by genetic algorithm. They showed that to attain the optimum trade-off between the power and utilization, the current of the fuel cell should be less than 0.9 mW cm⁻².

Although recently a few multi-objective optimizations have been performed for the fuel cell system, the optimizations of CCL are restricted to single-objective ones, such as that of cost or performance. Since the objectives of optimization affect each other, considering the objective functions separately would not be realistic and accurate, so objective functions of CCL must be solved simultaneously. In all cases above, the interaction between the goals of the CCL was not taken into consideration, each goal was optimized separately. In this study, a multi-objective multivariate optimization (MOMO) based on an agglomerate model is performed for CCL of PEM fuel cell. This optimization utilized to study the cost and the performance trade-off concerned with the model of CCL. The fminimax and bvp4c functions of MATLAB software are aided in optimization and modelling stage, respectively. Objective functions are current density and cost of CCL, and decision variables include platinum loading, ionomer volume fraction, agglomerate radius and porosity, and water saturation.

This paper is organized as follows: Section 2 presents the CCL modelling. Section 3 describes the CCL optimization formulation based on this model. Section 4 provides the important results from the investigation of objectives and variables. Section 5 concludes the paper.

CATHODE CATALYST LAYER MODELLING

Before any optimization can be done, the problem must first be modelled. The catalyst layer was modelled as an ultra-thin layer in the earlier models. Afterward, the catalyst layer is considered to be of finite thickness. Recently, microscopic images (SEM and TEM) have shown that the catalyst layer is built of Platinum/Carbon particles and a Nafion film, called agglomerates [16]. Agglomerate models have numerous parameters, including operational parameters, namely temperature, pressure and saturated liquid water, and structural parameters such as platinum loading, ionomer volume fraction, porosity and CL thickness, radius and porosity of agglomerate, etc.

Since the major variations occur in the diffusion direction of reactants (Z direction), a high-precision, one-dimensional model is applied to speed up the implementation of written code in the optimization stage. It's reasonable to assume an isothermal model in the low-temperature fuel cell where the generated heat is spent on the heating of the produced water.

In this study, a one-dimensional, isothermal, steady-state, agglomerate model is considered and developed for the CCL of a PEM fuel cell.

The agglomerate CL consists of Nafion ionomer, platinum and carbon particles as shown in Fig. 1. There are more details of agglomerate models in the references [3, 6, 12, 17].

Other assumptions of modelling are:

The void spaces between the agglomerates may be partially or fully filled with water

The PEMFC operates at steady-state and isothermal condition

The agglomerate particles are spherical in shape

Reaction kinetics are first-order with respect to the oxygen concentration

The gases are assumed to be ideal.

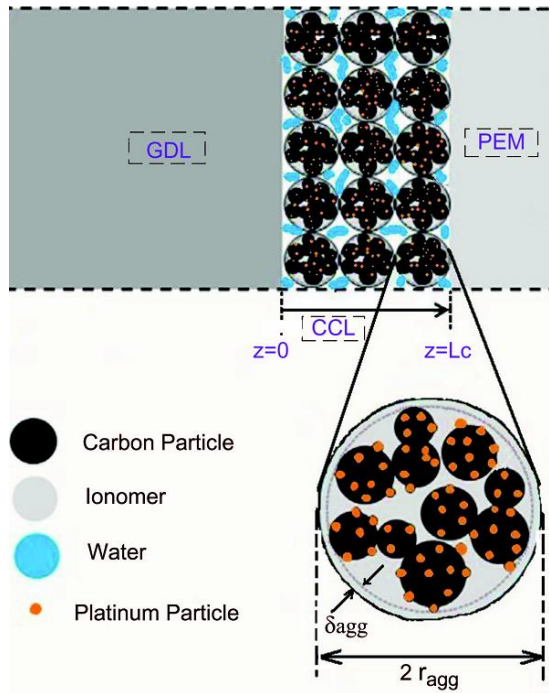


Fig. 1. Cathode catalyst layer based on agglomerate model.

GOVERNING EQUATIONS

As the considered model is one-dimensional, isothermal and steady state, the CL phenomena consist of proton transfer, oxygen diffusion and overpotential losses along the vertical direction of catalyst layer (Z direction). Ohmic and concentration

losses will be calculated when these parameters have been determined.

Current Profile

The oxygen conservation within agglomerate in steady-state indicates:

$$\nabla \cdot N_{O_2} = R_{O_2} \quad (1)$$

Where R_{O_2} represents the oxygen consumption rate and N_{O_2} shows flux of oxygen in the Nafion that is defined by Fick's diffusion law:

$$N_{O_2} = -D_{O_2,agg}^{eff} \nabla C_{O_2} \quad (2)$$

Where $D_{O_2,agg}^{eff}$ is the effective diffusion coefficient of oxygen inside agglomerate that is calculated by the Bruggeman's relation [6].

A combination of Eqs. (1) and (2) and expanding the equation leads to:

$$\frac{D_{O_2,agg}^{eff}}{r^2} \frac{d}{dr} \left(r^2 \frac{dC_{O_2}}{dr} \right) - k_1 \cdot a \cdot C_{O_2} = 0 \quad (3)$$

Equation (3) is a 2nd-order ODE which is solved analytically [17]:

$$C^* = \frac{\sinh(3\phi r)}{r^* \sinh(3\phi)}$$

$$\left(\text{Where: } \phi = \frac{r_{agg}}{3} \sqrt{\frac{k_1 \cdot a}{D_{O_2,agg}^{eff}}} \right), (4)$$

Now, we define E_r as the agglomerate effectiveness factor as [17]:

$$E_r = \frac{R_{O_2}}{R_{O_2,max}} = \left[\frac{1}{\phi} \left(\frac{1}{\tanh(3\phi)} - \frac{1}{3\phi} \right) \right], \quad (5)$$

The consumption rate of oxygen per unit volume of the catalyst layer can be linked to the current of protons i as:

$$R_{O_2} \frac{A}{a} = \frac{1}{4F} \nabla \cdot i, \quad (6)$$

Where $\nabla \cdot i$ can be substituted by di/dz for a one-dimensional study [10]:

$$\frac{di}{dz} = 4F \left(\frac{1}{E_r k_1 A} + \frac{\delta}{a_{agg} D_{O_2,N}} \frac{r_{agg+\delta}}{r_{agg}} \right)^{-1} \frac{C_{O_2}}{H_{O_2}}, \quad (7)$$

Oxygen Profile

For the ORR, the consumption rate of oxygen is $(i_{tot}-i)/nF$. Hence the distribution of oxygen concentration in the CL is [6]:

$$\frac{dC_{O_2}}{dz} = \frac{i-I_\delta}{4FD_{O_2,CL}^{eff}}, \quad (8)$$

Overpotential Loss Profile

The resistance against the migration of electron and proton in the catalyst layer is defined by Ohm's law [6]:

$$\frac{d\eta}{dz} = \frac{i}{k^{eff}} + \frac{i-I_\delta}{\sigma^{eff}}, \quad (9)$$

Boundary Conditions

According to Fig. 1 and ideal gas assumption, boundary conditions at $Z=0$ are:

$$C_{O_2}|_{z=0} = \frac{P_{O_2}}{RT} = \frac{P_{O_2}}{1.33 \exp(-\frac{6666}{T})}, \quad i|_{z=0} = 0, \quad (10)$$

And boundary condition at $Z=L_c$ is:

$$i|_{z=L_c} = I_\delta, \quad (11)$$

Solution method

Equations (7-9) along with boundary conditions Eqs. (10) and (11) form a coupled system of nonlinear ODEs with the unknown independent variables i , C_{O_2} and η that control the transfer of protons, oxygen and electrons within the catalyst layer. In this study, the coupled system of equations is solved through coding in MATLAB software by shooting method, as shown in Fig. 2. After solving the system of equations and calculating the losses, the performance curve is drawn.

Model validation

This model was verified using a comparison with the experimental data conducted by Chang et al. [18] and also the non-isothermal, two-phase and three-dimensional model by Obut et al. [19] in Fig. 3. As seen over the whole range of the performance curve, a very good agreement between all results is obtained; therefore, if the agglomerate model including numerous operational and structural parameters were used, considering the assumptions such as the isothermal, one-dimensional and steady state could not reduce the accuracy of the results. The values of the input variables for the base case are shown in Table 1.

Cathode catalyst layer optimization

After the CL modelling has been conducted and its precision has been confirmed, CL optimization is performed. Modelling offers powerful tools and guidance for performance optimization.

To cut the costs of the fuel cells, the studies progress in two routes: replacing the platinum with suitable non-precious metal alternatives [20] and optimal design of the fuel cell to predict and understand phenomena occurring in the cell. Optimal designs of catalyst layers will be further classified according to their composition and structure [21].

The optimization problems sometime include more than one objective function needing to be optimized simultaneously. The process of

optimizing a number of objective functions is called multi-objective optimization [4]. MOO is also known as multi-criteria [22] or multi-attribute optimization. In MOO it is not possible to find a single solution as an optimal solution for all of the functions together [4]. MOO consists of three phases: model building, optimization and decision making. After having found some solutions of the MOO problem, we must select a solution from this set [23]. One of the benefits of MOO is that it takes the interaction between the objectives into consideration.

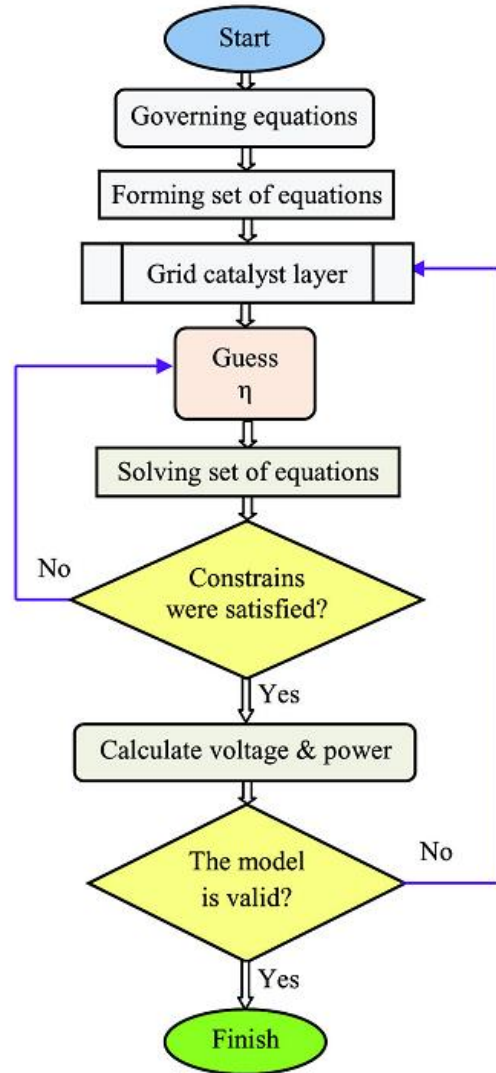


Fig. 2. Algorithm for solving the differential equations of CCL.

Objective Functions

Objective functions of CL optimization usually contain maximization of current density, output power, current density per Pt loading, and minimization of voltage losses, fuel cell size, and CL cost per power. This simulation can optimize many objective functions simultaneously but here, in order

to compare our results with existing results, two objective functions namely current density and CL's cost are used.

The CL is a combination of Pt/C and ionomer solution; therefore, the sum of platinum and ionomer costs is a good indicator of CL's cost. So in order to create the cost function of CL, the expression below is procured from curve fitting of r_{Pt} and related cost data and the cost of Nafion solution [11]. The

manufacture cost of CL depends on the synthesis technology and the laboratory, and could be added to the cost function of the catalyst layer only if it was determined.

The objective function of current density is also obtained from solving the modelling equations. A minus is added by the current density function, so that the two objective functions could be minimized.

Table 1. Input data used for base case in modelling stage [10, 17-19].

Parameters	Quantity	Value / Units
T	Temperature	60 °C
P	Pressure	1.1 bar
X _{O2}	Oxygen mole fraction in CCL	21 %
s	Liquid water saturation	0.5
L _C	Catalyst layer thickness	30 μm
R _{ohmic}	Ohmic resistance	0.47×10 ⁻⁴ Ωm ²
m _{Pt}	Pt mass loading	0.003 kg m ⁻²
ρ _{Pt}	Density of Pt	21,400 kg m ⁻³
ρ _C	Density of Carbon	1800 kg m ⁻³
r _{Pt/c}	Platinum mass ratio on Pt/C particles	0.2
C _{O2, ref}	Reference O ₂ concentration	2.28 mol m ⁻³
α _C	Transfer factor of Cathode	1.0
α _a	Transfer factor of Anode	0.5
κ	Protonic conductivity	300 Ω ⁻¹ m ⁻¹
σ	Electronic conductivity	72,000 Ω ⁻¹ m ⁻¹
τ	CL tortuosity	1.5
r _{agg}	Radius of agglomerate	0.3 μm
ε _{agg}	Spherical agglomerate porosity	0.45
δ _{agg}	Thickness of agglomerate	30 nm
ε _{CL}	CL porosity	0.2
ε _g	GDL porosity	0.74
L _{mc}	Volume fraction of membrane in the CL	0.3
L _{gc}	Volume fraction of GDL in the CL	0.1
A _p	Adjustable parameter	If i < 2000 Ap=3 else Ap=0.3

Table 2. Comparing the results of multi-objective optimization and optimization of Ref. [11].

Results of Ref. [11]:							
Voltage (V)	Current density / mA cm ⁻²		Cost function / \$ W ⁻¹		% Gain in performance	% Gain in cost	
	Base case	Optimized case	Base case	Optimized case			
0.8	265.47	292.02	0.61182	0.5212	10	14.81	
0.6	1081.7	1189.9	0.2002	0.1339	10	33.12	
0.4	1895.3	2084.8	0.17139	0.1021	10	40.43	
Results of this work:							
0.8	265	290	0.613	0.523	10	14.68	
0.6	1070	1180	0.201	0.152	10	24.38	
0.4	1880	1980	0.173	0.128	5	26.01	

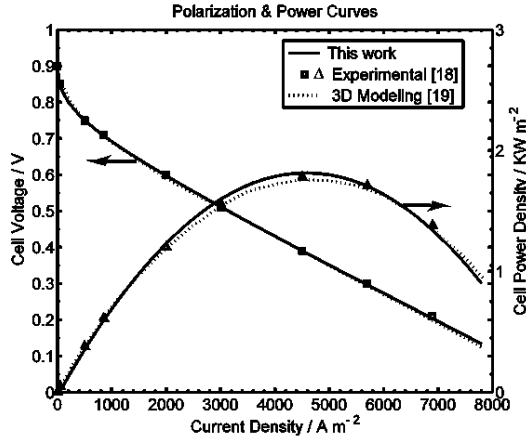


Fig. 3. Comparing the modelling results with results in [18, 19].

Finally, the following relations are used for the cost function of carbon-supported platinum and the cost function of ionomer, respectively:

$$C_1 = 251.7 r_{Pt/C} + 6.6092, C_2 = 24.0566 \quad / \$ g^{-1}, (12)$$

Weight of carbon-supported platinum and weight of ionomer come from the following relations, respectively:

$$\begin{cases} W_{Pt} + W_C = m_{Pt} \times 10^{-3} \text{ Area} / r_{Pt/C} \quad / g, & (13) \\ W_i = m_{Pt} \times 10^{-3} \text{ Area} / r_{Pt/C} \times f_i / (1 - f_i) \quad / g \end{cases}$$

Where f_i (mass ionomer ratio) will be obtained from the following relation:

$$f_i = \frac{L_{mc} \rho_i r_{Pt/C} L_C \times 10^5}{m_{Pt} + L_{mc} \rho_i r_{Pt/C} L_C \times 10^5}, (14)$$

Finally, the objective functions are obtained from the following relations:

$$f_1 = -I_{\delta} \quad / A \text{ cm}^{-2}, (15)$$

$$f_2 = (C_1 (W_{Pt} + W_C) + C_2 W_i) \quad / \$, (16)$$

Variables and constraints

There are many variables in the catalyst layer structure that influence the efficiency of the fuel cells. These variables are a combination of structural and operational parameters. Operational parameters include temperature, pressure and water saturation, and structural variables include thickness of Nafion film, agglomerate radius and porosity, catalyst loading, carbon loading, carbon-platinum ratio, Nafion fraction, GDL passing into CL, GDL porosity, CL porosity and thickness.

Although this study is theoretical, the decision variables can be controlled during the manufacture of the PEM fuel cell as follows: Agglomerate radius and porosity, and water saturation can be controlled through the synthetic techniques of MEA, pore formers, and water management, respectively. The catalyst layer thickness and ionomer fraction depend

on the amount of used ionomer, carbon and platinum.

In a written program, we can investigate all variables simultaneously, but here only important or measurable parameters are scrutinized. These parameters include: platinum loading, ionomer volume fraction, agglomerate porosity, agglomerate radius and water saturation.

To avoid unrealistic design criteria, the upper and lower limits below are applied to the parameters:

$$\begin{cases} x = [m_{Pt}, L_{mc}, \varepsilon_{agg}, r_{agg}, S] \\ lb = [0.01, 0.1, 0.1, .01, .01]; \\ ub = [2.0, 0.9, 0.9, 0.5, 0.7]; \end{cases} (17)$$

Constraints of the multi-objective optimization problem can be imposed on problem variables or objective functions. Constraints of variables are defined as volume fraction of solid, ionomer and void in the CL:

$$\begin{cases} \varepsilon_v = \varepsilon_{CL} = 1 - \frac{m_{Pt}}{L_C} \left(\frac{1}{\rho_{Pt}} + \frac{1 - r_{Pt/C}}{r_{Pt/C} \cdot \rho_C} \right) - \\ L_{mc} \quad 0 < \varepsilon_v < 1 \\ \varepsilon_i = L_{mc} = \frac{f_i}{1 - f_i} \frac{1}{\rho_i} \frac{m_{Pt}}{r_{Pt/C} L_C} \quad 0 < \varepsilon_i < 1, \\ \varepsilon_s = 1 - \varepsilon_v - \varepsilon_i = \frac{m_{Pt}}{L_C} \left(\frac{1}{\rho_{Pt}} + \frac{1 - r_{Pt/C}}{r_{Pt/C} \cdot \rho_C} \right) \quad 0 < \varepsilon_s < 1 \end{cases} (18)$$

In addition, constraints imposed on objective functions, such as the cost and the performance, could be seen as CL cost less than a specific value (e.g., base cost) or its performance greater than the base value, e.g., up to 20 %.

$$\left\{ \begin{array}{l} CL \text{ cost}_{Optimized} < CL \text{ cost}_{Base case} \\ \text{Curren density}_{Optimized} \\ - \text{Curren density}_{Base case} \\ > (0 - 20) \% \end{array} \right. (19)$$

Solution algorithm

However the possible solutions to the MOO are usually in conflict with several objectives, but the Pareto set has minimum conflict [24]. One of the methods most used to solve a MOO in order to obtain a Pareto-optimal set is the min-max method. This method tries to find a feasible design that minimizes its distance from the ideal design [25]. This method also uses the nonlinear programming algorithm, a sequential quadratic programming (SQP). There are two functions to solve constrained nonlinear MOO in MATLAB: `fminimax` and `fgoalattain`, both of which use a SQP method [26, 27].

In this study, we use the `fminimax` method because the `fgoalattain` method is more complicated

due to use the weighting coefficients. However, both methods have local solutions [5]. Due to the low range of variables and because a local minimum for a convex function is always a global minimum, this disadvantage does not cause difficulties. On the other hand, same results are obtained for different initial guesses.

In this research, the current density and the cost of CL are optimized under various conditions through the MOO technique using the min-max method. First of all, coding with MATLAB software, the set of equations obtained from the modelling stage is calculated using the bvp4c function as shown in the algorithm in Fig. 2. Then, MOO functions are solved through fminimax function and via Eq. (20). The fminimax is formed of objective functions, variables and constraints according to Eq. (20). The optimization algorithm is shown in Fig. 4.

$$\begin{cases} \text{fminimax} & f_1, f_2 \\ \text{w.r.t.:} & m_{pt}, l_{mc}, \epsilon_{agg}, r_{agg}, s \quad (20) \end{cases}$$

Subject to: $0 \leq \epsilon_v \leq 1, 0 \leq \epsilon_i \leq 1$ and $0 \leq \epsilon_s \leq 1$

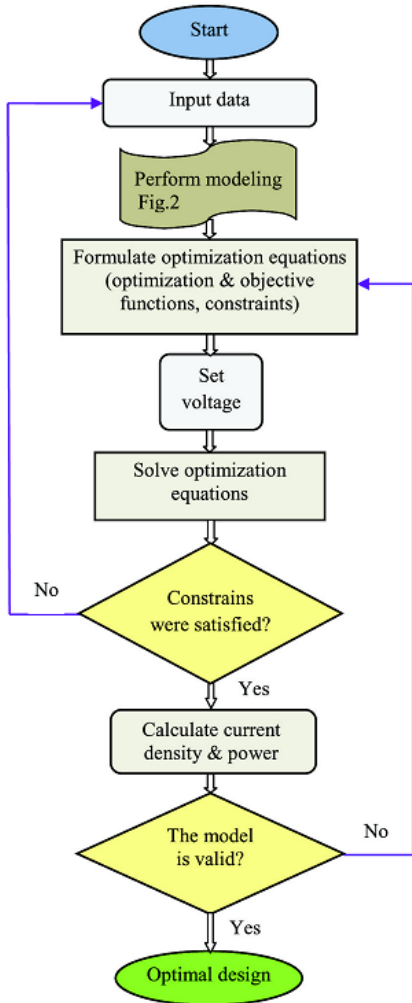


Fig. 4. Algorithm for performed multi-objective optimization.

Optimization validation

This simulation can optimize many objective functions simultaneously, but here, in order to compare our results with the available result, only two objective functions, namely maximization of current density and minimization of CL cost, are used. Our results are arranged in such a way that they can be compared with results in Ref. [11]. Input data are also the same as those of Ref. [11], with the rest of the data used in Table 1. Many variables are also considered in the catalyst layer modelling, but here only important or measurable parameters are scrutinized. These parameters include: platinum loading, carbon-platinum ratio, ionomer volume fraction, agglomerate porosity and radius, and water saturation.

Optimization results at three voltages, including high, medium and low voltages, and two states, base case and optimized case, are compared in Table 2 and Fig. 5. As can be seen, the results of both models at the base case conformed at high, medium and low voltages; therefore, their results can be compared. Optimization results show a good agreement at low current density. Increasing current density, which causes an increase in losses and cost-saving resulting from using less platinum, makes a divergence appear between optimizations. It occurs because in the above-mentioned reference, two objectives are actually optimized through a single objective manner, while in our study two objectives are used separately and simultaneously, so interactive effects of objectives are considered.

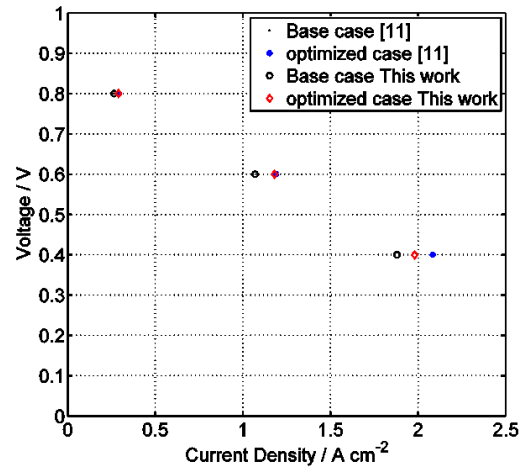


Fig. 5. Comparing these results and results in [11] at base case and optimized case.

RESULTS AND DISCUSSION

Since the amount of catalyst is the most important factor influencing the optimization objectives of the catalyst layer (performance and cost), before any

optimization is done, the effect of platinum on the performance is investigated in various voltages.

Pt loading diagram is drawn vs. current density and cost at the voltages of 0.8, 0.6 and 0.4 V in Fig. 6. The slope of the curve is very small where the platinum loading is larger than 0.4 mg cm^{-2} ; that is, increasing a large amount of platinum leads to small changes in current density, so it would not be economical to increase the platinum loading any more than that. By contrast, the slope of the curve is very sharp where the platinum loading is less than 0.1 mg cm^{-2} ; it means that, in order to reduce the cost, a large drop in the current density occurs through reducing Pt in small scales; therefore, the reduction of Pt in larger scales would not be technically justified. So, the best compromise between the cost and the performance should be achieved within this platinum range.

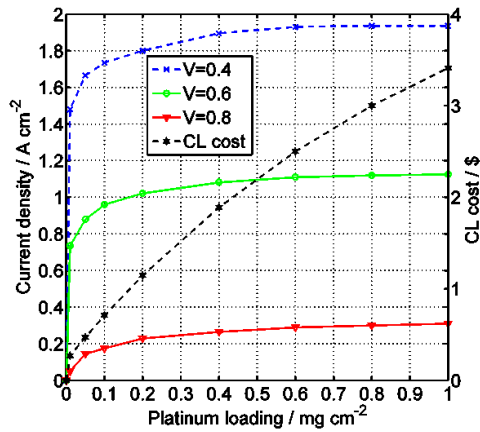


Fig. 6. Diagram of platinum loading vs. current density at the voltages of 0.8, 0.6 and 0.4 volt.

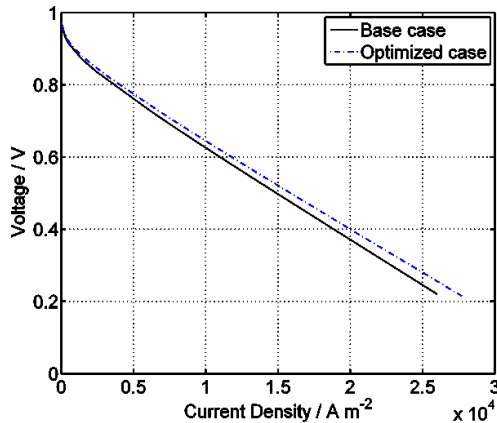


Fig. 7. Performance curve of fuel cell for both the base case and the multi-objective optimization case.

The catalyst layer cost increases 166 % at all three voltages in the above platinum ranges while the current density increases by 51.4 % at the voltage of 0.8 V, 12.7 % at the voltage of 0.6 V and 9.2 % at the voltage of 0.4 V; thus, the current is more dependent on the amount of platinum at high

voltages, due to the importance of activation overpotential, instead, it is far less dependent at low voltages.

Figure 7 demonstrates the performance curve of the fuel cell in both cases; base case and multi-objective optimization case. In Fig. 7, one of the objectives, namely cost, is considered the same as base cost, and another objective, namely performance, is optimized. Although the amount of increase in the CL performance is higher at the high currents, its relative increase is higher at the low current densities.

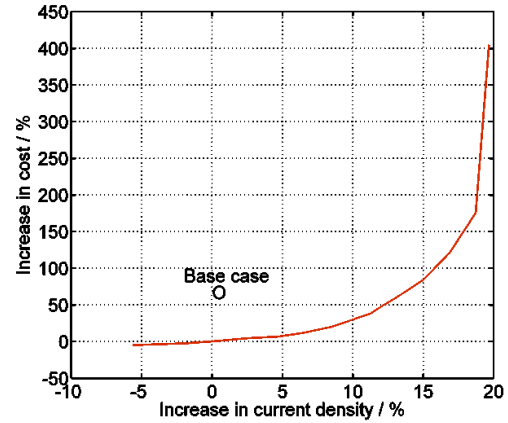


Fig. 8. Pareto curve for multi-objective optimization of catalyst layer at the voltage of 0.6 V.

In Fig. 8, a Pareto curve is drawn to optimize the objectives of performance and cost of the CL at the voltage of 0.6 V, where the base case (voltage 0.6 V, current 1.07 A cm^{-2} and cost 1.819 \$) is also marked with a circle. With multi-objective optimization at the base case current density, first the cost suddenly dropped compared to the base case, and then to increase the current density, the cost gradually increases. As shown in the graph on the left, the slope of the curve is very smooth, which shows that increasing the current density does not lead to too high a price; therefore, the current density can be increased as necessary. In the graph on the right, a slight rise in current leads to an increase in the cost several times, so increasing the performance in this area would not be economical; therefore, the trade-off between the cost and the performance is achieved, depending on the kind of application, when the current density increases in the range of 5 % to 12 %. In this range, the optimization objectives are met simultaneously; that is, the current is more than the base and the cost is lower than the base case.

In Fig. 9, a Pareto curve is drawn as the cost-power ratio vs. current at the voltage of 0.6 V. The above base case is also marked with a circle to compare. Here, a compromise is achieved between the objectives of cost-power ratio and current density

in the current density range of 1.13-1.23 A cm⁻² depending on the decision maker. Likewise, the current is more than the base and the cost is lower than the base case simultaneously.

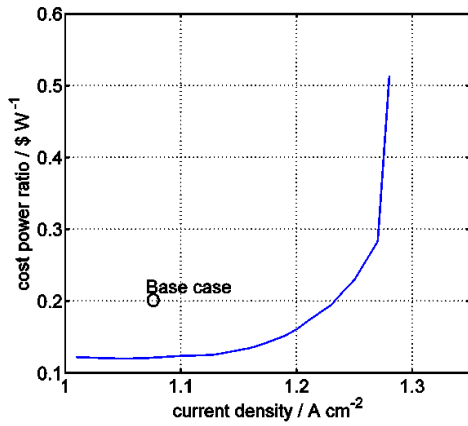


Fig. 9. Pareto curve for multi-objective optimization of catalyst layer at the voltage of 0.6 V: as term of cost power ratio vs. current density.

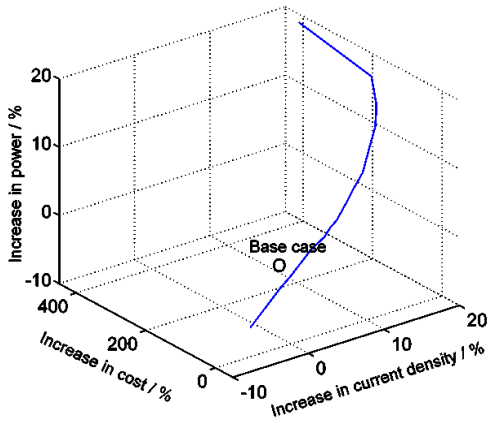


Fig. 10. Pareto curve as term of current density, cost, and power at the voltage of 0.6 V.

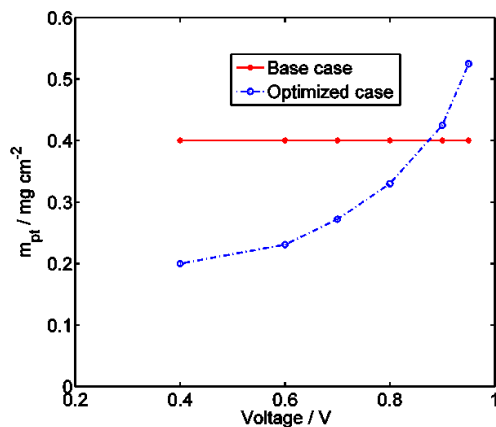


Fig. 11. Comparing the amount of platinum loading in both the base case and optimized case.

A Pareto curve for the three objective functions of current density, cost and power is drawn at the voltage of 0.6 V in Fig. 10. The diagram is drawn three-dimensionally in order to compare those

variations caused by price, although the two functions of current density and power are not independent. As shown, the slopes of the current and the power are smooth, but the slope of the cost will be steep, particularly at the high currents; so even if the cost increases so much at higher currents, the current in these conditions cannot increase more than 20 %.

In Fig. 11, the platinum loading is compared in the base case and optimized case. As can be seen, a large amount of platinum is necessary due to the importance of activation overpotential caused by beginning the reaction at the high voltages. Even the Pt loading in the optimized case is higher than the base case. Conversely, less platinum is required at low voltages or high current densities because of the stronger effect of ohmic and mass transport losses. So, less platinum is consumed and costs are saved more significantly.

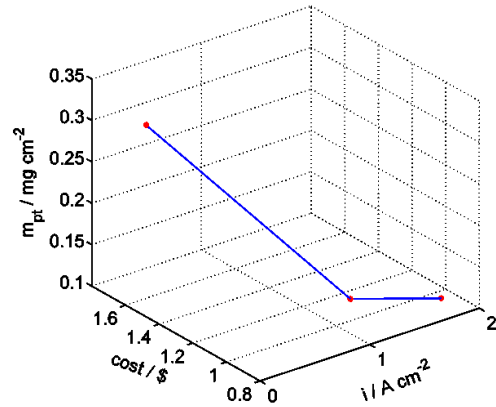


Fig. 12. Objective functions vs. platinum loading (m_{Pt}).

In this section, objective functions of current density and cost are plotted vs. two optimized decision variables at the voltages of 0.8, 0.6 and 0.4 volts. In Figs. 12, 13, current density is considered the same as base case and cost is optimized.

In Fig. 12, objective functions are plotted vs. platinum loading (m_{Pt}). Platinum loading has a direct and strong effect on CL cost, so usage of it must be reduced as far as possible. As shown, at low current densities, large amounts of platinum are necessary due to the activation overpotential caused by beginning the reaction that leads to increase in cost. Conversely, for the same reasons as in Fig. 11, less platinum is required at high current densities, so the cost decreases.

In Fig. 13, objective functions are plotted vs. ionomer volume fraction (l_{mc}). Ionomer content also directly effects CL cost, so usage of it must be reduced as far as possible. Ionomer volume fraction has two opposing effects on CL performance. Large

amounts of I_{mc} lead to reduced catalyst layer porosity, and as a result a decrease in the oxygen diffusion coefficient. On the other hand, according to Bruggeman's correction, the effective protonic conductivity increases, and hence CL performance increases. In high current densities, the effect of effective protonic conductivity dominates more clearly the effect of oxygen diffusion. Therefore, as shown, although more ionomer is used at high current densities, total cost is decreased.

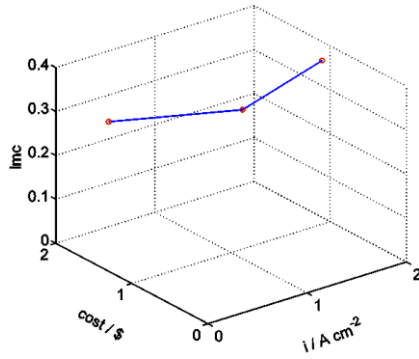


Fig. 13. Objective functions vs. ionomer volume fraction (I_{mc})

CONCLUSIONS

After the CL modelling has been conducted and its precision has been confirmed, catalyst layer optimization is performed. In this study, objective functions such as power, current density and CL cost are optimized under various conditions using the multi-objective optimization technique through the min-max method.

The results of this study were compared with those of Ref. [11] to validate the performed optimization. This comparison suggested that the results of optimizations are in good agreement at low currents, however when increasing the current the results diverge, caused by increasing the amount and the number of losses. In fact, this deviation is due to the number of objectives; that is, whether single-objective or multi-objective optimization is employed.

The Pt loading curve is drawn vs. current density and cost at the voltages of 0.8, 0.6 and 0.4 V. It determines that increasing a large platinum loading leads to small changes in current density where the platinum loading is larger than 0.4 mg cm^{-2} . Conversely, a large drop in the current density occurs through reducing Pt at small scales, where the platinum loading is less than 0.1 mg cm^{-2} . So the best compromise between the efficiency and the cost should be attained within this platinum range.

The performance curve demonstrates that in both cases, base case and multi-objective optimization case, although the increase in the CL performance is

higher at high currents, its relative increase is higher at low currents.

The Pareto curve demonstrates that to optimize the objectives of performance and cost of the CL at the voltage of 0.6 V, the trade-off between the cost and the performance is achieved, depending on the kind of application, when the current density increases in the range of 5 % to 12 %. In this range, the optimization objectives are met simultaneously; that is, the current is more than the base form and the cost is lower than the base form.

The platinum loading is compared in the base form and optimized form, where the large amount of platinum is necessary due to the importance of activation overpotential caused by beginning the reaction at high voltages. Even the Pt loading in the optimized case is higher than the base case. Conversely, less platinum is required at low voltages or high current densities. So, lower platinum is consumed and costs are saved more significantly.

Nomenclature

a	active surface area within the agglomerate / m^{-1}
a_{agg}	total external area of active sites of agglomerate per unit volume of CL / m^{-1}
A	total active area of agglomerate per unit volume of CL / m^{-1}
c	concentration / mol m^{-3}
CL	Catalyst Layer
D_{O_2}	diffusion coefficient / $\text{m}^2 \text{ s}^{-1}$
D_{K_n}	Knudsen diffusion coefficient / $\text{m}^2 \text{ s}^{-1}$
E_r	effectiveness factor
f _i	mass ionomer ratio
F	Faraday constant 96,485 /coulombs mol^{-1}
GDL	Gas Diffusion Layer
H_{O_2}	dimensionless Henry's constant
i	local current density / A m^{-2}
I_0	cell current density / A m^{-2}
k_1	reaction rate constant / m s^{-1}
L_c	catalyst layer thickness / m
$L_{g,c}$	volume fraction of GDL penetrating into the CL
$L_{m,c}$	volume fraction of ionomer phase in the CL
m_{Pt}	platinum mass loading / kg m^{-2}
m_c	carbon mass loading / kg m^{-2}
NO_2	molar flux of dissolved oxygen in the ionomer phase of an agglomerate
ODE	Ordinary Differential Equation
P	Pressure / Pa
r_{agg}	agglomerate radius / m
r_{Pt}	mass fraction of platinum to Pt/C articles
R	dissolved oxygen rate per unit of agglomerate / $\text{mol m}^{-3} \text{ s}^{-1}$
\bar{R}	universal gas constant 8.314 / $\text{J mol}^{-1} \text{ K}^{-1}$
s	liquid water saturation
T	temperature / K
W	weight
r, z	coordinate / m
δ_{agg}	ionomer film thickness, m
ϵ_{agg}	spherical agglomerate porosity
ϵ_{CL}	CL porosity
ϵ_g	GDL porosity
ϵ_i	volume fraction of ionomer
ϵ_s	volume fraction of solids
ϵ_v	
η	

ρ_c	volume fraction of voides
ρ_{Pt}	activation overpotential / V
σ	carbon density / kg m ⁻³
κ	platinum density / kg m ⁻³
ϕ	electronic conductivity / Sm ⁻¹
τ	protonic conductivity / Sm ⁻¹
	Thiele module
a	CL tortuosity
c	Subscriptions
agg	anode
O ₂	cathode
N	agglomerate
r	oxygen
l	Nafion
CL	radius
C	first-order reaction
ref.	catalyst layer
tot.	catalyst layer boundary
	reference condition
eff	total
*	Superscriptions
	effective
	concentration or radius ratio

REFERENCES:

1. A.A. Kulikovskiy, *Electrochim. Acta*, **130**, 826 (2014).
2. L. Xing, X. Song, K. Scott, V. Pickert, W. Cao, *Int. J. Hydrogen Energy*, **38**, 14295 (2013).
3. F.C. Cetinbas, S.G. Advani, A.K. Prasad, *J. Electrochem. Soc.* **161**, F803 (2014).
4. E. Goodarzi, M. Ziaei, E. Zia Hosseinipour, *Introduction to Optimization Analysis in Hydrosystem Engineering*, Springer, Switzerland, 2014.
5. D. Song, Q. Wang, Z. Liu, M. Eikerling, Z. Xie, T. Navessin, S. Holdcroft, *Electrochim. Acta*, **50**, 3347 (2005).
6. R. Madhusudana Rao, R. Rengaswamy, *Chem. Eng. Res. Des.* **84**, 952(2007).
7. W. Na, B. Gou, *J. Power Sources* **166**, 411 (2007).
8. S.M.C. Ang, D.J.L. Brett, S. Fraga, *J. Power Sources*, **195**, 2754 (2010).
9. S.M.C. Ang, S. Fraga, N.P. Brandon, D. Brett, *Int. J. Hydrogen Energy* **36**, 14678 (2011).
10. M. Secanell, R. Songprakorp, A. Suleman, N. Djilali, *Energy Environ. Sci.*, **1**, 378 (2008).
11. M. Srinivasarao, D. Bhattacharyya, R. Rengaswamy, S. Narasimhan, *Chem. Eng. Res. Des.*, **89**, 10 (2011).
12. N. Khajeh-Hosseini-Dalasm, M. Fesanghary, K. Fushinobu, K. Okazaki, *Electrochim. Acta*, **60**, 55 (2012).
13. A.A. Tahmasbi, A. Hoseini, R. Roshandel, *Int J Sustain Energ* , **34**, 283 (2015).
14. S.O. Mert, Z. Özçelik, *Int. J. Energy Res.*, **37**, 1256 (2013).
15. M.S. Feali, M. Fathipour, *Russ. J. Electrochem.*, **50**, 561 (2014).
16. D. Castagne, *Mathematical modeling of PEM Fuel Cell cathodes*, MS Thesis, Department of Chemical Engineering, Queen's University, Kingston, Ontario, Canada, 2008.
17. M. Moein-Jahromi, M.J. Kermani, *Int. J. Hydrogen Energy*, **37**, 17954 (2012).
18. W.R. Chang, J.J. Hwang, F.B. Weng, S.H. Chan, *J. Power Sources* , **166**, 149 (2007).
19. S. Obut, E. Alper, *J. Power Sources* **196**, 1920 (2011).
20. R. Othman, A.L. Dicks, Z. Zhu, *Int. J. Hydrogen Energy* **37**, 357 (2012).
21. D.P. Wilkinson, J. Zhang, R. Hui, J. Fergus, X. Li, *Proton Exchange Membrane Fuel Cells: Materials Properties and Performance*. Taylor and Francis Group, USA, 2010.
22. G.P. Rangaiah, A. Bonilla-Petriciolet. *Multi-objective optimization in chemical engineering: developments and applications*, John Wiley & Sons, 2013.
23. Y. Collette, P. Siarry. *Multiobjective Optimization Principles and Case Studies*. Springer, New York, 2004.
24. S.O. Mert, Z. Özçelik, Y. Özçelik, I. Dinçer, *Appl. Therm. Eng.* , **31**, 2171 (2011).
25. O.B. Augusto, F. Bennis, S. Caro, *Pesquisa Operacional* ,**32**, 331 (2012).
26. E.B. Magrab, Sh. Azarm, B. Balachanran, J.H. Duncan, K.E. Herold, G.C. Walsh, *An Engineer's Guide to MATLAB with Applications from Mechanical, Aerospace, Electrical, Civil, and Biological Systems Engineering*. Third Edition, Prentice Hall, USA, 2011.
27. *Optimization Toolbox of Matlab: User's Guide* (2011b). MathWorks Incorporated; 2011.

Determination of methane hydrate interfacial tension from measurement of induction time in methane hydrate crystallization

Alireza Azimi, Masoomeh Mirzaei , Seyed Mostafa Tabatabaee Ghomshe

Department of Chemical Engineering, Mahshahr Branch, Islamic Azad University, Mahshahr, Iran.

Submitted

Abstract: In this work the interfacial tension between methane hydrate and water at various temperatures, pressures and solution concentrations is determined. The Induction time in methane hydrate crystallization has been evaluated in a batch system and correlation of the induction time with the solution supersaturation has been drawn by the Classical Nucleation Theory (CNT). The results have shown that the induction time decreases with increasing solution concentration at any constant temperature while the interfacial tension increases with rising temperature. Experimental values of Hydrate – Water interfacial tension are evaluated 1.22, 1.957 and 4.16 at three temperatures as 273.15, 273.65 and 274.65 K. An empirical correlation has been used and the order of nucleation is thereby obtained to be 1.189.

Key words: Interfacial tension, Methane hydrate, Induction time, Crystallization, Nucleation

INTRODUCTION

Gas hydrates are ice-like compounds that are formed by a mixture of water and light gas molecules such as methane, ethane, CO₂, H₂S, Ar, Kr, Xe, ... at low temperatures and high pressures [1-4]. The crystal lattice is made up of water molecules which are strongly hydrogen bonded "host" and gas molecules "guest" that are engaged in cavities formed in the clathrates [5,6]. Gas hydrates are non-stoichiometric crystalline inclusion compounds comprised of approximately 85 mol% water, 15 mol% guest gas, and thermodynamically stable at low temperatures and high pressures [7]. Kinetics models proved that gas hydrate formation in general is a crystallization process including nucleation and growth steps [8-10]. Nucleation is an interfacial phenomenon, so interfacial properties like interfacial tension has a high effect on the rate of hydrate formation [11-13]. In this work the interfacial tension between methane hydrate and water has been determined by measurement of the induction time in methane hydrate crystallization. Induction time of crystallization depends on the temperature and the level of supersaturation [14]. In general, the induction time decreases with increasing supersaturation and rising temperature [15,16].

PROBLEM DESCRIPTION

A relation to evaluate the nucleation rate in supersaturated solutions is derived from classical nucleation theory (CNT) by Mullin [17]:

$$B = B^0 \exp\left(-\frac{\Delta G}{kT}\right) \quad (1)$$

In Equation (1) ΔG is the change of Gibbs free energy between a small particle of the dissolved substance and the solute in solution including two terms: the surface free energy and the volume free energy.

$$\Delta G_s = 4\pi r^2 \gamma, \quad \Delta G_v = \frac{4}{3}\pi r^3 g_v \quad (2)$$

Considering the maximum value of ΔG at the critical nucleus size, Mullin [17] derived Gibbs-Thomson relation to calculate the nucleation rate.

$$B = B^0 \exp\left(-\frac{16\pi \gamma^3 V_m^2}{3(kT)^3 \ln S^2}\right) \quad (3)$$

Where $S = C/C^*$ is supersaturation, k is Boltzmann constant by value of $k = 1.3805 \times 10^{-23} \frac{J}{K}$, T is temperature, γ is the interfacial tension and V_m is the molecular volume of methane which is calculated from following equation:

$$V_m = \frac{z R T}{P N_A} \quad (4)$$

In Equation (4) z is the compressibility factor of methane, $R = 8.314 \frac{N.m}{mol.K}$ is the gas constant and N_A is the Avogadro's number.

The induction time is assumed to be inversely proportional to the nucleation rate, $t_{ind} \propto \frac{1}{B}$, which gives Mullin [17] and Ghader [14]:

$$t_{ind} = K \exp\left(\frac{16\pi\gamma^3 V_m^2}{3(kT)^3 (\ln S)^2}\right) \quad (5)$$

$$\ln(t_{ind}) = \ln(K) + \left(\frac{16\pi\gamma^3 V_m^2}{3(kT)^3 (\ln S)^2}\right) \quad (6)$$

Which means that at different temperatures, a plot of $\ln(t_{ind})$ versus $\frac{1}{T^3 (\ln S)^2}$ should yield a straight line with slope m defined as:

$$m = \frac{16\pi\gamma^3 V_m^2}{3k^3} \quad (7)$$

The interfacial tension between the nuclei and solution is therefore:

$$\gamma = k \left(\frac{3m}{16\pi V_m^2}\right)^{\frac{1}{3}} \quad (8)$$

EXPERIMENTAL INVESTIGATION

Material

Required methane with 99.995 mol% purity was prepared by the Technical Gas Services co. and distilled water was applied as pure water.

Apparatus

The pressure cell made of 316 stainless steel has a volume of about 460 ml. For visual observation a glass window has been placed in the hydrate cell and an ultramodern CCD camera with high focus power is used for monitoring gas hydrate formation.

The data from camera is sent to a computer using Honestech TVR software. The stirring rate of vessel is 60 rpm. Cooling of the vessel is supplied by

ethanol circulation in the jackets (Figure 1). To monitor and report temperature in different places into the shell of the cell three thermocouples are used with $\pm 0.1K$ accuracy at 0.1s time intervals. The accuracy and time interval of cell pressure measurement are 0.1 bar and 0.1 s, respectively. Schematic diagram of the experimental apparatus is shown in Figure (1).

Procedure

At first, the cell was washed with deionized water. To ensure that all parts of set up is free of any air; inner parts were evacuated with a vacuum pump. 100 ml of deionized water was entered into the cell at room temperature and atmospheric pressure. To achieve the desired pressure the cell the cell was charged with methane. After the cell was pressurized, the system was cooled. Initial temperature is about 5K below the anticipated hydrate-formation temperature. As temperature and pressure were monitored continuously, initial nucleation was eventually verified through visualization of the cell content. This was further confirmed by the fact that at the instance of hydrate formation, migration of methane to the solid phase leads to the release of the crystallization energy and a drop in methane concentration in water. This in turn causes a more tendency of methane to be absorbed in water from the gas and the release of absorption energy. The overall outcome is a relatively sudden decrease in the vessel pressure and an increase in the temperature. These events can only be observed if the rate of heat transfer to the coolant ethanol is temporarily kept at nearly zero when nucleation is about to take place, which turns the procedure into one which needs lots of delicate control. Results are later analyzed through

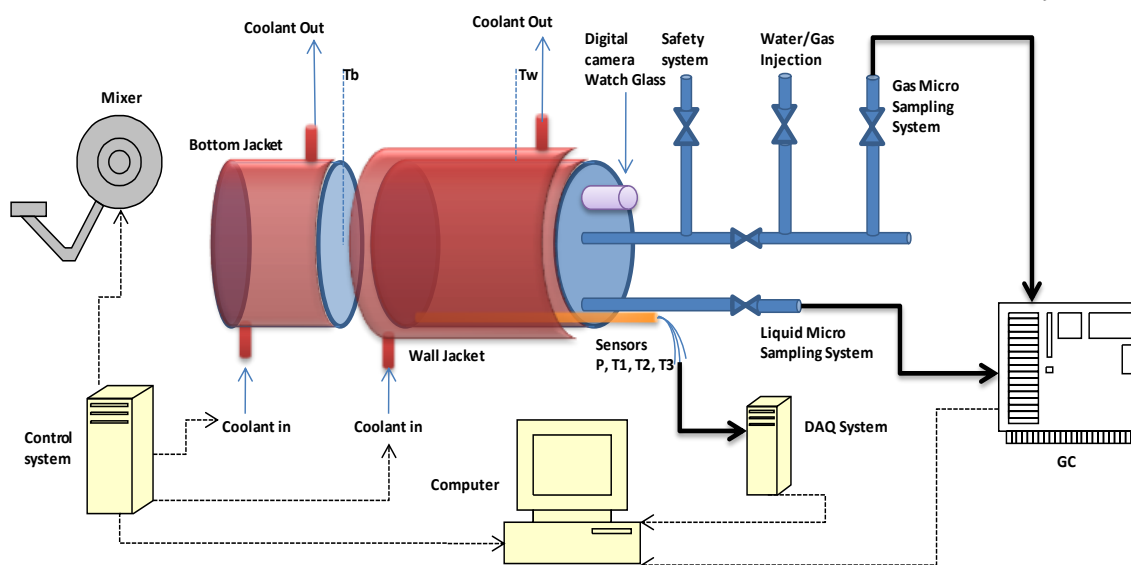


Fig.1. Schematic diagram of experimental apparatus

study of the temperature and pressure profiles and the judged moments of nucleation are compared with results of the visual observations.

RESULTS AND DISCUSSION

Cell temperature and pressure were monitored and measured throughout the experiments. Using these data, the effect of parameters such as supersaturation and temperature on the induction time has been investigated. The cell pressure-temperature profiles during one of the experiments have been drawn in Figure 2. The first section of Figure 2 is shown in Figure 3 in larger scale to help determining the induction time from temperature and pressure profiles with higher accuracy. As seen in Figure 3, at the first stages of the experiment, while cooling the cell, a decline in the pressure is observed which can be attributed to lowering the temperature

and gas dissolution in water. These drops in temperature and pressure approach a minimum as the vessel temperature comes close to that of the coolant ethanol. Under this delicately controlled condition, when the methane concentration in water reaches a maximum value and a peak in its concentration and supersaturation in the aqueous media is achieved, the pressure and temperature profiles become flat. This condition will remain unchanged till the eruption of nucleation. The induction time will then be accurately measured by determination of the duration of constant temperature and pressure in this procedure. In each experiment, the instance of nucleation has been determined both by monitoring the end of the flat period in the temperature-pressure profiles from Figure 3 and also by the turbidity observed by the visual apparatus. A comparison of the results is shown in Figure 4.

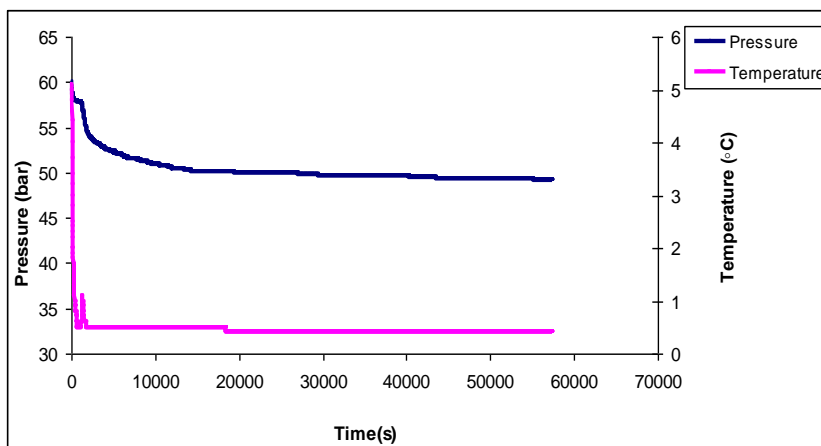


Fig. 2: Cell pressure and temperature profiles for Run (7).

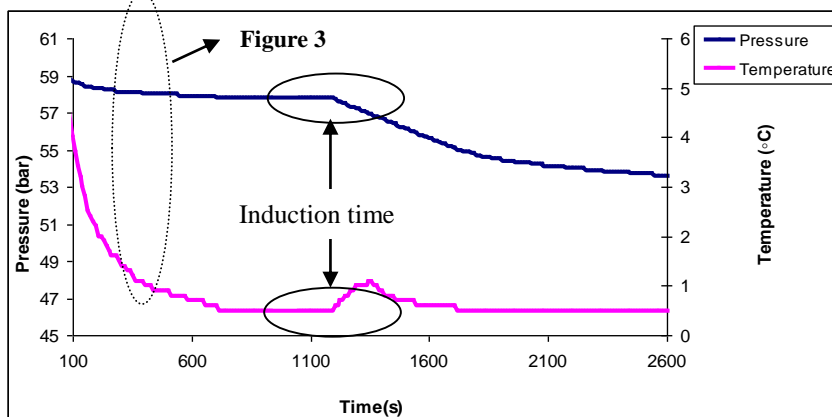


Fig. 3. Induction time determination from the pressure and temperature data for Run (7).

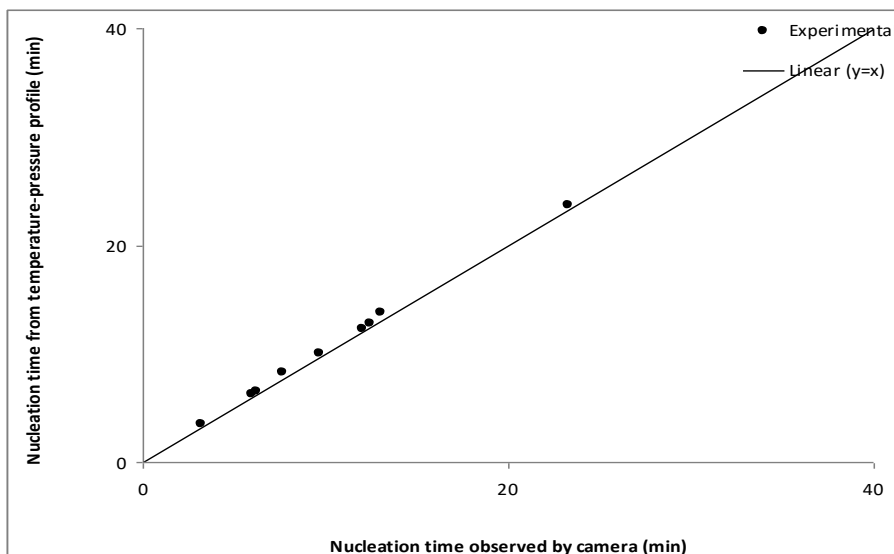


Fig. 4. Comparison of the nucleation time determined by visual observation and pin-pointed from the temperature-pressure profile.

In this figure, the vertical axis is nucleation time determined by temperature-pressure profiles and the axial axis is the nucleation time observed by camera. By drawing a straight line from the origin with the slope 1, it can be seen that the occurrence of nucleation phenomenon can be determined by both methods equally well.

SUPERSATURATION EFFECT

Solubility of methane hydrate in water has been gathered from literature [18]. Results show that the

induction time decreases with increasing supersaturation, satisfying the general trend in Equation (6). In order to compare the experimental induction time results with predictions from the CNT at constant temperature $\ln t_{ind}$ was plotted against $\frac{1}{(\ln S)^2}$. Figure 5 illustrates that a linear relation can be concluded. The values of R^2 of the linear regression are 0.959, 0.967, and 0.960, respectively.

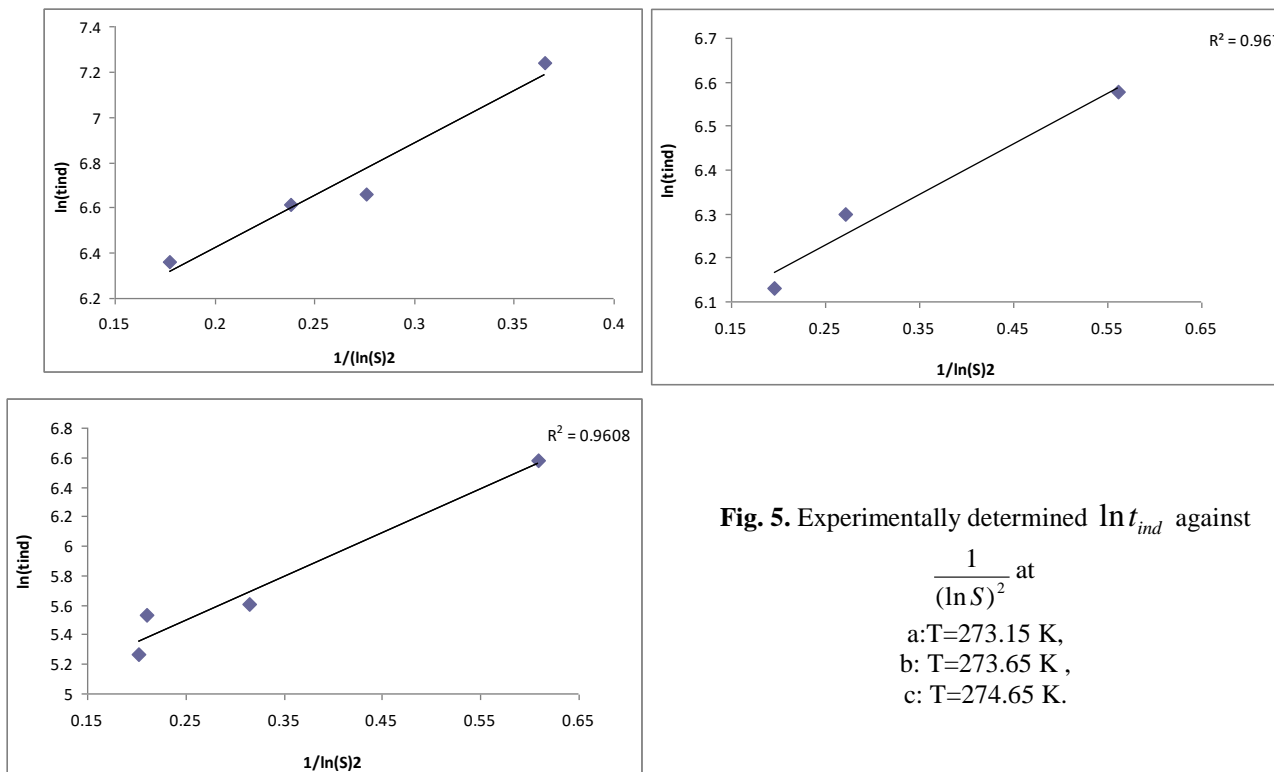


Fig. 5. Experimentally determined $\ln t_{ind}$ against

$$\frac{1}{(\ln S)^2} \text{ at}$$

a: T=273.15 K,
 b: T=273.65 K,
 c: T=274.65 K.

Determination of the interfacial tension

As Equation (6) shows, the classical nucleation theory (CNT) predicts that at different temperatures a linear relation between $\ln t_{ind}$ and $\frac{1}{T^3(\ln S)^2}$ (with slope m) should exist. All induction time data of

methane hydrate at $T=273.15$ K, $T=273.65$ K and $T=274.65$ K are presented in Figure (6) and the prediction of the Classical Nucleation Theory is presented by the slanted line.

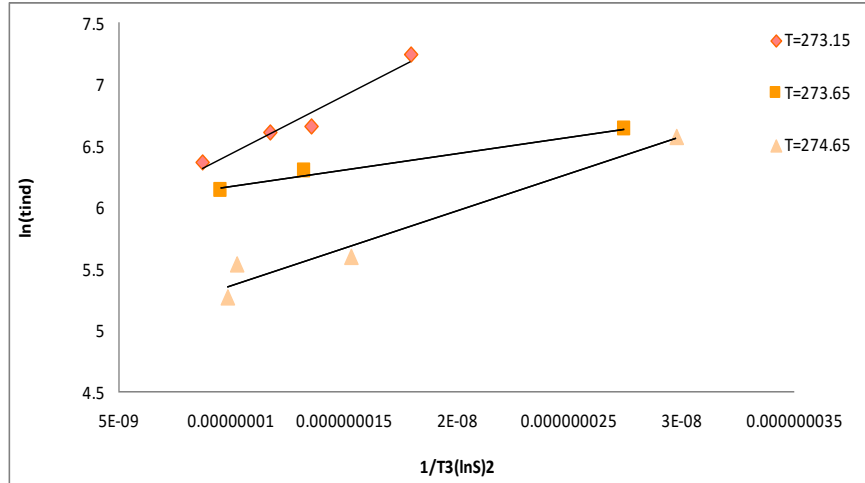


Fig. 6. Measured data of $\ln t_{ind}$ vs. $\frac{1}{T^3(\ln S)^2}$ at different temperatures.

A linear relation is observed. Equation (8) has been used to determine the values of the interfacial tension. The estimated interfacial tension values at different temperatures are shown in Table (1). The results show that Interfacial tension value is rising with temperature increasing. The temperature dependence of the solubility of gas in liquid and the Induction time is the main cause of the interfacial tension variation by temperature.

The findings can be compared with the results given by Equations (9) and (10).

$$\gamma = 0.414k.T(C_s.N_A)^{\frac{2}{3}} \ln\left(\frac{C_s}{C^*}\right) \text{ Mersmann [19]} \quad (9)$$

$$\gamma = k.T.V_m^{-\frac{2}{3}}(0.25)(0.7 - \ln x^*), \quad \text{cf. Bennema and Sohnel [20] (10)}$$

In Equation (9) C_s is concentration of methane hydrate in the liquid phase, C^* is the solubility of methane hydrate in water. The experimental values of C^* are estimated 0.059, 0.061 and 0.064 at three temperatures as 273.15, 273.65 and 274.65 K respectively [18]. In equation (10) x^* is the solubility mole fraction of methane hydrate in water is calculated by values of C^* . The results of Equations (9) and (10) are also shown in Table. 1 for comparison. It is found that the values of the interfacial tension obtained in this work compare with predictions by Equation (10) rather more

satisfactorily than by Equation (9). It may be attributed to the presence of the term $V_m^{-\frac{2}{3}}$ in both Equations (8) and (10). In Figure (7) the interfacial tension values at different temperatures and levels of supersaturation are shown. It is obvious that changes in supersaturation have little effect on the interfacial tension.

Table 1. Interfacial tension of methane hydrate at different temperatures as estimated by applying experimental results into the CNT and values calculated using Equation (9) and Equation (10).

Temperature (K)	Experimental γ (mN/m)	Equation (9) γ (mN/m)	Equation (10) γ (mN/m)
273.15	1.22	0.011176	9.378
273.65	1.957	0.0134	9.4394
274.65	4.16	0.0149	9.4898

Determination of the order of the nucleation

An empirical correlation is used to correlate the nucleation rate with the level of supersaturation.

$$B = K_b S^n \quad (11)$$

$$t_{ind} = K S^{-n} \quad (12)$$

$$\ln t_{ind} = \ln K - n \ln S \quad (13)$$

Fitting a straight line to the data of $\ln t_{ind}$ vs. $\ln S$ yields the value of the nucleation order.

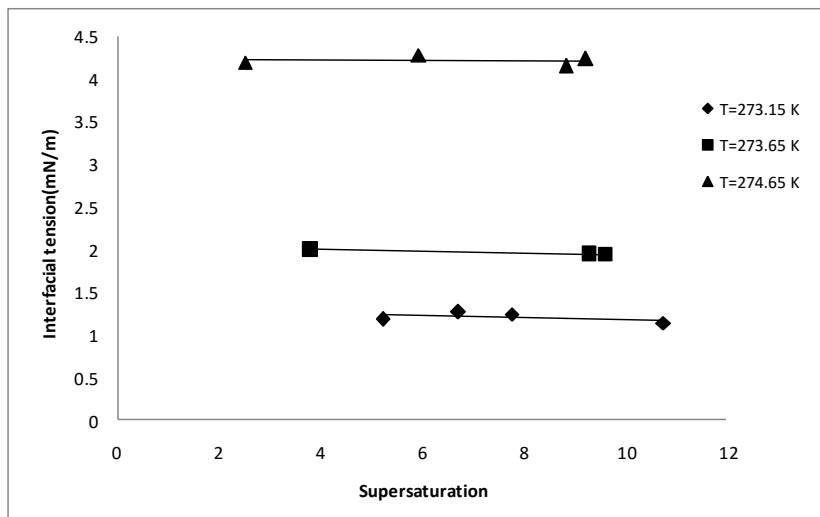


Fig. 7. Interfacial tension values at different temperatures and supersaturation values.

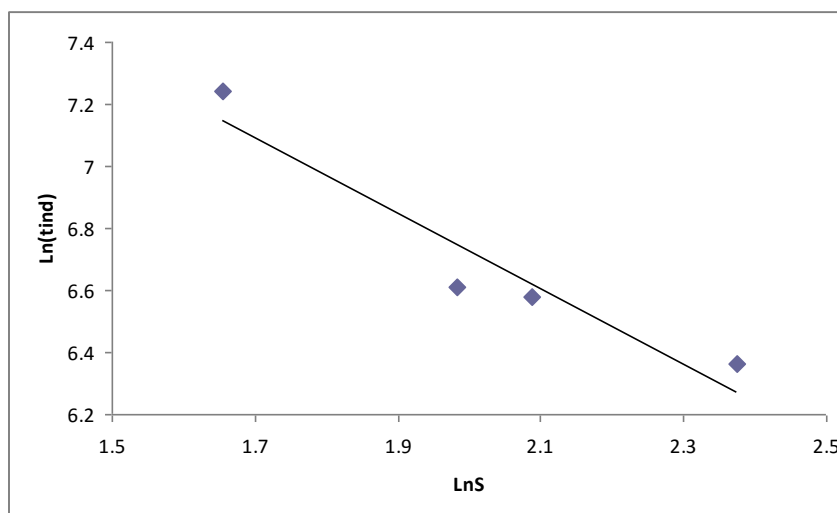


Fig. 8. A plot of Eq. (13) for calculation of the nucleation order at T=273.15 K.

In Figure 8, $\ln t_{ind}$ is plotted against $\ln S$ for calculation of the nucleation order at $T = 273.15$ K. The values of R^2 of the linear regression are 0.938 and $n = 1.189$.

CONCLUSION

The induction time of methane hydrate crystallization is measured at various temperatures and supersaturation values. The experimental data indicate that the induction time decreased with increasing supersaturation at each constant temperature. The induction time data have satisfactorily been fitted into the Classical Nucleation Theory and the interfacial tension between methane hydrate and the solution has thereby been determined at 3 temperatures. The interfacial tension has been found to increase with rising temperature but changes in supersaturation has little effect. The nucleation

order has also been determined by applying the results into the power law correlation for nucleation.

Acknowledgement: This paper was extracted from a research project entitled "Modeling of methane hydrate crystallization using particle size distribution". Financial assistance from the Islamic Azad University - Mahshahr Branch is gratefully acknowledged.

Nomenclature

- B, $Number/m^3.s$ - nucleation rate
- B^0 , $Number/m^3.s$ - pre-exponential value
- C, mol/L - concentration
- C_s , mol/L - concentration of hydrate in the liquid phase
- C^* , mol/L - saturation concentration
- k, $J/(mol.K)$ - Boltzmann constant
- K, (-) - proportionality constant

M , kg/mol	- molecular mass
N_A , Number/mol	- Avogadro's number
r , m	- radius of nucleus
t_{ind} , s	- induction time
V_m , m ³	- molecular volume
ΔG , J	- excess Gibbs free energy factor

Greek Symbol

γ , mN/m - interfacial tension

Superscript

* - saturation

Subscript

S - solid

REFERENCES

1. E. D. Sloan, C. A. Koh, "Clathrate Hydrates of Natural Gases", Taylor & Francis, CRC Press, 2008.
2. J. D. Lee, R. Susilo, and P. Englezos, *Chem. Eng. Sci.* **60**,4203, 2005.
3. H. Ganji, M. Manteghian, K. Sadaghianizadeh, M. R. Omidkhah, H. RahimiMofrad, *Fuel Process.Technol.* **86**, 434, 2007.
4. Y. F. Makogon, *J. Nat. Gas. Sci. Eng.* **2**, 49, 2010.
5. C. Y. Sun, G. J. Chen, *Fluid Phase Equilib.*, **242**, 123, 2006.
6. C. F. Ma, G. J. Chen, F. Wang, C. Y. Sun, T. M. Guo, *Fluid Phase Equilib.*, **191**, 41, 2001.
7. M. Erik, M. Freer, M. S. Selim, E. D. Sloan, *Fluid Phase Equilib.* p **185**, 65, 2001.
8. M. Clarke, and P. Bishnoi, "Measuring and modeling the rate of decomposition of gas hydrates formed from mixtures of methane and ethane", *Chem. Eng. Sci.* **56**, 4715, 2001.
9. P. Englezos, N. Kalogerakis, P. D. Dholabhai, P. R. Bishnoi, *Chem. Eng. Sci.* p **42**, 2647, 1987.
10. H.C. Kim, P.R. Bishnoi, R. A. Heidemann, S.S.H. Rizvi, *Chem. Eng. Sci.*, **42**, 1645, 1987.
11. H. Luo, C. Sun, Q. Huang, B. Peng, G. Chen, *J. Colloid. Interface. Sci.*, **297**, 266, 2006.
12. M. Lin, G.J. Chen, C.Y. Sun, *Chem. Eng. Sci.*, **59**, 44, 2004.
13. Z.G. Sun, R.Z. Wang, R. S. Ma, "Natural Gas Storage in Hydrates with the Presence of Promoters", *Energy. Converse. Manage.* **44**, 27, 2003.
14. S. Ghader, M. Manteghian, M. Kokabi, R. Sarraf, *Chem. Eng. Technol.*, **30**, 8, 2007.
15. C.Y. Tai, W.C. Chien, *J. Cryst. Growth*, **237**, 2142, 2002.
16. J. W. Mullin, Zacek, *J. Cryst. Growth*, **253**, 515, 2003.
17. J.W. Mullin, "Crystallization" ,Butterworth–Heinemann, Oxford, 2001.
18. P. Tishchenko, C. Hensen, K. Wallmann, C. S. Wong, *Chem. Geology*, **219**, 37, 2005.
19. A. Mersmann *J. Cryst. Growth*, **102**, 841, 1990.
20. P. Bennema, O. Sohnel, *J. Cryst. Growth*, **102**, 547, 1990.

The effects of anionic surfactants on the strength and environmental impacts of foamed concrete

Amir Hossein Fani^{*}, Afshin Pourafshar

Department of Civil Engineering, College of Engineering, University of Tehran, 16-Azar Str., Tehran, Iran

Received June 26, 2015, Revised September 10, 2015

Foamed concrete is an all-around material that can be applied in a wide range of construction projects due to its low self-weight, high workability, controlled low strength, excellent thermal properties, etc. Foamed concrete is produced by injecting preformed stable foam or by adding a special air-entraining admixture known as a foaming agent such as synthetic surfactants into a base mix of cement paste or mortar. The hydrophilic and hydrophobic structure of the surfactant molecules helps entrain air bubbles and stabilizes them in the fresh cement paste. The aim of this paper is to investigate the effects of two types of anionic surfactants on the mechanical and physical properties and, moreover, the environmental impacts of foamed concrete. Additionally, the potential of polypropylene fibers in foamed concrete to enhance compressive and tensile strength is examined. Twenty-four different mixtures were cast with two types of anionic surfactant foaming agents (with densities of 960 and 1200 kg/m³), Portland cement contents between 350 and 450 kg/m³, two ratio of water to cement (w/c), and polypropylene fibers. The results of compressive and tensile strength, water absorption, and heat transfer coefficient tests are reported and analyzed.

Keywords: Foamed concrete; Surfactant; Mechanical properties; Environmental impact

INTRODUCTION

Foamed concrete is a kind of lightweight concrete which is lighter than normal concrete by mixing foams like surfactant foaming agents into cement slurry. The difference between foamed concrete and normal concrete is the use of aggregate in the foam concrete is eliminated and been replaced by the homogeneous cells created by air in the form of small bubble which utilize a stable air cell structure rather than tradition aggregates [1].

Foamed concrete is a highly workable, low-density material which can incorporate up to 50 per cent entrained air. It has a number of attractive characteristics. It requires no compaction, but will flow readily from an outlet to fill restricted and irregular cavities, and it can be pumped over significant distances and heights. Moreover, it has suitable compressive and tensile strength regarding its application and significant reduction of overall weight results in saving structural frames, footing or piles [2, 3]. Foamed concrete has good thermal and acoustic insulation as its structure is porous due to usage of surfactant foam [4]. Liquid water absorption into foamed concrete is low, while retaining high water vapor permeability. Freez-thaw resistance is excellent [5]. Foamed concrete is used for a variety of applications, ranging from thermal insulation and fire protection to void-filling and building elements with successively increasing

density and strength requirements [6, 7].

Foamed concrete is made from Portland cement, water, foaming agent, and other additives if required. Portland cement is a hydraulic material which shall consist of at least two-thirds by mass of calcium silicates (CaO-SiO₂), the remainder consisting of aluminium and iron containing clinker phases and other compounds. The ratio of CaO to SiO₂ shall not be less than 2. The magnesium oxide content (MgO) shall not exceed 5.0% by mass [8].

Synthetic or protein-based foaming agents (surfactants) can be used to produce foam. In this study, we perform tests using two types of synthetic surfactant foaming agents. The chemical composition of a surfactant must be stable in the alkaline environment of concrete. Foam bubbles are formed under the condition where air can be flowed into the solution through stirring or air injection after reducing the surface tension of solution with the surfactant. The surface tension of water is generally 72~73 mN/m but the surface tension of solution with the surfactant lowers to 40~50 mN/m so foam bubbles are easily formed [9, 10].

Synthetic surfactants are classified into four main types according to the nature of their hydrophilic group, i.e. that part of the molecule that is soluble in water. Figure 1 shows four types of surfactants and their structures. Hydrophilic and hydrophobic nature of the surfactant molecules helps entrain air bubbles and stabilizes them in the fresh cement paste [11].

To whom all correspondence should be sent:
E-mail: amir.fani@ut.ac.ir

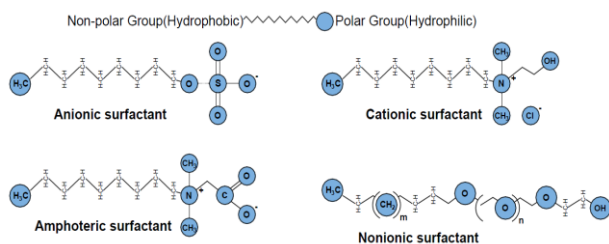


Fig 1. Classification and chemical structure of surfactants

There are many studies in the literature on foam concrete in terms of foaming agents, constituent materials, mix proportioning, production methods, and fresh and hardened properties of foam concrete [12]. A description of commonly used natural material-based and synthetic foaming agents have been presented by Valore [13], Taylor [14] and Laukaitis et al [15]. Du and Folliard [16] attempted to provide a framework for understanding the fundamental aspects of air entrainment in concrete. An investigation was carried out by Nambiar and Ramamurthy [17] on characterizing the air-void structure of foam concrete by identifying few parameters and influence of these parameters on density and strength. Additionally, Cui-hua [18] discussed the effects of the amount of surfactants on improving foam stability using change of foaming times and foam volume along with time as the evaluation indexes for performance of the foaming agent.

Puttappa and Ibrahim [19] designed 27 mixtures of foamed concrete and carried out an experimental and analytical study to evaluate the mechanical properties of lightweight foamed concrete. Chindapasirt and Rattanasak [20] and Nambiar and Ramamurthy [21] presented the shrinkage behavior of preformed foam concrete for the influences of basic parameters such as density, moisture content, composition like filler-cement ratio, levels of replacement of sand with fly ash, and foam volume. Moreover, mechanical, thermal insulation, thermal resistance and acoustic absorption properties of geopolymer foamed concrete were tested and analyzed by Zhang et al. [22]. In addition, Brady et al. [6] and Tian et al. [23] discussed the application of foamed concrete in construction, geotechnical and roadway projects.

This paper examines the effects of two types of anionic surfactants on the mechanical and physical properties and the environmental impacts of foamed concrete. The environmental impacts are investigated in terms of energy consumption. Moreover, the potential of polypropylene fibers in foamed concrete to improve compressive and tensile strength is studied. Twenty-four different mix-

tures were cast with two types of anionic surfactant foaming agents (with densities of 960 and 1200 kg/m³), Portland cement contents (350, 400 and 450 kg/m³), the ratio of water to cement (w/c) of 0.5 and 0.55, and polypropylene fibers. The results of compressive and tensile strength, water absorption, and Heat transfer coefficient tests undertaken in this study are reported and analyzed in order to evaluate the influence of surfactants and other factors.

EXPERIMENTAL METHOD

The best method for evaluating the performance of new mixtures is conducting tests which can assess the properties of the mixtures. In this paper, we carry out a laboratory study to measure the strength, durability and environmental criterion of foamed concrete. The compressive strength, indirect tensile strength, water absorption, and heat transfer coefficient tests are performed to analyze the properties of the mixtures.

Materials

Foamed concrete typically consists of cement, water, foaming agent and other additives. The cement used in this study is Portland cement type II of Tehran meeting Iran standard specification No. 389 ISIRI [24]. Portland cement type II in Iran is used to produce concrete which the medium hydration heat is required for and the sulphate attack is in the moderate range. This kind of cement is applicable in all concrete structures and in soil and water environments in which sulfate ion concentration is relatively low.

The quality of water in concrete is significant in view of the fact that the impurities in water may affect the cement setting and also have an adverse effect on the strength of concrete. As a general rule, the water with the PH level between 6 and 8 and without salty taste can be applied for constructing concrete. To avoid any possible errors in the mixtures, distilled water with electrical conductivity (EC) of 8.5 to 11 μ Siemens/cm, total dissolved solids (TDS) about 9.5 to 11 ppm, the maximum amount of silica (SiO₂) equal to 0.105 ppm, and PH level about 6.5 to 7.5 is used for the mixtures.

In this study, polypropylene fibers are applied to prevent shrinkage and cracking of foamed concrete at early ages (plastic shrinkage) in some mixtures. Polypropylene fibers are used to obtain a much better and stable surface and more resistant piece of foamed concrete. It reduces the danger of micro cracks greatly. It predicts that this increases the lifetime of the foamed concrete specifically where this is exposed to changing weather condition. The half

of mixtures are constructed by polypropylene fibers with a short cut of 12 mm and the ratio of 0.5 kg/m³.

Hydrophilic and hydrophobic structure of the surfactant molecules helps entrain air bubbles and stabilizes them in the fresh cement paste. Surfactant molecules, defined as surface-active agents, consist of a hydrophobic and a hydrophilic moiety that are clearly separated in the molecular structure. The polar part engages in electrostatic interactions (hydrogen bonding, dipolar interactions, ionic bonding etc.) with surrounding molecules, e.g. water and ions. The non-polar part, on the other hand, associates with neighboring non-polar structures via hydrophobic and van der Waals interactions. In mixed foaming, the surface active agent is mixed along with base mix ingredients and during the process of mixing, foam is produced resulting in cellular structure in concrete [9].

Increase of surfactant concentration is not proportional to decline of surface tension and this is because the CMC (Critical Micelle Concentration) is consistent according to the surfactant. However, the molecular activity varies depending on the type of the surfactant so the surface tension differs as well. In this study, two types of anionic surfactants is used to construct the specimens and evaluate the effects of them on the properties of foamed concrete. The first surfactant foaming agent which is named as surfactant type A in this study has a density of 960 kg/m³, foaming agent dilution of 1:25, PH value of 7, and foam stability time of 35 minutes. In addition, the second anionic surfactant foam has a density of 1200 kg/m³, foaming agent dilution of 1:25, PH value of 7, and foam stability time of 45 minutes. It is named as surfactant type B in the production of the specimens of this study.

Laboratory equipment and constructing specimens

Laboratory equipment required for constructing foamed concrete mixtures include foam generator, foamed concrete mixer which has a horizontal axis of rotation, laboratory oven to dry samples, caliper, molds, laboratory balance, and curing pond. After removing the specimens from the molds, they are stored in a saturated limewater to achieve the desired properties for its intended use. The curing pond is kept at a temperature of 25°C.

As mentioned before, 24 mixtures of foamed concrete are designed in order to carry out tests. 3 cube molds with dimensions of 15 cm, 3 standard cylindrical molds with a diameter of 15 and a height of 30 cm, 3 cube molds with dimensions of 10 cm, and 3 cubic molds with dimensions of

10×10×2 cm are employed for compressive strength, indirect tensile strength, water absorption and heat transfer coefficient tests, respectively. In general, weight ratio is not used for foamed concrete mixture because density of hardened concrete varies up to 10 percent. Therefore, foamed concrete is introduced usually based on the volume ratio. In this study, the design of all mixtures is volumetric. It means that the foam volume in the mixture is achieved regarding specifying volume of water and cement and ignoring the volume of polypropylene fibers (which are used in some mix designs) as shown in equations 1 and 2. Moreover, according to equation 3, the amount and volume of surfactant is achieved based on the mixing ratio of water and foaming agent. In the following equations, V_c , V_w , V_s and $V_{p,p}$ denote cement, water, surfactant, and polypropylene volume, respectively.

$$V_c + V_w + V_s + V_{p,p} = 1000 \text{ liter} \quad (1)$$

$$V_{p,p} \cong 0, V_c = \frac{M_c}{\rho_c}, V_w = \frac{M_w}{\rho_w} \quad (2)$$

$$V_s = 1000 - \frac{M_c}{\rho_c} - \frac{M_w}{\rho_w} \quad (3)$$

In general, in these 24 mixtures, two different types of anionic surfactant foaming agents which are introduced in the previous section, three cement content (350, 400 and 450 kg/m³), two water to cement ratio (w/c=0.5 and w/c=0.55), and two state for consume polypropylene (without polypropylene fibers and with polypropylene fibers) are used.

In order to construct laboratory specimens, three steps of preparation laboratory equipment and weighing raw material, mixing the material in the blender, and molding are required. In this study, the same mixing method is used for all 24 mixtures in the laboratory. In the first step, the blender is turned and the weighed water is poured into the blender. As the blender is running, the weighing cement is poured within 30 seconds. After pouring the cement completely in the blender, cement and water should be mixed completely for 90 seconds. At the end of 90 seconds, the surfactant foam is added slowly to the mixture by turning on the foam generator and simultaneously, blender is working and mixing when the foam poured in the blender tank.

Polypropylene fibers are used in the half of the designed mixtures. The time of adding the fiber into the blender tank is after the injection of surfactant into the blender. After completing foam injection into the blender, it is necessary to mix the materials for 4 minutes in the blender tank for homogenizing the mix. After making the mixtures, specimens should be cured. They are embedded in a saturated

limewater to achieve the desired properties for its intended use. The curing pond is kept at a temperature of 25°C.

Tests

Compressive strength tests

Since the compressive strength is one of the important properties of concrete and foamed concrete, information about this parameter has an important role in quality control of foamed concrete. Compressive strength testing in standard ASTM C869-91 [25] is done on cylindrical specimens of 30 × 15 cm and in the standard BSI [26] compressive strength tests is done on cube specimens of 15 cm. In this study, cube mold with dimensions of 15 cm is used to test the 28-day compressive strength. Before performing tests, the specimen dimensions must be measured with an accuracy of at least mm and then placed in a hydraulic jack. Loading speed is 50 KN per minute. Compressive strength is measured based on Equation 4.

$$f_c = \frac{P}{A_c} \quad (4)$$

In equation 4, P is the imposed force of hydraulic jacks on specimens in kg and A_c (in square centimeters) is side of the specimens placed under load. The compressive strength of the specimens (f_c) is obtained in terms of kg per square centimeter.

Tensile strength test

The purpose of this test is to determine the tensile strength of concrete by split method of cylindrical specimens. In this method by applying a diameter compressive force on the cylindrical specimen of foamed concrete placed horizontally between two pages of test device, tensile strength is determined by split method. Forms that can be used in this experiment are cylindrical which its height is twice its diameter. ASTM C496-96 [27] standard is used to test the tensile strength and the used molds have 15 cm of diameter and 30 centimeter of height.

Performing this test is required to use two pieces of steel with a thickness of 5 mm and a width of 2 cm and a length of at least 30 cm above and below the point of support on the jack. Loading speed in this test like the compressive strength is 50 KN per minute. The relationships between tensile stresses of split method and the applied load is shown in equation 5.

$$f_t = \frac{2 \times P}{\pi \times L \times D} \quad (5)$$

In this equation, f_t is splitting tensile strength in kg per square centimeter, P is the maximum load in kg, and L and D are the height and diameter of the cylindrical specimen, respectively.

Water absorption

The water absorption determination test is done by modeling ASTM C642 [28] standard on three cube specimens of 10 cm. After incubating in the water for 27 days, these specimens are transferred to the stove with ventilation a temperature of 45 °C. The dry weight of the specimens are measured after 14 days in a way that the obtained weight difference by weighing the interval of 24 hours is less than 0.1% of the weight of dried specimen. Afterwards, the dried specimens were immersed in water and the water level is within 5 ± 25 mm above the surface of specimens. Specimens at intervals of 1, 3, 24, 48 and 72 hours were taken out of the water and surface water were dried by a fabric and weighed. Thus, the percentage of absorbed water is determined regarding the weight of the dry specimen and the weight at mentioned time intervals.

Heat transfer coefficient

The high thermal resistance of foamed concrete in comparison with conventional concrete results in saving energy. To illustrate this feature in foamed concrete, heat transfer coefficient tests are conducted. Heat transfer coefficient expresses the rate of heat transfer between a solid surface and the liquid by convection. This test is performed on the simple method proposed by Raeisi et al. [29] on 3 specimens with dimensions of 10 × 10 × 2 cm. In the paper of Raeisi et al., a simple laboratory method is introduced to calculate the heat transfer coefficient of foamed concrete based on empirical formula to determine the heat flow.

RESULTS AND DISCUSSION

In this section, the results of laboratory tests, including compressive strength, indirect tensile strength, water absorption, and heat transfer coefficient, are reported and analyzed. All experiments are carried out in the laboratory of concrete and building materials of University of Tehran.

The 28-day compressive strength of foamed concrete is a function of some characteristics such as the type of surfactant foaming agent, the content of cement, water to cement ratio, and polypropylene fibers. In order to evaluate the effects of various factors on the compressive strength, a diagram of compressive strength according to dry density and water to cement ratio of 0.5 and 0.55 is plotted in figures 2-1 and 2-2.

The effects of the type of surfactant and polypropylene fibers on the compressive strength are shown in Figures 2-3 and 2-4. Figure 2-3 is related to the specimens containing surfactant foam type A and figure 2 is related to the foam type B. Moreover, in these figures, dashed lines present the mixtures containing fiber.

As shown in Figures 2.1 and 2.2, dry density and also the 28-day compressive strength are increased with the increase of the cement content in the mixtures. Changes in 28-day compressive strength in terms of dry density are shown by fitting a line to the water-cement ratio of 0.5 and 0.55. Comparison of Figures 2-1 and 2-2 shows that the increase in water to cement ratio from 0.5 to 0.55 reduces the 28-day compressive strength by 19.9 percent in average.

By comparing Figures 2-3 and 2-4, we find that the use of foam type B has a greater effect on improving the compressive strength and increases it by 8.3 percent. Moreover, figures 2-3 and 2-4 represent that using polypropylene fibers enhance the 28-day compressive strength significantly.

As shown in Figure 3, various factors influence the tensile strength of foamed concrete. Figures 3-1 and 3-2 are related to mixtures without fiber and with fiber, respectively. In these Figures, the tensile strength obtained by Brazilian cylinder test is fitted by a straight line according to dry density. As shown in figures, the increase in the cement content brings about higher dry density and tensile strength. Adding polypropylene fiber to the mixtures improves the tensile strength of all designs.

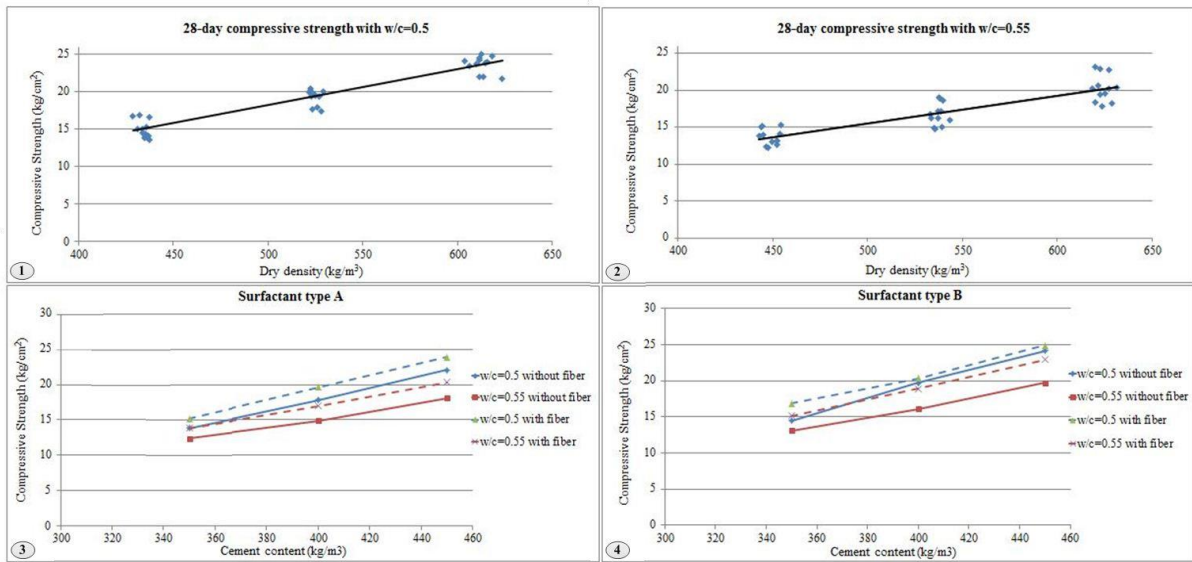


Fig. 2. Results of compressive strength test.

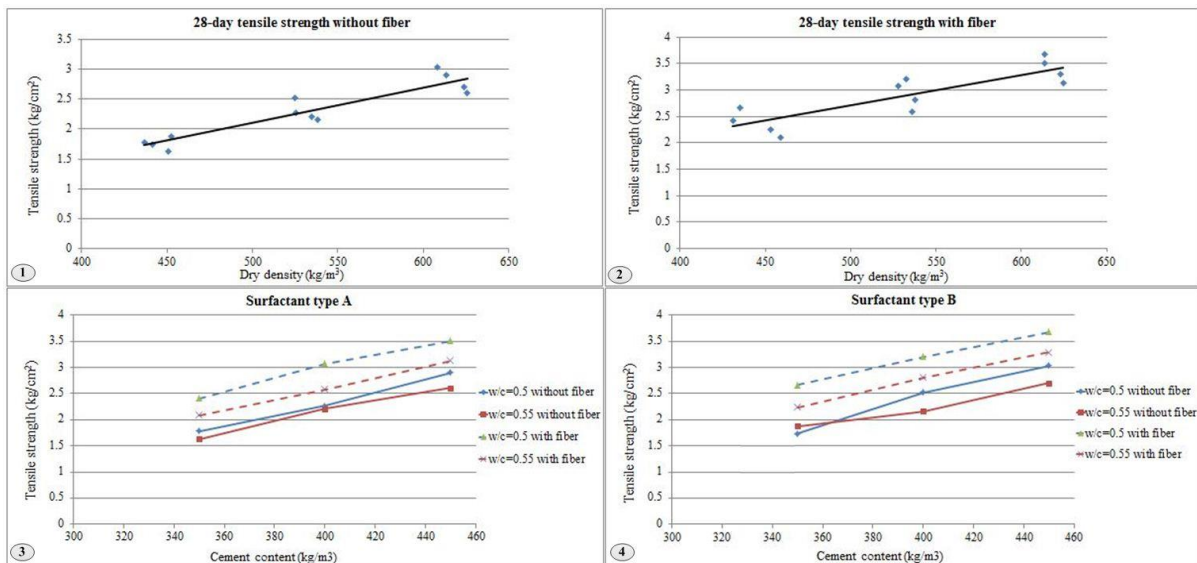


Fig. 3. Results of indirect tensile strength test.

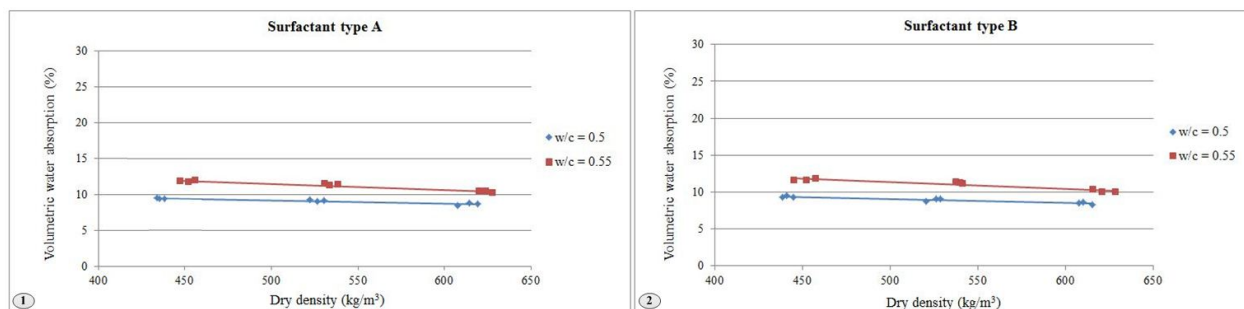


Fig. 4. Results of water absorption test.

Figures 3-3 and 3-4 are related to the specimens containing surfactant foam type A and type B, respectively. Additionally, dashed lines show the results of the specimens with fiber. The increase in water to cement ratio from 0.5 to 0.55 decreases the tensile strength by 10.6 percent. It can be concluded from figures 3-3 and 3-4 that the tensile strength of mixtures designed by surfactant type B is higher than type A by 5.8 percent. Moreover, adding polypropylene fibers has a positive effect on the tensile strength. The positive effect of using fibers in enhancing the tensile strength is more than the negative effect of the increase in the water to cement ratio.

ASTM standards accepted the volumetric water absorption criterion for determining the water absorption of specimens. In Figure 4, the effects of different factors such as the type of surfactant foam, content of cement, and water to cement ratio are displayed. According to the results in figure 4, the increase in density has little effect in reducing the volume of water absorption. The most important factor which influences the volumetric water absorption is water to cement ratio. As the ratio of water to cement is lowered from 0.55 to 0.5, the volumetric water absorption is also reduced by 22.7 percent. Additionally, the type of surfactant has approximately no effect on the water absorption.

Heat transfer coefficient of the mixtures containing surfactant type B is equal to 0.16 W/mk in average and foam type A is 0.18 W/mk. As can be concluded from the results, the performance of the mixtures with surfactant foam type B is slightly better than foam type A in terms of reducing energy loss, whereas the heat transfer coefficient of all mixtures is significantly lower than conventional concrete and natural lightweight aggregate concrete.

Heat transfer coefficient of natural lightweight aggregate concrete is approximately equal to 0.45 W/mk and conventional concrete is about 1.2 W/mk [29]. As a result, the performance of foam concrete in terms of thermal conductivity is much

better than conventional concrete due to its lower density. Therefore, it can be led to reduce energy loss significantly.

CONCLUSION

Foamed concrete is a vastly workable, low density material incorporating up to 50% entrained air. Surfactant foaming agents can be used to produce foam. Surfactant molecules, defined as surface-active agents, consist of a hydrophobic and a hydrophilic moiety and help entrain air bubbles and stabilize them in the fresh cement paste. In this paper, the mechanical properties and environmental impacts of foamed concrete under the influence of surfactant chemical foaming is studied. For this purpose, 28-day compressive strength, indirect tensile strength, water absorption, and heat transfer coefficient tests were conducted on 24 designed mixtures.

Two types of anionic surfactant foaming agents (type A and type B) were employed to design the foamed concrete mixtures. The compressive and tensile strength of the experimental specimens with surfactant type B were higher than type A by 8.3 and 5.8 percent, respectively. The specimens of both types of surfactants showed the same performance regarding water absorption. Additionally, the thermal conductivity of the specimens with surfactant type B were slightly better than type A, whereas the heat transfer coefficient of all mixtures is significantly lower than conventional concrete and natural lightweight aggregate concrete. For instance, heat transfer coefficient of the foamed concrete mixtures are roughly 3 times better than natural lightweight aggregate concrete which leads to considerable lower energy loss.

Three cement contents of 350, 400 and 450 kg/m³ were used in experiments and it was shown that the increase in the cement contents improves the compressive and tensile strength and reduces the volume of water absorption fairly. Moreover, the water to cement ratio of 0.5 and 0.55 were applied in the mixtures. It was presented that, In gen-

eral, the increase in water to cement ratio from 0.5 to 0.55 increases water absorption by 22.7 percent and reduces the compressive and tensile strength by 19.9 and 10.6 percent, respectively. In addition, the effect of polypropylene fibers on the compressive and tensile strength of foamed concrete was investigated. It was found that the 28-day strength of foamed concrete was substantially improved by the addition 0.5 percent by weight of polypropylene fibers.

REFERENCES

1. G. Bowen, L. Kaiping, *New Wall Materials*, **7**, 30-32, (2008).
2. Z. Yunyan, *Engineering Forum*, **15**, 134-156, (2005).
3. E. K. K. Nambiar, K. Ramamurthy, **20**, 2 (2008).
4. S. Ganesan, M. A. Othuman Mydin, M. Y. Mohd Yunos, M. N. Mohd Nawi, *Applied Mechanics and Materials*, **747**, 230-233, (2015).
5. P. J. Tikalsky, J. Pospisil, W. MacDonald, *Cement and Concrete Research*, **34**(5), 889 (2004).
6. K. C. Brady, M. J. Green, *Foamed concrete: A Review of Materials, Methods of Production and Applications*, project report/ CE/149/97 Transport Research Foundation Group of Companies, 1997.
7. L. Qing, J. Kang, *Petrochemical Engineering and Construction*, **28**, 5 (2006).
8. G. C. Bye, *Portland Cement: Composition, Production and Properties*, Thomas Telford Limited, London, second edition, 1999.
9. J. Ji-Yong, K. Jin-Man, *Journal of the Korea Institute of Building Construction*, **11**(6), 557 (2011).
10. T. Zhang, S. Shang, F. Yin, A. Aishah, A. Salmiah, T. L. Ooi, *Cement and Concrete Research*, **31**, 1009, (2001).
11. I. Girmiene, A. Laukaitis, A. Dudik, *Materials Science*, **6**(4), 316-320, (2000).
12. K. Ramamurthy, E.K. K. Nambiar, G. I. S. Ranjani, *Cement and Concrete Composites*, **31**(6), 388 (2009).
13. R.C. Valore, *ACI J*, **50**, 773 (1954).
14. W.H. Taylor, *Concrete Technology and Practice*, Angus and Robertson, London, 1969.
15. A. Laukaitis, R. Zurasukas, J. Keriene, *Cem Concr Comp*, **27**, 41 (2005).
16. L. Du, K. J. Folliard, *Cement and Concrete Research*, **35**(8), 1463 (2005).
17. E. K. Kunhanandan Nambiar, K. Ramamurthy, *Cement and Concrete Research*, **37**(2), 221 (2007).
18. W. Cui-hua, *Chemical Materials for Construction*, **3**, 47-49, (2006).
19. C.G. Puttappa, A. Ibrahim, K.U. Muthu, H.S Raghavendra, in: *International Conference on Construction and Building Technology*, 491-500, (2008).
20. P. Chindaprasirt, U. Rattanasak, *Materials and Design*, **32**, 2 (2011).
21. E. K. Kunhanandan Nambiar, K. Ramamurthy, *Materials in Civil Engineering ASCE*, **21**, 11 (2009).
22. Z. Zhang, J. L. Provis, A. Reid, H. Wang, *Cement and Concrete Composites*, **62**, 22-32, (2015).
23. W. Tian, L. Li, X. Zhao, M. Zhou, N. Wang, in: *International Conference on Transportation Engineering*, ASCE, Southwest Jiaotong University, Chengdu, China, 2009.
24. [http:// http://www.isiri.com/](http://www.isiri.com/)
25. ASTM, *Standard Specification for Foaming Agents Used in Making Preformed Foam for Cellular Concrete*, C869- 91 (2006).
26. BSI, *Methods of test for mortar for masonry – part 11: Determination of flexural and compressive strength of hardened mortar*, British Standards Institution, London, 1999.
27. ASTM, *Standard Test Method for Splitting Tensile Strength of Cylindrical Concrete Specimens*, C496-96 (2012).
28. ASTM, *Standard Test Method for Density, Absorption, and Voids in Hardened Concrete*, C642 (2006).
29. M. Raeisi, M. J. Mehrani, S. Nouri, in: *5th National Conference of Concrete*, Tehran, Iran, 2013.

Optimization of the electrocoagulation process for sulfate removal using response surface methodology

Hooshyar Hossini¹, Poursan Makhdoumi², Seyed Omid Rastegar³, Fazel Mohammadi-Moghadam⁴,
Hamid Reza Ghaffari⁵, Allahbakhsh Javid⁶, Nezam Mirzaei^{7,8*}

¹Department of Environmental Health Engineering, School of Public Health, Kermanshah University of Medical Sciences, Kermanshah, Iran.

²Department of pharmacodynamics and toxicology, School of pharmacy, Mashhad University of Medical Sciences, Mashhad, Iran.

³Chemical Engineering Department, Tarbiat Modares University, Tehran, Iran.

⁴Department of Environmental Health Engineering, School of Health, Shahrekord University of Medical Sciences, Shahrekord, Iran

⁵Social Determinants in Health Promotion Research Center, Hormozgan University of Medical Sciences, Bandar Abbas, Iran.

⁶School of Public Health, Shahroud University of Medical Sciences, Shahroud, Iran.

⁷Environmental Health Research Center, Kurdistan University of Medical Sciences, Sanandaj, Iran.

⁸Department of Environmental Health Engineering, School of Public Health, Tehran University of Medical Sciences, Tehran, Iran.

Received June 26, 2015, Revised September 10, 2015

Sulfate concentrations affected on the natural sulfur cycle in the anaerobic treatment, therefore pretreatment of wastewater containing sulfate must be considered. In this work electrocoagulation techniques have considered as an effective and environmentally friendly process for desulfurization from wastewater. Three factors including initial pH, initial sulfate concentration and current density were selected as the effective factors and were optimized using response surface methodology. An initial pH of 8, initial sulfate concentration of 80mg/l and current density of 12mA/cm² were determined to be optimum values by the statistical models. The maximum sulfate removal and minimum sludge generation under optimal conditions were 68.5% and 0.075g, respectively. The kinetics of sulfate removal study investigated the pseudo-first models were better described experimental data and was selected as overall kinetic removal of sulfate.

Keywords: Sulfate removal; Electrocoagulation; Response surface methodology; Kinetics; Optimization

INTRODUCTION

High sulfate concentration in the wastewater faces important restrictions to anaerobic treatment due to several factors, including competition between sulfate reducing bacteria (SRB) and methanogenic microorganisms, non-competitive inhibition of methanogenesis due to SRB-generated sulfide, and finally the corrosive, dangerous and malodorous characteristics of sulfide. However, pretreatment of sulfate wastewater using the physical and chemical processes must be considered as an alternative [1]. Normally pulp and paper, petrochemical, edible oil, sugar-cane and solvent plants are industries that produce large amounts of wastewater containing high sulfate concentration [2]. To remove the sulfate several processes can be applied encompassing (i)

Membrane (such as reverse osmosis, electrical dialysis and filtration), (ii) Chemical precipitation (gypsum, limestone/lime, barite, barium salts or ettringite, $\text{Ca}_6\text{Al}_2(\text{SO}_4)_3(\text{OH})_{12}\cdot 26\text{H}_2\text{O}$, (iii) ion-exchange technologies and (iv) biological treatment using sulfate-reducing microorganisms [3]. When sulfate is present in the wastewater, sulfate-reducing bacteria (SRB) are able to couple the oxidation of organic compounds and hydrogen to sulfate reduction [4].

In latest decade, electrocoagulation techniques have considered as an effective and environmentally friendly process for wastewater treatment. Due to several advantages of electrocoagulation techniques, treatment of various pollutants and contaminants such as heavy metals (Cr, Zn, Ni, and Cu), chemical oxygen demand, total organic carbon, total dissolved solids, oil and

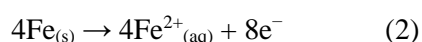
grease, phosphate, fluoride, chloride and etc. have been done [5-8]. These benefits are due to no chemical requirements, little sludge generation, strong oxidation ability, fast reaction rate and lower need space [9].

Based on electrochemical process, the electrodes (such as iron or aluminum) are generally better than other reported electrode materials. When iron is used as electrode materials, following reactions are occurred [10].

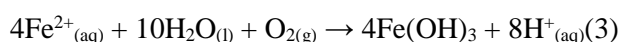
At the cathode:



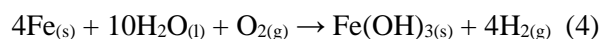
At the anode:



and with dissolved oxygen in solution:



overall reaction:



During electrocoagulation with iron various species are formed such as: $\text{Fe}(\text{OH})_4^-$, $\text{Fe}(\text{H}_2\text{O})_3(\text{OH})_3^0$, $\text{Fe}(\text{H}_2\text{O})_6^{3+}$, $\text{Fe}(\text{H}_2\text{O})_5(\text{OH})^{2+}$, $\text{Fe}(\text{H}_2\text{O})_4(\text{OH})^{2+}$, $\text{Fe}_2(\text{H}_2\text{O})_8(\text{OH})_2^{4+}$, and $\text{Fe}(\text{H}_2\text{O})_6(\text{OH})_4^{4+}$ [11, 12]. In addition, depending on pH, Fe^{3+} and/or Fe^{2+} ions form various monomeric and/or polymeric metal hydroxides complexes. The most common complex is the hydrated ion $[\text{Fe}(\text{H}_2\text{O})_6]^{3+}$. In acidic pH (pH 4–5) the hydroxo complexes reorient to a bi-nuclear iron complex species having a high surface charge, and the bi-nuclear ions have sufficient stability to exist in appreciable concentrations in solutions. In $\text{pH} > 4$, the octahedral hexaaquaions, $[\text{Fe}(\text{H}_2\text{O})_6]^{3+}$, gives a red-brownish gelatinous precipitate of hydrous oxide [11-13].

The sulfidic compound was removed in the form of metal sulfide in the presence of iron or aluminum anode. Sulfite and sulfate ions are getting removed possibly by adsorption on metal oxides/hydroxides. Sulfite and sulfate ions are possibly enmeshed in the porous metal oxide/hydroxide precipitate [14]. In the electrocoagulation process, some parameters such as initial pH, reaction time, initial concentration, current density and some other parameters were considered as effective factors but

a methodology is required to optimize these parameters and to identify their interactions. Response surface methodology (RSM) is an efficient experimental tool based on statistical analysis to determine optimal conditions for a multivariable system. Statistical optimization can determine the role of each component and the interactions among the parameters, which can save time, decrease the need for instrumentation, chemicals, and manpower [15, 16]. In the present investigation, the electrode sulfuration technique is explored for instantaneous and effective removal of sulfate ion with the lowest sludge rate production. Optimization of operating conditions and effective parameters like working time, pH, sulfate concentration and current density has been done using RSM.

MATERIALS AND METHODS

Synthetic wastewater

All reagents such as HCl, NaOH, Na_2SO_4 , BaCl_2 , $\text{MgCl}_2 \cdot 6\text{H}_2\text{O}$, Sodium acetate ($\text{CH}_3\text{COONa} \cdot 3\text{H}_2\text{O}$), KNO_3 , acetic acid (CH_3COOH (99%)) were prepared in analytical grade, and deionized water was used in all preparations. Stock solution of sulfate (SO_4^{2-}) was made by adding the specific values of sodium sulfate (Na_2SO_4) in deionized water. The synthetic wastewater was prepared from the stock solution by dilution. The desirable concentrations of sulfate were fabricated according to design of experiment runs. For all test the pH was adjusted using 1 M HCl and 1 M NaOH.

Electro-desulfurization setup

Electro-desulfurization was carried out in the batch reactors with a 500 mL capacity using iron (Fe/Fe) electrodes with a monopolar mode. Other appurtenance of electro-desulfurization unit consist of the DC power supply (TEK-8051, 30 V and 5 A double), and two electrodes with the dimensions $140 \times 60 \times 2$ mm at a fixed distance of 1.5 cm. The contents of the electrocoagulation react or were gently aerated with a magnetic rotator (Alfa, HS-860) with 70 rpm. **Fig. 1** shows the experimental set-up. Before starting-up the each test, electrodes impurity were cleaned with 1 M H_2SO_4 and rinsed with deionized water.

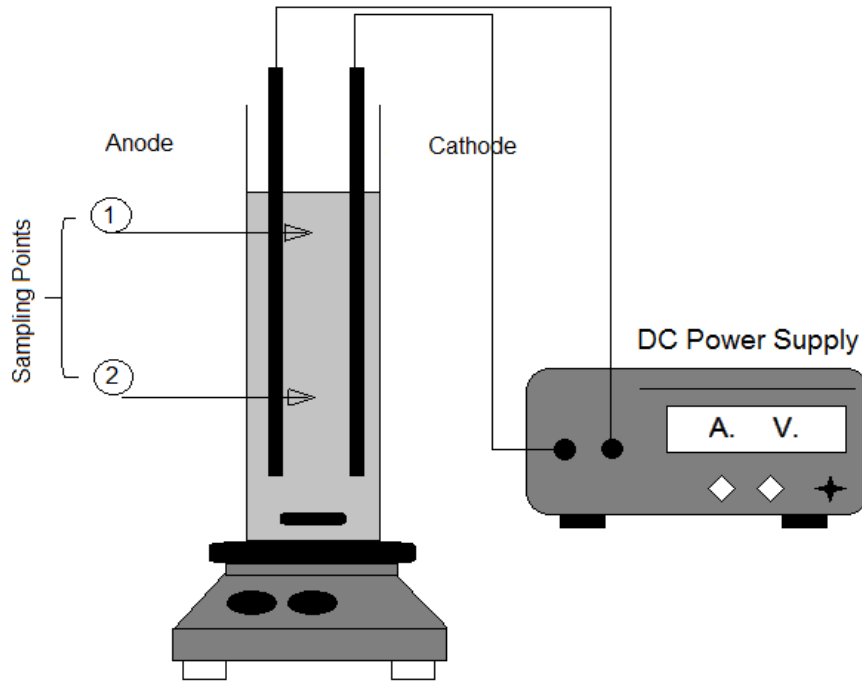


Fig. 1 Experimental set-up.

Sampling and analytical method

The samples were collected from the two points of reactor (upper and lower portions) and were filtered by Watman 0.45 μm to remove the flock and interference material. The residual sulfate was determined according to Environmental Protection Agency (EPA) procedure (Turbidimetric Method 9038)[17]. Sulfate concentration was measured by turbidimetric method by UV-spectrophotometer at 420 nm (Rayleigh UV 9200, China). The other experiments were performed regard to standard methods for the examination of water and wastewater[18].

Electrochemical experiments based on RSM

RSM is a collection of mathematical and statistical techniques for empirical model building. By careful design of experiments, the objective is to optimize a response (output variable) which is influenced by several independent variables (input variables). Central composite design (CCD) was widely used for fitting a polynomial model. By using this method, modeling is possible and it requires only a minimum number of experiments. It is not necessary during the modeling procedure to know the detailed reaction mechanism since the mathematical model is empirical. According to CCD method with total number of $2k + n_{\alpha} + n_0$ trials, where k is the number of independent variables, n_{α} is axial points and n_0 center points. In this work using Design-Expert 7.1.4a 8 (2³)

factorial design, 6 (2×3) axial points with 6 central points was selected. The behavior of the system is explained by the quadratic polynomial empirical model.

$$y = \beta_0 + \sum_{i=1}^3 \beta_i X_i + \sum_{i=1}^3 \beta_{ii} X_i^2 + \sum_{i<j}^3 \sum_{j=1}^3 \beta_{ij} X_i X_j + \varepsilon \quad (5)$$

where, y is the expected value of the response variable, β_0 , β_{ii} , β_{ij} are the model parameters, X_i and X_j are the coded factors evaluated. In this study, y represents the sulfate removal and sludge generation in the different empirical models.

Confirmation experiments

To check the validity of the models, a confirmatory experiment was done at optimal values predicted by the models. Values of sulfate removal and amount of sludge generation obtained from mentioned experiment were compared with the results predicted by the models and checked to be in the range of low and high confidence intervals.

RESULTS AND DISCUSSION

Statistical analysis

Influent pH, time, initial sulfate concentration and current density for a three-factor-five-level CCD design were used to determine the optimal values. Table 1 showed the range and levels of the variables in this study. Each factor was varied at

five different levels while the other parameters were kept constant. Once the desired ranges of the variables had been defined, they were coded to lie at ± 1 for the factorial points, 0 for the center points, and $\pm \alpha$ for the axial points [19]. The experimental conditions and their responses designed using CCD method is shown in Table 2. A total of 20 experiments were required for this procedure. In order to investigate the effect of each factor including initial pH, initial sulfate concentration and current density on the response of the system, analysis of variance (ANOVA) results were calculated as shown in Table 3.

This statistical tool is required to test the significance and adequacy of the model. The mean

squares (MS) were calculated as $MS=SS/DF$, where: SS is the sum of squares of each variation source and DF is the degrees of freedom [15, 16]. The Fischer variation ratio (F-value) is a measure of how well the factors describe the variation in the data about the mean. Data has some variation around its mean value; the greater the F-value from unity, the more acceptable is this variation. The amount of p-value values for the models which were less than 0.05 (<0.0001) indicated that the models were statistically significant with a 95% confidence interval.

Table 1. Experimental variables at different levels used for the bioleaching experiment.

Factor	$-\alpha$	-1	0	+1	$+\alpha$
A: pH	5	6	7	8	9
B: Initial sulfate conc. (mg/l)	40	80	120	160	200
C: Current density (mA/cm ²)	4	8	12	16	20

Table 2. Experimental plan based on CCD and the results.

Run	A: pH	B: Initial Sulfate Conc. (mg/l)	C: Current Density (mA/cm ²)	Sulfate Removal %	Sludge generation (g)
1	8	80	8	48.8	0.04
2	6	160	16	45	0.21
3	7	120	12	47.1	0.09
4	5	120	12	43.6	0.11
5	8	160	8	42.4	0.05
6	7	120	12	49.6	0.11
7	7	40	12	55.0	0.10
8	6	80	8	33.3	0.04
9	7	200	12	30.3	0.01
10	8	160	16	59.8	0.08
11	7	120	4	26.6	0.03
12	7	120	12	49.7	0.11
13	7	120	12	49.5	0.09
14	7	120	12	49.5	0.11
15	6	80	8	48.8	0.1
16	6	80	16	55	0.22
17	8	80	16	50.5	0.1
18	6	160	8	42.5	0.12
19	8	160	16	74.34	0.2
20	7	120	20	73.9	0.18

Table 3. ANOVA for response surface models applied.

Response	Model	ANOVA					
		Source	S.S.	Df	M.S.	F Value	Prob> F
Sulfate removal	quadratic	Model	5449.0797	9	605.45	27.55973	< 0.0001
		A-pH	2734.9248	1	2734.92	124.4915	< 0.0001
		B-Conc.	392.03108	1	392.03	17.84493	0.0004
		C-Current	1323.1091	1	1323.10	60.22683	< 0.0001
		AB	2.6405383	1	2.64	0.120195	0.7324
		AC	163.3284	1	163.32	7.434573	0.0130
		BC	10.465232	1	10.46	0.476368	0.4980
		A ²	644.2403	1	644.24	29.32528	< 0.0001
		B ²	99.96883	1	99.96	4.550498	0.0455
		C ²	0.0773501	1	0.077	0.003520	0.9533
		Residual	439.37531	20	21.96		
			(R ² = 0.92)		R ² _{adj} = 0.89)		
Sludge generation	quadratic model	Model	0.0152038	9	0.002	38.00663	< 0.0001
		A-pH	0.0039784	1	0.004	89.50644	< 0.0001
		B-Initial sulfate Conc.	0.0039784	1	0.004	89.50644	< 0.0001
		C-Current density	0.005251	1	0.005	118.1392	< 0.0001
		AB	0.0003151	1	0.00031	7.088352	0.0150
		AC	0.0003516	1	0.00035	7.909538	0.0108
		BC	0.0002031	1	0.0002	4.568549	0.0451
		A ²	0.0007176	1	0.0007	16.14495	0.0007
		B ²	0.0002626	1	0.00026	5.908249	0.0246
		C ²	3.161E-05	1	0.00003	0.711155	0.4090
		Residual	0.000889	20	0.00004		
			(R ² =0.94)		R ² _{adj} =0.91)		

Sulfate removal

The model equation for coded values in a quadratic model fitting the experimental results for sulfate removal can be seen in Eq. (6).

$$\text{Removal} = 48.63 + 10.67A - 4.04B + 7.42C + 0.41AB + 3.19AC + 0.81BC + 4.80A^2 - 1.89B^2 + 0.053C^2 \quad (6)$$

where A is pH, B is initial sulfate concentration and C is current density (mA/cm²). It should be noted that polynomial models are reasonable approximations of the true functional relationship over relatively small regions of the entire space of independent variables [20]. Fig. 2 shows the predicted data (data that was gathered from model to percentage of metals recovery) versus actual data (data that was gathered from experimental condition to percentage of metals recovery). Results show the very good agreement between the experimental and predicted values. The relatively high R² and adjusted R² (R²_{adj}) (0.92 and 89 respectively) values that presented in Table 3 indicate that the modified quadratic model is capable of representing the system under the given experimental conditions.

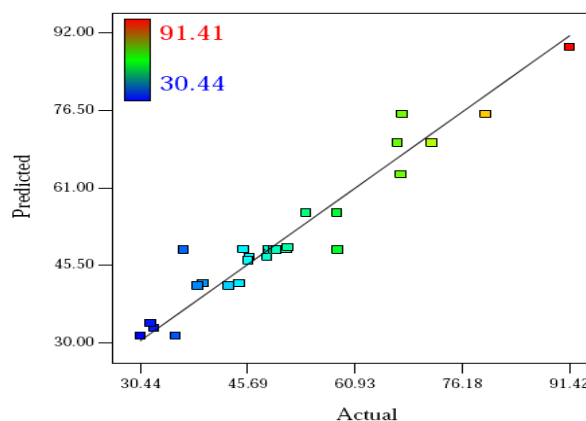


Fig. 2. Predicted vs. actual values for sulfate removal.

Fig.3 shows the sulfate removal efficiency contour plots. There is clearly in Fig. 3a a combined effect of pH and initial sulfate concentration on sulfate removal at a constant current density (16 mA/cm²). The maximum sulfate removal (>73%) was observed for initial sulfate concentration of 80 mg/land pH of 8.

Fig. 3b shows combined effect of initial pH and current density on the sulfate removal at a constant initial sulfate concentration of 80 mg/l. With current density increasing from 8 mA/cm² to 16

mA/cm², the sulfate removal efficiency increased. The maximum sulfate removal (>73%) was observed for the current density 16 mA/cm² and initial pH 8. Current density increasing result in higher production of iron complexes means coagulant concentration was increased in the aqueous phase; therefore the efficiency of sulfate was increased that is compatible with Faraday's law.

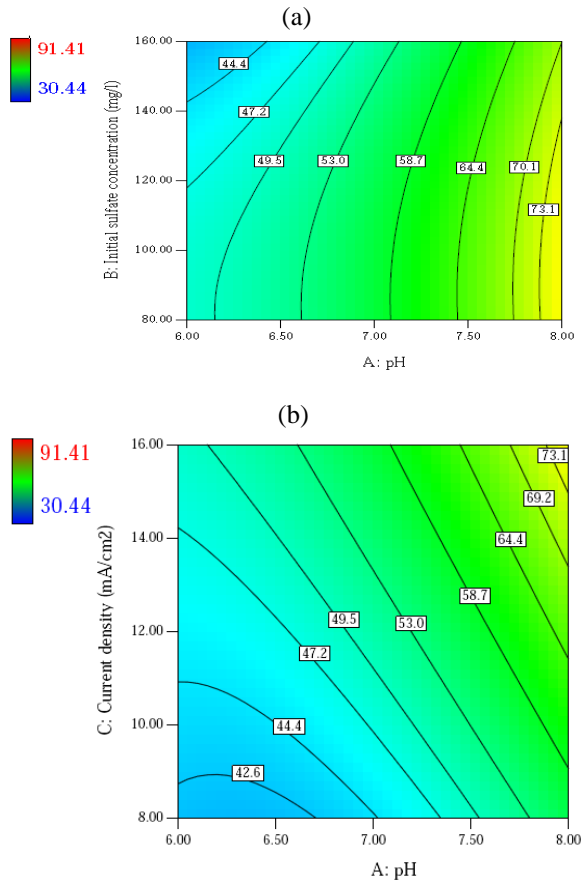


Fig.3. Contour plots of the interactive effect for sulfate removal: (a) effect of initial pH and initial sulfate concentration at the constant current density of 16 mA/cm² and (b) effect of initial pH and current density at the constant initial sulfate concentration of 80 mg/l.

Sludge generation

The model equation for coded values in the quadratic model fitting the experimental results of sludge production can be seen in Eq.(7):

$$\begin{aligned} \text{Sludge generation} = & 0.074 + 0.013 A \\ & + 0.013 B + 0.015 C + 4.438 E-003 AB + 4.688 E-003 \\ & AC + 3.563 E-003 BC + 5.062 E-003 A^2 - 3.062 E- \\ & 003 B^2 + 1.063 E-003 C^2 \end{aligned} \quad (7)$$

where A is pH, B is initial sulfate concentration and C is current density (mA/cm²). Fig.4 shows the actual and the predicted sludge generation. The clustering of the points around the diagonal line

indicates a satisfactory correlation between the experimental data and the predicted values, confirming the robustness of the model. R² and adjusted R² (R²adj) were found to be 0.94 and 0.91, respectively indicating that actual and predicted sludge generation were in agreement. The effect of pH and initial sulfate concentration on the amount of sludge generation is shown in Fig. 5a. According to this figure amount of sludge will be decreased from 0.13 g to 0.06 g by pH decreasing from 8 to 6 and initial sulfate decreasing from 160 mg/l to 80 mg/l at a constant current density 16 mA/cm².

Fig. 5b shows the interaction between pH and current density. According to this figure, the amount of sludge generation decreased by the decreasing of pH from 8 to 6 and the current density from 16 mA/cm² to 8 mA/cm² at a constant initial sulfate 120 mg/l. It should be said that in the pH below of isoelectric point (iep), iep of iron oxide/hydroxide was 7.7, the mechanism of removal sulfate is precipitation and in the pH higher than it the mechanism of removal sulfate is adsorption [14]. By increasing the current density, the bubble flux and in turn the collision probability is increased. At the same time, the dissolution of anode and in turn concentration of metal ions also increases. At higher current densities the consumption of electrodes is high [14]. Thus current density plays an important role in achieving optimum results.

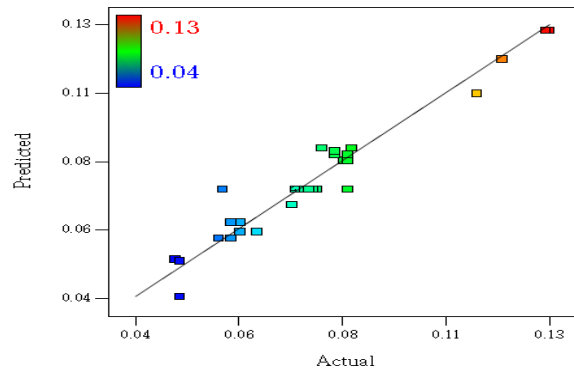


Fig.4. Predicted vs. actual values for sludge production.

Process optimization

In the numerical optimization, a minimum and a maximum level must be provided for each parameter. The goals are combined into an overall desirability function. Desirability is an objective function that ranges from zero outside of the limits to one at the goal. The program seeks to maximize this function. By starting from several points in the design space chances improve for finding the best local maximum are high [21]. A multiple response method was applied for optimization of any

combination of two goals namely sulfate removal and sludge generation. Level of all parameters within the range of investigation was set for maximum sulfate removal and minimum sludge generation. According to numerical optimization by Design-Expert 7.1.4, at optimal conditions as follows: pH 8, initial sulfate concentration 80 mg/l and current density 12 mA/cm², the maximum sulfate removal and minimum sludge generation were predicted as 68.5% and 0.075 g, respectively.

Confirmatory experiments

To test the validity of the optimized conditions given by the model, an experiment was carried out with the parameter suggested by the model. Table 4 presents the results of the experiment conducted at the optimal conditions and showed that verification experiment and the predicted values from fitted correlations were in close agreement at a 95% confidence interval. These results confirmed the validity of the model, and the experimental values were determined to be quite close to the predicted values. Under these conditions, the experimental value for the sulfate removal and sludge generation was found to be 68.5% and 0.075 g, respectively. The 95% confidence interval (C.I.) is the range in which the process average was expected to fall 95% of the time.

Kinetic study

Fig. 6 shows the trend of sulfate removal efficiency under optimal conditions including initial pH 8, initial sulfate concentration 80 mg/l and current density 16 mA/cm². Accordingly, large portion of sulfate was removed in first 5 min, and then the removal efficiency is increased, gradually. Maximum removal efficiency was determined around 85% at endpoint of 90 min. To evaluate the kinetics of sulfate removal, two of the most used kinetic models pseudo-first order (Eq. 8) and pseudo-second order (Eq. 9) were fitted to experimental results. The equation of two used kinetic are define as following[22]:

$$\ln C_t = \ln C_0 - k_1 t, \quad (8)$$

$$\frac{1}{C_t} = k_2 t + \frac{1}{C_0}, \quad (9)$$

Table 4. Verification of the model at optimum condition.

Response (%)	Target	Correlation Predicted (%)	Confirmation Experiment (%)	95% CI Low	95% CI High
Sulfate removal (%)	Maximize	66.6	68.5±0.2	62.2	71
Sludge generation (g)	Minimize	0.07	0.075±0.005	0.06	0.08

where C₀ is the initial sulfate concentration and C_t is the sulfate concentration after time t; k₁ and k₂ are the first and second-order kinetic constants, respectively. The linear equations of the kinetic plots and their correlation factor were shown in the Fig. 7. The kinetic constants values of the k₁ and k₂ were obtained about 0.0214 min⁻¹ and 0.00081.g⁻¹min⁻¹, respectively. The correlation factor (R²) of the straight lines was 0.97 for the pseudo-first order and 0.95 for the pseudo-second order. It was evident that the correlation coefficient for the pseudo-first-order kinetic model was higher than pseudo-second order; therefore the removal of sulfate using electrocoagulation method follows the pseudo-first-order kinetic model for the entire process.

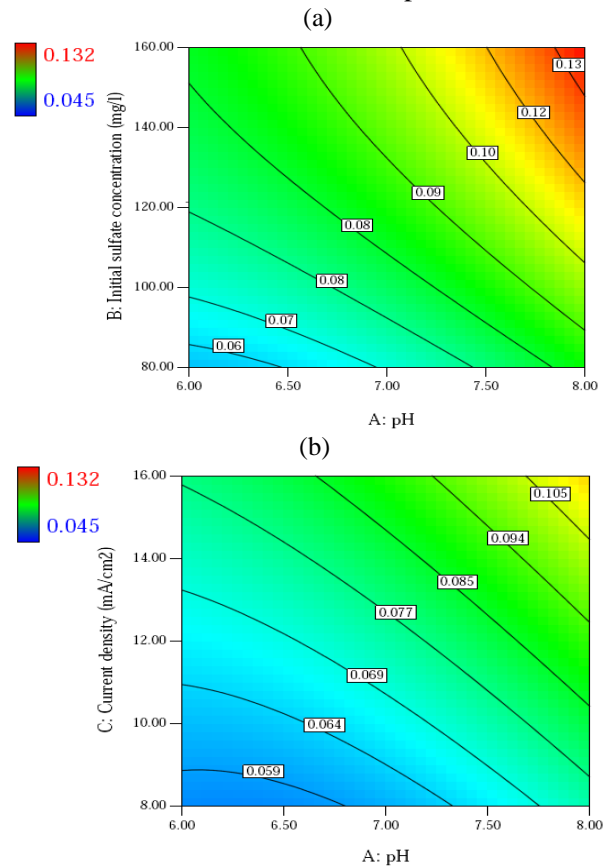


Fig.5. Contour plots of the interactive effect for sludge production: (a) effect of initial pH and initial sulfate concentration at the constant current density of 16 mA/cm² and (b) effect of initial pH and current density at the constant initial sulfate concentration of 120 mg/l.

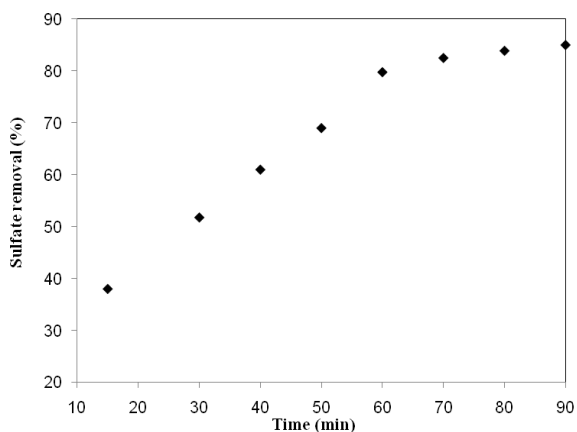
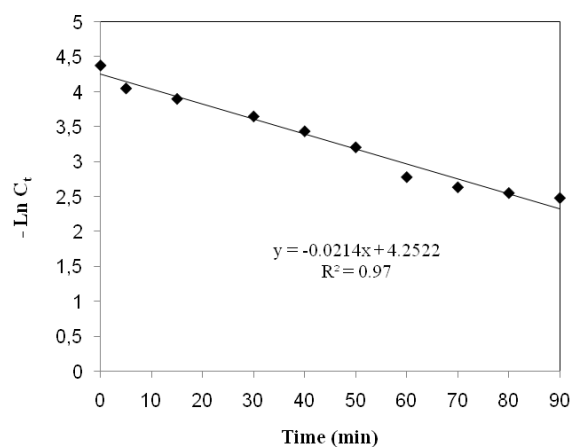


Fig. 6. Sulfate removal efficiency vs. time under optimal condition (initial pH 8, initial sulfate 80 mg/l and current density 12 mA/cm²).

(a)



(b)

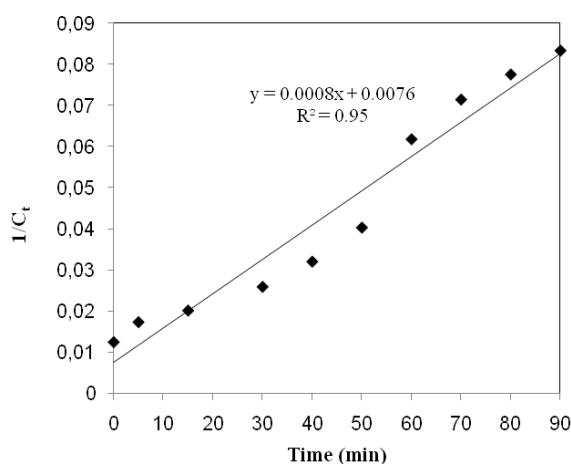


Fig. 7. The plots of the kinetic model (a) Pseudo first order (b) Pseudo second order.

CONCLUSION

Removal of sulfate from synthetic effluents was studied using electrocoagulation method. CCD was fitted with a modified quadratic model polynomial

equation for both sulfate removal and sludge production. The optimum values for variables were pH 8, initial sulfate concentration 80 mg/l and current density 12 mA/cm². Maximum sulfate removal and minimum sludge generation were obtained as 68.5% and 0.075g, respectively. The kinetics of sulfate removal was investigated using the pseudo-first and second order models. Results showed the experimental data were better described by pseudo-first order and was selected as overall kinetic removal of sulfate.

Acknowledgement: The authors acknowledge all non-financial supports provided by Tehran University of Medical Sciences and Kermanshah University of Medical Sciences. The authors declare that there is no conflict of interest.

REFERENCES

1. D.R. Jr Paula, E. Foresti, *Braz J Chem Eng.*, **26**, 669 (2009).
2. M. H. R. Z. Damianovic, E. Foresti, *Environ. Eng. Sci.*, **24**, 383 (2007).
3. R. J. Bowell, R. J. Connelly, J. Ellis, J. Cowan, A. Wood, J. Barta, P. Edwards, Proceedings of the International Mine Water Association symposium, 2004, part 2, p. 75.
4. A. J. Silva, M. B. Varesche, E. Foresti, M. Zaiat, *Process Biochem.*, **37**, 927 (2002).
5. N.M.Mahmoodi, A.Dalvand, *Desalin. Water Treat.*, **51**, 1 (2013).
6. F. Ozyonar, B. Karagozoglu, *Polish. J. Environ. Stud.*, **20**, 173 (2011).
7. A. Rezaee, H. Hossini, H. Masoumbeigi, R. Darvishi Cheshma Soltani, *IJESD*, **2**, 294(2011).
8. R. Khosravi, M. Fazlzadehdavil, B. Barikbin, H. Hossini, *Desalin. Water Treat.*, **55**, 3152 (2015).
9. A. Attour, M. Touati, M. Tlili, M. Ben Amor, F. Lapique, J. P. Leclerc, *Sep. Purif. Technol.*, **123**, 124 (2014).
10. A. K. Golder, A. N. Samanta, S. Ray, *Sep. Purif. Technol.*, **53**, 33 (2007).
11. I. Zongo, J. P. Leclerc, H. A. Maïga, B. Wéthé, F. Lapique, *Sep. Purif. Technol.*, **66**, 159 (2009).
12. A. K. Golder, N. Hridaya, A. N. Samanta, S. Ray, *J. hazard. Mater.*, **127**, 134 (2005).
13. M. Murugananthan, G. B. Raju, S. Prabhakar, *J. hazard. Mater.*, **109**, 37 (2004).
14. S. O. Rastegar, S. M. Mousavi, M. Rezaei, S. A. Shojaosadati, *J. Ind. Eng. Chem.*, **20**, 3096 (2014).
15. H. Hossini, A. Rezaee, B. Ayati, A. H. Mahvi, *Desalin. Water Treat.*
Doi: 10.1080/19443994.2015.1046946.
16. US EPA, Method 9038-sulfate (turbidimetric). Washington, DC,(1986).
17. APHA, AWWA, WPCF, Standard Methods for the Examination of Water and Wastewater, 21st ed., American Public Health Association, Washington, DC, 2005.

18. S. O. Rastegar, S. M. Mousavi, S. A. Shojaosadati, S. Sheibani, *J. Hazard. Mate.*, **197**, 26 (2011).
19. B. Ebrahimi, S. A. Shojaosadati, S. O. Ranaie, S. M. Mousavi, *Process. Biochem.*, **45**, 81 (2010).
20. S. M. J. Mirazimi, F. Rashchi, M. Saba, *Sep. Purif. Technol.*, **116**, 175 (2013).
21. G. Moussavi, R. Khosravi, M. Farzadkia, *Desalination.*, **278**, 288 (2011).

Kinetics, equilibrium, and thermodynamic studies of sulphate adsorption from aqueous solution using activated carbon derived from rice straw

E. Farahmand^{1*}, B. Rezai², F. Doulati Ardejani³, S.Z. Shafaei Tonekaboni³

¹Department of Mining Engineering, Science and Research Branch, Islamic Azad University, Tehran, Iran

²Department of Mining and Metallurgical Engineering, Amirkabir University, Tehran, Iran.

³School of Mining, College of Engineering, University of Tehran, Tehran, Iran

Received June 26, 2015, Revised September 10, 2015

In this study, the possibility of sulphate adsorption from a synthetic solution containing sodium sulphate was investigated using activated carbon derived from rice straw by $ZnCl_2$ activation. The structural and morphological characteristics of rice straw and activated carbon were evaluated applying SEM, FTIR, and EDS techniques. Influence of various parameters such as agitation time, pH, temperature, sulphate concentration and adsorbent dose at 5 levels was also studied. The highest uptake of sulphate ions was determined as 56.49 mg/g (1.8 mg/g compared to adsorption by raw straw). Adsorption kinetics and sulphate adsorption equilibrium behaviour were studied. It was found that the adsorption process follows second-order kinetics model and Langmuir isotherm fits well the equilibrium data. ΔG^0 was found to be -3.208, -3.230, -3.317, -3.372, -3.427 and -3.482 KJ/mol at 20, 25, 30, 35, 40, and 45°C, respectively. ΔS^0 and ΔH^0 of the adsorption were 10.95 J/K/mol and 0.001076 KJ/mol, respectively. The results further show that the adsorption process was a spontaneous and endothermic reaction and the activated carbon derived from rice straw by $ZnCl_2$ chemical activation can be considered as an effective adsorbent for sulphate adsorption from the aqueous solutions.

Key words: Adsorption; Activated Carbon; Sulphate; Isotherm; Adsorption Kinetic; $ZnCl_2$ activation.

INTRODUCTION

Pollutants release, generation of the variety of organic and inorganic chemical compounds due to the rapid development of chemical industry, and entry of toxic and hazardous substances to natural resources have become a serious threat to environment. Analysis of the effluents from mining industry has shown that this type of waste is considered among the most dangerous industrial waste. Besides, they contain high concentrations of toxic elements due to high levels of the variety of minerals. The annual costs which are paid for the treatment of such polluted effluents are considerable [1]. Sulphate ion is one of the major oxidation products of sulphide minerals in the tailings of ore processing plant and low-grade waste dumps containing sulphide minerals. Rapid oxidation of sulphide minerals in particular pyrite in the presence of oxygen and moisture produces acid mine drainage (AMD). Acid mine drainage results in death of vegetation, death of aquatic life, surface and groundwater pollution and corrosion of mine equipment [2]. Common methods of removing toxic elements from the the industrial effluents include precipitation, coagulation, ion exchange, electro-dialysis, electro-conglutination,

reverse osmosis, evaporation, and filtration [3, 4]. Although there are several techniques for removing dangerous elements from the aqueous solutions, most processes have significant disadvantages such as need for high energy and costly process, low efficiency, production of high amounts of sludge, sludge disposal problems, high levels of trace elements, high cost of specialty chemicals, and reclamation processes [3, 5]. Therefore, due to technical and economic constraints of the previous methods, the search for new methods is recommended and, in this regard, the biological uptake as a new option has been considered [6]. Biological adsorption or biosorption, is the process of using biological materials such as bacteria, fungi, algae, and agricultural waste through the creation of complex to toxic elements. Biological adsorption mechanism involves in chemical bonding between the metal ions and adsorbent surface groups or ion exchange reaction due to high ion exchange capacity of the adsorbent. Since this process is low-cost, and eco-friendly as well as having high performance in adsorption, it is an efficient alternative to the traditional methods in terms of removal of toxic elements [7]. Thus, in recent years, the use of agricultural byproducts and residuals like bark, sawdust, pistachio skin, almond skin, rice and wheat bran, corn residue, etc. due to the presence of cellulose compounds, carbon, and

To whom all correspondence should be sent:
E-mail: Farahmand.ehsan@yahoo.com

silica in their chemical structures has highly increased to adsorb toxic elements from the water and wastewater [8]. These biological materials are overabundant and available. However, they are not used specifically. Activated carbon as an adsorbent with high adsorption capacity has many applications in adsorption processes of liquid or gas phase. Activated carbon could be produced using both physical and chemical methods [9, 10]. The purpose of activation is the creation of porous structure with a high free surface area in raw materials [11]. In this study, rice straw is used by chemical activation to produce activated carbon.

EXPERIMENTAL PROCEDURE

Material and methods

Chemicals used in this study included sodium sulphate from Merck, deionised water to prepare the solution containing sulphate, hydrochloric acid and ammonia for pH adjustment from Merck, zinc chloride with the purity of 98 to 100 percent as well as molar mass of 136.28 g/mol, and distilled water to dilute solution system. Rice straw used in this research was prepared from the agricultural lands in Mazandaran Province in the north of Iran. In order to prepare the adsorbent, the rice straw was minced in an electric mill; then, it was washed several times with double distilled water and the oven was kept at 60°C to dry the adsorbent completely.

Raw material was mixed with ZnCl₂ boiling solution to combine them in a 2: 1 ratio and, the mixture was put on the heater at 100°C in order to evaporate the moisture. It was then put in the oven for 4 h at 150°C when completely dried. The resulting material was placed in a vacuum furnace for 1 h at 500°C. The adsorbent obtained was washed with the distilled water and then dried in the oven at 100°C. The obtained activated carbon was screened to reach the size of 250-500 μ using ASTM E11, 45 mesh sieve. Scanning electronic microscope (SEM) shows a layer of raw straw and activated carbon, as presented in Fig. 1. In addition, Fig. 2 demonstrate the functional groups and their links as well as their areas for raw straw and activated carbon using Fourier transform infrared spectroscopy (FTIR). The broader adsorption peak around 3440 cm⁻¹ could be attributed to the stretching of H-bonded hydroxyl groups. The other adsorption at 2914 cm⁻¹ relates to the C-H stretching. The band at 1649.15 cm⁻¹ is assigned to the bending mode of the adsorbed water [12]. In contrast to raw rice straw, there is a sharp adsorption peak of the stretching vibration of C-N

bond at 603.68 cm⁻¹ in ZnCl₂ activated rice straw carbon.

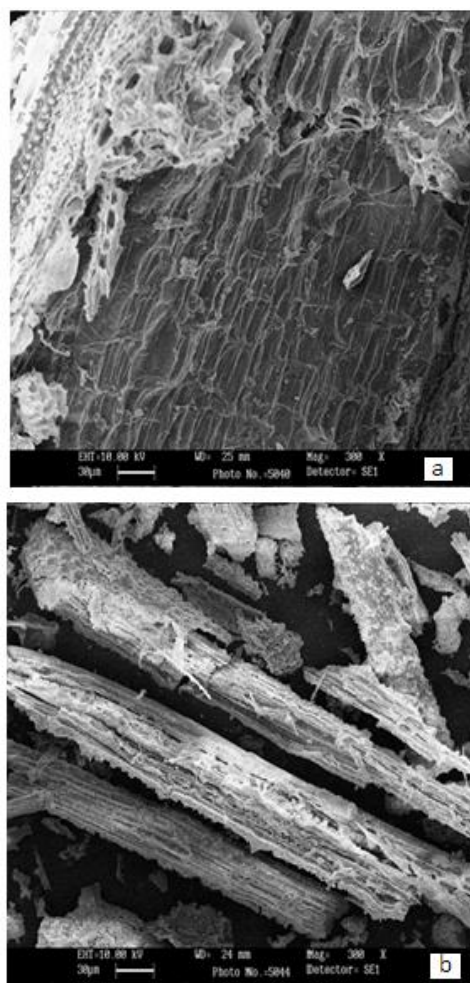


Fig. 1. SEM images of raw straw (a) and activated carbon mixed with ZnCl₂ (b).

Adsorption studies

Adsorption experiments were carried out in a batch system to determine solution pH, equilibrium time, optimum temperature, adsorbent dose, adsorption capacity, as well as the optimal kinetics and isotherm models and calculate the thermodynamic parameters. In this study, during the reaction time, a mixture of the certain amount of adsorbent and 30 mL solution containing a definite concentration of sulphate were placed on a thermostated rotary shaker for stirring intensity at 200 rpm and, after each experiment, the amount of remaining sulphate in the solution was measured and the amount of sulphate uptake was determined in each experiment. After completing the reaction, the amount of adsorbed sulphate was determined by calculating the difference between the initial and final concentrations and the quantity of adsorbed sulphate ions was calculated by the following equation:

$$q_e = \frac{(C_0 - C_e)v}{m}, \quad (1)$$

where q_e is the amount of adsorbed sulphate (mg/g), C_0 and C_e represent the initial and equilibrium concentrations of sulphate (mg/L), m denotes mass of adsorbent (g), and v stands for the volume of the solution (L).

In this study, influence of various parameters such as contact time, pH, temperature, sulphate concentration, and adsorbent dose using experimental design at five levels has been studied.

The optimization study of sulphate adsorption are presented in Table 1.

Effect of temperature

Temperature change is an important factor in determining the adsorption capacity. Effect of temperature on sulphate adsorption was studied at 20, 25, 30, 35, 40, and 45°C in the thermostated rotary shaker and the results show that the uptake slightly increased linearly with the temperature. It remained constant at temperatures above 25°C. Studies reveal that this increase is related to the increased temperature, the number of active sites,

and adsorption rate. Besides, at higher temperatures, the adsorption of sulphate might be decreased due to the damage and destruction of the active sites [13,19]. Fig. 3 shows the effect of temperature on the sulphate adsorption process.

Effect of contact time

Contact time is one of the effective factors in bioadsorption study. It plays an important role in improving the adsorption reaction and leads the reaction to the equilibrium. As shown in Fig. 4, during the first few minutes of the process, the adsorption rate increased intensely. It increased again with a gradual rate. The adsorption reached the maximum value after 90 min. After that, the adsorption remained constant with time [13]. The reason is that at the beginning of the adsorption reaction the number of sites available for adsorption is high. This results in high adsorption. The remaining sites are filled due to the repulsive force between sulphate ions in the liquid phase and activated carbon in solid phase. As a result, the amount of adsorption is reduced gradually.

Table 1. Values of sulphate adsorption parameters of 5 levels.

Exam Number	Time (min)	pH	Temperature (°C)	Concentration (mg/L)	Adsorbent dose (g)	Uptake (mg/g)
1	5	2	20	250	0.02	51
2	5	3	25	350	0.04	5.25
3	5	4	30	450	0.06	10
4	5	5	35	550	0.08	8.3
5	5	6	40	650	0.1	6.9
6	10	2	25	450	0.08	6.37
7	10	3	30	550	0.1	8.4
8	10	4	35	650	0.02	1.5
9	10	5	40	250	0.04	14.25
10	10	6	20	350	0.06	23.5
11	20	2	30	650	0.04	22.5
12	20	3	35	250	0.06	1
13	20	4	40	350	0.08	10.12
14	20	5	20	450	0.1	3.6
15	20	6	25	550	0.02	6
16	45	2	35	350	0.1	0.5
17	45	3	40	450	0.02	10.5
18	45	4	20	550	0.04	3
19	45	5	25	650	0.06	12.5
20	45	6	30	250	0.08	12.75
21	90	2	40	550	0.06	1.5
22	90	3	20	650	0.08	7.5
23	90	4	25	250	0.1	4.2
24	90	5	30	350	0.02	55.5
25	90	6	35	450	0.04	2.1

Effect of initial sulphate concentration

In order to evaluate the effect of initial sulphate concentration on adsorption process, several solutions were prepared with different concentrations in the range of 250-650 mg/L under optimal conditions. The results in Fig. 5 show that, by increasing the initial sulphate concentration to 350 mg/L, the adsorption rate increased almost linearly. It increased again at lower rate as concentration was increased from 350 mg/L to 650 mg/L.

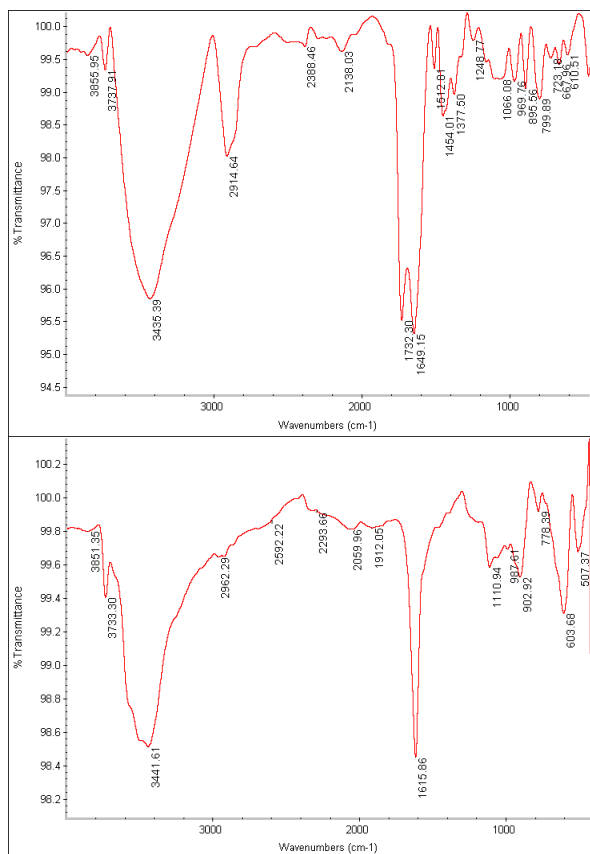


Fig. 2. The FTIR spectrum of raw rice straw (top), and activated carbon mixed with ZnCl₂ (down).

RESULTS AND DISCUSSION

Adsorption isotherm

One of the appropriate tools to model the thermodynamics and kinetics of adsorption process is the use of different methods for determining the adsorption isotherm, which is the relationship between the concentration of adsorbed onto solid surfaces and concentration of contaminants in the liquid phase at equilibrium and constant temperature [14]. The adsorption isotherms are obtained in the laboratory by batch systems [15, 16]. The results obtained from the experimental data are often shown using Langmuir, Freundlich, and Temkin adsorption isotherm models [17,18].

Langmuir isotherm

Langmuir model suggests a monolayer adsorption with no lateral interaction between the adsorbed molecules [19, 20]. This model can be expressed as follows:

$$\frac{C_e}{q_e} = \frac{1}{Q_{max} b} + \frac{C_e}{Q_{max}}, \quad (2)$$

where C_e is the equilibrium concentration of sulphate in solution (mg/L). Q_{max} represents the theoretical monolayer adsorption capacity (mg/g) and b denotes the energy of adsorption (L/mg).

Fig. 6 shows the linearised Langmuir isotherm and the adsorption isotherm parameters are presented in Table 2.

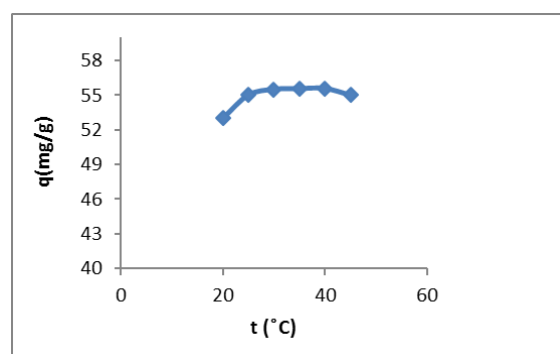


Fig. 3. The effect of temperature on sulfate adsorption (adsorbent dose = 0.02 gr , pH = 5, stirring intensity =200 rpm, sulfate concentration= 350 mg/L and contact time = 90 min).

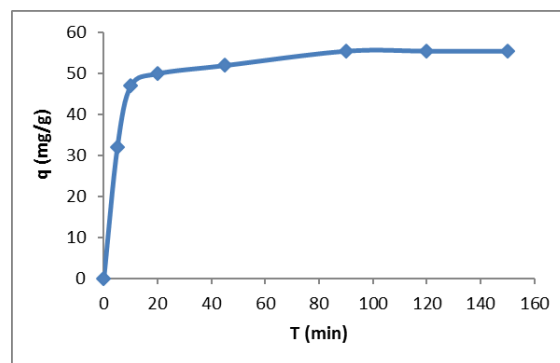


Fig. 4. The effect of contact time on sulphate adsorption (adsorbent dose = 0.02 gr, pH = 5, stirring intensity =200 rpm, sulphate concentration= 350 mg/L and temperature = 30 °C).

Freundlich isotherm

Freundlich model assumes a heterogeneous adsorption process due to the diversity of sorption sites or diverse nature of the ions adsorbed, free or hydrolyzed species [21,22]. The Freundlich model is expressed as follows:

$$\log q_e = \log K_f + 1/n \log C_e, \quad (3)$$

where K_f is the Freundlich constant and n expresses adsorption intensity. By plotting $\text{Log } q$ versus $\text{Log } C_e$, Freundlich isotherm parameters (Fig. 7) can be achieved. The results for Freundlich isotherm parameters are given in Table 2.

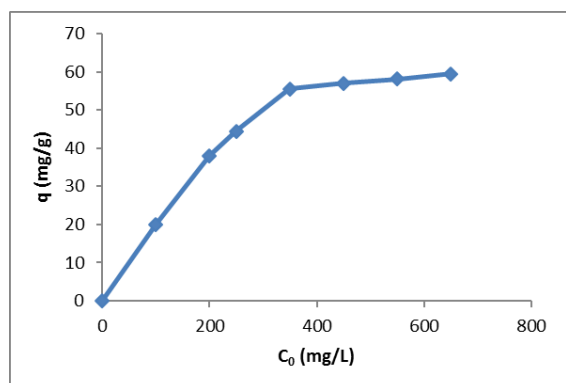


Fig. 5. The effect of initial concentration on sulphate adsorption (adsorbent dose = 0.02 gr , pH = 5, stirring intensity =200 rpm, contact time = 90 min and temperature = 30 ° C).

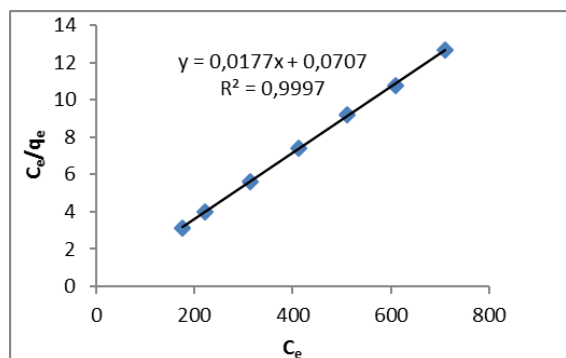


Fig. 6. Linearised Langmuir plot for adsorption of sulphate by activated carbon derived from Rice Straw.

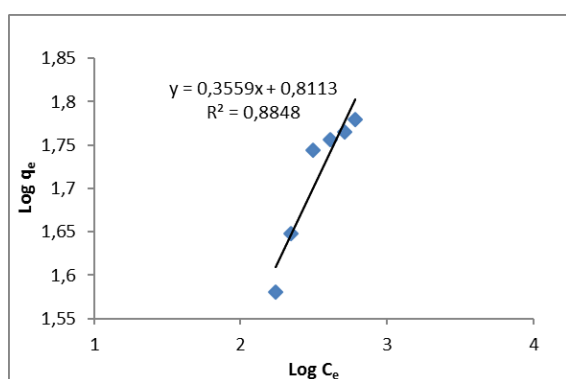


Fig. 7. Linearised Freundlich plot for adsorption of sulphate by activated carbon derived from Rice Straw.

Temkin isotherm

This isotherm contains a factor that explicitly taking into the account of adsorbent-adsorbate interactions. By ignoring the extremely low and large value of concentrations, the model assumes that heat of adsorption (function of temperature) of

all molecules in the layer would decrease linearly rather than logarithmic with coverage. This type of adsorption is expressed as follows:

$$q_e = B \ln A + B \ln C_e, \quad (4)$$

where B is the Temkin constant related to the adsorption heat ($B=RT/b$) and A represents the equilibrium constant hybrid (L/g) that corresponds to the maximum hybrid energy [23,24]. By plotting q versus $\text{Ln}C_e$, the parameters of Temkin isotherm can be calculated (Fig. 8 and Table 2).

As Table 2 shows, the Langmuir equation with a correlation coefficient (R^2) of 0.999 fits well the equilibrium data.

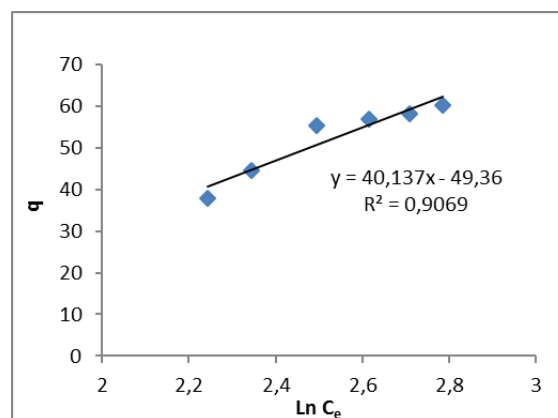


Fig. 8. Linearised Temkin plot for adsorption of sulphate by activated carbon derived from Rice Straw.

Adsorption kinetics

In order to understand the dynamics of adsorption reaction, adsorption kinetics data were studied. It was observed that, with increasing time, the uptake increased. It reached equilibrium state after 90 min of the adsorption process, (Fig. 4). The equilibrium and adsorption process depend upon the initial concentration of the absorbed substance. At the early stage (first phase), the adsorption was rapid and, in the second phase, a gradual decline in adsorption can be observed where the diffusion phenomenon was under control. The final phase was the stage of the equilibrium state. Several mathematical models have described the kinetics of adsorption [25]. In this study, first- and second- order kinetics models, inter-particle diffusion kinetics model, and Elovich kinetics model were investigated.

First-order kinetics model

The kinetics data of sulphate were analysed using Lagergren first-order rate equation [26,27,28]:

$$\log(q_e - q_t) = \log q_e - \frac{K_1}{2.303} t, \quad (5)$$

where q_e and q_t are the amounts of sulphate adsorbed (mg/g) at equilibrium and at time t , respectively, and K_1 represents the rate constant of first-order adsorption (1/min). Values of q_e and K_1 are calculated from the slope and intercept of the plot of $\log(q_e - q_t)$ vs t (Fig. 9, Table 3).

Second-order kinetics model

The adsorption kinetics data could be also described by a second-order equation [29,30,31] given below:

$$\frac{t}{q_t} = \frac{1}{K_2 q_e^2} + \frac{1}{q_e} t, \quad (6)$$

where K_2 is the equilibrium rate constant of second-order adsorption (g/mg/min). Values of K_2 and q_e are calculated from the slope and intercept of the plot of t/q vs t (Fig. 10, Table 3).

Inter-particle diffusion kinetics model

This model is based on the diffusion of adsorbed molecules into the adsorption sites within the adsorbent that are available to be checked. The mathematical expression of inter-particle diffusion kinetics model is as follows:

$$q_t = K_p t^{0.5} + C, \quad (7)$$

where K_p is the inter-particle diffusion rate constant ((mg/g).min^{-0.5}) and C denotes inter-particle diffusion constant (mg/g) [32]. Constant values of inter particle diffusion kinetics model are calculated from plot of q_t versus $t^{0.5}$ (Fig. 11, Table 3).

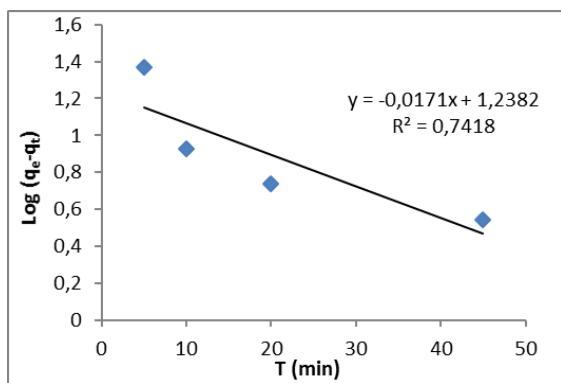


Fig. 9. Plot of the first-order kinetics model for adsorption of sulphate.

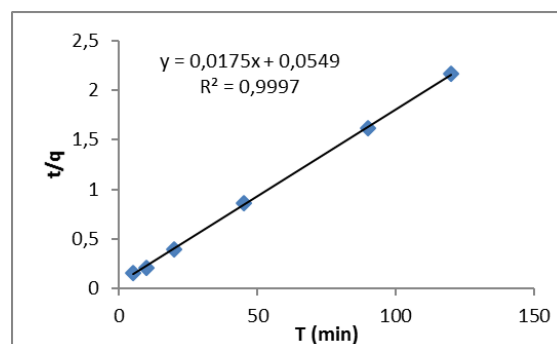


Fig. 10. Plot of the second-order kinetics model for adsorption of sulphate.

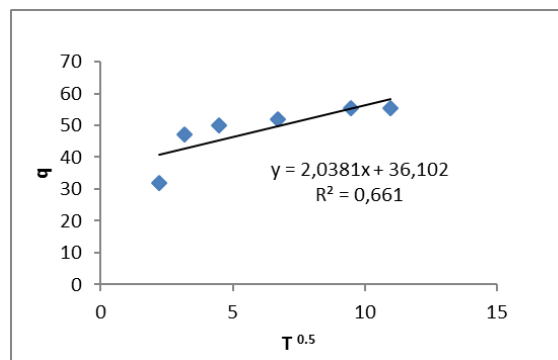


Fig. 11. Plot of the inter particle diffusion kinetics model for adsorption of sulphate.

Elovich kinetics model

The Elovich kinetics equation describes the adsorption and desorption kinetics of minerals used in solid chemistry and can be expressed as follows [32]:

$$q = \left(\frac{1}{\beta}\right) \ln(\alpha\beta) + \left(\frac{1}{\beta}\right) \ln t, \quad (8)$$

where α and β are Elovich constants which are calculated from the plot of q versus $\ln t$ (Fig. 12, Table 3).

As shown in Table 3, based on the analysis of kinetics data on the adsorption process, correlation coefficient was higher for the second-order kinetics model than the other models. This describes that the second-order kinetics model suits well the equilibrium data related to sulphate adsorption by the adsorbent used in this study.

Table 2. Parameters of various isotherm models for sulphate adsorption by activated carbon derived from rice straw.

Langmuir Parameters			Freundlich Parameters			Temkin Parameters		
R ²	q _{max}	b	R ²	k _f	n	R ²	A	B
0.999	56.49	0.25	0.884	6.475	2.81	0.906	3.42	40.14

Table 3. Values of sulphate adsorption kinetics parameters of various models used in this study.

Kinetics models	Parameters		
First-order kinetic	K_1 0.039	q_e 1.23	R^2 0.741
Second-order kinetic	K_1 0.00591	q_e 57.1	R^2 0.999
Inter-particle diffusion kinetic		K_p 2.038	R^2 0.661
Elovich kinetic	α 6.4	β 0.158	R^2 0.806

Table 4. Thermodynamic parameters for the adsorption of sulphate on activated carbon.

ΔG (kJ/mol)						ΔH (kJ/mol)	ΔS (kJ/mol)
T (°C)							
20	25	30	35	40	45	0.001076	10.95
-3.208	-3.230	-3.317	-3.372	-3.427	-3.482		

Thermodynamic studies of adsorption

The relationship between the distribution coefficient (K_d) and temperature in the form of Vant Hoff equation can be expressed as:

$$\ln K_d = \frac{\Delta S}{R} - \frac{\Delta H}{RT} \tag{9}$$

where ΔH is the enthalpy change (kJ/mol), ΔS stands for the entropy change (J/mol.K), R denotes gas constant, and T represents the temperature in Kelvin. The values of ΔH and ΔS are calculated from the slope and intercept of linear regression of $\ln K_d$ versus $1/T$.

The Gibbs free energy change (ΔG) values (kJ/mol) are calculated from the following equation [33-36]:

$$\Delta G = \Delta H - T\Delta S \tag{10}$$

Fig. 13 shows a Linearized plot of Eq. 9 and Table 4 gives the values of thermodynamic parameters. It was found that, the nature of the adsorption reaction is spontaneous and endothermic and the reaction tends to increase the irregularities.

Using EDS and applying SEM analysis the chemical components of the adsorbent were analysed after adsorption process. Results of the interactions of electron beam and activated carbon, plot of the distribution of different chemical elements in the adsorbent and measurement of the percentage of the elements are shown in Figs.14 and 15. In addition, Fig. 16 demonstrates the FTIR spectrum of activated carbon after the adsorption process.

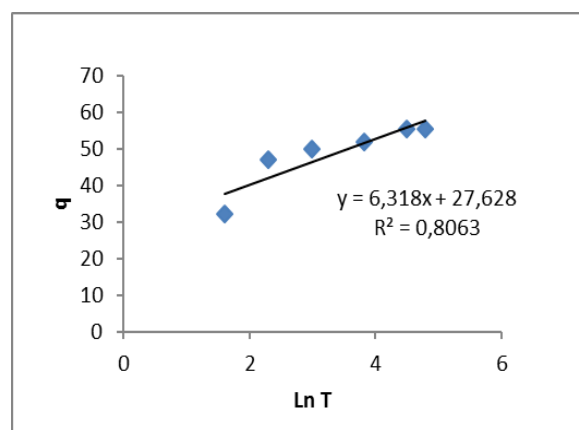


Fig. 12. Plot of the Elovich kinetics model for adsorption of sulphate.

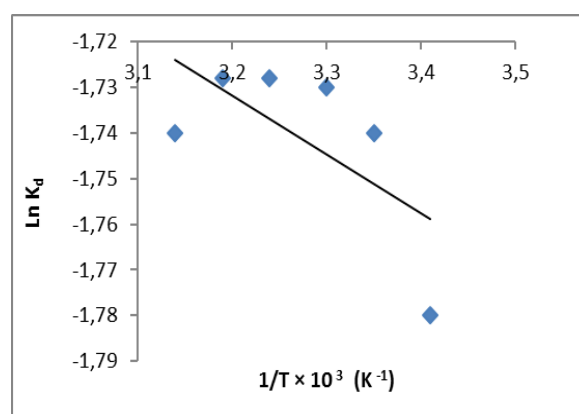


Fig. 13. Plot of $\ln K_d$ vs. $1/T$ for sulphate adsorption on activated carbon.

Distribution of the chemical elements in the adsorbent is presented in Table 5.

Table 5. Distribution of chemical elements in the adsorbent obtained by EDS.

Element. (c/s)	Line 2-sig	Intensity	Weight	Concentration (wt. %)
Si	Ka	6.32	1.005	34.243
S	Ka	0.71	0.338	3.690
Cl	Ka	0.61	0.311	3.078
Zn	Ka	2.55	0.639	58.989
Total				100

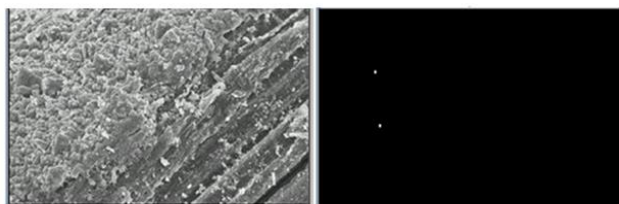


Fig. 14. The image of activated carbon after sulphate adsorption by EDS.

Comparison of ZnCl₂ activated rice straw carbon with other adsorbents

The application of low-cost and easily available materials in wastewater treatment has been widely investigated during recent years. Particularly, the sulphate adsorption on different materials has been extensively studied during recent years. Similar results were also observed for sulphate adsorption using other adsorbents. To illustrate the potential in the use of ZnCl₂ activated rice straw carbon in real applications, a comparative evaluation of the adsorption capacities of various types of adsorbents for the adsorption of sulphate species is provided in Table 6. The results achieved in comparison with the results obtained by others are significant, and so studied adsorbent in sulphate adsorption can be important, in this regard carry out a series of complementary experiments on other characteristics including desorption needs to be done.

Table 6. Adsorption capacity (q) of various adsorbents reported in literature.

Adsorbent	pH	q (mg/g)	Reference
γ-Al ₂ O ₃	5.7	7.7	[38]
Chitin-based shrimp shells	4.5	156	[39]
Powdered TiO ₂	1	0.9	[40]
Soil	4.1	1.42	[41]
Volcanic Ash	4	0.14 (m mol/g)	[42]
Soil	6.2	2.06	[43]
Granite Sand	6.2	1.2	[44]
Coir Pith Carbon	4	0.06	[45]
ZnCl ₂ Activated Coir Pith Carbon	4	4.9	[19]
Magnetite	4	15.4	[46]
LDH (nano particles)	Acidic	30.22	[47]
Rice Straw	Acidic	74.76	[48]
Raw Date Palm Seeds	3.5	3.19	[13]
LDH (nano particles)	7	21 (Percent removal)	[49]
Soil	6.3	0.003	[50]
Poly(m-Phenyl enediamine)	1.75	108.5	[51]
LDH (nano particles)	7	0.13 (m mol/g)	[52]
AMX Membrane	Acidic	80	[53]
ZnCl ₂ Activated Rice Straw Carbon	5	56.49	Present study

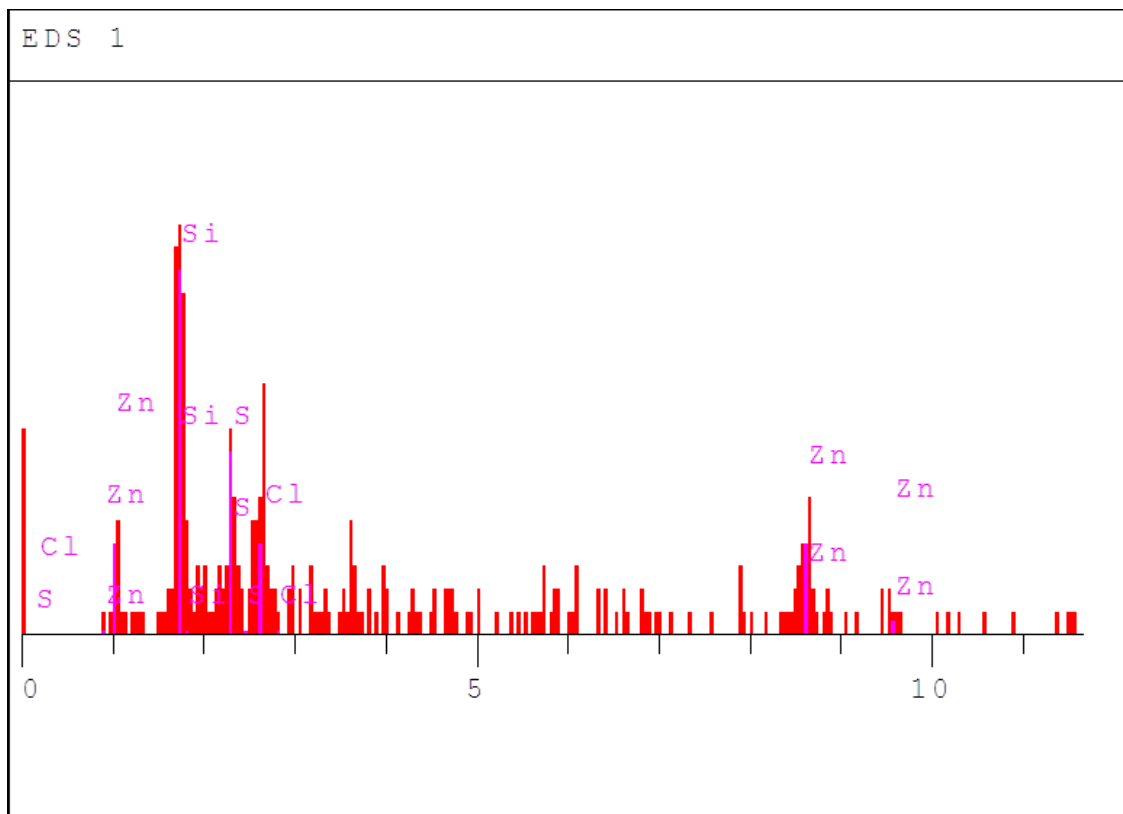


Fig. 15. Distribution of various chemical elements in activated carbon.

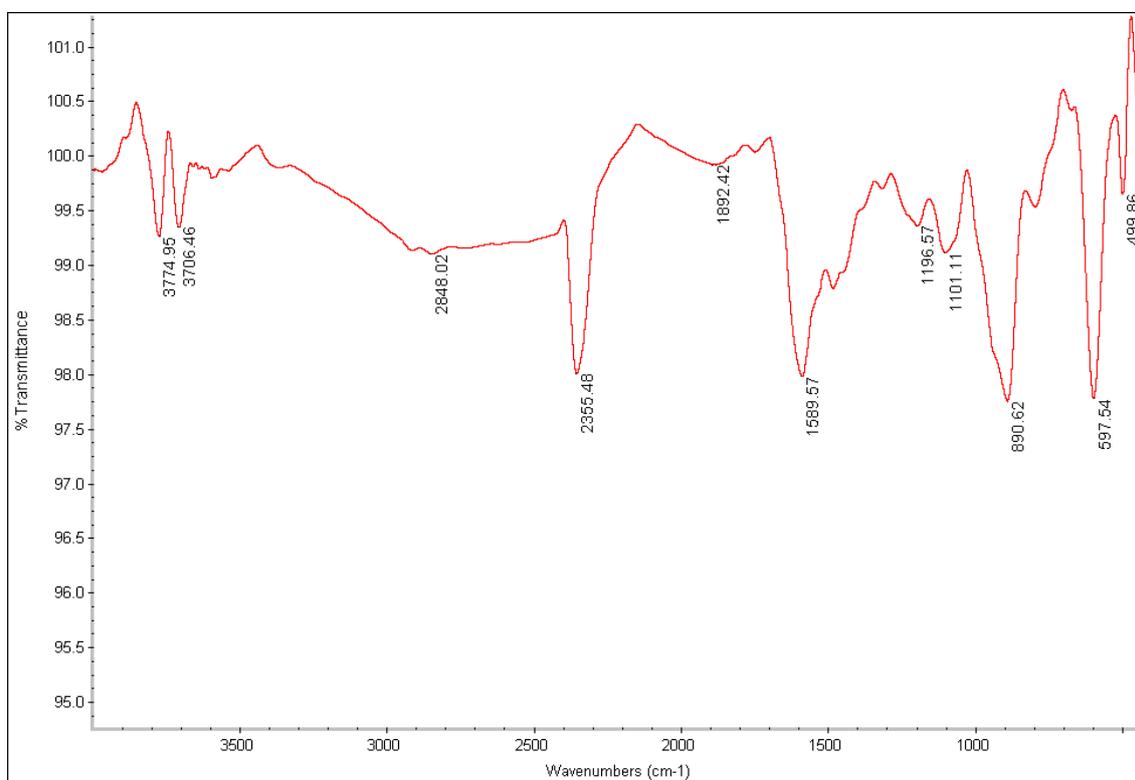


Fig. 16. The FTIR spectrum of activated carbon after adsorption process.

CONCLUSIONS

This study shows that the activated carbon obtained from rice straw and ZnCl₂ boiling solution is an effective absorbent for the removal of sulphate from aqueous solutions. The adsorption equilibrium data was followed by Langmuir isotherm and a second-order model describes the kinetics of process. The maximum absorption capacity was 56.49 mg/g at pH =5, contact time of 90 min, temperature of 30°C, sulphate concentration of 350 ppm, and adsorbent dose of 0.02 gr. Adsorption rate slowly increased with increasing temperature. The adsorption rate was directly proportional to the initial concentration and contact time. The positive values of ΔH^0 , and the negative values ΔG^0 confirmed the endothermic and spontaneous nature of adsorption, respectively.

REFERENCES

1. R.A. Anthony, C.A. Philip, C.J. Peter, S. Leone, N. Daniel, R. Warwick, V. Nafty, *J. Polyhedron.*, **26**, 3479 (2007).
2. G. Sangita, *IJEP*, **30**(11), 953 (2010).
3. A. Maleki, M.B.K. Erfan, A. Mohammadi, R. Ebrahim, *Pakistan J. Biol. Sci.*, **10**, 2348 (2007).
4. A. Maleki, A.H. Mahvi, R. Rezaee, *Sci. J. Kurdistan*, **16**, 65 (2011).
5. S. Lameiras, C. Quintelas, T. Tavares, *Biores. Technol.*, **99**, 801 (2008).
6. A. Maleki, M.A. Zarasvand, *Southeast Asian J. Tropical Medicine & Public Health*, **39**, 335 (2008).
7. C. Quintelas, B. Fonseca, B. Silva, H. Figueiredo, T. Tavares, *Biores. Technol.*, **100**, 220 (2009).
8. D. Sud, G. Mahajan, M.P. Kaur, *Biores. Technol.*, **99**, 6017 (2008).
9. J. M. Dias, M.C.M. Alvim-Ferraz, *J. Environ. Management*, **85**, 833 (2007).
10. A.A. Nunes, A. S. Franca, *Biores. Technol.*, **100**, 1786 (2009).
11. A. Ahmadpour, D.D. Do, *Carbon*, **35**, 1723 (1997).
12. C.F. Liu, F. Xu, J.X. Sun, J.L. Ren, S. Curling, R.C. Sun, *Carbohydrate Res.*, **341**(16), 2677 (2006).
13. S. Koumaiti, K. Riahi, F. Ounaies., B. Thayer, *J. Environ. Sci. Eng.*, **5**, 1570 (2011).
14. K.M. Khoda, Adsorption Isotherms, Nanyang: Nanyang Technological University, 2009.
15. B.H. Hameed, *J. Hazard. Mater.*, **162**, 939 (2009).
16. F. D.Ardejani, K. Badii, N.Y. Limaee, S. Shafaei, A. Mirhabibi, *J. Hazard. Mater.*, **151**, 730 (2008).
17. I. Langmuir, *J. Am. Chem. Soc.*, **40**, 1361 (1918).
18. H. Freundlich, *Z. Phys. Chem.*, **57**, 387 (1906).
19. C. Namasivayam, D. Sangeetha, *Desalination*, **219**, 1 (2008).
20. A.E. Nemr, *J. Hazard. Mater.*, **161**, 132 (2009).
21. B. Subramanyam, A. Das, *Int. J. Environ. Sci. & Technol.*, **6**, 633 (2009).
22. O. Altin, O. Ho, T. Dogu, *J. Colloid Interface Sci.*, **198**, 130 (1998).
23. S. Lagergren, *Hand Linger*, **24**, 1 (1898).
24. M. Temkin, J.A.V. Pyzhev, *Acta Physiochem.*, **12**, (1940) 217.
25. G.S. Khorramabadi, R.D.C. Soltani, S. Jorfi, *J. Water & Wastewater*, **1**, 57 (2010).
26. H. Qiu, L. Lv, B.C. Pan, Q. Zhang, W. Zhang, Q. Zhang, *J. Zhejiang Univ. Science A*, **10**(5), 716 (2009).
27. X. Fan, D.J. Parker, M.D. Smith, *Water Res.*, **37**, 4929 (2003).
28. S Lagergren, *PA Norstedt & Söner*, **24**, 1 (1898).
29. Y. Ho, *J. Hazard. Mater.*, **136**, 103 (2006).
30. Y.S. Ho, G. McKay, *Chem. Eng. J.*, **70**, 115 (1998).
31. W. Enos, K.M. Gerald, M. Paul, J. Karanja, *Eurasian J. Sci. Res.*, **4**, 317 (2009).
32. J. Wu, H.Q. Yu, *Biores. Technol.*, **98**, 253 (2007).
33. D.L. Sparks, in: Soil Physical Chemistry, CRC Press LLC, 1999, 38.
34. M. Torab-Mostaedi, *Chem. Ind. & Chem. Engineering Quart.*, **19**, 79 (2013).
35. S.J. Malakooti, S.Z.S. Tonkaboni, M. Noaparast, F.D. Ardejani, R. Naseh, *Environ. Earth Sci.*, **71**, 2267 (2014).
36. A. Halajnia, S. Oustan, N. Najafi, A.R. Khataee, A. Lakzian, *Appl. Clay Sci.*, **80-81**, 305 (2013).
37. A. Kumar, V. Kumar, *J. Chem. Pharm. Res.*, **7**, 685 (2015).
38. C.H. Wu, C.Y. Kuo, C.F. Lin, S.L. Lo, *Chemosphere*, **47**, 283 (2002).
39. A. Moret, J. Rubio, *Minerals Eng.*, **16**, 715 (2003).
40. G. Horanyi, *J. Colloid Interface Sci.*, **261**, 580 (2003).
41. M.E. Alves, A. Larorenti, *Geoderma*, **118**, 89 (2004).
42. T. Delfosse, P. Delmelle, B. Delvaux, *Geoderma*, **136**, 716 (2006).
43. V.E. Osodeke, A.F. Ubah, *Agric. J.I.*, **2**, 48 (2006).
44. M.N. Khan, U. Zareen, *J. Hazard. Mater. B*, **133**, 269 (2006).
45. C. Namasivayam, *J. Environ. Eng. Management*, **17**, 129 (2007).
46. P. Roonasi, A. Holmgren, *J. Colloid Interface Sci.*, **333**, 27 (2009).
47. K. Khalatbari, E. Jorjani, S. Bazgir, Study Sulfate Adsorption of Copper Sulfate Using LDH nano particles, Department of Technology, Science and Research Branch, Islamic Azad University, Tehran, Iran, 2010, p. 1.
48. W. Cao, Z. Dang, X.Q. Zhou, X.Y. Yi, P.X. Wu, N.W. Zhu, and G.N. Lu, *Carbohydrate Polym.*, **85**, 571 (2011).
49. U. Rafique., A Imtiaz, A.K. Khan, *J. Water Sustain.*, **2**, 233 (2012).
50. G. K. Ghosh, N. R. Dash, *Animal & Environ. Sci.*, **2**, 2231 (2012).
51. P.L. Sang, Y.Y. Wang, L.Y. Zhang, L.Y. Chai, and H.Y. Wang, *Trans. Nonferrous Metals Soc. China*, **23**, 243 (2013).
52. A. Halajnia, S. Oustan, N. Najafi, A.R. Khataee, A. Lakzian, *Appl. Clay Sci.*, **80-81**, 305 (2013).
53. Ch. Hannachi, F. Guesmi, Kh. Missaoui, *Int. J. Technol.*, **5**, 60 (2014).

Effect of surface modification agent and calcination process on the preparation of the hydrophobic magnetic silica aerogels by ambient pressure drying method

L. Amirkhani¹, J. Moghaddas^{1*}, H. Jafarizadeh¹

¹Faculty of Chemical Engineering, Sahand University of Technology, Tabriz, Iran

Received June 26, 2015, Revised September 10, 2015

Silica aerogel-iron oxide nanocomposites have been synthesized with sodium silicate precursor, iron oxide nanoparticles and ambient pressure drying method in this research successfully. For composite synthesis cogelation of the matrix precursor and the nanoparticles suspension method were used. Trimethylchlorosilane (TMCS) and hexamethyldisilazane (HMDZ) as modification agents were used to synthesize magnetic silica aerogel nanocomposite and their effects were studied. The properties of nanocomposites were determined by XRD, BET, VSM, AAS, FTIR, TEM and SEM methods. The results showed that by HMDZ modification agent, the magnetic and physical properties of iron oxide nanoparticles in silica matrix were retained. The XRD patterns proved the existence of magnetite in nanocomposite that was oxidized to maghemite after heating in 500°C for 2 hr. The effect of iron oxide nanoparticles content also were studied and the results indicated that the density and specific surface area of the aerogels were increased with increasing the iron oxide amount.

Keywords: Silica aerogel, Iron oxide, Magnetic, Ambient pressure drying, Sodium silicate.

INTRODUCTION

Magnetic zero-dimensional nanoparticles especially magnetite (Fe₃O₄) and maghemite (γ -Fe₂O₃) have very important application in many technological area such as catalysts, sensors, nuclear waste separation, biotechnology/ biomedical and magnetic recording systems [1-3]. But applications of these fine particles usually are difficult because of their tending to aggregation and chemically active natures that causes they become oxidized in air easily. One method to solve these problems is coating nanoparticles with inorganic layers such as carbon and silica [4, 5]. Continuous matrix such as silica aerogel also can be used to disperse iron nanoparticles [6, 7]. Silica aerogels and their composites has recently attracted so much considerations because of their unusual properties such as very low density, high porosity, high specific surface area, low dielectric constant and excellent heat insulation value. Aerogels are synthesized by sol-gel method and the liquid of the gels must be exit by special drying method so that the solid structure are retained. If the gels are dried in ambient pressure and temperature, they lost their porosity because the effects of the capillary forces and in that condition the xerogels are formed. Supercritical drying is the usual method to synthesize aerogel and their composites. But this method is dangerous and very costly. By solvent

exchange and surface modification of the gels, capillary stresses can be avoided and the shrinkages are decreased considerably [8, 9].

All the reported literature in the field of synthesis iron oxide- silica aerogel nanocomposites have used supercritical drying method and mainly silicon alkoxides such as tetramethyl orthosilicate (TMOS) and tetraethyl orthosilicate (TEOS) as silica precursors [3, 6, 7, 10-22]. Several materials such as iron acetylacetonate [10, 11, 13, 19, 20, 23, 24], iron acetate [19], iron nitrate [3, 6, 7, 14-16, 18, 25], iron carbonyl [12] and iron chloride [17, 22] were used as iron oxide precursor. Most of above mentioned studies used cogelation matrix precursor and the inorganic precursor to synthesis nanocomposite. In this method the creation favorite iron oxide phase is difficult. In this work, silica aerogel- iron oxide nanocomposite were synthesized by simple ambient pressure drying method and water glass as a cheap precursor for first time. Magnetite nanoparticles as iron precursor and co-gelation of the nanoparticles and the matrix precursor were used to synthesize nanocomposites. This approach offers the advantage of producing materials with a controllable loading of nanoparticles. Trimethylchlorosilane (TMCS) and hexamethyldisilazane (HMDZ) as modification agents were used to synthesize silica aerogel-iron oxide nanocomposite and their effects were studied. The effect of iron oxide content on nanocomposite properties was investigated. Moreover, synthesis steps were summarized in this work. The alcohol and solvent were added to hydrogel in one step,

To whom all correspondence should be sent:

E-mail: jafar.moghaddas@sut.ac.ir

therefore the synthesis was done in one day less than previous procedure [26].

EXPERIMENTAL

Chemicals and Characterization Tools

Iron oxide nanoparticles were prepared from US Research Nanomaterials Company. The other materials were purchased from Merck Company. The bulk density of the nanocomposites was calculated using a microbalance scale, (10^{-5} g precision) and coulisse. The surface area was determined by Brunauer–Emmett–Teller (BET) method (BEL, JAPAN) from the amount of N_2 gas adsorbed at various partial pressures. The Fe content in the samples were determined using an atomic absorption spectrophotometer (AAS, GBC Avanta). Organic and inorganic bonds present in an composite samples were studied by Fourier transform infrared spectroscopy (FTIR) using a IR spectrophotometer (PU 9800, from Philips) which gave the information about the various chemical bonding such as –OH, Si–OH, Si–O–Si, Si–C, C–H and Fe–O. The pore structure and particle morphology were characterized by field emission scanning electron microscopy (FESEM, Mira 3-XMU) and transmission electron microscopy (TEM, Philips EM208). X-ray diffraction (XRD) measurements were performed at room temperature using a Bruker D8 advance X-ray diffractometer. Magnetic properties of samples were studied by a vibrating sample magnetometer (VSM, Daghigh Meghnatis Kashan Co.) at room temperature.

Synthesis

At first step for synthesis of silica aerogel- iron oxide nanocomposite, certain weight (0.02 -1 g) of iron oxide nanoparticles were dispersed in 20 cc deionized water by an ultrasonic mixer. The power of the mixer was 70 watt, and solutions were mixed for 1 hr. Then water glass was added to the mixture in 1 to 4 ratios. The solution pH was ~ 12 in this step. After well mixing, amberlite resin was used to exchange the ion Na^+ with H^+ and solution pH became 2-3. The hydrogel was prepared by controlled addition of the NH_4OH solution (1 M) to the obtained sol. In this step to prevent deposition of Fe_3O_4 nanoparticles, the pH was adjusted so that the gelation time was limited in 1 minute. The mixture was transferred to Teflon vessels in airtight condition and $50\text{ }^\circ\text{C}$ temperature. After 3 hours aging, 2-propanol and n-hexane in equal ratios were added to hydrogel to exchange the solvent. This step lasted 14-20 hours. The modification agent was prepared by adding 25% TMCS or HMDZ in n-

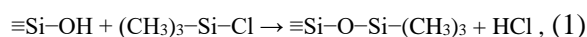
Hexane solution. After evacuation of propanol-hexane solution, surface modification agent was added to the gel. After 14-20 hours, the modification agent was extracted and the gels were dried. To drying, the gels were given in ambient temperature for one day. After that raising temperature program was applied from $50\text{ }^\circ\text{C}$ to $140\text{ }^\circ\text{C}$ slowly in one day.

Beside iron oxide- silica aerogel nanocomposite, iron oxide- silica xerogel nanocomposite and pure silica aerogel were synthesized and their properties were compared together. For synthesis xerogel nanocomposite, the first steps were done similar to iron oxide- silica aerogel synthesis, but after gelation, the gels were dried without any excess operation in $50\text{ }^\circ\text{C}$. In pure silica aerogel, iron oxide nanoparticles weren't added to the sol and the other steps were repeated.

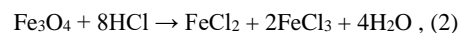
RESULTS AND DISCUSSION

Two modification agents, trimethylchlorosilane (TMCS) and hexamethyldisilazane (HMDZ), were used to change surface functional groups and prevent xerogel formation. The samples that were modified with HMDZ and TMCS will be named as "AH" and "AT" respectively.

Apparent color of AT nanocomposites was altered in modification step. In the first step, the formation gel was dark brown. This gel kept its color in solvent exchange step. But after modification, the gel became transparent and colorless and the final product became white (Figure 1 b, c, d). Surface modification of the silica gel with TMCS was done as below reaction [27]:

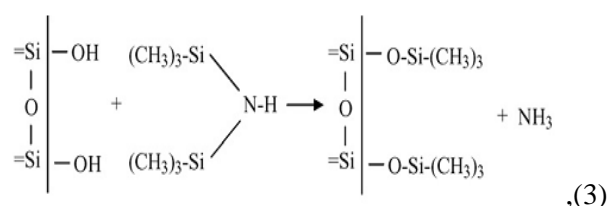


It seems that after formation of HCl, the following reaction between iron oxide entrapped in the pores and hydrochloride acid was happened [28].



Thus resulting composition was iron chloride-silica aerogel nanocomposite and didn't have any respond to external magnetic field.

Apparent color of samples AH remained constant in all steps (Fig. 1 b', c', d'). Surface modification of the silica gel with HMDZ was done as below reaction [29]:



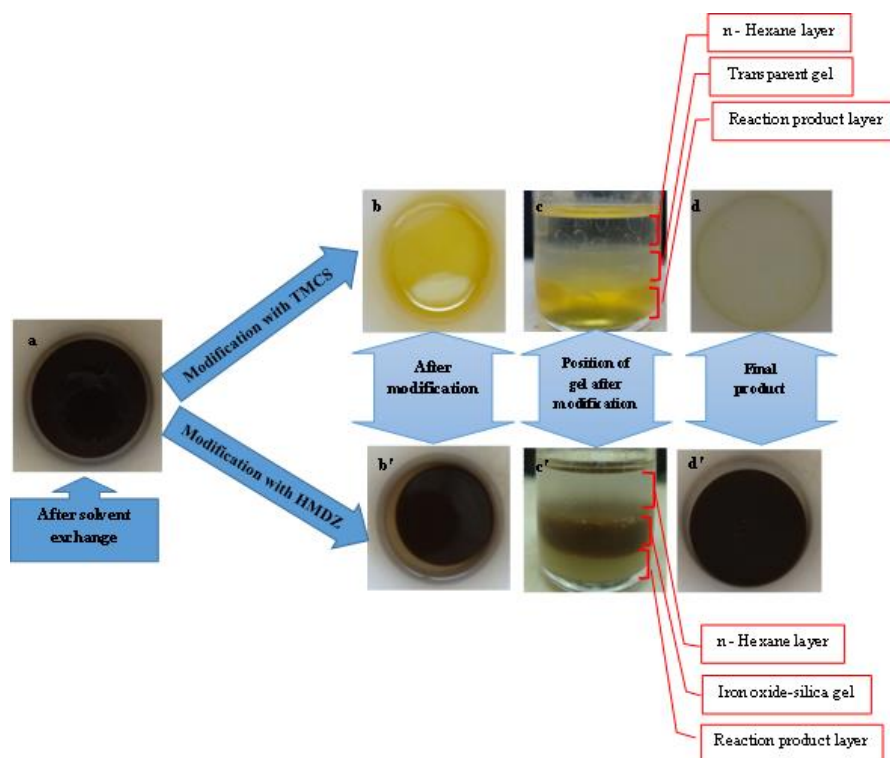


Fig. 1. Change in apparent color of iron oxide-silica gel in different steps (a) After solvent exchange; (b) and (b') samples AT and AH after modification respectively; (c) and (c') Position of gels after modification for samples AT and AH respectively; (d) and (d') Final product of samples AT and AH respectively.

NH₃ didn't react with Fe₃O₄ nanoparticles in modification step. Thus the structure and magnetic properties of Fe₃O₄ nanoparticles were retained. Resulting nanocomposites responded to external magnetic field strongly, so the main studies were done about samples AH.

Table 1 shows the effect of iron oxide initial weights on density and specific surface area of samples AH. Six initial weights of iron oxide nanoparticles (0.08, 0.1, 0.2, 0.5, 0.6 and 0.8 g) were examined and dispersed in 20cc deionized water in first step of synthesis. The properties of pure iron oxide, silica aerogel and iron oxide-silica xerogel also were measured for comparison. The iron contents of samples were measured by atomic absorption spectroscopy (AAS). The measured Fe contents of samples were less than the additive amount in initial step. This was probably due to the leakage of a part of iron oxide nanoparticle at exchanging the solvent and surface modification steps from the pores. The other little part of iron oxide particles were attracted by ultrasonic mixer probe. As shown in table 1 the Fe content of sample AH with 0.5 g initial weight of iron oxide was less (5.74%) than its related xerogel (7.1%). Because in xerogel synthesis there wasn't any solvent exchange and modification steps, so the leakage of iron oxide nanoparticles was less than aerogel in these steps.

Table 1. The effect of initial weight of iron oxide on nanocomposite property.

Sample	Density (g/cm ³)	specific surface area (m ² /g)	Fe content (%)
Pure silica aerogel	0.12	589	0
AH (0.08)*	0.35	366.8	3.02
AH (0.1)	0.36	368.07	3.74
AH (0.2)	0.39	430.1	4.63
AH (0.5)	0.42	499	5.74
AH (0.6)	0.51	509	6.81
AH (0.8)	0.58	517	7.49
Iron oxide-silica xerogel (0.5)	2.2	521	7.1
Pure Fe ₃ O ₄	5.1	82	100

* The numbers in parentheses are the initial amounts of iron oxide added to 20cc deionized water in first step

The results showed that the density of samples AH were increased with increasing the iron oxide amount. The reaction between some of Fe_3O_4 nanoparticles and SiO_2 and formation of Fe-O-Si bonds led to decrease modification of SiO_2 with silylating agent. This increased volume shrinkage and density. The values of density for the samples AH were between 0.35-0.58 g/cm^3 . For iron oxide-silica xerogel samples this value was 2.2 g/cm^3 and for pure silica aerogel was 0.12 g/cm^3 . These results showed iron oxide-silica aerogel surface modification were done less than pure silica aerogel and more than xerogel samples. Thus the porosity of pure silica aerogels was larger than their composites. On the other hand the density of pure iron oxide was 5.1 g/cm^3 that reduced the density of composites. Figure 2 compares the apparent properties of sample AH with initial 0.5 g Fe_3O_4 , its related xerogel and pure silica aerogel.

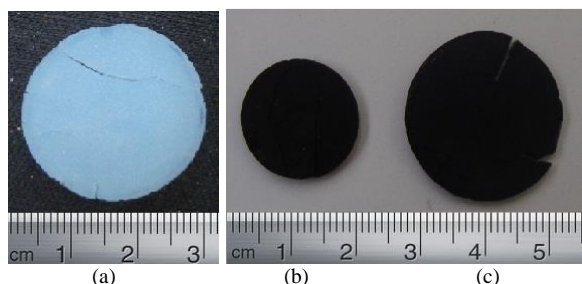


Fig. 2. Photographs of (a) pure silica aerogel; (b) magnetite-silica xerogel; (c) sample AH.

Two factors can affect on the nanocomposites specific surface area. The first factor is the presence of iron oxide nanoparticles with a low specific surface area that reduce the specific surface area of the composites considerably. The specific surface area of bare magnetite was 82 m^2/g . Thus with iron oxide doping, the specific surface area of the composite was decreased respect to pure silica aerogel (Table 1). The second factor is the small pores volume in the dense structures leading to an increase in specific surface area of the composites. Increasing surface area with increasing the initial amount of iron oxide and decreasing the density in table 2 was for this reason. So with adding the appropriate amount of iron oxide, the properties of nanocomposites can be regulated.

Figure 3 shows the result of XRD patterns of the magnetite and sample AH with 0.5 g iron oxide before annealing. The pattern for sample AH had four characteristic peaks at 30.3° (220), 35.7° (311), 57.2° (511) and 62.7° (440) which was consistent with the standard pattern of Fe_3O_4 (00-019-0629). The broad peak between 20 and 30 degree in pattern of sample AH, was due to amorphous silica. This

proved the existence of both amorphous silica and magnetite in nanocomposite before annealing.

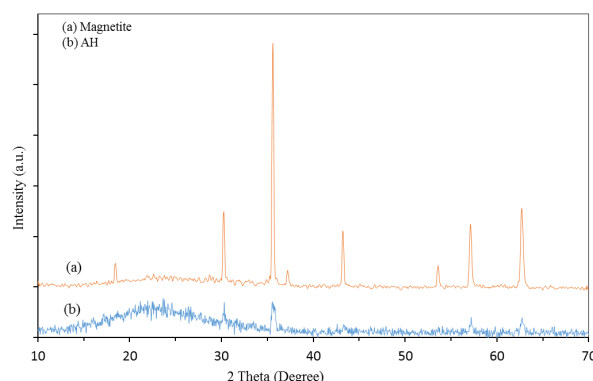


Fig. 3. The XRD pattern of (a) magnetite and (b) sample AH.

After annealing silica aerogel-magnetite nanocomposites in 500°C for 2 hr their apparent color was changed from dark brown to light brown. Figure 4 shows the XRD patterns of the magnetite and sample AH after annealing. There were ten characteristic peaks at 24.2°(210), 30.4°(220), 33.3°(310), 35.8°(311), 41°(321), 49.6°(421), 54.2°(430), 57.6°(511), 62.5°(440) and 64.1°(441) for annealing magnetite and seven characteristic peaks for annealing sample AH at 22.6° (210), 30.4°(220), 35.8°(311), 43.4°(400), 53.9°(422), 57.5°(511) and 63.1°(440) that corresponded to Fe_2O_3 (00-039-1346).

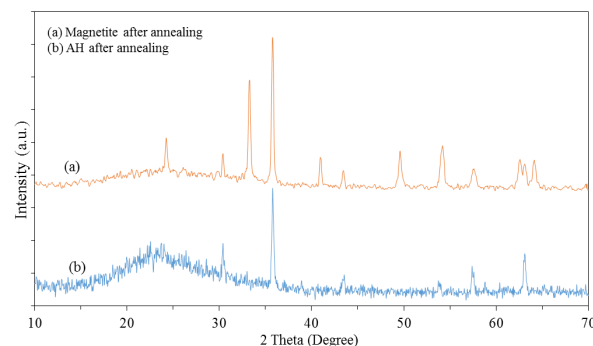


Fig. 4. The XRD pattern of (a) magnetite and (b) sample AH after annealing in 500°C for 2 hr.

These patterns showed that magnetite and sample AH were oxidized to maghemite and maghemite composite after heating in 500°C for 2 hr. The broad amorphous silica peak was also seen in maghemite composite pattern. The result composite showed strong response to the external magnetic field that was also evidence of formation maghemite polymorph.

Figure 5 (a) and (b) shows the XRD pattern of the AT sample before and after heating in 500°C for 2 hr respectively. Except of broad silica peak, any

other obvious peak wasn't seen. This showed that there wasn't any crystalline phase in silica structure that modified with TMCS.

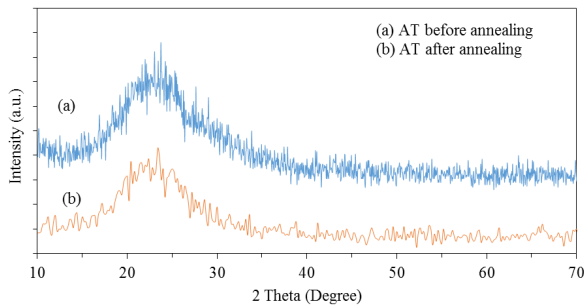


Fig. 5. The XRD pattern of sample AT: (a) before heating; (b) after heating in 500°C for 2 hr.

Crystallite size (D) is calculated using the Debye-Scherer's formula: [30]

$$D = \frac{k\lambda}{\beta \cos\theta}, \quad (4)$$

Where β is the full width at half maximum (FWHM) of the corresponding XRD peak, k is a constant (~ 1), λ is X-ray wavelength and θ is the Bragg angle. Crystallite size of magnetite and sample AH before and after annealing were calculated by the Scherrer formula and are shown in table 2. These results were confirmed nano crystallite size of structures.

Table 2. Crystallite size of samples magnetite and AH before and after annealing at 500°C, calculated by the Scherrer formula.

sample	Crystallite size (nm)	
	Before annealing	After annealing
magnetite	42	34
AH	21	40

Figure 6 shows field emission scanning electron micrographs for sample AH with 0.5 g iron oxide in two resolution and pure silica aerogel. The structures were uniform and porous. Comparison between SEM images of pure silica aerogel and magnetic silica aerogel showed that, the porosity of composite was less than pure silica aerogel in agreement with the results of BET analysis. The figures also showed that the particles and the pores size is less than 50 nm in agreement with XRD results.

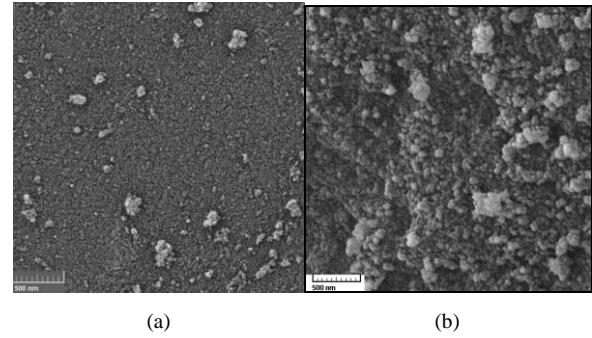


Fig. 6. FESEM image of sample (a) AH with 0.5 g iron oxide (b) pure silica aerogel

The TEM images of the pure silica aerogel and sample AH were obtained at the scales of 25 nm and 20 nm, respectively (Figure 7). This analysis showed that iron oxide nanoparticles were surrounded by porous silica aerogel matrix. When the magnetic particles disperse in silica sol, the inherent affinity between the silica and iron molecules is caused the formation of silica gel around the iron oxide nanoparticles.

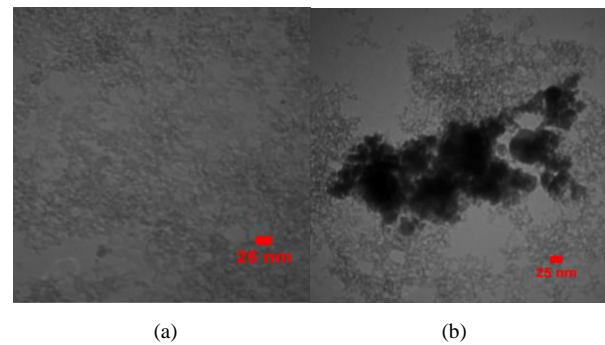


Fig. 7. TEM images of (a) pure silica aerogel (b) iron oxide-silica aerogel composite

Magnetization curve in room temperature are shown in Figure 8. Measurements were obtained by the use of vibrating sample magnetometer (VSM) with maximum magnetic field of 10 kOe. This hysteresis loop shows 0.74 emu/g for Remanence magnetization (M_R), 6.65 emu/g for Saturation magnetization (M_S) and 97.5 Oe for coercive field (H_C).

The inset of Figure 8 is the magnetization curve of Fe_3O_4 nanoparticles that was measured in company. As could be seen from this picture, the value of M_S for nanoparticles is 60.45 emu/g. Decrease in saturation magnetization is possibly due to the non-magnetic silica aerogel layer that decreases surface moments. On the other hand in nanocomposite structure there is a little amount of ferromagnetic nanoparticles per unit weight [31].

Figure 9 shows the FTIR investigations of (a) sample AH and (b) sample AT. In Figure 9a the absorption peak at 585cm^{-1} is the characteristic

absorption of a Fe–O bond that confirm the presence of Fe₃O₄ nanoparticles [32]. This peak in Figure 9b is very weak that prove the reaction of Fe₃O₄ nanoparticles in this sample. The major peaks at around 3500 and 1650 cm⁻¹ are attributed to O–H bonding. In samples that were modified with TMCS these peaks are very weak. It shows that the surface modification with TMCS is more effective than HMDZ and the most of O–H groups are replaced with O–Si–(CH₃)₃.

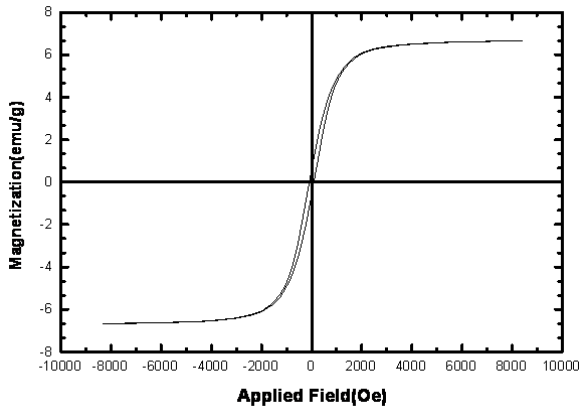


Fig. 8. Room temperature magnetization curve for iron oxide- silica aerogel nanocomposite. Inset figure is the magnetization curve of Fe₃O₄ nanoparticle

The peaks at around 2900 and 1450 cm⁻¹ indicates to C–H bonds that were seen in two samples and were stronger in HMDZ samples due to

two branches of (CH₃)₃ groups in this material. The peaks at around 1092 and 854 cm⁻¹ show asymmetric and symmetric of SiO₂ respectively. The strong peak in 469 cm⁻¹ are attributed to O–Si–O bond that exist in two graphs [33].

CONCLUSION

In this research, iron oxide- silica aerogel nanocomposites were synthesized successfully by sodium silicate precursor and ambient pressure drying method. Co-gelation of the nanoparticles and the matrix precursor were used to synthesize nanocomposites. The effect of two modification agents (HMDZ and TMCS) and the iron oxide content were investigated on the nanocomposite properties. The BET, AAS, SEM, TEM, VSM, FTIR and XRD method were used to characterize the result structures. HMDZ modified the gels without any effect on iron oxide nanoparticles and these particles retained their magnetic properties. By increasing the iron content of the samples, the density and specific surface area were increased. The minimum density of the synthesized samples by HMDZ in this research were 0.485 g/cm³ and the maximum specific surface area were 494.7 m²/g. The other analysis revealed the formation of porous magnetic silica aerogel. These structures can have many applications such as chemical and biochemical catalysts.

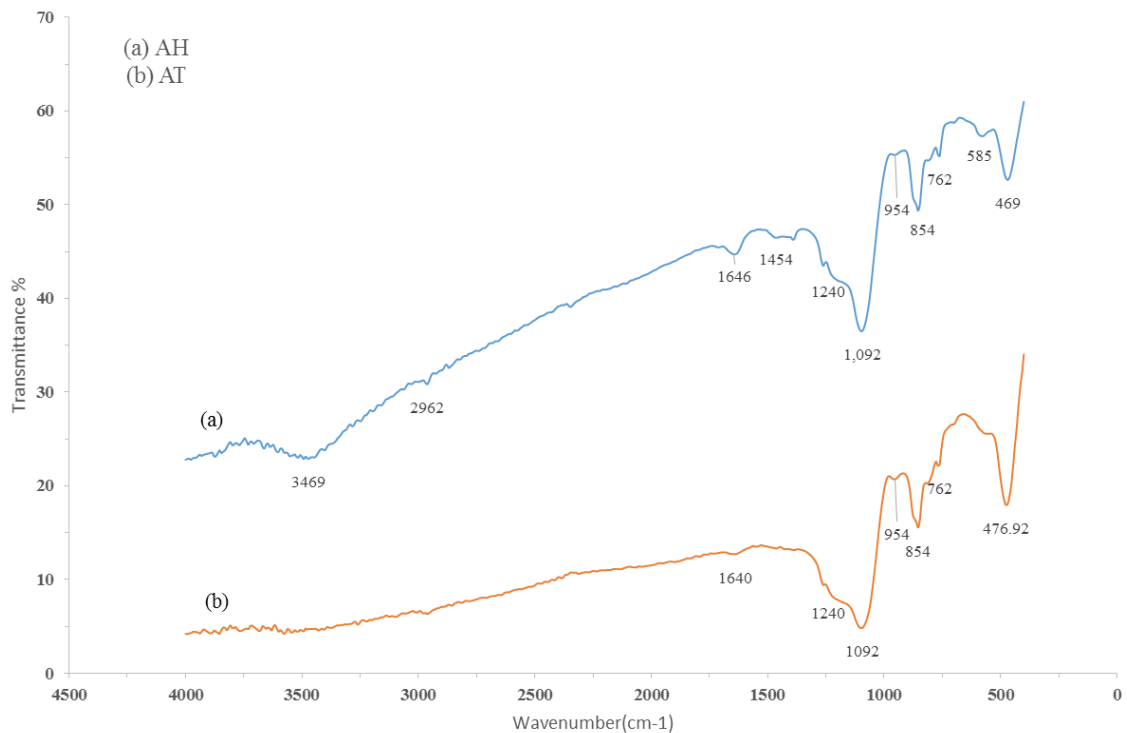


Fig. 9. FTIR spectra of (a) sample AH and (b) sample AT.

REFERENCES

1. S. Santra, R. Tapeç, N. Theodoropoulou, J. Dobson, A. Hebard, W. Tan, *Langmuir*, **17**, 2900 (2001).
2. S.P. Gubin, Y.A. Koksharov, G.B. Khomutov, G.Y. Yurkov, *Russ. Chem. Rev.*, **74**, 489 (2005).
3. C. Cannas, M. F. Casula, G. Concas, A. Corrias, D. Gatteschi, A. Falqui, A. Musinu, C. Sangregorioc, G. Spano, *J. Mater. Chem.*, **11**, 180 (2001).
4. A.-H. Lu, E.L. Salabas, F. Schuth, *Angew. Chem. Int. Edit.*, **46**, 1222 (2007).
5. M.E. Khosroshahi, L. Ghazanfari, M. Tahriri, *J. Exp. Nanosci.*, **6**, 580 (2011).
6. L. Casas, A. Roig, E. Rodriguez, E. Molins, J. Tejada, J. Sort, *J. Non-Cryst. Solids*, **285**, 37 (2001).
7. P.M. Zelis, M.B.F. van Raap, L.M. Socolovsky, A.G. Leyva, F.H. Sanchez, *Physica B*, **407**, 3113 (2012).
8. A.S. Dorcheh, M.H. Abbasi, *J. Mater. Process. Tech.*, **199**, 10 (2008).
9. F. Schwertfeger, D. Frank, M. Schmidt, *J. Non-Cryst. Solids*, **225**, 24 (1998).
10. F. Blanchard, B. Pommier, J.P. Reymond, S.J. Teichner, *Stud. Surf. Sci. Catal.*, **16**, 395 (1983).
11. M. Soufyani, D. Bourret, A. Sivade, R. empere, *J. Non-Cryst. Solids*, **145**, 60 (1992).
12. M.R. Ayres, X.Y. Song, A.J. Hunt, *J. Mater. Sci.*, **31**, 6251 (1996).
13. C.T. Wang, R.J. Willey, *J. Non-Cryst. Solids*, **225**, 173 (1998).
14. M.F. Casula, A. Corrias, G. Paschina, *J. Non-Cryst. Solids*, **25**, 293 (2001).
15. P. Fabriziooli, T. Burgi, A. Baiker, *J. Catal.*, **206**, 143 (2002).
16. M.B.F. van Raap, F.H. Sanchez, R.C.E. Torres, L. Casas, A. Roig, E. Molins, *J. Phys-Condens Mat.*, **17**, 6519 (2005).
17. B.J. Clapsaddle, A.E. Gash, J.H.Jr. Satcher, R.L.Simpson, *J. Non-Cryst. Solids*, **331**, 190 (2003).
18. S. Martinez, M. Meseguer, L. Casas, E. Rodriguez, E. Molins, M. Moreno-Manas, A. Roig, R.M. Sebastian, A. Vallribera, *Tetrahedron*, **59**, 1553 (2003).
19. M. Popovici, M. Gich, A. Roig, L. Casas, E. Molins, C. Savii, D. Becherescu, J. Sort, S. Surinach, J.S. Munoz, M. Dolores Baro, J. Nogues, *Langmuir*, **20**, 1425 (2004).
20. A. Lancok, K. Zaveta, M. Popovici, C. Savii, M. Gich, A. Roig, E. Molins, K. Barcova, *Hyperfine Interact.*, **165**, 203 (2006).
21. K. Racka, M. Gich, A. Slawska-Waniewska, A. Roig, E. Molins, *J. Magn. Magn. Mater.*, **127**, 290 (2005).
22. S. Masoudian, Hosseini H. Monfared, A. Aghaei, *Transition Met. Chem.*, **36**, 521 (2011). DOI 10.1007/s11243-011-9498-7.
23. C.T. Wang, R.J. Willey, *Catal. Today*, **52**, 83 (1999).
24. C.T. Wang, R.J. Willey, *J. Catal.*, **202**, 211 (2001).
25. M.B.F. van Raap, F.H. Sanchez, A.G. Leyva, M.L. Japas, E. Cabanillas, H. Troiani, *Physica B*, **398**, 229 (2007).
26. H. Bargozin, L. Amirkhani, J.S. Moghaddas, M.M. Ahadian, *Sci Iran*, **17**, 122 (2010).
27. U.K.H. Bangi, A.V. Rao, A.P. Rao, *Sci. Technol. Adv. Mater.*, **9**, 1 (2008). DOI 10.1088/1468-6996/9/3/035006
28. W.F. Kladnig, *J. Iron Steel Res. Int.*, **15**, 1 (2008).
29. A.P. Rao, A.V. Rao, G.M. Pajonk, P.M. Shewale, *J. Mater. Sci.*, **42**, 8418 (2007).
30. H.P. Klug, , L.E. Alexander, X-ray Diffraction, Wiley, New York, 1974, 132
31. H. Xu, N. Tong, L. Cui, Y. Lu, H. Gu, *J. Magn. Magn. Mater.*, **311**, 125 (2007).
32. K. Khoshnevisan, M. Barkhi, D. Zare, D. Davoodi, M. Tabatabaei, *Synth. React. Inorg. M.*, **42**, 644 (2012).
33. R. Al-Oweini, H. El-Rassy, *J. Mol. Struct.*, **919**, 140 (2009).

The kinetics study and reaction mechanism of acrylate grouting materials

Tao Wei^{1, 2, 3*}, Da Zhang^{1, 2, 3}, Liang Chen^{1, 2, 3}

¹ Materials and Structural Department, Changjiang River Scientific Research Institute, Wuhan 430010, China

² Collaborative Innovation Center for Geo-hazards and Eco-Environment in Three Gorges Area, Yichang 443002

³ National Dam Safety Research Center, Wuhan 430010, China

Received June 26, 2015, Revised September 10, 2015

Acrylate grouting material has been widely used in dams, tunnels and other underground buildings. This paper introduces the basic components of acrylate grouting material, then the reaction mechanism and dynamics of gelation process are discussed based on the theory of free radical polymerization. By measuring the relationship between gelation time and the concentration of initiator ammonium persulfate, the chain termination of free radical is confirmed to be single-base termination reaction. The gelation time is inversely proportional with the concentration of initiator and is directly proportional to the natural logarithm of the ratio of the initial concentration $[M]_0$ and a time component concentration $[M]$ of the acrylate monomer. The quantitative relation between them was derived. The result has a guiding significance on the material design and the gelation control of acrylate grouting material.

Key words: Kinetics, Reaction mechanism, Grouting material, Acrylate.

INTRODUCTION

Chemical grouting is a common method for the treatment of waterproof sealing [1, 2]. Chemical grouting material was filling into the formation or crack, which diffused, coagulated and cured, to increase the formation strength, reduce the permeability of the formation [3], prevent the formation of deformation [4, 5], or repair of cracks on concrete building [6, 7]. Acrylate is an important kind of chemical grouting material. Since the United States halted sales of acrylamide grouting in 1978 because of the pollution risk, the research and application of acrylic acid salts grouting material got the attention of the countries [8]. In 1980, acrylate polymer (AC-400) slurry began to instead of acrylamide grout materials. The AC-400 used now is the mixture of calcium, magnesium acrylate monomer, a small amount of methyl double acrylamide, triethanolamine, ammonium persulfate and water. In the 70s, China began to study acrylate grouting materials. The Changjiang River Scientific Research Institute carried out a study of acrylamide non-toxic alternatives, develop less toxic acrylic mixed salts of calcium and magnesium, which was successfully applied in Wan'an hydropower and dam seepage in the Three Gorges Project.

In recent years, a new crosslinking agent instead of methylene-bis-acrylamide was developed making acrylate grouting material more accord with

the requirement of environmental protection, at the same time there is the component increasing inflation performance as well as antagonists to eliminate the toxicity, and it improved the production technology to make them more outstanding performance [9]. To synthesize a kind of environmental crosslinking agents, and a water-soluble, non-toxic, replacing the original acrylic chemical grouting material used methylene bis-acrylamide cross-linker solved methylene bis-acrylamide difficult to dissolve and pollute the environment. This kind of crosslinking agent as raw materials in the preparation of acrylate chemical grouting material has low viscosity, good fluidity, can be poured into the tiny cracks in the gelation time control, low permeability, and high compressive strength of solid sand. Acrylate grouting material has been used in the dam foundation tunnels, sewers, underground buildings plugging and weak strata stabilization process, as well as other aspects of drilling wall has been widely used. Han's group explored the dynamics of gelation time in the oxidant ammonium persulfate and reductant sodium thiosulfate.

The reaction mechanism of grouting material is important because they can direct the actual application in engineering [10]. The kinetics of acrylate in ammonium persulfate oxidizer and triethanolamine accelerator was rarely reported. In this paper, bases on the theoretical basis of the radical polymerization, the reaction mechanism of acrylate grouting material in the present of the oxidizer ammonium persulfate and triethanolamine

To whom all correspondence should be sent:

E-mail: weitao@mail.crsri.cn, zhangda@mail.crsri.cn, chenliang@mail.crsri.cn

accelerator were described and the reaction kinetics of acrylate grouting material was discussed.

EXPERIMENTAL

The basic compositions of the chemical grouting material are the acrylate, crosslinking agent, initiator, accelerator, retarder and water. The crosslinking agent has two or more functional group which can be reacted with the primary agent. The gelation time can be controlled by adjusting the amount of retarder in the slurry between several minutes to several tens of minutes. There are a lot of acrylate monomer can be used in grouting, such as calcium acrylate, magnesium acrylate, zinc acrylate, potassium acrylate and sodium acrylate. Calcium acrylate was added as antagonists to get a lower toxicity and good performance of the gel. In this paper the mixture of calcium acrylate and magnesium acrylate solution were selected as the main agent.

Through a large number of tests, the best proportion of basic composition was determined, shown in Table 1.

Table 1. The basic composition of acrylate grouting material.

Materials composition	Mass percentage (%)
Acrylate monomer	10 ~ 20
Accelerant	1 ~ 2
Crosslinker	2 ~ 5
Initiator	0.5 ~ 2
Solvent	70 ~ 80
Retarder	be adjusted according to the curing time

RESULTS AND DISCUSSION

Radical polymerization mechanism

Acrylate grouting material is carried out in accordance with the mechanism of free radical polymerization. Radical chain polymerization is a chain reaction, consisting of a sequence of three steps: initiation, propagation, and termination.

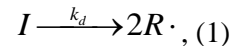
With ammonium persulfate as initiator and triethanolamine as accelerator in water, primary free radicals formed and stimulated the acrylate monomers coupled to double bond structure of crosslinking agent. The primary radicals inspired by acrylate monomer could form monomer free radicals. Polymer with space network was formed structure by radical polymerization. Retarder can capture the primary radicals and extend the time of the combination of free radicals and monomers,

which made the induction period of polymerization longer, thereby controlling the gelation time.

It is assumed that the initiator ammonium persulfate generate the primary radical. (M, acrylate monomer or crosslinking agent; Mn•, the growing polymer chain) According to the theory of free radical polymerization, each elementary reaction expression was discussed as follows:

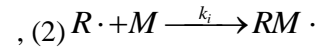
Step 1: Chain initiation

Chain initiation is the reaction of forming free radical of monomer, consisting of the following two steps. The first step is that the initiator decomposed to form a primary radical R•.



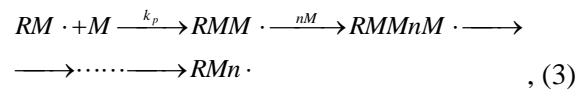
where k_d is the rate constant for the initiator dissociation

The second step is that monomer free radicals formed with the addition of monomer to primary radicals



Step 2: Chain propagation

As the propagation continues, each monomer unit was added. The radical has the same identity as the previous radical. Therefore, Eq.(3) of chain propagation was shown as following:



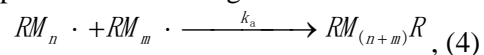
In which k_p is the rate constant for the Chain propagation.

Step 3: Chain termination

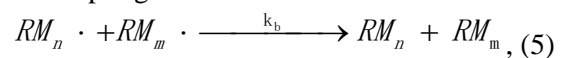
The growth of the chain takes place very rapidly to form higher weight polymer. But at some point, the polymer chain stops growing because the propagating radical could be terminated at the end.

The termination of the radical occurs by the bimolecular reaction between two radicals. They reacted with each other by coupling or disproportionation.

The two different modes of termination can be expressed as following:



(Coupling termination)



(Disproportionation termination)

In which k_a and k_b are the rate constants for terminations by coupling and, respectively.

Free radical polymerization kinetics of acrylate grouting material

The polymerization process of acrylate grouting material includes chain initiation, chain propagation and chain termination. Here the reaction rate of the reaction material (monomer and crosslinking agent) is represented. According to the law of mass action, the reaction rate equation can be derived.

The chain initiation rate equation was shown as following:

$$R_d = d[R\cdot]/dt = 2fk_d[I], (6)$$

In which k_d denotes the rate constant of chain initiation, R_d denotes the reaction rate of chain initiation, f denotes the initiator efficiency of initiation, and $[I]$ denotes the concentration of the initiator.

The overall rate of polymerization (R_p) can be considered as the rate of disappearance of monomer with respecting to time of $d[M]/dt$. This depletion is due to the initiator-monomer reaction and the propagation reaction.

$$R_p = -d[M]/dt = k_p[M\cdot][M], (7)$$

In which k_p denotes the rate constant of the chain propagation, $[M]$ denotes the concentration of monomer and crosslinker, $[M\cdot]$ denotes the total concentration of all the radical.

The rate of chain termination (R_t) can be considered as the disappearance rate of all the monomer radical, with respecting to time $d[M]/dt$, including coupling and disproportionation termination:

$$R_t = -d[M\cdot]/dt = 2k_t[M\cdot]^2, (8)$$

In which k_t denotes the rate constants for termination by coupling and disproportionation, and k_t is the sum of k_a and k_b .

In theory, three basic assumptions were introduced in polymerization kinetics, as the activity, large degree of polymerization and steady process. With three basic assumptions, the basic equations of polymerization kinetics can be introduced as following.

$$R_p = k_p[M] \left(\frac{fk_d}{k_t} \right)^{1/2} [I]^a, (9)$$

In which a is a reaction coefficient between 0.5 and 1.

In Eq.(9) R_p is also the consumption rate of monomer M , so R_p may be expressed as:

$$R_p = -d[M]/dt, (10)$$

Supposing the starting concentration of monomer M equals $[M]_0$, the combining of Eq.(9) and Eq.(10) can yield the time t as

$$t = \frac{I_n \frac{[M]_0}{[M]}}{k \left(\frac{fk_d}{k_t} \right)^{1/2} [I]^{1/2}} = \frac{I_n [M]_0}{k [I]^{1/2}}, (11)$$

Eq.(11) shows the relation between gelation time t and monomer concentration $[M]$, with reaction rate constant of k .

According to kinetics theory, free radicals reacted with one another to be terminated by coupling, and the rate of polymerization is proportional to the square of initiator concentration. When they react with one another to be terminated by disproportionation, the rate of polymerization is proportional to the initiator concentration. One molecule of acrylate could form free radicals. Therefore it is impossible for one molecule of acrylate to be terminated by coupling. So Eq.(11) is transformed into Eq.(12).

$$t = \frac{I_n \frac{[M]_0}{[M]}}{k_p \left(\frac{fk_d}{k_t} \right)^{1/2} [I]^{1/2}}, (12)$$

Eq.(12) shows that the gelation time is inversely proportional to ammonium concentration of persulfate initiator in temperature constant

For a given concentration of acrylate materials, the ratio $[M]_0/[M]$ is fixed at different process of solidification. When the grouting material gels, Eq.(12) is transformed into the Eq.(13):

$$C = t \times [I], (13)$$

To verify the correctness of the above Eq.(12), a set of experimental data was done (in Table 2), showing the influence of ammonium persulfate dosage on the gelation time.

If equation (12) is correct, the gelation time t multiplied by the concentration of ammonium persulfate should be a constant. So the data in Table 1 was plugged into equation (13) to calculate the value of product concentration C , when the concentration of ammonium persulfate was different (Table 3).

In Table 3, C is basically a constant. The results show that the gelation time of acrylate grouting material is inversely proportional to concentration of catalyst ammonium peroxydisulfate. Eq.(12) shows the relation between gelation time and initiator concentration. It also could be obtained that the acrylate grouting material chain termination reaction is a single-terminated reaction.

Table 2. Effect of $(\text{NH}_4)_2\text{S}_2\text{O}_8$ on the gelation time.

Concentration ($\text{mol}\cdot\text{L}^{-1}$)	0.0286	0.0491	0.07365	0.0982
Gelation time (s)	163	95	63	47

Note: Concentration of acrylate grouting material equals 25%, concentration of triethanolamine equals 1.0%, and the temperature is 25°C.

Table 3. The relationship of ammonium peroxydisulfate concentration and product concentration.

Concentration ($\text{mol}\cdot\text{L}^{-1}$)	0.0286	0.0491	0.0736	0.0982
Product concentration C	4.66	4.66	4.64	4.62

CONCLUSIONS

The reaction mechanism acrylate grouting material belongs radical polymerization reaction. The gelation time is inversely proportional with the concentration of initiator ammonium persulfate and is directly proportional to the natural logarithm of the ratio of the initial concentration $[\text{M}]_0$ and a time component concentration $[\text{M}]$ of the acrylate monomer. The quantitative relation between them is given. Its mathematical formula can be concluded. This formula has a guiding significance on gelation time for the formula design and the construction control of acrylate grouting material.

Acknowledgements: This work was financially supported by National Natural Science Foundation of China (Grant No. 51378078) and Ministry of Water Resources non-profit industry research project (Grant No. 201301023).

REFERENCES

1. H. B. Wallace, ASCE, New York, 1982.
2. D. Romanov, F. Gabrovser, W. Dreybrodt, *Engineering Geology*, **12**, 17 (2003).
3. A. Frnasson, *Tunnell. Undergroup Space Technol.*, **4**, 331 (2001).
4. W.G. Smoak, *Concrete International*, **13**, 33 (1991).
5. M.I. Yesilnacar, *Tunnell. Undergroup Space technol.*, **4**, 321 (2003).
6. O. Minemura, V. Sakata, S. Yuyama, *Construction and Building Materials*, **12**, 385 (1998).
7. A.A. Darrag, *Tunnell. Underground Space Technol.*, **3**, 319 (1999).
8. M. Weideborg, T. Kallqvist, K. E. Degard, *Norway Water Research*, **11**, 2645 (2001).
9. L.C. Lopez-Ureta, E.o Orozco-Guareño, L.E. Cruz-Barba, A. Gonzalez-Alvarez, F. Bautista-Rico, *J. Polymer Sci., Part A: Polymer Chemistry*, **8**, 2667 (2008).
10. Z. Kowalczyk, K.E. Olinski, *Mathematical Problems in Engineering*, doi:10.1155/2012/142060, (2012).

First-principles calculation of stacking fault energies and mechanical properties for high entropy solid solution $\text{Al}_x\text{CoCrCuFeNi}$ with different mole fraction of Al

Lan-xin Wang¹, Shan Yao^{1*}, Bin Wen²

¹School of Materials Science and Engineering, Dalian University of Technology, Dalian 116023, China

²State Key Laboratory of Metastable Materials Science and Technology, Yanshan University, Qinhuangdao 066004, China

Received June 26, 2015, Revised September 10, 2015

The ab initio calculations have been used to study the generalized stacking fault energy (GSFE) for the closed-packed (1 1 1) plane along <1 1 2>direction in FCC high entropy solid solutions $\text{Al}_x\text{CoCrCuFeNi}$ with $x=0, 0.5, 1, 1.5$ and 2 , respectively. The GSFE curves have been calculated by the first principle. Our calculated results of the GSFEs for FCC Al are agreement with previous calculation. The GSFE curves of high entropy solid solutions $\text{Al}_x\text{CoCrCuFeNi}$ are similar to which of FCC Al. The intrinsic stacking fault energy (ISFE) γ_{isf} of $\text{Al}_x\text{CoCrCuFeNi}$ with $x=1$ is the maximum, and with $x=2$ is the least. The unstable stacking fault energy (USFE) γ_{us} of $\text{Al}_x\text{CoCrCuFeNi}$ with $x=1$ is maximum, and with $x=0$ is the least. The high entropy solid solution $\text{Al}_x\text{CoCrCuFeNi}$ with $x=1$ has the lowest $\gamma_{\text{us}}/\gamma_{\text{isf}}$ ratio value, so full dislocation will be observed easily. We calculated the Peierls stress by Peierls-Nabarro model with GSFE curve, the changing of Peierls stress is similar to USFE with the different mole fraction of Al.

Key words: High entropy solid solution, Generalized stacking fault energy, Intrinsic stacking fault, Unstable stacking fault energy, First principle.

INTRODUCTION

High entropy alloys (HEAs) are a multicomponent system of 5 to 13 metallic elements with equiatomic or nearly equiatomic compositions [1-9]. The HEA AlCoCrCuFeNi was first synthesized by Yeh et al [7-11]. The most studies were about it. There are wear resistance and high-temperature compression strength of $\text{Al}_{0.5}\text{CoCrCuFeNi}$ [5]; adhesive wear behaviour of $\text{Al}_x\text{CoCrCuFeNi}$ [9]; microstructure characterization of $\text{Al}_x\text{CoCrCuFeNi}$ [12]; mechanical performance of the $\text{Al}_x\text{CoCrCuFeNi}$ [13] and so on. These researches indicate that it is impact on microstructure characterization, adhesive wear behaviour, wear resistance, tensile property, compression strength and mechanical performance by the mole fraction of Al changed. Mechanical properties of metals depend on phenomena is a hierarchical structure from atomic up to a macroscopic length scale [14]. The generalized-stacking-fault energy (GSFE), which was introduced by Vitek [14, 15], plays an important role in proposed model for the brittle-ductile transition and dislocation properties [16, 17]. However, it is possible to form material at the microscopic and nanoscopic length scales using deposition methods such as chemical vapour deposition, physical vapour deposition and molecular-beam epitaxy. In order to

minimize the quantity of defect, researchers need to know the mechanisms of dislocation nucleation, possibly leading to a criterion that determines when a dislocation will be created.

The GSFE is the interplanar potential energy for sliding one half of a crystal over the other half. Returning to the issue of dislocation nucleation in a crystal, it is desirable to know the shape of the entire GSFE curve, and to use it in a criterion for nucleation. Currently, such a potential can nowadays be determined from the embedded atom method (EAM), molecular dynamics (MD) calculations, and first-principles calculations [18]. The first-principles method has been successful in calculating the grains [19], so more accurate investigation of GSFE for FCC metals is needed. For example, Wu et. al calculated the generalized stacking fault surfaces and surface energies for FCC metals by first principle [18]; Muzyk et. al calculated the generalized stacking fault energy in aluminium alloys by first principle [20]; Wang et. al calculated the dislocation properties in magnesium by first principle [21]; Yan et. al calculated the generalized stacking fault energy and dislocation properties in BCC Fe by first principle [22], and so on.

The energy-displacement curve, known formally as the GSFE curve and introduced by Vitek [15, 23], cannot be measured experimentally except for a single point known as the intrinsic stacking fault energy (ISFE) γ_{sf} . The simulation region was

To whom all correspondence should be sent:

E-mail: yaoshan@dlut.edu.cn

rectangular with faces in the $\langle 1\ 1\ 2 \rangle$, $\langle 1\ 1\ 0 \rangle$ and $\langle 1\ 1\ 1 \rangle$ directions. Periodic boundary conditions were used in the $\langle 1\ 1\ 2 \rangle$ and $\langle 1\ 1\ 0 \rangle$ directions; the $(1\ 1\ 1)$ faces was free. The lattice was divided in half (cut by a $(1\ 1\ 1)$ plane), with the lower-half remaining fixed and the upper-half displaced in the $\langle 1\ 1\ 2 \rangle$ direction in small increments. The average energy/atom was used to calculate energy per unit area of the slip plane. For slip in some directions, such as the $\langle 1\ 1\ 2 \rangle$ directions of a FCC crystal, positions exist at which the lattice is stable, although the crystal is not in its bulk equilibrium structure. This stable configuration is known as the intrinsic stacking fault (ISF). So slip in the $\langle 1\ 1\ 2 \rangle$ directions is common because the unstable stacking fault energy (USFE) γ_{us} is the lowest in those directions [24].

In this paper, we present the GSFE for $(1\ 1\ 1)$ plane $\langle 1\ 1\ 2 \rangle$ direction in FCC structure using first-principle calculations employing CASTEP package for high entropy solid solution $\text{Al}_x\text{CoCrCuFeNi}$ with $x=0, 0.5, 1, 1.5$ and 2 , respectively. The slab calculation is used to obtain the GSFE curves for FCC structures. Then the Peierls stresses were calculated by Peierls-Nabarro model with GSFE curves.

COMPUTATIONAL METHOD

The total-energy calculations based on the density functional theory (DFT) embodied in the CASTEP package [25] are employed in the present study. The Perdew-Burke-Ernzerhof (PBE) [26] exchange-correlation functional for the generalized-gradient-approximation (GGA) [27] is used. A plane-wave basis set is employed within the framework of the projector augmented wave (PAW) method [28, 29]. The ion-electron interaction was modeled using norm-conserving pseudopotentials [30]. The model of high entropy solid solution $\text{Al}_x\text{CoCrCuFeNi}$ with $x=0, 0.5, 1, 1.5$, and 2 was built using the virtual crystal approximation (VCA) [31-33]. On the basis of tests, it is chosen the energy cut-off 250eV . For first-Brillouin-zone integrals, reciprocal space is represented by Monkhorst-Pack-special k point scheme [34] with $2 \times 4 \times 3$ grid meshes for FCC structure. The equilibrium theoretical lattice structure is determined by minimizing the Hellmann-Feynman force on the atoms and stress on the unit cell. The convergence of energy is $2 \times 10^{-5}\text{eV}$. In the present study, we calculated the GSFE curve for the $\langle 1\ 1\ 2 \rangle$ direction, since the slip between the closed-packed surface is most easily for FCC Al. The ideal FCC structure closed-packed surfaces have the configurationABCABC..... stacking

sequence of the atomic planes. To simulate the block shear process we use a slab consisting of 6 atomic layers in the $\langle 1\ 1\ 2 \rangle$ direction. Between periodically repeated slab the vacuum gap 15\AA normal to $(1\ 1\ 1)$ plane is chosen to avoid interactions between two slabs.

RESULTS AND DISCUSSION

First, we calculated the GSFE curve of FCC Al, shows the GSFE curve along $1/6 \langle 1\ 1\ 2 \rangle$ direction in FCC Al. The energy minimum value corresponds to the ISFE, where a full dislocation dissociates into a pair of Shockley partials. The energy maximum value is the USFE, which represents the lowest energy barrier for dislocation nucleation [18]. The trend of GSFE curve for the $\langle 1\ 1\ 2 \rangle$ direction in FCC Al crystal was agreement with previous calculation [17, 24, 35-40]. As can be seen from Fig. 1, it is found that γ_{us} and γ_{isf} are 144 and 100mJ/m^2 for FCC Al, respectively. Table 1 lists the corresponding unstable and intrinsic stable stacking fault energies for FCC Al along with other calculated values published in literature [39, 41-43].

These indicated that the set was reasonable. So we calculated the GSFE for the $\langle 1\ 1\ 2 \rangle$ direction in FCC high entropy solid solution $\text{Al}_x\text{CoCrCuFeNi}$ with $x=0, 0.5, 1, 1.5$ and 2 , respectively.

Using above set, we calculated the GSFE curve of the high entropy solid solution $\text{Al}_x\text{CoCrCuFeNi}$ with $x=0, 0.5, 1, 1.5$ and 2 , respectively. Fig. 1 showed the GSFE curve along $1/6 \langle 1\ 1\ 2 \rangle$ direction in FCC high entropy solid solution $\text{Al}_x\text{CoCrCuFeNi}$ with $x=0, 0.5, 1, 1.5$ and 2 , respectively. It is found from Fig. 1 that the GSFE of the high entropy solid solution $\text{Al}_x\text{CoCrCuFeNi}$ with $x=1$ is the largest at the same slide place, it indicate that the high entropy solid solution $\text{Al}_x\text{CoCrCuFeNi}$ with $x=1$ is difficult to slide, so its plastic property is better than the others high entropy solid solutions.

To further study the ISFE and USFE, Fig. 2(a) shows the ISFE and USFE of the high entropy solid solution $\text{Al}_x\text{CoCrCuFeNi}$, respectively. The calculated USFEs and ISFEs are listed in Table 1. With the values of γ_{us} and γ_{isf} is increasing, the potential barrier to form the stacking fault increased, and therefore it is difficult to form the stacking fault, and it is not easily deformed. It is normally that the stacking fault energy is closely related to the plastic deformation of the materials. The material having low stacking fault energy which can easily produce large plastic deformation slip dislocations further excited by twinning, and it is difficult to form stacking fault due to the high stacking fault energy, so the material having high stacking energy is poor

plastic deformability. However, it is found from Fig. 2 (a) that when the mole fraction of Al is 1, the ISFE and the USFE are the maximum. The ISFE is conducive to further stimulate the dislocation slip to improve the mechanical properties of materials. The ISFE and USFE increase first and then decrease by mole fraction of Al increasing, it indicate that the potential barrier which to form stacking fault is increased when the ISFE and USFE are increased, so it is difficult to form stacking fault, and is not easily deformed. For all high entropy solid solutions, the AlCoCrCuFeNi has the best plastic property due to the largest ISFE and USFE. It has been known that the deformation mechanism in crystals cannot be explained by the absolute value of ISFE γ_{isf} alone [44].

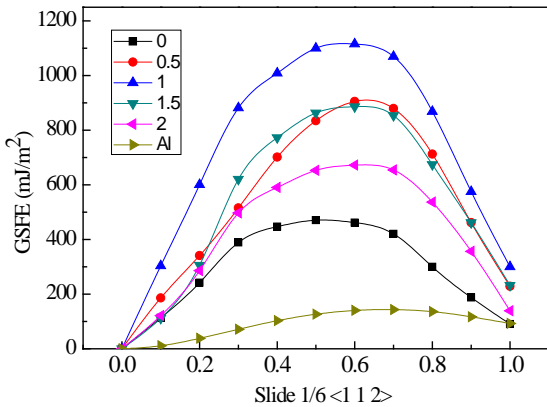
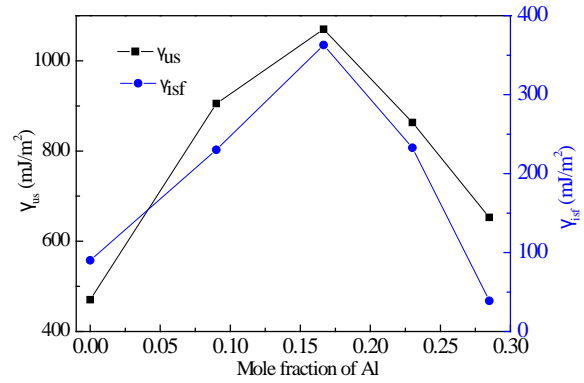


Fig.1. The GSFE curve along 1/6 the $\langle 1\ 1\ 2 \rangle$ direction for FCC Al and FCC high entropy alloy $\text{Al}_x\text{CoCrCuFeNi}$ with $x=0, 0.5, 1, 1.5$ and 2 , respectively.

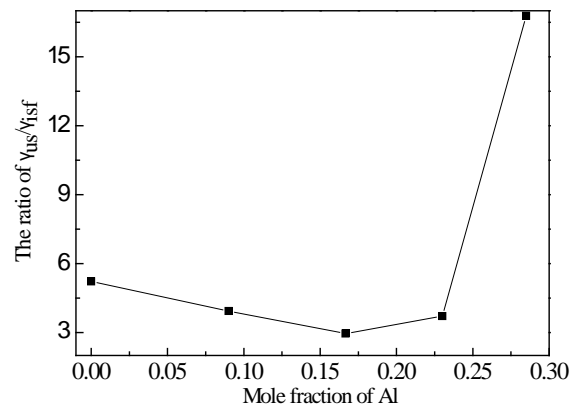
Although γ_{us} is not commonly used as fitting parameter for empirical potentials, the GSFE curves show the same qualitative trends for each type of materials. However, when applying a constant stress resulting in similar strain rates for both potentials, similar deformation mechanisms are observed, underlining the importance of the ratio of γ_{us}/γ is and not the absolute value of γ_{isf} [18, 44]. Although the stacking fault energy is higher, full dislocation will be observed more easily, but when this ratio is large, the energy increase necessary for nucleating the trailing partials substantial.

The value of ratio is more low, the more easy to generate dislocations, otherwise easy to generate partial dislocations.

Fig. 2(b) shows the ratios of γ_{us}/γ is for the high entropy solid solution $\text{Al}_x\text{CoCrCuFeNi}$. It is found that the ratio was the least when the mole



(a) The USFE and ISFE for the high entropy solid solutions $\text{Al}_x\text{CoCrCuFeNi}$



(b) The ratio of γ_{us}/γ_{isf} for the high entropy solid solutions $\text{Al}_x\text{CoCrCuFeNi}$

Fig.2. The USFE, ISFE and ratio of γ_{us}/γ_{isf} of the high entropy solid solution $\text{Al}_x\text{CoCrCuFeNi}$

fraction of Al is 1, it indicate that the high entropy solid solution AlCoCrCuFeNi may generate dislocation easily, then when the mole fraction of Al is 0 or 2, although the ISFE γ is little, it is hard to generate dislocation, because the ratio of γ_{us}/γ is large, especially mole fraction of Al is 2 for FCC high entropy alloy $\text{Al}_x\text{CoCrCuFeNi}$.

To describe the dislocation profile and other properties related to the core of a dislocation the atomic scale discreteness has to be considered. Peierls-Nabarro (P-N) [45-47] model provides a conceptual framework and combined with atomic forces derived from the GSFE. The PN model for planar dislocations provides a continuum solution for the disregistry of the dislocation from which a misfit energy can be computed and thus also energy barriers and stresses for dislocation motion. In the PN model, a dislocation is introduced into a lattice and it generates stresses at the interface/glide plane which are calculated according to elasticity theory.

The elastic stresses are restored by atomic forces acting on either side of the glide plane due to the misfit of atomic planes[48]. First, we calculated the lattice parameters and elastic constants of FCC Al and high entropy solid solutions $Al_xCoCrCuFeNi$ by first-principle, the results were listed in Table 2. The anisotropic factor depends on the elastic constants. It is noticed that the anisotropic factor of FCC Al or high entropy solid solutions are not 1, so we calculated the Peierls stress of FCC Al and high entropy solid solutions $Al_xCoCrCuFeNi$ with improved P-N model [21, 49]. The calculated results and yield strengths are listed in Table 3. We found from Table 3 that the Peierls stresses of all the high entropy solid solutions are larger than FCC Al, it indicates that the yield strengths of high entropy solid solution is larger than FCC Al, so the high entropy solid solution is difficult to yield, which is better than FCC Al. The Peierls stresses and yield strengths of high entropy solid solutions $Al_xCoCrCuFeNi$ with the different mole fraction of Al are shown in Fig. 3.

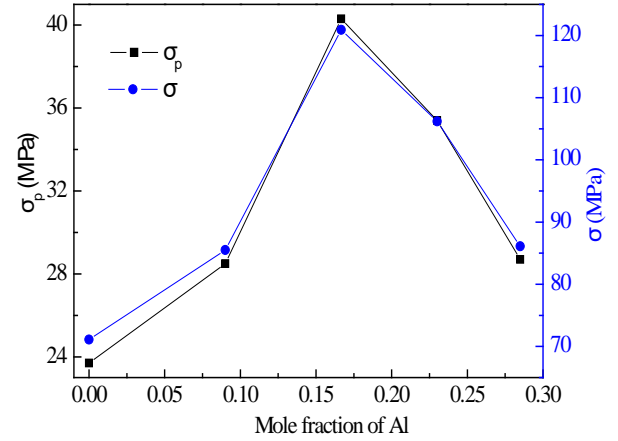


Fig. 3. The Peierls stress and yield strength of high entropy solid solutions $Al_xCoCrCuFeNi$.

It is noticed that the changing of Peierls stress with the different mole fraction of Al is similar to the USFE, this can explain that Peierls stress increases with the USFE increased [38, 50, 51, 52].

Table 1. Unstable and intrinsic stacking fault energies calculated in the present work for FCC Al and previously published literature values, and the calculated values for high entropy solid solutions $Al_xCoCrCuFeNi$. All values are given in mJ/m^2 .

	γ_{us} (mJ/m^2)	γ_{isf} (mJ/m^2)	Reference
Al	144	100	This work
	178 ^a	146 ^a	Brandl et al. [39]
	129 ^b	126 ^b	Jahnaek et al. [41]
	162 ^c	130 ^c	Kibet et al. [42]
	140 ^d	112 ^d	Jin and Dunham [43]
$Al_0CoCrCuFeNi$	470.4	90.1	This work
$Al_{0.5}CoCrCuFeNi$	905.4	230.1	This work
$Al_1CoCrCuFeNi$	1070.1	362.8	This work
$Al_{1.5}CoCrCuFeNi$	863.3	232.6	This work
$Al_2CoCrCuFeNi$	652.8	38.9	This work

a. Ref. [39]: using VASP-PAW-GGA; b. Ref. [41]: using VASP-US-GGA;

c. Ref. [42]: using VASP-PAW-GGA; d. Ref. [43]: using VASP-PAW-GGA, NEB-DFT method.

Table 2. The lattice parameters, elastic constants and anisotropy factor of FCC Al and high entropy solid solutions

	$Al_xCoCrCuFeNi$				
	a (\AA)	C_{11} (GPa)	C_{12} (GPa)	C_{44} (GPa)	$A=2C_{44}/(C_{11}-C_{12})$
Al	4.05	114.3	61.92	31.62	1.21
$Al_0CoCrCuFeNi$	3.57	359.1	156.6	182.5	1.81
$Al_{0.5}CoCrCuFeNi$	3.49	699.8	228.9	321.4	1.36
$Al_1CoCrCuFeNi$	3.48	888.1	292.7	288.7	0.97
$Al_{1.5}CoCrCuFeNi$	3.51	941.6	303.3	174.9	0.54
$Al_2CoCrCuFeNi$	3.59	323.8	442.2	-339.1	5.72

Table 3. The Peierls stress of FCC Al and high entropy solid solutions $Al_xCoCrCuFeNi$.

	σ_p (MPa)	σ_s (MPa)
Al	12.2	36.6
$Al_0CoCrCuFeNi$	23.7	71.1
$Al_{0.5}CoCrCuFeNi$	28.5	85.5
$Al_1CoCrCuFeNi$	40.3	120.9
$Al_{1.5}CoCrCuFeNi$	35.4	106.2
$Al_2CoCrCuFeNi$	28.7	86.1

CONCLUSION

In conclusions, we present ab initio calculations on the GSFE on $\langle 112 \rangle$ directions for the closed-packed (111) plane in FCC high entropy solid solutions $Al_xCoCrCuFeNi$. The density functional theory (DFT) within generalized gradient approximation (GGA) is employed. Our values of the GSFEs are in better agreement with previous calculated results. The calculated results indicate that the USFE γ_{us} and ISFE γ_{isf} of FCC high entropy alloy $Al_xCoCrCuFeNi$ with $x = 1$ is the maximum. We analyze the ratio of γ_{us}/γ_{isf} and positions for the ISF and USF. The high entropy solid solution $Al_xCoCrCuFeNi$ with $x=1$ has the lowest γ_{us}/γ_{isf} ratio value, so full dislocation will be observed easily. The calculated results of Peierls stresses indicate the high entropy solid solutions are difficult to yield, which is better than FCC Al.

REFERENCES

1. T. Masuko, A. Minami, N. Iwasaki, T. Majima, S. Nishimura, Y. C. Lee, *Anal Biochem.*, **69**, 339 (2005).
2. S. Ranganathan, *Current Science.*, **85**, 1404 (2003).
3. L. Liu, J. Zhu, C. Zhang, J. Li, Q. Jiang, *Materials Science and Engineering.*, **64**, 548 (2012).
4. X. Yang, Y. Zhang, P. Liaw, *Procedia Engineering*, **36**, 292 (2012).
5. Y. Zhang, X. Yang, P. Liaw, *JOM*, **64**, 830 (2012).
6. C.Y. Hsu, J. W. Yeh, S.K. Chen, T.T. Shun, *Metallurgical and Materials Transactions A*, **35**, 1465 (2004).
7. J.W. Yeh, S.K. Chen, S.J. Lin, J.Y. Gan, T.S. Chin, T.T. Shun, C.H. Tsau, S.Y. Chang, *Advanced Engineering Materials.*, **6**, 299 (2004).
8. J.W. Yeh, S.J. Lin, T.S. Chin, J.Y. Gan, S.K. Chen, T.T. Shun, C.H. Tsau, S.Y. Chou, *Metallurgical and Materials Transactions A*, **35**, 2533 (2004).
9. P.K. Huang, J.W. Yeh, T.T. Shun, S.K. Chen, *Advanced Engineering Materials*, **6**, 74 (2004).
10. J.M. Wu, S.J. Lin, J.W. Yeh, S.K. Chen, Y.S. Huang, H.C. Chen, *Wear.*, **261**, 513 (2006).
11. C.C. Tung, J.W. Yeh, T.T. Shun, S.K. Chen, Y.S. Huang,

- H.C. Chen, *Materials letters.*, **61**, 1 (2007).
12. S. Singh, N. Wanderka, B. Murty, U. Glatzel, J. Banhart, *Acta Materialia*, **59**, 182 (2011).
13. C.J. Tong, Y.L. Chen, J.W. Yeh, S.J. Lin, S.K. Chen, T.T. Shun, C.H. Tsau, S.Y. Chang, *Metallurgical and Materials Transactions A*, **36**, 881 (2005).
14. C.J. Tong, M.R. Chen, J.W. Yeh, S.J. Lin, S.K. Chen, T.T. Shun, S.Y. Chang, *Metallurgical and Materials Transactions A*, **36**, 1263 (2005).
15. V. Vitek, *Lattice Defects*, **5**, 1 (1974).
16. V. Vitek, *Philosophical Magazine*, **18**, 773 (1968).
17. R. Thomson, *Physical Review B*, **52**, 7214 (1995).
18. Y. Sun, E. Kaxiras, *Philosophical Magazine A*, **75**, 1117 (1997).
19. X.Z. Wu, R. Wang, S.F. Wang, Q.Y. Wei, *Applied Surface Science*, **256**, 6345 (2010).
20. R.W. X.Z. Wu, S.F. Wang, *Applied Surface Science*, **256**, 3409 (2009).
21. M. Muzyk, Z. Pakielna, K. Kurzydowski, *Scripta Materialia*, **64**, 916, (2011).
22. R. Wang, S.F. Wang, X.Z. Wu, Q.Y. Wei, *Physica Scripta*, **81**, 601 (2010).
23. J.-A. Yan, C.-Y. Wang, S.Y. Wang, *Physical Review B*, **70**, 105 (2004).
24. V. Vitek, *Physica Status Solidi.*, **18**, 687 (1966).
25. J.A. Zimmerman, H. Gao, F.F. Abraham, *Modelling and Simulation in Materials Science and Engineering*, **8**, 103 (2000).
26. M. Segall, P.J. Lindan, M. Probert, C. Pickard, P. Hasnip, S. Clark, M. Payne, *Journal of Physics*, **14**, 2717 (2002).
27. J.P. Perdew, K. Burke, M. Ernzerhof, *Physical review letters*, **77**, 3865 (1996).
28. M.C. Payne, M.P. Teter, D.C. Allan, T. Arias, J. Joannopoulos, *Reviews of Modern Physics*, **64**, 1045 (1992).
29. P.E. Blöchl, *Physical Review B*, **50**, 17953 (1994).
30. G. Kresse, D. Joubert, *Physical Review B.*, **59**, 1758, (1999).
31. D. Hamann, M. Schlüter, C. Chiang. *Physical Review Letters*, **43**, 1494 (1979).
32. L. Bellaiche, D. Vanderbilt, *Physical Review B*, **61**, 7877 (2000).
33. B. Winkler, C. Pickard, V. Milman, *Chemical Physics Letters*, **362**, 266 (2002).
34. J.M. Larkin, A.J. McGaughey, *J. Appl. Physics*, **114**, 023507 (2013).
35. H.J. Monkhorst, J.D. Pack, *Physical Review B*, **13**, 5188 (1976).
36. G. Lu, N. Kioussis, V.V. Bulatov, E. Kaxiras, *Physical Review B*, **62**, 3099 (2000).
37. S. Ogata, J. Li, S. Yip, *Science*, **298**, 807 (2002).
38. P. Denteneer, J. Soler, *Solid State Commun.*, **78**, 857 (1991).
39. J. Hartford, B. Von Sydow, G. Wahnström, B. Lundqvist, *Physical Review B*, **58**, 2487 (1998).
40. C. Brandl, P. Derlet, H. Van Swygenhoven, *Physical Review B*, **76**, 54 (2007).
41. A.F. Wright, M.S. Daw, C. Fong, *Phil. Magazine A*, **66**, 387 (1992).

42. M. Jahnátek, J. Hafner, M. Krajčí, *Physical Review B*, **79**, 224103 (2009).
43. S. Kibey, J. Liu, D. Johnson, H. Sehitoglu, *ActaMaterialia*, **55**, 6843 (2007).
44. Z. Jin, S. Dunham, H. Gleiter, H. Hahn, P. Gumbsch, *ScriptaMaterialia*, **64**, 605 (2011).
45. H. Van Swygenhoven, P. Derlet, A. Frøseth, *Nature Materials*, **3**, 399 (2004).
46. R. Peierls, *Proc. Phys. Soc.*, **52**, 34 (1940).
47. F. Nabarro, *Proceedings of the Physical Society*, **59**, 256 (1947).
48. J.P. Hirth, J. Lothe, *Theory of Dislocations*, **12**, 127 (1982).
49. B.v. Sydow, J. Hartford, G. Wahnström, *Computational Materials Science*, **15**, 367, (1999).
50. S.F. Wang, *Journal of Physics A: Mathematical and Theoretical*, **42**, 025208 (2009).
51. O.N. Mryasov, Y.N. Gornostyrev, *Physical Review B*, **58**, 11927 (1998).
52. W. Xiao-Zhi, W. Shao-Feng, L. Rui-Ping, *Chinese Physics B*, **18**, 2905 (2009).

Extraction of vanadium from sulfuric acid leaching solution of stone coal by ion exchange

Xiao Yang, Yi-min Zhang*, Shen-xu Bao

School of Resources and Environmental Engineering, Wuhan University of Technology, 122 Luoshi Road, Wuhan, Hubei 430070, PR China

Received June 26, 2015; Revised September 10, 2015

The extraction of vanadium from the acid leaching solution contained high concentration of impurities from stone coal by ion exchange was studied. Experimental results showed that vanadium can be effectively separated and extracted from the solution containing 2.68 g/L V, 3.82 g/L Fe, 18.63 g/L Al, 5.67 g/L Mg, 5.94 g/L K, 1.43 g/L P and 0.62 g/L Si by ion exchange and selective scrubbing and chemical precipitation. The proper pH range for ion exchange was 1.8-2.0. It was found that 98.5% of vanadium with 9.5% of iron and 7.41% phosphorus and 8.89% silicon were adsorbed by the resin D201 from the feed solution. Loaded iron can be selectively scrubbed by 0.5 mol/L HCl. 99.68% of vanadium with the same proportion of phosphorus and silicon was eluted by 2 mol/L NaOH. The removal of P and Si from the eluted solution was performed by adding 2 times stoichiometry of MgSO₄ at pH 8.0 and 80 °C for 1 h. After precipitation of metavanadate and calcination, high purity of V₂O₅ was obtained.

Keywords: Stone coal, vanadium extraction, ion exchange

INTRODUCTION

Vanadium-bearing stone coal is an important vanadium resource in China, hence, vanadium extraction from stone coal is paid more attention to in this country. At present, acid leaching with H₂SO₄ have been widely adopted for vanadium leaching from stone coal due to the merits of high vanadium recovery and low pollution [1, 2]. In order to improve the vanadium leaching rate, the high H₂SO₄ concentration is needed in acid leaching process commonly. Therefore, many impurities, such as Al, Mg and Fe ions are also leached along with vanadium from stone coal, which results in the complex vanadium-bearing leaching solution with high concentrations of impurities elements and low pH value. These impurities are detrimental to the recovery of vanadium from the acid leaching solution and need further separation and purification [3].

In order to find an effective route for separating vanadium and iron, researchers have paid special attention to this subject in recent years. Solvent extraction [4, 5] and ion exchange [6, 7, 8] are widely used to recover vanadium from the leaching solution. The separation of vanadium from the acid leaching solution with the mixed reagent D2EHPA/TBP has been studied by many authors [9, 10]. Tavakoli and Dreisinger [11] studied the

separation of vanadium from iron by solvent extraction using acidic and neutral organophosphorus extractants and indicated that Cyanex 923 could selectively extract V(V) over Fe(III) and D2EHPA revealed a suitable separation for V(IV) over Fe(II). The separation of V(IV) and Fe(III) from the acid leach solution of stone coal by D2EHPA/TBP was studied by Ma [3]. However, separation of vanadium and iron is not complete in solvent extraction with the above extractants. Compared to solvent extraction, ion exchange has the advantage of simply in operation and high purity of product. However, the study of extraction of vanadium by iron exchange mainly focus on low-acid solution with fewer impurities [6, 7, 8]. Moreover, little information has been found regarding the separation of vanadium from strong acid solution with high concentration of impurities by ion exchange. In our previous study, Al, Mg, Na and K almost have no effect on vanadium adsorption while it was difficult to separate V(V) from Fe(III) when weak base anion resin was selected [12]. Recently, by accident, it was found that the separation of vanadium and other ions from the acid leaching solution can be directly carried out with a strong base anion exchange resin D201. In this study, the loading behavior of D201 for vanadium at the optimum loading condition was determined. The recovery process of vanadium from the sulfuric acid leaching solution is reported.

To whom all correspondence should be sent:
E-mail: zym126135@126.com

Table 1. Composition of the solution (g/L).

Elements	V	Fe	Al	Mg	K	P	Si
Acid leaching solution	2.68	3.82	18.63	5.67	5.94	1.49	0.49
Filtrate at pH 2.0	2.56	2.24	18.51	5.65	5.72	1.25	0.45
Effluent	0.04	2.02	18.49	5.65	5.71	1.16	0.33
Eluted solution	15.36	0.012	0.011	0.002	0.003	0.18	0.037
Purified solution	15.29	0.002	0.001	0.001	0.002	0.009	0.006

EXPERIMENTAL

Anion-exchange resin

The strong base anion exchange resin D201 with function group of $[-N(CH_3)_3]$ and structure of crosslinking acrylate was obtained from Hangzhou Zhengguang Chemical Company of China. The diameter of more than 95% resin beads is in the range of 0.45-1.00 mm. The resin was first soaked in distilled water for 24 h, and then alternately soaked in 2 mol/L NaOH and 2 mol/L HCl for 12 h, repeated three times as this way, at last activated with 2 mol/L HCl and rinsed with distilled water before use. After adsorption, the loaded resin was eluted by 2 mol/L NaOH and regenerated by 2 mol/L HCl.

Sample solution and analysis

The sulfuric acid leaching solution of stone coal was prepared by roasting the stone coal at 850 °C for 1 h followed by leaching with 15% (v/v) H_2SO_4 and 5% (wt) $NaClO_3$ (as oxidant) at 95 °C and for 6 h. Due to roasting and oxidative leaching, vanadium and iron in the leaching solution existed predominantly in the form of V(V) and Fe(III). The composition of this solution was listed in Table 1 and the pH value of the solution was 0.4. The adjustment of pH using CaO and H_2SO_4 . After pH adjustment the solution was kept standing for 24 h and then the filtration was conducted. Vanadium concentration was titrated with ammonium ferrous sulphate [13]. The concentrations of other ions were determined by inductively coupled plasma-optical emission spectrometer (ICP-OES, Optima 4300DV, USA) after suitable dilution. The pH was determined with S220 SevenCompact™ pH meter (Mettler Toledo, Switzerland), and the degree of accuracy is 0.001.

Batch adsorption experiments

The experiments were carried out in the conical flask (500 mL) on the constant temperature bath oscillator at 150 rpm, at room temperature (25 ± 0.5 °C) for 24 h, the volumes of the solution and the wet resin were fixed in 200 mL and 10 mL respectively. After adsorption, the suspension was

filtered, and the solution was analyzed for vanadium and other ions concentrations. Ion uptakes were obtained by determining the ion concentrations before and after contact with the resin.

Column experiments

Trials were carried out in a glass column $\Phi 2.5 \times 30$ cm which operated with the leaching solution at the ambient temperature. Forty (40) mL of the pretreated resin, were wet-packed into the glass column. The operation was performed by downstream flow at a certain flow rate. Samples were collected periodically from the column eluate and analysed to determine ion content. The adsorption is stopped once the concentration of vanadium in the effluent reaches 0.05 g/L. 2 mol/L NaOH solution is then used to elute the loaded resin and the resin is then regenerated using 2 mol/L HCl.

Experiment fundamental

Fig.1 is the forms of vanadium (V) existing in sulfate solution under different pH and concentration [14]. As can be seen, vanadium (V) in the sulfate solution ($\log(V(V)) = -1.28$) is mainly in the forms of $VO_2SO_4^-$, $H_2V_{10}O_{28}^{4-}$, $HV_{10}O_{28}^{5-}$ between pH 1 and 4. These anionic vanadium species with other anionic species such as PO_4^{3-} , SiO_3^{2-} in the feed solution can be adsorbed by anion resin while cations such as Al^{3+} , Mg^{2+} , K^+ and Na^+ remain in the solution. It has been reported that iron(III) has a tendency to combination with sulfate to form the complexes $Fe(SO_4)_2^-$ [15], which can also be adsorbed by anion resin. Loading reaction of vanadium and other ions can be represented as Eqs.(1) to (6) and RCl represents chloride form of D201.



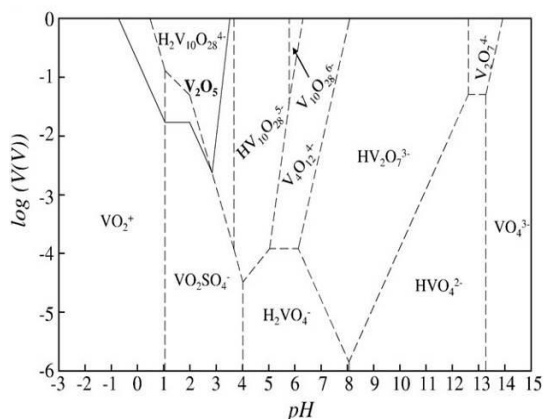


Fig. 1. Activity–pH diagram for vanadium(V)–water–sulfur–water system at 298.15 K [14].

RESULTS AND DISCUSSION

Batch experiments

Effect of solution pH

In order to investigate the effect of solution pH on the loading of vanadium and other metal ions from sulfuric acid leaching solution, experiments were carried out in the solution pH range from 0.5 to 2.4. Fig. 2 shows that pH value is an important condition for the vanadium adsorption in the solution and the adsorption efficiency of the resin for the vanadium increases with the pH from 0.5 to 2.4. The loading behavior of vanadium with the acidity of the solution can be explained using the activity–pH diagram of vanadium shown in Fig. 1. From Fig. 1 it can be observed that with pH increasing, the predominant form of vanadium changed from VO_2^+ to VO_2SO_4^- , $\text{H}_2\text{V}_{10}\text{O}_{28}^{4-}$ and $\text{HV}_{10}\text{O}_{28}^{5-}$. It is well known that the higher the charge of ion the better adsorption performance of it, thereby the adsorption rate of vanadium increases with pH. Iron adsorption increases slowly with pH increase and the total adsorption is below 20%. However, both phosphorus and silicon adsorption decrease with pH increase. Since the charge of $\text{H}_2\text{V}_{10}\text{O}_{28}^{4-}$ and $\text{HV}_{10}\text{O}_{28}^{5-}$ is higher than PO_4^{3-} , SiO_3^{2-} and $\text{Fe}(\text{SO}_4)_2^-$, the adsorption performance of vanadium is much better than that of phosphorus, silicon and iron. The adsorption percentage of Al, Mg, K was negligible in our experimental range which indicates that vanadium can be separated from Al, Mg, K.

Although higher pH value is beneficial for vanadium adsorption, it was found that when pH is over 1.6, iron, phosphorus, silicon and vanadium gradually precipitated, which made the loss of vanadium. As showed in Fig. 3, the precipitation of the above ions increases with pH increases. Moreover, the loss of vanadium increases slowly with pH increased from 1.6 to 2.0 and increases rapidly with pH increased from 2.0 to 2.4. Hence,

to maximise vanadium adsorption and minimise vanadium loss, accordingly, the solution pH was strictly controlled between 1.8-2.0.

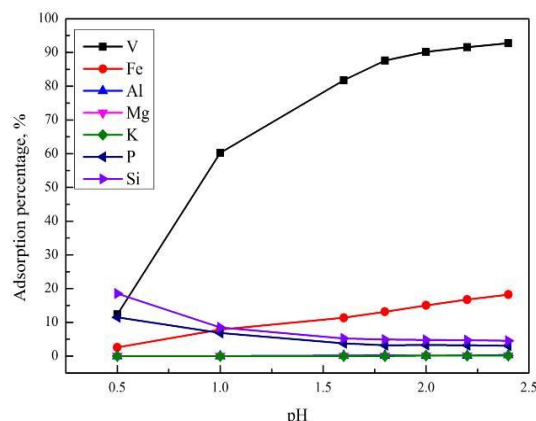


Fig. 2. Influence of pH value on vanadium and other metal ions adsorption.

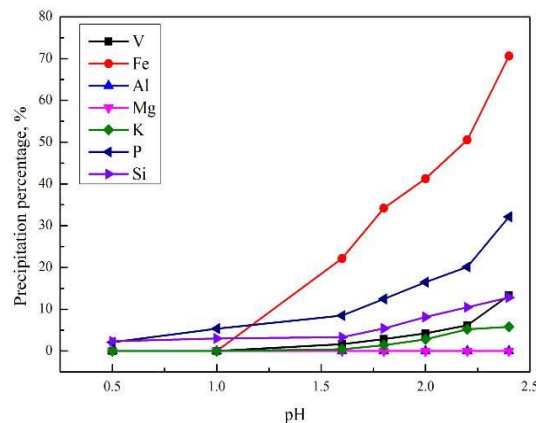


Fig. 3. Ions precipitation with pH.

Scrubbing of impurities

As mentioned above, the impurities of iron, phosphorus and silicon were adsorbed along with vanadium, and the scrub of these impurities from the loaded resin is necessary. The loaded resin was scrubbed by 0.5 mol/L HCl at the HCl/resin volume ratio of 2 and the results were shown in Table 2.

Table 2. Scrubbing ions from loaded resin.

Ion	V	Fe	P	Si
Scrubbing efficiency, %	5.17	94.19	15.23	23.15

It was shown that 94.19% of loaded iron and 15.23% of phosphorus and 23.15% silicon can be scrubbed by 0.5 mol/L HCl while 5.17% of vanadium was scrubbed off given a further separation of vanadium and iron, phosphorus and silicon. After scrubbing, there was a very small amount of impurities which may not effect the elution of vanadium.

Elution of vanadium

In vanadium ion exchange process, NaOH is usually adopted as eluant and the pH of the eluate is higher than 13. It can be seen from Fig.1 that vanadium mainly exist in the form of VO_4^{3-} under the pH value is higher than 13. Thus, the elution reaction can be represented by Eqs.(7) to (9), where ROH represents the hydroxide form of D201.



In this study, batch elution experiments were carried out with different concentration of NaOH, and the results are presented in Fig.3. As is shown in Fig.3, the elution percentage of vanadium increased rapidly from 42% to 92% with the increase of NaOH concentration from 0.5 to 2 mol/L. Due to there was little difference in the elution performance of vanadium with NaOH concentration increasing from 2 mol/L to 4 mol/L, 2 mol/L NaOH solution was chosen for the elution of vanadium in further experiments.

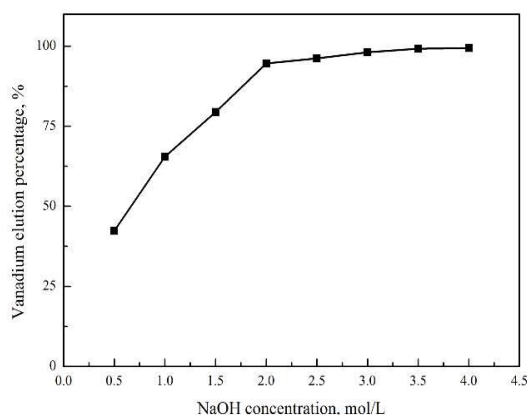


Fig. 4. Effect of NaOH concentration on the elution of vanadium.

Column experiment

Continuous column experiments were performed under pH of 2.0 and a constant flow rate of 100 mL/h. The adsorption results of vanadium and other ions are shown in Fig. 4. As can be seen in Fig. 5, the concentrations of iron, phosphorus and silicon increased rapidly in the effluent with the increasing of effluent/resin ratio. When effluent/resin volume ratio reached 18, in the effluent, iron concentration was the same as that of the feed solution, while vanadium concentration was close to 0.03 g/L at this time. It was interesting that the concentration of iron in the effluent was slightly higher than that in feed solution after the volume ratio was above 12, which indicated that

iron was eluted when effluent/resin volume ratio was about 12, and the concentration of iron indicating that some iron adsorbed in the resin was replaced by vanadium, the same phenomenon was observed by Fan [16]. There was no further adsorption of phosphorus and silicon once the effluent/resin volume ratio increased to 14 and 16 respectively. The concentration of vanadium is not more than 0.03 g/L in the effluent until the volume ratio over 20. From Fig. 5 it can be seen that if the breakthrough point was 0.05 g/L vanadium, the volume ratio would be 30, and the average concentration of vanadium is less than 0.05 g/L in the collected effluent, suggesting that the vanadium can be removed effectively from the iron, phosphorus and silicon contained solution with the resin. The raffinate contained 0.04 g/L vanadium, 2.02 g/L iron, 1.16 g/L phosphorus and 0.41 g/L silicon, which equate to 98.44% vanadium extraction whilst about 9.83% of iron together with of 7.41% phosphorus and 8.89% silicon were extracted.

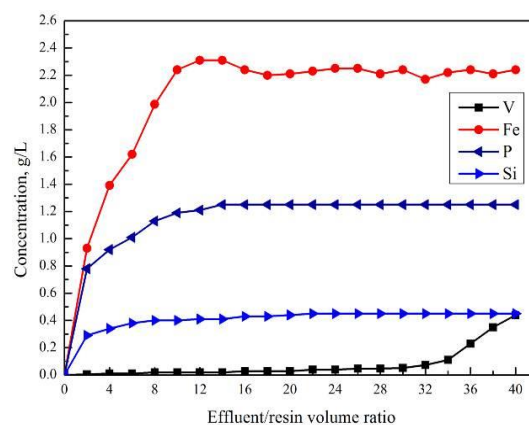


Fig. 5. Adsorption curves of the resin for iron.

Loaded resin was scrubbed by 0.5 mol/L HCl, the scrubbing curves were represented in Fig. 6. The results showed that iron can be effectively scrubbed from the loaded resin while only a small amount of loaded vanadium was scrubbed off. The scrubbing efficiency of phosphorus and silicon was in the range of 7%~20%. The differences of the scrubbing behavior of vanadium, iron, phosphorus and silicon indicating that vanadium and iron can be completely separated in the scrubbing process while the completely separation of vanadium and phosphorus and silicon need further operation. The scrubbing of iron was increased from 50.86% to 92.46% when the HCl to resin volume ratio was increased from 0.5 to 2. No significant difference was observed in the results obtained within the HCl to resin volume ratio range from 2 to 3. Therefore, HCl to resin volume ratio of 2 was selected for further investigations.

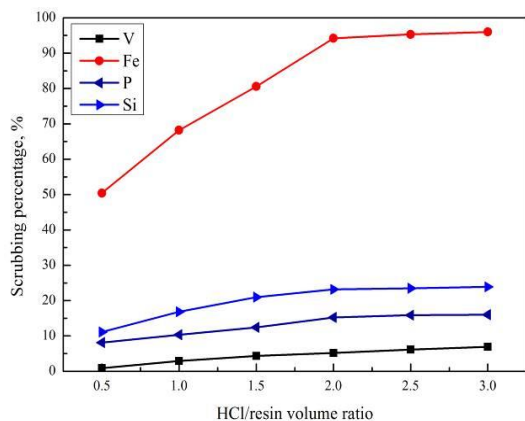


Fig. 6. Scrubbing of ions from the loaded resin using 0.5 mol/L HCl.

The scrubbed resin was eluted using 2 mol/L NaOH under the constant flow rate of 50 mL/h at room temperature, and the results were shown in Fig. 7.

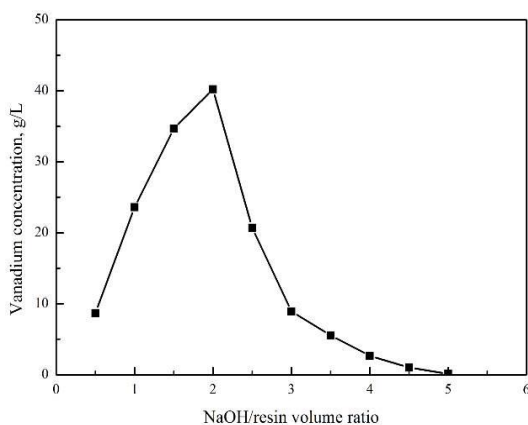


Fig. 7. Desorption curves of the loaded resin.

It was shown that the peak value of vanadium concentration in the effluent appeared when effluent/resin volume ratio was near 2, then the concentration of vanadium in the effluent was less than 0.1 g/L when the effluent/resin volume ratio was above 5, which can be regarded as the terminal

point of the elution, and the desorption of vanadium reached 99.68% at this time. Phosphorus and silicon were eluted along with vanadium in the same proportion and need further purification. Then the resin was regenerated by 2 mol/L HCl and reused in adsorption. The concentrations of vanadium and other ions in the eluted solution were shown in Table 1. From Table 1, it can be seen that phosphorus and silicon were eluted along with vanadium and need further purification. To remove phosphorus and silicon, the chemical precipitation method was usually adopted. The pH of eluted solution was adjusted to 8.0-9.0, then 2 times of stoichiometry $MgSO_4$ solution was added at 80 °C under stirring for 1 h to precipitate phosphorus and silicon as $Mg_3(PO_4)_2$ and $MgSiO_3$ [8]. After purification, the impurities concentrations are all below 0.01 g/L indicating that the purified solution is qualified feed solution for vanadium precipitation.

Preparation of V_2O_5

The purified solution was mixed with 2 times of stoichiometry $(NH_4)_2SO_4$ to precipitate metavanadate for 4 hour at 60 °C. Precipitation was obtained after filtration, scrubbing with water and calcination at 550 °C for 2 h. The product of V_2O_5 with purity of 99.52% was achieved, indicating that the product was of high quality.

Process for the separation and extraction of vanadium from sulfuric acid leaching solution

According to the previously mentioned test results, a process flowsheet of separation of vanadium and iron from acid leaching solution is shown in Fig. 8.

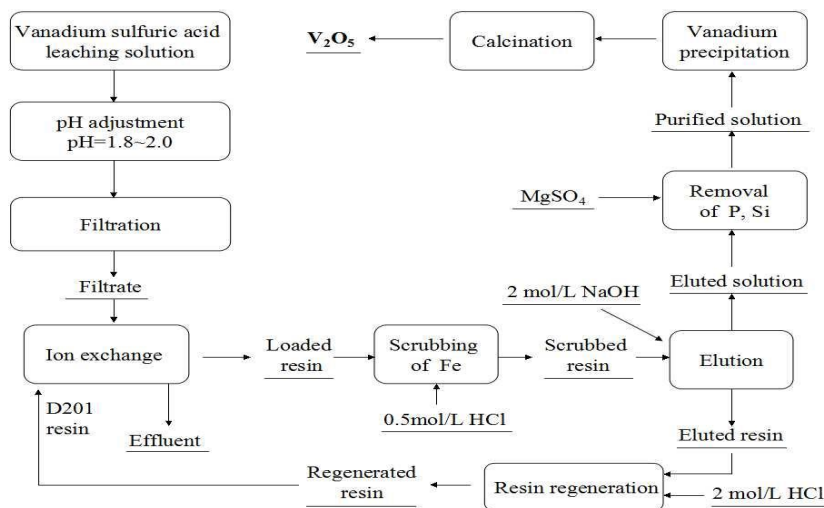


Fig. 8. Flowsheet of recovery of vanadium from sulfuric acid leaching solution of stone coal.

First, the solution pH was adjusted between 1.8~2.0 and then filtration was taken. Then the filtrate was contacted with the D201 resin and above 98% of vanadium and a small amount of iron, phosphorus and silicon was adsorbed by the resin. Loaded resin was scrubbed by 0.5 mol/L HCl and almost all the loaded iron can be scrubbed. Then the resin was eluted by 2 mol/L NaOH solution for vanadium desorption and then the resin was regenerated by 2 mol/L HCl. The eluted solution was purified by MgSO₄ to remove phosphorus and silicon. After precipitation and calcination, high purity of V₂O₅ can be obtained.

CONCLUSION

Batch adsorption experiments and column experiments have been carried out to verify the applicability of ion exchange for the separation of vanadium from the acid leaching solution of stone coal. The separation and recovery of vanadium from sulfuric acid leaching solution of stone coal in the presence of Fe, Al, Mg, K, P and Si were investigated using anion resin D201. The optimum pH value for the separation of vanadium with the resin was in the range of 1.8-2.0. Most of the vanadium together with a small amount of iron, phosphorus and silicon were selectively loaded by the resin at pH 2.0 but the loaded iron was separated from vanadium during scrubbing with 0.5 mol/L HCl solution. The loaded vanadium was successfully eluted by using 2 mol/L NaOH solution. The impurities of phosphorus and silicon in the eluted solution were removed by MgSO₄. After metavanadate precipitation and calcination, V₂O₅ with purity of 99.52% can be obtained.

Acknowledgements: This research was financially supported by the National Key Science-Technology Support Programs of China (NO.

2015BAB03B05), the National Nature Science Foundation of China (NO. 51404177).

REFERENCES

1. M. Li, C. Wei, G. Fan, C. Li, Z. Deng, X. Li, *Hydrometallurgy*, **98**, 308 (2009).
2. X. Zhang, K. Yang, X. Tian, W. Qin, *Int. J. Miner. Process.*, **100**, 184 (2011).
3. Y. Ma, X. Wang, M. Wang, C. Jiang, X. Xiang, X. Zhang, *Hydrometallurgy*, **153**, 38 (2015).
4. M. Noori, F. Rashchi, A. Babakhani, E. Vahidi, *Sep. Purif. Technol.*, **136**, 265 (2014).
5. X. Li, C. Wei, J. Wu, M. Li, Z. Deng, C. Li, H. Xu, *Sep. Purif. Technol.*, **86**, 64 (2012).
6. T. H. Nguyen, M. S. Lee, *Hydrometallurgy*, **147-148**, 142 (2014).
7. L. Zeng, Q. Li, L. Xiao, *Hydrometallurgy*, **97**, 194 (2009).
8. X. Wang, M. Wang, L. Shi, J. Hu, P. Qiao, *Hydrometallurgy*, **104**, 317 (2010).
9. X. Li, C. Wei, Z. Deng, M. Li, C. Li, G. Fan, *Hydrometallurgy*, **105**, 359 (2011).
10. G. Hu, D. Chen, L. Wang, J. Liu, H. Zhao, Y. Liu, T. Qi, C. Zhang, P. Yu, *Sep. Purif. Technol.*, **125**, 59 (2014).
11. M.R. Tavakoli, D.B. Dreisinger, *Hydrometallurgy*, **141**, 17 (2014).
12. W. Li, Y. Zhang, T. Liu, J. Huang, Y. Wang, *Hydrometallurgy*, **131-132**, 1 (2013).
13. GB/T8704.5, National Standard of People's Republic of China, Ferrovandium-Determination of Vanadium Content- the Ammonium Ferrous Sulfate Titrimetric Method and the Potentionmetric Titrimetric Method, 2007. (In Chinese)
14. X. Zhou, C. Wei, M. Li, S. Qiu, X. Li, *Hydrometallurgy*, **106**, 104 (2011).
15. M.C. Martí-Calatayud, D.C. Buzzi, M. García-Gabaldón, E. Ortega, A.M. Bernardes, J.A.S. Tenório, V. Pérez-Herranz, *Desalination*, **343**, 120 (2014).
16. Y. Fan, X. Wang, M. Wang, *Hydrometallurgy*, **136**, 31 (2013).

Statistical optimization of surfactant assisted dispersive liquid-liquid microextraction for trace mercury determination by GF-AAS

A. Gholami*, H. Noorizade

University of Kashan, Faculty of Chemistry, Department of Analytical Chemistry, Kashan, P.O. Box 87317-51167
Islamic Republic of Iran

Received June 26, 2015; Revised September 10, 2015

A new method of surfactant assisted dispersive liquid-liquid microextraction prior to graphite furnace atomic absorption spectroscopy (GF-AAS) has been developed for determination of trace amounts of mercury in aqueous solutions. In this method, Triton X-114 (TX-114), a non-ionic surfactant, compared with DLLME, was substituted as disperser solvent and emulsifier agent that could afford effective emulsification and make the extraction comparatively greener.

The effects of different experimental factors on the extraction was examined using two experimental design methods; a screening design to identify more effective parameters and a central composite design at five levels of the operating parameters to find out optimum values.

Under the optimal conditions, the limit of detection (LOD) for mercury was $0.023 \mu\text{g.L}^{-1}$, with enhancement factor (EF) of 125 and the relative standard deviation (RSD) of 8.1% ($n=5$, $C=1.0 \mu\text{g.L}^{-1}$).

The proposed method was applied for preconcentration and determination of mercury in different aqueous samples and the recoveries for the spiked samples were in the range of 95 – 106%.

Keywords: Surfactant assisted dispersive liquid-liquid microextraction, Triton X-114, Mercury, Experimental design

INTRODUCTION

Mercury could be released to the nature from two major sources, weathering of rocks that contain Hg and industrial activities; also using mercury-containing fungicides may lead to releasing Hg to the environment. Another and major source of Hg contamination includes waste incinerators and coal-fired utilities [1].

Rise in environmental mercury occurred in condition that this element is very harmful for health. According to the researches, mercury pollutants could affect many different areas of the brain and its associated functions, resulting in a variety of symptoms. These include personality changes (shyness, irritability, and nervousness), changes in vision (constriction of the visual field), tremors, loss of sensation, deafness, muscle incoordination and difficulties with memory [2].

Mercury compounds also have been introduced by the US Environmental Protection Agency as possible human carcinogens. Therefore, the development of rapid and accurate determination methods for monitoring the levels of mercury in natural waters is absolutely necessary [3].

Regardless of good developments in the modern analytical instruments, direct trace determination of

analytes at low concentrations is often a difficulty for analytical chemists and so a sample-preparation step is necessary [4,5].

Convention sample preconcentration and preparation methods such as solid phase extraction (SPE) and liquid-liquid extraction (LLE) are time consuming, laborious and need a large amount of organic solvents.

In recent years, many researchers have focused on these methods to provide alternative pre ecological solvent-free extraction methods or techniques employing a minimal amount of solvents.

LLE is one of the oldest extraction techniques used most frequently in the case of aqueous samples with complex matrix composition [6].

First attempts to miniaturized LLE methods lead to introducing liquid phase microextraction (LPME) and then dispersive liquid- liquid microextraction (DLLME) methods [7]. The latter is basically consists of a proper mixture of disperser and extraction solvent that is injected into the aqueous sample containing analyte(s) rapidly. The cloudy solution is formed as a result of the formation of fine droplets of extraction and disperser solvent in the solution. Finally, the cloudy solution is centrifuged and small sedimented phase containing extracted analyte(s) is analyzed by appropriate analytical instruments [8].

To whom all correspondence should be sent.

A. Gholami Tel.: +983155912380; fax: +98 3155552935

DLLME is a low cost, fast and efficient extraction method but not completely environmental friendly. The main disadvantage of DLLME is using relatively high volume of disperser solvents (in ml range) such as acetonitrile or methanol. Usual disperser solvent are harmful and environmentally unfriendly. Another disadvantage is decreasing extraction efficiency because of increasing analyte solubility in the presence of a disperser solvent [9,10].

Among the efforts made to solve these problems and to develop miniaturized extracting method, one has led to surfactant-assisted dispersive liquid-liquid microextraction (SA-DLLME) [11-13]. In this method, surfactant was used as an environmental friendly emulsifier. Surfactants are surface (or interface) active chemicals that have both hydrophobic and hydrophilic parts, and are soluble in organic solvents and water. Because of particular properties, these compounds are considered good choices as disperser solvents in DLLME [14].

In the present study, SA-DLLME method for determination of Hg contamination in trace levels in an aqueous sample has been developed.

The first step in Hg²⁺ extraction into organic solvent from the aqueous phase is forming a suitable complex with acceptable hydrophobicity. Diethyldithiocarbamate (DDTC), an appreciate chelating agent, was used in this study to extract Hg ions from aqueous solutions.

DDTC can form complexes with many metallic ions under suitable pH to extract metal ions into appreciate organic solvents. It is a common chelating agent which forms stable complexes with transition metals [15,16].

In SA-DLLME, a surfactant is used as a substitute of traditional disperser solvents in DLLME. The Triton X-114 (TX-114) is the most widely used surfactant that has been used in surfactant-assisted DLLME method [17,18] and was applied in this study. TX-114 is a Non-ionic surfactant with good emulsification properties which makes the extraction relatively greener.

A few microliters of an organic solvent containing suitable amount of TX-114 were used to extract the Hg from water samples.

Some affecting parameters on extraction process that must be optimized are as follows: volume of extraction solvent, concentration of chelating agent, time of extraction, pH, sample volume and salting out effect. One method for obtaining the best condition is using an experimental design method intended to: (1) Investigating the effect of different factors can affect enrichment factor in the extraction procedure. (2) Identifying the factors that have

higher impact on the extraction results. (3) Obtaining a better insight about the method that would help us to find optimized conditions considering the interactions between factors. These steps have been done by Plackett Burman [19,20] design, central composite design [21,22] and response surface methods [23], respectively.

The extracted analytes were determined by graphite furnace atomic absorption spectroscopy (GF-AAS). The analytical efficiency and possible application of the method in real water sample analysis were also investigated.

EXPERIMENTAL

Material and methods

Reagents and chemicals. All used reagents were of analytical grade purity purchased from Merck (Germany). Stock solution of mercury (1000 mgL⁻¹) was prepared by dissolving the appropriate amount of HgCl₂ (Merck, Darmstadt, Germany). Working standard solutions were prepared daily by appropriate dilutions of the standard stock solution. Working standard solutions were prepared daily by stepwise diluting of stock standard solutions.

Diethyldithiocarbamate (DDTC) was solution prepared by dissolving suitable amount of the compound (Shanghai Reagent Factory, Shanghai, China) in 100 ml of deionized water.

Apparatus. An atomic absorption spectrometer (Unicam AA929) equipped with continuous source background correction (deuterium lamp) and graphite furnace atomizer (GF90) were employed. Hollow cathode lamps were utilized as the radiation source for each element. Instrumental parameters for mercury are shown in Table 1. The pH was measured by using a pH meter (Metrohm 691 pH meter).

Table 1: Instrumental parameters for Mercury

Instrumental parameters	Mercury		
Wavelength (nm)	253.7		
Bandwidth	0.5		
Atomizer type	Electrographite		
Injected sample volume (μl)	20		
Background correction	D ₂		
Furnace heating program			
Step	Temperature Hg (°C)	Time (Sec)	Ramp (°C.S ⁻¹)
Drying	120	30	10
Pyrolysis	500	10	50
Atomization	1400	3	0
Cleaning	1900	6	0

DLLME Procedure. 10 ml of sample solution after PH adjustment was placed in conical test tube. Then appreciate concentration of ligand (DDTC) was

transferred into the vessel leading to form hydrophobic complex. Then, optimal amounts of surfactant (TX-140) were added into the solution and 180 μL of extractant (CCl_4) was injected rapidly into the solution using a syringe. After the injection and shaking manually for 1 min, the solution became turbid because of the presence of emulsifier (surfactant) and so CCl_4 was dispersed into fine droplets to extract the analytes. After this step, Cloudy solution was centrifuged to remove sedimented extraction phase at the bottom of conical test tube and finally it was placed in the graphite furnace cuvette using 20 μl Hamilton syringe for AAS analyses.

RESULT AND DISCUSSION

Optimization Step

Some factors had effects on determination of Hg by SA-DLLME and should be optimized. Therefore, enrichment factor (EF) was chosen as an analytical response under different conditions. The enrichment factor as a response is defined in Eq. (1):

$$EF = C_{\text{sed}} / C_0 \quad (1)$$

where EF is enrichment factor; C_{sed} and C_0 are analyte concentration in sedimented phase and primary analyte concentration in aqueous phase, respectively. C_{sed} was obtained from conventional LLE-ETAAS calibration curve (extraction condition: 10 ml of standard water sample, ligand concentration of 0.024M, 10 ml CCl_4 and pH at 5.06).

Extraction solvent optimization

The first step in SA-DLLME is finding a suitable extraction solvent. The extraction solvent must meet some conditions such as low solubility in water and low volatility, high capacity for analyte extraction and having density more than water. Generally extraction solvent conditions in SA-DLLME are very similar to conventional DLLME.

Three solvents that have these properties including CH_2Cl_2 , CHCl_3 and CCl_4 were examined. The highest enrichment factor at same condition was obtained for CCl_4 , so CCl_4 was chosen as extraction solvent.

Experimental design

Some factors affect SA-DLLME and should be optimized, such as extraction solvent volume (A), ionic strength (B), pH (C), concentration of surfactant (D), extraction time (E), and ligand concentration (F).

Optimization of these several factors requires a lot of experiments and it is a time-consuming and costly procedure. A screening experimental design method called Plackett Burman was used to find

main effects with significant influence on resonance. After choosing significant factors, a central composite design (CCD) combined with response surface method (RSM) was used to derived response surface equation and to find optimized values for each factor.

Plackett Burman Design

A Plackett Burman design containing 12 runs was used to determined significant factors. Low and high levels for all factors were selected based on preliminary experiments. In order to eliminate nuisance and extraneous variables, these 12 runs were carried out randomly and after that, the ANOVA results were estimated for determining main effects.

Plackett Burman design values for each parameter in coded and uncoded values are shown in Table 2.

Table 2. Two level Plackett Burman design values

Parameters	Low (-1)	High (+1)
extraction solvent volume	50 μL	250 μL
ionic strength	5mmol/L	100mmol/L
Ph	3	9
concentration of surfactant	0.01 %v/v	0.05% v/v
extraction time	2 min	5 min
ligand concentration	0.01M	0.1M

Pareto chart of the studied variables has been obtained from screening experiment and are shown in Fig 1. The normalized effect of each variable is shown by horizontal bars and vertical line at 95% confidence level judges the effects that are statistically noteworthy.

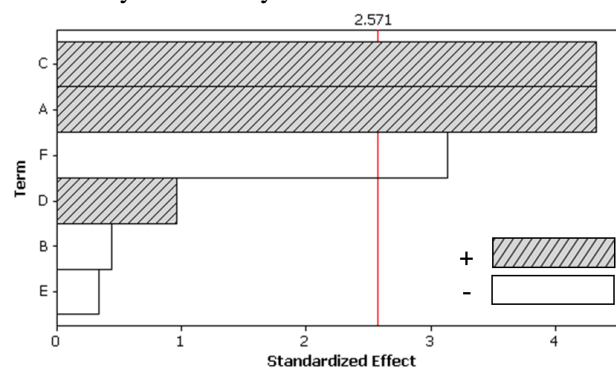


Fig. 1: Standardized ($P = 0.05$) Pareto chart, representing the estimated the most effective parameters, extraction solvent volume (A), ionic strength (B), pH (C), concentration of surfactant (D), extraction time (E), and ligand concentration (F).

Results indicate that the volume of extraction solvent (A), pH (C) and ligand concentration (F) were the most significant variables with noteworthy effects on the RF which were evaluated using CCD

for further assessment. Ionic strength (B) extraction time (E) and concentration of surfactant (D) were negligible parameters. The values of B and E were fixed at up level for further experiments because of their positive effects on extraction process. Commonly in DLLME experiments the extraction time (E) has no effect on extraction efficiency. It has been illustrated that due to the very large contact surface between the fine drops of extraction solvent and aqueous phase, DLLME process is a fast process. As it's shown here this parameter has positive and also unimportant effect on extraction process. Ionic strength (B) also was studied in 5 and 100 mmol/L of NaCl showing a positive negligible effect. Concentration of surfactant (D) was fixed at lower level because of their negative effect according to Pareto chart.

Considering the result of Plackett Burman design, three variables were fixed at suitable values (extraction time of 5 minutes, salt addition of 100 mmol/L of NaCl and surfactant concentration of 0.01% v/v of TX-114)

These factors had no significant effect on the ER and thus were eliminated for further studies by CCD.

Central composite design

According to screening design results pH(x₁), extraction solvent volume (x₂) and Ligand concentration(x₃) are effective variables on extraction results by SA-DLLME and should be optimized by a multivariate experimental design method.

A central composite design followed by response surface methodology was used to optimize the SA-DLLME process of mercury extraction. The CCD matrix with 3 independent variables (factor), N (number of experiments) = 20 and three repeats, r =4 was applied for model development.

The design matrix in coded and uncoded values, as well as the responses obtained from 20 experiments of a solution containing 1 µg.L⁻¹ of mercury have been shown in Table 3 and Table 4.

Table 3: The variables and values used for central composite design (CCD)

Variable name	Coded variable				
	-2	-1	0	1	2
Ph	3	4	5	6	7
extraction solvent volume	100	150	200	250	300
Ligand concentration	0.01	0.02	0.03	0.04	0.05

(mol/L)

Table 4: List of experiments in the CCD for model optimization (coded values) and the responses

Design points	Factors levels			Response
	F1	F2	F3	Enrichment factor
1	0	2	0	55.6
2	0	0	0	117.2
3	0	0	2	49.5
4	-2	0	0	51.8
5	2	0	0	45.2
6	-1	1	1	57.6
7	-1	-1	-1	99.1
8	0	0	0	119.0
9	0	0	-2	106.5
10	0	0	0	118.1
11	1	-1	1	74.2
12	1	1	-1	95.8
13	1	1	1	44.6
14	0	0	0	118.1
15	0	0	0	117.9
16	1	-1	-1	105.3
17	-1	1	-1	82.2
18	0	0	0	116.9
19	-1	-1	1	90.8
20	0	-2	0	101.4

Analysis Of Variance (ANOVA) test has been done on the obtained results. The ANOVA results (Table 5) are used to evaluate model suitability and adequacy of the fitted model and also to select suitable model terms.

The value of the adjusted R² = 0.9991 shows that this model has good predictive ability and there is acceptable match between predicted and experimental values.

The Model F-value of 2472.41 implies the model is significant. There is only a 0.01% chance that a "Model F-Value" this large could occur due to noise. Values of "Prob > F" less than 0.05 indicate that the model terms are significant. In this case x₁, x₂, x₃, x₁x₂, x₁x₃, x₂x₃, x₁², x₂², x₃² are significant model terms. Values greater than 0.05 indicate that the model terms are not significant. The "Lack of Fit F-value" of 1.44 implies that the Lack of Fit is not significant relative to the pure error. There is a 34.91% chance that a "Lack of Fit F-value" this large could occur due to noise. Non-significant lack of fit is good because we wish the model to fit.

Table 5: ANOVA results for CCD model

	DF	Seq SS	Adj SS	Adj MS	F	P
Regression	9	15064.9	15064.9	1673.88	2472.41	0.000
Linear	3	5359.4	5359.4	1786.46	2638.71	0.000
x ₁	1	33.1	33.1	33.06	48.84	0.000
x ₂	1	2043.0	2043.0	2043.04	3017.68	0.000
x ₃	1	3283.3	3283.3	3283.29	4849.60	0.000
Square	3	9219.7	9219.7	3073.23	4539.33	0.000
(x ₁) ²	1	5193.2	5193.2	5193.23	7523.03	0.000
(x ₂) ²	1	1550.9	1550.9	1550.90	2413.60	0.000
(x ₃) ²	1	2475.6	2475.6	2475.58	3656.57	0.000
Interaction	3	485.8	485.8	161.93	239.18	0.000
x ₁ x ₂	1	15.1	15.1	15.12	22.34	0.001
x ₁ x ₃	1	305.0	305.0	305.04	450.57	0.000
x ₂ x ₃	1	165.6	165.6	165.62	244.63	0.000
Residual Error	10	6.8	6.8	0.68		
Lack-of-Fit	5	4.0	4.0	0.80	1.44	0.349
pure Error	5	2.8	2.8	0.55		
Total	19	15071.6				

The following equation was obtained for the response relating to x₁, x₂ and x₃:

$$y = 117.95 - 1.43x_1 - 11.30x_2 - 14.32x_3 - 17.29(x_1)^2 - 9.79(x_2)^2 - 9.92(x_3)^2 + 1.37x_1x_2 - 6.17x_1x_3 - 4.55x_2x_3$$

The optimum values were obtained by graphical analysis of response surface plots (Fig. 2). The response surface is a graph of a response as a function of effective factors. This model was optimized with respect to maximum signal that is proportional to 180 µl of extraction solvent volume and ligand concentration of 0.024M at pH 5.06. These optimized values were used for determination of mercury in the following experiments.

Performance of the SA-DLLME for mercury determination

The analytical efficiency of the proposed method was evaluated by determining the limit of detection, linear dynamic range and relative standard deviation (RSD).

The LOD was calculated as 3s_b/a where s_b is the standard deviation of the blank signal and "a" is the slope of calibration curve.

To evaluate these parameters, a series of solutions at 12 different concentration ranging from 0 to 3 µg.L⁻¹ were prepared.

Linearity was observed over the range of 0.08 to 2 µg/L with an acceptable correlation coefficient value. LOD value for mercury determination was obtained 0.023 µg/L and relative standard deviation (RSD) was 8.1%.

Results of proposed method compared with other published method are summarized in Table 6. It has been obviously concluded that this method is comparable with other published method and the

extraction time of this method is shorter than other extraction methods.

Table 6: Results of proposed method in compare with other published method

Method	Sample volume (ml)	EF	RSD	LOD (µg L ⁻¹)	Ref.
LLE-CV-AAS	1000	-	1.2	0.01	24
SPE-CV-AAS	250-400	300	0.8-1.7	0.01	25
LLE-FI-CV-AAS	20	36	2.8	0.0023	26
DLLME-CV-AAS	10	310	4	0.03	27
CPE-UV-VIS	50	6	4.8	14	28
SPE-UV-VIS	1000	100	2.5	4	29
SPE-UV-VIS	100	50	1.6	15	30
DLLME-UV-VIS	10	18.6	1.7	3.9	2
DLLME-HPLC-DA D	5	107	4.1-7.3	0.32	31
HF-LPME-ETV-IC P-MS	2.5	73	6.1	0.0048	16
SA-DLLME-GF-AAS	10	125	8.1	0.023	this work

The effect of foreign ions on Hg²⁺ determination by the proposed method was studied in the presence of common metal ions such as Na⁺, K⁺, Mg²⁺, Ca²⁺, Al³⁺, Cu²⁺ and Fe³⁺. For this reason, solutions containing 1 µg.L⁻¹ of Hg²⁺ and different concentration of foreign ions were prepared. The amount of these ions that would be tolerated without interference effects were examined and are demonstrated in Table 7. The results showed that the presence of large concentration of these common ions in water samples had no considerable effect on Hg determination by proposed SA-DLLME.

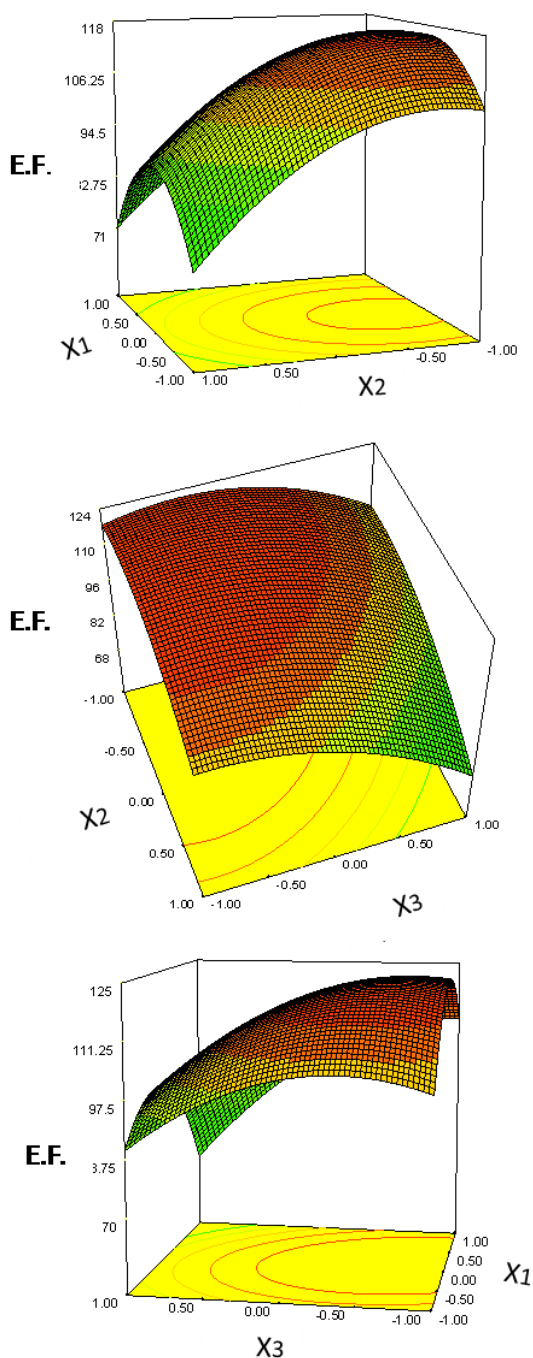


Fig. 2: Three surface plots that can be explained the optimal condition

Table 7: Tolerance limit of some coexisting ion (results within 10% error)

Ion	Tolerance limit $C_{ion}/C_{Analyte}$
Na	160000
K+	140000
Mg ²⁺	40000
Ca ²⁺	40000
Cu ²⁺	1400
Fe ³⁺	1000
Al ³⁺	4000

Real samples

The proposed SA-DLLME method was applied for Hg determination in water sample. In condition in which there is no standard reference with certified content as a target analyte, recovery study can be used as an alternative method for validation studies [24]. Tap and river water sample were collected as real samples. Kashan tap water was collected from our lab in Kashan University (Kashan, Iran). The river water sample was collected from Zayanderud River (Isfahan, Iran).

The recovery percentage was calculated by equation (3) where m_s and m_e are total amount of analyte and extracted amount into extraction solvent, respectively.

Also C_s , C_e , V_s and V_e are initial concentration of analyte in aqueous sample, concentration of analyte in extractant, volume of sample solution and volume of extraction solvent, respectively. C_e was obtained from calibration graph of Hg²⁺ complex using GF-AAS results.

$$R\% = \frac{m_e}{m_s} \times 100 = \frac{C_e V_e}{C_s V_s} \times 100 \quad (3)$$

Real sample were filtered by Millipore Membranes and then were extracted by the proposed method. Hg residues were found in the tap and river water samples at the concentration of 0.6 and 1.2 µg/L, respectively. The Percentage of Recoveries where standard solution of Hg was added at two different levels (0.5 and 1 µg/L) was also investigated and results are listed in Table 8. Results show that the recoveries for the spiked samples are within a satisfactory range (95 to 106 %) and so the proposed method is applicable for Hg preconcentration and determination in water samples.

In SA-DLLME a surfactant was used as a substitution for traditional disperser solvents in DLLME. The Triton X-114 is the most widely used surfactant that has been used in surfactant-assisted DLLME method and was applied in this study. TX-114 is a non-ionic surfactant with good emulsification properties which makes the extraction relatively greener.

CONCLUSION

In this paper, a new, reliable and disperser solvent free method based on SADLLME using DDTC chelating agent combined with GF-AAS was developed for mercury analysis in aqueous samples.

The method was fully optimized by screening design and multivariate methodology and it has been demonstrated that these are useful methods which enable us to determine significant variables and also

Table 8: Analytical results (mean \pm SD, n = 3) for trace Hg, in real water samples ($\mu\text{g/L}$)

Sample	Tap Water			River Water		
	Added ($\mu\text{g/L}$)	Determination ($\mu\text{g/L}$)	Recovery (%)	Added ($\mu\text{g/L}$)	Determination ($\mu\text{g/L}$)	Recovery (%)
Hg	0	0.60 \pm 0.08		0	1.2 \pm 0.07	
	0.5	1.05 \pm 0.07	95	0.5	1.65 \pm 0.07	103
	1	1.64 \pm 0.06	103	1	2.33 \pm 0.05	106

to evaluate the interaction of variables and determining the correct optimization.

The established method also was applied for the determination of mercury in some real water samples with satisfactory analytical results.

Some considerable features of this method include low cost and matrix effect, good extraction efficiency and recovery, more environmental friendly method compared with DLLME, because of the absence of organic disperser solvent, and also acceptable sensitivity and precision.

Acknowledgement. Authors are grateful to University of Kashan for supporting this work by Grant NO. 463609/1.

REFERENCES

- [1] D. M. Roundhill, *Journal of Chemical Education*, 2004, 81, 275.
- [2] M. Gharehbaghi, F. Shemirani and M. Baghdadi, *International Journal of Environmental and Analytical Chemistry*, 2009, 89, 21-33.
- [3] U. ATSDR, *Atlanta: Agency for Toxic Substances and Disease Registry, US Department of Health and Human Services*, 1999.
- [4] D. L. Rocha, A. D. Batista, F. R. Rocha, G. L. Donati and J. A. Nobrega, *TrAC Trends in Analytical Chemistry*, 2013, 45, 79-92.
- [5] H. Al-Saidi and A. A. Emar, *Journal of Saudi Chemical Society*, 2014, 18, 745-761.
- [6] E. Müller, R. Berger, E. Blass, D. Sluyts and A. Pfennig, *Ullmann's Encyclopedia of Industrial Chemistry*, 1985.
- [7] M. El-Shahawi and H. Al-Saidi, *TrAC Trends in Analytical Chemistry*, 2013, 44, 12-24.
- [8] C. B. Ojeda and F. S. Rojas, *Chromatographia*, 2009, 69, 1149-1159.
- [9] Y. Han, X. Jia, X. Liu, T. Duan and H. Chen, *Chromatographia*, 2010, 72, 351-355.
- [10] S. Li, S. Cai, W. Hu, H. Chen and H. Liu, *Spectrochimica Acta Part B: Atomic Spectroscopy*, 2009, 64, 666-671.
- [11] M. Saraji and A. A. H. Bidgoli, *Analytical and bioanalytical chemistry*, 2010, 397, 3107-3115.
- [12] M. S. Tehrani, M. H. Givianrad and N. Mahoor, *Analytical Methods*, 2012, 4, 1357-1364.
- [13] M. Moradi, Y. Yamini, A. Esrafil and S. Seidi, *Talanta*, 2010, 82, 1864-1869.
- [14] M. Rezaee, Y. Yamini and M. Faraji, *Journal of Chromatography A*, 2010, 1217, 2342-2357.
- [15] R. S. Amis and C. R. T. Tarley, *Canadian Journal of Analytical Sciences and Spectroscopy*, 2008, 53, 131-140.
- [16] L. Xia, Y. Wu and B. Hu, *Journal of Mass Spectrometry*, 2007, 42, 803-810.
- [17] Q. Deng, M. Chen, L. Kong, X. Zhao, J. Guo and X. Wen, *Spectrochimica Acta Part A: Molecular and Biomolecular Spectroscopy*, 2013, 104, 64-69.
- [18] V. A. Lemos, M. S. Santos, G. T. David, M. V. Maciel and M. de Almeida Bezerra, *Journal of Hazardous materials*, 2008, 159, 245-251.
- [19] H. Ebrahimzadeh, Y. Yamini and F. Kamarei, *Talanta*, 2009, 79, 1472-1477.
- [20] A. N. Panagiotou, V. A. Sakkas and T. A. Albanis, *Analytica Chimica Acta*, 2009, 649, 135-140.
- [21] M. A. Farajzadeh, M. Bahram and M. R. Vardast, *CLEAN–Soil, Air, Water*, 2010, 38, 466-477.
- [22] S. Khodadoust and M. Ghaedi, *Journal of Separation science*, 2013, 36, 1734-1742.
- [23] H. Sereshti, M. Karimi and S. Samadi, *Journal of Chromatography A*, 2009, 1216, 198-204.
- [24] E. Prichard, G. MacKay and J. Points, *Trace analysis: a structured approach to obtaining reliable results*, Royal Society of Chemistry, 1996.

Evaluation of the minerals content and fatty acids profiles in *Descurainia Sophia* and *Sisymbrium Irio*

Seyed Mostafa Kazemeini^{1*}, Babak Ghiassi Tarzi¹, Hossein Bakhoda², Kambiz Larijani³, Parasto Damanafshan⁴

¹Department of Food Science and Technology, Faculty of Agriculture, Science and Research Branch, Islamic Azad University, Tehran, Iran

²Department of Agricultural Mechanization, Faculty of Agriculture, Science and Research Branch, Islamic Azad University, Tehran, Iran

³Department of Chemistry, Islamic Azad University, Science and Research Branch, Tehran, Iran

⁴Department of Food Science and Technology, Shahr-e-Qods Branch, Islamic Azad University, Tehran, Iran

Abstract

The flixweed grain as a known medicinal herb is consumed more in Iran due to its beneficial properties. There are two known species of *Descurainina Sophia* and *Sisymbrium Irio*. The *Descurainina Sophia* is highly used in Iran and this species has significant health benefits. The aim of this research is to examine some of the minerals and also fatty acids profiles in the *Descurainina Sophia* and *Sisymbrium Irio* and also compare them with other food products. In this study, the moisture, calcium, iron, sodium and potassium contents were measured in both species. The results revealed that the *Descurainina Sophia* is superior to *Sisymbrium Irio* in all parameters significantly. Measuring minerals content showed that the *Descurainina Sophia* had high moisture, calcium, iron and potassium content and *Sisymbrium Irio* had high sodium content which was considered as the main property of the *Descurainina Sophia*. The results of measuring fatty acids of both species depict high amount of essential fatty acids particularly in *Descurainina Sophia*.

Keywords: *Descurainina Sophia*, *Sisymbrium Irio*, minerals, fatty acids

1. INTRODUCTION

Medicinal herbs have been considered since old times and most of the medicinal effective substances have been extracted from these herbs [1]. Medicinal herbs have played a determinant role in traditional treatment methods for thousands of years [2]. These herbs are used in traditional medicine for control and remedy of most diseases. Humans have had a close relationship with medicinal herbs and traditional medicine. According to the WHO report, nowadays more than eighty percent of the world people consume medicinal herbs for remedial purposes [1]. This organization estimated that annual consumption of medicinal herbs will increase from 14 billion dollars to 5 trillion dollars in 2050 [2]. Medicinal herbs can produce a broad scope of chemicals which are very important physiologically. These herbs include active medicinal compounds used for production of drugs [1]. The producers produce these herbs in the forms of pill, capsule, syrup or cream and herbal tea as a new form [3]. Low side effects compared to synthetic herbs, lack of drug resistance, health and environmental hygiene are advantages of medicinal herbs. Due to climatic diversity, Iran has a broad

and unique biodiversity. This diversity is seen in the herbs particularly in the medicinal herbs. Among the medicinal herbs, flixweed has been considered by numerous therapeutic properties. Flixweed is an annual and biennial herb from Mustard family grows in non-agricultural and relatively humid areas as wilding herb. The seed of this herb is small and yellow or light brown. In Iran traditional medicine, the flixweed grain is used as laxative, stomach tonic and also as an appetizer. The grain is bitter and consumed for remedy of chest pain and reducing fever in case of bronchitis [4].

In this research two species of *Descurainia Sophia* (Flixweed) and *Sisymbrium Irio* (London rocket seed) were evaluated. *Descurainia Sophia* is popular species in Iran characterized by specific feature of being healthy which has caused to be considered as a traditional medicinal herb. It is a very popular beverage. In botany, *Descurainia Sophia* has a lot of leaves and the fruits growing on the short branch bent inside and the herb is white and grows in the ruins and low water areas in spring. *Sisymbrium irio* is consumed less than *Descurainia Sophia* species and it is used only in some parts of Iran. *Sisymbrium irio* has large leaves, seen along streams in the spring and it is an annual or biennial herb [5].

In 1980 and 1992, *Descurainia Sophia* was examined as a good source for medicinal herb. In

*To whom all correspondence should be sent.

these research, their presence or absence was determined, in many combinations due to the available facilities cf. Baghi [5] and Dehdar [6]. In 2005, the microbial effect of *Descurainia Sophia* on inhibiting the standard *Escherichia coli* and *Staphylococcus aureus* strains growth were evaluated [7]. In 2007, the effect of consumption of *Descurainia Sophia* in late pregnancy on spontaneous onset of delivery in women with first pregnancy was examined. The results showed that this herb influences delivery process by opening the uterus cervical and increase possibility of vaginal delivery. Therefore, it is recommended to use it as facilitator of delivery [8]. In 2009, a study was conducted on the chemical constitutes of *Descurainia Sophia* and its biological activity. In this study, whole herb was examined. The herbs were collected from northern part of Egypt. Proteins, amino acids, fatty acids compounds and carbohydrates were determined [9].

Research on the *Sisymbrium irio* and *Descurainia Sophia* nutrition value was very limited so that the latest research on the medicinal use of this herb dates back 20 years ago. However, need for transparency and more information about some micronutrients seems necessary. For this reason, this study aimed to examine some basic components involved in feeding as oral administration.

2. MATERIALS AND METHODS

2.1. Primary materials

Two varieties of *Sisymbrium Irio* and *Descurainia Sophia* were collected randomly from the west of Tehran. Then their grains were approved by the Department of Herbarium at Tehran University.

2.2. Methods

The moisture of the species was determined using the oven according to the Iran National Standard No.6330. For determination of ash percentage, samples of both species were measured using an electric furnace [10]. Using Atomic Absorption Spectrometry some minerals such as calcium and iron were measured [11] and the amount of sodium and potassium in *Descurainia Sophia* and *Sisymbrium Irio* were measured using a flame photometer device [12]. Their oil was extracted from the seeds of two species by cold method using petroleum ether [9] and then the fatty acids became volatile derivatives by converting to methyl ester and prepared for GC analyses [10].

2.3. Statistical analysis

The results of comparison of the chemical compounds (nutritional value) of *Descurainia Sophia* and *Sisymbrium Irio* were analyzed through simple random using SPSS software Version 19. In comparison of treatments means the T-student test were used for statistical analysis.

3. RESULTS AND DISCUSSION

3.1. Determination of moisture percentage

The content of moisture of *Descurainia Sophia* and *Sisymbrium Irio* is shown in Fig. 1. As it is seen there is a significant difference in 1% in both species moisture percentage ($P < 0.05$) so that the *Descurainia Sophia* has high moisture percentage compared with *Sisymbrium Irio*. It is likely physiologic conditions of these herbs are effective in significance of their moisture percentage.

The main point on *Descurainia Sophia* is that this medicinal herb is not considered among nutrients as source of water but since it is consumed as a drink with significant amount of water, it plays an important role in meeting body need for water particularly in hot seasons due to tendency toward consumption of this herb.

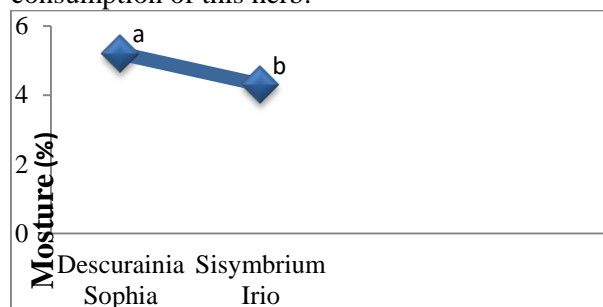


Fig 1: *Descurainia Sophia* and *Sisymbrium Irio* moisture content. Different letters depict significance of the treatments, mean in 1%.

3.3. Determination of calcium and iron in both flixweed species with atomic absorption system and comparison with other resources

The calcium content was measured in both species using atomic absorption system. The results showed that there is a significant amount of calcium in both species and compared to other resources, milk is the common resource of calcium which has low content of calcium compared to flixweed [15]. It is necessary to point that when the food products including calcium are examined, calcium content is less important; however, since most of the food resources have not been described accurately in research so biological availability has not considered as a factor for determining daily needs for calcium [13].

Calcium constitutes 1% to 2% of the body weight of an adult. The highest need for daily calcium in men is in age range 14-18 years (1094 mg or 22.2 mol/day) while for women this range is 9-13 years (889 mg or 22.2 mol/day) [13]. Approximately 236 ml fatless milk includes 300 mg calcium so drinking one glass of milk provides a part of the body required calcium [3]. Therefore, consuming diaries particularly milk plays an important role in meeting daily calcium need. However, some people suffer from digestive disorder by drinking milk [14] which reduces drinking milk. It should be pointed that the calcium content in the prepared grains is about 36763.2 mg/kg which includes highest content of calcium in highly consumed food products [15]. Although this amount is more than *Sisymbrium irio* calcium content, but it is less than *Descurainia Sophia* calcium content significantly.

It is necessary to point that a glass of drink including 4 grams *Descurainia Sophia* meets 20% of calcium dietary reference intake (DRI) (approximately 900 mg).

Shamsa et al. [16] measured the *Descurainia Sophia* calcium content 24270 mg/kg which this content is very lower than amount measured in this research. One of the reasons can be considered as the weather that the herb grows in it. The diagram in Fig. 2 depicts the *Descurainia Sophia* and *Sisymbrium Irio* calcium content measured by atomic absorption system compared to other resources.

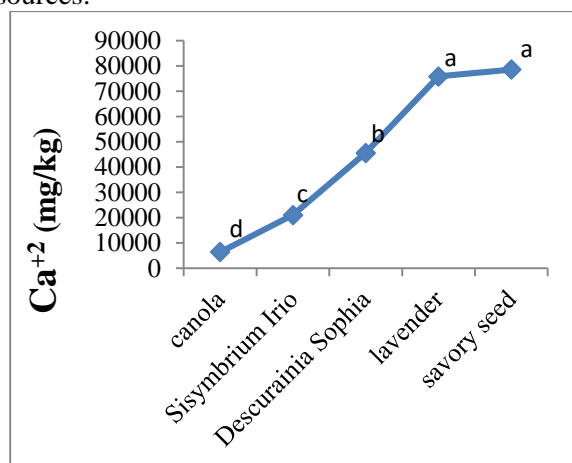


Fig. 2. Calcium content in both flixweed species compared to other resources. Different letters depict significance of the treatments mean in 1%.

Osteoporosis is one of the common diseases in this century. Calcium deficit is the main cause of this disease. Reduction of dairy products and enhancement of eating fast foods are the main reasons for calcium deficit. In addition some people cannot drink milk as the enriched source of calcium

due to intolerance of lactose. Thus, according to the results of this research flixweed is recommended as a resource enriched with calcium in the people suffering from osteoporosis and of lactose intolerance.

2.3. Iron. Iron has been known as an essential nutrient for more than one century [17]. The daily reference intake of iron is 12-16 mg/day which it reaches to 18 mg/day in women older than 50 years. Anemia is one of the main problems in developed and developing countries. The major resource of iron is liver and then marine foods including oyster and fish, kidney, heart and red meat [18]. The results of this research revealed that flixweed particularly *Descurainia Sophia* is a good resource for iron so that the iron content in this species has no significant difference with other resources particularly red meat ($P > 0.05$). According to the results, *Descurainia Sophia* has significant iron compared with *Sisymbrium Irio* ($P < 0.05$).

In a research conducted in 2009 the content of iron was measured in ten medicinal herbs. The results showed that iron content in *Descurainia Sophia* is higher than other medicinal herbs [19]. However, due to outbreak of anemia resultant from iron deficit on one hand and unavailability of red meat resources due to economic problems flixweed is considered as an enriched and effective resource of iron besides other food products.

Also, anemia is one of the main problems in hot areas so flixweed drink can be effective in these areas. It should be pointed that high amount of iron cannot be considered as a reason for appropriateness of this resource as providing body iron. The aim is to use this product besides other products for meeting iron and other essential minerals reference intake [19].

Fig. 3 depicts iron content in *Descurainia Sophia* and *Sisymbrium Irio* and other foods containing iron.

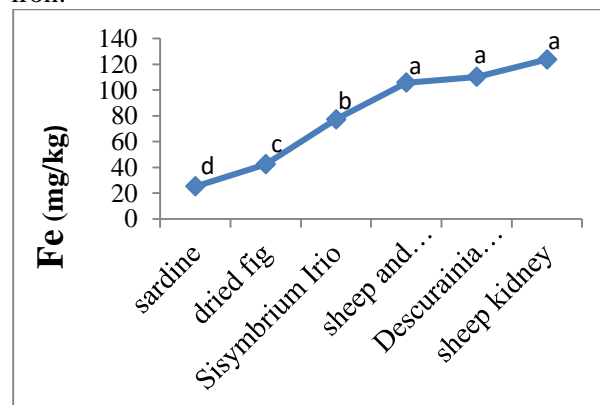


Fig. 3. Iron content in *Descurainia Sophia* and *Sisymbrium Irio* and other foods containing iron. Different letters depict significance of the treatments mean in 1%.

3.4. Determining sodium and potassium content using flame photometer

3.4.1. Sodium. Sodium is the main cation of the extracellular fluids. Measuring sodium content in both species showed that sodium content is higher in *Sisymbrium Irio* than *Descurainia Sophia* although there is no significant difference in sodium content in both species ($p>0.05$).

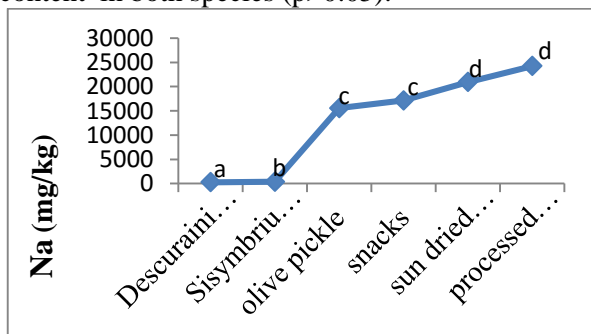


Fig. 4. Sodium content in both flixweed species compared to other resources. Different letters depict significance of the treatments mean in 1%.

Salt is the main resource of sodium in the body. More than 40% of the salt body is sodium. Sodium amount is high in salt about 380000 mg/kg. Totally, the lowest DRI of sodium is 0.2 gram equal 0.5 gram of chloride sodium. Also, the results of a research conducted in Harvard University showed the effect of consuming more sodium on blood pressure and its direct association with cardiovascular diseases. According to the reports of this research of ten morbidities related to cardiovascular diseases one is related to consumption of more than 2000 mg/kg/day sodium. The result of measuring sodium compounds content is shown in Fig. 4 which depicts among different products, flixweed has less sodium. Since sodium content is low in flixweed, so this drink can be considered as a drink with very low sodium. When the sodium content of a drink is low it can be drunk with proteins without concern [3]. In addition since the sodium content is very low in flixweed so drinking flixweed is useful for patients with blood pressure and kidney disorder.

3.4.2. Potassium. Potassium content in *Descurainia Sophia* and *Sisymbrium Irio* was measured by photometry and the results are shown in Fig. 5. The results showed significant increase of potassium in *Descurainia Sophia* compared to *Sisymbrium Irio* ($P<0.05$).

Potassium is the main intracellular cation that balances the cells osmosis pressure and acidity and base of the body. Sodium and potassium are two main ions controlled in the patients with kidney disorder [1]. These compounds have similar

functions in the body but their functional ways are completely different. The individuals who consume low sodium and in contrary high potassium, their blood pressure and diseases resultant from blood pressure are reduced Potassium plays adjusting role in blood pressure. The studies showed that if potassium content reaches 400 mg/day the morbidity resultant from stroke is reduced by 40% [14]. It should be pointed that potassium has a direct

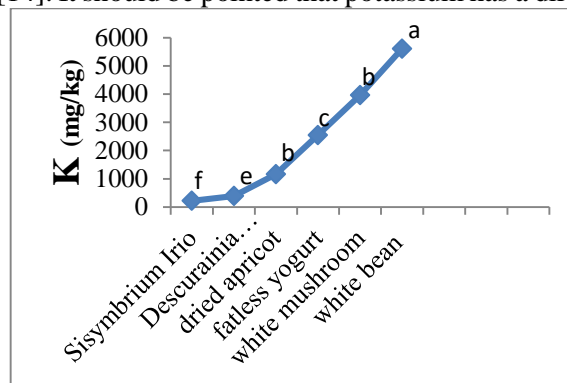


Fig. 5. Potassium content in both species of flixweed compared to other resources. Different letters depict significance of the treatments mean in 1%.

association with sweating. The daily reference intake of potassium in adults is 4.7 g or 120 Mmol/day. High sweating as a result of physical activities and hot weather causes to reduction of potassium. Potassium concentration in sweating is 4-5 mmol/day or 0.2 gram in a day. However, this content reaches 14 mmol or 0.5 gram in a day in hot weather. Sweating in hot weather can reach 11 liters which loss potassium content is about 60 mmol/day or 2.3 gram in a day that complete loss can be 116 mmol/day or 4.5 gram/day more than the body dietary reference intake. For this reason, need to potassium is high [13]. Thus it is likely that one of the reasons for heat exhaustion is losing much more potassium which in such cases consumption of the compounds with high amount of potassium is useful. Flixweed (as a drink) is one of the resources enriched in potassium and since it is considered as a good resource for providing potassium so these compounds are effective in the case of heat exhaustion for meeting needs for lost potassium and water.

3.5. Fatty acids profiles in *Descurainia Sophia* and *Sisymbrium Irio*

Fatty acids in *Descurainia Sophia* and *Sisymbrium Irio* were measured by gas chromatography. The results showed that *Descurainia Sophia* has higher fatty acids than *Sisymbrium Irio*, cf. Table 1.

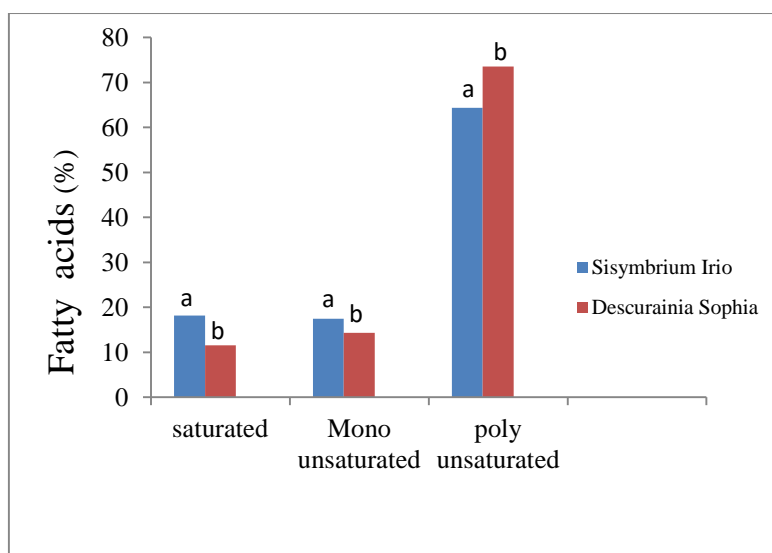


Fig. 6. Type and content of fatty acids in both flixweed species. Different letters depict significance of the treatments mean in 1%.

Table 1. Fatty acid content.

Flixweed	Mean %
<i>Descurainia Sophia</i>	29.21 ± 0.108
<i>Sisymbrium Irio</i>	25.05 ± 0.350

Some research has introduced *Descurainia Sophia* as a good resource for meeting edible oil in the body (Peng et al. [20]; Peng et al. [21]; Zhang et al. [22]; Shie [23]).

In a research it was tried to use canola oil production [24]. Canola oil is produced from *Brassica napus* and *Brassica rapa* which are genetically modified and contain low erusic acid [25]. Accordingly, it was tried to produce a hybrid of *Descurainia Sophia* and *Brassica napus* which its erusic acid is less than 0.5%. In this research the produced hybrid was recommended for edible oil industrial production [24].

Both of the flixweed species were the same in fatty acids type but they were different in levels of them. Fig. 6 depicts types and content of fatty acids in both flixweed species.

Amount and mean of saturated and unsaturated fatty acids are shown in Fig. 6. According to the results, unsaturated fatty acid in *Descurainia Sophia* is 88.41% and in *Sisymbrium Irio* is 81.80%.

Among varieties of fatty acids both linoleic acid and linolenic acid are essential fatty acids. Essential fatty acids are one of the constituents of oils and the major fatty acids are omega 3 and omega 6. Generally, fatty acids in human regimes are more important than total consumed oils [26]. Also, fatty acids ratio is very important in nutritional and economic value [27]. Among fatty acids, omega 3 (essential and unsaturated fatty acid) is considered essential fatty acid that body cannot produce and synthesis it and it is provided by food. The body

should receive balanced amount of omega 3 and omega 6 existed in foods in order to convert them to required derivatives. Nowadays, due to benefits of omega 3 fatty acids they have been considered in daily foods. WHO recommends that the ratio of omega 6 to omega 3 unsaturated fatty acids should be minimum 5 to 1 and maximum 10 to 1. In other words, in daily nutrition the content of omega 6 is minimum 5 and maximum 10 times of omega 3. The role of omega 3 fatty acids has been proved in prevention of cardiovascular diseases [28]. According to the results of this research, flixweed compared to other resources is considered as a good resource of essential fatty acids Table 2 depicts the level and type of fatty acids measured in this research.

The results of measuring types and levels of fatty acids in both flixweed species showed that linolenic acid is the common fatty acid in both *Descurainia Sophia* and *Sisymbrium Irio*, by this difference that this fatty acid amount was higher in *Descurainia Sophia* than *Sisymbrium Irio*. After linolenic acid, linoleic acid was in the second rank of the fatty acids in both species which its content was high in *Descurainia Sophia*. Hence, *Descurainia Sophia* is very important in omega 3 and omega 6 content and it can be used as a proper resource of essential fatty acids. Also, by comparison of essential fatty acids in the two flixweed samples it was specified that essential fatty acids in the sample flixweed was high compared with cottonseed oil, soybean oil, sunflower oil and Turkish olive oil and on the other hand, unsaturated fatty acids in the *Descurainia Sophia* was higher in amount of all mentioned oils.

Table 2. Fatty acid content in both flaxweed species.

Fatty acid	Carbon No.	RT (min)		Ratio (%)	
		<i>Descurainia sophia</i>	<i>Sisymbrio irio</i>	<i>Descurainia sophia</i>	<i>Sisymbrio irio</i>
Luric Acid	12:0	13.74	13.71	0.008	0.013
Miristic Acid	14:0	14.99	14.96	0.066	0.089
Pentadecanoic acid	15:0	15.88	15.83	0.050	0.051
Palmitic Acid	16:0	17.02	16.98	7.418	13.013
Palmitoleic Acid	16:1	-	18.18	-	0.465
Stearic Acid	17:0	18.23	-	0.435	-
Stearic Acid	18:0	20.21	20.15	2.356	4.240
Oleic Acid	18:1	21.98	21.87	13.551	15.713
Linoleic Acid	18:2	24.83	24.65	20.204	19.471
Linolenic Acid	18:3	29.10	28.80	53.855	44.854
Arachidic Acid	20:0	31.97	31.87	1.256	0.789
Erusic Acid	22:1	33.40	33.31	0.801	1.301

4. CONCLUSION

Medicinal herbs have played a very important role for thousands years in traditional treatment of diseases. These compounds are known as a valuable, ready to use and reliable source for individuals. One of the varieties of medicinal herbs is *Descurainia Sophia* as the oldest drinks consumed among Iranians. There are *Descurainia Sophia* and *Sisymbrium Irio* grains known as medicinal herbs in Iran with high usage because of its beneficial properties. *Descurainia Sophia* is consumed more in Iran and it has a lot of health benefits. On the other hand, *Sisymbrium Irio* is consumed in some parts of the country and it used less due to its bitterness. The results obtained in this study showed that *Descurainia Sophia* elements superiority is connected perfectly with its great popularity. So that in most of the factors measured, *Descurainia Sophia* elements were superior and only the amount of sodium was high in *Sisymbrium Irio* and since low intake of sodium is considered as favorable property, so sodium deficit is considered as advantage of *Descurainia Sophia*. In addition, the moisture, calcium, iron and potassium contents were high in *Descurainia Sophia*. Measuring the amount and types of fatty acids in two species of *Descurainia Sophia* showed that it is an excellent source of essential fatty acids. The essential fatty acids content is higher in *Descurainia Sophia* than other resources enriched with essential fatty acids. However, according to the obtained results using this herbal drink is recommended for supplying some required minerals in the body.

REFERENCES

1. M. Millikan, A. Kolassani, H. Xu, *Food Chem.*, **127**, 465 (2011).
2. A. Saha, V. Tripathy, B.B. Basak, T.S. Varghese, *Phytochem. Lett.*, **14**, 67 (2015).
3. A.C. Marshall, R.N. Gallaher, K. Gallaher, A.J. Marshall, *J. Food Composition Analysis*, **19**, S53 (2006).
4. H. Mirheydar, Plant introduction: the use of herbs in the prevention and treatment of diseases with the latest scientific scholars and scientists research (In Persian). Tehran's Islamic culture, pp. 121-123, 2010.
5. Baghi, A. 1980. Chemical evaluation of *Sisymbrium sophia* traditional plant. PhD dissertation on Pharmacology (In Persian). Department of Pharmacology and Pharmaceutical Sciences. Isfahan University of Medical Sciences. pp. 10-16.
6. F. Dehdar, Evaluation of quantity and quality of ingredients of Turkish, *Artemisia*, *Fumaria* and *Stochys inflala* benth. PhD dissertation on Pharmacology (In Persian), Department of Pharmacology and Pharmaceutical Sciences. Isfahan University of Medical Sciences, 1992.
7. Z. Shahande, Molana, T. Farinosh (In Persian), *J. Babol Univ. Medical Sci.*, **8**, (5) (2005).
8. N. Mohammadi Niya, M. Rezaei, Loripoor, R. Vazirinejad. *Tabib Sharq Journal* (In Persian) **10**, issue 3 (2007)
9. N.H. Mohamed, A.E. Mahrous., Chemical constituents of *Descurainia sophia L.* and its biological activity, Egypt (2009).
10. C.S. James, Analytical Chemistry of Foods, Springer-Science+ Business Media.B.V., 1995.
11. Nielson. S.S., Food Analysis, Springer- Science+ Business Media LLC, fourth edition (2010).
12. K.V. Shah, P.K. Kapupara, T.R. Desai, Determination of sodium. Potassium, calcium and lithium in a wheat grass by flame photometry, *Pharma Science Monitor*, India, 2010.
13. Dietary reference intakes (for calcium, phosphorus, magnesium, vitamin D, and fluoride), Standing Committee on the Scientific, Evaluation of Dietary Reference Intakes, Food and Nutrition Board, Institute of Medicine, 1997.
14. N. Rajabzadeh, Healthy eating: food miracle from medical point of view (In Persian). Publication of Science and Literature. Tehran, pp. 170-185 (2006).
15. F. Greer, N. Krebs, *Pediatrics*, **117**, 578 (2006).

16. F. Shamsa, S. Reza zadeh, H. Shamsa, K. Abdi, A quantitative investigation on some toxic and non-toxic metals in popular medicinal herbs in Iranian market, Department of Pharmaceutical Chemistry, Faculty of Pharmacy, Tehran University of Medical Sciences, Tehran, Islamic Republic of Iran (2009).
17. F. Gaucheron, *Trends Food Sci. Technol.*, **11**, 403 (2000).
18. K.L. Mahan, S. Escott-Stump, J.L. Raymond, , Krause's Food and the Nutrition Care Process, by Saunders. An imprint of Elsevier Inc., 2012.
19. C. Chhabra, J. Ouma, C. Sumeh, G. Nyagah, *J. Ethnopharmacol.*, **58**, 97 (1997).
20. G. Peng, F. Hongbo, C. Zhaolin, Z. Songdong, Y. Jiaming, *Descurainia sophia*, an oil plant species with special uses, Institute of Botany, Sichuan Union University, China (1998).
21. G. Peng, Y. Yi, G. Fu-li, L. Ze-qu, A preliminary study on the introduction of *Descurainia sophia*, an oil plant species for industrial uses, Botanical Institute, Sichuan Union University, China (1996).
22. Zhang.Z.C, Li.X.F, Luo.P, *J. Agric. Sci.*, **3**, 19 (1990).
23. Shie.S.Y., Wild oil crops, *Sichuan agriculture*: **2**, 64 (1958).
24. Xin.R, Zhou.C, Chen.J, Jiang.S, Zhang.L, Guan.R, New canola germplasm of high oil content created by somatic hybrids between *Brassica napus* and *Descurainia Sophia*, China (2010).
25. F.D. Gunstone, Vegetable oils in food technology: composition, properties and uses, Blackwell Publishing Ltd,
26. G.P. Savage, D.L. McNeil, P.C. Dutta, *Acta Hort.*, **544**, 557 (2001).
27. M. Venkatachalam, S.K. Sathe, *J. Agric. Food Chem.*, **13**, 4705 (2006).
28. J.M. Bourre, *J. Nutrition, Health Aging*, **1**, 31 (2005).
- 29.

Molecular characteristics of drug activities in *Vitex negundo* woody extractives

Q. Ma^{1,2}, Z. Li¹, Z. Zhang^{1*}, H. Hou¹, Y. Furuta^{2*}, M. Ohkoshi^{2*}

¹Central South University of Forestry and Technology, Changsha 410000, China

²Laboratory of Biomaterials Science, Kyoto Prefectural University, Kyoto 6068799, Japan

Received June 26, 2015, Revised September 10, 2015

The molecular characteristics of stem extractives from *Vitex negundo* were studied to be known and further utilize the drug resources. Fresh *Vitex negundo* stems were pound to pieces and extracted by single extraction and sequential extraction. And then the extractives were obtained and analyzed by GC/MS. The leaching rule of stem extractives from *Vitex negundo* was obvious. What's more, the stem extractives contained drug activities, such as eicosane, 3,3,7,11-tetramethyltricyclo [5.4.0.0(4,11)] undecan-1-ol, etc. The stem extractives of *Vitex negundo* could be used to prepare the rich and rare drug activities.

Keywords: Drug activities, *Vitex negundo*, Stem extractives, Molecular, GC-MS

INTRODUCTION

Vitex negundo, which was a deciduous shrub, was widely distributed in North China. It was often born in the mountain slope to form dense thickets and abundant resources. [1, 2] And *Vitex negundo* was used as drugs for a long time. *Vitex negundo* real was bitter, warm and non-toxic; the leaf was bitter, cold and non-toxic; the root was sweet, bitter and non-toxic; the stem was sweet, flat and non-toxic. *Vitex negundo* as traditional Chinese medicine was recorded in the Pharmacopoeias such as “Herbal classic variorum”, “Materials Science”, “Qian Jin Fang”, and so on. [3] *Vitex negundo* could attend the symptoms including leucorrhoea, small intestine hernia, wet phlegm turbid urine and deafness. *Vitex negundo* leaf could be used to heal the nine orifices bleeding, piss hematuria; stems could do burning boil heat and wind toothache. [4, 5]. So *Vitex negundo* had the drug effect.

Vitex negundo had antiasthmatic, antitussive, expectorant effect, on cardiovascular function, blood pressure lowering effect, and other effects [3]. However, the researches on the active ingredients in *Vitex negundo* were less done, and concentrated in seed. For example, β -caryophyllene, caryophyllene oxide, β -elemene, α -pinene, P-cymene, 1,8-cineole, vanillic acid, alkaloids, and amino acid were found in the volatile oil of *Vitex negundo* seed. Peng et al. had studied the molecular identification methods, many woody extractives and biomass' chemical composition [7-21]. The researches were very effective and had great reference value. Therefore, the molecular

characteristics of the stem extractives in *Vitex negundo* were investigated and analyzed by the optimized extraction techniques so as to further utilize the drug resources.

MATERIALS AND METHODS

Materials

Fresh *Vitex negundo* stems were collected from the Tongbai Mountain, Henan Province, China. The fresh stems were pound to pieces and kept in vacuum. Acetic ether, methanol, benzene, petroleum ether and ethanol were chromatographic grade, preparing for the experiments. Cotton thread and bag were both done in benzene/ethanol extraction for 12 h..

Experimental methods

Single extraction. Weighed 54 pieces of *Vitex negundo* stems, each was about 20 g (0.1 mg accuracy) and finally parceled into the cotton bag and then tied by cotton thread, and signed. Extraction was carried out in 350 ml solvents by the Foss method for 1, 3, 4, 5, 6, 7 hours. Ethanol/methanol ($V_{\text{ethanol}}/V_{\text{methanol}}=2$), petroleum ether/acetic ether ($V_{\text{petroleum ether}}/V_{\text{acetic ether}}=2$), and benzene/ethanol ($V_{\text{ethanol}}/V_{\text{benzene}}=2$) extraction were done at the temperature of 75°C, 90°C and 95°C, respectively. After extraction, the one portion was dried in 105°C to oven dry, and weighed. The extractives were obtained by evaporation in 60 - 70°C.

Sequential extraction. Weighed 27 pieces of stems, each was 20 g (1.0 mg accuracy), and finally parceled into cotton bag tied by cotton thread, and signed. Three-step extractions were carried out by large-caliber Soxhletor by ethanol/methanol \rightarrow

To whom all correspondence should be sent:
E-mail: csfuzzf@163.com, furuta@kpu.ac.jp,
mohkoshi@kpu.ac.jp

petroleum ether/acetic ether → benzene/ethanol (JY-YS-BC), petroleum ether/acetic ether → benzene/ethanol → ethanol/methanol (YS-BC-JY), benzene/ethanol → ethanol/methanol → petroleum ether/acetic ether (BC-JY-YS), respectively. After every step extraction, the one portion was dried in 105°C to oven dry, and weighed. The extractives were obtained by evaporation in 60°C - 70°C.

GC/MS condition. Among the above extractives, the JY extractives in JY-YS-BC extraction, BC extractives in BC-JY-YS extraction, jyYS extractives in JY-YS-BC extraction, and bcJY extractives in BC-JY-YS extraction were analyzed, respectively. Each 0.5 mg extractives was analyzed by online linked GC/MS, respectively. The GC/MS analysis was carried out as the same as the documents [13, 14, 15, 16].

RESULTS AND DISSCUSION

The leaching rates of single extraction and three-step extraction were listed in Table 1 and Table 2, respectively. And the JY, BC, jyYS and bcJY extractives were obtained. The total ion chromatograms of four extractives by GC/MS were shown in Figure 1, respectively.

Leaching rule of stem extractives of *Vitex negundo*

The trend of leaching rates of stem extractives from *Vitex negundo* in different solvents was described in Table 2. It was observed that during ethanol/methanol extraction, the leaching rate of stem extractives fluctuated, and reached the maximum (9.79%) when extraction time was 5 h.

During petroleum ether/acetic ether extraction, the leaching rate of stem extractives first increased and then decreased, and reached the maximum (3.70%) when extraction time was 4 h. During benzene/alcohol extraction, the leaching rate of stem extractives fluctuated, and reached the

maximum (5.19%) when extraction time was 7 h. And the optimal extraction time of ethanol/methanol extraction, petroleum ether/acetic ether extraction, and benzene/alcohol extraction were 5 h, 4 h, and 7 h, respectively.

During the three-step extractions, the ethanol/methanol extraction, petroleum ether/acetic ether extraction, and benzene/alcohol extraction were done for 5 h, 4 h, and 7 h, respectively. The statistical results showed that the leaching rate of *Vitex negundo* stem extractives by JY-YS-BC extraction was 28.42%, 24.23% by YS-BC-JY extraction, and 28.22% by BC-JY-YS extraction. Comparing with table 2, it was observed that the leaching rate of each single extraction was less than that of table 1, suggesting that the solvent effect also existed in the leaching periods of stem extractives. During the three-step extractions, JY-YS-BC extraction was the optimum extraction mode for the leaching rate was 28.42%.

Molecular properties of *Vitex negundo* stem extractives

Analyzing the MS data, the NIST standard MS map by computer, open-published books and papers, then components and their contents were identified.

According to GC/MS result, 7 components were identified from JY extractives of *Vitex negundo* stem. The result showed that the main components were cyclotrisiloxane, hexamethyl- (36.588%), 3,3,7,11-tetramethyltricyclo [5.4.0.0(4,11)] undecan-1-ol (34.642%), 1,2-benzenedi-carboxylic acid, butyl 2-methylpropyl ester (10.074%), silicic acid, diethyl bis (trimethylsilyl) ester (8.153%), hexanedioic acid, bis (2-ethylhexyl) ester (2.456%), eicosane (2.111%), 1,2-benzenedicarboxylic acid, mono (2-ethylhexyl) ester (5.977%).

Table 1. Leaching rates of each single extraction [%].

Extraction time [h]	ethanol/methanol	petroleum ether/acetic ether	benzene/ethanol
1	5.53	1.20	0.90
3	8.63	1.22	3.21
4	7.16	3.70	4.23
5	9.79	3.44	3.84
6	7.01	3.51	3.48
7	7.22	1.02	5.19

Table 2. Leaching rates of three-step extractions.

Extraction	JY-YS-BC			YS-BC-JY			BC-JY-YS			
	Time [h]	4	7	5	7	5	4	5	4	7
Step		1 st	2 nd	3 rd	1 st	2 nd	3 rd	1 st	2 nd	3 rd
Leaching rate [%]		9.22	7.52	11.68	5.99	7.56	10.68	9.81	9.52	8.89

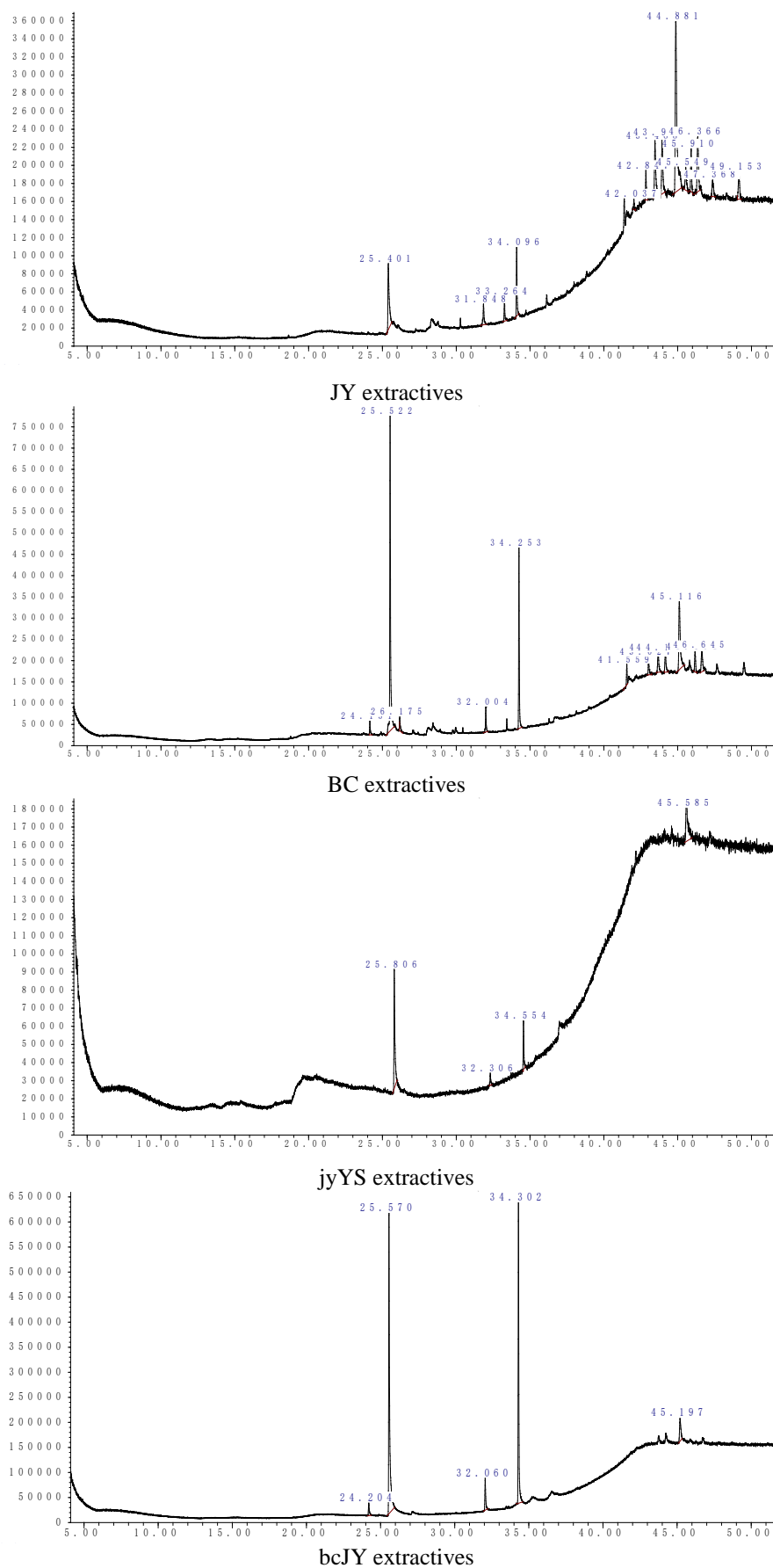


Fig. 1. Total ion chromatogram of four extractives of *Vitex negundo* stems by GC/MS

The 7 components were identified from BC extractives of *Vitex negundo* stem. The result showed that the main components were dibutyl phthalate (40.003%), 1,2-benzenedicarboxylic acid, mono(2-ethylhexyl) ester (18.803%), cyclotrisiloxane, hexamethyl- (19.351%), 1,1,1,3,5,5,5-heptamethyl-trisiloxane (15.402%), hexanedioic acid, bis (2-ethylhexyl) ester (2.965%), phthalic acid, isobutyl nonyl ester (1.58%), benzo [g] pteridine, 2,4-diamino-6,7,8,9-tetrahydro -7-methyl- (1.895%).

The 4 components were identified from jyYS extractives of *Vitex negundo* stem. The result showed that the main components were dibutyl phthalate (45.37%), cyclotrisiloxane, hexamethyl- (35.713%), cyclohexanecarboxylic acid, dodecyl ester (4.003%), 1,2-benzene -dicarboxylic acid, mono (2-ethylhexyl) ester (14.914%).

The 5 components were identified from bcJY extractives of *Vitex negundo* stem. The result showed that the main components were dibutyl phthalate (49.917%), 1,2-benzenedicarboxylic acid, mono(2-ethylhexyl) ester (38.537%), 1,2-benzenedicarboxylic acid, bis(2-methylpropyl) ester (2.037%), silicic acid, diethyl bis (trimethylsilyl) ester (5.075%), hexanedioic acid, bis (2-ethylhexyl) ester (4.435%).

Resource Properties of Stem Extractives of *Vitex Negundo*

There were many biomedical components in the stem extractives of *Vitex negundo*. Because of their public role and value, dibutyl phthalate was a pesticide to keep the environment homeostasis. [15, 16] 1, 2-benzenedicarboxylic acid, butyl 2-methylpropyl ester was hydrolyzed to 1,2-benzenedicarboxylic acid which could be used to make some drugs.

Hexanedioic acid, bis (2 -ethylhexyl) ester could be used in various products such as cosmetics, auto interior protectant, and lubricant (www.chemicalsubstances.gc.ca). Eicosane was the main compositions of rose essential oil which had the remarkable beauty effect and health care efficacy [22]. 3,3,7,11-Tetramethyltricyclo[5.4.0.0(4,11)] undecan-1-ol was the significant alcohol of volatile compositions in needle and branch of *Picea crassifolia* which could lure *Ips typographus* Linnaeus [23]. Phthalic acid, isobutyl nonyl ester was the main small constituents of *Elaeagnaceae* plant which might cure chronic cardiovascular and cerebrovascular diseases and had anti-tumor, anti-inflammatory, antibacterial functions [24]. The components were rare medicinal herbs including hexanedioic acid, bis

(2-ethylhexyl) ester, cyclohexanecarboxylic acid, dodecyl ester. And there were some drug activities of the stem extractives from *Vitex negundo*.

CONCLUSION

The leaching rule of stem extractives from *Vitex negundo* was obvious. The optimal extraction time of ethanol/methanol, petroleum ether/acetic ether, and benzene/alcohol extraction were 5 h, 4 h, and 7 h, respectively. The leaching rates of each single extraction were less than those of three-step extractions, and JY-YS-BC extraction was the optimum extraction mode with the leaching rate of 28.42%. What's more, the stem extractives of *Vitex negundo*, which was rich in drug activities. For example, hexanedioic acid, bis (2-ethylhexyl) ester was used in Canada in cosmetics, care products, heavy-duty hand cleanser and lubricant; eicosane was the major composition of the rose essential oil which had the remarkable beauty effect and health care efficacy; 3,3,7,11-tetramethyltricyclo [5.4.0.0 (4,11)] undecan-1-ol could lure *Ips typographus* Linnaeus. And the stem extractives of *Vitex negundo* contained many rare drug activities.

Acknowledgments: This work was financially supported by Invitation Fellowship Programs for Research in Japan of Japan Society for the Promotion of Science (ID No. L14713), Program for New Century Excellent Talents in University (NCET-12-0725), Project supported by the Natural Science Foundation of Hunan Province, China (14JJ4053), the Research Foundation of Education Bureau of Hunan Province, China (12B134), and Project of Forestry Science and Technology Extension([2012] 60).

REFERENCES

1. W. Tuanrong, *J. Hebei Forestry Sci. Technol.*, **4**, 10 (1998)
2. X. Boshu, D. Chunlei, L. Hongrong, *Land Greening*, **2**, 43 (2006).
3. F. S. Wang, S. X. Ren, D. P. Yang, C. S. Zhu, H. N. Lu, *J. Chinese Mass Spectrom. Soc.*, **1**, 1 (2004).
4. J. C. Xie, B. G. Sun, F. P. Zheng, M. Yu, *Food Sci.*, **26**, 281 (2005).
5. J. C. Xie, B. G. Sun, M. Yu, *Food & Fermentation Ind.*, **7**, 100 (2005).
6. X. B. Liu, H. Cao, G. H. Tian, *Amino Acids and Biotic Resour.*, **1**, 75 (2010).
7. H. C. Qi, W. X. Peng, Y. Q. Wu, S. B. Wu, G. J. Xu, *J. Comput. Theor. Nanosci.*, **9**, 1525 (2012)..
8. L. S. Wang, W. X. Peng, M. L. Zhang, Z. Lin, *J. Pure Appl. Microbiol.*, **7**(SE), 59 (2013).
9. L. S. Wang, W. X. Peng, Z. Lin, M. L. Zhang, *J. Pure Appl. Microbiol.*, **7**, 1345 (2013).

10. W. X. Peng, L. S. Wang, F. J. Wu, Q. Xu, *Acta Crystallographica Section E-Structure Reports Online*, **67**, 2329 (2011)..
11. W. X. Peng, F. J. Wu, L. S. Wang, Q. Xu, Z. *Kristallographie-New Crystal Structures*, **227**, 61 (2012).
12. E. Atasoy, *Oxidation Commun.*, **38**, 222 (2015).
13. W. X. Peng, C. Le, Z. *Kristallographie-New Crystal Structures.*, **227**(2), 267 (2012).
14. W. X. Peng, L. S. Wang, Q. Xu, Q. D. Wu, S. L. Xiang, *J. Comput. Theor. Nanosci.*, **9**, 1431 (2012)..
15. W. X. Peng, L. S. Wang, Z. Lin, M. L. Zhang, *J. Pure Appl. Microbiol.*, **7**(SE), 67 (2013).
16. W. X. Peng, Z. Lin, J. B. Chang, F. L. Gu, X. W. Zhu, *Biotechnol. Biotechnolog. Equip.*, **27**, 4311 (2013).
17. W. X. Peng, L. S. Wang, M. L. Zhang, Z. Lin, *Pakistan J. Pharm. Sci.*, **27**(3s), 723 (2014)..
18. D. L. Li, W. X. Peng, S. B. Ge, B. Mo, Z. F. Zhang, D. C. Qin, *Pakistan J. Pharm. Sci.*, **27**(6s), 2061 (2014)
19. W. X. Peng, S. B. Ge, D. L. Li, B. Mo, M. Ohkoshi, *Pakistan J. Pharm. Sci.*, **27** (6s), 2133 (2014).
20. Y. C. Sun, Z. Lin, W. X. Peng, T. Q. Yuan, F. Xu, Y. Q. Wu, et al., *BioResources*, **9**, 1055 (2014).
21. Z. P. Xiao Z. Y. Peng, J. J. Dong, R. C. Deng, X. D. Wang, H. Ouyang, P. Yang, J. He, Y. F. Wang, M. Zhu, X. C. Peng, W. X. Peng, H. L. Zhu, *Eur. J. Medicinal Chem.*, **68**, 212 (2013).
22. F. Yu, B. Zhang, W. Zhou, J. Ren, G. Y. Wang, *Natural Product Res. Dev.*, **24**, 784 (2012).
23. R. J. Shi, S. A. Xie, W. Zhao, S. J. Lv, X. B. Song, X. R. Guo, *J. Northwest Forestry Univ.*, **6**, 95 (2011).
24. H. Huang, X. Zhao, B. Jian, *Chinese Traditional and Herbal Drugs*, **37**, 307 (2006).

Performance of NaClO in selective oxidation of salix microcrystalline cellulose

Y. Li, J. Huang*

School of Materials Science & Art Design, Inner Mongolia Agricultural University, Huhehot 010018, China

Received June 26, 2015, Revised September 10, 2015

By oxidizing primary hydroxyl on surface of the salix microcrystalline cellulose with NaClO, we studied the effects onto performance of salix microcrystalline cellulose resulted from oxidant in different amounts. Performance of salix microcrystalline cellulose having been oxidized takes on attributes including lower degree of polymerization, stronger hydrophilicity due to increased carboxyl, which also resulted in larger water retention values; oxidation at paracrystalline areas began to oxidize crystallization areas, making the oxidized cellulose have higher pyrolysis temperature, significantly smaller granularity and increased specific surface, which caused some damage to superficial and internal structures, so that changes occurred in form of the cellulose.

Keywords: Salix Cellulose, Selective Oxidation, Performance

INTRODUCTION

During selective oxidation of the cellulose, intramolecular hydroxyl will be oxidized into carboxylic acid group, which will enhance cellulose's reactive activity and adsorptive capacity for ion. In the process of preparing composite material in the solution, dispersion degree of carboxylic acidified cellulose has also been improved, which greatly expanded the application range of cellulose in different fields. Together with biocompatibility and degradability, cellulose has been under the spotlight in fields of nanophase materials and biomedicine [1, 2, 3, 4, 5]. Richard K. Johnson used to utilize TEMPO to oxidize cellulose and study the application of cellulose in the field of nanocomposites, where content of carboxyl group reached up to 1.1 mmol/g after cellulose having been carboxylic acidified. Youssef Habibi [6, 7] carboxylic acidified the nano-cellulose, microcrystalline cellulose and cellulose whiskers they have prepared. Flocculation didn't appear in those cellulose having been treated and birefringence occurred in the cellulose whiskers under polarizing microscope. He also prepared nano-composite materials with those carboxylated cellulose. After the study, he found that carboxylic acidification could greatly improve adsorptive capacity of the fiber, which serves as the best template for nanocomposites. T. Saito et al [8] conducted attribute analysis on aldehyde content and carboxylic acid group of the carboxylated cellulose with different cellulosic feedstocks and oxidation processes and studied changes of

performance index with polymerized degree, pattern, crystal structure, crystallinity, water retention value and so on. A. Isogai et al [9] oxidized cellulose materials with the TEMPO / NaClO / NaBr oxidation system. A lot of experiments showed that amount of TEMPO had great impact onto polymerization degree of the product. Both regenerated fiber and mercerized fiber can be completely oxidized. However, natural cellulose can't realize complete selective oxidation, mainly due to high crystallinity of native cellulose affects the oxidation effect..

EXPERIMENTAL

Disperse the prepared salix microcrystalline cellulose in deionized water to make 2.0% solution of microcrystalline cellulose, add TEMPO (0.1 mmol/g) and NaBr (1 mmol/g) to make stable solution for later use, adjust PH to 10.75 with sodium carbonate/sodium bicarbonate solution as a buffer, add a certain amount of 9% NaClO solution, adjust PH to be constant with ammonia, and then finish the preparation of salix cellulose with different levels of carboxylic acid groups. As PH value keeps unchanged during reaction, add a certain amount of absolute ethanol to terminate the reaction. Stir for 10 minutes, centrifuge at high speed and then obtain the carboxylated salix cellulose. Repeatedly wash with deionized water, add 0.1 mol/L AgNO₃, test to make sure no presence of chloride ions, dry at low temperatures for later use.

To whom all correspondence should be sent:
E-mail: jintian_h@163.com

To Determine Content of Carboxylic Acid Group in Salix Cellulose

Obtain carboxylic acid in free state by the replacement reaction between calcium acetate and carboxylic acid group on the salix cellulose, and then use standard NaOH solution to titrate. The principle as follows:



Weigh 1 g of the sample mentioned above, soak the sample with 50 ml of 0.1 mol/L newly-prepared calcium acetate in a 100 ml iodine flask, place for 24 hours with stirring. Take 10ml of solution mentioned above and place in a 250 ml conical flask, add mixed indicator of cresol red - thymol blue, select 0.1 mol/L standard NaOH solution as the titration reagent, observe colour of the solution changing from yellow to purple, record consumption volume of NaOH solution as V, take another 10ml of solution mentioned above for blank test, titrate with standard NaOH solution at $c = 0.1 \text{ mol/L}$, and record volume of the standard NaOH solution as V_0 .

Formula for calculating content of the carboxylic acid group as follows:

$$\text{Carboxyl group content (mmol} \cdot \text{g}^{-1}) = (V - V_0) \times 5c / W$$

Where, W is the absolutely dry mass of test sample under accurate weighing.

To Determine Polymerization of Salix Cellulose with Carboxylic Acid Group

Adopt the Uno Viscosity Method to calculate the degree of polymerization. Dissolve 0.05 g of salix microcrystalline cellulose and 0.05 g of oxidation product respectively in 1 M of copper ammonia solution and 0.1 M of NaCl solution, and analyze viscosity of the solution in a thermostat. Draw 15 ml of the prepared solution and inject into the viscometer, keep temperature of the viscometer constant, let the solution flow from end opening of the viscometer, and record the time for solution to flow through the viscometer with a stopwatch. Repeat the test for three times, ensuring time difference among the three tests to be 0.2 s. Determine relevant value at T2 with the same method, adding 5 ml, 15 ml and 25 ml of copper ammonia solution respectively. And then determine relevant values at T3, T4 and T5. Obtain viscosity of the salix cellulose at 25°C -- $[\eta]$. In the same way, obtain viscosity of the carboxylated salix cellulose at 25°C -- $[\eta]$.

To Determine Water Retention Value of the Salix Cellulose with Carboxylic Acid Group

Weigh 0.25 g of absolutely-dry cellulose with carboxylic acid group, put into stainless-steel strainer, and make absorption at 25°C for 30 minutes. Put the strainer with sample into high speed centrifuge at 6000 rev / min for 15 minutes. Take out the sample and weigh, and record the weight as W1. Place the sample in a vacuum drying oven at 105°C for 4 hours, weigh the sample and record the weight as W2. Use the following formula to calculate the water retention value (WRV%):

$$WRV = 100(W1 - W2) / W2$$

RESULTS AND DISCUSSION

Effect of the Amount of NaClO onto Carboxyl Content of Salix Cellulose

Figure 1 showed that carboxyl content of salix cellulose increased along with the amount of NaClO getting larger. As amount of NaClO increased to 5.0 mmol/g from 1.0 mmol/g, content of carboxylic acid group in the salix cellulose increased to 0.90 mmol/g from 0.21 mmol/g, indicating that larger amounts of NaClO could break crystalline areas on the surface of salix cellulose and thus enhance the degree of oxidation in crystalline areas of the salix cellulose. A small amount of hemicellulose contained in the salix cellulose may serve as another reason, because hemicellulose has the lower molecular weight whose pentosan can be easily carboxylated.

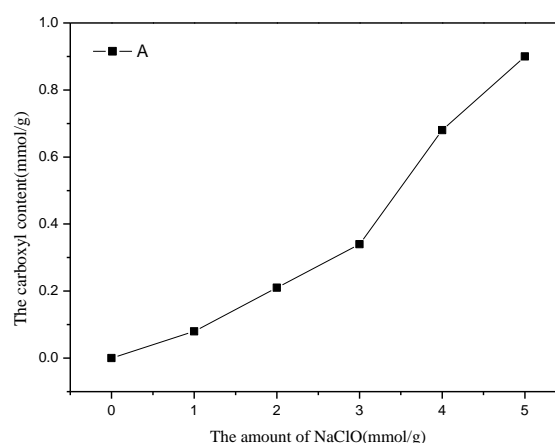


Fig. 1. Effect of the amount of NaClO onto carboxyl content of salix cellulose.

Effect of The Amount of NaClO onto Polymerization of Salix Cellulose

In general, water retention value of the cellulose is related to length of the cellulose, swelling resistance of the cellulose, fibrillation and other factors.

As having been oxidized, amount of small pieces in the cellulose will increase. However, water retention value of the oxidized cellulose gets larger due to increased amount of carboxyl group which has the hydrophilicity. Therefore, as amounts of NaClO changing, salix cellulose will change and water retention value will get larger. As shown in the figure 2, water retention value increased for 198% as amount of NaClO reached to 5 mmol/g, which was one time larger than the water retention value of non-oxidized cellulose.

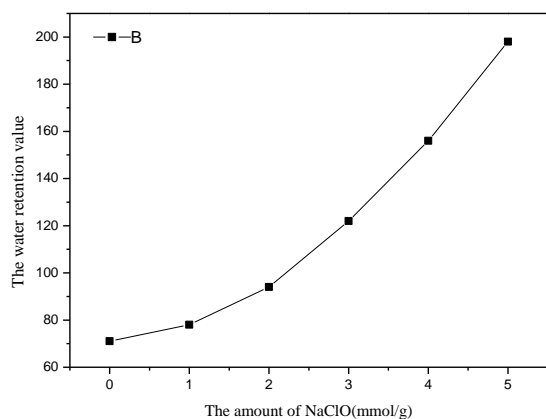


Fig. 2. Effect of the amount of NaClO onto water retention value of salix cellulose.

Ultra-Red Adsorption Spectroscopy on NaClO Amounts Used for Salix Cellulose

As shown in Figure 3, increased amount of NaClO enhanced the oxidizing power of the oxidation system for salix microcrystalline cellulose. Along with changing amounts of NaClO, oxidized salix microcrystalline cellulose showed strengthened absorption peak at 1650 cm^{-1} site, which was mainly the carbonyl absorption peak. Because carboxyl groups were introduced onto macromolecule chain of the salix cellulose having been oxidized. Content of carboxylic acid group increases along with increased amounts of NaClO, where absorption strength and width of the peak also enhanced. There were no changes at other major absorption peaks, which indicated that other functional groups had no changes and congruous chemical structures during the oxidation. However, stretching peaks of the secondary hydroxyl group at sites of 1110 cm^{-1} and 1175 cm^{-1} showed significantly decreased vibration, because secondary hydroxyl groups at C2 and C3 on macromolecular chains of salix cellulose had been oxidized into aldehyde groups. Therefore, it indicated that selective oxidation mainly occurred in the oxidation process which produced the dialdehyde-oxidized salix cellulose. Also shown in the figure, absorption peak at the 1650 cm^{-1} site had

no obvious changes as amounts of NaClO increasing from 1 mmol/g to 3 mmol/g. Changes on absorption peak at the 1650 cm^{-1} site became obvious as amounts of NaClO increasing from 3 mmol/g to 5 mmol/g. Because NaClO at the amount between 1 mmol/g and 3 mmol/g mainly oxidized paracrystalline areas of the microcrystalline cellulose. As the amount continued to grow, oxidation in the paracrystalline area finished and began to occur in the crystalline area, which caused enhanced absorption peak at 1650 cm^{-1} site and increased exposure of secondary hydroxyl group in the crystalline area, where stretching peaks of the secondary hydroxyl group at sites of 1110 cm^{-1} and 1175 cm^{-1} showed enhanced vibration.

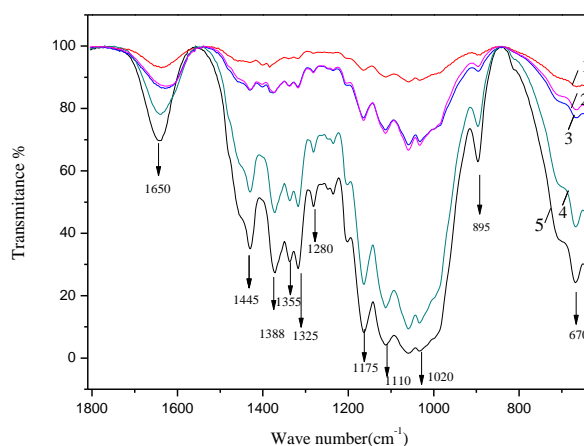


Fig. 3. Ultra-red adsorption spectroscopy on different NaClO amounts used for salix cellulose.

Thermo-Gravimetry for Salix Cellulose Based on NaClO Amounts

Figure 4 to Figure 8 showed that heat resistance of the carboxylated cellulose changed along with the amounts of NaClO going as 1 mmol/g, 2 mmol/g, 3 mmol/g, 4 mmol/g and 5 mmol/g. Free water contained in the carboxylated cellulose acts as the reason for weight loss at 150°C. In an amount of 1.0 mmol/g NaClO, weight loss started at 215°C and ended at 408°C. When the amount of NaClO reached to 2.0 mmol/g, initial temperature for weight loss had no obvious changes and termination temperature was at 443°C. In an amount of 3.0 mmol/g NaClO, termination temperature for weight loss was at 476°C. In an amount 4.0 mmol/g NaClO, termination temperature for weight loss was at 528°C. When the amount reached to 5.0 mmol/g, termination temperature for weight loss was at 551°C. Strengthened oxidation in the salix microcrystalline cellulose caused the thermal decomposition temperature presenting an upward trend. As oxidation in the microcrystalline cellulose getting

deepened, non-crystalline areas on the surface will be oxidized and degraded. As a result of oxidation getting into the crystalline area, amount of cellulose will get larger and thus termination temperature will get higher. In addition, absorption peaks on thermal decomposition became significantly moderate, which was mainly caused by a large amount of oligosaccharides produced during oxidation.

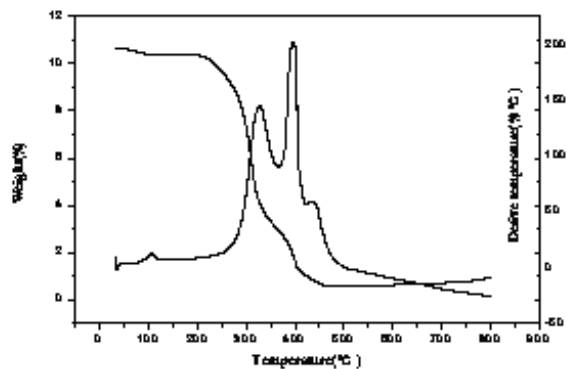


Fig. 4. TG diagram under 1.0 mmol/g NaClO.

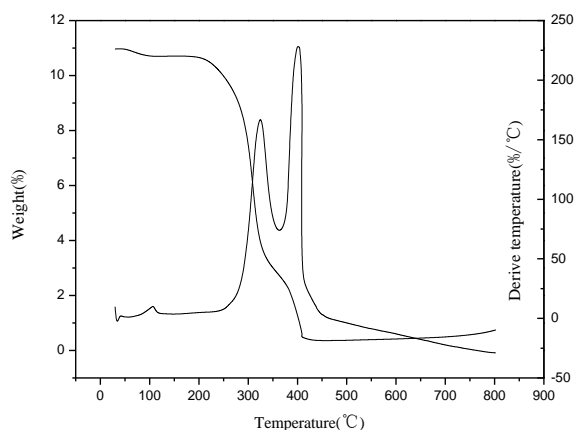


Fig. 5. TG diagram under 2.0 mmol/g NaClO.

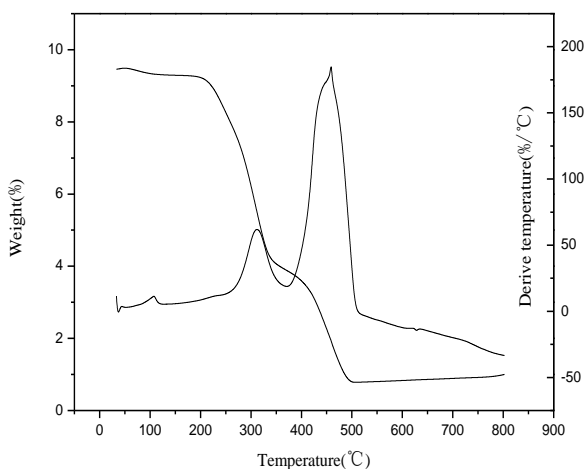


Fig. 6. TG diagram under 3.0 mmol/g NaClO.

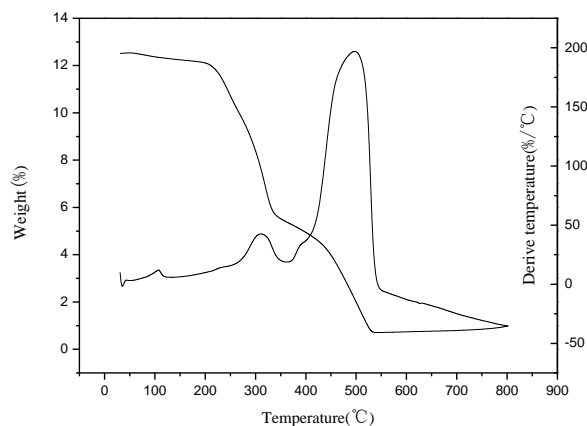


Fig. 7. TG diagram under 4.0 mmol/g NaClO.

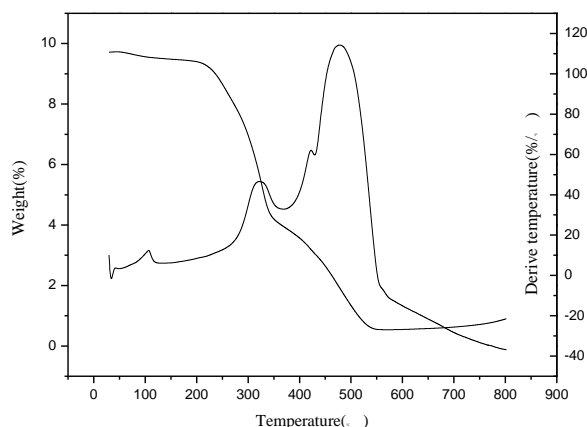


Fig. 8. TG diagram under 5.0 mmol/g NaClO.

Sem Analysis for *Salix* Cellulose Based on *Nacl* Amounts

As seen from figure 9-13, changes occurred on surface of the cellulose with continuous adding of NaClO. When NaClO added in an amount of 1.0 mmol/g, surface of the cellulose having been carboxylated became rough, interface on the surface became blurred and began to show coarseness. When NaClO added in an amount of 3.0 mmol/g, orientation of the cellulose deteriorated. When NaClO added in an amount of 4.0 mmol/g, orientation of the cellulose disappeared. When NaClO added in an amount of 5.0 mmol/g, cavities began to appear on the surface, which mainly because larger amounts of oxidant continuously got into crystalline areas of the cellulose and resulted in oxidation. Meanwhile, granularity of the cellulose became significantly small and specific surface became larger, which indicated that increasing amounts of oxidizer were liable to cause some damage for surface and internal structures of the suit fiber, making forms of the cellulose change.

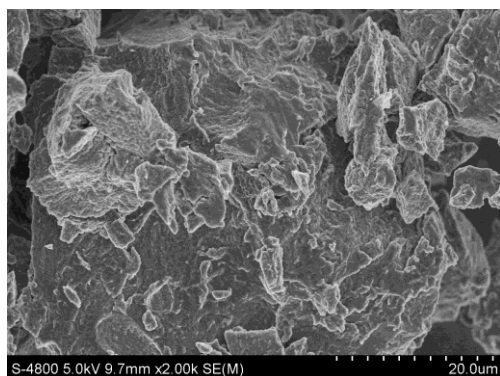


Fig. 9. Scanning electron micrograph under 1.0 mmol/g NaClO.

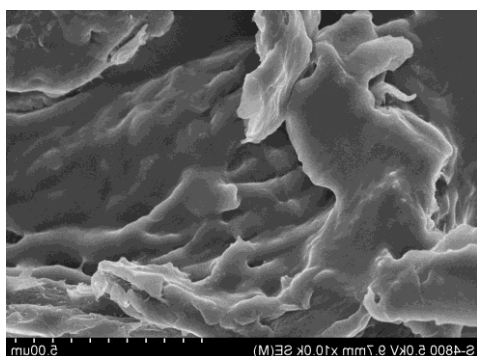


Fig. 10. Scanning electron micrograph under 2.0 mmol/g NaClO.



Fig. 11. Scanning electron micrograph under 3.0 mmol/g NaClO.

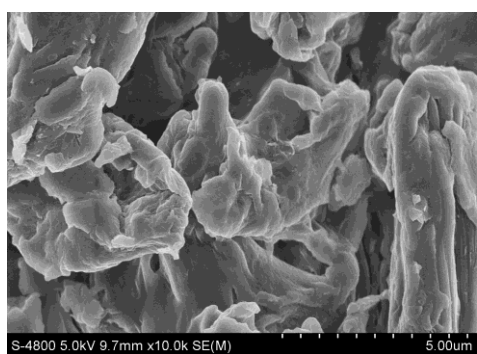


Fig. 12. Scanning electron micrograph under 4.0 mmol/g NaClO.

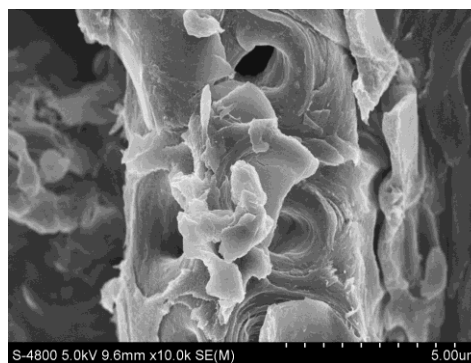


Fig. 13. Scanning electron micrograph under 5.0 mmol/g NaClO.

CONCLUSION

1. With the increasing amounts of NaClO, number of carboxylic acid groups becomes larger during selective oxidation of salix cellulose, changing from 1.0mmol/g to 5.0mmol/g. On the contrary, increasing amounts of NaClO can decrease polymerized degree of the salix cellulose, which indicates that carboxylicly acidified degree of the salix cellulose is related to the polymerized degree. After cellulose having been oxidized, content of carboxyl groups will get larger, leading to stronger hydrophilicity. As amounts of NaClO changing, salix cellulose will change and water retention value will get larger accordingly. Water retention value increased for 198% as amount of NaClO reached to 5 mmol/g, which was one time larger than the water retention value of non-oxidized cellulose.

2. NaClO at the amount between 1 mmol/g and 3 mmol/g mainly oxidized para-crystalline areas of the microcrystalline cellulose. As the amount continued to grow, oxidation in the para-crystalline area finished and began to occur in the crystalline area, which caused enhanced absorption peak at 1650cm⁻¹ site and increased exposure of secondary hydroxyl group in the crystalline area, where stretching peaks of the secondary hydroxyl group at sites of 1110 cm⁻¹ and 1175 cm⁻¹ showed enhanced vibration.

3. As amount of NaClO added in larger amounts, strengthened oxidation in the salix microcrystalline cellulose will cause the thermal decomposition temperature presenting an upward trend. Along with oxidation in the microcrystalline cellulose getting deepened, non-crystalline areas on the surface will be oxidized and degraded. As a result of oxidation getting into the crystalline area, amount of cellulose will get larger and thus termination temperature will get higher. Absorption peaks on thermal decomposition became significantly moderate, which was mainly caused

by a large amount of oligosaccharides produced during oxidation.

4. Larger amounts of oxidant continuously will get into crystalline areas of the cellulose and result in oxidation. Meanwhile, granularity of the cellulose became significantly small and specific surface became larger, which indicated that increasing amounts of oxidizer were liable to cause some damage for surface and internal structures of the suit fiber, making forms of the cellulose change.

Acknowledgments: Fund Project: State Forestry Administration 948 project on introduction of foreign advanced technology (2011-4-7); Inner Mongolia Science and Technology Department, major project under natural science foundation (2011ZD07).

REFERENCES

1. C. Tsiptsias, I. Tsivintzelis, L. Papadopoulou., *Materials Science and Engineering*, **29**, 159 (2009).
2. E. Lasseguette, *Cellulose*, **15**, 571 (2008).
3. T. Tatrishvili, N. Jalagonia, K. Gelashvili, *Oxidation Communications*, **1**, 13 (2015).
4. Saito. T. Nishiyama Y, Putaux. J. L. *Biomacromolecules*, **7** (6), 1687 (2006).
5. C. Aulin, S. Ahola, P. Josefsson., Nanoscale Cellulose Films with Different Crystallinities and Messtructures: Their Surface Properties and Interaction with Water, *Langmuir Article*, 2009.
6. S. Ifuku, M. Tsuji, *Biomacromolecules*, **10**, 2714 (2009).
7. Y. Habibi, H. Chanzy, *Cellulose*, **13**, 679 (2006).
8. T. Saito, A. Isogai, *Biomacromolecules*, **5**, 1983 (2004)..
9. A. Isogai, Y. Kato, *Cellulose*, **5**, 153 (1998).

Molecular characteristics of immune activities in *Cercis chinensis* stem extractives for physical anthropology

Q. Ma^{1,2}, D. Zhang^{1*}, F. Yuzo^{2*}, H. Deng¹

¹ Central South University of Forestry and Technology, Changsha, China

² Laboratory of Biomaterials Science, Kyoto Prefectural University, Kyoto, Japan

Received June 26, 2015, Revised September 10, 2015

As one of dominant species of medicinal plants in North China, *Cercis chinensis* was also considered as the important immune active drug resources for physical anthropology, however, the molecule constituents of *Cercis chinensis* stems was not known. Therefore, the molecular characteristics of extractives from *Cercis chinensis* stems were studied to further utilize the drug resources. The GC/MS analysis results showed that 6, 13, 3, and 8 components were identified by GC/MS in the SY extractives, syJC extractives, syjcBY extractives, jcsyBY extractives from *Cercis chinensis* stems, respectively. The multi-steps extraction method was fit to extraction and separation for the particular extractives from *Cercis chinensis* stems. What's more, the extractives of *Cercis chinensis* stems contained biomedical constituents, such as phytol, 4,6-di-O- methyl- .alpha.-d-galactose, 2-C-methyl-myo-Inositol, and so on. The analytical result suggested that the extractives of *Cercis chinensis* stems were used to prepare the rich and rare immune activities for the better physical anthropology.

Keywords: Immune activity, Physical anthropology, *Cercis chinensis* stem, Extractives molecule, GC/MS

INTRODUCTION

Cercis chinensis, which easily growing in average, medium and well-drained soil, should be planted when young and left undisturbed. *Cercis chinensis* was native in central and southern China, commonly called Chinese redbud, and usually grown much smaller as an open, densely branched, multi-stemmed shrub or small tree to 8-15' tall [1]. Its leaves would turn a respectable yellow in fall [2]. Especially, Chinese redbud was less affected by the common diseases and pests of our native redbud. *Cercis chinensis* was also an important ornamental shrubs for large beautiful flowers with bright color, and then was widely welcomed for good adaptability, high survival rate, low price, and good greening effect. *Cercis chinensis* tree should be transplanted in the bud before or after the leaves, roots could be cultivated, but could not be the first root transplanting and colonization [3, 4]. *Cercis chinensis* had the well-developed root system, and was not easy to cut so as to avoid tearing the root bark. When transplanting the proper pruning, part old branches should be updated each year before germination. It need be fertilized for 2-3 times during the growth period.

Cercis chinensis was a tree which had economic value. In the past, *Cercis chinensis* stems were

mainly used in furniture and building. However, *Cercis chinensis* stems were always abandoned. *Cercis chinensis* biomass had the functions of clearing heat and cooling blood, detoxification, activating blood flow, swelling pain [5, 6, 7, 8]. It could cure rheumatism, traumatic injury, wind cold dampness arthralgia, amenorrhea, snake bite, bloodfeud, rabies and other diseases [2]. Its bark was bitter and flat to activate blood flow and swell detoxification for wind cold dampness arthralgia, amenorrhea, blood gas pain, sore throat, stranguria, carbuncle swollen, tinea cabies, traumatic injury, insect and snake bite. Its wood was bitter and flat to promote blood circulation, stranguria for blood stasis dysmenorrhea, abdominal pain and stranguria; Its flowers had heat-cleared detoxification for rheumatism muscles pain and nasal abscess; Its fruit was used for coughs and pregnant women [1, 5, 6]. *Cercis chinensis* biomass was also used as traditional Chinese medicine for thousands of years. However, the medicinal components of *Cercis chinensis* were less recorded. Yanyan *et al.* [9] found N naphthyl 2 aniline, biocyclomahanimbine, mahanimbine and girinimbine in *Bauhinia variegata*. Wanxi *et al.* [10, 11, 12, 13, 14, 15, 16, 17]; Lansheng *et al.* [18] had studied many woody extractives and their pyrolysis products [11, 19]. Zhu-Ping *et al.* [20] had studied the synthetic bio-drugs [21, 22, 23, 24, 25, 26, 27]. Some researchers had explored a variety of immune biological active ingredients [5, 6, 7, 8, 28, 19, 29, 30, 18, 31, 32, 33]. And *Cercis chinensis* was also

To whom all correspondence should be sent:
E-mail: 1171008963@qq.com, zhangdangquan@163.com.,
mohkoshi@kpu.ac.jp, csfucyc@163.com

considered as the important immune active drug resources to maintain and enhance the fine physical anthropology. However, the molecule constituents of immune activities from *Cercis chinensis* stems were not known. Therefore, the molecular characteristics of the stems extractives from *Cercis chinensis* were investigated and analyzed by the optimized extracting techniques in order to better utilize immune activities from *Cercis chinensis* stems as bio-drug resources for the better physical anthropology.

EXPERIMENTAL

Materials

In winter, fresh *Cercis chinensis* stems were collected from the Tongbai Mountain, Henan Province, China. The fresh stems were directly pound to pieces and kept in the dryer. Acetic ether, methanol, benzene, petroleum ether and ethanol, which were prepared for the subsequent experiments, were chromatographic grade. Cotton thread and cotton bag were both extracted in benzene/ethanol solution ($V_{\text{ethanol}}/V_{\text{benzene}} = 2$) for the treatment time of 12 h.

Experimental methods

Weighed 27 pieces of stems, each was 20 g (1.0 mg accuracy), and finally parceled by cotton bag tied by cotton thread. Method of three-step extraction was carried out by large-caliber Soxhlet according to the solution's different orders combined by JC-SY-BY (methanol \rightarrow petroleum ether/acetic ether ($V_{\text{petroleum ether}}/V_{\text{acetic ether}} = 2$) \rightarrow benzene/ethanol), SY-BY-JC (petroleum ether/acetic ether \rightarrow benzene/ethanol \rightarrow methanol), BY-JC-SY (benzene/ethanol \rightarrow methanol \rightarrow petroleum ether/acetic ether), respectively. After each step extraction, the extractives solutions were removed and evaporate in 60°C-70°C air, and then kinds of extractives of *Cercis chinensis* stems were obtained. The extraction times were both 2.5 hours.

GC/MS condition

Among the above extractives, the SY extractives in SY-JC-BY method (Number LD-120), syJC extractives in SY-JC-BY method (Number LD-123), syjcBY extractives in SY-JC-BY method (Number LD-125), and jcsyBY extractives in JC-SY-BY method (Number LD-127) were analyzed, respectively. Each 0.5 mg extractives was analyzed by online linked GC/MS (gas chromatograph / mass spectrometer), respectively. The GC/MS analysis

was done as the same as the documents [18, 12, 13, 14, 15].

EXPERIMENTAL RESULTS

Results of stem extractives from *Cercis chinensis*

The SY extractives, syJC extractives, jcsyBY extractives, and syjcBY extractives were obtained respectively. The total ion chromatograms of four extractives by GC/MS were shown in Figure 1. Relative content of each component was counted by area normalization. The components and their contents were identified by analyzing the MS data, the NIST standard MS map, open-published books and papers. And the results were listed in table 1, table 2, table 3 and table 4, respectively.

RESULTS' ANALYSES

Molecular properties of stem extractives from *Cercis chinensis*

According to GC/MS result, 6 components were identified from SY extractives of *Cercis chinensis* stems. The result showed that the main components were 2-butanone, 4,4-dimethoxy- (14.602%), 4,6-di-O- methyl-.alpha.-d-galactose (50.990%), n-hexadecanoic acid (1.811%), 9,12-octadecadienoic acid, methyl ester (4.059%), tetrasiloxane, decamethyl- (7.041%), 1H-indole, 1-methyl-2-phenyl- (21.497%).

The 13 components were identified from syJC extractives of *Cercis chinensis* stems. The result showed that the main components were 1,3-hexadien-5-yne (2.619%), benzene, 1-pentynyl- (0.392%), 5,6-epoxy-6- methyl-2-heptanone (1.114%), diazene, butyl[1-(2,2-dimethylhydrazino)ethyl]- (87.380%), myo-Inositol, 2-C-methyl- (0.278%), n-hexadecanoic acid (0.543%), dibutyl phthalate (0.897%), (R)-(-)-14-methyl- 8-hexadecyn-1-ol (0.140%), phytol (0.377%), 9,12-octadecadienoic acid (Z,Z)- (0.914%), 2-bromo- 4,5-dimethoxycinnamic acid (2.730%), 2,4,6-cycloheptatrien-1-one, 3,5-bis-trimethylsilyl- (0.550%), 1H-indole, 1-methyl-2-phenyl- (2.068%).

The 3 components were identified from syjcBY extractives of *Cercis chinensis* stems. The result showed that the main components were 2,4-hexadiyne (92.924%), dibutyl phthalate (4.520%), 1,2-benzenedicarboxylic acid, diisooctyl ester (2.555%).

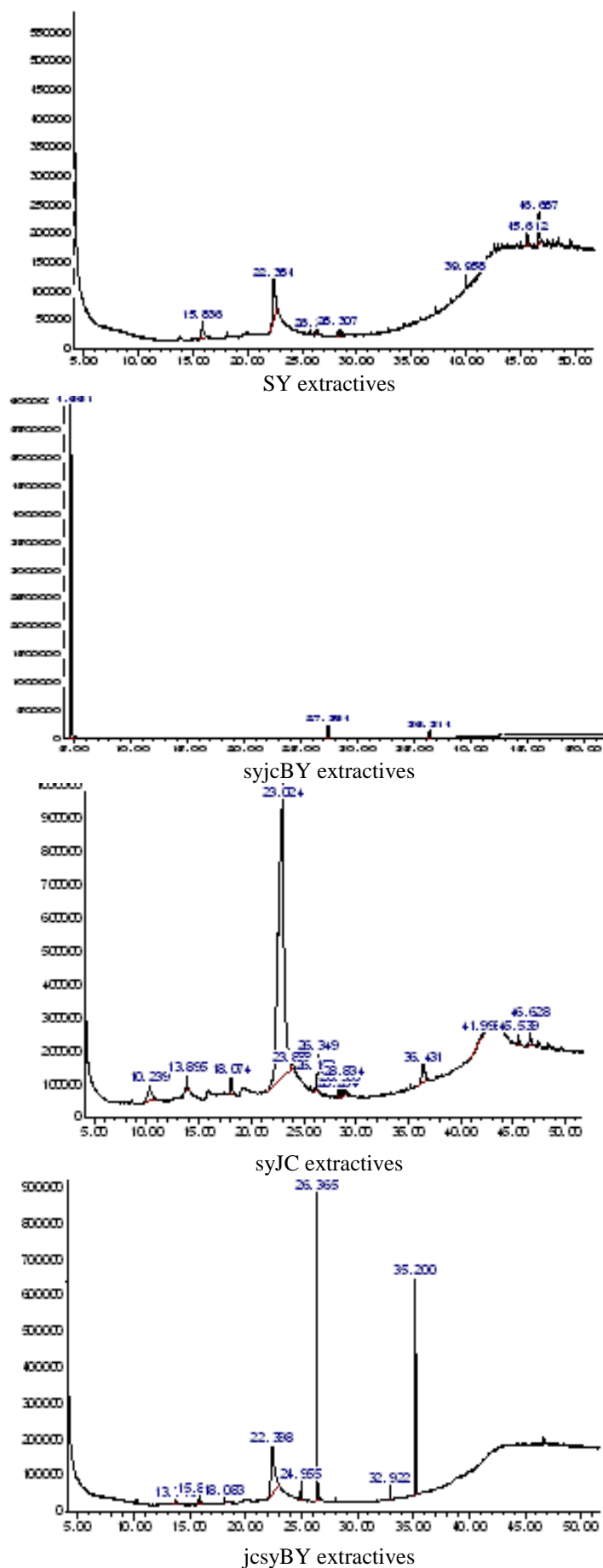


Fig. 1. Total ion chromatograms of four stem extractives of *Cercis chinensis* by GC/MS.

Table 1. The compounds of SY extractives of *Cercis chinensis* stems by GC/MS.

No.	Retention time [min]	Peak area [%]	Chemical compound
1	15.836	14.602	2-Butanone, 4,4-dimethoxy-
2	22.384	50.990	4,6-Di-O-methyl-.alpha.-d-galactose
3	26.223	1.811	n-Hexadecanoic acid
4	28.307	4.059	9,12-Octadecadienoic acid, methyl ester
5	39.958	3.154	1H-Indole, 1-methyl-2-phenyl-
6	45.612	7.041	Tetrasiloxane, decamethyl-
7	46.687	18.343	1H-Indole, 1-methyl-2-phenyl-

Table 2. The compounds of syJC extractives of *Cercis chinensis* stems by GC/MS.

No.	Retention time [min]	Peak area [%]	Chemical compound
1	10.239	2.619	1,3-Hexadien-5-yne
2	13.895	0.392	Benzene, 1-pentynyl-
3	18.074	1.114	5,6-Epoxy-6-methyl-2-heptanone
4	23.024	87.380	Diazene, butyl[1-(2,2-dimethylhydrazino)ethyl]-
5	23.888	0.278	Myo-Inositol, 2-C-methyl-
6	26.152	0.543	n-Hexadecanoic acid
7	26.349	0.897	Dibutyl phthalate
8	28.264	0.140	(R)-(-)-14-Methyl-8-hexadecyn-1-ol
9	28.556	0.377	Phytol
10	28.834	0.914	9,12-Octadecadienoic acid (Z,Z)-
11	36.431	2.730	2-Bromo-4,5-dimethoxycinnamic acid
12	41.998	0.370	1H-Indole, 1-methyl-2-phenyl-
13	45.539	0.550	2,4,6-Cycloheptatrien-1-one, 3,5-bis-trimethylsilyl-
14	46.628	1.698	1H-Indole, 1-methyl-2-phenyl-

Table 3. The compounds of syjcBY extractives of *Cercis chinensis* stems by GC/MS.

No.	Retention time [min]	Peak area [%]	Chemical compound
1	4.661	92.924	2,4-Hexadiyne
2	27.364	4.520	Dibutyl phthalate
3	36.314	2.555	1,2-Benzenedicarboxylic acid, diisooctyl ester

Table 4. The compounds of jcsyBY extractives of *Cercis chinensis* stems by GC/MS.

No.	Retention time [min]	Peak area [%]	Chemical compound
1	13.716	1.425	Ethanone, 1-(2,4,5-trimethylphenyl)-
2	15.817	2.909	2-Butanone, 4,4-dimethoxy-
3	18.083	0.980	3,3'-Thiodipropanol
4	22.398	34.002	4,6-Di-O-methyl-.alpha.-d-galactose
5	24.955	1.854	Phthalic acid, isopropyl propyl ester
6	26.365	35.106	Dibutyl phthalate
7	32.922	1.380	Hexanedioic acid, bis(2-ethylhexyl) ester
8	35.2	22.344	Phthalic acid, 2-ethylhexyl hexyl ester

The 8 components were identified from jcsyBY extractives of *Cercis chinensis* stems. The result showed that the main components were ethanone, 1-(2,4,5-trimethylphenyl)- (1.425%), 2-butanone, 4,4-dimethoxy-(2.909%), 3,3'-thiodipropanol (0.980%), 4,6-di-O-methyl-.alpha.-d-galactose

(34.002%), phthalic acid, isopropyl propyl ester (1.854%), dibutyl phthalate (35.106%), hexanedioic acid, bis(2-ethylhexyl) ester (1.380%), phthalic acid, 2-ethylhexyl hexyl ester (22.344%).

Based on the above molecular properties, kinds of extractives *Cercis chinensis* stems were

significantly different in several solvents and extraction order. There were the vast differences in the different three-step extraction method. Therefore, the multi-step extraction method was fit to extraction and separation of the particular *Cercis chinensis* extractives.

Resource properties of stem extractives from Cercis chinensis

There were many biomedicine and drug components in stem extractives of *Cercis chinensis*. Because of its bio-drug value, dibutyl phthalate was a pesticide to keep internal environment homeostasis [16]. Phthalic acid, isobutyl nonyl ester, which had the potential efficacy on curing chronic cardiovascular and cerebrovascular diseases, had anti-tumor, anti-inflammatory, antibacterial functions [34]. Phytol, which was an acyclic diterpene alcohol that could be used as a precursor for the manufacture of synthetic forms of vitamin E and vitamin K1, was used not only as food which converted to phytanic acid and stored in fats of body, but also in the fragrance industry, cosmetics, shampoos, toilet soaps, household cleaners, and detergents [35, 36, 37, 38]. 4, 6-di-O-methyl-.alpha.-d-galactose was a form of sugar that could provide a great deal of energy in a very small amount of product, enhance nutrient properties, and be used as a nutritive sweetener. The n-hexadecanoic acid was an anti-inflammatory agents whose binding energy was calculated by in silico method and compared with known inhibitors [39]. Myo-Inositol, 2-C-methyl, which are found in many foods, in particular fruit, especially cantaloupe and oranges, played an important role as the structural basis for a number of secondary messengers in eukaryotic cells, the various inositol phosphates, and had a taste which has been assayed at half the sweetness of table sugar. 2, 4, 6-cycloheptatrien-1-one, 3,5-bis-trimethylsilyl- was one of the bioactive components of *Microcosmus exasperatus* which might heal some diseases [41]. 9,12-octadecadienoic acid, methyl ester, and 9,12-octadecadienoic acid (Z,Z)- had been identified as the main medical component of dried worms, and has diuretic, swelling and detoxification properties [41, 15]. Hexanedioic acid was also rare medicinal herbs. The analytical result suggested that there were many bio-drug activities in kinds of extractives from *Cercis chinensis* stems..

CONCLUSION

The analytical analysis result of different *Cercis chinensis* stem extractives was obtained. 6, 13, 3, and 8 components were identified by GC/MS in SY

extractives, syJC extractives, syjcBY extractives, jcsyBY extractives, respectively. There were the vast differences in the different three-step extraction methods. The multi-step extraction method was fit to extraction and separation of the particular extractives from *Cercis chinensis* stem. What's more, the kinds of extractives from *Cercis chinensis* stem were rich in bio-drug activities, such as Phytol was used not only as food which converted to phytanic acid and stored in fats of body, but also in the fragrance industry, cosmetics, shampoos, toilet soaps, household cleaners, and detergents; 4,6-di-O-methyl-.alpha.-d-galactose was used as a nutritive sweetener; myo-Inositol, 2-C-methyl played an important role as the structural basis for a number of secondary messengers in eukaryotic cells, and so on. And the stem extractives of *Cercis chinensis* were rich in rare bioimmune-drug activities for the better physical anthropology.

Acknowledgments: This work was financially supported by the National Natural Science Fund of China (31172257), Invitation Fellowship Programs for Research in Japan of Japan Society for the Promotion of Science (ID No. L14713), and Key Plan Projects of Hunan Province (2014FJ2004), The National Forestry Technology Popularization Project (2012]37; 2012]60; [2012]62).

REFERENCES

1. L. H. Mu, Study on chemical constituents and biological activity of *Cercis chinensis* redbud part., Peking Union Medical College, 2007.
2. L. Yuan, Study on chemical constituents and biological activity of Cao Shanhu, Bauhinia and Lobular Shi Nan, Doctoral Dissertation of Peking Union Medical College, 2006.
3. W. Tuanrong, *J. Hebei Forest Sci Technol.*, **4**, 10 (1998).
4. X. Boshu, D. Chunlei, L. Hongrong, *Land Gree.*, **2**, 43 (2006).
5. J. C. Xie, B. G. Sun, F. P. Zheng, Y. U. Min, *Food Sci.*, **26**, 281 (2005a).
6. J. C. Xie, B. G. Sun, Y. U. Min, *Food and Fermentation Ind.*, **7**, 100 (2005b).
7. X. B. Liu, H. Cao, *Amino Acids Biotic Resour.*, **1**, 75 (2010)
8. F. S. Wang, S. X. Ren, D. P. Yang, C. S. Zhu, H. N., *J Chin Mass Spectr Soc.*, **1**, 1 (2004)..
9. Z. Yanyan, C. Chengbin, C. Bin, H. Bing, S. Qishi, *Chin J Med Chem.*, **14**, 169 (2004).
10. Q. Z. Ma, W. X. Peng, Y. Q. Wu, X. Zhang, H. P. Deng, *Applied Electromagnetics And Mechanics (II)*, **13**, 373 (2009).
11. W. X. Peng, F. J. Wang, L. S. Wang, X, Z Qiu. *Kristallogr. NCS*, **227**, 61 (2012a).

12. W. X. Peng, L. S. Wang, Z. Lin, M. L. Zhang, *J. Pure Appl. Microbio.*, **7**(SE), 67 (2013a).
13. W. X. Peng, Z. Lin, J. B. Cao, F. L. Gao, X. W. Zhao, Z. F. Zhang, *J. Pure Appl. Microbio.*, **7**(2), 1237 (2013b).
14. W. X. Peng, Z. F. Zhang, Z. Lin, M. Ohkoshi, J. B. Cao, F. L. Gao, X. W. Zhao, *J. Pure Appl. Microbio.*, **7**, 2017 (2013c).
15. W. X. Peng, Z. Lin, J. B. Cao, F. L. Gao, X. W. Zhao, *Biotechnol. Biotec. Eq.*, **27**, 4311 (2013d).
16. W. X. Peng, Wang, Z. Lin, M. L. Zhang, Z. Lin, *Pak. J. Pharm. Sci.*, **27**(3S3), 723 (2014a).
17. W. X. Peng, X. Qiu, O. Makoto, *Pak. J. Pharm. Sci.*, **27**(4S), 991 (2014b).
18. L. S. Wang, W. X. Peng, M. L. Zhang, Z. Lin. *J. Pure Appl. Microbio.*, **7**(SE), 59 (2013a).
19. H. C. Qiu, W. X. Peng, Y. Q. Wang, S. B. Wang, G. J. Xu, *J. Comput. Theor. Nanos.*, **9**, 1525 (2012).
20. Z. P. Xu, Z. Y. Peng, Jing-Jun D, Rui-Cheng D, Xu-Dong W, Hui O, Pan Y, Juan H, Yuan-Feng W, Man Z, Xiao-Chun P, Wan-Xi P, Hai-Liang Z, *Eur. J. Med. Chem.*, **68**, 212 (2013).
21. R. Chaiyarat, C. Sookjam, K. Eiam-Ampai, P. Damrongphol, *Sci Asia*, **40**, 198 (2014).
22. S. Ruangsanka, *Sci Asia*, **40**, 204 (2014).
23. C. H. Lu, W. L. Liao, T. Y. Wang, C. C. Chen, Y. H. Chen, S. S. Tang, Y. C. Han, F. J. J, *Sci Asia*, **40**, 212 (2014).
24. W. X. Peng, L. S. Wang, F. J. Wang, Q. Xu. *Acta Crystallog. E*, **67**, O2329 (2011).
25. W. X. Peng, L. Cao, Z. *Kristallogr. NCS*, **227**, 267 (2012).
26. W. X. Peng, L. S. Wang, Q. Xu, Q. D. Wu, S. L. Xiang, *J. Comput. Theor. Nanos.*, **9**, 1431 (2012c).
27. I. Gunes, K. Aslantaş, S. Ulker, S. Taktak, *Journal of the Balkan Tribological Association*, **38**, 173 (2015).
28. Y. C. Sun, Z. Lin, W. X. Peng, T. Q. Yuan, F. Xu, Y. Q. Wang, J. Yang, Y. S. Wang, R. C. Song, *BioResources*, **9**, 1055 (2014).
29. Q. Xue, W. X. Peng, M. Ohkoshi, *Pak. J. Pharm. Sci.*, **27**, 975 (2014).
30. C. Le, P. Wanxi, S. Zhengjun, S. Lili, C. Guoning, *Pak. J. Pharm. Sci.*, **27**(4S), 1083 (2014).
31. L. S. Wang, W. X. Peng, Z. Lin, M. L. Zhao, *J. Pure Appl. Microbiol.*, **7**, 1345 (2013b).
32. R. S. Clements Jr, B. Darnell, *Am J Clin Nutr.*, **33**(9), 1954 (1980).
33. V. L. Boyadzhieva, P. Georeva, T. Kuneva, N. Stoilov, *Oxidation Commun.*, **38**, 271 (2015).u
34. H. Huang, X. Zhao, B. Jiang, *Chinese Tradit. & Herb. Drugs*, **37**, 307 (2006).
35. T. Netscher, *Synthesis of Vitamin E. Vita Horm.*, **76**, 155 (2007).
36. M. D. Alison, J. P. Richard, E. H. Mark, D. A. Andrew, *Curr Org Chem.*, **7**, 1625 (2003).
37. D. M. V. D. Brink, R. J. A. Wanders, *Cell Mol Life Sci.*, **63**, 1752 (2006).
38. D. McGinty, C. S. Letizia, A. M. Api McGinty, *Food Chem Toxicol*, **48**, S59 (2010).6
39. V. Aparna, K. V. Dileep, P. K. Mandal, P. Karthe, C. Sadasivan, M. Haridas, *Chem. Biol. Drug Des.*, **80**, 434 (2012).
40. V. K. Meenakshi, S. Gomathy, *J. Curr. Chem, Pharm, Sc*, **2**, 271 (2012).
41. C. Guo, D. Wei, *Chin. J. Anal. Chem.*, **34**, 15 (2006).

Highly efficient and easy synthesis of biscoumarin catalyzed by pentafluoropropionic acid (PFPA) as a new catalyst in aqueous medium

Naser Montazeri*, Vahid Vahabi

Department of Chemistry, Tonekabon Branch, Islamic Azad University, Tonekabon, Iran

Received June 26, 2015, Revised September 10, 2015

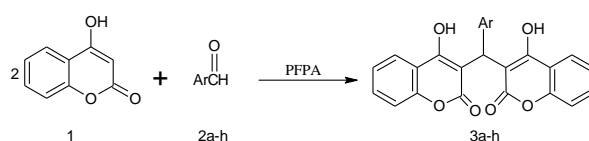
Pentafluoropropionic acid efficiently catalyzes the one-pot reaction of 4-hydroxycoumarin and aryl aldehydes under mild reaction conditions to yield biscoumarin derivatives in high yields. The products were obtained in short reaction times. We believe this applicability of pentafluoropropionic acid with mentioned advantages makes our method superior over previous reported methods to the synthesis of biscoumarins.

Keywords: Biscoumarins, 4-hydroxycoumarin, Aryl aldehydes, Pentafluoropropionic acid.

INTRODUCTION

Coumarin derivatives and especially biscoumarins are important classes of heterocyclic compounds because their biological activities [1-5]. Compounds with these ring system have diverse pharmaceutical activities such as cytotoxicity, antithrombotic, anticancer, anti-HIV, antioxidant, anticoagulant, urease inhibitory and enzyme inhibitory [6-10]. A number of structurally different natural and synthetic coumarin derivatives have been reported to exert notably antimicrobial as well as antifungal activity [11-13]. Moreover a number of biscoumarins are useful as malignant melanoma, metastatic renal cell carcinoma and prostate cancer drugs [14-16]. Therefore, the development of new and efficient methodologies for the synthesis of biscoumarin derivatives will be interesting in both synthetic organic and medicinal chemistry. The general method for synthesis of biscoumarin derivatives involves the reaction of 4-hydroxycoumarin with aryl aldehydes in the presence of different catalyst such as cellulose sulfonic acid [17], nano TiO₂ [18], Zn(proline)₂ [19], ruthenium (III) chloride hydrate [20], tetrabutylammonium bromide (TBAB) [21], molecular iodine [22], [bmin]BF₄ [23], SO₃H-functionalized ionic liquid [24], nano silica chloride [25], sodium dodecyl sulfate [26], piperidine [27], n-dodecylbenzene sulfonic acid (DBSA) [28], heteropolyacids [29], phosphotungstic acid [30], POCl₃ in dry DMF [31], 1,8-diazabicyclo [5.4.0] undec-7-ene (DBU) [32], manganous chloride [33], and tetrabutylammonium hexatungstate [34]. Although these methods may be effective, some of

them have relatively long reaction times and tedious work up. These finding prompted us toward further investigation in search for a new catalyst, which will carry out the synthesis of biscoumarins under simpler experimental set up and eco-friendly conditions. In this article, we present a one-pot reaction for the synthesis of biscoumarin derivatives in the presence of pentafluoropropionic acid (PFPA) in aqueous medium (Scheme 1).



Scheme 1. PFPA catalyzed synthesis of biscoumarins.

EXPERIMENTAL

Chemical were purchased from Merck and used without further purification. All yields refer to the isolated products. The purity determination of the substrate and reaction monitoring were accompanied by thin layer chromatography (TLC) on Silica-gel Polygram SILG-UV 254 plates. Melting points were recorded on an Electrothermal type 9100 melting point apparatus. The IR spectra were obtained on a 4300 Shimadzu spectrophotometer in KBr disks. The ¹H NMR (500 MHz) spectra were recorded on a Bruker-Ac-500 spectrometer.

TYPICAL PROCEDURE

A mixture of 4-hydroxycoumarin **1** (2 mmol), an aromatic aldehyde **2a-h** (1 mmol) and PFPA (0.4 mmol) in H₂O (10 mL) was heated on the oil bath under reflux with stirring for the time period as indicated in Table 1. The progress of the reaction

To whom all correspondence should be sent:
E-mail: montazer1350@gmail.com

was monitored by TLC. After completion of reaction, the mixture was cooled to room temperature and the solid product was collected by filtration, and washed with cold water. The solid product was obtained by recrystallization in ethanol. Products were characterized by their physical constants (m.p.), IR and ¹H NMR spectroscopy and comparison with authentic samples.

RESULT AND DISCUSSION

In order to optimize the reaction conditions, including solvents and temperature, the reaction was conducted under various conditions and the results are listed in Table 1. In an optimized reaction condition, 4-hydroxycoumarin (2 mmol) and benzaldehyde (1 mmol) in H₂O (10 mL) were mixed in the presence of PFPA (0.4 mmol) as catalyst for 60-100 min. The reaction proceeds very cleanly under reflux and was free of side products. After completion of the reaction (monitored by

TLC), a simple work up affords the products in high yields (Table 2).

Among the solvents tested, the reaction in CHCl₃ using 40 mol% of the catalyst gave a low yield of desired product. Ethanol, methanol and CH₃CN gave moderate to good yields under these conditions. Without catalyst, in refluxing EtOH, MeOH, H₂O, CHCl₃ and CH₃CN the reactions times are prolonged and the yields are poor. However, the reaction at reflux in H₂O with 40mol% of catalyst afforded desired product in high yield. In the solvent free conditions, even in the presence of 50 mol% of the catalyst at 120 °C, the yields are low. We also evaluated the amount of PFPA required for this transformation. It was found that the yield of product was affected by the catalyst amount. Increasing the amount of the catalyst up to 40 mol% at reflux in H₂O increased the yield of the product. Further increase in the catalyst amount did not increase the yield noticeably. In order to show generality and scope.

Table 1. Optimizing the reaction conditions^a.

Entry	Catalyst (mol%)	Solvent	Condition	Time (min)	Yield (%)
1	--	EtOH	Reflux	180	25
2	--	MeOH	Reflux	180	20
3	--	H ₂ O	Reflux	180	30
4	--	CHCl ₃	Reflux	240	Trace
5	--	CH ₃ CN	Reflux	180	28
6	30	--	120 °C	60	40
7	40	--	120 °C	60	45
8	50	--	120 °C	60	45
9	30	H ₂ O	Reflux	100	82
10	40	H ₂ O	Reflux	80	88
11	50	H ₂ O	Reflux	80	87
12	40	EtOH	Reflux	80	75
13	40	MeOH	Reflux	100	64
14	40	CHCl ₃	Reflux	100	40
15	40	CH ₃ CN	Reflux	100	72

^a Benzaldehyde (1 mmol) and 4-hydroxycoumarin (2 mmol)

^b Isolated yields

Table 2. Synthesis of biscoumarins using pentafluoropropionic acid as catalyst ^a.

Entry	Ar	Product ^b	Time (min)	Yield (%) ^c	m.p. (°C) [reference]
1	3-NO ₂ C ₆ H ₄	4a	60	92	234-235 [25]
2	4-HOC ₆ H ₄	4b	100	86	223-225 [19]
3	4-NO ₂ C ₆ H ₄	4c	60	90	233-235 [25]
4	C ₆ H ₅	4d	80	88	227-229 [19]
5	4-ClC ₆ H ₄	4e	80	87	250-252 [20]
6	4-MeOC ₆ H ₄	4f	80	87	243-245 [20]
7	4-MeC ₆ H ₄	4g	80	89	267-268 [25]
8	2-ClC ₆ H ₄	4h	100	86	221-223 [25]

^a 4-hydroxycoumarin (2 mmol), aryl aldehyde (1 mmol) and PFPA (40 mol%).

^b The product were characterized by comparison of their spectroscopic and physical data with those reported in the literature.

^c Isolated yield.

Table 3. Comparison of efficiency of various catalyst in synthesis of biscoumarin derivatives.

Entry	Catalyst	Conditions	Time (min)	Yield (%) ^c	Reference
1	Cellulose sulfonic acid	H ₂ O, reflux	100-150	80-90	[17]
2	Nano TiO ₂	H ₂ O, reflux	5-10	84-96	[18]
3	Zn[proline] ₂	H ₂ O, reflux	5-9	91-96	[19]
4	RuCl ₃ .nH ₂ O	H ₂ O, 80 °C	25-35	75-95	[20]
5	Nano SiO ₂ Cl	CH ₂ Cl ₂ , 40 °C	60-360	68-95	[25]
6	SDS	H ₂ O, 60 °C	138-180	84-98	[26]
7	DBSA	H ₂ O, 40 °C	60	78-92	[28]
8	[TBA] ₂ [W ₆ O ₁₉]	EtOH, reflux	5-10	85-92	[34]
9	PFFA	H ₂ O, reflux	60-100	86-92	This work

Of this new protocol, we used various substituted aromatic aldehydes and the results obtained are summarized in table 2. In all cases, aromatic aldehydes with substituents carrying either electron-donating or electron-withdrawing groups reacted successfully and gave the expected products in high yields. The type of aldehyde had no significant effect on the reaction. The efficiency of PFFA as a catalyst for the synthesis of the biscoumarin derivatives was compared with that of other catalysts reported in the literature. Some of the results are summarized in table 3. It is clear from this table that PFFA is an efficient catalyst which could be useful in the synthesis of a series of biscoumarin derivatives.

CONCLUSION

In conclusion, we have developed new method for the one-pot synthesis of biscoumarin derivatives from 4-hydroxycoumarin and aryl aldehydes using pentafluoropropionic acid (PFFA) catalyst. Easy work up, ready commercial availability of the catalyst, short reaction time and high yield, make the procedure an attractive alternative to the existing methods for the synthesis of biscoumarin derivatives.

Acknowledgment: This research has been supported by the Islamic Azad University Tonekabon Branch.

REFERENCE

- J. C. Jung, O. S. Park, *Molecules*, **14**, 4790 (2009).
- S. Stanchev, G. Momekov, F. Jensen, I. Manolov, *Eur. J. Med. Chem.*, **20**, 1 (2007).
- Jung, J. C.; Lee, J. H.; Oh, S.; Leed, J. G.; Parkeb, O. *S. Bioorg. Med. Chem. Lett.* **2004**, 14, 5527.
- V. D. Kancheva, V. P. Boranova, J. J. Nechev, I. I. Manolov, *Biochimie*, **92**, 1138 (2010).
- I. Manolov, C. Maichle-Moessmer, N. Danchev, *Eur. J. Med. Chem.*, **41**, 882 (2006).
- B. Musicki, A. M. Periers, P. Lavrin, D. Ferroud, Y. Benedetti, S. Lachaud, F. Chatreaux, J. L. Haesslein, A. Itlis, C. Pierre, *Bioorg. Med. Chem. Lett.*, **10**, 1695 (2000).
- Z. H. Chohan, A. U. Shaikh, A. Rauf, C. T. Supuran, *J. Enzyme Inhib. Med. Chem.*, **21**, 741 (2006).
- I. Kostova, G. Momekov, M. Zaharieva, M. Karaivanova, *Eur. J. Med. Chem.*, **40**, 542 (2005).
- M. I. Choudhary, N. Fatima, K. M. Khan, S. Jalil, S. Iqbal, Atta-ur. Rahman, *Bioorg. Med. Chem.*, **14**, 8066 (2006).
- P. C. M. Mao, J. F. Mouscadet, L. Leh, C. Auclair, L. Y. Hsu, *Chem. Pharm. Bull.*, **50**, 1634 (2002).
- I. Singh, H. Kaur, S. Kumar, A. Kumar, S. Lata, *Int. J. Chem. Tech. Res.*, **2**, 1745 (2010).
- M. Mladenovic, N. Vukovic, S. Sukdolak, S. Solujic, *Molecules*, **15**(6), 4294 (2010).
- N. Hamdi, M. C. Puerta, P. Valerga, *Eur. J. Med. Chem.*, **43**, 2541 (2008).
- J. L. Mohler, L. G. Gomella, E. D. Grawford, L. M. Glode, C. D. Zippe, W. R. Fair, M. E. Marshal, *Prostate*, **20**, 123 (1992).
- M. E. Marshall, K. Bulter, A. Fried, *Mol. Biother.*, **3**, 170 (1991).
- R. D. Thornes, L. Daly, G. Lyneh, B. Breslin, H. Browne, H. Y. Browne, T. Corrigan, P. Daly, G. Edwards, E. Gaffney, *J. Cancer. Res. Clin. Oncol.*, **120**, S32 (1994).
- M. Sedigi, N. Montazeri, *Adv. Stud. Bio.*, **7**, 89 (2015).
- H. Babaei, N. Montazeri, *Oreint. J. Chem.*, **30**, 577 (2014).
- Z. N. Siddiqui, F. Farooq, *Cat. Sci. & Tech.*, **1**, 810 (2011).
- K. Tabatabaeian, H. Heidari, A. Khorshidi, M. Mamaghani, N. O. Mahmoodi, *J. Serb. Chem. Soc.*, **7**, 407 (2012).
- J. M. Khurana, S. Kumar, *Tetrahedron Lett.*, **50**, 4125 (2009).
- M. Kidwai, V. Bansal, P. Mothra, S. Saxena, R. K. Somvanshi, S. Dey, T. P. Singh, *J. Mol. Catal. A*, **268**, 76 (2007).
- J. M. Khurana, S. Kumar, *Monatsh. Chem.*, **141**, 561 (2010).
- W. Li, Y. Wang, Z. Wang, L. Dai, Y. Wang, *Cat. Lett.*, **141**, 1651 (2011).
- R. Karimian, F. Piri, A. A. Safari, S. J. Davapanah, *J. Nano Str. Chem.*, **3**, 52 (2013).
- H. Mehrabi, H. Abusaidi, *J. Iran. Chem. Soc.*, **7**, 890 (2010).

27. K. M. Khan, S. Iqbal, M. A. Lodhi, G. M. Maharvi, Z. Ullah, M. I. Choudhary, Atta-ur. Rahman, S. Perveen, *Bioorg. Med. Chem.*, **14**, 8066 (2006).
28. B. Pawar, V. Shinde, A. Chaskar, *Green. Sust. Chem.*, **3**, 56 (2013).
29. M. M. Heravi, S. Sadjadi, N. Haj Mokhtari, H. Oskooie, F. F. Bamoharram, *Catal. Commun.*, **10**, 1643 (2009).
30. P. Singh, P. Kumar, A. Katyal, R. Karla, S. K. Dass, S. Parkash, R. Chandra, *Catal. Lett.*, **134**, 303 (2010).
31. M. H. A. Elgamal, N. M. M. Shalaby, M. A. Shaban, H. Duddeck, B. Mikhova, A. Simon, G. Toth, *Monatsh. Chem.*, **128**, 701 (1997).
32. H. Hagiwara, N. Fujimoto, T. Suzuki, M. Ando, *Heterocyclic.*, **53**, 549 (2000).
33. J. N. Sangshetti, N. D. Kokare, D. B. Shinde, *Green. Chem. Lett. Rev.*, **2**, 233 (2009).
34. A. Davoodnia, *Bull. Korean. Chem. Soc.*, **32**, 4286 (2011).

Kinetic study of superheated water extraction of berberine from *Berberis vulgaris* root

N. Rahimi¹, M. Shiva², S. Ali Mortazavi³, A. Hossein Elhamirad⁴, A. Majid Maskooki⁵,
G. Rajabzadeh⁶

¹Department of Food Science & Technology, Birjand Branch, Islamic Azad University, Birjand, Iran

²Department of Chemical engineering, Birjand University of Technology, Birjand, Iran.

³Department of Food Science and Technology, Agriculture Faculty, Ferdowsi University of Mashhad, Iran

⁴Department of Food Science & Technology, Sabzevar Branch, Islamic Azad University, Sabzevar, Iran.

⁵Department of Food Technology, Research Institute of Food Science and Technology, Mashhad, Iran

⁶Department of Food Nanotechnology, Research Institute of Food Science and Technology, Mashhad, Iran

Received June 26, 2015, Revised September 10, 2015

The kinetics of superheated water extraction of berberine from *Berberis vulgaris* root was investigated. Response surface methodology was employed to reduce the experimental efforts of the kinetic study. A response surface model was successfully developed for berberine extracted concentration on the basis of the experimental data that gathered according to a central composite design and it was employed to generate several simulated data. The simulated response surface data was then employed to develop a kinetic model for berberine extraction. It was found that a second order kinetic model is able to fit the experimental/simulated data. The activation energy for the superheated water extraction kinetics of berberine with sample/solvent ratio of 0.03 and 0.02 was found to be $E_a = 61.4 \text{ kJmol}^{-1}$ and 37.93 , respectively.

Key Words: Kinetic modeling, superheated water Extraction, Berberine, Design of Experiments

INTRODUCTION

Extraction of bioactive materials from herbal plants may be interesting due to the growing trend of using herbal remedies and food additives instead of chemical ones. For the chemical standardization of botanicals and herbal preparations, the extraction of bioactive components is an essential step. Extraction is the process of separating active portions of plant (or animal) tissues using selective solvents through standard procedures [1, 2]. The products obtained from plants are relatively complex mixtures of metabolites, either in liquid or semi liquid or dry powder [2, 3 and 4]. The seedless barberry plant (*Berberis vulgaris* L. family *Berberidaceae*), is one of the commercial shrub trees. The fruit and various extracts obtained from the plants of this family are widely used in commercial scale and as food additive in folk food systems and medicines. All species of *Berberidaceae* produce alkaloids. The main component of *Berberis vulgaris* (barberry) stem and root extract is berberine which is a quaternary ammonium salt derived from the protoberberine

group of isoquinoline alkaloids. Berberine (BBR) is the major compound identified in the root, rhizome and stem bark of many plants. Berberine has been used for over 2000 years in traditional Eastern medicine and is also effective in the prevention and treatment of some illnesses [5-9]. These properties were summarized in recent reviews [5, 6, 8]. The conventional extraction techniques include maceration, infusion, percolation, digestion, decoction, Soxhlet, counter-current extraction, aqueous- alcoholic extraction. For a general extraction such as solvent extraction, there are few adjustable parameters to control the selectivity of extraction processes. Consequently, the application of alternative extraction techniques with higher selectivity and efficiency is desirable [10, 12]. Pressurized solvent extraction (PES) is a solid-Liquid extraction (SLE) technique which has been developed as an alternative to current extraction methods. When water is used as the extraction solvent, the technique is named as Pressurized Hot Water Extraction (PHWE), Sub-critical Water Extraction or super heated water extraction [4, 10-12]. SCW extraction, using water under external pressurization above its boiling point offers an efficient, non-toxic, and environmental-friendly

To whom all correspondence should be sent:

E-mail: n.rahimi@iaubir.ac.ir

alternative to extract polar or slightly polar compounds. The polarity of subcritical water is much less than that of water at ambient condition ($\epsilon = 79$ at 298 K). The dielectric constant of SCW is in the range of 20-40 depending on temperature and pressure. It is very similar to the dielectric constant of methanol ($\epsilon = 33$ at 298 K) or ethanol ($\epsilon = 25$ at 298 K). In addition, the densities of subcritical water are high (0.82- 0.98g/cm³ at 4.0MPa). Thus, desired polar or slightly polar components, that are not soluble well in water at ambient conditions, can be much more soluble in subcritical water [10-13]. The effect of general operating parameters such as the extraction solvent, solvent to feed ratio, sample particle size, time and temperature extraction are mentioned as important factors for both conventional and non conventional techniques. The non-conventional extraction techniques are presumed to replace conventional solvent techniques, which make studying their kinetics mechanisms and modeling essential. Such studies enable prediction of the extraction behavior which is considered to be useful for scaling up of the process [14-16].

Many studies have been carried out on the kinetic modeling of continuous solvent extraction such as supercritical fluid extraction. Following the experimental determination of the extraction yield, using non-conventional extraction techniques modeling is the next important step, not only for predicting the extraction yield at unmeasured operational conditions but also for optimizing the process and determining the best process parameters [15]. Nowadays, there is a wide spectrum of mathematical models that a number of studies have applied in order to describe the process of extraction from plant materials. Based on the last approach, these models can be classified into three groups. The first is empirical models which are used when there is no information about the mass transfer mechanisms for extraction process. In the second group models, second Fick's law of diffusion is combined with the heat-mass transfer in order to obtain analytical solutions of the model equations. The third groups of models consist of models based on setting and solving the mass balance equations [16]. So far, berberine has been extracted from various plant sources using conventional and non-conventional methods. Considering the accessible literature data, there is no reported kinetic study of berberine extraction. This study was aimed to develop a kinetic model for berberine extraction by sub critical water.

MATERIAL AND METHODS

Preparation of plant material

The barberry root was collected from Barberry gardens around Birjand (South Khorasan Province, Iran) at the end of the harvest season, subsequently dried in Vacuum oven at 50°C for 72hrs and ground into fine powder. In order to avoid any sort of confusion between samples, the powder was classified in 3 groups with three kinds of sieves (mesh No. 24, mesh No. 35, mesh No. 45 sieves)

SCW Extraction Instrumentation

Subcritical water extraction processes were performed using a reactor that was designed and manufactured in the novel technologies laboratory of Research Institute of Food Science and Technology, Mashhad, Iran. This reactor was made from stainless steel 316. The temperature values were measured by a digital thermometer. Pressure was controlled by pressure gauge manometer (with an accuracy of 2 bars). Thermal supply was an electrical element fed with 220V alternative current (AC). The glycerol was an intermediate to transfer stable heat.

Design of Experiments

In this study, a three factors central composite design (CCD) was employed for SCW modeling. The factors and their levels are as follows:

Temperature: 110-170 °C, time: 30-70 mins, Sample/Solvent Ratio: 0.01-0.03. Totally 20 points were designed and extraction was performed by subcritical water according to each experiment condition. Design of experiments as well as statistical analysis was performed by MINITAB 16.

HPLC Conditions

Preparation of reference standards. Some standard berberine solutions (10, 50, 100, 250 and 500 µg/ml) were prepared in methanol. Calibration curve was prepared by plotting respective peak areas of berberine against concentration. Then Quantization was done using standard berberine calibration curve.

Measurement of berberine concentration. The crude extracts were passed through Whatman No. 1 filter and were analyzed by Knauer HPLC including HPLC pump (k-1001), C₁₈ Column, UV-detector (k-2600) measuring wavelengths used in 330 nm. Injection volume was 20 micro liters. The conditions of solvent mixtures (methanol + water) were supposed to run as follows.

The 20% methanol /80% water solution becomes a 100% methanol solution in 10 mins and

remains for 5 mins in this mode. It gets back to its earlier mode in 5 mins and stays the same for another 5 mins. It took 25 minutes altogether. The extracts obtained from each batch of subcritical water extractions were quantitatively analyzed by HPLC and berberine concentration $\mu\text{gr/ml}$ (extract) was calculated. As indicated in the chromatogram (Fig.1) the berberine peak is visible in the chromatogram after approximately 9.4 minutes.

Response surface models

In this study, berberine concentration was analyzed by multiple regressions through the least squares method to fit the following equation:

$$Y = B_0 + \sum B_i x_i + \sum B_{ii} x_i^2 + \sum B_{ij} x_i x_j, \quad (1)$$

Where, Y is the predicted response variable; B_0 , B_i , B_{ii} , and B_{ij} are constant regression coefficients of the model, and x_i , x_j ($i = 1,2,3$; $j = 1,2,3$; $i \neq j$) represent the independent variables in the form of coded values according to the following transformation equation:

$$x_i = \frac{X_i - X_0}{\Delta X}, \quad (2)$$

Where x is the dimensionless coded value of the variable X_i , X_0 is the value of X_i at the center point, and ΔX is the step change [17-19].

The second-order polynomial coefficients were calculated using the software MINITAB 16 to estimate the responses of the dependent variable.

Kinetic modeling of berberine extraction

The aim of kinetic study is to develop a kinetic model for berberine extraction by superheated water. The kinetic data were employed to fit several kinetic rate equations and it was found the following kinetic rate equation is able to fit the data:

$$C = \frac{t}{A + Bt}, \quad (3)$$

C : Concentration of Berberine in the solution at any time.

The above kinetic rate has been derived according to the assumption of a second order rate law for berberine extraction:

$$\frac{dC}{dt} = k(C - C_s), \quad (4)$$

k is the second-order extraction rate constant, $\text{mL} \cdot \mu\text{g}^{-1} \cdot \text{min}^{-1}$.

C_s is the extraction capacity (concentration of berberine at saturation in g L^{-1})

By considering the boundary condition $t = 0-t$ and $C_t = 0-C_t$, the integrated rate law for a second-order extraction was obtained:

$$C = \frac{C_s^2 kt}{1 + C_s kt}, \quad (5)$$

or

$$C = \frac{t}{\frac{1}{C_s^2 k} + \frac{t}{C_s}}, \quad (6)$$

$$A = C_s^2 k, \quad (7)$$

$$B = \frac{1}{C_s} \quad (8)$$

For a second order system, the rate constants increase with temperature and may be described by the Arrhenius law:

$$k = k_0 e^{-E/RT}, \quad (9)$$

Where: k is the extraction rate constant ($\text{L mg}^{-1} \text{min}^{-1}$), k_0 is the temperature independent (pre-exponential) factor ($\text{L mg}^{-1} \text{min}^{-1}$), E is the activation energy (J mol^{-1}), R is the gas constant ($8.314 \text{ J mol}^{-1} \text{K}^{-1}$), T is the absolute suspension temperature (K).

RESULTS AND DISCUSSION

Development of the response surface model

Table 1 shows the experimental data of SCW berberine extraction in different process conditions. The estimated regression coefficients of response surface model were presented in Table 2. The estimated regression coefficients of polynomials in coded unit, the standard errors of coefficients and their t-statistic and P-values are shown in Table 2. The correlation coefficient and adjusted correlation coefficient of the fitted model are also presented in the Table.

The principal model analysis is based on analysis of variance (Table 2), which provides numerical information for the F -value and the P -value. A summary of the analysis of variances (ANOVA) is given in Table 2. The ANOVA of regression model reveals that the model is highly significant as evident from Fisher's F-test value being 68.84 with a low probability value ($P_{\text{model}} < 0.0001$). The goodness of the fit of the model was checked by determination coefficients, $R^2 = 98.41\%$ and $R^2_{\text{adj}} = 96.98\%$ that revealed that there is a good agreement between experimental and predicted value of concentration. The RSM predicted data are presented in Table 1.

Table 1. Design of Experiments (CCD) for barberry root and prediction of berberine concentration by RSM.

Points	Temperature	Time (min)	Ratio	Concentration Experimental Data (µg/ml)	Concentration Predicted Data (µg/ml)
1	170	70	0.03	281.128	256.385
2	140	50	0.02	77.683	66.748
3	170	30	0.01	90.739	76.129
4	170	50	0.02	141.572	144.120
5	140	50	0.03	110.906	119.066
6	110	30	0.01	20.739	28.600
7	170	30	0.03	226.072	215.056
8	140	50	0.02	80.239	66.748
9	110	70	0.01	31.183	25.822
10	110	50	0.02	31.906	18.175
11	140	50	0.02	75.294	66.748
12	140	50	0.01	54.906	36.256
13	140	70	0.02	76.128	77.820
14	110	70	0.03	54.461	52.604
15	140	50	0.02	75.80	66.748
16	140	50	0.02	78.80	66.748
17	170	70	0.01	84.572	77.233
18	140	30	0.02	70.406	58.299
19	110	30	0.03	23.628	14.576
20	140	50	0.02	66.683	66.748

Table 2. Estimated regression coefficients of response surface model, the standard errors of estimated coefficient, the statistics and ANOVA results

Term	Coef	SE Coef	T	P
Constant	74.102	3.840	19.299	0.000
Temperature	66.2167	3.532	18.748	0.000
Time	9.5889	3.532	2.715	0.022
Ratio	41.4056	3.532	11.723	0.000
Temperature* Temperature	14.7468	6.735	2.190	0.053
Time* Time	1.2745	6.735	0.189	0.854
Ratio *Ratio	10.9134	6.735	1.620	0.136
Temperature* Time	0.9514	3.949	0.241	0.814
Temperature* Ratio	38.2153	3.949	9.678	0.000
Time* Ratio	10.2014	3.949	2.583	0.027

F. Regression= 68.84; R-Sq= 98.41%; P_value = 0.000; R-Sq(adj) =96.98%

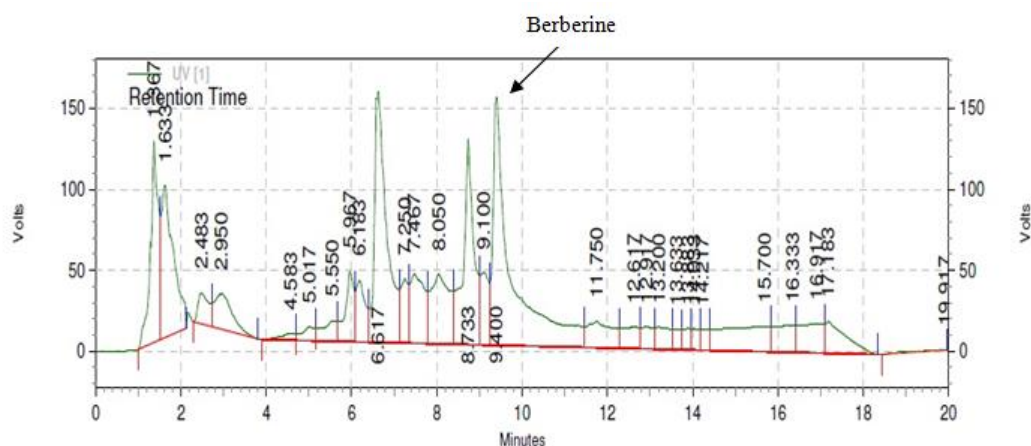


Fig.1. Chromatogram obtained for berberine in barberry root by SCW extraction.

All three factors (time, temperature and sample/liquid ratio) have statistically significant effect on the berberine concentration according to the t-student test and corresponding P-value of each coefficient. However, the higher value of estimated regression coefficient for temperature indicates that temperature has more effect.

Kinetic study

According to the second order nature of the kinetic model, temperature should have an increasing effect on the berberine concentration. However, this behavior is not observed in low temperatures in the range of 110-120°C. To reduce the errors of parameter estimation, the kinetic study was limited to temperature range of 120-170°C. In addition, the dependency of berberine concentration on time is significantly affected by the ratio according to the response surface results. So, the ratio has the significant effect of the kinetics of extraction and the kinetic study should be conducted in fixed ratios. If we develop a kinetic model separately in each ratio, the number of experimental points that are necessary for an efficient parameter estimation of the kinetic model significantly decreases. For example, the number of experimental points in ratio of 0.03 is 5 according to the Table 1. So, to increase the points we employed response surface model to generate several simulated data and conduct the kinetic study with simulated data. So for the purpose of the kinetic study, the response surface model was first employed to generate several simulated data, sample/water ratio of 0.03 at temperatures 120, 130, 140, 150, 160 and 170°C, time 20-70 mins (stepwise 1 min). A total of 246 points were produced for berberine concentration (41 points in each temperature). This procedure was repeated for ratio of 0.02 and 246 points were produced from a similar manner. Each data set was employed to fit the second order kinetic model (Eq. 6). The estimated coefficients of the kinetic model with their associated 95% confidence intervals as well as the statistical criteria are presented in the Table 3. The high R^2 and R^2_{adj} values of above 0.99 reveals that the regressed rate model fits the data well in agreement with the low values of RMSD and Variances as presented in Table 3 in different temperatures.

Calculation of activation energy

The estimated k values in the six temperatures are $2.69E-05$ (120°C), $1.05E-04$ (130°C), $1.71E-04$ (140 °C), $2.19E-04$ (150°C), $2.54E-04$

(160°C) and $2.79E-04$ (170°C) in the case of sample/water = 0.03.

Linearization of Eq. 9 as shown below will give the value of the activation energy (E) and the temperature independent factor (k_0) from $\ln(k)$ against $1/T$ plot:

$$\ln k = \ln k_0 - \left(\frac{E}{RT} \right), \quad (11)$$

Fig. 2 presents the plot of $\ln k$ against $1/T$. The activation energy for berberine extraction is calculated as 61.4 kJ mol^{-1} from the slop of the fitted line (see Fig. 2).

The pre-exponential factor of this extraction (k_0) is evaluated as 6734.5 from interception of fitted line (see Fig. 2)

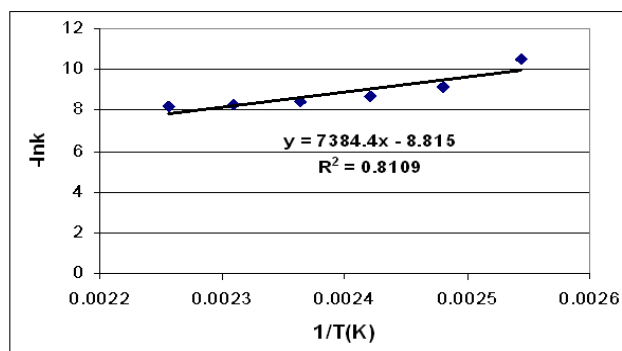


Fig. 2. Linear relationship between second order extraction constant, $\ln(k)$ and temperature for superheated water extraction of berberine (sample/ratio=0.03).

The estimated k values of ratio=0.02 are $1.50E-04$ (120 °C), $3.19E-04$ (130 °C), $4.43E-04$ (140 °C), $5.26E-04$ (150 °C) , $5.81E-04$ (160 °C) and $6.15E-04$ (170 °C) as presented in Table 3.

The plot of $\ln k$ against $1/T$ is presented in Fig. 3. The slop of the fitted plot presents the E/R value and the activation energy is 37.93 kJ/mol . It is clear that the activation energy significantly decreases (about 24 kJ/mol) when sample/water ratio decreases from 0.03 to 0.02. So the activation energy depends to the ratio. Further kinetic study (not presented here) showed that activation energy approaches to zero in lower ratios (0.02 to 0.015). This means that temperature dependency of berberine extraction decreases significantly.

When sample/liquid ratio was low, the concentration gradient was high and, thus, the transfer rate increased. Goula [20], Qu et al. [21], Rakotondramasy-Rabesiaka et al. [22] , Zhang et al. [23] and Li et al. [24] reported the same effect of sample/liquid ratio on concentration of pomegranate seed oil, antioxidant from pomegranate, protopine, oil from flaxseed and chlorogenic acid from *Ecommia ulmodies*.

Table 3. Parameter estimates with associated confidence intervals for Equation 3.1 regressed from the simulated/ experimental data set.

	T	A	B	Cs	k	R ²	R ² _{adj}	RMSD	Variance
Ratio=0.03	120	0.5785±0.01867	0.0039±34E-05	253.6	2.69E-05	0.995	0.995	0.156	1.074
	130	0.2630±0.0128	0.0053±25E-05	190.1	1.05E-04	0.992	0.992	0.249	2.747
	140	0.1423±0.0082	0.0049±16E-05	202.8	1.71E-04	0.992	0.992	0.304	4.09
	150	0.0858±0.0054	0.0043±11E-05	230.7	2.19E-04	0.993	0.993	0.341	5.14
	160	0.0557±0.0037	0.004±7.6E-05	266.0	2.54E-04	0.995	0.995	0.368	5.98
	170	0.0382±0.0026	0.0033±5.5E-05	306.4	2.79E-04	0.996	0.996	0.389	6.69
Estimated Activation Energy, E(kJ/mol):61.4					Pre-exponential Factor, k ₀ :6734.5				
Ratio=0.02	120	0.7908±0.0448	0.0109±0.00085	91.9	1.50E-04	0.988	0.987	0.132	0.7659
	130	0.3686±0.0251	0.0108±0.00049	92.1	3.19E-04	0.988	0.988	0.168	1.2397
	140	0.1962±0.0146	0.0093±0.00029	107.2	4.43E-04	0.990	0.990	0.192	1.6192
	150	0.1148±0.0090	0.0078±0.00019	128.6	5.26E-04	0.993	0.993	0.2094	1.9330
	160	0.0721±0.0058	0.0065±0.00012	154.5	5.81E-04	0.995	0.995	0.2236	2.2039
	170	0.0478±0.0039	0.0054±8.27E-05	184.4	6.15E-04	0.996	0.996	0.2355	2.4473
Estimated Activation Energy, E(kJ/mol): 37.93					Pre-exponential Factor, k ₀ : 22.18				

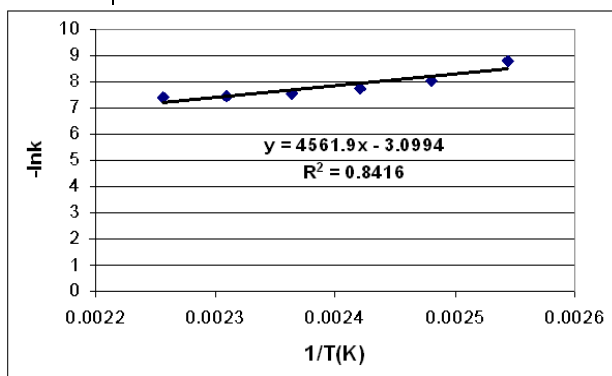


Fig. 3. Linear relationship between second order extraction constant, $\ln(k)$ and temperature for superheated water extraction of berberine (sample ratio = 0.02)

Fig. 4 and Fig. 5 present the predicted kinetic model in different temperatures in sample/water ratio 0.03 and 0.02 respectively. The experimental points and some RSM simulated data are also presented. The graphs clearly show the capability of the kinetic model for demonstration of experimental and simulated data. It is important to note that the model is applicable in sample/water ratio of 0.02-0.03 and the temperature range of 120°C -170°C.

Generally, the solid-liquid extraction process can be considered as the reverse of an adsorption process. Due to this, the kinetic equations of

adsorption process can be applied to solid-liquid extraction. So, the second-order law gives the best fits for the extraction rate. Whereas, mechanistic models provide more from a basic understanding of a given system, a greater basis for extrapolation and a representation of a response function that is more precise than one attained empirically. [14, 15]

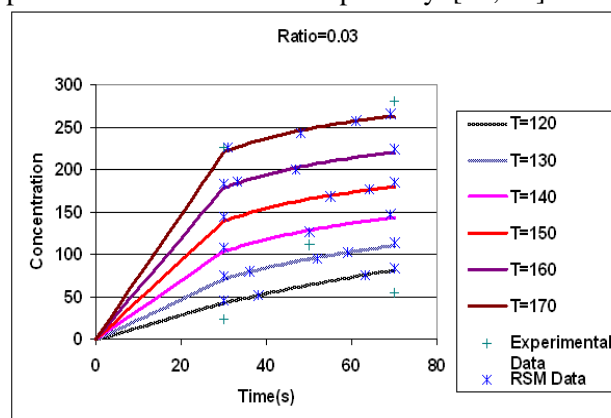


Fig. 4. Extraction of berberine using superheated water at different temperatures and sample/ratio of 0.03: comparison between experimental data, response surface simulated data and second order kinetic models.

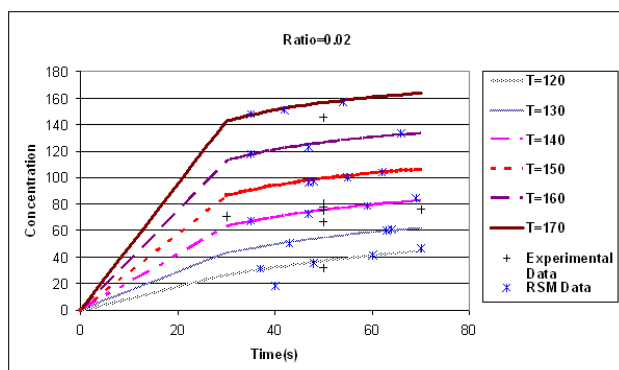


Fig. 5. Extraction of berberine using superheated water at different temperatures and sample/ratio of 0.02: comparison between experimental data, response surface simulated data and second order kinetic model

CONCLUSION

Combined RSM/kinetic modelling was employed to study the rate of berberine extraction from *Berberis vulgaris* root using superheated water at various temperatures, times and sample/solvent ratios. It was found that a second order kinetic model can describe the berberine extraction process. The experimental trials showed that k has high values at high temperatures. The activation energy depends on sample/solvent ratio, as increase of sample/solvent ratio increases the activation energy of extraction. Superheated water extraction technique is a notably faster extraction method than conventional extraction techniques, as well as being clean, cheap, and environment-friendly.

Acknowledgments: The authors would like to extend their gratitude to Research Institute of Food Science and Technology (Novel Technology Laboratory), Mashhad and Pharmacognosy Lab of Medicine Faculty of Mashhad university of Medical Sciences.

REFERENCES

1. E.S. Ong, S.M. Len, *Analytical Chemica Acta*, **482**, 81 (2003).

2. S. S. Handa, An overview of extraction Techniques for Medicinal and Aromatic plants, in: *Extraction Techniques for Medicinal and Aromatic plants*. First Edition, International Center for Science and High Technology, Trieste, 2008, p 21.
3. L. Wang, C. L. Weller, *Food Sci. Technol.*, **17**, 300 (2006).
4. B. Kaufmann, Ph. Christen, *Phytochem. Anal.*, **13**,105 (2002).
5. M. Imanshahidi, H. Hosseinzadeh, *Phytother Res.*, **22**(8), 999 (2008).
6. S. M. Javadzadeh, S. R. Fallah, *Int. J. Agric.Crop Sci.*, **4-7**,404 (2012).
7. R. Suau, R. Rico, J. M. Lopez-Romero, F. Najera, A. Cuevas, *Phytochemistry*, **49**, 2545 (1998).
8. M. Fatehi, T.M. Saleh, Z. Fatehi- Hassanabad, M. Tarek, Kh. Farrokhfal, M. Jafarzadeh, S. Davodi, *J. Ethnopharmacology*, **10**, 46 (2005).
9. N. L. Pfoze, Y. Kumuar , B. Myrboh , R. K. Bhagobaty , S. R. Joshi, *J. Medicinal Plants Res.*, **5**, 859 (2011).
10. A. Mustafa, C. Turner, *Analytica Chimica Acta*, **703**, 8 (2011).
11. E.S. Ong, S. O. Woo, Y. L. Yong, *J. Chromatography A*, **313**, 57 (2000).
12. B. E. Richter, B. A. Jones, J.L. Ezzell, N.L. Porter, N. Avdalovic, C. Pohl, *Analytical Chemistry*, **68**(6) 1033 (1996).
13. W. J. Kim, B. Veriansyah, Y. W. Lee, J. Kim, J.D. Kim, *J. Ind. Eng. Chem.*,**16**, 425 (2010).
14. C. H. Chan, R. Yusoff, G. C. Ngoh, *Chem. Eng. Res. Design*, **92**, 1169 (2014).
15. T. Hatami, L. S. Moura, M. Khamfroush, M. Angela, A. Meireles, *J. Supercrit. Fluids*, **85**, 62 (2014).
16. M. Stamenic, I. Zizovic. *Computers Chem. Eng.*, **48**, 89 (2013).
17. B. D. Hibbert, *J. Chromatography B*, **910**, 2 (2012).
18. D. Bas, I. H. Boyaci, *J. Food Eng.*, **78**, 836 (2007).
19. D. Bas, I. H. Boyaci, *J. Food Eng.*, **78**, 846 (200).
20. M. A. Goula, *J. Food Eng.*, **117**, 492 (2013).
21. W. Qu, Z. Pan, H. Ma, *J. Food Eng.*, **99**, 16 (2010).
22. L. Rakotondramasy- Rabesiaka, J.L. Havet, C. Porte, H. Fauduet, *Ind. Crops. Prod.*, **29**, 516 (2009).
23. Z. S. Zhang, L.J. Wang, D. Li, S.S. Jiao, X.D. Chen, Z.H. Mao, *Purif. Technol.*, **62**, 192 (2008).
24. H. Li, B. Chen, S.Z. Yao, *Ultrason. Sonochem.*, **12**, 295 (2005).

Preparation of pegylated nanoliposomal oxaliplatin and investigation of its Efficacy on breast cancer cell lines MCF-7 and MDA-MB-231

Delaram Ahmadi¹, Azim Akbarzadeh*², Mahdi Arjmand³, Amir Heidarinasab⁴

¹ Department of Chemical Engineering, Science and Research Branch, Islamic Azad University, Tehran, Iran

² Department of Pilot Biotechnology, Pasteur Institute of Iran, Tehran, Iran

³ Department of Chemical Engineering, South Tehran Branch, Islamic Azad University, Tehran, Iran

⁴ Department of Chemical Engineering, Science and Research Branch, Islamic Azad University, Tehran, Iran

Cancer is an important issue and cause of death among human breast cancer is the most common form of cancer types within women population in world. Oxaliplatin is a chemotherapy compound for treatment of cancer with side effects. Drug delivery system (DDS) and using of nanocarriers are known as one of the effective methods for cancer treatment. In this study, nanotechnology was applied to decrease drug side effects and enhancement of therapeutic index. In order to improve chemotherapeutic effective of Oxaliplatin, Nanoliposomation is used in pharmacological as beneficial developments. To achieve this results polymers, such as polyethylene glycol can reduce interactions with reticuloendothelial system (RES) and increase the circulation lifetime of the drug. In this work, pegylated nanoliposomal oxaliplatin was synthesized by reverse phase evaporation technique. The particle size and zeta potential were confirmed with dynamic light scattering (DLS). The results showed that the size of pegylated nanoliposomal oxaliplatin was 147.7 nm. The zeta potential of pegylated nanoliposomal oxaliplatin assessed -20.5 mv. Zeta potential exhibits stability of pegylated nanoliposomal preparation. Morphology of liposomal nanodrug were examined by scanning electron microscopy (SEM). Entrapment efficiency of pegylated nanoliposomal oxaliplatin was determined 40.2%. Cytotoxicity effects of drug-loaded nanoparticles and pure drug were evaluated for MCF-7 and MDA-MB-231 breast cancer cell lines by MTT assay. The IC₅₀ values for pegylated nanoliposomal oxaliplatin and pure oxaliplatin were assessed 0.1046 mg/ml and 0.2307 mg/ml respectively for MCF-7 and 0.05125 mg/ml and 0.1023 mg/ml respectively for MDA-MB-231, hence the IC₅₀ values of pegylated nanoliposomal oxaliplatin was estimated as 1/2 the IC₅₀ of pure oxaliplatin. This indicated cytotoxicity of oxaliplatin-loaded nanoparticle was decreased in comparison to pure drug. Finally, in this investigation, effect of pegylated nanoliposomal oxaliplatin on MDA-MB-231 showed 2-times decrease of (in) IC₅₀ value in comparison with MCF-7 at 96 h incubation.

Keywords: Breast cancer, Oxaliplatin, Liposome, polyethylene glycol, Nano drug delivery

1. INTRODUCTION

Cancer represents one of the most common diseases in the world. As shown in figure 1 the breast cancer is the major cause of mortality among women world [1]. Breast cancer increases with age and all women are at risk. It is always caused by a genetic abnormality. However, only 5-10% of cancers are due to abnormality inherited from parents. About the 90% of breast cancers are due to genetic abnormalities that happen as a result of the aging process and the “wear and tear” of life in general. Treatment of breast cancer is consists of surgery, radiotherapy, hormonal therapy and chemotherapy [2]. Oxaliplatin is a chemotherapy drug based on platinum for curing breast cancer. Platinum compounds is include of cisplatin, carboplatin, oxaliplatin, satraplatin, nadaplatin, triplatin, etc [3]. Oxaliplatin antitumor compound is third generation platinum (Pt) [4]. The mechanism action of

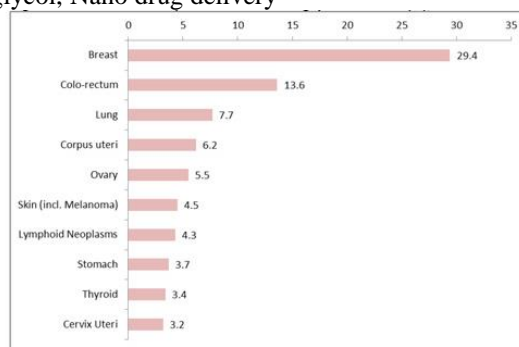


Figure 1. The most common cancer in women.

Oxaliplatin is similar to mechanism of cisplatin, involving DNA cross linking mechanisms [5]. Oxaliplatin is one of potent compounds be used in treatment of cancer, which inhibits DNA replication and transcription [6].

In order to improve chemotherapeutic effective of oxaliplatin, nanoliposomation is used in pharmacological as beneficial developments. Liposomes are colloidal, spherically shape vesicles of one or more lipid closed bilayers phospholipid systems and were used as drug delivery systems [7]. To achieve this results polymers, such as polyethylene glycol can reduce interactions with

To whom all correspondence should be sent:
E-mail: azimakbarzadeh1326@gmail.com

reticuloendothelial system (RES) and increase the circulation lifetime of the drug. Liposomes are able to pass successfully through biological barriers protection of drugs against destructive conditions and compounds, delivering the drug to the target tissue [8]. Polyethylene glycol used to increase resistance, applicability and solubility and extending the circulation lifetime of liposomes [9, 10]. Polyethylene glycol is used to reduce interactions with reticuloendothelial cells and not to be taken up by them [11]. Liposomal drug nanoparticles can self-load the drug as a carrier and prevents damage to non-cancerous tissues. Moreover, they can increase the rate of drug delivery to target cells (figure (2)). Indeed, liposome uptake by tumors relies primarily on the enhanced permeability and retention (EPR) effect [12, 13].

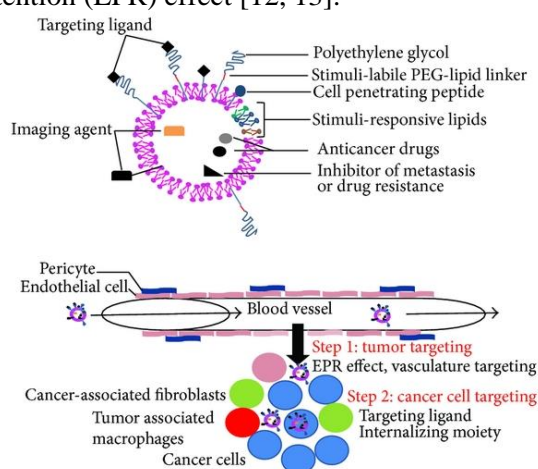


Figure 2. Schematic picture of a liposomal nanocarrier and its effect on cancer cell [13].

This article aimed to improve the drug therapeutic index and decreasing its side effects by preparation of pegylated nanoliposomal of oxaliplatin.

2. MATERIALS AND METHODS

2.1 Materials

Phosphatidylcholine, cholesterol, polyethylene glycol 2000 (PEG 2000) and MTT (3-(4,5-dimethylthiazolyl-2)-2, 5-di-phenyltetrazolium bromide), were purchased from sigma company (SIGMA, USA). Ethanol and Isopropanol purchased from Merck Company (Merck, Germany). The RPMI-1640 culture medium was purchased from Invitrogen (Invitrogen, USA) and Oxaliplatin was prepared from Sobhan Ancology Company. Breast cancer cell lines (MCF-7) were purchased from cell bank of Pasteur institute Iran.

2.2 Preparation of pegylated nanoliposomal oxaliplatin

In order to produce pegylated liposomal oxaliplatin, phosphatidylcholine (50mg) and cholesterol (10mg)

and polyethylene glycol 2000 (15mg) were dissolved in 15 ml chloroform and then 5 ml of oxaliplatin solution (1 mg/ml) added to resultant mixture. The resultant solution was stirred (at 300 rpm, at room temperature, 1h) to gain a transparent, yellow suspension. The solvent phase was removed by rotary evaporator (Heidoiph, Germany). The buffer phosphate saline (pH 7.4) (30 ml) was added to resultant film. Resultant solution was stirred (150 rpm, room temperature, 24 h). Also control solution was prepared without oxaliplatin. The emulsion was sonicated (Bandelin Sonorex Digital, 60 HZ) for 10 min to reduce the size of liposomes. [14] Then resultant solution was homogenised (7000 rpm, 5 min) and then was extruded through a polycarbonate membrane (200 nm pore size) (pegylated nanoliposomal oxaliplatin and pegylated nanoliposomal).

2.3 The particle size and zeta potential measurement

The particle size and zeta potential were measured by Zeta sizer (Malvern, Instruments Ltd, Worcestershire, Zen 3600 UK) [15].

Charges present on the surface of the vesicles indicate in vivo performance of the liposomes. Thus the zeta potential demonstrates the degree of repulsion between adjacent vesicles.

3. Entrapment efficiency

For evaluation of encapsulated oxaliplatin, 1 ml from formulation was centrifuged at 13,000 rpm for 2 h at 4°C and the optical density (OD) of the upper phase of solutions were measured at 210 nm wavelength by spectrophotometer (UV-160IPC, Shimadzu, Japan). Calculations were performed by using the standard curve. The standard curve of oxaliplatin was obtained by different concentration of pure oxaliplatin and their optical density(OD) were determined (measured) at 210 nm 254 nm wavelength by spectrophotometer. Encapsulation efficiencies were calculated as follows [16]:

$$\eta_{ox} = \frac{OX_a}{OX_t} \times 100 \quad (1)$$

Where, η is the oxaliplatin encapsulation efficiency, OX_a and OX_t are actual and theory amount of oxaliplatin loaded in nanoparticles respectively.

3.1. In vitro release study

In order to determine of the oxaliplatin release rate from liposomes employed membrane diffusion method, thus 1 ml from oxaliplatin and pegylated nanoliposomal oxaliplatin added to the dialysis bags (cut off 12000Da, sigma) separately and dialysis bags were transported to 25 ml phosphate buffer, pH 7.4, and left on the magnetic stirrer (37 °C, 120 rpm,

24 h) separately. At certain intervals, 1.5 ml of phosphate buffer around dialysis bags was taken and replaced with an equal volume of the phosphate buffer. The optical density samples were separately measured by spectrophotometer at 210 nm wavelength. Then the amounts of released oxaliplatin and pegylated nanoliposomal oxaliplatin in phosphate buffer were assessed by spectrophotometer and standard curve [17].

3.2 Evaluation of cellular cytotoxicity

Cellular cytotoxicity was evaluated on breast cancer cell lines MCF-7 and MDA-MB-231 by MTT assay.

A sample of 100 μ L of cells suspension contained 10,000 cells were seeded onto 96-well plates in 1 ml of RPMI 1640 medium containing 10% fetal bovine serum (FBS) and incubated for 24 hours under 10% carbon dioxide at 37 $^{\circ}$ C. Subsequent to 24 hours of cells culturing, the supernatant was removed and various concentrations of formulations of pure oxaliplatin and pegylated nano liposomal oxaliplatin and its control was substituted and then incubated for 96 hours at 37 $^{\circ}$ C. After 96 h of incubation again culture supernatants were poured off and 100 μ L the 3-(4,5-dimethylthiazol-2-yl)-2,5diphenyl tetrazolium Bromide (MTT) solution with pH equal to 4.7 was added to each well and incubated for 3 h. MTT solution was replaced with 100 μ L Isopropanol and stirred to dissolve the formed Formazan crystals. The optical absorption was determined at 570 nm by a spectrophotometer. The cell viability rate was calculated from the ratio of treated cells absorption with different formulations of the drug to the absorption of control cells, and the results were assessed by the Pharm program. IC50 values (IC50 values expressed drug concentrations that cause 50% cell death) was determined for each of the samples. The experiment was performed in triplicates. Cytotoxicity effects of drug nanoparticles and pure drug were evaluated for breast cancer cell lines MCF-7 and MDA-MB-231 by MTT assay.

4. RESULT AND DISCUSSION

Polyethylene glycol- coated liposomes can reduce interactions with reticuloendothelial cells and increase the circulation lifetime for the drug [17].

Zeta potential increases repulsive forces, while electrostatic repulsion of particles with the same electric charge prevents aggregation of the spheres particles [18].

Oxaliplatin is a third generation of platinum (Pt) anti-tumor compound and has minimum ototoxicity and nephro-toxicity in comparison to cisplatin and carboplatin platinum compounds [19, 20].

4.1. Morphology and determination of particle sizes and zeta potential

The mean diameter of pegylated nano-liposomal oxaliplatin was determined as 147/7 nm. The zeta potential of pegylated nanoliposomal oxaliplatin was assessed -20.5 mv. Zeta potential exhibit stability of pegylated nano liposomal preparation.

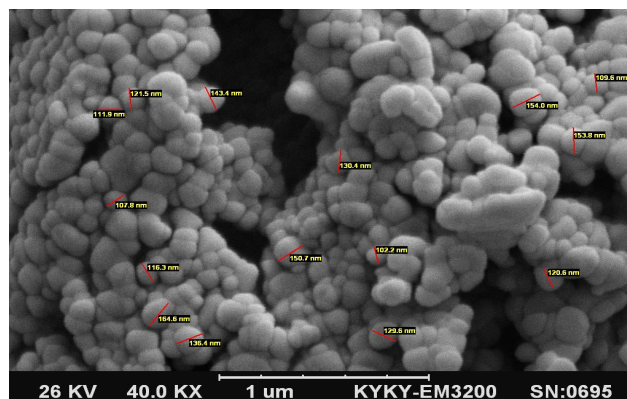


Figure 3. Representative scanning electron microscopy (SEM) image of nanodrug.

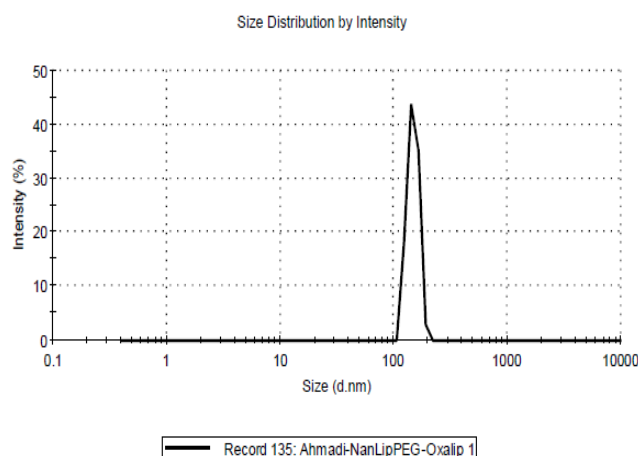


Figure 4. Dynamic light scattering (DLS) examination for the particle size distribution.

4.2. Entrapment efficiency

The entrapment efficiency was calculated according to the standard curve and using the encapsulation formula. The percent of encapsulation was 40.2%.

4.3. In vitro release study

The values of released oxaliplatin from two formulations of pure oxaliplatin and pegylated nanoliposomal oxaliplatin in phosphate buffer was assessed at 1, 2, 3, 4, 5, 6, 17, 18, 20, 22, 24, 48, 96, 120 hours. Our results demonstrate the release of oxaliplatin from pegylated nanoliposomal was gradually increased over time at 6 hours about 38% and at 120 h there was an increase of over 80% and pure oxaliplatin exhibited the highest level at 2,3,4 hours about 90% .

4.4. Cytotoxicity assay

In our investigation, pegylated nanoliposomal oxaliplatin exhibited slightly decrease of cytotoxicity when cell viability was evaluated (determined) at 24 and 48 h and it showed increase of cytotoxicity when cell viability was evaluated (determined) at 96 h. This could be due to retard release of oxaliplatin from pegylated nanoliposomal oxaliplatin in compared to pure oxaliplatin. Cause of this observation is reduction of oxaliplatin release rate from liposomes at 48 h and a drastic increase of oxaliplatin release rate from liposomes at 96 h.

IC₅₀ values express (represent) drug concentrations that cause 50% cell death for the pure oxaliplatin and pegylated nano liposomal oxaliplatin. Results demonstrated the higher effectiveness of the pegylated nano liposomal oxaliplatin formulation in comparison to pure oxaliplatin. Also, it depicted that the cytotoxicity of the empty pegylated nano liposomal was low.

In MTT assay, the IC₅₀ of the pegylated nano liposomal oxaliplatin formulation was about 1/2 the IC₅₀ of pure oxaliplatin at 96 h incubation. (MCF-7 and MDA-MB-231 breast cancer cell lines).

Effect of pegylated nanoliposomal oxaliplatin on MDA-MB-231 showed about 2-times decrease in IC₅₀ value in comparison to MCF-7 at 96 h incubation. This could originate from increasing of cellular uptake by MDA-MB-231 cell line in comparison to MCF-7 cell line.

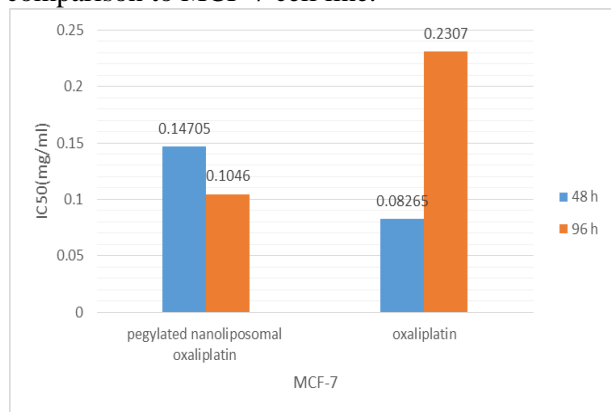


Figure 5. The IC₅₀ of pegylated nanoliposomal oxaliplatin and pure oxaliplatin was assessed for MCF-7 cell line by using MTT assay at 48h and 96h.

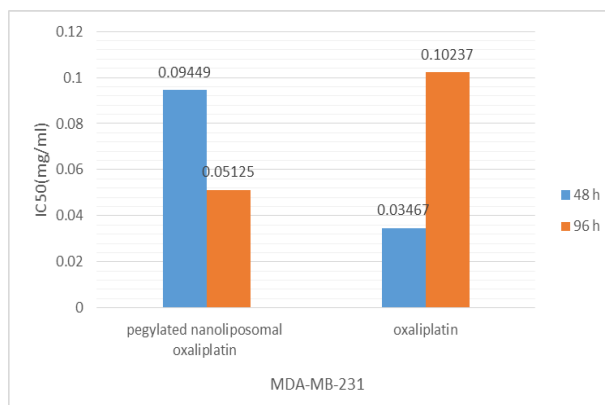


Figure 6. The IC₅₀ of pegylated nanoliposomal oxaliplatin and pure oxaliplatin was assessed for MDA-MB-231 cell line by using MTT assay at 48h and 96h.

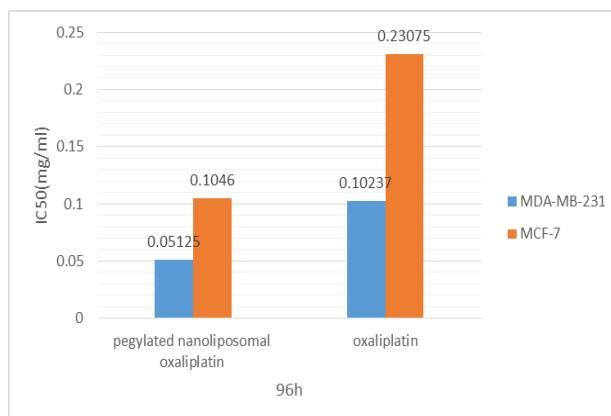


Figure 7. The IC₅₀ values of pegylated nanoliposomal oxaliplatin and pure oxaliplatin were evaluated on breast cancer cell lines MCF-7 and MDA-MB-231 by MTT assay.

5. CONCLUSION

In this paper, a novel method was proposed that Pegylated liposomes at nano scale carry oxaliplatin in order to increase the effectiveness and decrease the side effects of the drug. Pegylated nanoliposomal oxaliplatin formulation was successfully prepared by reverse phase evaporation method. The results indicated that cytotoxicity of pegylated nanoliposomal oxaliplatin formulations was better. In this approach, it was found that pegylated nanoliposomal oxaliplatin had a slower release of oxaliplatin to prevent drug dispersion before reaching the cancer cells. The in vitro release study showed that pegylated nanoliposomal oxaliplatin on MDA-MB-231 showed about 2-times decrease in IC₅₀ value compared with MCF-7 at 96 h incubation.

REFERENCES

1. A.T. Vo, R.M. Millis, *Obstet Gynecol Int*, **2012**, 6022 (2012).
2. Wang X, Yang L, Chen ZG, Shin DM, *CA Cancer J Clin.*, **58**, 97 (2008).
3. L. Kelland, *Nat. Rev. Cancer*, **7**, 573 (2007).

4. A. Ibrahim, S. Hirschfeld, M.H. Cohen, D.J. Griebel, G.A. Williams, R. Pazdur, *Oncologist*, **9**, 8 (2004).
5. E. Raymond, S. Faivre, S. Chaney, J.M. Woynarowski, *Molecular Cancer Therapy*, **1**, 227 (2002).
6. H. Bleiberg, *Br. J. Cancer*, **77**, 1 (1998).
7. N. Maurer, D.B. Fenske, P.R. Cullis, *Expert Opin Biol Ther.*, **1**, 923 (2001).
8. L. Costantino, D. Boraschi, *Drug Discov Today*. **17**, 367 (2012).
9. T.M. Allen, C. Hansen, F. Martin, C. Redemann, A Yau-Young, *Biochim. Biophys. Acta*, **1066**, 29 (1991).
10. C. Allen, N. Dos Santos, R. Gallagher, Chiu G.N., Shu Y., Li W.M., S.A. Johnstone, A.S. Janoff, L.D. Mayer, M.S. Webb, M.B. Bally, *Biosci. Rep.*, **22**, 225 (2002).
11. A. Gabizon, D. Papahadjopoulos, *Proc. Natl. Acad. Sci. USA*, **85**, 6949 (1988).
12. S. Zalipsky, M. Saad, R. Kiwan, E. Ber, N. Yu T. Minko, *J. Drug Targeting*, **15**, 518 (2007).
13. F. Perche, P. Torchilin, *J. Drug Delivery*, **70**, 52 (2013).
14. Yang T., Choi M.K., Cui F.D., Kim J.S., Chung S..J, Shim C.K., Kim D.D., *J. Control Release*, **31**, 169 (2007).
15. R. Patel, S.K. Singh, S. Singh, N.R. Sheth, R..Gendle, *J. Pharm. Sci Res.*, **1**, 71 (2009).
16. Zhang Z., Feng S.S., *Biomaterials*, **27**, 4025 (2006).
17. N. Jawahar, D.N. Venkatesh, R. Sureshkumar, V. Senthil, G.N.K. Ganesh, P. Vinoth, *J. Pharm. Sci. Res.* **1**, 123 (2009).
18. A.C. Salome, C.O. Godswill, I.O. Ikechukwu, *Res. J. Pharm. Biol. Chem. Sci.*, **4**, 97 (2013).
19. A. Gabizon, D. Papahadjopoulos, *Proc. Natl. Acad. Sci. USA*, **85**,:6949 (1988).
20. S. Feng, G. Huang, *J. Control. Release*, **71**,53 (2001).

Dispersion model for assessing oily components of produced water discharges from South Pars Gas offshore

G. Bahmannia¹, A.H. Javid^{2*}, A.M. Moradi², S.A. Mirbagheri¹

¹Department of Environment and Energy, Science and Research Branch, Islamic Azad University, Tehran, Iran

²Department of Marine Science and Technology, Science and Research Branch, Islamic Azad University, Tehran, Iran

Received June 26, 2015, Revised September 10, 2015

The discharge of produced water accounts for the largest volume of waste associated with offshore oil and gas production operations. With the development and expansion of Iran's offshore gas reserves in the South Pars fields, there is concern over the potential long-term impacts of produced water discharges in the Persian Gulf. To deal with this emerging issue, the present study focused on modeling and assessment of environmental impacts associated with produced water discharges based on the integration of Gulf hydrodynamic and oily components dispersion models. It provides three-dimensional hydrodynamic input to a Random Walk model focused on the dispersion of oily pollutant components within the produced water effluent stream at a regional spatial scale. In this paper at first the quantity and quality of produced water are measured and reported for one year and some statistical reviews has done. Determination of the oil content of effluent water - Extraction and infra-red spectrometric and OSPAR Reference Method which is the standard method for dispersed oil in produced water analysis in the UK for both oil and gas facilities was used as standard method. Advection, diffusion and fate of oil spills by wind and tidal currents and transport are indirectly taken into account in this study. Hydrodynamic, oil spill and path of the oil pollutants in Offshore Gas Platforms in South Pars Gas Field in 3 month has been simulated in a few scenarios. The results of modeling in this research approved the risk of oily components pollution nearby of onshore ecosystems through 3 months.

Key Words: Modeling, Dispersion, Oil, Offshore, Persian Gulf

INTRODUCTION

The most significant energy development project, the South Pars field, produces about 44 percent of total natural gas in Iran. Discovered in 1990 and located 62 miles offshore in the Persian Gulf, South Pars has a 24-phase development scheme. Phases 1-10, which are operational and are allocated for the domestic market for consumption and reinjection for EOR Produced water is the largest effluent discharge associated with South Pars offshore gas production. (Fig. 1&2) The total volume of produced water effluent is expected to increase with future anticipated development of offshore gas reserve. The environmental impact potentially which is caused by produced water is related to the fate and transport of its individual components including organic and inorganic compounds (e.g., petroleum hydrocarbons, heavy metals, nutrients, natural radionuclide), as well as the formation water and treating chemicals. Although produced water discharges are associated with rapid dilution and low-to-trace levels of pollutants, the potential for cumulative toxic effects

under regional ocean currents warrants a need to assess the long-term risks on the marine ecosystems. Recently, the increasing development of economy has considerably raised the demand for fossil fuels all over the world. Consequently, oil spill disasters in coastal areas, which may be the result of oil production or transportation, have become one of the most serious threats against marine environment. Understanding the nature of oil spills in coastal areas plays a crucial role in alleviating destructive impacts of oil spill disasters on marine environment [1]. Produced water consists of water naturally present in the oil and gas reservoir (formation water); flood water previously injected into the formation, and/or, in the case of some gas production condensed water. Produced water is part of the well stream together with oil and/or gas. Oil and/or gas are separated from the produced water on the production platform. The produced water is treated to reduce the dispersed oil content to below the regulatory maximum limit of 40 mg/l, set by OSPAR, before it is discharged from the production platform.

Typical produced water flow diagrams of studied platforms are shown in Fig.3. The package is designed to process a feed rate of 2000 bpd liquids and to reduce suspended oil in water content of the separated water to 40 ppm wt. max.

To whom all correspondence should be sent:

E-mail: a.javid@srbiau.ac.ir



Fig. 1. A typical platform.



Fig. 2. The South Pars Gas Field location

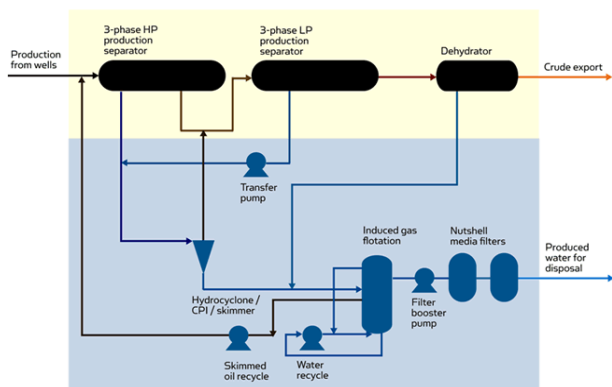
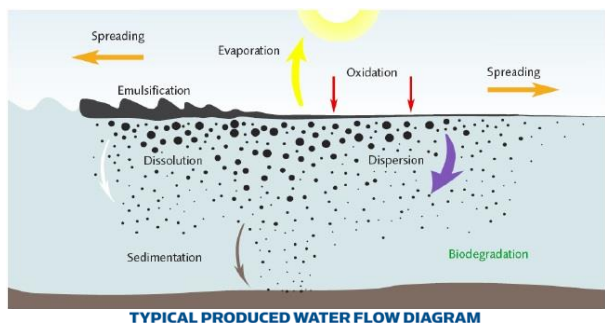


Fig. 3. Typical produced water flow diagram of platforms and oil spills changes in Sea.

MATERIALS AND METHODS

Sampling, preparation and measurement of total petroleum hydrocarbons (TPH) as main oily components in produced water of each platforms has done based on OSPAR Agreement 2005-15 and ISO 9377-2 and ISO 5667-3 test methods[3]. The calibrated GC-FID as an accurate laboratory equipment used for all 52 times analysis of samples and expert personnel through a year carried out reliable tests (Fig. 4).

The MIKE 21/3 software provides three-dimensional hydrodynamic input to a Random Walk model focused on the dispersion of oily pollutant components within the produced water effluent stream at a regional spatial scale.



Fig. 4. GC- FID test equipment and lab experts.

RESULTS

The quantity and quality of produced water are measured and reported for one year and assumed for modeling and some statistical reviews. Table 1 includes oil content of produced water discharge within 3 months on the platform No.5. An average of daily BBL of produced water discharges per each platforms and average of TPH components are shown in Table 1.

Table 1. Data of oil content in platforms no. 5.

Oil	Gasoline (C6-C10)	Diesel (C10-C20)	Heavy Oil (C20-C28)
160	92	53	15
180	101	67	12
177	98	62	17
165	105	51	9
155	80	56	9
145	100	38	7
176	111	55	11
160	115	35	10
166	107	48	11
154	99	41	14
166	111	45	10
170	135	30	5
163	109	41	13
144	88	46	10
130	75	48	17
134	85	35	14
144	92	42	10
136	87	43	6
190	122	60	8
185	129	51	5

Statistical review by SPSS started with Manova method for 8 platforms TPH data in 26 times measurement. It assumed that sampling was random and error of first type was $\alpha = 0.05$.

This analysis shows that data of platforms are acceptable and useful for mathematical modeling input which is an effective tool for the management of Persian Gulf operational platforms' oily water discharges.

MODEL SETUP

In order to the model input data the bathymetry is used by structure distances of geographical width 2 minute in Southern- Northern direction, and the geographical 2 minute in Western-Eastern direction related to ETOPO1 altimetry data in NOAA site. So by the use of these data in 0.10 structure, the altimetry features of the place is counted and rendered in model (Fig. 5). Tidal surface elevation in Hormuz station utilized for Flow Model FM boundary condition that is shown in Fig 6. Also constant coefficients of oil spill model of Mike 21 are shown in Table 3.

Table 2. Data of platforms.

Platforms	SPD1&2	SPD3	SPD4	SPD5	SPD6	SPD7	SPD8	SPD9	SPD10	SPD11
Water bbl./D	541	167	326	732	1664	389	430	304	2042	1987
Ave. TPH mg/L	43	0	0	155	192	215	330	177	143	208

Table 3. Multivariate Tests.

	Effect	Value	F	Hypo-thesis df	Error df	Sig.
Intercept	Pillai's Trace	.999	38754.175 ^a	4.000	197.000	.000
	Wilks' Lambda	.001	38754.175 ^a	4.000	197.000	.000
	Hotelling's Trace	786.887	38754.175 ^a	4.000	197.000	.000
	Roy's Largest Root	786.887	38754.175 ^a	4.000	197.000	.000
platform	Pillai's Trace	1.686	20.822	28.000	800.000	.000
	Wilks' Lambda	.002	109.934	28.000	711.716	.000
	Hotelling's Trace	149.993	1047.271	28.000	782.000	.000
	Roy's Largest Root	148.352	4238.641 ^b	7.000	200.000	.000

a. Exact statistic-

b. The statistic is an upper bound on F that yields a lower bound on the significance level.

c. Design: Intercept + platform

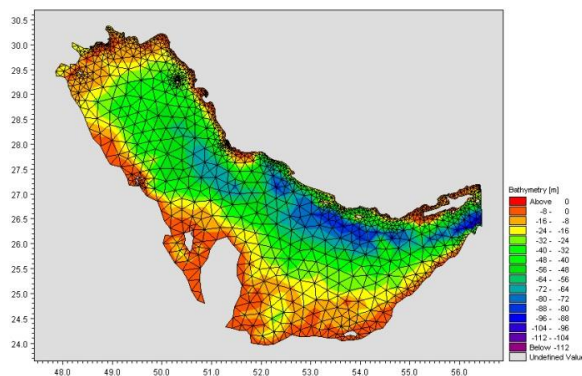


Fig. 5. Mesh Data of Hydrodynamic and Oil Spill model.

Table 3. Constant coefficients of oil spill model.

No	Description	Class	Value
1	Evaporation: Submit number (dim. less)	1	2.6
2	Evaporation: Average molecular weight of volatile fraction of oil (g/mol)	1	60
3	Evaporation: Vapor pressure (atm)	1	0.04
4	Spreading: Terminal thickness (mm)	1	0.005
5	Spreading: Maximum oil-front velocity (m/s)	1	0.4
6	Biodegradation: Decay rate (per day)	1	0.01
7	Emulsification: Rate (s/m ²)	1	2e-006
8	Emulsification: Maximum water fraction (m ³ /m ³)	1	0.6
9	Emulsification: Constant Kao equal 3.3 at 293 K (dimentionless)	1	3.3
10	Emulsification: Constant Kao equal 200 at 293 K (dimentionless)	1	200
11	Emulsification: Fraction of asphaltene (g/g)	1	0.01
12	Emulsification: Fraction of wax (g/g)	1	0.05
13	Buoyancy: Density of original oil at 20 °C volatile fraction (kg/m ³)	1	950
14	Buoyancy: Density of original oil at 20 °C heavy fraction (kg/m ³)	1	980
15	Buoyancy: Grain diameter of oil particles (mm)	1	0.001
16	Photooxydation: Decay rate (per day) at 100 watt/m ²	1	0.001
17	Photooxydation: Light extinction coefficient (1/m)	1	1
18	Dissolution: Rate light fraction (per day)	1	0.1
19	Dissolution: Rate heavy fraction (per day)	1	0.005
20	Vertical dispersion: Fraction of wave height (dim. less)	1	0.1
21	Vertical dispersion: Parameter for wave break	1	0.001

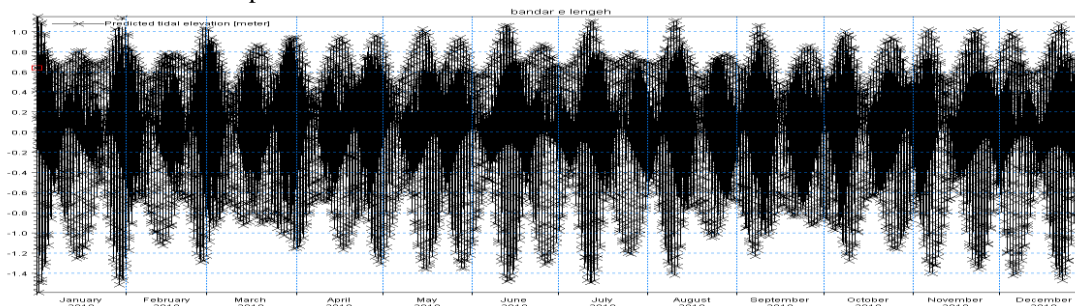


Fig. 6. Tidal elevations at Hormuz station used as boundary conditions for the Flow Model.

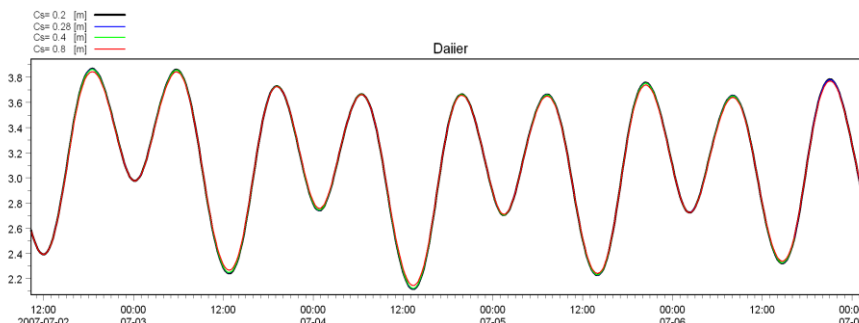


Fig. 7. Model Validation and Sensitive Analysis between Numerical Model and Measurement Data

RESULTS

In this research, hydrodynamic parameters such as tidal surface elevation that measured in Daiier Port have been used for model validation (Fig 6). Comparing numerical results and field measurements shows a good agreement between numerical results and field measurements in Daiier Port. Hydrodynamic results of are shown in Fig 7. Oil dispersion model, which includes hydrodynamic model and qualitative water model from produced water, has been done for a year for each discharge location. Oil spill modeling in Offshore Gas Platforms in South Pars Gas Field is shown in Fig 8. Path of the oil pollutants in Offshore Gas Platforms in South Pars Gas Field is shown in Fig 9.

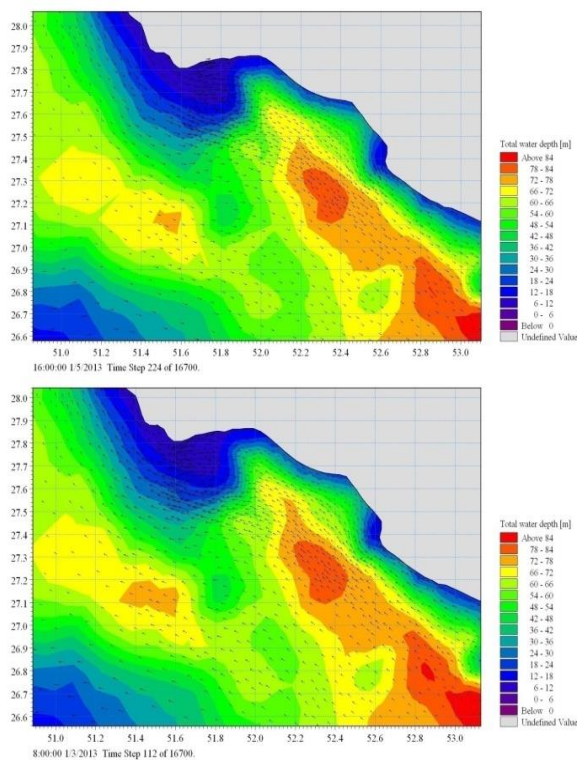


Fig. 8. Flow velocity vectors in the surrounding area of Asalooye.

CONCLUSIONS AND DISCUSSION

Comparing Industry development and growing marine transportation, together with oil spill disasters in the seas and oceans have resulted in contamination of marine environments. Advection, diffusion and fate of oil spills by wind and tidal currents and transport are indirectly taken into account in this study. This study was done on Gas Platforms in South Pars Gas Field in Iran; however there are other platforms belonging to Qatar, so there are actually produced water discharges and pollutants from those platforms, too. Therefore,

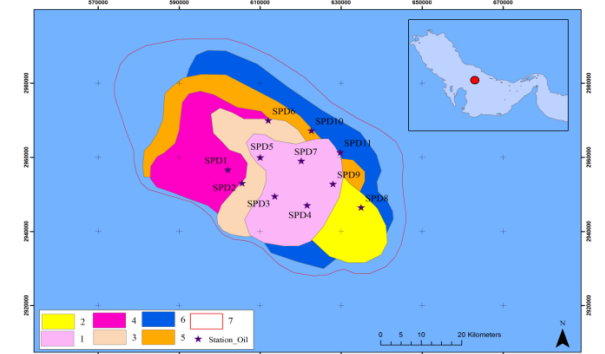
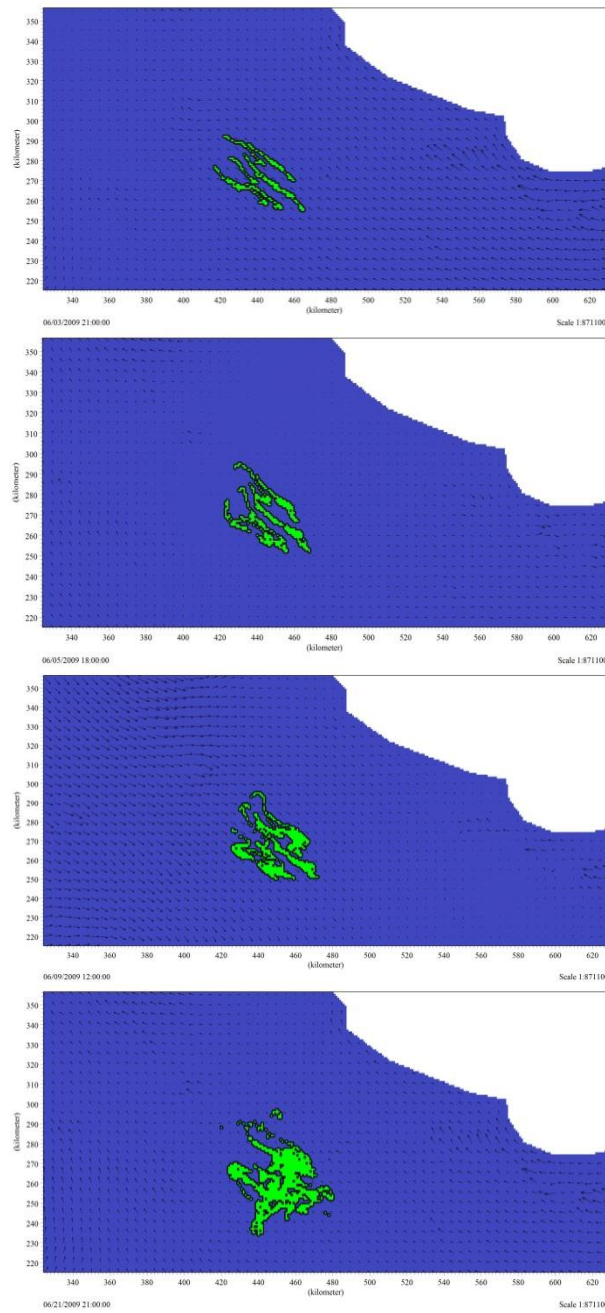


Fig. 9. Path of the oil pollutants in offshore gas platforms in South Pars Gas Field during the simulation period.

future studies can be done on other platforms in South Pars Gas Field and the obtained results can be compared, so better and more accurate results can be achieved.

REFERENCES

1. P. Tkalich, X. B. Chao, Accurate Simulation of Oil Slicks, Proceedings of the International Oil Spill Conference 26-29 March 2001, Florida, Washington DC, 2001, p. 1133.
2. J.A. Fay, The Spread of Oil Slick on a Calm Sea, Houtt, D.P. (Ed), Oil on the Sea. Plenum Press, New York, NY , 1969, p. 53.
3. R. Perianez, Modeling the Dispersion of Radio Nuclides in the Marine Environment, Springer, 2005.
4. D. Mackay, S. Paterson, K. Trudel, A Mathematical Model of Oil Spill Behavior, Environmental Protection Service, Fisheries and Environmen, Canada, 1980.
5. A. Johansen, *Spill Technol. Newslett.*, **III**, 134 (1982).
6. M. Fingas, *J. Adv. Marine Technol.*, **11**, 41 (1994).
7. A.J. Elliot, *Deutsche Hydrographische Zeitschrift*, **39**, 113 (1986).

Chemical characterization and statistical analysis of heavy metals produced discharges from South Pars Gas offshore for dispersion modeling

S.H. Fatemi^{1*}, A.H. Javid², P. Nasiri¹, M. Mirilavasani¹

¹Graduate School of Environmental Engineering, Science and Research Branch, Islamic Azad University, Tehran, Iran

²Graduate School of Marine Science and Technology, Science and Research Branch, Islamic Azad University, Tehran, Iran

Received June 26, 2015, Revised September 10, 2015

The most significant energy development project, the South Pars field, produces about 44 percent of total natural gas in Iran. Discovered in 1990 and located 62 miles offshore in the Persian Gulf, South Pars has a 24-phase development scheme. Phases 1-10, which are in production mode and are allocated for the domestic market for consumption and reinjection for EOR Produced water is the largest effluent discharge associated with South Pars offshore gas production. The total volume of produced water effluent is expected to increase with future anticipated development of offshore gas reserve. The environmental impact potentially caused by produced water is related to the fate and transport of its individual components including organic and inorganic compounds (e.g., petroleum hydrocarbons, heavy metals, nutrients, natural radionuclides) associated with the formation water and treating chemicals. Although produced water discharges are associated with rapid dilution and low-to-trace levels of pollutants, the potential for cumulative toxic effects under regional ocean currents warrants a need to assess the long-term risks to the marine ecosystems. In this paper at first the quantity and quality of produced water are measured and reported for one year and some statistical reviews has done. Determination of the heavy metals of effluent water - extraction and infra-red spectrometric and OSPAR reference method which is the standard method for dispersed heavy metals in produced water analysis in the UK for both oil and gas facilities used as standard method. Advection, diffusion and fate of heavy metal by wind and tidal currents and transport are indirectly taken into account in this study. Hydrodynamic, heavy metal and path of the heavy metal in Offshore Gas Platforms in South Pars Gas Field in 3 month has been simulated.

Keywords: Heavy Metals, Dispersion, Statistical, Analysis, Modelling, Persian Gulf

INTRODUCTION

Increasingly, offshore outfalls are being used for the disposal of wastewater in coastal areas. Because the discharged effluents generally exert different velocity, temperature, and density compared with the receiving water body, waste discharges form plumes and jets with high momentum and different densities [1,2,3]. The mixing and dispersion processes of a continuous discharge into a receiving water body can be divided into near-field, far-field, and intermediate regions according to length and time scale. In the vicinity of the discharge point, the jet trajectory and mixing are dominated by the momentum of the discharges and the density differences between discharges and the receiving water body. This region is referred to as the near field, where the typical time and length scales of the plume are in the order of minutes and water depths (tens to hundreds of meters), respectively.

After some time, or some distance, from the discharge point, the influence of the inflow

characteristics dissipates and ambient flow conditions then control transport and mixing of the discharges. This region, where the diluted effluents are diffused with ocean currents, is referred to as the far field, where the typical time and length scales are in the order of hours and kilometers. Between these two regions, there is a zone called the intermediate field, which starts at the end of the jet regime [2,4,5]. The intermediate field may extend over distances greater than the water depth under conditions of weak ambient flow; however, under strong ambient conditions, intermediate-field processes can be far less significant than far-field dispersion processes. There is increasing environmental concern over the ocean discharge of contaminants, such as metals and hydrocarbons, in produced water because of their potential for bioaccumulation and toxicity, particularly by those dissolved in the water phase. It is noted that hydrocarbons and heavy metals show different fate and transport mechanisms due to their differences in physico-chemical properties. Low concentrations of hydrocarbons in a large discharge of produced water can be rapidly diluted by tidal currents and decay over time due to aerobic degradation. Thus,

To whom all correspondence should be sent:
E-mail: hamidrezafatemi@yahoo.com;

the effects of hydrocarbons associated with produced water discharges are primarily linked to localized areas and unlikely to cause large-scale environmental impacts. In contrast, a large number of heavy metals are stable, environmentally persistent, and highly toxic. Furthermore, they can be accumulated by marine life in concentrations several thousand times higher than those in the surrounding seawater [3]. For example, lead (Pb) is a highly toxic metal with persistent adverse effects in the marine ecosystem, and the toxic effects on shellfish can occur even in the presence of a very low concentration of Pb [5, 6, 7].

Produced water is the largest volume waste stream in the exploration and production process of oil and gas. Over the economic life of a producing field, the volume produced water can exceed by ten times the volume of hydrocarbon produced. During the later stages of production, produced water can account for as much as 98 % of the extracted fluids. Typical water production rates from oil platforms are from 2 400 to 40 000 m³/day and for gas platforms 1, 6-30 m³/day [6, 8]. These amounts to an expected discharge of produced water to the North Sea in 1998 of 3, 4 x 10⁸ m³. When discharged the produced water still contains a wide range of components: dissolved organic components, various production chemical trace metals, naturally occurring radioactive material, inorganic salts. In addition the discharged water is almost depleted for oxygen and has an average COD or BOD value of 4 000 mg O₂/l [5, 8, 9, 10]. In addition to the organic components trace elements as Pb, Cd, Cu, Hg, Ni, Zn, As and Cr are dissolved in the produced water in considerably greater concentrations than in sea water [11, 12].

In this field, 11 platforms (we know as SPD) are in production mode and very platforms normally have 10-12 gas wells. The layout and configuration of these platforms has shown in Fig. 1.

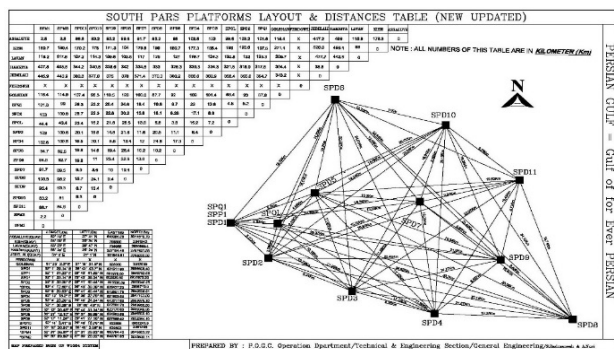


Fig. 1. The South Pars Gas Platforms layout

On the platforms, in process diagram separated water from the FWKO (Free Water Knock Out) drums and Coalesces is routed to the Oily Water

Treatment Package that is common to both trains [13]. Typical produced water flow diagrams of platforms which are studied are shown in Fig.2.

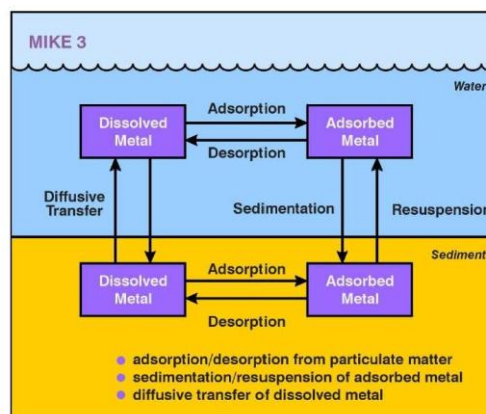


Fig. 2. Typical produced water flow diagram of platforms and Heavy Metal Changes in Sea

The package is designed to process a feed rate of 2000 bpd (barrels per day) liquids and to reduce suspended oil in water content of the separated water to 40 ppm wt. max [8]. Prior to disposal overboard via a disposal caisson. The Oily Water Treatment Package comprises:

- Hydro cyclones (two per FWKO Drum – one operating, one installed spare - and one for Test Separator).
- A water degassing drum – this handles the water from the hydro cyclones and the coalescing vessels. Reject oil from the hydro cyclones enters directly into the oil compartment of the drum.
- Filters and coalescer filters – these handle water from degassing drum before discharge to sea.

The treated water from the coalescer filters is discharged to the sea via the caisson. The reject stream from the OWTP (recovered condensate in water) is recycled back to the inlet of the FWKO Drum via the Flare KO Drum and Condensate Injection Pumps, due to its high water content.

METHOD

The data of produced water discharges and analytical results are gathered through one year and a statistical review has done. The IP 426:98 (04), Determination of the oil content of effluent water - Extraction and infra-red spectrometric and OSPAR Reference Method which is the standard method for dispersed oil in produced water analysis in the UK for both oil and gas facilities used as standard method (See Figure 3).

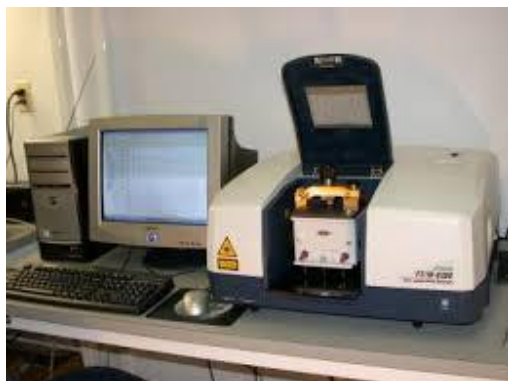


Fig.3. Infra-red spectroscope

In this method a sample of the discharge water to be analyzed is acidified to a low pH (<2), extracted with two volumes of Tetrachloroethylene (TTCE) or an alternative solvent approved by DECC, and the IR absorbance measured using an infrared analyzer with a fixed wavelength of 2930 cm^{-1} . The oil content of the sample is determined by comparison of the infrared absorbencies of the extract against a calibration graph prepared using a series of standards containing a known heavy metals [9]. The SPSS software for statistical assessment is used for analysis of produced water rate and oil content in all platforms.

MEASUREMENT DATA

The quantity and quality of produced water are measured and reported for one year and assumed for modeling and some statistical reviews. Table 1 includes oil content of produced water discharge and heavy metals within 3 months on the platform no5. An average of daily BBL of produced water discharges per each platforms and average of heavy metals components are shown in Table 1.

Statistical review by SPSS started with Manova method for 8 platforms heavy metals data in 26 times measurement. It assumed that sampling was random and error of first type was $\alpha=0.05$.

This analysis shows that data of platforms are acceptable and useful for input of mathematical modeling which is an effective tool for the management of Persian Gulf operational platforms' oily water discharges. Two soft wares; MIKE 21/3 (DHI 2007) and Delft3D (Delft3D 2009) are proposed software's for predictions of ocean hydrodynamics; pollutant fate and transport in the far field; water quality and sediment processes (See Figure 4 and Figure 5).

MODEL SETUP

To order the model input data the bathymetry is used by structure distances of geographical width 2

minute in Southern- Northern direction, and the geographical 2 minute in Western-Eastern direction related to ETOPO1 altimetry data in NOAA site. So by the use of these data in 0.10 structure, the altimetry features of the place is counted and rendered in model (Fig. 4 and Fig. 5). Tidal surface elevation in Hormoz station utilized for Flow Model FM boundary condition that shown in Fig 5. By using Particle Tracking model of MIKE21, DHI, path of heavy metal has been simulated.

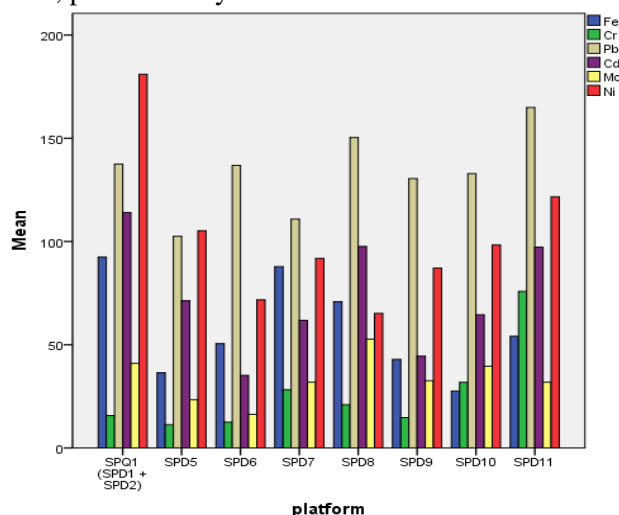


Fig.4. Measurement data gathering in gas platforms

Table 1. Data of heavy metals in platforms no. 5

	Fe	Cr	Pb	Cd	Mo	Ni
101	11	146	129	55	200	
99	12	150	111	50	201	
97	15	134	100	48	199	
90	9	135	120	48	188	
90	10	142	118	44	189	
92	11	141	117	34	199	
98	17	120	110	30	167	
100	14	122	120	46	168	
86	19	160	121	43	155	
93	23	165	119	42	185	
90	15	133	101	46	183	
81	15	133	102	48	190	
81	15	140	109	40	199	
78	17	138	115	38	193	
78	18	132	114	37	188	
102	17	119	115	34	193	
102	11	123	119	43	170	
93	10	125	118	39	173	
95	16	140	117	51	190	
99	16	139	110	33	177	
92	16	147	103	39	160	
91	15	148	111	41	161	
100	23	134	124	40	171	
103	22	130	127	31	155	
88	21	136	109	34	163	
85	20	143	107	32	190	

Table 2. Multivariate Tests

	Effect	Value	F	Hypothesis df	Error df	Sig.
Intercept	Pillai's Trace	.999	38754.175 ^a	4.000	197.000	.000
	Wilks' Lambda	.001	38754.175 ^a	4.000	197.000	.000
	Hotelling's Trace	786.887	38754.175 ^a	4.000	197.000	.000
	Roy's Largest Root	786.887	38754.175 ^a	4.000	197.000	.000
Platform	Pillai's Trace	1.686	20.822	28.000	800.000	.000
	Wilks' Lambda	.002	109.934	28.000	711.716	.000
	Hotelling's Trace	149.993	1047.271	28.000	782.000	.000
	Roy's Largest Root	148.352	4238.641 ^b	7.000	200.000	.000

a. Exact statistic b. The statistic is an upper bound on F that yields a lower bound on the significance level.
 c. Design: Intercept + platform

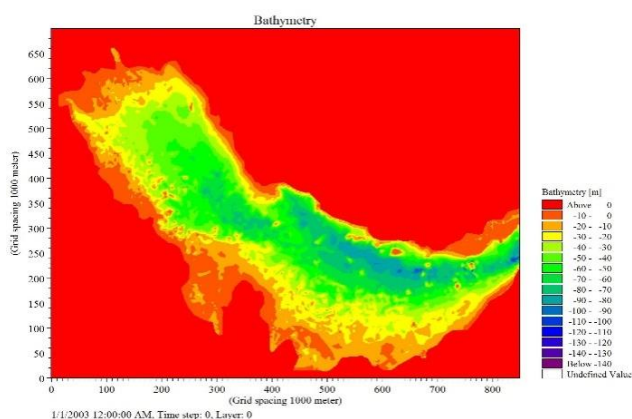


Fig. 5. Bathymetric data particle tracking models.

RESULTS

In this research hydrodynamic parameters such as tidal surface elevation that measured in in Daiier Port have been used for model validation. Compare between numerical results and field measurements shown a good agreement between numerical results and field measurements in Daiier Port. Hydrodynamic results of model have been shown in Fig 6. The model shows the tracking of heavy metals from in offshore gas platforms in South Pars Gas Field for 6 month (See the 4 Shapes in Fig 6). Dispersion modeling of heavy metals, which

includes hydrodynamic model and qualitative water model from produced water which has been done for a year for each discharge location.

CONCLUSIONS AND DISCUSSION

Gathering of sound and acceptable data for modeling is very important step of work. In this paper we submit a few tables of data which has produced by standard sampling and lab tests. Then a statistical review report has submitted based on SPSS software and it proved that these data are useful for next step of modeling. In this paper at first the quantity and quality of produced water are measured and reported for one year and some statistical reviews has done.

In addition to the organic components trace elements as Pb, Cd, Cu, Hg, Ni, Zn, As and Cr are dissolved in the produced water in considerably greater concentrations than in sea water the risk assessment of that high environment risk near Booshehr seaside and transition of heavy metals was indirect of northwest of Persian gulf.

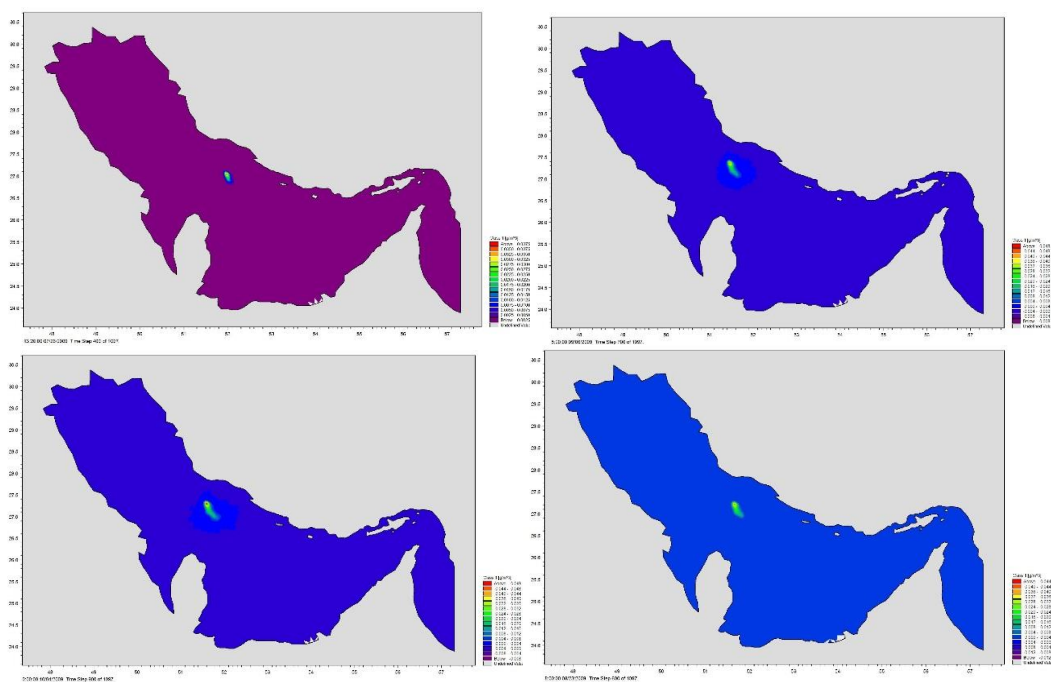


Fig. 6. Tracking of heavy metals from in offshore gas platforms in South Pars Gas Field for 6 month.

REFERENCES

1. P. Tkalich, X. B. Chao, Proceedings of the International Oil Spill Conference, 26-29 March 2001, Florida, Washington DC, 2001, p. 1133.
2. J.A. Fay, The Spread of Oil Slick on a Calm Sea, Hoult, D.P. (Ed), Oil on the Sea. Plenum Press, New York, NY, 1969, p. 53.
3. Perianez, R.2005, "Modeling the Dispersion of Radio Nuclides in the Marine Environment" Springer
4. D Mackay, S. Paterson, K. Trudel, A Mathematical Model of Oil Spill Behavior, Environmental Protection Service, Fisheries and Environmen Canada, 1980.
5. A. Johansen., *Spill Technol. Newslett.*, **III**, 134 (1982).
6. M. Fingas, *J. Advance Marine Technol.*, **11**, 41 (1994).
7. A.J. Elliot, *Deutsche Hydrographische Zeitschrift*, **39**, 113 (1986).
8. A. F.Blumberg, G. L .Mellor, A description of a three-dimensional coastal ocean circulation model. Geophysical Fluid Dynamics Program, Princeton University, Princeton, NJ, 1987.
9. G. W. Bryan, W. J. Langston, *Environ. Pollut.*, **76**, 89 (1982).
10. Z. Chen, G. H. Huang, *J. of Environ. Eng. Div. ASCE*, **129**(1), 79 (2003).
11. J. R. Dojlido, G.A. Best, Chemistry of water and water pollution. Ellis Horwood Ltd, Chichester, UK. 1993.
12. P. Foster, *Environ. Pollut.*, **10**, 45 (1976).
13. P. A. Gillibrand, R .Stagg, W. R. Turrell, *ICES CM/c* , **11**, 421 (1995).

Studying changes amount of useful chemical elements for pistachio trees in vermicompost animal manure than initial animal manure

Saman Haj Mohammadi¹, Sohrab Haj Mohammadi²

¹Department of Chemistry, Sirjan Branch, Islamic Azad University, Sirjan, Iran

²Young Researchers and Elites Club, Sirjan Branch, Islamic Azad University, Sirjan, Iran

Received June 26, 2015; Revised September 10, 2015

Today, vermicompost process with earthworms has been focused to stabilize waste materials. Consistent and rapid steady passing of materials from congestive system of earthworm along crushing, grinding, stirring, and mixing it in various parts of this path and staining these materials with all types of congestive system secretions of this animal, and finally providing proper conditions to synthesize humic acid lead to produce a totally different material in properties from sank materials that is called vermicompost. Since there are contradicted records about vermicompost nutritious materials (K, P, N, Fe, Ca, Mg, B, S, Cu, Zn, Mo Mn), the first matter arising for a former is about amount of nutritious materials in vermicomposts and also organic materials and proportion of carbon to nitrogen in obtained vermicomposts from animal manures (sheep, cow, chicken, and fish) and whether it has significant changes from initial animal manures or not. According to affluent benefits of vermicomposts, the necessity of developing its producing system and supporting its producers is one of important today global needs with significant help to reduce costs and keeping environment that humans are dependent on it for living. This study explores nutritious materials needed for pistachio trees in vermicomposts manure. Obtained vermicomposts is a proper organic modifier to improve agricultural soils fertilization for pistachio trees.

Keywords: animal manure, decomposition process, pistachio tree, quality control

INTRODUCTION

Farmers spend too high costs for animal manures annually. This manures are used for soil fertilization and fertility of pistachio trees. Costs of buying and transferring these manures are problems for farmers. Therefore, composting chemical manures has been focused recently. Composting is a proper method, because it is affordable economically. Composting by organic materials by microbial, thermal, and aerobic methods is done by a great population of natural microorganisms leading to stability, handling, removing undesirable odors, and producing high humic materials. Compost is easy to store and supply for selling [13]. Many researchers have emphasized on efficiency of using earthworms in changing chemical manures to usable vermicompost manures in agricultural lands [2]. Adding earthworms to process of vermicompost is a proper technology to manage chemical manures. Earthworms' activities protect aerobic condition and increase speed of microbial decomposition. Weights of alive earthworms increase and their rich nutritious wastes are produced in this process [12]. Adding plumping

materials to animal manures increases worm activities and improve production quality [14]., 1999). Gondek&Filipek-Mazur [3] used conifer sawdust, cardboard trinkets, and straw trinkets as plumping by proportion of 15% mixture to prepare vermicompost manure. Arumuga et al. [15] used mixture of sludge, rice straw, and animal manure to prepare vermicompost in 2004. Vigueros& Ramirez-Camperos [10] used water hyacinth as plumping material. These researchers also saw significant reduction in population of coliform bacteria and parasite eggs. Eastman et al. [9] showed that population of fecal coliform bacteria and parasite eggs in vermicomposts were very lower than compost and producing vermicompost is a very proper substitute method for compost class A. Studies have been so limited in Iran particularly no study was about using native worms and effect of various plumping materials and their mixture proportion to sludge and worms reproductions. Naddafi et al. [16] (2004) used *Eisenia foetida* species in experimental level to produce vermicomposts from sewage sludge of Tehran. In Shahmansuri et al. [17] (2005) experiment, aggregation of heavy elements in native and importing earthworms, *Eisenia foetida* species, was explored in production process of vermicompost. The purpose of this study is exploring feasibility of

To whom all correspondence should be sent:
E-mail: samalbert_908@yahoo.com

changing animal manure to organic manure using native vermicomposts and changing useful chemical elements to feed pistachio trees in these manures. In addition, the best and most proper plumping material were examined for these manures.

METHODS AND MATERIALS

This study was done in a workshop near Sirjan city. Experiment was in framework of split factorial that steps of changing animal manure was considered as the main factor and type of plumping materials and mixture percentage were considered as factorial. Samples of animal manures were bought in bulk and initial experiments were performed to determine the present elements in these manures. Samples of manure types were dried and ground under 50 °C during 48 hr. 1 gr of this material was burnt in electric furnace and extracted by HCL 2N acid. The obtained extraction was used to determine all chemical elements (Jones et al,

1999). Chemical properties of manures in various decomposition steps were measured including PH, EC in extraction 1:5 (distilled water and materials), organic carbon by Walkley Black method, total nitrogen by Kjeldahl automatic system made by Gerhard Co. model 2020, total phosphorus by colorimetric method, total sodium and potash by flame photometer method, calcium and magnesium by complexometry, and Iron, copper, and zinc by spectrophotometry (Sparks, 1996). The most proper changing step, type of plumping materials, and proportion of mixing manures with plumping materials was determined using one-way variance analysis tests and Duncan compare means test by Spss and MSTATE software. Differences in mixture of manure with plumping was considered by proportion of 0%, 15%, 30%, and 45% and worm number in 1*1 environment was considered as 300 worms.

Table 1. Chemical properties of animal manures in initial decomposition step.

Properties	Sampling step			
	Sheep manure	Cow manure	Chicken manure	Fish manure
PH	8.00	7.5	7.5	7.2
Electric conduction (dS/m)	25.33	19.74	46.00	41.02
Organic carbon (%)	77.30	85	73.63	80.25
Total nitrogen (%)	3.22	2.71	4.08	3.55
C/N proportion	6.36	6.45	3.34	4.87
Phosphorus (%)	0.78	0.59	1.98	1.59
Potash (%)	2.98	2.24	1.76	3.35
Calcium (%)	1.80	1.42	7.11	4.45
Magnesium (%)	0.47	0.45	0.89	0.77
Sodium (%)	0.21	0.15	0.35	0.32
Iron (mg/kg)	4368.5	1856.13	1681.22	2023.10
Zinc (mg/kg)	148	209.8	462	380.70
Copper (mg/kg)	26.97	54.77	123.5	134.40
Magnesium (mg/kg)	352.78	238	528.39	446.23

Table 2. Chemical properties of plumping materials used in the test.

Properties	Plumping materials	
	Leaf of pistachio tree	Wood chip of pistachio tree
Organic carbon (%)	18.8	22.5
Total nitrogen (%)	1.12	0.092
C/N proportion	16.8	244.6
Phosphorus (%)	0.199	0.018
Potash (%)	0.21	0.11
Calcium (%)	3.2	4.8
Magnesium (%)	2.4	3.7
Sodium (%)	0.62	0.45
Iron (mg/kg)	23	19
Zinc (mg/kg)	0.2	0.5
Copper (mg/kg)	1.2	0.7
Magnesium (mg/kg)	3.45	3.6

Table 3. Comparison interactive effects of factors on worms' weights

Material	Mixture percentage	Worm weight
leaf	0 %	11.23 c
Leaf	15 (%)	19.23 bc
Leaf	30 (%)	14.99 c
Leaf	45(%)	13.04 c
Wood chip	0 (%)	12.99 c
Wood chip	15 (%)	21.17 b
Wood chip	30 (%)	32.79 a
Wood chip	45 (%)	24.35 b

Table 4. Chemical properties of animal manures in final step of analysis

Properties	Sampling step			
	Sheep manure	Cow manure	Chicken manure	Fish manure
PH	7.5	7.00	7.1	7.5
Electric conduction (dS/m)	28.23	23.13	49.13	45.60
Organic carbon (%)	81.45	91.50	79.12	89.33
Total nitrogen (%)	2.90	2.13	3.38	2.88
Phosphorus (%)	1.09	0.63	2.32	1.67
Potash (%)	3.34	2.54	1.97	3.67
Calcium (%)	1.85	1.45	7.12	4.40
Magnesium (%)	0.50	0.45	0.91	0.80
Sodium (%)	0.32	0.27	0.46	0.44
Iron (mg/kg)	4634.43	1987.87	1875.09	2365.37
Zinc (mg/kg)	156	231	495	410
Copper (mg/kg)	33.29	61.80	139.20	145.78
Magnesium (mg/kg)	355	241	530	448

RESULTS

Chemical properties of manures are shown in Table 1:

As it is seen, these manures have neutral PH and relatively proper EC for plants growth particularly pistachio tree. C/N for all 4 manures is proper (for cow manure is more than others) and this issue reduces necessity of using plumping materials to compensate carbon. Analysis of plumping materials (leaf and chips of pistachio trees) is collected in Table 2:

In this research, leaf of pistachio tree is used as plumping material for having proper C/N.

Leaf of pistachio tree was fully dried and mixed to 15% of animal manure and explored to 300 worms during 2 months. Results of table 4 shows analysis of composed animal manure by worms:

CONCLUSION AND DISCUSSION

Vermicompost is biologic organic manure obtaining by consistent steady passing of organic materials while decomposition in digestive system of earthworms species and removal of these materials from worms body. By passing these materials from worm body, they are stained to digestive system (Mucus), vitamins, and enzymes which are finally produced and used as a rich organic and very

useful manure for construction and soil nutritious elements improvement. To be assure of quality and security of organic manure, some parameters are controlled during composing process. These parameters are examined based on physical, chemical, and microbial analyses from the first to the end of process based on standards.

By comparison results of table 1 and 4, we can see that PH and EC didn't change so much. Organic carbon increased as interaction of animal manures with secretion materials of worms' digestive systems and nitrogen reduced for removal of some nitrogen compounds in worms as N₂ gas from the obtained compost. Other elements such as phosphorus, iron, zinc, and potash changed significantly which are really effective in growth of pistachio tree. According to increase in useful elements of vermicompost than initial manure, it is useful for pistachio trees, but usage amount should be mentioned, because some elements are not only harmful for pistachio trees, but also cause irreversible damages in their products.

REFERENCES

1. A.R. Parvaresh, H. Movahhedian, L. Hamidian, *Water & Waste Water*, **15**, 29 (2004).
2. C. Elvira, L. Sampedro, J. Dominguez, S. Mato, *Soil Biol. Biochem.*, **29**, 759 (1997).
3. K. Gondek, B. Filipek-Mazur, *Electronic Journal of Polish Agricultural Universities, Environmental Development*, **4** (2) (2001).
4. G. D. Harris, W.L. Platt, B.C. Price, *Biocycle*, **31**, 48 (1990).
5. J. B. Jones, B. Wolf, H.A. Mills, *Plant analysis handbook: A practical sampling, preparation, analysis and interpretation guide*. Macro-Micro Pub. Inc., Athens, GA, 1991, p. 23.
6. M. S. Maboeta, L. van Rensburg, *Water, Air Soil Poll.*, **150**, 219 (2003).
7. T. Manios, E.I. Stenifored, *J. Environ. Sci. Health*, **41**, 1235 (2006).
8. D.L. Sparks, *Methods of Soil Analysis, Part 3, Chemical Methods*. SSSA Book Series Number 5, Soil Science Society of America, Madison, WI, 1996.
9. B.R. Eastman, P.N. Kane, C.A. Edwards, L. Trytek, B. Gunadi, A.L. Stermer, J.R. Mobley, *Compost Sci. & Utilization*, **9**, 38 (2001).
10. C. Vigueros, E. Ramirez-Camperos, *Water Sci. Technol.*, **46**, 153 (2002).
11. <http://www.ejpau.media.pl/series/volume4/issue2/environment/art-01.html>.
12. E. Benitez, R. Nogales, C. Elvira, G. Masciandaro, B. Ceccanti, *Bioresource Technol.*, **67**, 297 (1999).
13. A. Quatmane, M. R. Provenzano, M. Hafidi, N. Senesi, *Compost Sci. & Utilization*, **8**, 124 (2000).
14. J. Dominguez, C. A. Edwards, M. Webster, *Pedobiologia*, **43**, 372 (1999).
15. G.K. Arumuga, S. Ganesan, R. Kandasamy, R. Balasubramani D.R. Burusa, 2004. Municipal Solid Waste Management through Anaecic Earthworm, *Lampito Mauritti* and their Role in Microbial Modification. Eco Service International, Available at: <http://www.eco-web.com/editorial/040831.html>
16. K. Naddafi, M. Zamanzadeh, A.A. Azimi, G.A. Omrani, A.R. Mesdaghinia, E. Mobedi, *Pakistan J. Biol. Sci.*, **7**, 1217 (2004).
17. M.R. Shahmansouri, H. Pourmoghadas, A.R. Parvaresh, H. Alidadi, *Iranian J. Env. Health Sci. Eng.*, **2**, 28 (2005).

Phytoremediation of cadmium, lead and zinc by *Medicago sativa* L. (alfalfa): A study of different period

Fu-qiang Wang^{*1,2}, Yu-juan Li¹, Qian Zhang³, Jiao Qu³

1 Department of Water Conservancy Engineering, North China University of Water Conservancy and Electric Power, Zhengzhou, Henan 450011, P. R. China

2 Collaborative Innovation Center of Water Resources Efficient Utilization and Protection Engineering, Henan Province, Zhengzhou 450045

3 School of Chemistry and Chemical Engineering, Bohai University, Jinzhou, Liaoning 121013, P. R. China

Received June 26, 2015; Revised September 10, 2015

Medicago sativa L. (alfalfa) has been reported to be extremely resistant to contaminants as well as a bioaccumulator. However, heavy metals accumulated by alfalfa in different period was less analyzed and reported. In the present experiment, the alfalfas grew for 10 days, 40 days and 80 days in different soils which were polluted by Cd, Pb, and Zn. It was found that: alfalfa could be applied for phytoremediation of soil polluted moderately by Cd, Pb, and Zn. Alfalfa could transfer heavy metals from roots to shoots in seedling period. Alfalfas had the higher biomass in maturation period. However, biomass of alfalfa was not significant difference in the same period. In different period, alfalfa showed the similar ability of accumulating Cd, Pb and Zn in roots and shoots. Compared with the shoots, the contents of Cd, Pb and Zn in the roots were higher. BCF (bioconcentration factor) values of alfalfa in Cd, Pb and Zn were higher in maturation period. Alfalfa had a better ability of accumulating Cd. TF (translocation factor) values of alfalfa were low and tended to decrease with the increasing contents of Cd, Pb and Zn in the soils.

Keywords: Heavy metals, Biomass, Bioconcentration factor, Translocation factor, *Medicago sativa* L

INTRODUCTION

Anthropogenic activities have concentrated some heavy metals in certain areas up to dangerous levels for living organisms [1]. Activities such as mining and agriculture have polluted extensive areas throughout the world [2, 3, 4, 5]. As well known, Cadmium (Cd) and lead (Pb) have long been considered as a major contamination problem, not only for working conditions but also for the environment [6, 7]. Cd and Pb were environmental pollutants mainly of anthropogenic origin [8, 9]. It was well known that zinc (Zn) in low concentrations was essential for plant growth [10, 11], nevertheless, beyond certain a threshold concentration, it became toxic for most plant species [12, 13].

Recently, there have been some studies on the ability of biomaterials or biomass to extract heavy metals from the environment, and phytoremediation has emerged as one of the alternative technologies for removing pollutants from the environment. Interest in using plants for environmental remediation was increasing due to their natural capacity to accumulate heavy metals and degrade organic compounds [14]. Phytoremediation was

defined as the use of plants to remove pollutants from the environment or to render them harmless [15]. Alfalfa was also found to show highly resistant to contaminants as well as a bioaccumulator [16]. Previously, Angle and Chaney [17] reported that alfalfa has the ability to accumulate concentrations of heavy metals well above the tolerance levels of other plants. Alfalfa may be a good source of plant tissues because it has been found to tolerate heavy metals and grow well in contaminated soils [18]. Further, alfalfa was shown to be used as a potential source of biomaterials for the removal and recovery of heavy metals [19]. In this work, the accumulation of Cd, Pb, and Zn by alfalfa in different period (seedling period, vegetation period, and maturation period) was investigated.

EXPERIMENTAL

Soil sources and preparation

The soil samples were collected from the Bohai University in Jinzhou city of Liaoning Province, China. The climate style belongs to the warm temperate zone, the annual average parameters were as follows: temperature 9.2 °C, rainfall 436.7 mm. The major heavy metals in the soil were Cd, Pb, and Zn. The physical and chemical properties of the soil were shown in Table 1.

To whom all correspondence should be sent:

E-mail: fortunewang@163.com

The salts used in this study included $\text{Cd}(\text{NO}_3)_2$, $\text{Pb}(\text{NO}_3)_2$, and $\text{Zn}(\text{NO}_3)_2$. The collected soils (5 kg) were added into each pot. The salts were separately diluted with deionized water, and all solutions were adjusted to pH 7.5-7.7 with HNO_3 and NaOH before being added into pots. The urea was added into soils of the pot to keep the N at the same level. Treatments were prepared at the concentrations of (1) control, Cd 7.843 mg/kg + Pb 55.120 mg/kg + Zn 221.078 mg/kg (following as S0); (2) treatment 1, Cd 8.143 mg/kg + Pb 105.120 mg/kg + Zn 271.078 mg/kg (following as S1); (3) treatment 2, Cd 8.843 mg/kg + Pb 155.120 mg/kg + Zn 346.078 mg/kg (following as S2); (4) treatment 3, Cd 17.843 mg/kg + Pb 355.120 mg/kg + Zn 471.078 mg/kg (following as S3); (5) treatment 4, Cd 27.843 mg/kg + Pb 555.120 mg/kg + Zn 771.078 mg/kg (following as S4).

Table 1. The physicochemical properties and patterns of soils.

Parameter	Soil
pH	7.63
organic matter	5.26 %
CEC	8.64 cmol/kg
total N	0.12 %
total P	0.06 %
total K	1.13 %
Cd	7.84±2.38 mg/kg ^b
Pb	55.12±5.07 mg/kg ^a
Zn	221.08±10.55 mg/kg ^a

^aSignificant at $p < 0.01$.

^bSignificant at $p < 0.05$. n=10.

Plant culture

Seeds of alfalfa were obtained from Tai Yuan Seed Company. Seeds were surface sterilized by immersion in 2% (v/v) H_2O_2 and shaken at 144 rpm on an orbital shaker in sterile deionized water for 6 h [20]. They were then sown onto stainless plates with aseptic gauze in incubator, and the temperature and moisture were kept at 25 °C and 60%, respectively. Seedlings grew at a length of 2 cm and then 60 seedlings were transplanted to each pot in a green house. After 2 days, pots were migrated and grew under natural conditions.

Analysis

In the experiment, 10 alfalfas were harvested by clipping the shoots and pulling out the roots randomly after they have grown for 10 days (seedling period), 40 days (vegetation period), and 80 days (maturation period), respectively. After the roots and shoots were washed with deionized water and dried in an oven at 70 °C for 72 h, the dry weights were recorded by electronic balance. The roots and shoots of alfalfa were digested at 150 °C for 200 min with 10 ml mixture of $\text{HNO}_3/\text{HClO}_4$ (4:1) [21]. The digestion was accomplished using the simple setting- furnace digestion and big cuvettes. Subsequently, the volume of digested sample was adjusted to 20 ml with double deionized water and analyzed using ICP-OES.

Two bio-concentration factors, BCF (bio-concentration factor, defined as concentration ratio of plant shoot to soil) and TF (translocation factor, defined as concentration ratio of shoot to root) computed from the treatments concentrations would be used to discuss the results of this study. All the data obtained from this study were analyzed by SPSS 13.0. The Duncan multiple range test was used to determine the statistical significant ($P < 0.05$). Controls and treatments were in triplicates for analysis.

RESULTS AND DISCUSSION

Biomass of alfalfa

After 10 days, 40 days and 80 days, 10 alfalfas were dried and recorded by electronic balance (table 2). The biomass of alfalfa, grown in soil polluted by different concentration of heavy metal, was not significantly different in the same period ($P < 0.05$). Appropriate heavy metals could promote alfalfa to accumulate the biomass, but high contents of heavy metals were harmful to alfalfa. It meant the alfalfa growing has been affected under the contents of the Cd, Pb, and Zn in soil.

Bioaccumulation of Cd, Pb, and Zn by alfalfa

After 10 days, 40 days and 80 days, alfalfa could uptake Cd, Pb, and Zn from the soil. Figure 1-3 show the total mass of heavy metals in the alfalfa's shoots and roots in three periods.

Table 2. Biomass of alfalfa.

Time	S0	S1	S2	S3	S4
10 days	12.98±1.12 ^b	14.57±1.39 ^b	13.30±0.82 ^a	13.26±1.01 ^a	11.12±0.78 ^a
40 days	39.64±2.99 ^a	46.70±2.63 ^a	41.29±1.93 ^a	43.71±2.67 ^a	32.06±1.48 ^a
80 days	56.32±3.23 ^a	68.15±3.71 ^a	62.37±2.54 ^a	65.22±2.48 ^a	40.80±3.85 ^b

Unit was mg/plant. ^aSignificant at $p < 0.01$. ^bSignificant at $p < 0.05$. n=10.

The contents of Cd, Pb, and Zn in alfalfa were the highest after alfalfas have grown for 80 days. Alfalfa accumulated more Cd and Zn with the increasing contents of Cd and Zn in the soils, but the contents of Cd, Pb, and Zn in alfalfa were not significant different in seedling period. Compared with the contents of Cd, Pb, and Zn in alfalfas which have grown for 80 days, 65.54%-94.58% of Zn, 63.98%-86.90% of Cd, and 60.38%-93.51% of Pb have been accumulated by them which have grown for 40 days. The contents of Cd, Pb, and Zn were higher in the roots than in the shoots, which may be it is related to both heavy metals uptake from the soils and xylem translocation from roots to shoots. The contents of Cd, Pb and Zn in alfalfa under treatment 3 level were highest in each period. It meant that Cd, Pb and Zn could be absorbed by alfalfa in soil polluted moderately. Alfalfa showed the similar ability of accumulating Cd, Pb and Zn in roots and shoots in the whole period. The accumulation of Cd, Pb, and Zn in both shoots and roots of alfalfas was increased with the increasing contents of Cd, Pb, and Zn in the soils, but the accumulation was decreasing after the contents of Cd, Pb, and Zn (especially for Pb) were achieved treatment 3 level in three periods, respectively. In general, Cd has greater toxic effects on plants than Pb and Zn. The damage to plants made by Cd could affect the growth of plants and tolerance to heavy metals much more than Pb and Zn. Thus, the content of Zn in the shoots was significantly higher than Cd and Pb, which was in accordance with the previous results found for alfalfa [22]. The content of Cd in roots of alfalfa was higher than Pb, and this result was agreed with that found for alfalfa [23]. The content of Pb in the alfalfa was low, and it was not agreed with the finding of alfalfa adsorbing metal order: $Pb > Zn > Cd$ [24], this may be due to the pH of soil and Pb bound by soil or alfalfa, the metal binding affinities for ligand in the soils, the antagonism of ions, chemical competition for multi-metal and physicochemical properties of Pb in the soils. Bioaccumulation depends not only on the characteristics of the organism itself, but also on the characteristics of the substance and the environment factors. With increasing contents of heavy metals in the soils, alfalfa showed performance to avoid and resist.

BCF and TF of alfalfa in Cd, Pb and Zn

BCF values were studied in each sample (Figure 4-6). BCF values of alfalfa in Cd, Pb and Zn were higher while alfalfas were grown, and BCF values of roots were higher than those of shoot. Also,

concentrations of heavy metals in soils could influence the abilities of phytoextraction, higher concentration maybe increase the contents of heavy metals in tissue compartments of plants [25].

The BCF values of shoots were nearly equivalent compared with roots in seedling period, since the xylem has not got formed during seedling period. After alfalfas have grown for 40 days, BCF values for Cd, Pb and Zn were higher. After alfalfas have grown for 80 days, BCF values for Cd were from 5.72 to 71.85 in shoots and from 13.75 to 571.97 in roots; BCF values for Pb were from 0.25 to 9.61 in shoots and from 0.34 to 98.25 in roots; BCF values for Zn were from 1.91 to 20.64 in shoots and from 2.75 to 43.65 in roots; the average BCF values of alfalfa for Cd, Pb, and Zn were 30.66, 3.63, and 7.47 in shoots and 250.21, 39.32 and 16.31 in roots, respectively. Values of BCF can be an index for the plant's ability to accumulate heavy metals. BCF values are different in response to concentrations, kinds of heavy metals, the accumulation ability, physiological factors of plants and environmental conditions. In this experiment, it was apparent that alfalfa had better ability of bioaccumulate Cd than Pb and Zn, the result was agreed with that found for alfalfa [20]. Alfalfa could uptake much Zn and Pb, but BCF values were not the highest, which may be due to the physiological and morphological characteristics of alfalfa, concentrations of heavy metal and conditions of environment.

The average values of TF were studied in each sample (table 3). The higher values of TF indicated that plants could move and distribute more heavy metals. The TF values of alfalfa were low, it showed that there were less Cd, Pb and Zn moved into shoots. The TF values of alfalfa tended to decrease with the increasing contents of Cd, Pb and Zn in the soils. The TF values in Zn were higher than Cd and Pb, maybe it is related to the characteristics of the alfalfa and characteristics of Cd, Pb and Zn in the soils. Since movement of heavy metal from roots to shoots was likely to occur via the xylem and to be driven by transpiration from the leaves, alfalfa could move much heavy metal from roots to shoots in seedling period. The study of heavy metals translocation and accumulation occurred predominantly via the phloem (Popelka et al., 1996). Cellular sequestration of Cd or Pb could have a large effect on the levels of free Cd or Pb in plants, thus, it can potentially influence the movement of Cd or Pb throughout the plant [20].

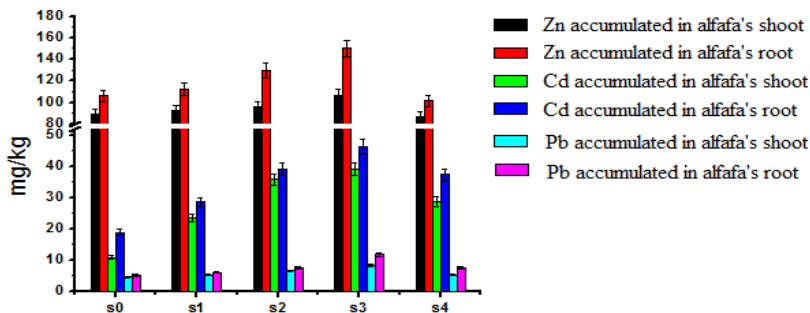


Fig. 1. Contents of Cd, Pb, and Zn accumulated in alfalfas after alfalfas have grown for 10 days. Significant at $p < 0.05$.

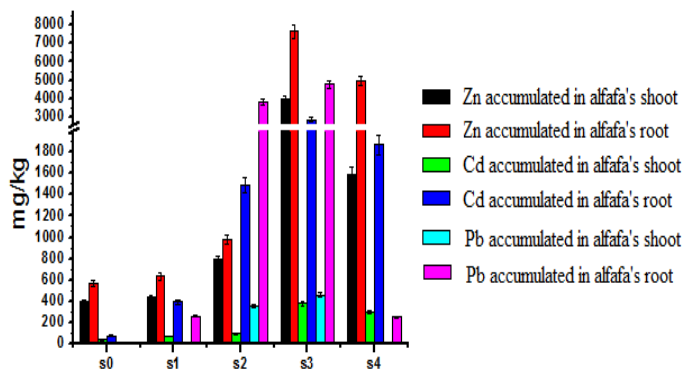


Fig. 2. Contents of Cd, Pb and Zn accumulated in alfalfas after alfalfas have grown for 40 days, Significant at $p < 0.05$.

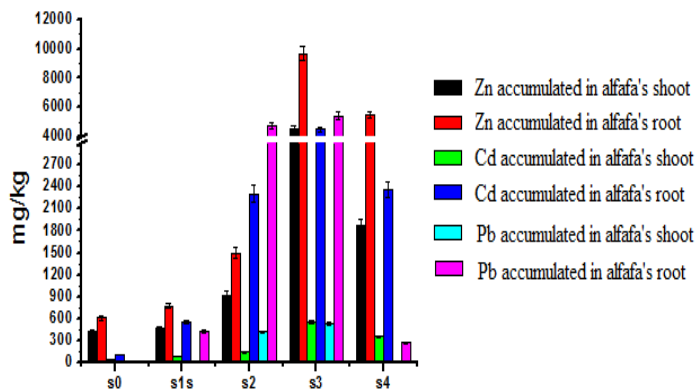


Fig. 3. Contents of Cd, Pb and Zn accumulated in alfalfas after alfalfas have grown for 80 days, Significant at $p < 0.05$.

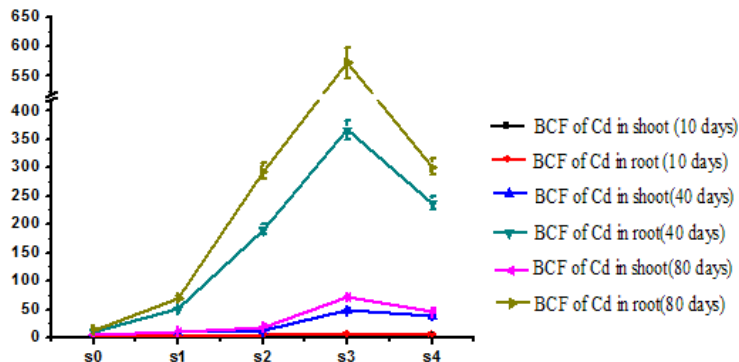


Fig. 4. Values of BCF of alfalfa for Cd. Significant at $p < 0.05$.

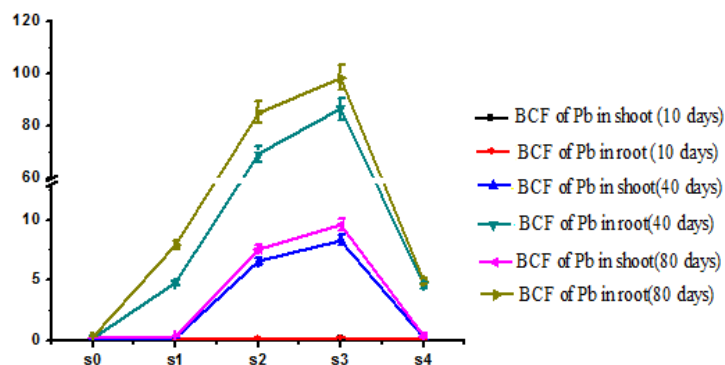


Fig. 5. Values of BCF of alfalfa for Pb. Significant at $p < 0.05$.

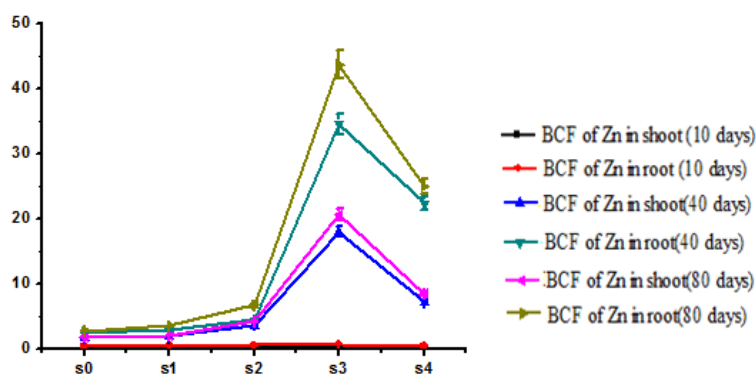


Fig. 6. Values of BCF of alfalfa for Zn, Significant at $p < 0.05$.

Table 3. The average TF values of alfalfa in Cd, Pb, and Zn.

days	Cd			Pb			Zn		
	10	40	80	10	40	80	10	40	80
S0	0.57	0.49	0.42	0.91	0.58	0.75	0.84	0.70	0.69
S1	0.82	0.18	0.15	0.87	0.06	0.05	0.83	0.69	0.61
S2	0.91	0.07	0.06	0.88	0.09	0.09	0.74	0.81	0.62
S3	0.85	0.13	0.13	0.71	0.10	0.10	0.71	0.52	0.47
S4	0.77	0.16	0.15	0.69	0.06	0.06	0.86	0.32	0.34

CONCLUSIONS

In this work, the accumulation of Cd, Pb, and Zn by alfalfa in different period was investigated. The results indicated that alfalfa had the higher biomass while alfalfa was grown. However, biomass of alfalfa, grown in soil polluted by different concentration of heavy metals, was not significantly different in the same vegetation period; the contents of Cd, Pb, and Zn in alfalfas were the highest after they have grown for 80 days. Alfalfa accumulated further Cd, Pb, and Zn with increasing contents of Cd, Pb, and Zn in the soils, but the contents of heavy metal in alfalfa were not significantly different in seedling period. Alfalfa had better ability of bioaccumulate Cd than Pb and Zn; the TF values of alfalfa were low and tended to decrease with the increasing contents of Cd, Pb, and Zn in the soils. The TF values in Zn were higher than Cd and Pb. Alfalfa could be applied for phytoremediation of soil moderately polluted by Cd, Pb, and Zn.

Acknowledgements: The authors acknowledge the National Natural Science Foundation of People's Republic of China (51379078, 51579101, 51409103 and 51379079), Science-tech Innovation Talents in University of Henan Province (15HASTIT044) and National Key Technology Support Program (2012BAC19B03).

REFERENCES

1. J. Chatterjee, C. Chatterjee, *Environ. Pollution*, **109**, 69 (2000).
2. N. Herawati, S. Susuki, K. Hayashi, I. F. Rivai, H. Koyama, *Bull. Environ. Contamination Toxicol.*, **64**, 33 (2000).
3. L. A. Brun, J. Maillet, P. Hinsinger, M. Pepin, *Environmental Pollution*, **111**, 293 (2001).
4. N. Zantopoulos, V. Antoniou, E. Nikolaidis, *Bull. Environ. Contamination Toxicol.*, **62**, 691 (1999).
5. S. Shallari, C. Schwartz, A. Hasko, J. L. Morel, *The Science of the Total Environment*, **209**, 133 (1998).
6. L. Freiberg, G. F. Nordberg, B. Vouk, *Handbook on*

- the toxicology of metals. oxford: Elsevier/North Holland Biomedical Press, Amsterdam, New York, 1979.
7. E. Merian, *Metalle in der Umwelt*. Weinheim: Verlag Chemie, 1984.
 8. J. Nriagu, *Arsenic in the environment, part I: cycling and characterization*. New York, 1989.
 9. J. Nriagu, *Arsenic in the environment, part II: human health and ecosystem effects*. New York, 1994.
 10. H. Kahle, *Environ. Exper. Botany*, **33**, 99 (1993).
 11. N. C. Brady, R. R. Weil, *The Nature and Properties of Soils*, twelfth-ed. Prentice Hall, Upper Saddle River, New Jersey, 1999.
 12. S. Monni, M. Salemaa, N. Millar, *Environ. Pollution*, **109**, **221** (2000).
 13. M. J. Blaylock, J. W. Huang, Phyto-extraction of metals. In: Raskin, I., Ensley, B.D, Eds. John, 2000.
 14. C. D. Scott, *Biotechnol. Bioeng.*, **39**, 1064 (1992).
 15. D. E. Salt, R. C. Prince, I. J. Pickering, I. Raskin, *Plant Physiol.*, **109**, 1427 (1995).
 16. G. R. Carrillo, L. J. Cajuste, *J. Environ. Sci. Health. Part A: Environ. Sci. Eng. Toxicol.*, **27**, 1771 (1992).
 17. J. S. Angle, R. L. Chaney, *Water, Air and Soil Pollution*, **57-58**, 597 (1991).
 18. V. C. Baligar, T. A. Campbell, R. J. Wriugh, *Plant Nutrition*, **16**, 219 (1993).
 19. J. L. Gardea-Torresdey, J. H. Gonzalez, K. J. Tiemann, O. Rodriguez, G. Gamez, *J. Hazard. Mater.*, **57**, 29 (1998).
 20. Z. X. Niu, L. N. Sun, T. H. Sun, Y. S. Li, H. Wang, *J. Environ. Sci.*, **19**, 961 (2007).
 21. F. Queirolo, P. Valenta, *Fresenius' J. Anal. Chem.*, **32**, 93 (1987).
 22. J. L. Gardea-Torresdey, K. J. Tiemann, G. Gamez, G. Gamez, K. Dokken, *J. Hazard. Mater.*, **69**, 41 (1999).
 23. J. L. Gardea-Torresdey, K. J. Tiemann, J. H. Gonzalez, O. Rodriguez, *J. Hazard. Mater.*, **56**, 169 (1997).
 24. J. C. Popelka, S. Schubert, R. Schulz, A. P. Hansen, *Angewandte Botanik*, **70**, 140 (1996).
 25. X. Y. Lu, C. Q. He, *J. Agro-Environ. Sci.*, **24**, 674 (2005).

A novel subsurface flow constructed wetland system used in advanced wastewater treatment for nutrient removal in a cold area

Changlong Pang, Ang Li*, Shan Qiu, Li Wang, Jixian Yang, Fang Ma*, Nanqi Ren

State Key Lab of Urban Water Resource and Environment, School of Municipal and Environmental Engineering, Harbin Institute of Technology, Harbin 150090, People's Republic of China

Received June 26, 2015; Revised September 10, 2015

Due to the limitations of a cold climate to a conventionally constructed wetland system (CWS) during annual operation, a new type of compound double-layer subsurface flow wetland system was developed. A full-scale test trial of this system has been operated in the Northeast of China, which was used for advanced sewage treatment. By increasing the depth of the wetland structure, setting down insulating material layers, filling with a high-efficiency compound substrate and using the bioaugmentation technology. The purification efficiency and the operational stability of this CWS has been effectively improved. The new type of double-layer subsurface flow of the CWS still showed a high purification capacity for organic matter in the winter. It was hard to obtain a high purification effect for the ammonia with the wetland system in winter because of the limitation of nitrification at low temperatures, but the system had a significant effect in denitrification and nitrate-nitrogen removal. The compound substrates provide a high performance of the system in Total Phosphorus (TP) removal.

Key words: Constructed wetland; Horizontal subsurface flow; Nutrient Removal; Cold areas

INTRODUCTION

Contaminant and nutrient discharged from sewage into an aquatic environment can cause serious pollution and the nitrification of lakes, rivers and sea coasts and is one of the major environmental concerns in the world [16]. The traditional municipal wastewater treatment technology is a challenge to small towns, for it requires sophisticated maintenance and management, high investment and high running costs. Furthermore, the wastewater treatment systems used in small towns also cannot produce effluent with a high quality, especially in nitrogen and phosphorus removal. Therefore, it is of great importance to develop the process for advanced wastewater treatment in rural areas and small towns. The constructed wetland system (CWS) is an efficient system for secondary or tertiary sewage treatment and as such could significantly improve the quality of wastewater effluent [1,5,6]. CWSs are widely used for domestic wastewater, agricultural wastewater and industrial wastewater as these are cost-effective, technically feasible and enhance the landscape quality [11, 19].

In China, the constructed wetland system is very suitable for decentralized wastewater treatment in small towns and the countryside. However, the cold climate in the Northeast of China has negative effects on the conventional CWS while in operation

through out the whole year [2, 17], which makes the CWS unsuitable in the traditional view for sewage treatment in the Northeast of China. This limits the field application of the constructed wetland system in north China. Nivala et al. [15] pointed out that the low temperatures could cause; the wetland system pipes to rupture, plant dormancy, rhizosphere microbial metabolism slow down or even system stoppage and other phenomena. The results indicated that the rate of nitrification and denitrification with temperature are positively correlated in constructed wetlands. The nitrogen removal is significantly impacted by the low temperature in winter, which is caused by the low activity of microbes and plants in the wetlands at low temperatures [7, 10]. In the cold winter, the low temperature of the water affects the operating efficiency of constructed wetlands, which can decrease the adsorption capacity of the media, increase the viscosity of the water, lower the diffusion rate, decrease the rate of water molecule transport in the roots, reduce the oxygen transfer efficiency, decrease the metabolic rate of the bacteria and plants, stimulate the accumulation of organic matter particles in the packed media and cause soil clogging. In addition, the temperature can affect the dissolved oxygen concentration and it will directly impact the aerobic treatment process. At low temperatures, the purification of the sewage by the wetland is not stable, which may lead to a suspension of function [12, 14]. In conclusion, the effective operation of traditionally constructed

To whom all correspondence should be sent:
E-mail: ang.li.harbin@gmail.com,
mafang@hit.edu.cn

wetlands in the cold is elusive.

In cold regions, the design and construction of CWSs have special requirements on the structure of the wetland, the selection of media, and the insulation measures. Compared with natural wetlands, the pollutants removal rate of the constructed wetlands depends largely on the substrates. The contaminant removal in the wetland bed depends mainly on the purification of substrates and microorganisms, especially after the plants are harvested in the autumn and winter [11]. The cold climate can strongly affect the efficiency of CWSs as well as the wastewater characteristics and the filling material composing the wetland. Therefore, it is necessary to develop systems for low temperatures together with appropriate design and operational criteria. For the problems faced by CWSs in the cold winter, the Subsurface Flow Constructed Wetland is generally designed as a major wetland in the cold regions. The cover of the substrates on the surface of the subsurface flow constructed wetland can reduce the energy loss due to sewage evaporation, transportation and flow. It is able to maintain and improve the temperature inside the wetland, which can protect the constructed wetland internal micro-organisms from the influence of the external low temperature [22]. At present, several measures have been used to ensure the effective operation of the constructed wetlands and to improve the purification at low-temperature. It includes increasing the depth of the wetland structure, applying insulating materials, artificial aeration, extending the hydraulic retention time and effluent return. It is of great importance to solve the problem that CWSs cannot operate normally in the freezing winter and develop a highly efficient constructed wetland system to be used in cold areas, especially in small towns and the countryside to control the decentralized point source and non-point source pollution.

MATERIALS AND METHODS

Experiment site and raw water quality

A full-scale test trial of the system for advanced sewage treatment has been constructed and operated in the Harbin Taiping Wastewater Treatment Plant (45°49' 0.51"N, 126° 43' 8.91"E) in the northeast of China. The experimental site is in a sub-frigid monsoon climate zone which has a winter as long as 6 months and the lowest temperature in winter can be lower than -30°C. The average temperatures through out the trial period were -10°C in the winter (from February to April, 2010) and 23°C in the summer (from May to

August, 2010).

The main purpose for developing the novel Subsurface Flow CWSs was to treat the secondary effluent of the small treatment plants, especially focused on total nitrogen (TN) removal, because most small sewage treatment plants in China are without the process for TN removal. The untreated water was the effluent of a high load sewage biological treatment reactor with a jet loop technology, which was focused on the COD (Chemical Oxygen Demand) and Ammonia Nitrogen removal with the aeration condition. The contaminant concentration range of the untreated water involved COD of 85~120 mg/L, SS (Suspended Solids) of 18~27 mg/L, NH₄⁺-N (Ammonia Nitrogen) of 18~30 mg/L, TN (Total Nitrogen) of 24~45 mg/L, TP (Total Phosphorus) of 1.3~3.9 mg/L.

The configuration of the constructed wetland system

In accordance with the characteristics of the cold climate and the sewage composition in the northeast of China, a new type of the compound double-layer subsurface flow constructed wetland system has been developed based on the conventional CWSs research. As shown in Fig. 1, the system has a structure with two layers of horizontal subsurface flow wetland. The tank of the full-scale trial wetland system was constructed by a 5 mm welding steel plate with waterproof an epoxy coating and the total size of the tank was 11 m long × 4m wide × 3m deep. The system consists of three main parts, including: an influent tank (2m long), the double subsurface flow constructed wetland (8m long) and an effluent tank (1m long).

The core of the system consists of the two layers of horizontal subsurface flow wetland and the total size of the wetland tank was 8m long × 4m wide × 3m deep with each part having a 1.2m deep substrate layer and a baffle plate between the two layers. To improve the microorganism activity and remove the phosphorus, a compounded substrate was filled in the top layer with grit, haydite, cinders and lime stones, while the under layer was filled with gravel, volcanic rocks and lime stones.

Cold-proof measures and operation of the system

The two layer wetland of the system was operated in an alternating mode. In the winter the sublayer was operated as a bio-filtration bed and the top layer was frozen as a thermal insulation materials layer to protect the under layer from the cold weather. Another measure for cold-proof was to set a 10 cm cover of dry straw and reed over the

top surface of the top layer wetland. The system can operate stably by the combined of cold-proof measures during the frozen winter. In the summer, the top layer was used and the contaminant was removed by the combined purification of the substrate, microorganisms and plants.

The untreated water from the biological reactor was introduced into the effluent tank and then the wastewater was fed to the wetland with a submerged pump (QDX1.5-16-0.37KW, Shanghai People Pump Factory Co., Ltd.). A pre-aeration device was equipped in the influent tank to improve the DO (Dissolved Oxygen) of wastewater. The effluent of the wetland system was discharged into the effluent tank and pumped out batch-wise with a submerged pump. There was another submerged pump placed in the effluent tank, which recirculates the water from the effluent tank to the front of the wetland in order to obtain a higher performance of organic matter and nutrients purification. The flow rate of the CWSs was 1.5-2m³/h monitored by an Electromagnetic Flow Meter (SITRANS F M MAGFLO MAG 1100, SIEMES Co., Ltd.) and the hydraulic retention time (HRT) was 19~26h. The top layer wetland was planted with reeds at a density of 16 rhizome/m².

Rapid start-up with bio-augmentation

In order to render the system a rapid start-up and enhance the performance of organic and nitrogen removal in the frozen winter, the engineering bacterium agent with a psychrotolerant denitrification consortium obtained by fast enrichment and domestication [8] was added into the constructed wetland, which can remove the ammonia, nitrate and organic matter simultaneously and efficiently at a low water temperature (<10°C). At system start-up, 200L of bacterium agents were added to the wetland system every three days, 3 times in total.

Analytical methods of the effluent

The influent and effluent of the CWS was measured each day by detecting the chemical oxygen demand (COD), ammonia nitrogen (NH₄⁺-N), total nitrogen (TN) and total phosphorus (TP) according to the standard methods [2]. Every sample had been detected 3 times and the results shown in the paper were the average of the 3 time detections.

RESULTS AND DISCUSSION

The performance of the cold-proof measures

In order to investigate the performance of cold-proof measures, the temperatures of the influent,

effluent and atmosphere in the system during the winter have been recorded (Fig.2). The temperature data shows that the atmospheric temperatures were low in the first month when the system was started, the average temperature was below -10°C and the lowest temperature reached about -25°C. The temperature of the influent was relatively stable, the average temperature was 13°C during the operational period in the winter and the lowest

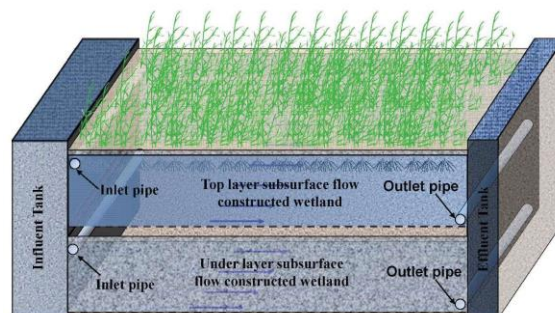


Fig.1 Double-layer subsurface flow constructed wetland system

temperature was 11°C. The temperatures of the effluent show that the cold-proof measures designed in the system can significantly reduce the heat loss from the inner wetland and the average temperature of the effluent was 10.6°C during the winter operation period with an average temperature drop less than 3°C. The temperatures of wetland effluent could still be above 7°C in the coldest period (temperatures about -25°C), which can allow for normal system operation and stable purification. In contrast, a pilot-scale wetland system (volume 4 m³) used in the previous winter was completely frozen when the air temperatures fell below -10°C. The results prove that the structural design of the double-layer constructed wetland and the cold-proof measures can make the system operate stably without freezing in the cold of Northeast China.

Organic matters and suspended solids removal

The purification effect of the system on organic matter during the two periods (winter and summer) is shown in Fig. 3. The results indicate that the system had a good performance for organic pollutant removal under at a low temperature and high hydraulic loading operational conditions. The main purpose for developing the novel CWSs was for the advanced treatment of the secondary effluent of the small treatment plants, focused on Total-Nitrogen removal, but the system can also purify the organic contaminant. The effluent COD concentrations were 43 to 55mg/L in winter and 40 to 50mg/L in summer, while the influent COD concentration was 85 to 120 mg/L. The average

effluent COD concentration of the CWSs was $46.4 \pm 4.3 \text{ mg/L}$ in winter and $41.4 \pm 2.2 \text{ mg/L}$ in summer, the average removal rate of the COD was 51.5 % in winter and 57.0 % in summer. The bio-augmentation with adding the psychrotolerant bacterium consortium agent has obviously improved the organic removal performance at low temperature. The average removal rate of the COD was 44.2 % in the first ten days and then the removal rate has been improved to about 55 % after adding bacterium agent.

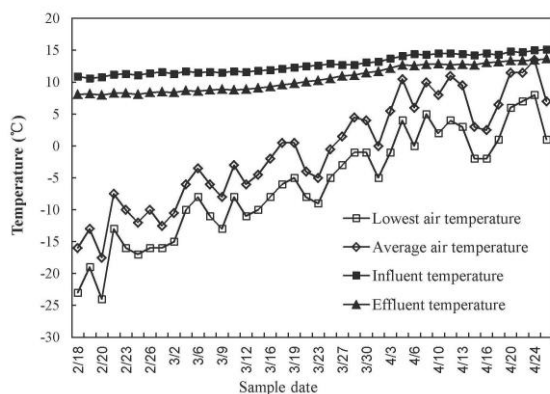


Fig. 2. The temperatures of the influent, effluent, and atmosphere in the system during the winter.

Furthermore, the CWSs had a good performance in Suspended Solid removal during the whole period of operation. The values for SS in the effluent were always lower than 10 mg/L and the effluent showed an excellent sensory indicator. The mechanisms of purification of SS by the wetland system mainly include the filtration of the suspended particulates with the substrate, the flocculation and settling of colloidal particulates with a bio-film attached to the substrate [4, 20]. This subsurface flow constructed wetland has played a role as a filter bed and the suspended solids have been removed effectively by the filtration of the fine and polyporous substrates.

The removal of the organic matter in the wetlands is largely regulated by microorganisms and their metabolism. The microbial biomass is a major sink for organic carbon and many nutrients. In the winter, the system was operated to purify the wastewater in the under layer. With the function of the top layer as an insulating materials layer and other anti-freezing measures, the inner temperature of the wetland has been improved significantly with the effluent at 8~10°C in the frozen winter. Without plants, the under layer subsurface wetland acts as a fixed-film bioreactor and the bio-augmentation has been used to improve the purification ability at low temperatures. The contaminant was removed by the combined purification of the substrate and

microorganisms. The mechanisms of the particulate organic matter removal were similar to suspended solids separation in the horizontal substrate beds. The dissolved organic matters from the influent or cycled from solids decomposition could likely be adsorbed on the biofilm surfaces attached to the media and they would be purified by the assimilation or degradation of the microorganisms. The predominant metabolic pathways leading to organic matter removal from the system were the aerobic reaction and denitrification. The aerobic reaction was most likely to occur in the front of the wetland because of the pre-aeration in the influent tank. The operation results suggest that the purification efficiency and the operation stability of the CWSs has been improved effectively by placing an insulating top substrate layer and surface materials cover filling into a high-efficiency compound substrate and applying the bio-augmentation technology. The new type of double-layer subsurface flow CWS still showed a high purification capacity of the organic matter in the winter.

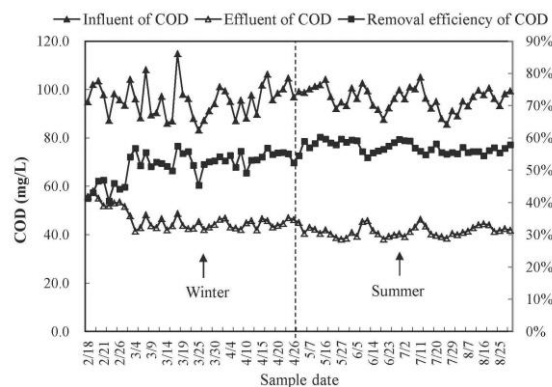


Fig. 3 The performance of COD removal in a CWS over the winter and summer.

Nitrogen removal

The concentrations of the TN, $\text{NH}_4^+\text{-N}$ and $\text{NO}_3^-\text{-N}$ in the influent and effluent of the CWSs during the winter and summer periods has been measured and the statistical results of 40 samples in winter and 41 samples in the summer is been shown in Fig. 4. The TN, $\text{NH}_4^+\text{-N}$, and $\text{NO}_3^-\text{-N}$ average concentrations of effluent were $19.7 \pm 4.5 \text{ mg/L}$ (range from 14 to 29mg/L), $15.7 \pm 3.9 \text{ mg/L}$ (11 to 21 mg/L), $4.6 \pm 2.5 \text{ mg/L}$ (3 to 8 mg/L) in the winter, and $16.6 \pm 3.6 \text{ mg/L}$ (9 to 27mg/L), $7.6 \pm 2.7 \text{ mg/L}$ (5 to 16 mg/L), $6.3 \pm 1.9 \text{ mg/L}$ (4 to 11 mg/L) in the summer, while the TN, $\text{NH}_4^+\text{-N}$ and $\text{NO}_3^-\text{-N}$ average concentration of influent were $34.0 \pm 7.7 \text{ mg/L}$ (24 to 45mg/L), $23.1 \pm 5.1 \text{ mg/L}$ (18 to 30mg/L) and $9.4 \pm 3.6 \text{ mg/L}$ (6 to 15 mg/L). This indicated that the under layer constructed wetland in the winter obtained a relatively higher removal

rate of $\text{NO}_3\text{-N}$ (average 51%), but a lower rate of $\text{NH}_4^+\text{-N}$ removal (average 32%) and the average removal rate of TN was 42% in the winter. In summer, the top layer constructed wetland, yields a much better performance for $\text{NH}_4^+\text{-N}$ removal (average 67%) than that in the winter and the average removal rate of TN was 51%.

The predominant pathways for nitrogen (N) removal in CWSs contain the assimilation and storage by plants and microorganisms, burial of organic N and the production/release of N_2 [21]. In these processes, N_2 release represents the only permanent removal mechanism of N from the waste stream. The production of N_2 in wetlands has been principally attributed to the process of nitrification-denitrification and the anammox process can also contribute to the N_2 production in CWSs [9, 18]. For this constructed wetland, the nitrogen removal pathways from the top layer of wetland in the summer was the combined nitrification/denitrification process by the microbes, the absorption and assimilation process by the plants. The under layer wetland can depend mainly on the nitrification/denitrification process to remove the nitrogen. On the other hand, the temperature was an important factor in the nitrification of constructed wetlands [23], the reaction likely slowed down by the low temperature. Therefore, by using this wetland system it was hard to obtain a high purification effect on the ammonia in the winter, but the system performed well in denitrification or the nitrate nitrogen removal at low temperatures.

Phosphorus removal

The purification performance of TP in the CWSs is shown in Fig. 5. The TP average concentrations of effluent were 0.49 ± 0.14 mg/L (0.38 to 0.69 mg/L) in the winter and 0.46 ± 0.13 mg/L (0.36 to 0.62 mg/L) in the summer, while the influent TP average concentration was 2.10 ± 0.95 mg/L (1.3 to 3.9 mg/L). The results pointed out that the wetland system showed a good performance of phosphorus removal both in the winter and summer. The average removal rates of TP were 76.7% in the winter and 78.1% in the summer.

The mechanisms of phosphate removal from wetland systems mainly include the uptake by plants, the transformation by microorganisms and the precipitation/exchange/sorption by the substrates [13].

Since there is no important gaseous component in the biogeochemical cycle, phosphorus tends to move to the sediment sink in natural systems and become scarce in the ecosystem. In fact, it is the accretion of mineral phosphates and biomass in the

sediment that is the primary mechanism for phosphorus removal in the wetland environment. The TP removal by the under layer wetland in the winter depends mainly on the adsorption of the substrates, the biofilm and the high performance of TP removal indicated, that the compound substrates of gravel, volcanic rocks and lime stones had a strong capability of phosphate removal.

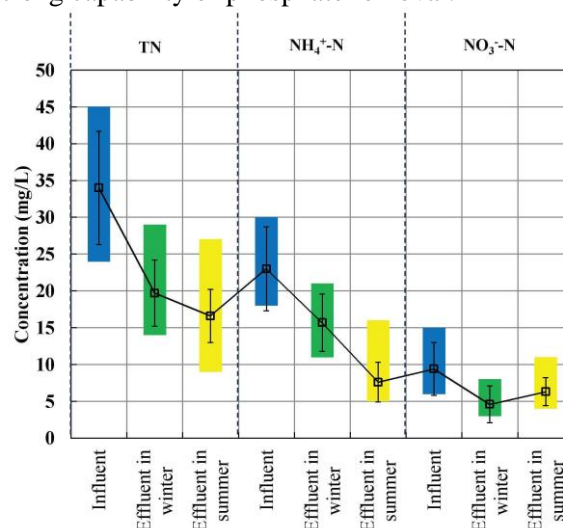


Fig. 4 Concentrations over the winter and summer of the Total Nitrogen, Ammonia Nitrogen and Nitrate-Nitrogen inflow and outflow of the wetland system.

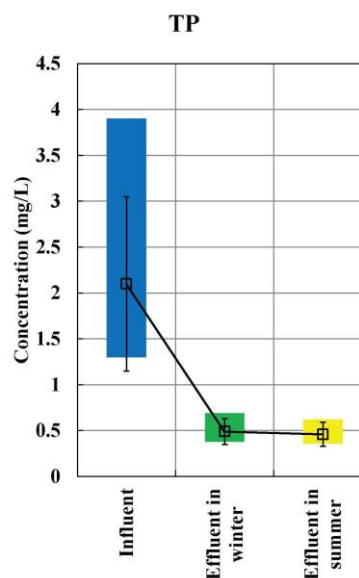


Fig. 5. Concentrations over the winter and summer of the Total Phosphorus inflow and outflow of the wetland system.

CONCLUSION

A novel compound double-layer subsurface flow constructed wetland system has been developed and a full-scale test trial of this system was used in advanced sewage treatment in the northeast of China. The design of the double-layer constructed wetland with an insulating surface materials cover

filling and a high-efficiency compound substrate applying the bio-augmentation technology, the operational stability of the CWSs have been improved effectively, while in use through the freezing winter. The novel double-layer subsurface flow constructed wetland system maintained a high purification capacity for the organic contaminants at low temperatures. There was a relatively low removal rate of the ammonia in the system during the winter because of the limitation of nitrification by the low temperature, but the system had a much better performance in denitrification for nitrate nitrogen removal, where the system average TN removal rate was about 42%. The compounded substrates provide the system with a high performance of TP removal. The results of this full-scale research study can be used for determination of the technologically feasible and applicability of advanced wastewater treatment systems in the northernmost province of China, which was considered unsuitable for using CWSs in the past. The novel structure of CWSs can be used to solve environmental problems caused by decentralized wastewater systems in small towns and the countryside in Northern China.

Acknowledgments: This work was supported by the National Creative Research Group from the National Natural Science Foundation of China (No. 51121062), the National Natural Science Foundation of China (Nos. 51108120, 51178139 and 51179041), the 4th Special Financial Grant from the China Postdoctoral Science Foundation (No. 201104430) and the 46th China Postdoctoral Science Foundation (No. 20090460901).

REFERENCES

1. T. Masuko, A. Minami, N. Iwasaki, T. Majima, S. Nishimura, Y. C. Lee, *Anal Biochem.*, **69**, 339 (2005).
2. C.S. Akrotosa, V.A. Tsihrintzis. *Ecol.Eng.*, **29**, 68 (2007).
3. APHA: Standard methods for the examination of water and wastewater. American Public Health Assoc, Washington DC, 2005.
4. A. Caselles-Osorio, J. García, *Water Res.*, **40**, 3603 (2006).
5. J E. Cloern, *Marine Ecol. Progr. Series.*, **210**, 223 (2001).
6. D. V. Erler, B. D. Eyre, L.Davison, *Environ. Sci. Technol.*, **42**, 9144 (2008).
7. S. Gray, J. Kinross, P. Read, A. Marland, *Water Res.*, **34**, 2183 (2000).
8. J.B. Guo, J. H. Wang, D. Cui, L. Wang, F. Ma, C.C. Chang, J.X. Yang, *Bioresource Technol.*, **101**, 6622 (2010).
9. R.H. Kadlec, C.C. Tanner, V.M. Hally, M.M. Gibbs. *Ecol. Eng.*, **25**, 365 (2005).
10. M.E. Kaseva, *Water Res.*, **38**, 681 (2004).
11. A.K. Kivaisi. *Ecol. Eng.*, **17**, 545, (2001).
12. P. Kuschik, A. Wiessner, U. Kappelmeyer, E. Weissbrodt, M. Kastner, U. Stottmeister, *Water Res.*, **37**, 4236 (2003).
13. I. Lawrence. Bowden, P. Adam. Jarvis, L. Paul. Younger, L. Karen. Johnson, *Environ. Sci. Technol.*, **43**, 2476 (2009).
14. P. Munoz, A. Drizo, W.C. Hession, *Water Res.*, **40**, 3209 (2006).
15. J. Nivala, S. Wallace, G. Parkin, *Sci. Total Environ.*, **15**, 19 (2007).
16. O. Oenema, C.W.J. Roest, *Water Sci. Technol.*, **37**, 19 (1998).
17. C. R. Picard, L. H. Fraser, D. Steer, *Bioresource Technol.*, **96**, 1039 (2005).
18. J. T. Scott, M. J. McCarthy, W. S. Gardner, R. D. Doyle, *Biogeochemistry.*, **87**, 99 (2008).
19. U.S. EPA: Constructed Wetlands Treatment of Municipal Wastewaters. Office of Research and Development, Ohio, U.S.EPA, 2000.
20. J. Vymazal, *Ecol. Eng.*, **25**, 478 (2005).
21. J. Vymazal, *Sci. Total Environ.*, **48**, 380 (2007).
22. H.B. Wittgren, T. Maehlum, *Water Sci. Technol.*, **35**, 45 (1997).
23. S. B. Wu, D. X. Zhang, D. Austin, R. J. Dong, C. L. Pang, *Ecol. Eng.*, **37**, 1789 (2011).

Optimization electrophotocatalytic removal of acid red 18 from drinking water by the Taguchi model

Kashi Giti^{1*}, Jaberzadee Narges²

¹Department of Environmental Health, School of Health, Islamic Azad University Tehran Medical Sciences Branch, Tehran, Iran

²Department of Natural Sources Engineering, Environmental Pollution, Department of Environmental, Islamic Azad University, Damavand Pardise Science and Research Branch, Damavand, Iran

Received June 26, 2015, Revised September 10, 2015

The aim of this applied-analytical research was to investigate acid red18(AR18)removal from water by a batch EPC reactor using zinc oxide (ZnO) nanoparticles immobilized on a zinc(Zn) sheet-copper electrode and an emitting dynode(LED)ultraviolet-A (UV-A) lamp. Various operating variables were tested; these include current density, initial concentration of AR 18, lamp intensity, concentration of ZnO nanoparticles, pH and radiation time. To prepare the ZnO films on the Zn electrode dry methods were used. The studied variables were pH(4-10), AR 18 concentration (100-300 mg L⁻¹), lamp intensity(120-360 mW cm⁻²), radiation time(0-45 min), concentration of zinc oxide nanoparticles(1.5-4.5 mg cm⁻²) and current density(3-9 mA cm⁻²). The AR 18 concentration was measured by a spectrophotometer. The optimal removal(0) was obtained at pH 4, a radiation time of 30 minutes, 3 mg cm⁻² of ZnO nanoparticles concentration, lamp intensity of 360 mW cm⁻² and a current density of 9 mA cm⁻². The AR 18 degradation followed a first order reaction. The results of AR 18 removal efficiency via the Taguchi model indicated that the concentration was the most important variable. The rate of degradation decreased at higher concentrations. Thus, batch experiments showed that the EPC reactor can be considered a promising technology for treating AR 18-polluted water.

Key words: Acid red 18 (AR 18), Drinking water, Electrophotocatalytic, Taguchi model, Zinc oxide.

INTRODUCTION

We deal with a variety of chemical materials in the textile effluent such as enzymes, detergents, dyes, sodas, salts and acids [1]. Annual azo dyes (-N=N-) production in the world during 2010 is estimated to be about 350000 tons, including red, yellow, orange, blue, black, green and violet [2]. The characteristics of acid red 18 (AR 18), C₂₀H₁₁N₂Na₃O₁₀S, is a low lethal dose (8000 mg kg⁻¹ bw in rat fed). AR 18 is approved for use as a food colorant and as a direct dye in semi-permanent hair dye. Azo dyes may be due to their toxicity a source of a potential danger to both human health and the environment [3]. The textile industry in Iran has been situated mainly in Yazd, Kashan and Mazandran states. The increase in AR 18 levels in the groundwater in the country of Iran has been mainly attributed to the discharge of dye effluent. The national emission standard for discharging into a surface water source has been promulgated as 75 TCU. A wide range of traditional methods are used for the treatment of AR 18-contaminated water including adsorption, chemical precipitation and

reverse osmosis [4]. In recent years, advanced oxidation processes (AOPs) such as electrophotocatalytic (EPC) are applied to treat the dye-contaminated water [5]. The presence of a catalyst in the electrical field or combined and direct photoelectrochemical application increases the treatment efficiency with lower energy consumption [6]. This process is a coupling of electrochemistry with heterogeneous photocatalysis to avoid photohole/photoelectron recombination [7]. The advantages of a thin layer electrophotocatalyst stabilized on a metal surface are; more homogeneous UV radiation of the catalyst and avoiding filtration [8]. Effective factors for the optimal performance of a thin layer electrophotocatalyst stabilized on a metal surface are: the catalyst gap bond, layer thickness, light intensity, oxygen and the presence of particles [9]. In this study the coupling of a light emitting dynode (LED) UV-A lamp and immobilized zinc oxide (ZnO) semiconductor on a zinc (Zn) electrode have introduced a new method to meet the efficient decay of AR 18. The aim of this study is the removal AR 18, an azo dye which is considered a dye stable to ultraviolet and visible light irradiation, from drinking water using a thin layer of photocatalytic ZnO nanoparticles stabilized on Zn.

To whom all correspondence should be sent:
E-mail: g.kashi11@yahoo.com

The studied variables are pH, the concentration of AR 18, the lamp intensity, the radiation time, the concentration of zinc oxide nanoparticles, and the current density.

EXPERIMENTAL

Materials

The ZnO nanoparticles with a special area of 50 m² g⁻¹ and particle size of 20 nm were supplied by Amohr Co. (Germany). Sulphuric acid, AR 18, and sodium hydroxide were purchased from Merck Co. (Germany). Sulphuric acid and sodium hydroxide (1 N) were applied for pH adjustment.

Preparation of ZnO nanoparticles

5 grams of ZnO nanoparticles were placed into 100 ml of distilled water. To improve the dispersion of ZnO, the suspension was mixed with a magnetic stirrer for 30 min and then sonicated in an ultrasonic bath (MATR.N.B., Italy) in distilled water at a frequency of 50 kHz for 22 min.

Immobilization of ZnO nanoparticles

To prepare the ZnO films, dry methods were used [10, 11]. After the pre-treatment, the Zn electrode was weighted, immersed in the colloidal solution and dried in an oven (Dyna, Iran) at 35°C for 30 min. The coated particles were then calcined in a muffle furnace (Shoele, Iran) at 105 and 320°C for 60 min.

Batch EPC reactor

The batch reactor was a 250-ml glass vessel (10×5×5 cm) (Figure 1). The characteristics of the electrodes were as follows: two electrodes of a thin layer of ZnO nanoparticles were immobilized on a Zn (anode) and a copper electrode (cathode). The area of each electrode was 40 cm² (10×4×0.1 cm). The distance between the LED UV-A lamp and the Zn/ZnO electrode was adjusted to 2 cm. The alternating current (AC) electrical source (Iran Jahesh, Iran) was equal to 1-5 A. The LED UV-A lamp (OSRAM, Holand) had a radiation intensity of 120 mW cm⁻², a wavelength of 395 nm and a voltage of 3.4 V. To evaluate the effect of the current densities, catalyst and UV light on the degradation process, samples underwent LED UV-A lamp treatment at (120, 240, and 360 mW cm⁻²), with an electrode and thin layer of ZnO nanoparticles immobilized on Zn of (1.5, 3, and 4.5 mg cm⁻²) at different current densities (3, 6, and 9 mA cm⁻²), different pHs (4, 7, and 10) and different radiation times (15, 30, and 45 min.).

Analytical methods

All tests were performed in triplicate and the mean data values were reported. The water samples were tested for AR 18, oxidation reduction potential (ORP), pH and temperature by EPC using a spectrophotometer (Hack, America), ORP-meter (CG, Malesia), pH-meter (Hack, America), respectively. The percentage of AR 18 removal was calculated in accordance with the following equation [12]:

$$R(\%) = [1 - (C_t / C_0)] \times 100 \quad (1)$$

where R was the percentage of AR 18 removed, C₀ and C_t were the average of AR 18 concentrations in milligrams per before and after treatment.

The kinetics reaction models were determined from the following Equations (2) and (3):

$$\ln C_t = \ln C_{t0} - K_1 t \quad (2)$$

$$1 / C_t = K_2 t + 1 / C_{t0} \quad (3)$$

where C₀ and C_t are the concentrations of AR 18 in the beginning and after a time (t) of the reaction, respectively. K₁ and K₂ were the first and second order reaction constants, respectively [13].

Preparation of water sample

AR 18-contaminated water samples used for EPC experiments were obtained from an urbane distribution system situated at the site of a laboratory in the Islamic Azad University Tehran Medical Sciences Branch in the city of Tehran. The AR 18 was measured by a standard method 2120 C at a wavelength of 510 nm [14]. After each round of the study, reactor water was picked and analyzed to evaluate the efficiency of the removal process. EPC experiments were duplicated and all samples were analyzed in triplicate.

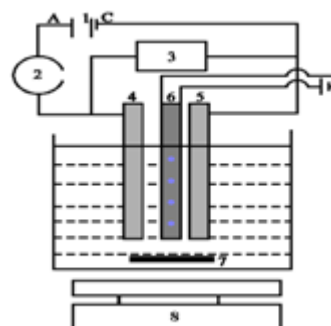


Fig. 1. The batch EPC reactor with a thin layer of ZnO nanoparticles immobilized on Zn (1.Power supply; 2.Current volume; 3.Voltage volume; 4.Copper electrode; 5. Zinc/Zinc oxide electrode; 6. Light emitted dynode ultraviolet-A lamp; 7. Magnetic stirrer bar; 8. Magnetic stirrer

RESULTS AND DISCUSSION

The effect of the initial concentration of AR 18 on the removal efficiency of the EPC process was investigated (Figure 2). The removal efficiency was decreased by an increase in the concentration from 100 to 300 mg L⁻¹. The EPC reactor showed that the removal percentage for an AR 18 concentration (100 mg L⁻¹) decreased from 100% to 82% as the pH increased from 4 to 10, with 15 min. irradiation. The EPC reactor showed the removal percentage for an AR 18 concentration (300 mg L⁻¹) decreased from 82% to 62% as the pH increased from 4 to 10, with 15 min. irradiation. This effect was attributed to increasing the concentration of AR 18 and accordingly fixed the number of photocatalytic sites and UV-A light due to an increase of the adsorbed AR 18 molecules on the catalyst surface. Therefore, fewer photons reached the catalyst surface and the production of OH[•] radicals decreased because the photocatalytic sites were occupied by AR 18 molecules. The Rate of degradation was decreased. The higher AR 18 concentration played an important role for the inhabitation of OH[•] radicals during production. Alizadeh *et al.* (2013) investigated the effect of electrocoagulation degradation on the dye reactive orange 16. These experiments were performed at an initial dye reactive orange 16 concentration in the range of 50 to 250 mg L⁻¹ at a reaction time of 5 min., a current density of 20 mA cm⁻² and the removal percentage for dye reactive orange 16 decreased to 10% as the concentration increased from 50 to 250 mg L⁻¹ [15]. Abdelwahaba *et al.* (2009) investigated the effect of electrocoagulation degradation on phenol. These experiments were performed at an initial phenol concentration in the range of 0 to 300 mg L⁻¹ at pH 7, a reaction time of 120 minute, a distance between the aluminum electrodes of 2 cm and a current density 19.3 mA cm⁻² [16]. At higher concentrations, the efficiency began to decrease. The EPC reactor reached the highest efficiency (100%) at pH 4, a radiation time of 15 minutes and a concentration of 100 mg L⁻¹. The photocatalytic exposure times required for complete degradation (100 and 200 mg L⁻¹) were 15 and 30 min. This finding was in agreement with previously published data. Saggiaro *et al.* (2011) performed an initial study with a C.I Reactive Black R 5 concentration in the range of 30 to 150 mg L⁻¹ at acidic pH, TiO₂ 0.1g L⁻¹, an irradiation time of 120 min. and a radiation intensity of 260 mW cm⁻² [17]. At lower concentrations, the photocatalytic exposure time required for complete AR 18 degradation began to decrease. Meena *et al.* (2013) indicated that Methylene Blue immobilized resin Dowex-11

(MBIRD) photocatalyst nanoparticles degraded 40 mg L⁻¹ of AR 18 in 160 minutes [18].

The degradation effect of this method was strongly dependent on pH and was enhanced by a decrease in pH. In the EPC process, different concentrations of OH[•] radicals from water were formed depending on the pH. These products played an important role in the removal of AR 18 concentrations in the EPC process. This effect was attributed to an increase in the availability of OH⁻ anions at an acidic pH that generated more OH[•] radicals due to decreasing ORP. Basiri *et al.* (2014) investigated the effect of ozone-electrolysis degradation on Azo dye CI AR 18 and informed that the optimum pH was 2 [19]. The decrease in AR 18 removal at pH 10 could be attributed to increasing the oxidation of hydroxide anions in the anode. The optimum pH for reaching the AR 18 standard was 4. The above increased mineralization activity was explained by a higher formation of ROS in the reactor due to accelerating the mass transfer by electron migration of the AR 18 towards the electrode. This effect was also attributed to a decrease in the reduction potential of the reactor at an acidic pH that generated more OH[•] radicals. The initial and final pH values were measured in this study in order to investigate the effect of pH more effectively. The initial pH was enhanced during EPC studies (Figure 2-3). The EPC reactor reached the highest efficiency (100%) at pH 4, radiation time 15 minutes, ZnO nanoparticles 3 mg/cm², distance between the LED UV-A lamp and Zn/ZnO electrodes 2 cm, LED UV-A lamp intensity 360 mW cm⁻², current density 3 mA cm⁻² and an AR 18 concentration of 100 mg L⁻¹. pH 4 requires a lower current density, compared with the two other current densities. The point zero charge point (zpc) of the ZnO was at pH 9.05. The excess positive charge at the ZnO surface, developed the power interaction of the dye with the SO₃⁻ groups in acidic conditions (pH ≤ pH_{ZPC}). The SO₃⁻ groups at AR 18 can gain or lose protons depending on the pH of the sample. Mahanpoor *et al.* (2008) reported using TiO₂ supported on clinoptilolite as a catalyst [20].

The removal percentage for an AR 18 concentration (300 mg L⁻¹) increased from 12% to 15% as the LED UV-A lamp intensity increased from 120 to 360 mW cm⁻², with 45 min. of radiation and at pH 4 (Figure 4). The removal efficiency of AR 18 was proportional to the LED UV-A lamp intensity and enhanced by an increase in the LED UV-A lamp intensity since the greater the number of photons produced, required more electrons to migrate from the valence band to the conduction band of the photocatalyst. Kundua *et al.*

(2009) reported the concentration 50 mg L^{-1} of 2,4-dichlorophenoxyacetic acid (2,4-D) decreased progressively from 49.5 mg L^{-1} to 30 mg L^{-1} as the UV-C lamp power increased from 100 to 400 W [21]. At a higher lamp intensity, the exposure time and current density start to decrease. The above increase in optical activity was explained by a higher formation of reactive oxygen species (ROS), such as electron donor OH^\cdot radicals from hydroxide anions of water and superoxide anion ($\text{O}_2^{\cdot-}$) radicals. This phenomenon was attributed to the efficient separation of photo generated holes and electrons, reducing their recombination by the application of an external electric bias. Consequently, more holes were available for the degradation of AR 18 and its intermediates; the photocatalytic process in the EPC process was more effective than the photoelectrochemical (PEC) process alone. This finding was consistent with photocatalytic experiments performed using Ti/TiO₂ nanoparticle electrodes [22]. The removal rate at the same reaction time during the EPC process was larger than the sum of for the PEC and electrochemical (EC) process. Therefore, a synergetic effect was proved, which is consistent with the result in Figure 4. The trend of a linear increase in the degradation rate for AR 18 at given UV-A lamp intensity was explained by producing more electron/hole pairs due to the availability of more photons for excitation at the Zn/ZnO surface.

The removal percentage for AR 18 concentrations dramatically increased in the presence of ZnO photocatalyst nanoparticles and the LED UV-A lamp since the availability of a greater catalyst surface area for absorption of photons and the interaction of AR 18 reaction with the ZnO catalyst led to an increase in the number of holes and OH^\cdot radicals generated (Figure 5). At a higher lamp intensity along with a higher amount of ZnO catalyst, up to 3 mg cm^{-2} , the exposure time, and current density start to decrease. At fixed lamp intensity, it was that an optimum catalyst amount would present where the photocatalyst would form a maximum concentration of ROS which could take part in a reaction at the outer film surface. The optimum amount of ZnO catalyst had the highest surface for decay of AR 18. The optimum amount of ZnO catalyst concentration and optimum intensity of the LED UV-A lamp reaching the AR 18 standard were 3 mg cm^{-2} and 360 mW cm^{-2} , respectively. While the removal efficiency decreased at 1.5 and 4.5 mg cm^{-2} of ZnO nanoparticle films, it reached the highest value (100%) for 3 mg cm^{-2} ZnO nanoparticle film. This finding was attributed to an increase in the surface

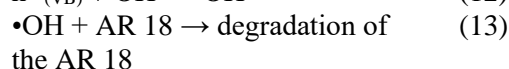
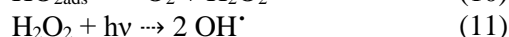
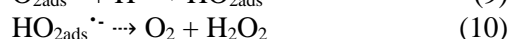
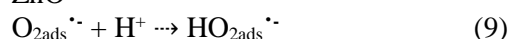
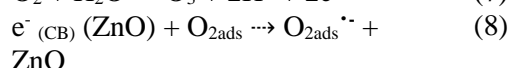
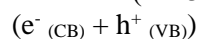
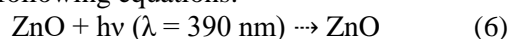
area for degradation of AR 18 concentrations. Elaziouti *et al.* (2011) concluded that the decay rate constant of Congo red (CR) was proportional to the ZnO concentration. The decay rate enhanced from 68.73 to 90.02% as the ZnO concentration was increased from 0.25 to 0.5 g/L. However, the increase in the ZnO concentration more than 0.5 g/L led to a decrease in the decay rate of CR [23]. However, a limiting value was observed for thick films due to an increase in opacity and light scattering leading to a decrease in the passage of irradiation through the film. At higher catalyst loadings (i.e. more than 3 mg cm^{-2}) the removal efficiency of AR 18 started to decrease due to the photo emission. This phenomenon was attributed to a decrease in UV penetration through the outer layers of the film and a decrease in protection due to the clusters blocking UV from reaching the catalyst surface. The presence of ZnO photocatalyst nanoparticles and UV-A led to increasing the removal efficiency of AR 18 and generation of OH^\cdot radicals. Nafie and Yasmen (2013) used ZnO and UV-A LED for degradation of phenol [24]. OH^\cdot radicals led to oxidation of AR 18. The $\text{O}_2^{\cdot-}$ hydroperoxyl radical and hydrogen peroxide generated by the reduction of dissolved oxygen in the anode, could also feed the photocatalytic degradation mechanism. These species were responsible for degrading the AR 18. Madhusudhana *et al.* (2012) reported the photocatalytic degradation of the Violet GL2B azo dye using CaO and TiO₂ nanoparticles [25].

A key variable parameter affecting the oxidation ability of EPC processes was the applied current density since it regulated the amounts of generated OH^\cdot radicals acting as oxidizing agents. At a lower current density and a lower radiation time the removal efficiency of AR 18 began to decrease (Figure 6). The optimum current density for AR 18 as a standard is 9 mA cm^{-2} . At lower initial concentration loadings, the photocatalytic treatment time required for complete degradation started to decrease. The experimental results show that the current density electrode enhances the resulting gradient separated electron-holes, thereby diminishing its recombination rate, enhancing the photocurrent rate and expediting the degradation as shown in Figure 3. Under higher applied current densities, the external electric field improved the direct and indirect electro-oxidation reactions at the anode. The degradation efficiency was proportional to the specific surface area of photocatalysts because the number of OH^\cdot was proportional to the specific surface area and inversely proportional to the electron-hole recombination rate. The

photoelectrocatalytic process accelerated the mass transfer by electro-migration of AR 18 towards the electrode. The selection of current densities is dependant on the removal efficiency of AR 18 and the cost of the consumed electrical energy. This finding is in unison with the photocatalytic experiments carried out using graphite-supported TiO₂ by Maljaei *et al.* (2009) [26]. The experimental results showed that the more intense the radiation penetrating the photocatalytic electrode, the faster the AR 18 degradation progressed. As expected, the current density and exposure time were enhanced accordingly the removal efficiency of AR 18 was increased as shown in Figure 3. This finding was the same as for the UVA photoelectro-Fenton degradation experiments carried out using the BDD reactor by El-Ghenmy *et al.* (2013) [27]. The increase in current density and exposure time led to faster generation of electrolysis products such as OH⁻ anions at the cathode electrode. This product was responsible for AR 18 degradation. Increased current density led to an increased drift force on the electrode surface, which was the main factor in the electrochemical processes. These finding are the same as the experiments performed using the electrode by Isarain-Chávez *et al.* (2010) [28]. The oxygen produced on the anode electrode led to the effect of higher degradation of AR 18, because the oxygen molecules play an important role at the stage of photocatalysis and transformed to O₂^{•-} radicals bound to the ZnO photocatalyst nanoparticles. This finding was the same as shown by the photocatalytic experiments performed using ZnO by Sushil *et al.* (2009) [29]. At a current density of more than 20 mA cm⁻², the removal efficiency started to decrease at higher temperatures in the reactor due to the disintegration of the OH[•] radicals. Farhadi and Aminzadeh (2012) showed that the COD removal efficiency was increased to 32% at 1.83 mA cm⁻² from 12% at 0.43 mA cm⁻² after 30 min. of reaction time [30].

The pattern of the EPC decay mechanism for AR 18 was distinguished by the complex structure of the -N=N- and SO₃⁻ groups. The negative charge of the AR 18 led to its absorption by the Zn/ZnO electrode and could be mineralized, eroded by strong oxidants such as positive holes and OH[•] radicals or reduced by electrons. The increase in current density and exposure time led to faster generation of electrolysis products such as OH⁻ and Cl⁻ anions at the cathode and anode electrodes, respectively. These products were responsible for AR 18 inactivation. Increased current density led to an increased drift force on the electrode surface,

which was the main factor in electrochemical processes. Therefore, it is obvious that the generation of an adequate quantity of reactive oxygen species for the oxidation of AR 18 requires the optimum radiation time (30 min). This finding was the same as for the experiments performed using an N-doped TiO₂ photoanode by Daghrir *et al.* (2014) [31]. Clearly, the band gap of the ZnO semiconductor (E_g = 3.2 eV) is close to that of the UV-A radiation LED lamp (E_{UV-A} = 3.4 eV). The photogenerated electron (e⁻)-hole (h⁺) pairs could be facily isolated and transferred to the semiconductor/adsorbate interface efficiently, therefore enhancing the photocatalytic activity. This finding is the same as the photocatalytic experiments carried out using a UV light by Tomasevic *et al.* (2009) [32]. The oxygen produced at the anode electrode led to a higher degradable effect of AR 18, because oxygen molecules play an important role at the photocatalysis stage and transformed to O₂^{•-} radicals as bonds in ZnO photocatalyst nanoparticles. These findings are the same as the photocatalytic experiments performed using TiO₂ by Pelaez *et al.* (2012) [33]. The efficiency of AR 18 absorption by a Zn electrode covered by a layer of ZnO nanoparticles as a positive pole (anode) is directly related to an increase in current density and exposure time. This electrophotocatalytic mechanism is illustrated by the following equations:



The results of the AR removal efficiency by the Taguchi model showed that the concentration was the most important variable (Figure 7). This finding was not consistent with the experiments performed using iron electrodes by Chandra *et al.* (2011) [34]. It was concluded that the influence of the initial pH of the solution on the photocatalysis kinetics was due to the amount of the dye adsorbed on ZnO. On the other hand the reaction developed the ZnO surface near the surface catalyst and not in the solution. This finding was consistent with the experiments performed using hydroxide/TiO₂ nanoparticles by Wang *et al.* (2008) [35].

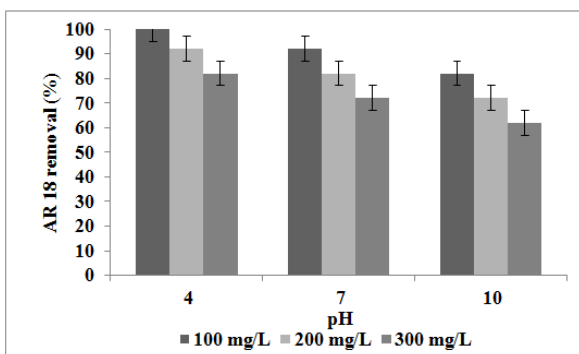


Fig. 2. Effect of the initial AR 18 concentration and pH on the efficiency of AR 18 removal (pH 4-10; Temperature 25°C; Radiation time 15 min; UV-A lamp intensity 360 mw cm⁻²; Initial AR 18 concentration 100-300 mg L⁻¹; Current density 3 mA cm⁻²; Zinc oxide concentration 3 mg L⁻¹).

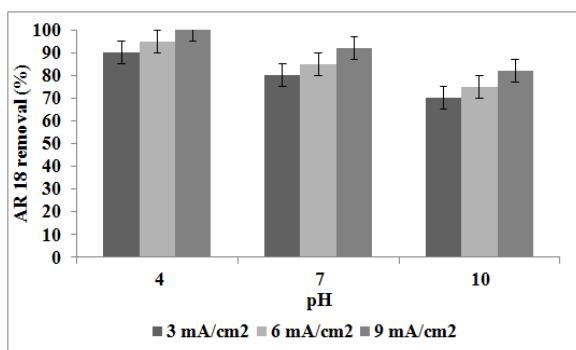


Fig. 3. Effect of the pH on the efficiency of AR 18 removal (pH 4-10; Temperature 25°C; Radiation time 30 min; UV-A lamp intensity 360 mw cm⁻²; Initial AR 18 concentration 300 mg L⁻¹; Zinc oxide concentration 3 mg L⁻¹).

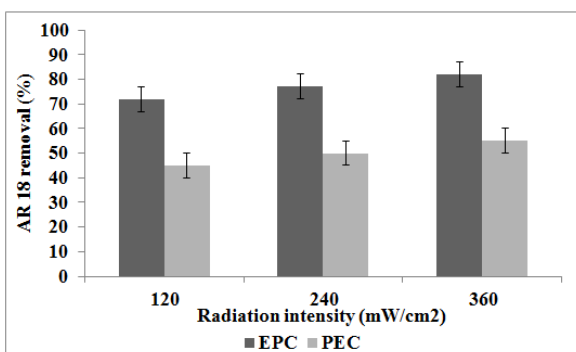


Fig. 4. Effect of the UV radiation and catalyst on the efficiency of AR 18 removal (pH 4; Temperature 25°C; Radiation time 15 min.; UV-A lamp intensity 120-360 mw cm⁻²; Initial AR 18 concentration 300 mg L⁻¹; current density 3 mA cm⁻²).

The experimental data are a better fit to the first order reaction (Figure 8). The regression coefficient for the fitted line was calculated to be $R^2 = 0.9898$ for AR 18. The apparent rate constant, K_1 and the half-life time, $t_{1/2}$ were calculated to be 0.013 min⁻¹

and 0.7 min. Mohammadlou *et al.* (2014) concluded that the electrocoagulation degradation of the CR follows first-order kinetics [36]

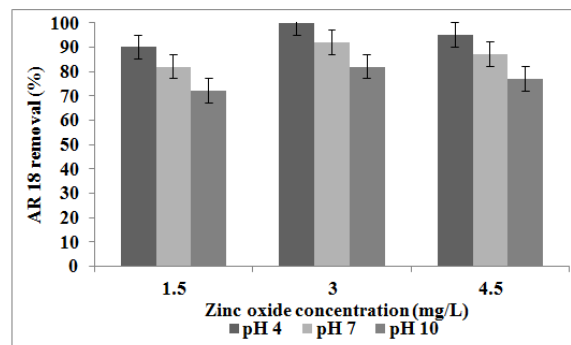


Fig. 5. Effect of the catalyst layer on the efficiency of AR 18 removal (pH 4-10; Temperature 25°C; Radiation time 15 min; UV-A lamp intensity 360 mw cm⁻²; Initial AR 18 concentration 300 mg L⁻¹; current density 3 mA cm⁻²).

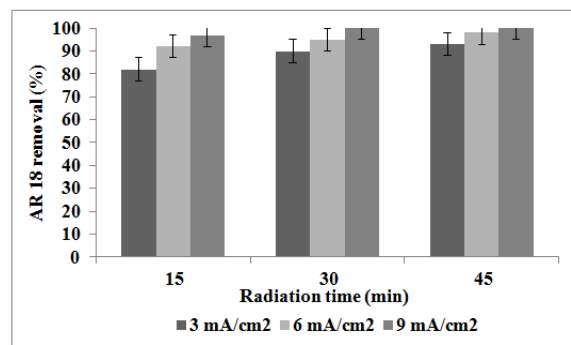


Fig. 6. Effect of the current density on the efficiency of AR 18 removal (pH 4; Temperature 25°C; Radiation time 15-45 min; UV-A lamp intensity 360 mw cm⁻²; Initial AR 18 concentration 300 mg L⁻¹; current density 3-9 mA cm⁻²; Zinc oxide concentration 3 mg L⁻¹).

CONCLUSION

The experimental results show that the batch EPC reactor is a practical and promising method in AR 18-contaminated water. The EPC reactor is more effective than the PEC reactor. AR 18 degradation is affected by the pH, the concentration of AR 18, the concentration of ZnO nanoparticles, the radiation time and current density. The EPC is capable of AR 18 removal at the pH value (4) investigated with a radiation time less than 15 min. Enhanced AR 18 removal is obtained with an increase in the radiation time and current density. It is purposed that the performance of process is studied the other electrode material.

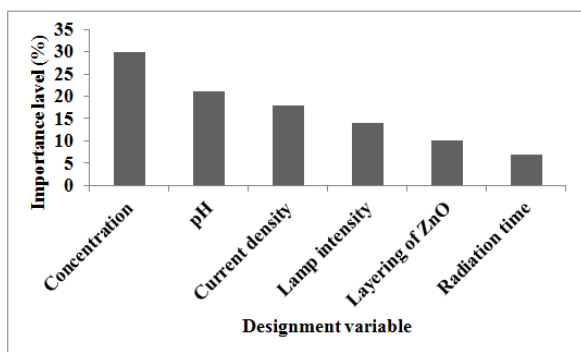


Fig. 7. The Taguchi model.

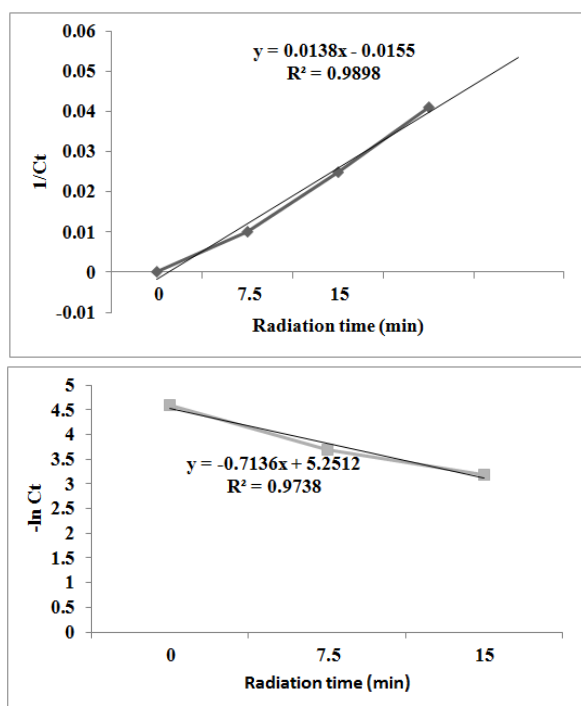


Fig. 8. The plots of first and second order reaction models fitted with the AR 18 removal experimental data in the batch EPC reactor (experimental conditions: 25 °C, pH: 7, reaction time: 0-15 min).

Acknowledgements: The author thanked the Department Environmental Health of Islamic Azad University, Tehran Medical Sciences Branch for financial and instrumental supports.

REFERENCES

1. M. Mukhlsh, B. Zobayer, M.M. Huq, M.S.I. Mazumder, M.R. Khan, M.A. Islam, *Int. Res. J. Environ. Sci.*, **2** (6), 49 (2013).
2. A. Maleki, A.H. Mahvi, R. Ebrahimi, Y. Zandsalimi, *J. Chem. Engin.*, **27**, 79 (2010).
3. I. Maghri, A. Kenz, M. Elkouali, O. Tanane, M. Talbi, *J. Mater. Environ. Sci.*, **3**, 121 (2012).
4. G.R.D. Oliveira, N.S. Fernandes, J.V.D. Melo, D.R.D. Silva, C. Urgeghe, C.A. Martínez- Huitle, *Chem. Engin. J.*, **168**, 208 (2011).

5. D. Arsene, C. Petronela Musteret, C. Catrinescu, P. Apopei, G. Brajoveanu, C. Teodosiu, *J. Environ. Engin. Manag.*, **10**, 1967 (2011).
6. C. Ratiu, F. Manea, C. Lazau, I. Grozescu, C. Radovan, J. Schoonman, *Desalin.*, **260**, 51 (2010).
7. I. Sirés, E. Brillas, *Env. Int.*, **40**, 212 (2012).
8. J. Georgieva, E. Valova, S. Armyanov, N. Philippidis, I. Poullos, S. Sotiropoulos, *J. Hazard. Mater.*, **211**, 30 (2012).
9. S. Guy, P. Yaron, *Int. J. Photoenergy.*, Article ID 596710, 1-7 (2011).
10. S. Malato, P. Fernandez-Ibanez, M.I. Maldonado, J. Blanco, W. Gernjak, *J. Catal. Today.*, **147**, 1 (2009).
11. C. Zuolian, T. Kok-Eng, T. Yong, G. Amos, Y. Xi-Jiang, *Sustain. Environ. Res.*, **20**, 281 (2010).
12. D. Hua, K. Cheuk, Z. Wei-ning, W. Chen, X. Chang-Fa, *J. Trans. Nanoferrous Met. Soc. China.*, **17**, 700 (2007).
13. A.O. Ifelebuegu, T.J. Mason, J. Eadaion, J. Onubogu, *Int. J. Environ. Sci. Technol.*, **11**, 1 (2014).
14. APHA: Standard methods for the examination of water and wastewater. 22st Edn. APHA, AWWA, WPCF, Washington DC, USA (2012).
15. M. Alizadeh, A.H. Mahvi, H. Jafari Mansoorian, R. Ardani, *Iranian J. Health, Safety & Environ.*, **1** (1), 1 (2013).
16. O. Abdelwahaba, N.K. Aminb, E-S.Z. El-Ashtoukhyb, *J. Hazard. Mater.*, **163**, 711 (2009).
17. E.M. Saggiaro, A.S. Oliveira, T. Pavesi, C. G. Maia, L.F. Vieira Ferreira, J.C. Moreira, *Molecules.*, **16**, 10370 (2011).
18. R.C. Meena, S. VermaHimakshi, S. Disha, *Int. Res. J. Environ. Sci.*, **2** (12), 35 (2013).
19. J. Basiri Parsa, M. Golmirzaei, M. Abbasi, *J. Industrial Engin. Chem.*, **20**, 689 (2014).
20. K. Mahanpoor, K. Gholivand, M. Nikazar, *J. Desalin.*, **219**, 293 (2008).
21. S. Kundua, A. Pala, A.K. Dikshit: UV induced degradation of herbicide 2,4-D: kinetics, mechanism and effect of various conditions on the degradation.
22. N. Philippidis, S. Sotiropoulos, A. Efstathiou, I. Poullos, *J. Photochem. Photobiol. A: Chem.*, **204**, 129 (2009).
23. E. Elaziouti, N. Laouedj, B. Ahmed, *J. Chem. Engin. Process Technol.*, **2** (2), 1 (2011).
24. A.A. Nafie, H.Z. Yasmen, *Global Res. Analtsis.*, **2** (1), 2013.
25. N. Madhusudhana, K. Yogendra, K.M. Mahadevan, *Int. J. Engin. Res. Applications.*, **2** (5), 1300 (2012).
26. A. Maljaei, M. Arami, N.M. Mahmoodi, *Desalin.*, **249**, 1074 (2009).
27. A. El-Ghenymy, N. Oturan, M. A. Oturan, J.A. Garrido, P.L. Cabot, F. Centellas, R.M. Rodríguez, E. Brillas, *Chem. Engin. J.*, **234**, 115 (2013).
28. E. Isarain-Chávez, C. Arias, P.L. Cabot, F. Centellas, R.M. Rodríguez, J.A. Garrido, E. Brillas, *Appl. Catal. B: Environ.*, **96**, 361 (2010).
29. K. Sushil, N.K. Kansal, S. Sukhmehar, *Nanoscale Res. Letter.*, **4**, 709 (2009).
30. S. Farhadi, B. Aminzadeh, *J. hazard. Mater.*, **35**, 219 (2012).

31. R. Daghrrir, P. Drogui, N. Delegan, M.A. El-Khakani, *Sci. Total Environ.*, **466-467**, 300 (2014).
32. A. Tomasevic, J. Đaja, S., Petrovic, E.E. Kiss, D. Mijina, *Chem. Industry Chem. Engin. Quarterly.*, **15**, 17 (2009).
33. M. Pelaez, N.T. Nolan, S.C. Pillai, *Appl. Catal. B- Environ.*, **125**, 331 (2012).
34. S.V. Chandra, D. Patil, S.K. Kumar, *Int. J. Chem. Reactor Engin.*, **9** (1), 1 (2011).
35. N. Wang, J. Li, L. Zhu, Y. Dong, H. Tang, *J. Photochem. Photobiol. A Chem.*, **198**, 282 (2008).
36. N. Mohammadlou, M.S. Rasoulifard, M. Vahedpour, M.R. Eskandarian, *J. Appl. Chem.Res.*, **8** (4), 123 (2014).

Removal of fluoride from urban drinking water by eggshell powder

Giti Kashi^{1*}, Azadee Mehree², Mozghan Zaeimdar³, Fariba Khoshab¹, Amir Mohades Madaree¹

¹Department of Environmental Health, Islamic Azad University Tehran Medical Sciences Branch, Tehran, Iran.

²Department of Natural Sources Engineering, Environmental Pollution, Department of Environmental, Islamic Azad University, Damavand Pardice and Research Branch, Damavand, Postal code: 39715/194, Iran.

³Department of Environment, North Tehran Branch, Islamic Azad University, Tehran, Iran

Received June 26, 2015, Revised September 10, 2015

The aim of this applied-analytical study was to investigate the feasibility of fluoride (F) removal from drinking water using a batch reactor by using eggshell powder. The variables under study involved are the pH, contact time, adsorbent doses, initial F concentration, reaction kinetics and eggshell powder characteristics. A sample of urban drinking water was prepared containing 3-12 mg/L of F. Eggshell powder was prepared in a laboratory oven at 105°C for 12 h. The F-containing water was introduced into a batch reactor and the F removal efficiency was studied in different cases for pH (4-10), contact time (0-80 min) and adsorbent doses (1-2.5 gr/dl). The characteristics of the eggshell powder showed that the average diameter in size of the eggshell powder particles is 2 µm. The main component of the eggshell powder was calcium carbonate (CaCO₃). The best conditions for F removal attained were at pH 6, contact time 60 min., an adsorbent dose of 3 gr. and an F concentration of 3 mg/L. The adsorption of F in eggshell powder was obtained from the Langmuir isotherm.

Keywords: Adsorbent, Calcium carbonate, Eggshell, Langmuir, Urban drinking water.

INTRODUCTION

Chemically, fluoride (F) is the most reactive and electronegative of all the elements due to its small radius/charge ratio. Low concentrations of F in the drinking water were proposed as necessary to prevent against dental caries and as an indispensable element to help build the dental enamel in humans [1]. The high concentrations of F (>1.5 mg/L) in drinking water results in serious diseases, such as dental fluorosis, skeletal fluorosis and non-skeletal fluorosis (including neurological, allergic, gastro-intestinal, bone cancer and urinary tract conditions) [2]. The maximum permissible level for F in potable water is 1.5 mg/L, according to the World Health Organization (WHO) [3]. The increase of F levels in the groundwater is mainly attributed to anthropogenic factors (rapid urbanization and the growth of modern industries) and natural phenomena (geochemical dissolution of F bearing minerals) [4]. The water interaction and volcanic rock activity were considered as the most effective factors for increasing the F concentration of groundwater and surface water [5]. It was estimated that there are at least 25 countries which are affected by fluorosis world-wide including Algeria, Argentina, Australia, China, Ethiopia,

India, Iran, Japan, Kenya, Mexico, Morocco, New Zealand, Senegal, Sri Lanka, Tanzania, Thailand, Turkey and the USA [6]. The defluoridation methods usually applied include adsorption, chemical precipitation, ion exchange, reverse osmosis, and electro dialysis [7-9]. The selection of the method was related to variables such as the area, concentration and availability of the resources. The most important disadvantage of the coagulation method was the high concentration of residual toxic chemicals such as aluminium and sulphate in the water after treatment. The main disadvantage of the ion exchange technique was the low selectivity of anions. The most important disadvantage of reverse osmosis was clogging, scaling and the fouling problem. The main disadvantage of the electro dialysis technique was the high capital and operational cost [10]. The advantages of the adsorption technology were applicable in batch and continuous arrangements, easier accessibility, economical and retain effectiveness at a low fluoride concentration [11]. Experiments have been done with many natural adsorbents such as defluoridation agents including Cynodon dactylon-activated carbon [12], Typha angustata-activated carbon [13], Pine wood and Pine bark chars [14]. The aim of this applied-analytical study was to investigate the feasibility of F removal from drinking water using a batch reactor by using eggshell powder. The variables under study involve the pH, contact time, adsorbent

To whom all correspondence should be sent:
E-mail: g.kashi11@yahoo.com

doses, initial F concentration, reaction kinetics and eggshell powder characteristics.

EXPERIMENTAL

Preparation of a water sample

F-contaminated water samples used for adsorption experiments were obtained from urban distribution systems situated at the site of a laboratory of the Islamic Azad University Tehran Medical Sciences Branch, in the city of Tehran. The samples were tested for the main physicochemical characteristics. The mean values of these water characteristics were presented in Table 1. All the reagents used were of an analytical grade. A solution of 3, 6, 9 and 12 mg/L of F was prepared by dissolving an appropriate amount of sodium fluoride (Merck, Germany) in deionized water.

Table 1. The main physicochemical characteristics of nitrate-contaminated urban water

Parameter	Unit	Value
Calcium	mg/L as CaCO ₃	162
Dissolved oxygen	mg/L	8.05
Nitrate	mg/L	9.5
ORP	mV	272
pH	-	7.19
Sulfate	mg/L	93.8
Temperature	°C	20
Total Alkalinity	mg/L as CaCO ₃	122

Preparation of eggshell powder

After collecting chicken eggshells from local markets in Tehran city, removing the waste matter such as colour and fat, boiling in deionized water for 30 minutes and washing with deionized water, eggshell powder was prepared by heating the collected eggshells in a hot air oven (Dena, Iran) at 105°C for 12 h, maybe, a temperature higher than 105°C led to a decrease in defluoridation due to damaging the calcium carbonate structure, while temperatures below 105°C led to developing a bad taste and odour in the treated water. Heat pretreatment removed the organic matter, the cause of taste and colour problems in the water. After heating, the eggshells were crushed by a laboratory electrical crusher (AIKA, Germany) for 20-30 second and were sieved several times to get a uniform fraction of eggshell of a specific size (60-100 mesh/0.25-0.104 mm), according to the ASTM standard [15]. The eggshell powder was stored in a desiccator after pretreatment containing a solution

of sodium hypo chloride (NaOCl) (Merck, Germany), to eliminate the dust particles [16].

Determination of the eggshell powder characteristics

A Scanning Electron Microscopy (SEM) image (Philips, XL 30, Holland) was prepared from the eggshell powder. X-ray diffraction patterns were measured using RINT 2000 (Rigaku Instrument Corp.) with Cu K α radiation to confirm the structure and mineral composition of the eggshells powder (Philips, Xpert, Holland). An eggshell powder composition was obtained by energy dispersive X-ray (EDX) analysis. The surface area of the eggshell powder was analyzed through nitrogen adsorption measurements at 77 K using Micromeritics Gemini 2370 equipment. The zeta potential was analyzed with a Nano Zetasizer (Philips, Holland).

Experimental set up

The batch reactor was a 250 ml plastic container (10×6×6 cm). To evaluate the effect of adsorption, on the F removal process, samples underwent treatment with different pH (ca. 4-10), different times (0-80 min), different concentrations of F (3-12 mg/L) and adsorbent dosages (1-2.5 gr/dl). The number of samples obtained was 256. A magnetic stirrer (AIKA, Germany) was used for the homogeneous mixing of water samples (120 rpm). For each test, 200 ml of sample water was poured into the reactor. All tests were performed at a laboratory temperature (20°C). Chloric acid and sodium hydroxide solutions (0.1 N) (Merck, Germany) were used for pH adjustment.

Analytical methods

All tests were performed in triplicate and the mean data values were reported. The water samples were tested for F after the adsorption process by using a spectrophotometer (Hach DR5000, America) at a wavelength of 580 nm. F was determined by a standard method 4500D [17]. The percentage of F removal was calculated in accordance with the following equation:

$$\text{Removal (\%)} = \left(1 - \frac{C_t}{C_{t0}}\right) \times 100, \quad (1)$$

Where the percentage of F removal (R , percentage) and the F value before and after treatment (C_0 and C_t , mg/L) are expressed.

The defluoridation capacity of the regenerated eggshell powder was calculated according to the following equation:

$$DC_{FC} = \left(\frac{S_0 - S_t}{X_{FC}} \right), (2)$$

Where the defluoridation capacity of the regenerated eggshell powder (DC_{FC} , mg/g) and the F concentration before and after treatment (S_0 and S_t , mg/L) are expressed.

RESULTS AND DISCUSSION

The reduction of F in urban drinking water was investigated in an adsorption reactor with filler particles made of charred chicken eggshells in a batch mode. Several operational variables were examined for the effects on process reduction efficiency. The following results were obtained from the experiments.

The characterization of eggshell powder

Figure 1 illustrates SEM images of the eggshell powder. As observed, the average diameter in size of the eggshell powder particles was 2 μm . Figure 2 illustrated X-ray dispersive (XRD) analysis of the eggshell powder. As found in Figure 2, the analyzed eggshell powder was composed of the elements calcium (Ca) and phosphor (P) as the main elements, respectively. Figure 3 illustrates the EDX analysis of the eggshell powder. As shown in Figure 3, the analyzed eggshell powder was composed of the elements calcium (Ca), oxygen (O), magnesium (Mg), carbon (C) and others. The spectrum of the analysed eggshell powder was adapted to the 2370 standard. The peaks confirmed that the main component of the eggshell powder was calcium carbonate (CaCO_3). The calcium to carbon (Ca/C) ratio of eggshell powder was 2.9. The SEM analysis was helpful to determine the surface morphology of an adsorbent. The agglomerate, non-adhesive, porous and irregular surface structure of the adsorbent is distinctly observed in the SEM image as indicated in Figure 1a. Furthermore, the pores of the adsorbent surface are regular, adhere to each other, but are heterogeneous as can be observed in Figure 1b. The heterogeneous pores represent a larger exposed surface area for the adsorption of fluoride. The diameters of the pores are symptomatic of the anticipated adsorption of fluoride molecules onto the surface of the adsorbent. It distinctly indicated the formation of a porous surface that supports the adsorbent with a large surface area and enhanced

adsorption capacity. The SEM analysis showed that the removal of fluoride affects the orientation of the eggshell powder particles. The treated sample illustrates a regular, adhesive appearance leading to a higher adsorption. F. Bhaumik et al. [18] reported that the particle size of the eggshell powder was 150-350 μm . The characteristics of the eggshell powder are shown in Table 2. Specific surface area, BET measurements were performed and the highest BET was obtained for an eggshell powder 7.43 m^2/g . Zulfikar et al. [19] reported the BET of eggshell powder to be 3.23 m^2/g . Tsai et al. [20] reported that the composition of eggshell powder consisted of calcium carbonate (94%); magnesium carbonate (1%); calcium phosphate (1%); and organic matter (4%). Agarwal and Gupta [21] reported that the compound in the eggshell powder with the highest content was calcium carbonate. Functional groups of eggshells were diagnosed by infrared analysis. The peaks at about 710, 875, 1420, 1807 and 2520 cm^{-1} coincide with those of pure CaCO_3 .

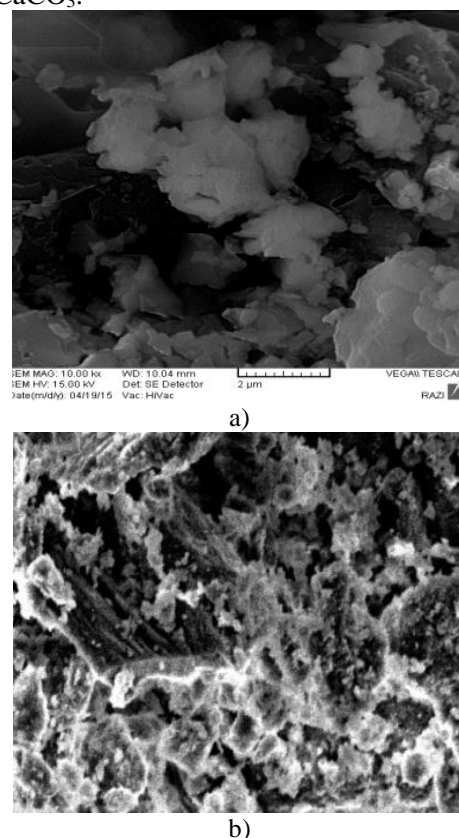


Fig. 1. SEM images of eggshell powder a) before treatment, b) after treatment.

Table 2. Characterization of BC_S particles

Particle	pH_{ZPC}	Density (g/cm^3)	Specific Surface Area, BET (m^2/g)	Diameter (μm)
Eggshell	8.2	1.148	7.43	2

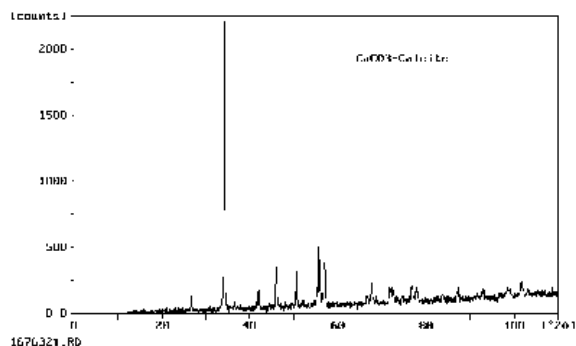


Fig. 2. XRD analysis of eggshell powder.

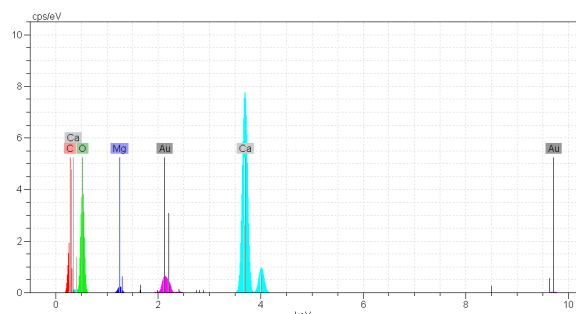


Fig. 3. EDX analysis of eggshell powder.

Effect of water pH

Adsorption experiments were carried out for pH values in the range of 4 to 10 and experimental conditions such as contact time (60 min), F concentration (6 mg/L) and amount of eggshell powder adsorbent (2 g). The mean F removal increased from 90% to 100% when the pH increased from 4 to 6 (Figure 4). F removal in the adsorption reactor was mainly influenced by the water pH. The pH had a significant effect on F reduction due to the surface charge of the adsorbent, with the highest reduction obtained at pH 6. It was connected by a competing potential of $[H^+]$ with the adsorbate ions and active sites on the adsorbent surface. The lower adsorption at acidic pH could be due to the formation of a weak hydrofluoric acid and a composition effect of the chemical and electrostatic interaction between the surface and the F ions. The removal of F ions in the alkaline condition is diminished and this can be due to strong competition from hydroxide ions at the active sites due to the prevailing OH^- and CO_3^{2-} . This was in agreement with Chowdhury et al. [22], who reported that the fastest removal rate occurred at a pH equal to 6.5. The pH at the point of zero charge (pH_{ZPC}) is an important parameter in F sorption, for it is the pH at which the sorbent has a neutral charge. When the pH is increased above the pH_{ZPC} , F sorption decreases due to electrostatic repulsion between the surface and the F anions, also, as a result of competition with the hydroxides

in solution. When pH_{ZPC} is increased above the pH, the F sorption is increased.

Effect of eggshell powder adsorbent dosage

Adsorption experiments were carried out with an initial adsorbent dosage in the range of 1 to 2.5 g at the experimental conditions such as contact time (60 min), F concentrations (6 mg/L) and a pH value (6). The mean F removal increased from 60% to 100% when the adsorbent dosage increased from 1 to 2 (Figure 5). Enhancing the adsorbent dosage increased the percentage of F that was attributed to enhancing of sportive surface area, since more active adsorption sites and a proper porosity were available. The optimum dosage of eggshell powder adsorbent was 2 g. It was seen that 2 g was a better adsorbent dosage than 1 g. This phenomenon can be due to the exposure of the active sites of the adsorbent which allowed the F ions of water to be in direct contact with the eggshell powder, therefor increasing adsorption capacity. Increasing the adsorbent dosage also led to decreasing the surface area between the eggshell powder adsorbent and the F adsorbate due to the formation of aggregates. Increasing the adsorbent dosage resulted in increasing the pH. Suneetha et al. [23] reported that the optimum dosage of active carbon derived from the barks of the *Vitex negundo* plant was 4.0 g/L. At a constant pH, the activity of F^- was directly proportional to the concentration of HCO_3^- . CaF_2 precipitated when the concentration of Ca^{+2} and F in water exceeded the solubility product of F. If Ca was present in the raw water, it precipitated out the F.

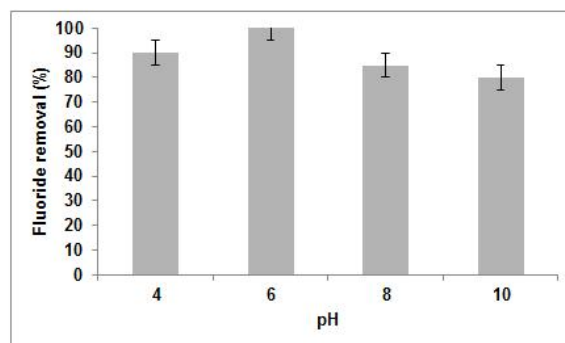


Fig. 4. The effect of water pH on fluoride removal in the batch adsorption reactor.

Effect of contact time

Adsorption experiments were carried out as a function of the time in the range of 0 to 80 min at the experimental conditions such as amount of eggshell powder adsorbent (2 g/dL), F concentration (6 mg/L) and pH value (6). The efficiency of F removal increased as the contact time increased. The mean F removal increased from

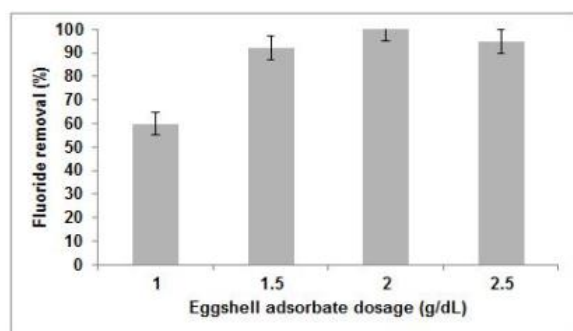


Fig. 5. The effect of eggshell powder adsorbent dosage on fluoride removal in the batch adsorption reactor.

82% to 100% when the contact time increased from 20 to 60 min (Figure 6). The efficiency of F removal initially increased as the contact time increased, but then gradually approached a more or less constant value, indicating a point of equilibrium. As there was no enhanced F removal efficiency between the 65th and 80th minute, an equilibrium time of 60 minutes was selected for the eggshell powder adsorbents. These variations could be due to the fact that initially, all the absorbent sites were empty and active, the solute concentration gradient was high and the opportunity for adsorption reactions was high. Then, the F adsorption rate on an eggshell powder adsorbent noticeably diminished due to a decrease of the absorbent sites. This phenomenon indicated a monolayer of F ions on the external surface and pores of eggshell powder and pore diffusion on to the internal surface of the eggshell powder. During this period the residual F fluctuated from a maximum value of 1.07 mg/L at 20 min. contact time to a minimum value of 0.0 mg/L for a contact time of 60 min. The highest removal capacity of eggshell powder (3 mg/g) was obtained for 60 min. An equilibrium time of 120 minutes was selected for the lemon leaves treated with a Ca^{+2} solution extracted from the eggshell adsorbent by Bhaumik et al [24].

Effect of initial F concentration

Adsorption experiments were carried out with an initial F concentration in the range of 3 to 12 mg/L at the experimental conditions such as contact time (20-80), amount of eggshell powder adsorbent (2 g/dL) and pH value (6). The mean F removal decreased from 100% to 84% when the initial F concentration increased from 3 to 12 mg/L for the duration of 60 minute (Figure 7). If the F ions were more than the absorbent sites, adsorption decreased due to saturation of the absorbent sites at a constant concentration. The F removal as a function of contact time was proportional to the F ions found in

the water. Due to enhancing the concentration gradient, as a driving force, the predominant mass transfer resistances of the fluoride between the solution and solid phase, resulted in enhancing the sorption equilibrium, until sorbent saturation was obtained. This was in agreement with Bahatti et al. [25], who reported that the defluoridation efficiency decreased when the initial F concentration was increased. In other hands, increasing the concentration of F led to shifting the pH_{ZPC} to a lower value and decreasing the electrostatic attraction between the sorbent surfaces and the F anions.

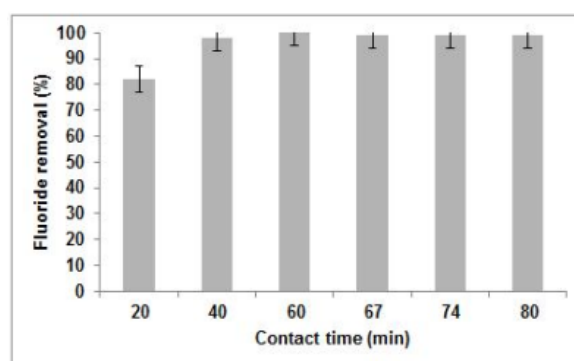


Fig. 6. The effect of contact time on fluoride removal in the batch adsorption reactor.

The proposed mechanism of the F uptake rate onto the eggshell powder surface involved the replacement (ion exchange adsorption) of the carbonate radicals of the eggshell powder, by F ions to form an insoluble fluorite. This compound could

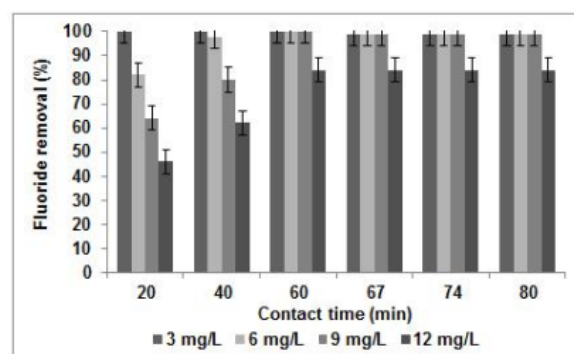
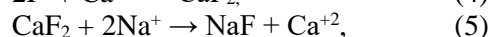
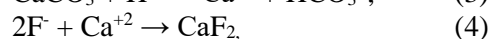
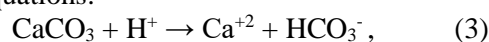


Fig. 7. The effect of initial fluoride concentration on fluoride removal in the batch adsorption reactor.

be returned to a form suitable for repetitive F adsorption with a caustic solution such as sodium hydroxide. This resulted in the formation of calcite (CaCO_3), with the F removed as sodium fluoride. This reaction could be represented by the following equations:



The application of 1% solution of sodium hydroxide for regeneration had been reported by Piddennavar and krishnappa [26]. F reduction followed a Langmuir isotherm model ($R^2 > 0.99$). Therefore, the eggshell powder adsorption reactor, in batch mode, was shown to be efficient and viable for meeting a high degree of F reduction from drinking water and was considered as a promising technology for treating F-polluted drinking water in developing countries. Water treated by eggshell powder gave allowable residual F, which was recommended by the WHO³ and Iranian National Standards [27].

CONCLUSIONS

The experimental results suggest that the batch chicken eggshell powdered reactor is a practical and promising method for the treatment of F-contaminated water. F removal was affected by pH, the concentration of F, the concentration of adsorbent and the reaction time. This reactor is capable of F removal at the pH value (6) investigated, with a reaction time of 60 min. It is proposed that the process can be successfully applied to study other materials.

Acknowledgments: The authors thank the Department of Environmental Health of the Islamic Azad University, Tehran Medical Sciences Branch for the financial and instrumental support.

REFERENCES

1. J.V. Kumar, M.E. Moss, *Dental Clinician North America*, **52**, 387 (2008).
2. O. Barbier, L. Arreola-Mendoza, L.M. Del Razo, *Che. Biol. Intera.*, **188**, 319 (2010).
3. World Health Organization (WHO). Guidelines for drinking water quality. Geneva: WHO; 2008.
4. J. Zhu, H. Zhao, N.I. Jinren, *Pur. Technol.*, **56**, 184 (2007).
5. A.D. Keçeci, B.U. Kaya, E. Guldaz, E. Saritekin, E. Şener, *Res. Report Fluoride.*, **47**, 119 (2014).
6. T. Vaishali, K. Dinesh, *Chem. Central J.*, **7**, 1 (2013).
7. E. Akbar, S.O. Maurice, O. Aoyi, A. Shigeo, *J. Hazard. Mater.*, **152**, 571 (2008).
8. S. Meenakshi, N. Viswanathan, *J. Colloid Interface Sci.*, **308**, 438 (2007).
9. S. Lahnid, M. Tahaikt, K. Elaroui, I. Idrissi, M. Hafsi, I. Laaziz, et al., *Desalin.*, **230**, 213 (2008).
10. P. Logathanan, S. Vigneswaran, J. Kasandamy, R. Naidu, *J. Hazard. Mater.*, **248**, 1 (2013).
11. S. Ayoob, A.K. Gupta, 2008. *J. Hazard. Mater.*, **152**, 976 (2008).
12. G. Alagumuthu, V. Veeraputhiran, R. Venkataraman, *Hem Industrial.*, **65**, 23 (2011).
13. Y. Hanumantharao, M. Kishore, K. Ravindhranath, *J. Analytical Sci. Technol.*, **3**, 167 (2012).
14. D. Mohan, R. Sharma, K. Vinod, P.S. Singh, C.U. Pittman, *Industrial Engin. Chem. Res.*, **51**, 900 (2012).
15. M.M. Than, P. Lawanprasert, S. Jateleela, Mahidol University *J. Pharmaceut. Sci.*, **39**, 32 (2012).
16. O.I. Isaac, C.O. Genevive, 2012. *American J. Polymer Sci.*, **2**, 56 (2012).
17. American Public Health Association/ American Water Works Association/ Water Environmental Federation. Standard methods for the examination of water and wastewater. 22th ed. Washington DC, USA; 2012.
18. R. Bhaumik, N.K. Mondal, B. Das, P. Roy, K.C. Pal, C. Das, et al., *Eur. J. Chem.*, **9**, 1457 (2012).
19. M.A. Zulfikar, E.D. Mariske, and S.D. Djajanti, Songklanakarin, *J. Sci. Technol.*, **34**, 309 (2012).
20. W.T. Tsai, K.J. Hsien, H.C. Hsu, C.M. Lin, K.Y. Lin, C.H. Chiu, *Bioresource Technol.*, **99**, 1623 (2008).
21. A. Agarwal, P.K. Gupta, *Advanced Appl. Sci. Res.*, **5**, 75 (2014).
22. S. Chowdhury, R. Misha, P. Saha, P. Kushwaha, *Desalin.*, **265**, 159 (2011).
23. M. Suneetha, B.S. Sundar, K. Ravindhranath, *J. Analytical Sci. Technol.*, **6**, 2 (2015).
24. R. Bhaumik, N.K. Mondal, S. Chatteraj, J.K. Datta, *American J. Analytical Chem.*, **4**, 404 (2013).
25. H.N. Bhatti, A.W. Nasir, M.A. Hanif, *Desalin.*, **253**, 78 (2010).
26. R. Piddennavar, P. krishnappa, *Int. J. Engin. Sci.*, **2**, 86 (2013).
27. Iranian National standards. No. 1053, Iran: Iranian Standard and Industrial Research Institute, 2014.

Short-term remediation of soil contaminated with landfill leachate using natural and microwave modified zeolite of the clinoptilolite type

Y. Liu¹, Z. Chen^{1*}, L. Yang², Z. Liao¹, T. Sun², J. Wang¹, H. Wang¹

¹*School of Environmental Science & Engineering, Huazhong University of Science and Technology, Wuhan 430074, PR China*

²*School of Resources and Environmental Engineering, Wuhan University of Technology, Wuhan 430070, PR China*

Received June 26, 2015, Revised September 10, 2015

The experiment was conducted to evaluate the effect of raw and microwave modified zeolite application on leachate contaminated soils. Soils treated with 50ml leachate were amended with 0, 15, 25 and 35g zeolite per 300g soil. Chemical oxygen demand (COD) and ammonium of soil extract, soil pH and leaching toxicity were compared between soils treated with and without zeolite. The results showed natural and microwave modified zeolites were both effective to increase soil pH, eliminate COD and ammonium in soil extraction and decrease leaching toxicity of leachate polluted soils. Above observations were more likely attributed to biologic degradation reactions in zeolites relative to sorption reactions. Microwave modification was helpful for ammonium removal, but with no benefit for COD removal and toxicity eliminating. Furthermore, excessive zeolite application could induce negative influences on soils for both natural zeolite and its microwave modified forms. Therefore application dosages would act as an essential factor in remediation process.

Keywords: Soil remediation, Landfill leachate, Natural zeolite, Leaching toxicity, Microwave modification

INTRODUCTION

Waste leachates are residual liquids that are generated by water percolating through stored trash and thus dissolving and hydrolyzing organic and inorganic matter [1]. Improper methods of disposing MSW such as unlined landfill cause leachate migration resulting in pollution of soil system [2] and groundwater [3,4]. Considerable attention has been paid to landfill leachate pollution and many research studies have been carried out on this topic during the past decades. Electrical resistivity surveys were used to evaluate groundwater and soil pollution in landfill areas and indicated pollution risks posed by leachate [4,5]. The content and immobilization of Cd in leachate was analyzed with the method of leaching tests [6]. Smith and Senior [7] selected pH, electrical conductivity and copper as indicators and proved that high removal of pollutants from landfill leachate can be achieved by passage through a soil with a low attenuation potential. However, few reports were found to be focused on the approaches to remediation of leachate contaminated soils and biological impacts posed by leachate.

The natural zeolites have already found extensive applications to the environmental remediation and restoration [8]. The use of natural zeolites and their modified forms offer as advantages the low-cost, the availability in big

quantities in many parts of the world, the good mechanical and thermal properties and the combination of high sorption capacity with the ability to modestly adjust the pH of the soil or the aqueous system. In addition, the natural zeolites, do not introduce additional pollution in the environment. Surface modifications such as heating, surfactant treatment, microwave irradiation etc., were usually used to promote sorption capacity or ion-exchange property [9]. Among various modified methods, microwave irradiation showed its advantages of notable promotion on the acidic and surface properties of zeolites as reported by González et al.[10]. Whereas little work was found about zeolite application on remediation of leachate contaminated soils in previous literatures. In this study, we attempted to adopt natural zeolite and its microwave modified forms as soil remediation materials.

Soil leaching toxicity is a typical indicator for migration properties of pollutants in soils to groundwater and surface waters, and simultaneously could be chosen as an effective indicator for effectiveness of soil remediation materials. Landfill leachate presents biotoxicity risks reasonably due to its content of heavy metals and persistent organic pollutants [11]. Our previous work suggested that high COD, ammonia and DEHP contents presented notable negative influences on microorganism growth [12]. In this study, *tetrahymena pyriformis* (TP) was chosen as leaching toxicity indicator due to its

To whom all correspondence should be sent:
E-mail: czlgroup@sina.com

wide distribution in natural waters and good sensitivity to hazardous substances, which made it reasonable to be used to assess soil toxicity mobility and the risk of further pollution to waters.

In this paper, the emphasis is placed on remediation effectiveness of zeolites on selected parameters of leachate-polluted soils. The objectives of this study are to attempt the application of raw and microwave modified zeolites on leachate-polluted soils and to figure out their effectiveness on pH, COD, ammonium and biotoxicity of soil extract. Thus, a short-term incubation was conducted to simulate the dark environment in deep polluted soils and analyse the remediation mechanisms of zeolites on above representative parameters of leachate-polluted soils.

MATERIALS AND METHODS

Materials

Soil samples up to 20 cm below ground was collected from Maanshan Forest Park in Wuhan, China. The soil samples were dried in drying oven for 1 week and passed through 2 mm sieve before being used in incubation experiments. Typical chemical characteristics of the soil are measured from three samples and listed in Table 1. Leachate was collected from Changshankou Landfill in Wuhan, China. The indicators for leachate were determined according to MEPC [13] and are presented in Table 2. Natural zeolite was purchased from Xinyang, Henan Province and Table 3 summarizes the chemical composition of the zeolite sample used in the experiments. Besides, modified methods of zeolites are listed in Table 4. All types of zeolites passed through 1 mm sieve before being used in incubation experiments.

Incubation experiment

The soil was treated with 50 ml leachate per 300 g soil. According to Smith and Senior [7], enough leachate would significantly affect soil pH and we estimate 50 ml leachate per 300 g soil could reach

the required level. The remediation was evaluated by repeated tests of chemical and biological soil properties (termed "indicators") in soils that were incubated for up to 35 days with three dosages (e.g. 15g, 25g and 35g) of zeolites treated with various microwave conditions (Table 4). Similar modified method was proposed by Shang et al.[14].

The soil samples treated with zeolites and leachate were thoroughly mixed and watered. The soil was then transferred to glass beakers (Ø=12 cm, Height=7 cm) and in each beaker 300 g soil was placed. Treatments were arranged in a completely randomized design with three replicates per treatment. The treated soils were maintained at 60% water holding capacity with deionized water. All beakers were incubated without illumination to simulate the dark environment in deep natural soil.

Analysis of samples

Soil extract was obtained from each soil sample according to CMEP [15]. Chemical oxygen demand (COD), biological oxygen demand (BOD), ammoniacal nitrogen (NH₃-N), and pH were measured using standard methods [13] after 35-day incubation. All chemicals used for the analytical determinations were of analytical grade.

Tetrahymena pyriformis (TP) (generously provided by Institute of Hydrobiology, Chinese Academy of Science) was used as a probing indicator for biotoxicity assessment. Leaching toxicity experiments using protozoan TP were conducted with the method of the 24h-LC₅₀ test (%) according to Tatara et al. [16]. TPs were tested in tissue culture plates containing 1 ml of test solution per sample. Test solutions consisted of six soil extract concentrations (6, 12, 25, 50, 75, and 100% of each soil extract) and a control with each replicated six times. TPs were incubated at 20°C for 24±1h, and the number dead was determined by visual inspection and probing the worms with a platinum wire under a dissecting microscope. This concentration response experiment was repeated three times for each zeolite type.

Table 1. Typical chemical characteristics of the soil.

Materials	pH	Organic matter (%)	Total P (mg/g)	Available P (mg/g)	NO ₃ ⁻ -N (mg/g)	NH ₄ ⁺ -N (mg/g)	Available K (mg/g)
Soil	7.12	1.204	0.824	0.017	0.007	0.019	0.082

Table 2. Chemical characteristic of landfill leachate.

pH	SS (mg/L)	COD _{Cr} (mg/L)	BOD ₅ (mg/L)	NH ₄ ⁺ -N (mg/L)	Total Cr (mg/L)	Cr ⁶⁺ (mg/L)	Hg (µg/L)	As (mg/L)
7.79	10700	38200	15200	1360	1.45	0.24	1.17	0.37

Quality control

All the glassware such as vials and bottles were first cleaned in an ultrasonic cleaner (20 KHz) assisted by liquor for 30min. Then they were further washed by tap water and deionized water for three times, respectively. Deionized water was obtained from a Millipore Milli-Q system (18.2mΩ cm). All chemicals used for the analytical determinations were of analytical grade. All parameters were measured with each replicated at least three times.

Table 3. Chemical composition of the natural zeolite (wt. %).

Composition	w%
SiO ₂	67.25
TiO ₂	0.17
Al ₂ O ₃	7.82
Fe ₂ O ₃	0.95
MnO	0.09
MgO	0.73
CaO	3.22
Na ₂ O	2.16
K ₂ O	3.84
H ₂ O	8.41
LOI	5.37

Table 4. Various types of zeolites for soil remediation.

Samples	Treatments
Control	No zeolite
NZ	Natural zeolite
MZ1	Natural zeolite+200W+3min
MZ2	Natural zeolite+500W+3min
MZ3	Natural zeolite+800W+3min

RESULTS AND DISCUSSION

Soil pH

Soil pH of contaminated soils in the absence and presence of various types of zeolite is demonstrated in Fig. 1. Soil pH is a typical and important parameter and widely used for assessing soil quality [17] and remediation effectiveness [18,19]. Undoubtedly, suitable soil pH is close to the neutral value of 7. However, significant decrease was observed in simulated polluted soils with a pH value of 5.2 in the control samples, respected to initial value of 7.12 (Fig. 1). Similar results was obtained by Smith and Senior [7] that pH value decreased to below 5 in initial period of leachate irrigation. This observation may be attributed to organic acids occurring during the organic matter degradation processes within leachate [1], especially for leachate from anaerobic landfill due

to lower content of inert COD [20], or the exchange of H⁺ and Al³⁺ ions from the soil colloids by cations from the leachate [7]. The acid soil environment is unsuitable for soil biological activities and easily results in the increase of heavy metal mobility. Simultaneously, acid soil environment may cause serious damage to plant root.

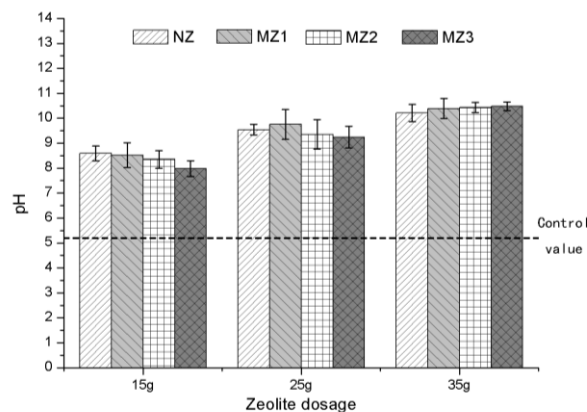


Fig. 1. Changes of soil pH in the presence and absence of zeolites.

With the addition of raw and microwave modified zeolites, notable pH increase was achieved with 36-day incubation and pH increased with the dosage of zeolite. It could be concluded that raw and microwave modified zeolites both increase soil pH in a short-term incubation. Our results show reasonably good agreement with other research reports. It has been reported that soil pH increased significantly with application of natural zeolites in lead-polluted soils [21], similar results were observed in wastewater treatment studies [22]. All above observations are probably attributed to the basic characters of ion exchange for natural zeolites and their modified forms. No regular changes are observed between raw and microwave modified zeolites on their effectiveness on soil pH. That means zeolite modification has no remarkable effect on their pH effectiveness. Consequently, raw and microwave modified zeolites are both effective to increase soil pH. Nevertheless, high alkalinity would undoubtedly induce negative influences to environment, therefore application dosages would act as an essential factor in remediation process.

COD removal of soil extract

High content of organic matter contained in landfill leachate puts a great threat on groundwater and surface water. Many experiments have been conducted to study the characters of leachate COD to find an effective approach to dealing with the complex wastewater (eg. [1,20]). While few studies are found to control the pollution of organic matters to soils from landfill leachate. COD of soil

extraction for samples treated with various type of zeolites is presented in Fig.2. It can be seen that higher COD removal was achieved with zeolite application, especially for 15g-dosage group. Zeolites has been reported to be applied in remediations of organic matter polluted soils [23] and dealing with organic wastewater [24]. It should be noted that the studies above are focused on some solely or low content of organic pollutants in soils or wastewaters. When the objectives are some complicated and special pollutants, the effectiveness of zeolites is uncertain. Landfill leachate is characterized by its complicated compositions and high content of organic pollutants. Halim et al. [25] adopted zeolite as adsorbent to investigate the the adsorption effectiveness of COD in leachate, and found that zeolite was effective to decrease leachate COD mainly due to its adsorption property.

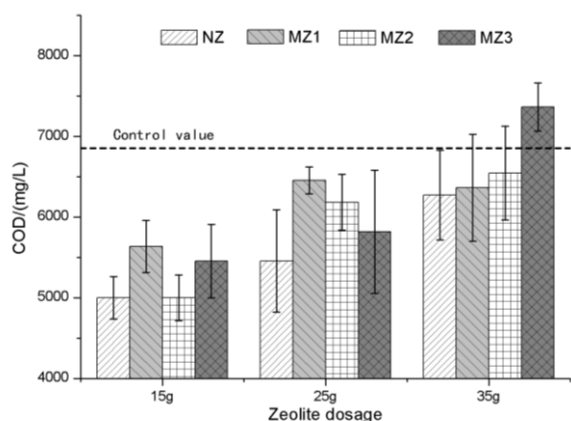


Fig. 2. Changes of COD in soil extract in the presence and absence of zeolites.

Fig.2 shows higher COD removal was achieved with zeolite application, but removal rate did not increase along with the increase of addition dosages. It was reported that zeolites are capable of sorbing into their cavities or channels different polar and non-polar inorganic or organic molecules [26]. If the COD removal was mainly attributed adsorption property of zeolites, the removal would be facilitated with the dosage increase. The results obtained in our study show a different trend for COD removal with the supposition above. As indicated in the literature zeolite was believed to act as two types of reactive media for contaminant removal [9]. Firstly, sorption reactions tend to be relatively fast, but eventually the maximum capacity of the medium will be reached, and there will be no further retention. The other media type is a degradation or transformation material. The contaminant will be transformed to a non-toxic compound after coming in contact with zeolites.

Degradation reactions tend to be kinetically slow relative to sorption reactions, and but the reactions are persistent. Similar standpoints are found in other studies [8] that zeolite particles could act as good carriers of microbe, which increase the biological activity in contaminated soil or wastewater. In this study, COD removal was more likely attributed to degradation reactions in zeolites relative to sorption reactions and the observations may indicate microwave modification had no remarkable effect on degradation reactions. Meanwhile, excessive zeolite application is indicated to show negative influences on degradation reactions probably due to unsuitable soil pH.

Ammonium removal of soil extraction

Ammonia nitrogen pollution results in eutrophication of lakes and rivers, dissolved oxygen depletion and fish toxicity in receiving waters. Higher concentration of ammonium will cause a sharp decrease of dissolved oxygen and obvious toxicity on aquatic organisms. Negative effects occur in ammonium polluted soils similarly. Zeolites has been proved as a good remediation material for ammonium according to previous studies [27]. Ammonium of soil extraction for samples treated with various type of zeolites is presented in Fig.3. Significant decrease of ammonium was observed in most zeolite treated soils respect to the control soil. More ideal removal was obtained in the 15g dosage group comparing to 25g and 35g dosage groups..

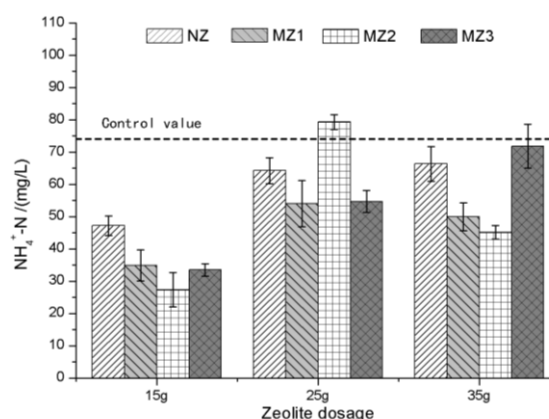


Fig. 3. Changes of ammonium in soil extract in the presence and absence of zeolites.

The removal mechanisms for ammonium probably are attributed to the three basic properties of zeolites: sorption, ion exchange and catalytic [26]. Fig. 3 demonstrated that the removal did not increase with the zeolite dosage added to soils. That leads us to believe the main mechanism was catalytic reaction rather than sorption and ion

exchange because natural zeolite could adsorb ammonium steadily at a wide pH range [28]. As described in Section 3.2, zeolite particles could act as good carriers of microbe, which increase the biological activity in contaminated soil. Zaman and Nguyen [29] used conducted a field experiment to investigate the effects of zeolites on N_2O and N_2 emissions from a pastoral soil treated with urine or nitrate-N fertilizer. They found nitrifier-denitrification and denitrification acted as a significant role in ammonium removal in urine treated soils. Wang et al. [22] found that zeolite could increase pH to a 7.0~8.0 and thus fulfilled the conditions for anaerobic digestion in ammonium-rich swine wastes. In our study, it can be concluded that the catalytic impact of zeolite on biological activities is the main mechanism for ammonium removal in leachate contaminated soils. Excessive zeolite did not promote ammonium removal due to too high pH values as demonstrated in Fig.3. A previous study conducted by Milan et al. [30] demonstrated that a zeolite dose of 10g/L could contribute to process inhibition for ammonium removal in piggery waste. All above may explain the lower removal obtained in zeolite doses of 25g and 35g.

Moreover, modified zeolites show a more notable promotion effect on ammonium removal as showed in Fig.3, which may be attributed to the positive influences of microwave treatment on surface properties of zeolites [10]. It can be concluded that ammonium removal was attributed to nitrifier-denitrification and denitrification and microwave modification had positive effect on biochemistry reactions. Negative influences would occur with excessive zeolite application due to process inhibition for biological activities.

Soil leaching toxicity

Soil leaching toxicity is a typical indicator for migration properties of pollutants in soils to groundwater and surface waters, and simultaneously could be chosen as an effective indicator for effectiveness of soil remediation materials. Soil leaching toxicity for soil samples treated with various type of zeolites is demonstrated in Fig.4. Leaching toxicity was significantly lower in 15g and 25g zeolite dose groups, with LC_{50} s of about 62% and 50% respectively respect to the control soils of 32%. However, no notable decrease was observed in the 35g dose group. There has been some relative views in our previous work. Liu et al. [11] found that leachate toxicity decreased as landfill age increased and was dependent on ammonia

concentration and COD with multivariate analysis. Liu et al. [12] suggested that high COD, ammonia and DEHP contents presented notable negative influences on microorganism growth. Heavy metals found in leachate (Table 2) are undoubtedly one of main toxic components and posed great threats on soils and natural waters near unlined landfills [31]. However, few studies are found to focus on decreasing biotoxicity or eliminating toxic pollutants from landfill leachate.

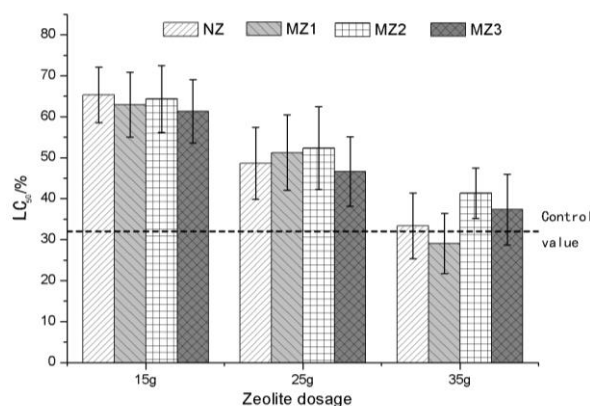


Fig. 4. Changes of leaching toxicity in the presence and absence of zeolites.

As demonstrated in Fig.4, leaching toxicity of leachate contaminated soils could be effectively decreased with suitable application of natural and modified zeolites. This may mainly be attributed to the catalytic property of zeolites. Other reports has been found to attempt to utilize zeolites for eliminating negative impacts of above pollutants. Burgess et al. [32] proved that zeolite could be effectively adopted to eliminate the toxic effects of ammonia in marine sediment in a laboratory scale. Shi et al. [33] studied the remediation effects of the lead-polluted garden soil by exogenous natural zeolite and humic acids, and found that the available fraction of lead compounds was reduced. Dercova et al. [34] proposed humic acids bound on zeolite reduced the potential toxicity of PCP to microbial community by lowering its bioavailability and thus facilitated its biodegradation. The results in this study has proved significant effectiveness of zeolites for COD and ammonium removal in soil extracts (Fig.2 and Fig.3). In fact, no notable decrease of leaching toxicity was observed in the 35g dose group. Strong basicity caused by excessive zeolite may explain the observations. As showed in Fig.1, pH values of above 10 were unsuitable for biological activities as described in Section 3.2 and 3.3. A previous study conducted by Milan et al. [30] demonstrated that high pH could contribute to

process inhibition for anaerobic digestion in piggery waste. It can be concluded that proper dosage of zeolites could effectively reduced the leaching toxicity of leachate polluted soils and there was no significant difference between natural zeolites and its modified forms for toxicity removal.

CONCLUSIONS

A fundamental research had been carried out to explore the remediation effectiveness of natural and microwave modified zeolites for leachate contaminated soils. The influences of application dosage and mechanisms of pollutant removal were investigated. Conclusions were drawn as follows:

(1) Natural and modified zeolites were both effective to increase soil pH. But excessive zeolites would cause high alkalinity, which would induce negative influences to biological activities.

(2) COD and ammonium in soil extraction could be effectively eliminated with zeolite application, and this may be more likely attributed to degradation reactions in zeolites relative to sorption reactions.

(3) Leaching toxicity of leachate polluted soils also got high removal with proper dosage of zeolites. Impacts on toxic pollutants such as heavy metals and persistent organic pollutants may explain the observations.

(4) Microwave modification was helpful for ammonium removal, but with no benefit for COD removal and toxicity eliminating. Besides, excessive zeolite application could induce negative influences on soils for both natural zeolite and its modified forms.

Acknowledgments: This work was supported by Program of Natural Science Foundation of China (No.51278212 and No. 51508430).

REFERENCES

1. L. Badoil, D. Benanou, *Anal. Bioanal. Chem.*, **393**, 1043 (2009).
2. B.M. Sunil, S. Shrihari, S. Nyayak, *Eng. Geol.*, 106, 20 (2009).
3. T.W. Assmuth, T. Strandberg, *Water Air Soil Pollut.*, **69**, 179 (1993).
4. A.M. Ahmed, W. N. Sulaiman, *Environ. Manag.*, **28**, 655 (2001).
5. P. R. Pujari, P. Pardhi, P. Muduli, P. Harkare M.V. Nanoti, *Environ. Monit. Assess.*, **131**, 489 (2007).
6. T.H. Christensen, *Water Air Soil Pollut.*, **44**, 43 (1989)..
7. D.C. Smith, E. SENIOR, H.M. Dicks, *Water Air Soil Pollut.*, **109**, 327 (1999).
8. P. Misaelides, *Microporous Mesoporous Mater.*, **144**, 15 (2011).
9. R.S. Bowman, *Microporous Mesoporous Mater.*, **61**, 43 (2003).
10. M.D. González, Y. Cesteros, P. Salagre, *Physics Procedia*, **8**, 104 (2010)..
11. T. Liu, Z.L. Chen, S. Chen, 5th International Conference on Bioinformatics and Biomedical Engineering, iCBBE 2011.
12. T. Liu, Z.L. Chen, S.Q. Tang, W.G. Xie, L. Yang, *Environ. Sci.* **31**, 541 (2010).
13. Ministry of Environmental Protection of China, Water and wastewater monitoring and analysis methods, China Environmental Science Press, Beijing, 2002
14. P. Shang, T.L. Liu, X.J. Kong, *Non-Metallic Mines*, **33**, 63 (2010).
15. CMEP (China's Ministry of Environmental Protection), HJ557-2010, 2010.
16. C.P. Tataru, M.C. Newman, J.T. McCloskeyb, P.L. Williams, *Aquat. Toxicol.*, **39**, 279 (1997)
17. Mijangos, R. Perez, I. Albizu, C. Garbisu, *Enzyme Microb. Technol.*, **40**, 100 (2006)
18. S. Kuo, M.S. Lai, C.W. Lin, *Environ. Pollut.*, **144**, 918 (2006).
19. L. Liu, H. Chen, P. Cai, W. Liang, Q. Huang, *J. Hazard. Mater.*, **163**, 563 (2009).
20. M. S. Bilgili, A. Demir, E. Akkaya, B. Ozkaya, *J. Hazard. Mater.*, **158**, 157 (2008).
21. H. Li, W.Y. Shi, H.B. Shao, M.A. Shao, *J. Hazard. Mater.*, **169**, 1106 (2009).
22. Q.H. Wang, Y.N. Yang, C. Yu, H. Huang, M. Kim, C.P. Feng, Z.Y. Zhang, *Bioresource Technol.*, **102**, 7064 (2011).
23. S. Gan, E.V. Lau, H.K. Ng, *J. Hazard. Mater.*, **172**, 532 (2009).
24. Meteš, D. Kovačević, D. Vujević, S. Papić, *Water Res.*, **38**, 3373 (2004).
25. A.A. Halim, H. A. Aziz, M.A. M. Johari, K.S. Ariffin, *Desalination*, **262**, 31 (2010).
26. M. Reháková, S. Čuvanová, M. Dživák, J. Rimár, Z. Gaval'ová, *Curr. Opin. Solid State Mater. Sci.*, **8**, 397 (2004).
27. S. Wang, Y. Peng, *Chem. Eng. J.*, **156**, 11 (2010).
28. M.Y. Li, X.Q. Zhu, F.H. Zhu, G. Ren, G. Cao, L. Song, *Desalination*, **271**, 295 (2011).
29. M. Zaman, M.L. Nguyen., *Agric. Ecosyst. Environ.*, **136**, 254 (2010).
30. Z. Milan, E. Sanchez, P. Weiland, R. Borja, A. Martin, K. Ilangovan, *Bioresource Technol.*, **80**, 37 (2001).
31. A. Kasassi, P. Rakimbei, A. Karagiannidis, A. Zabaniotou, K. Tsiouvaras, A. Nastis, K. Tzafeiropoulou, *Bioresource Technol.*, **99**, 8578 (2008).
32. R.M. Burgess, M.C. Pelletier, K.T. Ho, J.R. Serbst, S.A. Ryba, A. Kuhn, M.M. Perron, P. Raczewski, M.G. Cantwell, *Mar. Pollut. Bull.*, **46**, 607 (2003).
33. W.Y. Shi, H.B. Shao, H. Li, M.A. Shao, S. Du, *J. Hazard. Mater.*, **170**, 1 (2009).
34. K. Dercova, Z. Sejkova, M. Skokanova, G. Barancikova, J. Makovnikova, *Chemosphere*, **66**, 783 (2007)..

Effects of forest plantations on soil carbon sequestration in Chah Nimeh region of Sistan, Iran

E. Rouhi-Moghaddam^{1*}, F. Azarian-Moghaddam², A. Rashki³, R. Karami⁴

¹ University of Zabol, Faculty of Water and Soil, Department of Range and watershed Management, 98615-538 Zabol-IRAN

² University of Zabol, Faculty of Water and Soil, Department of Range and watershed Management, 98615-538 Zabol-IRAN

³ University of Ferdowsi, Faculty of Environment and Natural Resources, Department of Desert and Drylands Management, 9177948974 Mashhad-IRAN

⁴ University of Zabol, Hamoun International Wetland Research Institute, 98615-538 Zabol-IRAN

Received June 26, 2015, Revised September 10, 2015

Plantation forests are the most effective and ecologically friendly way of absorbing CO₂ and increasing carbon sinks in terrestrial ecosystems; mitigating global warming and beginning ecological restoration. This study was done in Chah Nimeh region located in Sistan and Baluchistan province, the southeastern part of Iran, near the Afghanistan border. In this study, soil samples were collected at depths of 0-15 cm and 16-30 cm in 10 replications. This study was done based on a completely randomized design in a factorial experiment in planted forests stands with bare lands surrounding (control areas). The obtained data were entered to SPSS software and were analyzed using One-way ANOVA and the effectiveness of species of *Eucalyptus camaldulensis*, *Tamarix aphylla*, *Olea europaea* and *Pinus eldarica* on soil carbon sequestration rate was calculated. The results showed that the carbon sequestration in soils under different species of afforestations in this area has significant difference at the 5% level in both depths. As, in the upper soil depth, carbon sequestration in Pine species (12.66 tons per hectare) is higher than Tamarisk (9.22 t/ha), Eucalyptus (8.18 t/ha), Olive (5.70 t/ha) species and the control area (6.30 t/ha). Also in the second depth of soil, carbon sequestration in Pine (11.61 t/ha) is higher than Olive (6.27 t/ha) species. There are no significant differences among Eucalyptus (10.41 t/ha), Tamarisk (9.77 t/ha) plantations and bare land (7.05 t/ha) in this soil depth. In this arid region, afforestation of Eucalyptus, Tamarisk and Pine species has increased the amount of carbon sequestration in soil.

Keywords: Afforestation, Arid Land, Soil Carbon Stock, Sistan Plain.

INTRODUCTION

Anthropogenic release of CO₂ into the atmosphere through the combustion of fossil fuels represents a growing threat to the global environment. Although, a permanent solution to this problem can only come through the development of technologies that do not depend on previously stored carbon, in the short-term, offsetting emissions of greenhouse gases together with other CO₂ abatement policies may provide some respite. The atmospheric carbon pool at 750 Pg [1] is considerably smaller than the quantity of carbon stored within soil (2200 Pg in top 1 m) of which approximately 1500 Pg is organic carbon [2]. Carbon is readily exchanged between these two pools [3].

The Kyoto Protocol to the Framework Convention on Climate Change, adopted by a majority of the world's nations in December, 1997,

sets specific targets and timetables for the reduction of greenhouse gas emissions by Annex I (industrialized) countries. There is currently a great deal of interest in converting non-forest to forest land (afforestation) to offset carbon dioxide (CO₂) emissions. Trees and other forest vegetation photosynthesize CO₂ to yield carbon, and since forests generally store more carbon than land in other uses (e.g. agriculture), afforestation can achieve a reduction in net greenhouse gas emissions [4,5].

The role of forests (or trees) in carbon cycles is well recognized and forests are a large sink of carbon [6]. There is considerable interest to increase the carbon storage capacity of terrestrial vegetation through land-use practices such as afforestation [7]. Gaining new carbon through forestation has become the most effective, hopeful, and ecologically friendly measure to enhance carbon sequestration in terrestrial ecosystems and mitigate increasing CO₂ concentrations in the atmosphere. Large scale forestation will establish large areas of new vegetation to enhance carbon

To whom all correspondence should be sent:
E-mail: erouhimm@uoz.ac.ir

sinks, conserve soils, and improve water quality [8,9]. Forestation is also the primary driving force for transformation between carbon sinks and sources [10]. Tree plantations allow the carbon to be sequestered in biomass, thus playing a vital role in the terrestrial carbon sink [11,12].

Carbon is stored in different parts of the land ecosystems the most important of which is soil. About 75% of carbon storage of the terrestrial ecosystems is found in soils (3 times more carbon stored in plants) [13]. Thus, soil plays a key role in carbon sequestration. Forest soils with reserves of 700 billion tons are the largest reservoir of carbon in forest ecosystems of the world [14]. Accurate and efficient estimation of soil C is vital to understanding and monitoring the role of afforestation in C sequestration [15]. Soil organic carbon (SOC) makes up a significant portion of the world's terrestrial carbon stocks, and changes in land-use and land cover are changing soil carbon stocks [16]. It has been reported that more than 50% of total SOC is stored in the subsoil (at a depth below 50 cm) [17].

Sequestering carbon in the soil, ultimately as stable humus, may well prove a more lasting solution than temporarily sequestering it in biomass [18,19]. Soil sequestration would be the most effective factor in mitigating climatic warming in the long term. However, like any large-scale land use change, plantations can have unintended environmental and socioeconomic impacts that can jeopardize the overall value of carbon mitigation projects [20]. The most important factors affecting change in soil C were previous land use, climate and the type of forest established [21].

Forests offer two main options. First, the volume of atmospheric CO₂ may be reduced by increasing forest biomass. This may be achieved through an expansion of forests—either by planting currently unforested land, or by allowing the existing forests to accumulate higher biomass. The second main approach is to utilize forest directly as a source of raw materials for energy production, usually referred to as bio-energy, which is considered a carbon-neutral energy source. Use of bio-energy represents a positive contribution towards the CO₂ concentration problem if it replaces fossil fuels. Since trees are a terrestrial carbon sink [22], managed forests in theory can sequester carbon both in situ (biomass and soil) and ex-situ (products) [23].

It is estimated that in the one hectare of forested land, an average of 12 to 50 tons of carbon is stored in above-ground biomass [24]. However, there is strong variation in the carbon sequestration

potential among different plantation species [25], regions and management. Hence, a careful choice of tree species used for the forestation occurring under the Kyoto protocol is needed to promote long-term climate change mitigation [26]. Variations in environmental conditions can affect carbon sequestration potential even within a relatively small geographic area [23,27].

Iran is located in the world's arid and semi-arid belt, where the lack of rain and its poor distribution, and high evaporation are its main climatic characteristics [28]. Carbon stored in Iran's forests is estimated 180 million tons and absorbed carbon dioxide is 662 million tons [29]. Annual carbon uptake and carbon dioxide in the forests of Iran is respectively, 8 and 30 million tons [30].

The half wells (known as Chah Nimeh) are main water reservoirs located in Sistan plain in Iran and Afghanistan border areas. Afforestations around Chah Nimeh were implemented in order to get to multiple objectives including biological restoration to counter desertification, creation of forest parks, wildlife refuges strengthened, and carminative as well as other conservation and environmental objectives. The current research is an attempt to evaluate the significance of these afforestations in terms of carbon sequestration in soils. Because in natural ecosystems the amount of carbon sequestration is higher, the higher will be its ecological capability.

MATERIALS AND METHODS

Study area

The half wells (known as Chah Nimeh) are large natural pits located in the distance of 50 kilometers from the city of Zabol. Excess water of the Helmand River flows into Chah Nimeh by a channel. The capacity of these reservoirs that have been converted as artificial lakes is 700 million cubic meters, located in the 41° 61' east and 54° 30' north latitude coordinates geographically (Fig 1). Plants from the families of *Tamaricaceae*, *Poaceae*, and *Chenopodiaceae* are more frequent in the region. 3800 hectares of Chah Nimeh area were dedicated to cultivating forest species. Afforestation species in this area include: *Eucalyptus camaldulensis*, *Tamarix aphylla*, *Olea europaea* and *Pinus eldarica*.

Study area in terms of the climate and weather classification, is considered a part of Iran' dry lands, because all the main characteristics of arid regions are found in this region such as the high level of solar radiation, the frequency range of daily and seasonal changes in temperature, low humidity,

strong winds accompanied by dust storms and sand, low and scattered rainfall and high temporal and spatial variations of the region's climatic conditions.

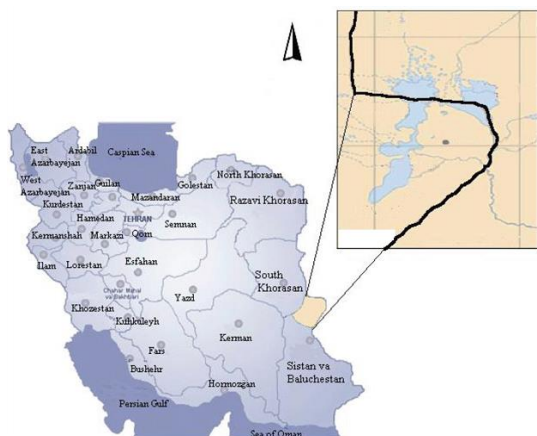


Fig. 1. The location of study area.

Maximum, minimum and average rainfalls in Sistan plain are respectively 123, 17 and 59 mm. Most of the atmospheric fallouts occur in winter, and January with 29 percent of total rainfall is the most rainfall month. Weather station data indicate that the minimum temperature and maximum temperature belong to January (1.24°C) and July (41.60°C), respectively. High temperatures and high sunshine hours made this region have the greatest amount of evaporation compared to other parts of the country (4775 mm per year). Another factor affecting the climate of the area is strong winds blowing in winter and spring alternately, and in summer constantly. These winds flow from the North and North West and are recognized as “120-day winds” during the warm season that begin in mid-June and continue until early October. The wind speed is 80 mph.

Sampling

Four forest stands of Pine, Tamarisk, Olive and Eucalyptus along with the surrounding bare lands (control plot) were selected randomly in this area. To reduce boundary effects, a few planting rows around each stand were not considered for sampling. In each forest stand, 10 plots (5m × 5m) were established in a systematic random way, and within each plot after removing litter layer, the soil from two depths 0-15cm and 16-30 cm was sampled.

To minimize error, the sampling was performed in combination. In this case, the soil samples were

taken from the four corners of the plot, then samples were pooled and one sample was harvested from each depth in every plot [31]. Thus, 10 combined samples were harvested in each depth in each forest stand and transferred to the laboratory. Samples were dried in air. Then, after crushing clods, separating the roots, rocks and other impurities, samples were milled and passed through sieve 5.0 mm [32,33]. Bulk density was studied by hunk in grams per cubic centimeter [34]. The organic carbon was determined using Walkley and Black method [35]. The amount of carbon sequestration was calculated according to the equation 1 [36].

$$Cs = 10000 \times OC (\%) \times Bd \times e \quad (1)$$

Where Cs = the amount of organic carbon sequestration (g/ m²); OC = organic carbon; Bd = Soil bulk density (gr/cm³); e = depth of sampling (cm)

Data analysis

To analyze the data, SPSS software version 19 was employed. Data normality and homogeneity of variance were analyzed using Smirnov-Kolmogorov test and Levene test, respectively. One-way ANOVA was used for total assessment of forest stands. Moreover, Duncan's test was used for multiple comparisons of means at the 5% level. Plot graph was prepared through Excel software.

RESULTS

Table 1 show the descriptive statistics of organic carbon (OC) and soil carbon sequestration (SCS) for 0-15 cm and 16-30 cm soil depths. Statistical analysis showed that there were significant differences between the types of afforestation in terms of organic carbon and SCS in soil (Table 2). Duncan's test showed that in depth of 0-15 cm soil, organic carbon in Pine stand (0.97%) is significantly greater than Olive plantation (0.50%) and the control (bare land) (0.42) ($p < 0.05$). In addition, the organic carbon in Tamarisk and Eucalyptus stands found to be more than the unplanted area at 95 percent level. Organic carbon averages in the 16-30 cm soil in Pine and Eucalyptus stands did not differ significantly, while they were more than the control (bare land). There was no significant difference between Tamarisk and Olive plantations in these terms (Table 3).

Table 1. Descriptive statistics of organic carbon (OC) and soil carbon sequestration (SCS) for 0-15 cm and 16-30 cm soil depths.

	N	Minimum	Maximum	Mean	Std. Deviation
OC (0-15 cm)	50	.10	1.90	.6680	.40327
OC (16-30 cm)	50	.04	2.00	.6786	.44181
SOC (0-15 cm)	50	1.05	24.80	8.4105	5.23077
SOC (16-30 cm)	50	1.14	24.80	9.0229	5.33725

Table 2. Statistical analysis (ANOVA) of organic carbon (OC) and soil carbon sequestration (SCS) for 0-15 cm and 16-30 cm soil depths.

		Sum of Squares	df	Mean Square	F	Sig.
OC (0-15 cm)	Between Groups	1.935	4	.484	3.607	.012
	Within Groups	6.034	45	.134		
	Total	7.969	49			
OC (16-30 cm)	Between Groups	2.129	4	.532	3.221	.021
	Within Groups	7.436	45	.165		
	Total	9.565	49			
SCS (0-15 cm)	Between Groups	305.489	4	76.372	3.320	.018
	Within Groups	1035.196	45	23.004		
	Total	1340.685	49			
SCS (16-30 cm)	Between Groups	206.733	4	51.683	1.956	.118
	Within Groups	1189.092	45	26.424		
	Total	1395.826	49			

Table 3. Organic carbon percent in two soil depths of afforestations with their standard error in the parenthesis.

	Pinus	Tamarisk	Eucalyptus	Olive	Bare land	ANOVA
0-15 cm	0.97(0.13) a	0.67 (0.10) abc	0.78 (0.16) ab	0.50 (0.06) bc	0.42 (0.08) c	*
16-30 cm	0.89 (0.13) a	0.71 (0.11) ab	0.89 (0.19) a	0.55 (0.08) ab	0.35 (0.09) b	**

ANOVA results: *, $p < 0.05$; **, $p < 0.01$. Mean values with the same letter within the soil layer do not differ significantly with each other (Duncan).

Also, Duncan's test showed that in the depth of 0-15 cm soil carbon sequestration in Pine stand (12.66 t/ha) was significantly greater than the control (Bare land) (6678 kg/ha) and Olive stand (6.27 T/ha) ($p < 0.01$). The carbon sequestration in Tamarisk (9.22 T/ha) and Eucalyptus (8.18 T/ha) did not indicate significant differences with other plantations and bare land at 95 percent level (Fig. 1). Carbon sequestration rate in the second depth of soil, in Pine (11.61 t/ha) was higher than Olive species (6.27 t/ha) ($p < 0.01$). There was no significant difference among Eucalyptus (10.41 t/ha), Tamarisk (9.77 t/ha), and bare land (7.05 t/ha) in this soil depth ($p < 0.05$, Fig. 2).

DISCUSSION

Soil C sequestration following afforestation has been the subject of a substantial body of research, which suggests that the direction and magnitude of SOC changes are determined by many factors and processes, such as climate, stand age and soil depth [37-39]. The major sources of carbon storage are

vegetation, especially forests. Forests serve as carbon reserves and stabilizers. When forests grow, they gradually store the carbon in wood textures and soil organic carbon matter over time [40]. Carbon is stored in plant tissues such as leaves and wood, and then in autumn dried leaves fell and decompose resulting in an increase in the amount of organic matter.

Carbon sequestration rate in upper soil in the Pine, Eucalyptus and Tamarisk is more than the bare area (control). This can be due to an accumulation of litter on the soil surface and its decomposition trend. Also, the amounts of organic matter derived from Walkley and Black method in Pine (1.66), Tamarisk (1.15) and Eucalyptus (1.34) afforestations were more than bare land (0.72). Vesterdal [41] in a study of 1 to 19 years old plantations, showed that the highest concentration of carbon is made in the soil depth of 5 cm. Woome *et al.* [42] studying on the amount of carbon stored in soils and plants in Senegal, concluded that about 60% of soil organic carbon is stored at a depth of 20 cm below the surface. The

rate of carbon sequestration in the soil surface of Olive afforestation is less than the control area and has the lowest carbon sequestration among other stands, suggesting afforestation with olive species is not able to increase carbon sequestration. Although the amount of organic matter in the soil of the Olive stand is somewhat more, but the average values of its soil bulk density was measured lower than bare land. For this reason, the amount of carbon stored in the soil under Olive plantation was calculated lower than the control area.

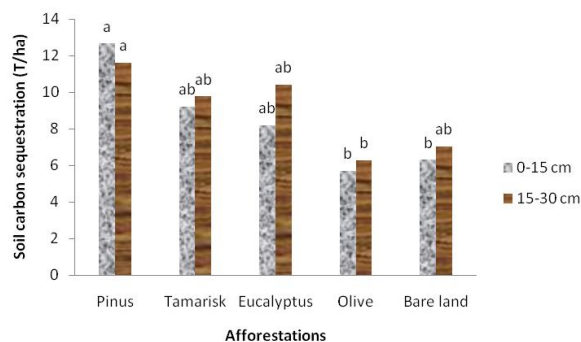


Fig. 2. Soil carbon sequestration in 0-15 cm and 15-30 cm depths in the different planted species

Also the results showed that the rate of carbon sequestration in depth of 16 to 30 cm of soil in the Pine, Eucalyptus and Tamarisk afforestations was higher than in bare land (control). To a certain proportion of annual precipitation, soil organic carbon storage increases as evapotranspiration decreases. Since evapotranspiration in Chah Nimeh is high, the organic carbon content sets low. Sequestration of carbon is associated with vegetation percent, plant species and amount of plant debris litter, type of land use and management. In case of appropriate establishment of vegetation in the area, soil organic carbon will increase in long-term, because soil organic carbon changes are gradual [43]. The root is an important component of ecosystems to sequester carbon, but because the study area is hot and dry and the ground water level is low in the region, the roots of trees did not have much development in this region. Roots and its coexistence with micro organisms are of the factors that affect carbon sequestration in soil including forested areas and afforestation areas. As a guess, the nitrogen fixing bacteria maybe low in the plants' roots. So, carbon sequestration is less in second depth of soil. Varamesh *et al.* [31] stated that soil organic carbon at a depth of 0-15 cm was more than 15-30 cm depth. Also, Amiqy *et al.* [44] measured the amount of organic carbon in the soil surface layer 0-25 cm to be greater than the 25- 50 cm layers. Zhao *et al.* [45] documented that

afforestation not only affects soil organic carbon (SOC) stocks in surface soil, but also strongly influences it in deep soil.

Forest type is also effective on carbon sequestration. Among land ecosystems, the conifer forests are the most important carbon-storing trees. Their contribution to mitigating climate change is considerable, because of their ability to absorb carbon dioxide from the atmosphere through photosynthesis and carbon storage potential in living and non-living components [46]. In this study it was found that carbon sequestration in soils beneath conifers (Pine) was greater than the soils under broadleaf species which is consistent with other studies [47-50] in their study in Scotland found that the conifer species increased density of surface litter, in other words, increased the soil organic carbon.

The results showed that the highest rates of carbon sequestration associated to Pine among the tree species, because the amount of its organic matter had the highest value in the surface, and so carbon sequestration in 0-15 cm of Pine plantation is more than 16-30 cm depth. Then the forest stands of Tamarisk and Eucalyptus had the most amount of carbon sequestration. This is because these species are resistant to dehydration and are salt-friendly. The carbon sequestration of these afforestations in second depth is greater than the first because their organic matter content is greater than the first depth, and perhaps due to the activity of root mass of the plant. In general, species that grow in dry areas have greater root biomass and volume. The olive stand had the least amount of carbon sequestration among the afforestations. Also, carbon sequestration in the second depth is greater than the first depth.

The different C content and stocks at 0-15 and 16-30cm depths is very important and determined by both organic matter dynamics and soil properties, which are in turn affected by vegetation. Reviews have shown that carbon biomass is influenced by forest type, climate, soil, topography, and human activity [24]. However, the changes in soil organic carbon that follow forestation are still under debate, and are influenced by vegetation production, soil conditions, land use history, the type of forest established, and forest management [27,51]. SOC after planting may increase [16,52-54] or decrease [12,51,55,56]. However, most reviews have presented initial losses in SOC, followed by slight increases [21,54,57,58].

CONCLUSIONS

The results showed that in this arid region, afforestation with species of Pine, Eucalyptus and Tamarisk increases the amount of carbon sequestration in soil. This research proved that the effects of afforestation varied with plant species. Moreover, it managed to show that needle leave species led to an increase in soil organic carbon storage more than hardwoods. Given that carbon sequestration is a measure of ecosystem stability, and by recognition of species which have a greater ability to sequester carbon, as well as through managing those factors affecting the process of carbon sequestration, reclamation and restoration of land can be achieved more successfully.

REFERENCES

1. IGBP, *Science*, **280**, 1393 (1998).
2. N.H. Batjes, *European Journal of Soil Science*, **47**, 151 (1996).
3. A. Farage, B.L.Ardo, C. Olsson, D. Rienzi, E. Ball, J.N. Pretty, *Soil and Tillage Research*, **94**, 457 (2007).
4. S. Matthews, R. O'Connor, A.J. Plantinga, *Ecological Economics*, **40**, 71 (2002).
5. S.Z. Zhong, L.S. Xiao, G.L. Xian, S.X. Zhen, *Journal of Soils Sediments*, **13**, 1043 (2013).
6. R.K. Dixon, S. Brown, R.A. Houghton, A.M. Solomon, M.C. Trexler, *Science*, **263**, 185 (1994).
7. I.K. Murthy, M. Gupta, S. Tomar, M. Munsri, R. Tiwari, G.T. Hegde, *Earth Science and Climatic Change*, **4**, 131 (2013).
8. R.B. Jackson, E.G. Jobbágy, R. Avissar, S.B. Roy, D.J. Barrett, C.W. Cook, *Science*, **310**, 1944 (2005).
9. K.A. Farley, *Annals of the Association of American Geographers*, **97**(4), 755 (2007).
10. M. Kraenzel, A. Castillo, T. Moore, *Forest Ecology and Management*, **173**, 213 (2003).
11. S. Nilsson, W. Schopfhauser, *Climatic Change*, **30**, 267 (1995).
12. P. Laclau, *Forest Ecology and Management*, **180**(1–3), 317 (2003).
13. E.Mahmoudi-Taleghani, Q. Zahedi-Amiri, J. Adeli, K. Sagheb-Talebi, *Journal of Forest and Poplar Research*, **15**, 241 (2007).
14. S.T. Gower, J.G. Vogel, J.M. Normal, C.J. Kucharic, S.J. Steele, T.K. Stow, *Journal of Geophysical Research Atmospheres*, **102**, 29029 (1997).
15. S.C. Cunningham, K.J. Metzeling, R. Mac Nally, J.R. Thomson, T.R. Cavagnaro, *Agriculture, Ecosystems and Environment*, **158**, 58 (2012).
16. S.Y. Korkance, *Catena*, **123**, 62 (2014).
17. R. Amundson, *Annual Review of Earth and Planetary Sciences*, **29**, 535 (2001).
18. N.H. Batjes, *Biology Fertility of Soils*, **27**, 230 (1998).
19. A. Thuille, E. Schulze, *Global Change Biology*, **12**(2), 325 (2006).
20. J.G. Canadell, *Science*, **320**, 1456 (2008).
21. K.I. Paul, P.J. Polglase, J.G. Nyakuengama, P.K. Khanna, *Forest Ecology and Management*, **168**(1–3): 241 (2002).
22. R.A. Houghton, E.A. Davidson, G.M. Woodwell, *Global Biogeochemical Cycles*, **12**, 25 (1998).
23. S. Fang, J. Xue, L. Tang, *Journal of Environmental Management*, **85**, 672 (2007).
24. T. Roosta, S.M. Hodjati, Forest soil management in relation to carbon sequestration - Fourth Conference of Environment, Tehran, Iran, 2010.
25. X. Zeng, W. Zhang, J. Cao, X. Liu, H. Shen, X. Zhao Changes in soil organic carbon, nitrogen, phosphorus, and bulk density after afforestation of the “Beijing–Tianjin Sandstorm Source Control” program in China – *Catena*, **118** (2), 2014, p.186.
26. L. Huang, J. Liu, Q. Shao, X. Xu, *Renewable and Sustainable Energy Reviews*, **16**, 1291 (2012).
27. H. Yan, M. Cao, J. Lieu, B. Tao, *Agriculture Ecosystems and Environment*, **121**, 352 (2007).
28. R. Lal, *Geoderma*, **123**, 1 (2004).
29. T. Roosta, An introduction to the importance of carbon sequestration role of forests soil in relation to climate change in Iran and the world - Fifth Conference on Environmental Engineering, Tehran, Iran, 2011.
30. E.A. Naghipour, M. Aghakhani, Q. Dianati, D. Kartulynejad, Carbon sequestration in Hyrcanian Forests, way to mitigate of climate change - Proceedings of the First international conference on climate change and dendrochronology in Caspian Ecosystem, Tehran, Iran, 2004.
31. S. Vramesh, S.M. Hosseini, N. Abdi, M. Akbarinia *Journal of Iranian Forest*, **2**(1), 25 (2010).
32. K.G. McDicken - A Guide to Monitoring Carbon Storage in Forestry and Agroforestry Projects. Winrock International Institute for Agricultural Development - Forest Carbon Monitoring Program, 1997, p.91.
33. R. Hernandez, P. Koohafkan, J. Antoine, Assessing Carbon Stocks and modeling win-win Scenarios of carbon sequestration through land-use change, Food and Agriculture Organization of the United Nations, Rome, 2004, p. 166.
34. G.R. Blake, K.H. Hartge, in: Klute, A. (Ed.), *Methods of Soil Analysis. Part I. Physical and Mineralogical Methods* - Soil Society America, Pub. No. 9. Part 1, 1986, p.363.
35. A. Walkley, I. Black, *Soil Science Society of America Journal*, **37**, 29 (1934).
36. G. Zahedi, in: Proceeding of the XII World Forestry Congress in Canada, Quebec, 2002, p. 357.
37. J. Laganière, D.A. Angers, *Global Change Biology*, **16**, 439 (2010).
38. Y. Yang, Y. Luo, A.C. Finzi, *New Phytologist*, **190**, 977 (2011).
39. D. Li, S. Niu, Y. Luo, *New Phytologist*, **195**, 172 (2012).
40. M. Mortenson, G.E. Schuman, Carbon sequestration in rangeland interseed with yellow flowering Alfalfa(*Medicago sativa* spp *Facata*) - USDA

- symposium on natural resource management to effect greenhouse gas emission in Uni of Wyoming, 2002.
41. L. Vesterdal, *Forest Ecology and Management*, **169**, 137 (2002).
42. D.L. Woomer, A. Tourc, M. Sall, *Journal of Arid Environments*, **59**, 499 (2004).
43. T. Chiti, G. Cerini, A. Puglisi, G. Sanesi, A. Capperucci, *Goderma journal*, **61**, 35 (2006).
44. S.J. Amiqy, H.M. Asgari, V. Berdy-Sheikh, F. Honardost, Effect of agroforestry on carbon sequestration in the soil - First National Conference on Desertification, International Desert Research Center, Tehran University, Tehran, Iran, 2012.
45. F. Zhao, D. Kang, X. Han, G. Yang, G. Yang, Y. Feng, G. Ren, *Ecological Engineering*, **74**, 415 (2015).
46. H. Gucinski, E. Vance, W.A. Reiners, in: Smith, W. K., Hinckley, T.M. (Eds), *Ecophysiology of Coniferous Forests*, Academic Press, New York, 1995, p. 309.
47. E.E. Nobakht, M. Pourmajidian, S.M. Hodjati, A. Fallah, *Journal of Forestry*, **3**(1), 23 (2011).
48. S. Varamesh, S.M. Hosseini, N. Abdi, *Journal of Soil Science*, **25** 187 (2011).
49. S. Sadat-Aryapak, M. Bayramzadeh, A. Moeini, *Journal of natural resource exploitation*, **1**, 15 (2012).
50. M.G. Cannel, R.C. Dewar, The carbon sinks provided by plantation forests and their products in Britain, Institute of Terrestrial Ecology, Scotland, 1993, p. 124.
51. Y.L. Zinn, D.V.S. Resck, J.E. Silva, *Forest Ecology and Management*, **166**, 285 (2002).
52. T. Charles, J.R. Garten, *Biomass and Bioenergy*, **23**(2), 93 (2002).
53. G.E. Schuman, H. Janzen J.E. Herrick, *Environmental Pollution*, **116**, 391 (2002).
54. S.Q. Wang, J.Y. Liu, G.R. Yu, Y.D. Pan, Q.M. Chen, K.R. Li, *Climatic Change*, **67**, 247 (2004).
55. D.D. Richter, D. Markewitz, S.E. Trumbore, C.G. Wells, *Nature*, **400**, 56 (1999).
56. A. Specht, P.W. West, *Biomass and Bioenergy*, **25**, 363 (2003).
57. J. Turner, M. Lambert, *Forest Ecology and Management*, **133**, 231 (2000).
58. M. Huang, J.J. Ji, K.R. Li, Y.F. Liu, F.T. Yang, *Tellus Series B*, **59**, 439 (2007).

Efficiency comparison of alum and ferric chloride coagulants in removal of dye and organic material from industrial wastewater - a case study

Davood Jalili Naghan¹, Mohammad Darvish Motevalli¹, Nezam Mirzaei², Allahbakhsh Javid³,
Hamid Reza Ghaffari⁴, Mohammad Ahmadpour⁵, Masoud Moradi^{6,7}, Kiomars Sharafi^{7,1*}

¹Department of Environmental Health Engineering, School of Public Health, Tehran University of Medical Sciences, Tehran, Iran.

²Environmental Health Research Center, Kurdistan University of Medical Sciences, Sanandaj, Iran.

³School of Public Health, Shahroud University of Medical Sciences, Shahroud, Iran.

⁴Social Determinants in Health Promotion Research Center, Hormozgan University of Medical Sciences, Bandar Abbas, Iran.

⁵Instructor, M.S.c, Department of Public Health, Maragheh University of Medical Sciences, Maragheh, Iran.

⁶Department of Environmental Health Engineering, Iran University of Medical Sciences, Tehran, Iran

⁷Department of Environmental Health Engineering, School of Public Health, Kermanshah University of Medical Sciences, Kermanshah, Iran

Received June 26, 2015, Revised September 10, 2015

Coagulation and flocculation are most widely methods used for dye and pollution removal from various wastewaters. The aim of this study is efficiency comparison of inorganic coagulant (Alum and Ferric Chloride) for treatment of textile factory wastewater. The appropriate coagulant was selected at optimum condition for treatment of textile's factory wastewater by measuring of dye, COD, BOD₅ and TSS parameters. The different pH (4, 5, 6, 7, 8 and 9) was used for determine the optimum pH. Totally, 240 samples were collected and examined according the standard methods of wastewater and water tests. Results showed that the ferric chloride has more removal efficiency than alum in removal of COD, TSS and dye. The most removal of COD, TSS and dye using alum was obtained 36, 19 and 68.8% while for ferric chloride was obtained 72, 60 and 98% respectively. The optimum pH 7 and 5 were obtained for alum and ferric chloride respectively. Based on the results, it can be concluded that COD, TSS and dye removal using ferric chloride has higher efficiency than alum. Therefore, application of ferric chloride in the same conditions is preferred than alum.

Keywords: wastewater treatment, textile's wastewater, coagulant, Alum, ferric chloride.

INTRODUCTION

High level pollutants have discharged into the environment at the recent decades due to develop of industrial activities on the one hand and non-compliance with environmental requirements. Accumulation of these organic compounds in the environment poses a serious threat to human health, environment, living organisms and ecosystems (1, 2). The textile industry is one of the oldest industries in the world. This industry from 5000 BC and was recognized when piece of linen clothing was found at Egyptians caves, and was developed with the invention of machines for spinning and weaving after the industrial revolution in England at the eighteenth century. The first man-made fabrics (rayon fibers) were presented to market in the twentieth century (1910). In the recent century, the process of textile factories has been automated

and computer-aided work due to technology development. The sewage of different processes units of textile industry has most important environmental issues compared to other waste such as solid waste as well as health and safety is more important. Textile dyeing industry is one of the largest water users that lead to produce the significant amounts of wastewater. This wastewater contains significant amounts of organic dye compounds. Exist of organic dye materials in industrial wastewater cause the irreversible damage to the environment due to decreasing the light penetration into the water and disruption of photosynthesis, reducing the oxygen transfer into the water and the solubility of gases. Also discharge of wastewater into rivers and lakes leads to decreasing water quality (3-7).

Generally, industrial wastewater contaminants include caustic soda, detergents, starch, wax, urea, ammonia, dyes and pigments lifting of biochemical and chemical oxygen demand, suspended solids and toxic substances. Hence, it is necessary the

To whom all correspondence should be sent:
E-mail: kio.sharafi@gmail.com

treatment of textile dye effluent before discharging into the environment. Biological treatment processes are rarely used for textile wastewater treatment. These processes commonly are effective in biochemical oxygen demand (BOD₅) and suspended solids (SS) removal, but are ineffective for the dyes removal from these wastewaters(8), because dye compounds are complex and resistant structures that cause the rate of biodegradation dyes to be slow. The most common method that used for the dyes removal from textile wastewater include physical-chemical methods such as coagulation and flocculation, adsorption, ozonation, reverse osmosis and advanced oxidation are using membrane filters(9-12). Each of these methods has advantages and disadvantages for the dyes removal from wastewater. Coagulation and flocculation processes are used one of the most common and effective method for treatment of effluents dyes (11, 13, and 14).The produce of non-toxic and non-harmful of intermediate products is main advantages of effluents dyes treatment with coagulation and flocculation. Beside, this method is cost effective and is implemented on a large scale (14, 15).In general, coagulation and flocculation is proper method for removal of organic compounds with high weight and larger molecular chains (11, 14 and 16).The aim of this study was to evaluate the effectiveness of alum and ferric chloride coagulants in treatment of one Type of industrial wastewater (textile factory wastewater). For this purpose, the effect of pH and concentration of coagulants are examined.

MATERIAL &METHODS

This study is a cross-sectional study. The samples were collected from sewage of textile factory and were properly transferred to the chemistry laboratory. Optimum pH was adjusted with sodium hydroxide (1N) and sulfuric acid (0.1N) respectively using pH-meter model of Microprocessor 537. At the first step, the pH=6 was selected to determine of appropriate coagulant amount, then coagulant gradually added to the 6 containers of Jar test and experiments were continues until visible flock with appropriate settling was observed. In the second step, after determination of approximate amount of suitable coagulant in previous step, the optimum pH was determined for each individual coagulant using Jar test with pH adjustment at 4, 5, 6, 7, 8 and 9. In the third step, considering the optimal pH obtained at second step, the different amounts of coagulant were added to containers for determine proper dosage of coagulant (2 containers with less than

amount coagulant of first step, 1 container with equal amount coagulant of first step and 3 containers with more than amount coagulant of first step) The efficiency removal of dye, COD and BOD₅ were applied as indicators to determine of appropriate coagulant dosage and optimum pH. The tests carried out for both coagulants at least twice in each load. After the addition of coagulant, the samples was transferred to Jar test containers (HACH model) and rapid mixing was conducted for destabilizing particles for one minute at speed of 90 rpm and slow mixing was conducted for create the settling flock for 3 minutes at speed of 30 rpm. After slow mixing, the sample for 15 minutes for sedimentation was kept in stasis. Dye was measured with optical density method at 470 nm using spectrophotometer Varian UV-120-02 models made in America and COD measuring was conducted using COD reactor HACH model with closed reflux method.

Experiments were accomplished thrice and in total 240 samples tested according standard methods for water and wastewater treatment were assessed (17). Used coagulants include Aluminum sulfate (Al₂(SO₄)₃) and ferric chloride (FeCl₃).

The removal efficiency was calculated as fallow equation:

$$\eta_{Color} = \frac{OD_0 - OD}{OD_0} \times 100 \quad (1)$$

Where

η_{Color}	Efficiency removal of Dye by coagulants
DO ₀	optical density of wastewater before coagulation
DO	optical density of wastewater after coagulation

RESULTS

Table 1 shows the performance compares of alum and ferric chloride coagulant in COD removal of wastewater at optimum pH. Figure 1 shows comparison the COD level after the addition of alum(550 mg/L) and ferric chloride (150 mg/L) and its percentage removal in samples at different pH and different COD of wastewater (1100 and 512 mg/L). Figure 2 shows comparison the COD level after the addition of alum (400 mg/L) and ferric chloride (250 mg/L) and its percentage removal in wastewater samples at different pH and different COD of wastewater (512 and 1280 mg/L). Figure 3 shows the comparison of COD level after the addition of alum (pH =7) and ferric chloride (pH =5) and its percentage removal textile factory wastewater with different COD concentrations in

raw wastewater (512 and 1280 mg/L), Figure 4 shows the comparison of TSS level after adding different amounts of alum (pH = 4) and ferric chloride (pH =5) and its percentage removal in textile factory wastewater with different TSS concentrations of raw sewage (240 and 320 mg/L), Figure 5 shows the dye removal at different pH and certain concentration of alum (500 mg/L) and ferric chloride (400 mg/L) and Figure 6 shows the percentage removal of dye with different concentrations of alum (pH=7) and ferric chloride (pH=9).

DISCUSSION

The results of other studies conducted by many researchers confirmed that pH is a significant factor in the coagulation and flocculation process. Each coagulant has an optimum pH which in that condition, coagulation and flocculation process for certain dosage of coagulant, the highest efficiency occurs in the shortest time. Therefore, determining of this factor is necessary to ensure the performance of coagulation and flocculation process (18). Thus, it is necessary determine of optimum pH for treatment of textile wastewater factory with alum and ferric chloride coagulant. The results showed that pH has effect on decreasing of COD level in treated wastewater use alum and ferric alum coagulants. So that the highest efficiency of COD and dye removal obtained for alum and ferric chloride coagulants at pH = 7 and pH =5-9 respectively. Alum with different dosage and pH=7 has low efficiency removal of COD even in low concentration (512 mg/L), but with 550 mg/L dosage and pH=7 has highest efficiency removal (36%) in high concentration of raw wastewater COD (1100 mg/L) and with 550 mg/L dosage was obtained highest efficiency removal of dye (75%). Ferric chloride with 150 mg/L and pH=5 has highest efficiency removal in low concentration of raw wastewater COD (68.75%) and with 250 mg/L

dosage and pH=5, removal efficiency of COD was obtained 60%. Ferric chloride with 400 mg/L dosage has highest removal efficiency of dye (98%).

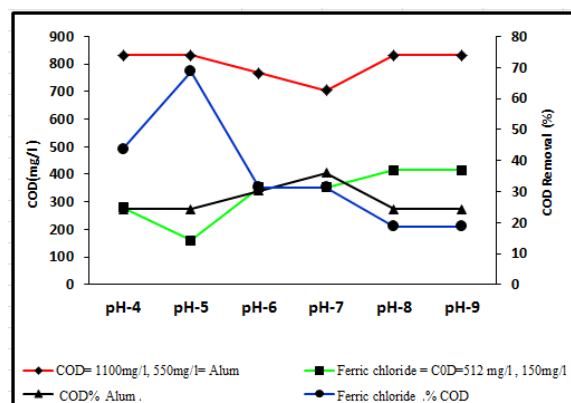


Fig. 1. Comparison of COD level after the addition of alum (550 mg/L) and ferric chloride (150 mg/L) and its percentage removal in samples at different pH and different COD of wastewater (1100 and 512 mg/L).

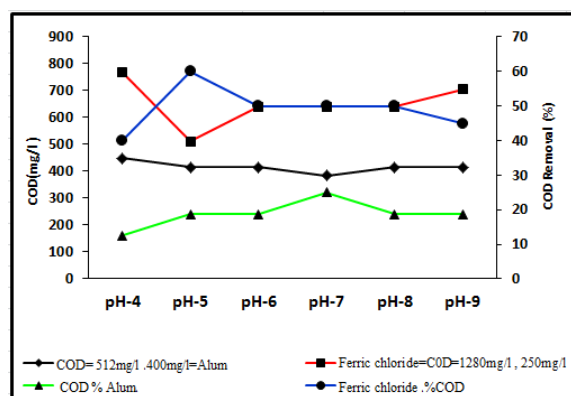


Fig. 2. Comparison of COD level after the addition of alum(400 mg/L) and ferric chloride (250 mg/L) and its percentage removal in wastewater samples at different pH and different COD of wastewater (512 and 1280 mg/L).

Table 1. The comparison COD level and its removal percentage in different pH, alum= 550 mg/L and ferric chloride =150 mg/L in different COD of raw sewage (512 and 1100 mg/L).

Coagulants	Parameters				
	Range of raw sewage COD (mg/l)	Range of sewage COD after Jar test (mg/l)	Optimum pH	Consumed coagulant (mg/l)	Efficiency removal of COD (%)
Alum	512 -1100	384 - 704	7	400 - 550	25 - 36
Ferric chloride	512 -1280	160 - 641	5	150 - 250	60 - 68.75

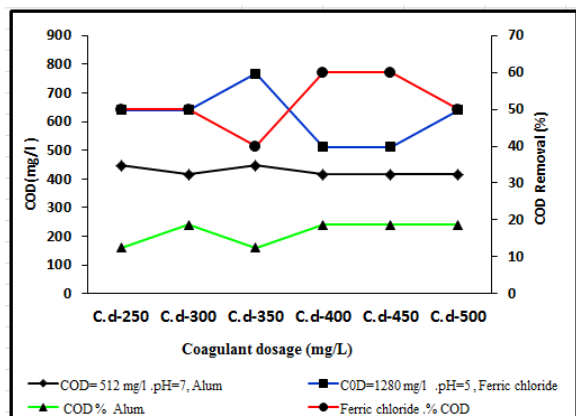


Fig. 3. Comparison of COD level after the addition of alum (pH =7) and ferric chloride (pH =5) and its percentage removal textile factory wastewater with different COD concentrations in raw wastewater (512 and 1280 mg/L).

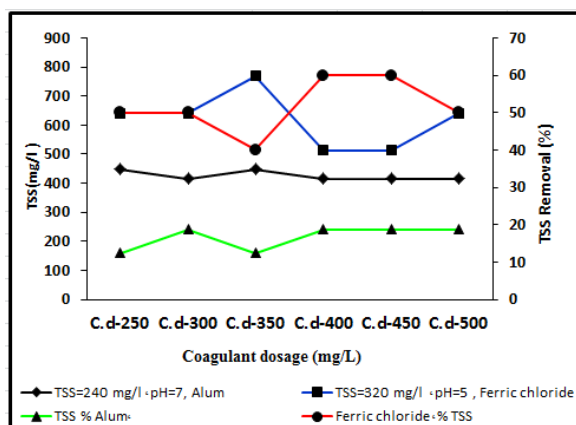


Fig. 4. Comparison of TSS level after adding different amounts of alum (pH = 4) and ferric chloride (pH =5) and its removal in textile factory wastewater with different TSS concentrations of raw sewage (240 and 320 mg/L).

Considering the results, ferric chloride with 150 and 250 mg/L was recommended for low and high concentration of COD respectively. This coagulant was selected for treatment of textile wastewater. The comparison of these results with results obtained from dye and COD removal using magnesium carbonate, PAC and combined treatment of textile wastewater using coagulation and oxidation with fenton (19-21). Indicated that ferric chloride has more efficiency removal than magnesium carbonate. Also, Jonaidy and Azizi (2008) reported that ferric chloride has best efficiency removal of dye than alum which confirms the results of this study (22).

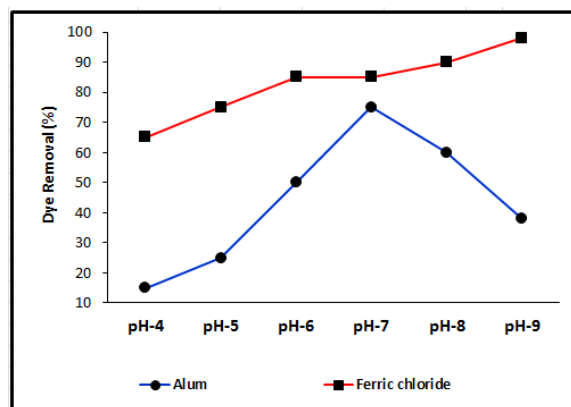


Fig. 5. The dye removal at different pH and constant concentration of alum (500 mg/L) and ferric chloride (400 mg/L).

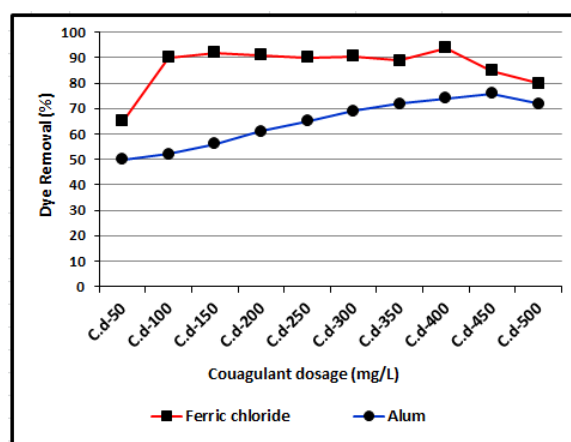


Fig. 6. The dye removal with different concentrations of alum (pH=7) and ferric chloride (pH=9).

CONCLUSION

Based on the findings, pH is effective parameters in terms of coagulation and flocculation process and it can be concluded that using ferric chloride to removal of COD, TSS and color of textile factory's wastewater had higher efficiency than alum and therefore its application in the same conditions than alum is preferred.

Acknowledgements: The authors acknowledge all non-financial supports provided by Kermanshah University of Medical Sciences and Tehran University of Medical Sciences. The authors declare that there is no conflict of interest.

REFERENCES

1. D. C. Kalyani, P. S. Patil, J. P. Gadhave, S. P. Govindwar, *Bioresource Technology*, **99**, 4635 (2008).
2. C. Hessel, C. Allegre, M. Maisseu, F. Charbit, P. Moulin, *Journal of Environmental Management*, **83**, 171 (2007).
3. N. Daneshvar, D. Salari, A.R. Khataee, *J. Photochem. Photobiol*, **157**, 111 (2003).

4. N. Daneshvar, D. Salari, A.R. Khataee, J. Photochem. Photobiol, 162, 317 (2004).
5. N. Supaka, K. Juntongjin, S. Damronglerd, Chemical Engineering Journal, 99, 169 (2004).
6. Y. M. Kolekar, Sh. P. Pawar, K. R. Gawai, P. D. Lokhande, Y.S. Shouche, K.M. Kodam, Bioresource Technology, 99, 8999 (2008).
7. J. Roussy, M.V. Vooren, B.A. Dempsey, E. Guibal, Water Research, 39, 3247 (2005).
8. M.C. Kay, J American Dyestuff Reporter, 68, 29 (1979).
9. B. H. Tan, T. T. Teng, A. K. Mohd, Water Res, 34(2),507 (2000).
10. G.R.N. Bidhendi, A. Torabian, H. Ehsani, N. Razmkhah, Iran.J. Environ. Health. Sci. Eng, 4, 29 (2007).
11. B. Shi, G. Li, D. Wang, C. Feng, H. Tang, J. Hazard. Mater, 143, 567 (2007).
12. Y. Yuan Y. Wen, X. Li, S. Luo, J. Zhejiang Univ. Sci. A, 7, 340 (2007).
13. G.R.N. Bidhendi, A. Torabian, H. Ehsani, N. Razmkhah, Iran. J. Environ. Health. Sci. Eng, 4, 29 (2007).
14. V. Golob, A. Vinder, M. Simonic, Dyes Pigments, 67, 93 (2005).
15. D. Wang, W. Sun, Y. Xu, H. Tang, J. Gregory, Colloids Surf. A: Physicochem. Eng. Aspects, 243, 1 (2004).
16. B. Gao, Q. Yue, Y. Wang, W. Zhou, J. Environ. Manage, 82, 167 (2007).
17. R. Sanghi, B. Bhattacharya, A. Dixit, V. Singh. J. Environ. Manage, 81, 36 (2006).
18. A. Torabian, J. Environmental. Stud, 23(20), 1 (1997).
19. M. H. Zonoozi, Environmental Engineering and Management Journal, 7(6), 695 (2008).
20. A. N. Nguyen, Water. Res, 30(35), 800 (2005).
21. J. Joneidi, S. Azizi, Comparison between color removal from synthetic wastewater using Alum and Chlorine. 11th National congress of environmental health, Zahedan University of Medical Sciences, Zahedan, Iran, 2008.
22. APHA, AWWA and WPCF. Standard method for the examination of water and wastewater. 21thed. Washington DC: American Public Health Association, 2005.

The effect of soil properties and plant species on the absorption of heavy metals in industrial sewage contaminated soil: A case study of Eshtehard Industrial Park

M.R.S. Benis^{1*}, A.H. Hassani², J. Nouri³, I. Mehregan⁴, F. Moattar²

¹Department of Natural Resources - Environmental Engineering, School of Environment and Energy, Science and Research Branch, Islamic Azad University, Tehran, Iran

²Department of Environmental Engineering, School of Environment and Energy, Science and Research Branch, Islamic Azad University, Tehran, Iran

³Department of Environmental Management, School of Environment and Energy, Science and Research Branch, Islamic Azad University, Tehran, Iran

⁴Department of Biology, School of Basic Sciences, Science and Research Branch, Islamic Azad University, Tehran, Iran

Received June 26, 2015; Revised September 10, 2015

In recent years, the rapid development of industries in developing countries has led to the excessive contamination of the soil in these areas. In Eshtehard Industrial Park, Iran, untreated industrial and domestic sewage containing heavy metals has entered the soil along the northern edges of the area. The present study has sought to measure the contamination of this particular area of soil with heavy metals including Cr, Zn, Cd, Pb and Ni, normally present in untreated sewage. The study also measured the absorption rate of heavy metals by local plants. The physicochemical properties of the soil were also examined through using standard methods. The results of the Kruskal-Wallis test showed that the species of the plant and its particular organs have an effect on the absorption of heavy metals. The Pearson test was used to assess the correlation between the physicochemical properties of the soil and the absorption of its heavy metal content by plants. The present study examined identified *Alhagi pseudalhagi* (M.B.) Desf., *Salvia aristata* Aucher ex Benth, *Stipa barbata* Desf., *Salsola kali* and *Peganum harmala* L., which have been examined for phytoremediation, for the first time, and identified them as hyperaccumulators according to the EPA definition. Planting the seeds of hyperaccumulating plants and adding DTPA to the soil helps absorb the heavy metal contaminants of the soil and constitutes a measure that can be used to purify the soil; the plants used can then be harvested, collected and disposed of as regular just like industrial sewage.

Keywords: Soil properties, phytoremediation, heavy metals, hyperaccumulating plants, Eshtehard Industrial Park

INTRODUCTION

Sanitary and industrial sewage have become massive sources of soil and water contamination in developing countries and the presence of heavy metals in raw industrial sewage constitutes a major health problem. Heavy metals are non-biodegradable types of metal that cause dangerous diseases. Through the proper treatment and careful observation of sewer standards [1], sanitary and industrial sewage can be used for agricultural irrigation, and the resulting sewage sludge [2] containing organic compounds and nutrients required for plants can be used as an inexpensive fertilizer if treated by standard criteria. The sanitary and industrial sewage exiting Eshtehard Industrial Park is currently contaminating the soil in the northern edges of the area, caused by miscalculations in the treatment plant's capacity given the number of industrial units built in the park and also the plant's frequent break-downs.

This untreated sewage contains heavy metals originated from various industrial processes such as plating, and is discharged into the soil in the northern part of the industrial park. The present study was conducted to investigate the contamination of soil with heavy metals including Cr, Zn, Cd, Pb and Ni. According to the standards set by Kabata-Pendias and Pendias, soil contamination is considered critical when the concentration of heavy metals in the soil falls in these ranges: 75 to 100 mg kg⁻¹ for Chromium, 70 to 400 for Zinc, 3 to 8 for Cadmium, 100 to 400 for Lead and 100 for Nickel; any concentration below these ranges is considered normal [3]. Phytoremediation is a bioremediation technique used for the phytoextraction and remediation of contaminated soil. This method is inexpensive and can be used on a large scale. Phytoaccumulation is one of the techniques used for phytoremediation, in which the removal of heavy metals from the soil depends on the plants' natural metal absorption capacity. Using hyperaccumulating plants therefore

To whom all correspondence should be sent:
E-mail: reza_sadeghia@yahoo.com

provides the best option available for the removal of heavy metals from the soil.

According to the EPA definition, a hyperaccumulating plant is a plant that accumulates metals in its shoot and root at the following total concentrations: 100 mg kg⁻¹ for Cadmium, 1000 mg kg⁻¹ for Chromium and Lead and over 10,000 mg kg⁻¹ for Zinc and Nickel [4]. The present study examines hyperaccumulating plants that can accumulate Cr, Zn, Cd, Pb and Ni. Ziarati used the hyperaccumulating plant *Amaranthus sp.* for the phytoremediation of soils contaminated with the heavy metals present in Tehran's municipal sewage [5]. The phytoremediation of heavy metal contaminated soils should be carried out with a full knowledge of the complex effects of plant-soil parameters. An important condition for the storage and accumulation of metal in a plant is to increase the metal's available concentration for the plant. In other words, a soluble form of the metal should remain near the root membrane of the plant in the soil for a set period of time. In geographical terms, factors affecting the solubility of the metal and its available form in the soil are vastly different and include the concentration and chemical form of the metal present in the soil, the physicochemical and biological properties of the soil (including pH, EC, OC, CCE, available phosphorus and soil texture) and additives such as DTPA. Hung conducted a study in Taiwan to examine the effects of the physicochemical properties of soil and the addition of DTPA on the absorption of heavy metals by plants [6]. Among the plants examined, some hyperaccumulators were discovered for the first time, and others were found to absorb high concentrations of heavy metals due to the changes made in the physicochemical and biological properties of the soil caused by its contamination with untreated sewage and were thus identified as hyperaccumulators for the first time.

EXPERIMENTAL

Study Site: The present study was conducted in areas contaminated with untreated sewage in Eshtehard Industrial Park, located at the longitude of 35° 42' 18" N and the latitude of 50° 18' 22" E and the mean altitude of 1200 m above sea level with a relatively dry climate and an average annual rainfall of 220 mm [7].

Sampling: Samples were collected between 2011 and 2013 during the period from early June to mid-September from mature plants in the contaminated areas and the control areas by the full removal of their shoot and root from the soil. Given the sparseness of vegetation in the contaminated

areas, sampling was conducted using systematic random sampling, i.e. without a frame and merely through observation [8]. The plant samples were then transferred to the herbarium of Islamic Azad University, Science and Research Branch, Tehran, Iran, where they were identified by name. Soil samples were collected separately from each plant's sampling area from the 0 to 20 cm depth of the rhizosphere soil. The soil samples were packed separately in polyethylene bags, and after being numbered and having their location and date detailed, they were sent to the environmental laboratory of Islamic Azad University, Science and Research Branch, Tehran, Iran.

Measuring Cr, Zn, Cd, Pb and Ni concentrations in the samples:

The researchers used the acid digestion method to determine the overall concentration of heavy metals in the soil samples [9]. They poured two grams of each soil sample into an Erlenmeyer flask with stopper and then added in 15 ml of 4 normal nitric acid. They then placed the flasks in a water bath at 80 °C for 12 hours. After passing the samples through a Whatman filter paper 42, the researchers recorded the samples' heavy metal concentrations using a Varian Spectraa 200 atomic absorption spectrophotometer made in Australia.

To measure the soil samples' concentrations of plant-available heavy metals, the researchers used Lindsay & Norval's [10] method with a DTPA extractor. To prepare the DTPA solution (Diethylene Triamine Penta-acetic Acid), they weighed 0.005 mol of DTPA salt (1.96 grams) and transferred it to a 1-liter flask containing 950 ml of distilled water. They then placed the flask on a shaker for the salt to dissolve, and then added in 1.4 grams of dehydrated calcium chloride and 13.3 ml of Triamine N(CH₂CH₂OH)₃, and raised the volume to 1000 ml by adding in distilled water and carefully stirring it. They then added 20ml of the produced extract to 2 grams of the soil sample and placed it for 2 hours on a shaker at 20-25 °C for 2 hours. They filtered the soil extract through a Whatman filter paper 42 and read the heavy metal concentrations using a Varian Spectraa 200 spectrophotometer.

To determine the exchangeable concentrations, the researchers used the Tessier extraction method [11]. They transferred 2 grams of each soil sample to an Erlenmeyer flask with stopper and added in 20 ml of 1 mol ammonium acetate (pH=7) and then placed the flask on a shaker at 20-25 °C for 30 minutes. They then filtered the soil extract through a Whatman filter paper 42 and used a Varian

Spectraa 200 spectrophotometer to read the heavy metal concentrations.

The researchers then carefully examined the physicochemical properties of the soils, including their pH, EC, OC, CCE, available phosphorus and soil texture, using standard methods [12].

To determine the total concentration of heavy metals in the plant samples, the researchers used the Dry Ash extraction method [13]. They transferred 2 grams of each plant sample to a crucible and placed it in an oven at 550 °C for 2 hours. They then added 5 ml of hydrochloric acid 2N to the samples and passed them through a filter paper. They used an atomic absorption spectrophotometer to read the heavy metal concentrations.

RESULTS AND DISCUSSION

The identified plants are presented in Table 1.

As seen in Table 1, the plants are coded.

The physicochemical properties of the soils were measured over 3 years in the contaminated

and control areas. Table 2 presents the mean values obtained for these properties in the sewage contaminated area.

As shown by table 2, the entry of sewage has changed the physicochemical properties of soil in the contaminated area compared to in the control area.

The concentration of heavy metals in the soil was measured in the contaminated and control areas. The control area was selected based on the physicochemical similarities of its soil to the contaminated soil (table 2).

Figure 1 shows the total, exchangeable, and extractable concentrations of heavy metals using DTPA extractor with a mean of 3 replicates in the area contaminated with sewage. Furthermore, to facilitate locating the sampled soil, each area was coded with the number of the plant grown in that area (as in Table 1). For example, soil No.1 was sampled from the area that *Launaea acanthodes* (Boiss.) O.Kuntze grew.

Table 1. The name of identified plants

Plant No	Plant species	Plant No	Plant species	Plant No	Plant species
1	<i>Launaea acanthodes</i> (Boiss.) O.Kuntze	10	<i>Salsola kali</i>	19	<i>Bromus tectorum</i> L.
2	<i>Thevenotia persica</i> DC	11	<i>Ceratocarpus arenarius</i> L.	20	<i>Phragmites australis</i> (Cav) Trin. ex Steud
3	<i>Carthamus oxyacantha</i> M.B	12	<i>Salsola persica</i> Bunge ex Boiss.	21	<i>Echinochloa crus-galli</i> (L.) P.Beauv.
4	<i>Artemisia herba-alba</i> Asso.	13	<i>Alhagi persarum</i> Boiss. & Buhse	22	<i>Hordeum vulgare</i> L.
5	<i>Amaranthus graecizans</i> L.	14	<i>Alhagi pseudalhagi</i> (M.B.) Desf.	23	<i>Stipa barbata</i> Desf.
6	<i>Nonnea persica</i> Boiss.	15	<i>Astragalus aureus</i> Wild	24	<i>Papaver piptostigma</i> Bienert ex Fedde
7	<i>Salsola nitraria</i> Pall.	16	<i>Alhagi camelorum</i> Fisch.	25	<i>Polygonum patulum</i> M.B.
8	<i>Atriplex aucheri</i> Moq.	17	<i>Erodium Cicutarium</i> (Jusl) L'Her.exaition	26	<i>Pteropryum aucheri</i> Jaub. & Spach
9	<i>Kochia scoparia</i> (L.) Shrad	18	<i>Salvia aristata</i> Aucher ex Benth	27	<i>Peganum harmala</i> L.

Table 2. The mean and standard deviation of the physicochemical properties of the sewage contaminated soils

The name of Area	Clay %	Sand %	Silt %	Soil texture	pH	EC dS m ⁻¹	OC %	CCE %	Available phosphorus mg kg ⁻¹
Contaminated area	18.7±6.6	44.4±3.4	36.8±9.9	Sandy Clay Loam and Loam Sandy Clay	6.5±0.2	1.8±0.6	0.6±0.1	5.7±1.2	24.3±4.2
Control area	19.8±7.1	45±2.5	35.1±10.1	Clay Loam and Loam	6.9±0.1	0.6±0.2	0.3±0.1	7.9±1.3	16.3±4.3

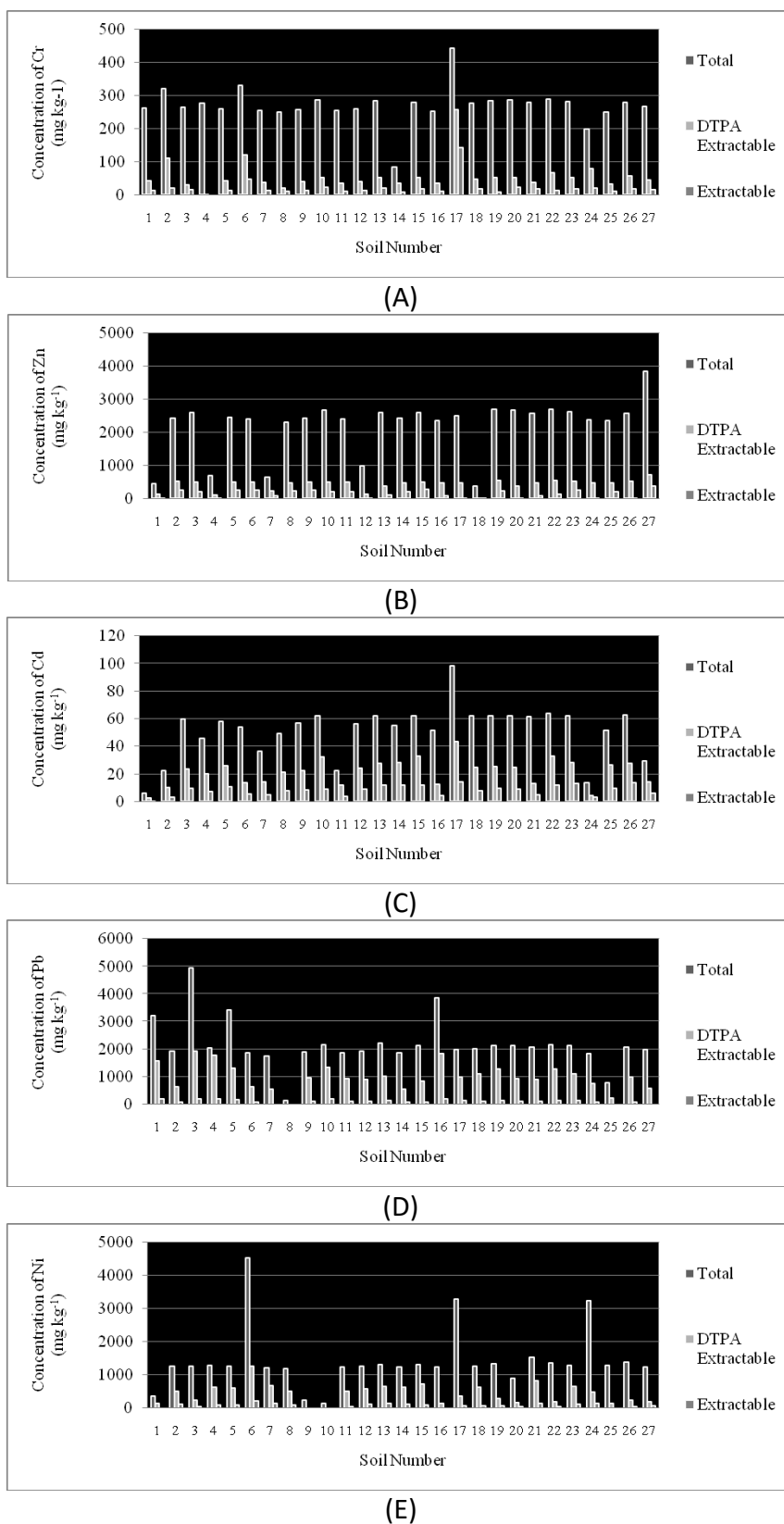


Fig. 1. The mean of concentrations of Cr (A), Zn (B), Cd (D), Pb (Pb) and Ni (Ni) in 3 replicates of soil samples contaminated with raw sewage (mg kg⁻¹ of soil).

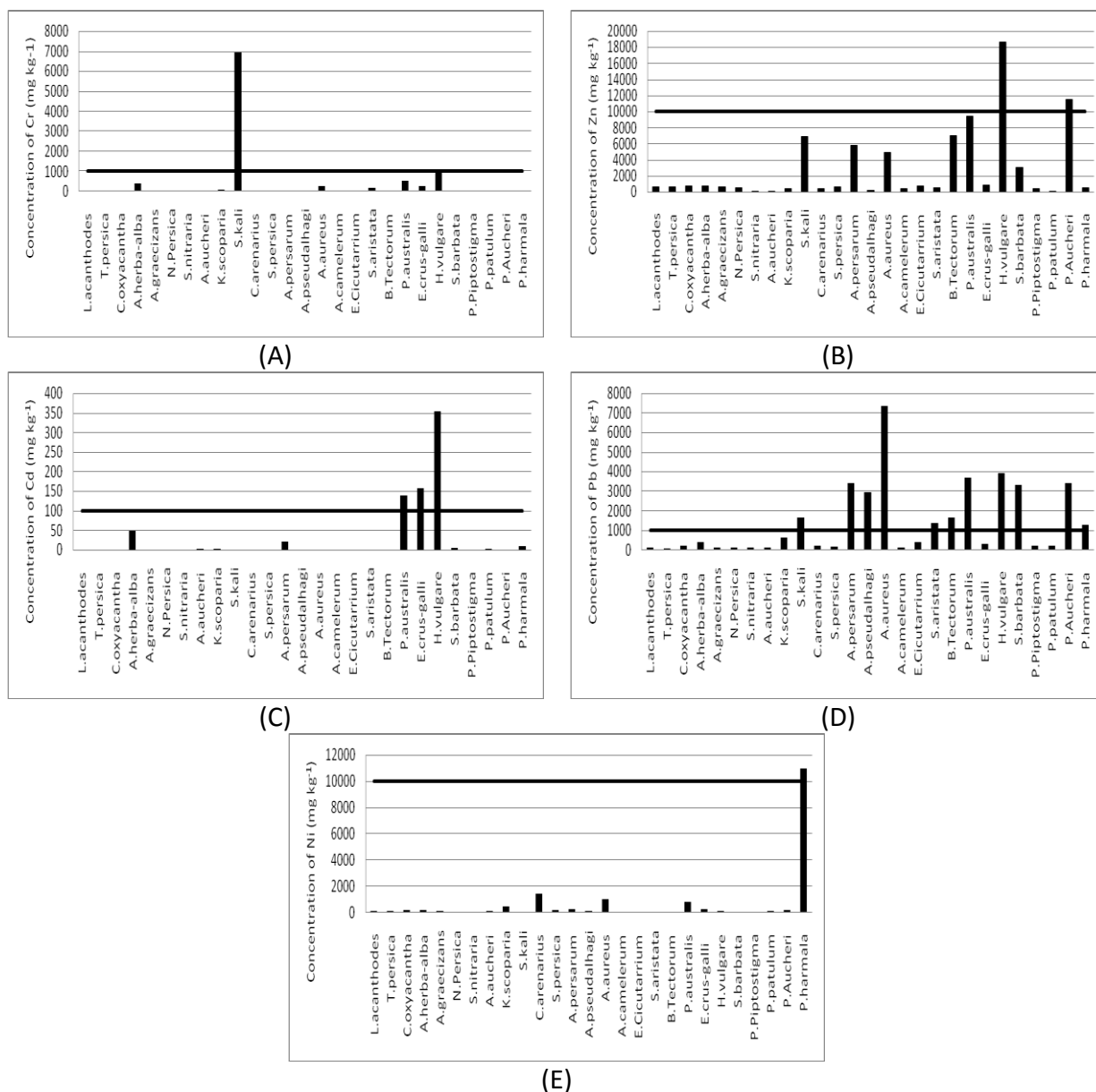


Fig. 2. Min of metal concentration of Cr (A), Zn (B), Cd (C), Pb (D) and Ni (E) in plants (shoots + roots) collected from raw sewage polluted area of Eshtehard industrial park (three replicates).

As shown in Figure 1, a decreasing trend can be observed for the total, DTPA-extractable and exchangeable concentrations of Cr, Zn, Cd, Pb and Ni. Some soil samples contained higher concentrations of heavy metals. The concentration of heavy metals was sampled and measured for all the plants in 3 replicates.

Figure 2 shows the total heavy metal concentration values in the shoot and root for identifying hyperaccumulating plants based on the EPA definition. For an easy identification of the minimum hyperaccumulation threshold in the plants based on the EPA definition, a horizontal line has been drawn on the diagrams.

As shown in figure 2, some of the plants absorb heavy metals beyond the minimum hyperaccumulation threshold.

The significance of the effect of the plant species and plant organs on the absorption of heavy metals was analyzed in SPSS using the Kruskal-Wallis test and is presented in tables 3 and 4.

As shown in tables 3 and 4, the correlations are significant.

The correlation between the physicochemical properties of the soil and the plants' heavy metal absorption rates in the study site was analyzed in SPSS using the Pearson correlation test and is shown in table 5.

Table 3. Kruskal-Wallis test results showing the effect of the plant species on the absorption of heavy metals in the sewage contaminated area.

	Heavy metal concentration in the plant				
	Cr	Zn	Cd	Pb	Ni
Chi-Square	48.30*	46.05*	48.72*	47.33*	49.24*
df	26	26	26	26	26
Asymp. Sig	0.00	0.00	0.00	0.00	0.00

*Differences of 0.05 and less considered significant

Table 4. Kruskal-Wallis results test showing the effect of the plant organs on the absorption of heavy metals in the sewage contaminated area

	Heavy metal concentration in the plant									
	Cr		Zn		Cd		Pb		Ni	
	Root	Shoot	Root	Shoot	Root	Shoot	Root	Shoot	Root	Shoot
Chi-Square	48.21*	48.01*	46.01*	35.13*	48.43*	48.81*	47.21*	47.34*	49.18*	48.20*
df	26	26	26	26	26	26	26	26	26	26
Asymp. Sig	0.00	0.00	0.00	0.00	0.00	0.00	0.00	0.00	0.00	0.00

*Differences of 0.05 and less considered significant

Table 5. The Pearson correlation coefficients between the concentrations of heavy metals absorbed by the plants examined and the physicochemical properties of the sewage contaminated soil

Heavy metal concentration in the plant	physicochemical properties of the soil								Heavy metal concentration	
	Clay	Silt	Sand	Available Phosphorus	OC	pH	EC	CCE	Total	DTPA Extractable
Cr	ns	+0.61**	ns	+0.58**	+0.71*	Ns	ns	-0.58*	ns	+0.44*
Zn	-0.51*	+0.66**	ns	+0.49*	Ns	-0.63**	ns	ns	+0.79**	+0.55**
Cd	ns	ns	ns	ns	-0.41*	-0.44*	+0.50**	-0.49*	ns	+0.64**
Pb	-0.55*	ns	-0.78**	ns	Ns	-0.59**	+0.60**	-0.42*	+0.61**	ns
Ni	ns	+0.59**	-0.71**	+0.68**	+0.89**	Ns	ns	-0.58*	ns	ns

* Correlation at the 0.05 level; ** Correlation at the 0.01 level; NS No correlation

As shown in table 5, the correlation between the physicochemical properties of the soil and the concentration of heavy metals can be either positive or negative, and NS indicates cases in which there are no significant correlations.

Table 2 shows that raw sewage has reduced the soil pH in the contaminated area. Heavy metal concentrations have also increased with the raw sewage, resulting in higher soil magnetism and consequently a higher electrical conductivity. Hung [6] found similar results in his study. As raw sewage increases, so does organic carbon (OC), which is an organic source of plant-available phosphorus. Calcium Carbonate Equivalent (CCE) indicates the soil's calcareous properties; the soil in the contaminated area was already slightly calcareous, but this property further increased with the entry of sewage. There was a slightly higher amount of silt in the contaminated area compared to in the control area due to the entry of sewage

sludge, which resulted in better conditions for plant growth.

As shown in Figure 1 and based on the Kabata-Pendias standards, the total concentration of heavy metals in the area was found to fall in the critical range, indicating the contamination of the soil. The control area was not contaminated, indicating that the entry of sewage has been fact the source of contamination. Figure 1 shows both the concentration of heavy metals that can be absorbed with a DTPA extractor by the plants and the naturally-exchangeable concentration of heavy metals and can thus be of use for the assessment of the correlation between them. As suggested by the Figure, the concentration of heavy metals that can be absorbed with a DTPA extractor by the plants is higher than the exchangeable concentration of heavy metals. DTPA can therefore make greater amounts of heavy metals available to the plants.

Figure 2 shows the heavy metal absorption rate of the whole plant (the shoot and root) separately for each plant examined. According to the EPA definition, heavy metal hyperaccumulating plants include:

Alhagi persarum Boiss. & Buhse absorbed 3418.23 mg kg⁻¹ of lead and *Pteropyrum Aucheri* Jaub. & Spach accumulated 11585.56 mg kg⁻¹ of zinc and 3408.47 mg kg⁻¹ of Lead and were therefore considered hyperaccumulators of these two metals. Ghaderian *et al.* [14] found similar results for *Alhagi persarum* Boiss. & Buhse; however, despite its high levels of zinc and lead accumulation, *Pteropyrum Aucheri* Jaub. & Spach was not considered a hyperaccumulating plant in this study. *Alhagi pseudalhagi* (M.B.) Desf. and *Salvia aristata* Aucher ex Benth absorbed 2959.01 mg kg⁻¹ and 1376.6 mg kg⁻¹ of lead and were therefore considered hyperaccumulators. *Salsola kali* absorbed 6948.97 mg kg⁻¹ of Chromium and 1651.4 mg kg⁻¹ of lead and was also considered a hyperaccumulator of these two metals. No studies have yet been conducted on phytoremediation in these three plants. *Astragalus aureus* Wild absorbed 7343.68 mg kg⁻¹ of lead and is considered a hyperaccumulating plant. Salari *et al.* [15] did not find this plant to be a hyperaccumulator despite its high accumulation of metals. Accumulating 1676.4 mg kg⁻¹ of lead, *Bromus Tectorum* L. was also found to be a hyperaccumulator. Parsadoost *et al.* also found similar results [16]. *Phragmites australis* (Cav) Trin. Ex Steud absorbed 140.23 mg kg⁻¹ of cadmium and 3703.3 mg kg⁻¹ of lead and is thus a hyperaccumulator of these two metals. Al-Taisan and Deng studied this plant's cadmium and lead absorption, respectively however, despite their high levels of metal accumulation, the plants were not considered hyperaccumulators [17, 18]. *Echinochloa crus-galli* (L.) P. Beauv absorbed 158.21 mg kg⁻¹ of cadmium through all of its organs and is therefore considered a hyperaccumulating plant. Messou also proposed this plant to be a hyperaccumulator of cadmium [19]. *Hordeum vulgare* L. accumulated 1032.37 mg kg⁻¹ of Chromium, 18628.83 mg kg⁻¹ of zinc, 325.83 mg kg⁻¹ of cadmium and 3930.7 mg kg⁻¹ of lead and is therefore considered a hyperaccumulator of these metals [20]. *Stipa barbata* Desf. absorbed 3316.4 mg kg⁻¹ of lead and is also a hyperaccumulating plant. Lorestani *et al.* [21] discovered the manganese stabilization of this plant, but the present study showed its lead hyperaccumulation capacity for the first time. *Peganum harmala* L. absorbed 10948.67 mg kg⁻¹ of nickel and 1274.37 mg kg⁻¹ of lead and is identified as a

hyperaccumulator of these two metals. Zamani *et al.* achieved similar results for lead, but no studies have yet been conducted to investigate Nickel accumulation [22].

Tables 3 and 4 and the Kruskal-Wallis test results, showing the significant effect of plant species and plant organs on the absorption of heavy metals in sewage contaminated areas, support the present study's hypothesis regarding plant species' and plant organs effects on the absorption of heavy metals.

Table 5 presents the study findings on the correlation between the physicochemical properties of the soil and the concentration of heavy metals in the plants and their underlying reasons.

A significant negative correlation was observed between the soil pH and the concentration of zinc, cadmium and lead in the plants, which is due to the sewage's reduction of the soil pH to about 6.5, turning insoluble metals to soluble ones and leading to their greater absorption by the plants. Ziarati and Alaedini achieved similar results in his study [5].

There was a significant positive correlation between soil EC and the concentration of cadmium and lead. The increased EC is due to the increased heavy metal concentrations caused by the entry of sewage into the area, resulting in a higher electrical conductivity in the soil. The increased heavy metal concentrations in the soil lead to an increased heavy metal concentration absorbed by the plants. Hung also found similar results [6].

A significant positive correlation was observed between organic matters in the soil and Chromium and nickel concentrations in plants; however, the correlation between organic matters in the soil and cadmium concentrations was found to be significant and negative. The reason for the negative correlation might be that organic matters present in soils have a potential for stabilizing heavy metals in an unavailable concentration, and the positive correlation is perhaps because organic matters can act as a chelate, increasing the usability and mobility of trace elements. Furthermore, the ligand bond formed between the metal and the organic matter affects its availability, as the ligand bond is capable of easily turning into an available form through the organic acids excreted by the plant roots and thus be absorbed by the plant. According to Nakatsu *et al.* the ligand may become available to the plants through certain soil-borne microorganism activities [23].

A significant positive correlation was found between the available phosphorus in the soil and Chromium, zinc and nickel concentrations in the plants. The positive correlation was due to the high

amounts of phosphorus present in sewage (phosphorus acts as a fertilizer) and the solubility of phosphorus due to the soil's reduced pH caused by the entry of sewage and therefore the increased availability of soluble phosphorus in the soil. Rato Nunes *et al.* achieved similar results in his study [24].

A significant negative correlation was found between Calcium Carbonate Equivalent (CCE) in the soil and Chromium, cadmium, lead and nickel concentrations in the plants. The negative correlation was because lime (CaCO_3) is a soil mineral that can produce a mechanism for metal absorption and retention through the chemical absorption of heavy metals and depositing metal cations and can then reduce the activity of the heavy metals' soluble form, thus making the metals unavailable to the plants. Mozafari *et al.* emphasized the negative effect of lime on the absorption of cadmium by plants [25].

There was a significant positive correlation between the total concentration of metal in the soil and zinc and lead concentrations in plants. A significant positive correlation was also found between DTPA-extractable metals concentrations and Chromium, zinc and cadmium concentrations in plants. Sharma *et al.* also achieved similar results [26].

A significant negative correlation was found between the concentration of clay in the soil and zinc and lead concentrations in plants. A significant negative correlation was also observed between the concentration of sand in the soil and lead and nickel concentrations in plants. A significant positive correlation was observed between the concentration of silt in the soil and Chromium, zinc and nickel concentrations in plants. The negative correlation between the clay concentration and plants is due to the surface absorption of heavy metals by fine-grained clay, which reduces the amount of heavy metals available to the roots of the plants. Although sand is larger-grained and has no surface absorbability, and although, in their soluble form, metals can freely be absorbed by plants, there is a negative correlation between sand concentrations and plants, as the presence of greater concentrations of sand in the soil creates a larger pore space in the soil and allows the metals to be easily washed away from the plant roots. The positive correlation between silt concentrations and plants is because silt improves the soil, resulting in better plant growth and increased heavy metal concentrations in the plants. Raj *et al.* achieved similar results about the effect of soil texture on the absorption of heavy metals [27].

CONCLUSION

Based on the Kabata-Pendias standards, the entry of raw sewage into the soil examined in the present study has contaminated it and reduced its pH and CCE and increased the soil its EC, OC, available phosphorus and silt. The results of the Kruskal-Wallis test demonstrated that plant species and plant organs affect the absorption of heavy metals. The Pearson correlation test was then used to assess the correlation between the physicochemical properties of soil and the absorption of heavy metals by the plants. The plant-absorption of some metals was found to have increased due to the entry of raw sewage into the soil. *Alhagi pseudalhagi* (M.B.) Desf., *Salvia aristata* Aucher ex Benth, *Stipa barbata* Desf. (*Pb*), *Salsola kali* (*Pb* and *Cr*), and *Peganum harmala* L. (*Ni*), studied for the first time for their phytoremediation capacity, were identified as hyperaccumulators based on the EPA definition. As already found by other researchers, *Alhagi persarum* Boiss. & Buhse, *Bromus Tectorum* L. and *Peganum harmala* L. (*Pb*), *Echinochloa crus-galli* (L.) P. Beauv. (*Cd*) and *Hordeum vulgare* L. (*Cr*, *Zn*, *Cd* and *Pb*) were also identified as hyperaccumulators. Compared to the findings of other studies, *Pteropyrum Aucheri* Jaub. & Spach (*Zn* and *Pb*), *Astragalus aureus* Wild (*Pb*) and *Phragmites australis* (Cav) Trin. Ex Steud (*Cd* and *Pb*) absorbed higher concentrations of heavy metals in the present study due to the high concentrations of environmental pollutants in the area examined and the changes in the physicochemical properties of its soil caused by the entry of raw sewage and are therefore deemed by this study to be hyperaccumulators of these metals. Planting the seeds of these hyperaccumulating plants and the addition of DTPA therefore comprises a suitable strategy for purifying soils through plants' absorption of heavy metals, and the plants themselves can then be harvested, collected and disposed of as regular industrial waste.

Acknowledgements: The researchers would like to express their gratitude to the Industrial Estate Corporation of Alborz Province and Eshtehard Industrial Park for their sincere cooperation.

REFERENCES

1. M.A. Shaeri, A. Rahmati, Wastewater discharge standard. Human Environmental Laws, Regulation Criteria and Standards; Iranian Department of Environment (DOE). 2012, p. 275.
2. M.A. Shaeri, A. Rahmati, Use of sewage sludge as fertilizer in agriculture work instruction. Human

- Environmental Laws, Regulation Criteria and Standards; Iranian Department of Environment (DOE). 2012. p. 292.
3. A. Kabata-Pendis, H. Pendis, Trace elements in soils and plants, CRC press. Boca Raton, Florida; 1984.
 4. E. Asari, Heavy Metal contamination of water and soil, Analysis, Assessment, and remediation strategies, Boca Raton, Florida, USA: CRC Press; 2014, p. 259.
 5. P. Ziarati, S. Alaedini, *Environmental & Analytical Toxicology*, **4**(208); OMICS publishing Group (2014); doi: 10.4172/2161-0525.1000208.
 6. Y. Hung, *International Journal of Phytoremediation*, **17**, 228 (2015). doi: 10.1080/15226514.2014.883493.
 7. A.H. Hassani, J. Nouri, I. Mehregan, F. Moatar, M.R.S. Benis, The Phytoremediation of contaminated Soils that have up taken heavy metals of Eshtehard industrial city wastewater by plants”, Ph.D Dissertation. Environment and Energy, Science and Research Branch, Islamic Azad University, Tehran, Iran; 2013.
 8. Neishabori A. Practical Ecology. payam noor university publication, 4th Edn., pp.35-46 Tehran; 2011.
 9. A.H. Hassani, J. Nouri, I. Mehregan, F. Moatta, M.R.S. Benis, *Journal of Environment and Earth Science*, **4**(19), IISTE (2014), ISSN 2224-3216.
 10. W.L. Lindsay, W.A. Norvell, *Soil Sci. Soc. Amer J.*, **42**, 421 (1978).
 11. A. Tessier, P. G. C. Campbell, M. Bisson, *Anal. Chem.*, **51**(7), 844 (1979), doi: 10.1021/ac50043a017.
 12. L.P. Van Reeuwijk, Procedure for soil analysis. International Soil Reference and Information Centre (ISRIC), Washington; 2002.
 13. A.J. Shaw, Heavy Metal Tolerance in Plant: Evolutionary Aspects”, CRC press, Florida. ISBN: 0849368529; 1989.
 14. S.M. Ghaderian, G.R. Hemmat, R.D. Reeves, A.J.M. Baker, *Journal of Applied Botany and Food Quality*, **81**(1), 145 (2007).
 15. H. Salari, H. Oloumi, D. Afzali, E.A. Mosavi, *African Journal of Biotechnology*, **11**(77), 14146 (2012), doi: 10.5897/AJB11.3613.
 16. F. Parsadoost, B. Bahreini, A. Nejad, K.S. Sanjani, M.M. Kaboli, *Pajouhesh & Sazandegi J.*, **75**, 54 (2007).
 17. W.A. Al-Taisan, *Journal of Environmental Sciences*, **5**(6), 740 (2009).
 18. H. Deng, Z.H. Ye, M.H. Wong, *Environmental pollution*, **132**, 29 (2004).
 19. A. Messou, L. Coulibaly, L. Doumbia, G. Gourene, *African Journal of Biotechnology*, **12**(3), 253 (2013). doi:10.5897/AJB12.1664.
 20. J. Ciura, M. Poniedziałek, A. Sękara, E. Jędruszczak, *Polish Journal of Environmental Studies*, **14**(1), 17 (2005).
 21. B. Lorestani, M. Cheraghi, N. Yousefi, *Engineering and Technology*, **53**, WASET (2011).
 22. A.A.R. Zamani, M. Shokri, R. Yaftian, A.H. Parizanganeh, *International Journal of Environmental Science and Technology*, **10**(1), 93 (2013).
 23. <http://dx.doi.org/10.1128/AEM.71.12.7679-7689.2005>.
 24. J.R. Nunes, J. Ramos-Miras, A. Lopez-Piñeiro, L. Loures, G. Carlos, J. Coelho, A. Loures, *Sustainability*, **6**, 9124 (2014), doi: 10.3390/su6129124.
 25. G.H. Mozafari, M. Fakri, H. Naghavi, Effect of lime and chicken manure on cadmium pollution in soil. Eleventh Seminar irrigation and reduce evaporation, Kerman, Iran; 2011.
 26. A. Sharma, A. Dhiman, J. Dhankar, Detection of Total and DTPA Extractable Nickel and Cadmium in Soil and Plants Irrigated with Industrial Effluent and Sewage Waste Water. 3rd International Conference on Ecological, Environmental and Biological Sciences (ICEEBS'2013), Singapore; 2013.
 27. R. Sudarsan, J.P. Kumar, P.C. Ranjan, *Indian Journal of Geo-Marine Sciences*, **42**(3), 370 (2013).

Determination and assessment of three heavy metal content (Cd, Pb and Zn) in *Scomberomorous commerson* fish caught from the Persian Gulf

E. Sadeghi¹, M. Mohammadi², K. Sharafi^{3,4}, S. Bohlouli^{5*}

¹Research Center for Environmental Determinants of Health (RCEDH), Kermanshah University of Medical Sciences, Kermanshah, Iran.

²Student Research Committee, Kermanshah University of Medical Sciences, Kermanshah, Iran.

³Department of Environmental Health Engineering, School of Public Health, Kermanshah University of Medical Sciences, Kermanshah, Iran

⁴Department of Environmental Health Engineering, School of Public Health, Tehran University of Medical Sciences, Tehran, Iran

⁵Department of Veterinary Medicine, Faculty of Agriculture, Kermanshah Branch, Islamic Azad University, Kermanshah, Iran

Received June 26, 2015, Revised September 10, 2015

Most of fish that sold in southern city of Iran captured from the Persian Gulf. Heavy metals are recognized as one of the most important pollutants, that effect on human health even in trace amount. A study was conducted to quantitate the concentrations of heavy metals, such as Cd, Pb and Zn in *Scomberomorous commerson* fish caught off the coast of Persian Gulf. 25 fish samples of *Scomberomorous commerson* were collected between June – May 2012 at three different sites from Persian Gulf. The Cd, Pb and Zn concentrations were determined with an atomic absorption Spectrophotometer. The results expressed in micrograms of metal per dry weight gram of fish ($\mu\text{g/g}$). Statistical analysis of data was carried out using SPSS 16.0 software. Pb, Cd and Zn concentration in muscle of *S.commerson* were obtained 1.43-2.02 ppm dry wt, 0.11-0.27 ppm dry wt and 7.39-8.73, respectively. Heavy metal accumulation in muscle order was $\text{Zn} > \text{Pb} > \text{Cd}$. Pb concentration was increased with increase of length of fish. ANOVA was reveal that concentration differences among the heavy metals were high ($p < 0.05$). In all samples, Zn level was higher than other metals and Cd was minimum. Pb concentrations exceeded FAO/WHO, IAEA-407, TFC, EC and Chine but had not exceeded the guidelines limits except for Range of International Standards. Zn values match with all noted Standards. The metal accumulation in the aquatic organism may be species and size -dependent.

Keywords: Heavy metal, *Scomberomorous commerson*, Persian Gulf.

INTRODUCTION

The contamination of receive waters with a wide range of heavy metals has become a matter of concern over the last few decades [1, 2]. Agricultural and industrial activities in an area directly increase the heavy metal of water [3] and also an important factor in the decline of water sediments and fish quality [4]. Heavy metals are dangerous because they tend to bio accumulate in marine organisms including fish and transfer to human through food chain [5, 6]. Fish, a part of being a good source of digestible protein vitamins, polyunsaturated fatty acids (PUFA) and minerals, are also an important source of heavy metals. Heavy metals have a specific density of more than 5 g/cm^3 [7] and are environmentally ubiquitous, readily dissolved and transported by water and taken up by fish, readily [8]. They can be classified as potentially toxic, probably essential and essential

[9]. Toxic elements are non-biodegradable and can be causing cytotoxic, mutagenic and carcinogenic effects in animals [10]. Levels of heavy metals in fish samples have been widely reported in the literature [9, 11-13]. This study was conducted to determine the concentration of Cd, Pb and Zn in *Scomberomorous commerson* caught in Persian Gulf. Concentration of zinc was determined as vital elements, while lead and cadmium as toxic elements.

MATERIAL AND METHOD

Study area

Bushehr province coasts, located in the northern coasts of the Persian Gulf (29°N, 38°E), was investigated. This area because of its ecological significance is important.

Sampling and analysis

The number of 25 *Scomberomorous commerson* fish samples measuring 12-30 cm were collected between June – May 2012 and were transported to

To whom all correspondence should be sent:

E-mail: sbohloli@yahoo.com

the laboratory in a thermos-flask with ice, also immediately frozen and stored at -20°C until dissection. During dissection in laboratory, Approximately 20 g of muscle fillets, from each sample were dissected, washed with deionized water, were dried in an oven at 60°C till constant weight. After that, they were digested with 2 ml nitric acid (65%, Merck, Germany) in Teflon bombs placed into a microwave digestion system [14]. After cooling, samples were transferred to a 50 ml volumetric flask and rinsed with triple distilled water. In order to check for possible contamination of the samples, one analytical blank was prepared as a control in the same manner, but without tissue samples.

Measurement of Zn, Pb and Cd

Atomic absorption spectrophotometer (Perkin-Elmer-5100) was used to measure the Zn, Pb and Cd concentrations (as $\mu\text{g/g}$ dry weight). The results were validated according to ISO 17025 accreditation [15].

Statistically analysis

Statistical analysis of data was carried out using SPSS 16.0 statistical package program (Chicago, IL). One-way analysis of variance (ANOVA) was employed to assess whether metal concentrations varied as significantly among fish (between heavy metal and length) and followed by Tukey post hoc comparisons for the source of statistically significant difference ($P < 0.05$). The results are presented as means \pm standard error.

RESULTS

Pb, Cd and Zn concentration in muscle of *S.commerson* were obtained 1.43-2.02 ppm dry wt, 0.11-0.27 ppm dry wt and 7.39-8.73, respectively. Mean concentrations of cadmium, lead and zinc in muscle is shown in figure 1.

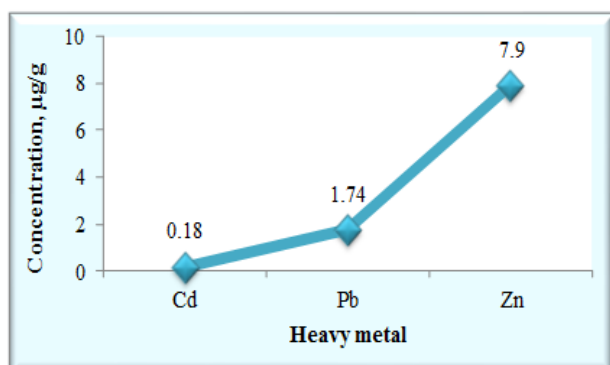


Fig. 1. Concentration of Cd, Zn and Pb ($\mu\text{g/g}$ dry weight) in *Scomberomorus commerson*

The highest concentrations were found Zn and the lowest levels were detected for Cd (Heavy metal accumulation order was $\text{Zn} > \text{Pb} > \text{Cd}$). Our results showed that different fish length contained different metal levels in their muscle. Statistically, significance analysis was performed among the heavy metal and our results showed that, the concentration differences among the heavy metals were high ($p < 0.05$). Also, relationship between the fish size and the metal levels for Cd and Zn was not significant ($P > 0.05$), whereas, for Pb was positive ($P < 0.05$). (Table 1 and Figure 2, 3 and 4)

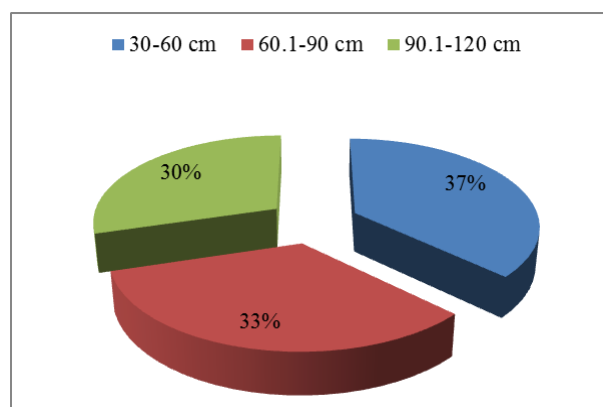


Fig. 2. Relative frequency (%) of Cd in *Scomberomorus commerson* base on size of fish

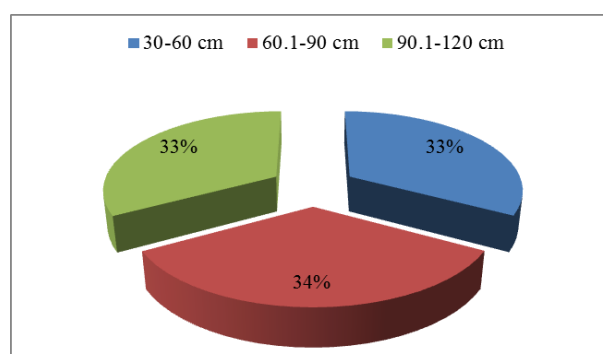


Fig. 3. Relative frequency (%) of Zn in *Scomberomorus commerson* base on size of fish

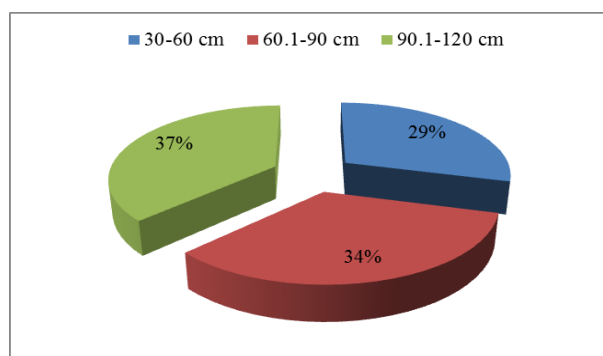


Fig. 4. Relative frequency (%) of Pb in *Scomberomorus commerson* base on size of fish

Table 1. Mean (\pm SD) concentrations of Cd, Zn and Pb ($\mu\text{g/g}$ dry weight) in *Scomberomorus commerson* base on size of fish

Size of fish, cm	Cd	Zn	Pb
30 - 60	0.2 ± 0.52	7.78 ± 0.25	1.53 ± 0.07
60.1 - 90	0.18 ± 0.03	8 ± 0.43	1.76 ± 0.87
90.1 - 120	0.16 ± 0.04	7.8 ± 0.16	1.95 ± 0.05

DISCUSSION

Fish may accumulate heavy metals by consumption of contaminated food and sediments [16]. The present work revealed marked presence of heavy metals concentration in muscles tissue of investigated fish. Fish are often at the top of the aquatic food chain, hence, fish contamination can also have major impacts on people and society [17]. The efficiency of metal uptake from contaminated water may differ in relation to size of fish [18]. The present work revealed marked increase of Pb concentration with increase of size of fish, simultaneously. It is generally accepted by Marijic et al [19]. The maximum Permissible doses for an adult are 3 mg Pb and 0.5 mg Cd per week, but the recommended doses are only one-fifth of those values [8]. Pb concentrations in this study exceeded FAO/WHO [8], IAEA-407 [20], TFC [21], EC [22] and China [23] but had not exceeded the guidelines limits except for Range of International Standards [24]. Zn is an essential metal which play an important role in metabolic processes and biological systems and is assimilated by the organisms over time, but it can also produce toxic influences when bioaccumulate and reach toxic level [25].

Protective effect of Zn against the Cd and Pb toxicity had been reported, Zn values in this study match with FAO/WHO (1989) [25], TFC (2002) [21], EC (2006) [22] and China and Range of International Standards [26]. Similar results had been reported by Özparlak, et al [8]. Cd content of muscles was lower that reported by Mohammadnabizadeh [15]. In research of Metwally and Fouad, Cd, Zn and Pb concentration in three different types of fishes (*Pagellus acarne*, *Sarpa salpa* and *Liza saliens*) were 0.062, 0.38 and 0.56 ppm, respectively that are lower in compare to this study [11]. Pb and zinc levels were reported as high as $0.064\mu\text{g/l}$ and $4.82\mu\text{g/l}$ in fish and shellfish in ABA river, from Nigeria by Ubalua [17]. Cd content of muscles was lower that reported by RAUF et al (2009) in fish collected from river Ravi, Pakistan [10] and muscle tissue of nine fish species from Beyşehir Lake, Turkey [8]. Also it was higher than reported from fish in Southeast

Coast of India [13]. Heavy metal concentrations in *Scomberomorus commerson* varied significantly depending upon the type of metal. The concentrations of heavy metals differed significantly ($p < 0.001$) depending upon the size of fish. According to investigations, the metal accumulation in the aquatic organism is size-dependent [10]. In general, accumulation of zinc is higher than lead and cadmium in fish tissues. This matter was confirming by Huang [16]. Zinc values ranged from 7.39-8.73 ppm and were lower Beyşehir Lake, Turkey [8], Croatia [27] and Köyceğiz Lake-Mugla [18] and Langkawi island, Malaysia [6]. This present study showed lower accumulation of cadmium than other two metals, too. Hence, knowledge of heavy metal concentrations in fish is important with respect to nature of management and human consumption of fish.

Ethical Consideration: *Ethical issues (Including plagiarism, informed consent, misconduct, data fabrication and/or falsification, double publication and/or submission, redundancy, etc.) have been completely observed by the authors.*

REFERENCES

1. S.S. Vutukuru, *Int. J. Environ. Res. Public Health*, **2**, 456 (2005).
2. R. Vinodhini, M. Narayanan, *Int. J. Environ. Sci. Tech.*, **5**, 179 (2008).
3. B. Staniskiene, P. Matusevicius, R. Budreckiene, K.A. Skibniewska, *Polish J. of Environ. Stud.*, **15**, 585 (2006).
4. Z. Zhang, L. He, J. Li, Z.B. Wu, *Polish J. of Environ. Stud.*, **16**, 959 (2007).
5. M. Tuzen, *Food Chem.*, **80**, 119 (2003).
6. J. Irwandi, O. Farida, *Int. Food Res. J.*, **16**, 105 (2009).
7. L. Järup, *British Medical Bulletin*, **68**, 167 (2003).
8. H. Özparlak, G. Arslan, E. Arslan, *Turkish J. Fisheries & Aquatic Sci.*, **12**, 761 (2012).
9. M. Zarei, A. Mollaie, M.H. Eskandari, S. Pakfetrat, S. Shekarforoush, *Global Veterinaria*, **5**, 259 (2010).
10. A. Rauf, M. Javed, M. Ubaidullah, *Pakistan Vet. J.*, **29**, 24 (2009).
11. M.A.A Metwally, I.M. Fouad, *Global Veterinaria*, **2**, 308 (2008).
12. S.M. Al-Weher, *Jordan J. Biol. Sci.*, **1**, 41 (2008).
13. R. Lakshmanan, K. Kesavan, P. Vijayanand, V. Rajaram, S. Rajagopal, *Adv. J. Food Sci. Technol.*, **1**, 63 (2009).
14. ABNT, NBR ISO/IEC 17025 (2005): Requisitos gerais para a competência de laboratórios de ensaio e calibração.

15. S. Mohammadnabizadeh, A. Poorkhabaz, *J. Iran Veterinary*, **1**, 64 (2013).
16. W.B. Huang *J. Food Drug Anal.*, **11**, 324 (2003).
17. A.O. Ubalua, U.C. Chijioke O.U. Ezeronye, *J. Fisheries International*, **1**, 106 (2006).
18. F. Yilmaz, *Turkish J. Sci. & Technol.*, **4**, 7 (2009).
19. V.F. Marijic, B. Raspor, *Toxicol. Lett.*, **168**, 292 (2007).
20. E.J. Wyse S. Azemard, S.J Mora, Report on the world wide inter comparison exercise for the determination of trace elements and methyl mercury in fish homogenate. IAEA. 407, IAEA/AL/144 (IAEA/MEL/72), IAEA, Monaco, 2003.
21. TFC Turkish Food Codes, Official Gazette, No: 24885, 2002.
22. EC No. 78/2005, amending Regulation (EC) No 466/2001 as regards heavy metals. (2005).
23. K.C. Cheung H.M. Leung, M.H. Wong, *Archi. Environ. Contamination Toxicol.*, **54**, 705 (2008).
24. A.K. Anim, E.K. Ahiale G.O. Duodu, M. Ackah N.O. Bentil, *Res. J. Environ. Earth Sci.*, **3**, 56 (2011).
25. FAO/WHO WHO Technical Report, Series No. 505 (1989).
26. E.E. Obasohan, *African J. General Agric.*, **3**, 141 (2008).
27. Z. Matasin V. Orescanin V.V. Jukic, S. Nejedli M. Matasin, I. Tlak Gajger, *J. Animal & Veterinary Adv.*, **10**, 1069 (2011).

A study on one-dimensional isothermal moisture migration in *Pinus yunnanensis*

Shao-jiang Zheng^{1,2}, Kui-yan Song^{1*}, Chun-lei Dong²

¹Material Science and Engineering College, Northeast Forestry University, Harbin 150040, China

²Material Engineering College, Southwest Forestry University, Kunming 650224, China

Received June 26, 2015; Revised September 10, 2015

Abstract: In this study, in order to acquire the quantitative distribution of wood moisture in a hygroscopic environment, *Pinus yunnanensis* was taken as the research target. In consideration of the phase equilibrium relationship among vapor and bonded water, unstable diffusivities of vapor and bonded water, and the relationship between the equilibrium moisture content of wood and surrounding moisture content, a model of one-dimensional isothermal moisture migration in wood was established beneath the fiber saturation point. Comparative analyses were then carried out on the model solution and experimental measurement results. It was found that the model could accurately predict the process of moisture migration in the wood in each hygroscopic range beneath the fiber saturation point, and the diffusivities of bonded-water D_{ls} and vapor D_{vs} increased with greater moisture content (MC) of wood, but they could be regarded as constant within a certain MC range. The larger the gap change range between the initial wood MC and surrounding equilibrium MC was, the greater the MC gradient of the wood interlayer would be, and the shorter the overall EMC time would be. Environment boundary was selected as the actual EMC of wood under the corresponding ERH.

Keywords: *Pinus yunnanensis*, One-dimensional isothermal migration, Moisture content gradient, Equilibrium moisture content

INTRODUCTION

In the relevant standards of each nation, the “wood moisture content” used for investigating wood mechanical properties actually refers to the equilibrium moisture content (EMC) of the wood with a specific test environment temperature and humidity, which is usually set as the constant temperature and humidity environment with the temperature (T) of 20°C and relative humidity (RH) of 65%. However, the bearing wood materials actually used are in an environment with dynamic changes in temperature and moisture content. When the influence of temperature on the wood mechanical properties is seen as a constant in the constant temperature range, the dynamic changes in the surrounding moisture content lead to uneven moisture distribution inside the wood, such as gradient moisture distribution, which seriously affects the bearing capacity of the wood [1, 2, 3]. Therefore, it is required to determine a scientific mathematical expression of wood moisture distribution state, in order to analyze the wood moisture distribution state and the relationship with wood mechanical properties.

Compared with general non-hygroscopic porous

materials, wood is characterized by porosity but a low effective conduction rate, high moisture content (water vapor, bonded water and free water), significant material anisotropy, and uneven structure [4, 5]. Combined with imperfect direct testing techniques and means of wood moisture distribution [6, 7, 8], difficulties are determined in the wood moisture migration mechanism and mathematical simulation. For example, in terms of water vapor (in the wood cell cavities), bonded water (in the wood cell walls) and free water (in the wood cell cavities), a series of problems will occur in the migration process, such as phase change, great difference in migration rate along different wood texture directions, migration rate changing with wood moisture content, and complex heat and mass transfer at the wood-environment boundary [5, 9, 10, 11].

Under the premise of vapor-bonded water phase equilibrium relationship, unstable diffusivities of vapor and bonded water, as well as the relationship between wood EMC and surrounding moisture content (SMC) considered in this paper, a one-dimensional isothermal migration model of wood moisture is established beneath the fiber saturation point. Then, analyses are carried out on the migration laws of wood moisture in different hygroscopic ranges, the relationship between

* To whom all correspondence should be sent
E-mail:44009146@qq.com, skuiyan@126.com

diffusivities of the vapor-bonded water and wood moisture content (MC), as well as other issues, and these are verified by experiments.

NUMERICAL SIMULATION

Description of wood isothermal moisture absorption process (physical model)

In a constant temperature convection environment, once the wood with moisture content beneath the fiber saturation point is placed in the environment with a surrounding equilibrium moisture content that is higher than the wood EMC, then immediate moisture migration occurs to the surrounding moisture at the environment-wood interface and in the wood. Its process is shown as follows. (1) The wood surface vapor (in the wood cell cavities) density is lower than the surrounding vapor density, and the water vapor is transferred from the environment to the wood surface by means of convective mass transfer between the environment and wood interface. Meanwhile, the water vapor in the cell cavities and environment is absorbed by the wood surface-layer cell wall and converted to liquid water, until phase equilibrium between the bonded water and water vapor is reached. (2) After the wood surface absorbs water, the water vapor density in the cell cavities will be greater than that in the wood inner cell cavities, and the water content absorbed by the cell walls will be greater than in the wood inner cell walls. In the driving of the density difference, the water vapor migrates from the surface wood cell cavity to the inner wood cell cavities by means of diffusion, while the bonded water migrates from the surface wood cell walls to the wood inner cell walls in the driving of the capillary force. Similarly, the bonded water in the wood cell walls and water vapor in the cell cavities is always in the dynamic phase equilibrium during the migration process. (3) The inward migration of the surface water vapor and bonded water mass is compensated by the direct input of surrounding water vapor and the condensation on the cell walls.

Therefore, the surrounding water vapor migrates from the wood surface to the wood inner cell walls through the above process, until an equal moisture content between the outer and inner wood is reached. Meanwhile, the wood moisture content under this environment is wood EMC.

Governing equation

Governing equation of liquid water (bonded water)

Wood is considered as a network porous material composed of large and small capillaries, of which the cell walls are connected, and the same is

true for the pores. Then the governing equation of bonded water [5] can be expressed as shown below:

$$\frac{\partial W}{\partial \tau} = D_{ls} \frac{\partial^2 W}{\partial z^2} - \frac{\dot{m}_v}{\rho_d} \quad (1)$$

Governing equation of water vapor

The existence of the wood internal air is ignored (except when calculating relative air humidity), regardless of air mass migration [5], then:

$$\dot{m}_v = \Phi \frac{\partial \rho_v}{\partial \tau} - D_{vs} \frac{\partial^2 \rho_v}{\partial z^2} \quad (2)$$

Phase equilibrium governing equation of liquid water and vapor

When the moisture content is unable to reach the surrounding equilibrium EMC, the water vapor in the wood cell cavities is always unsaturated water vapor, of which the pressure p and local wet air relative humidity φ should satisfy the following:

$$p_v = p_{sv} \varphi \quad (3)$$

Under atmospheric pressure, due to the low water vapor density in the wood cell cavities, it is close to the ideal gas, which can be assumed to satisfy the ideal gas equation:

$$\rho_v = p_v \frac{M_v}{RT} \quad (4)$$

Wood moisture content W , relative humidity φ and temperature t simultaneously satisfy the Simpson model [12] (to facilitate calculation, the inverse function is used herein):

$$\varphi = f_p^*(t, W) \quad (5)$$

Boundary conditions

Boundary conditions of wood surface and surrounding moisture exchange

The water vapor in surrounding wet air is attached to the wood surface in the form of condensation, thus the water vapor condensation rate \dot{m}_s on the wood surface is as shown below [5]:

$$\dot{m}_s = h_m^*(W_e - W_s) \quad (6)$$

Then, the mass exchange boundary condition of the wood surface and surrounding wet air is expressed as follows [5]:

$$\frac{\partial W}{\partial \tau} = D_{ls} \frac{\partial^2 W}{\partial z^2} - \frac{\dot{m}_v}{\rho_d} + \frac{\dot{m}_s}{\rho_d \Delta z} \quad (7)$$

In Eq. (6), W_e is the maximum actual equilibrium moisture content of the wood in the environment, rather than the theoretical maximum moisture content of the wood converted by the Simpson model.

Boundary conditions of wood inner

The wood inner moisture is composed of bonded water on the wood cell walls of the adjacent layers through diffusion, and water vapor in the wood cell cavities of the adjacent layers through diffusion; therefore:

$$\frac{\partial W}{\partial \tau} = D_{ls} \frac{\partial^2 W}{\partial z^2} + \frac{\dot{m}_v}{\rho_d} \quad (8)$$

EXPERIMENT ARRANGEMENT

Instruments and devices

(1) A Binder KMF720 climate chamber ((Gesellschaft Mit Beschränkter Haftung)) with temperature accuracy of 0.1°C and humidity accuracy of 1.5%.

(2) A digital electronic balance with a range of 500 g and precision of 0.01 g.

(3) A digital vernier caliper with a precision of 0.01 mm.

Experimental methods

Moisture absorption experiment of specimen

The research targets are six specimens of *Pinus yunnanensis* with the dimensions (length×width×thickness) of 480 mm × 20 mm × 20 mm, and side sealed by aluminum foil along the thickness direction (Fig. 1). These are placed into the constant temperature and humidity box, in which T = 20°C and RH = 42%. When the equilibrium in the specimen mass and environmental humidity (no changes in mass by weighting for three consecutive days) is achieved, then the RH is adjusted to 65%, 80% and 90% in turn. In the three moisture absorption ranges of RH = 42-65%, 65-80% and 80-90%, the specimen mass is weighted every day at 9 am and recorded, until the specimen mass no longer changes.

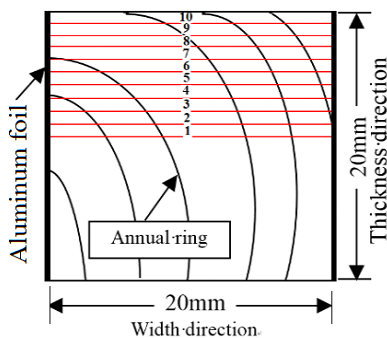


Fig.1. Specimen preparation

Measurement and determination of specimen D_s , D_{ls} and D_{vs} values

For the D_{ls} and D_{vs} values of the *Pinus yunnanensis* specimens with EMC less than 10%, refer to Reference 5. The bonded water diffusivities D_{ls} of *Pinus yunnanensis* with other moisture

contents are calculated for integer according to Eq. (9) [5].

$$D_{ls} = 0.5 \times 10^{-10} + \frac{W - 0.1}{W_{fsp} - 0.1} \times 0.78 \times 10^{-10} \quad (9)$$

In this experiment, three moisture absorption ranges of *Pinus yunnanensis* are calculated by

Empirical Eq. (9), and verified by the Crank method in Reference 11 with measured tests. Finally, it is comprehensively considered to take $D_{ls}=5.0 \times 10^{-11}$ m²/s (RH42%-65%), $D_{ls}=6.0 \times 10^{-11}$ m²/s (RH65%-80%) and $D_{ls}=6.0 \times 10^{-11}$ m²/s (RH80%-90%).

The water vapor diffusivity D_{vs} of *Pinus yunnanensis* is measured according to ASTM E96 / E96M - 05 Standard Test Methods for Water Vapor Transmission of Materials. The values are $D_{vs}=0.7 \times 10^{-6}$ m²/s (RH42%-65%), $D_{vs}=1.5 \times 10^{-6}$ m²/s (RH65%-80%), $D_{vs}=1.6 \times 10^{-6}$ m²/s (RH80%-90%).

DEFINITE CONDITION AND SOLUTION

Definite condition

The specimen thickness is divided into 20 layers, then $\Delta z = 1$ mm (as shown in Fig. 1), and the calculation step $\Delta \tau = 600$ s. Among them, the absolute dry density of *Pinus yunnanensis* $\rho_d = 519.74$ kg/m³ (measured), that of the cell wall material is 1540 kg/m³ [12], material surface mass transfer coefficient $h_m^* = 3.88 \times 10^{-6}$ kg/(m²·s) [5], and molar gas constant R = 8.315 J/(mol·k); for the bonded-water diffusivity D_{ls} and water vapor diffusivity D_{vs} in *Pinus yunnanensis*, refer to Section to *Experimental methods*

Solution of partial differential equation

Differential Eqs. (1-7) are transformed into explicit difference equations, and according to the above definite conditions, the moisture absorption laws of *Pinus yunnanensis* in each moisture absorption range can be obtained.

Considering the specimen geometry symmetry in this study, moisture migration is only solved within half specimen thickness (as shown in Fig. 1).

RESULTS AND ANALYSIS

Wood moisture absorption process and model validation

Based on the above mathematical model, definite condition and difference numerical method, the theoretical moisture content change curves of *Pinus yunnanensis* (solid squares in Figs. 2-4) in three moisture absorption ranges (RH = 42-65%, 65-80% and 80-90%) can be obtained. However, the measured average moisture content curves of six *Pinus yunnanensis* specimens (hollow triangles

in Figs. 2-4) consistently prove that this theoretical model can accurately reflect the wood moisture absorption process.

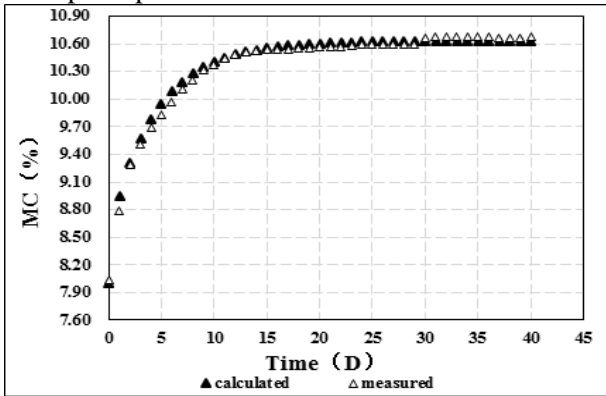


Fig. 2. MC-change curve of YNP along with time under RH42-65% environment.

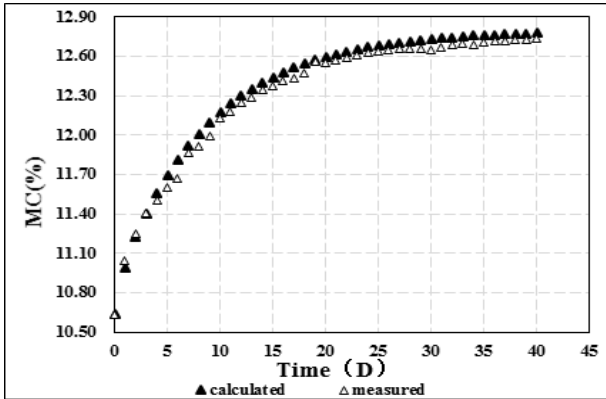


Fig. 3. MC-change curve of YNP along with time under RH65-80% environment

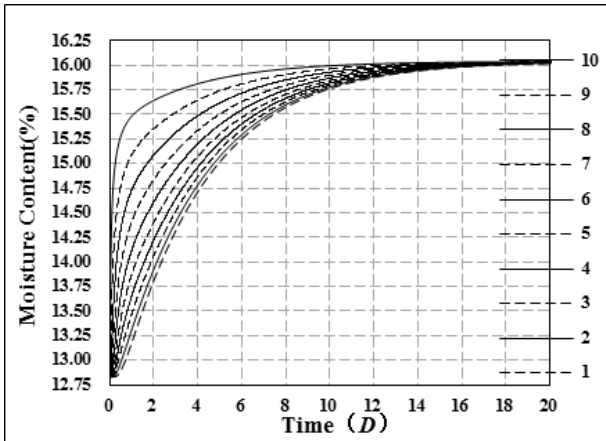


Fig. 4. MC-change curve of YNP along with time under RH80-90% environment

It also can be seen from Figs. 2-4 that the wood materials have different moisture absorption rates in different moisture absorption ranges (corresponding to the different wood moisture contents and moisture states). As a result, in the three moisture absorption ranges of RH = 42-65%, 65-80%

and 80-90%, *Pinus yunnanensis* respectively requires 30 d, 40 d and 25 d for moisture absorption to achieve a basic balance of water inside and outside respectively, i.e. to reach the equilibrium moisture content (EMC) under the target environment humidity. The reasons resulting for differences are as follows:

(1) In the above three moisture absorption ranges, the actual change ranges of moisture content in *Pinus yunnanensis* are 7.95-10.63%, 10.63-12.80% and 12.80-16.04%, i.e. the moisture content gradient differences are 2.68%, 2.17% and 3.24%, respectively. Therefore, the moisture content gradient difference is able to directly determine the above moisture absorption rates of *Pinus yunnanensis*.

(2) In the process of wood moisture absorption, the cell walls present a certain degree of swelling, thus leading to greater pit aperture, and the adsorption capacity of wood cell wall weaken gradually, so that the diffusivity of vapor (DOV) is increased to a certain degree [5,11] (as shown in Fig. 5).

(3) In a certain range of moisture content, with the increase of moisture content, the channel capacity of the micro capillary system in the wood cell walls is also enhanced to a certain degree, thereby resulting in the diffusivity of bonded water (DBW) also increasing [1] (as shown in Fig. 5).

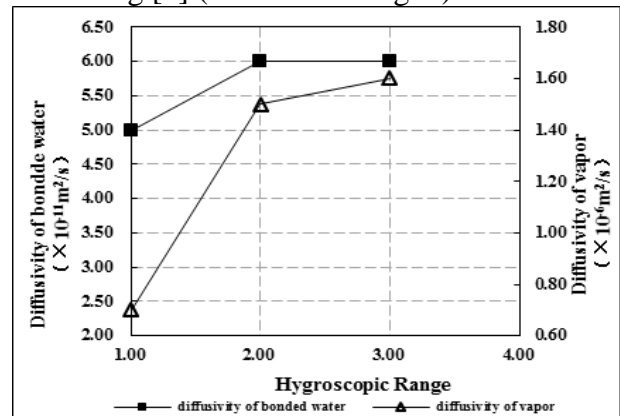


Fig. 5. Diffusivities of bonded-water and vapor in different hygroscopic ranges.

The relationship of the diffusivities of the wood bonded water and water vapor with wood moisture content is still inconclusive in academia at present, and thus requires further research.

Distribution of wood moisture content in moisture absorption process

Figs. 6, 8 and 10 respectively show the changes of moisture content in each layer of the *Pinus yunnanensis* specimens over time within three moisture absorption ranges during moisture absorption process, of which Layer 1 is the middle layer of the specimen, and Layer 10 is the boundary layer connected with the environment (see Fig. 1).

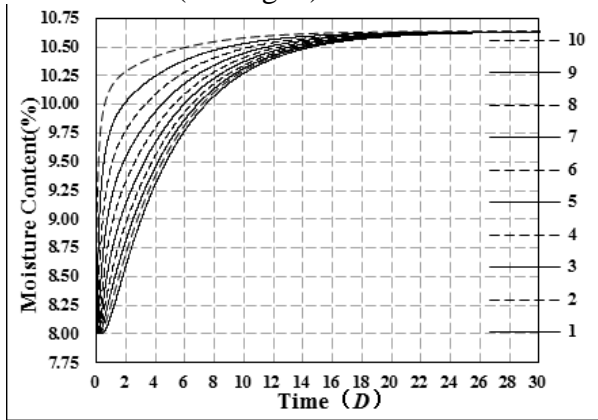


Fig. 6. MC distributions among different layers of YNP along with time under RH42-65% environment.

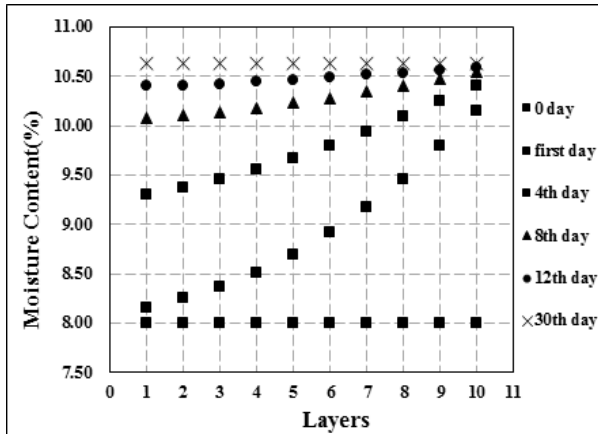


Fig. 7. MC gradients among different layers and time of YNP under RH42-65% environment.

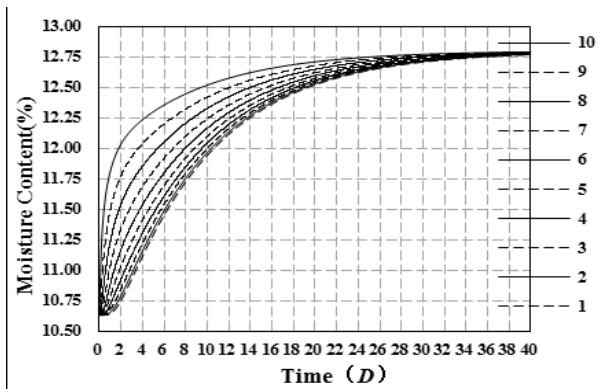


Fig. 8. MC distributions among different layers of YNP along with time under RH65-80% environment

Figs. 7, 9 and 11 respectively show the changes in the moisture content gradient of each layer on days 0, 1, 4, 8, 12 and 30 in the three moisture absorption ranges.

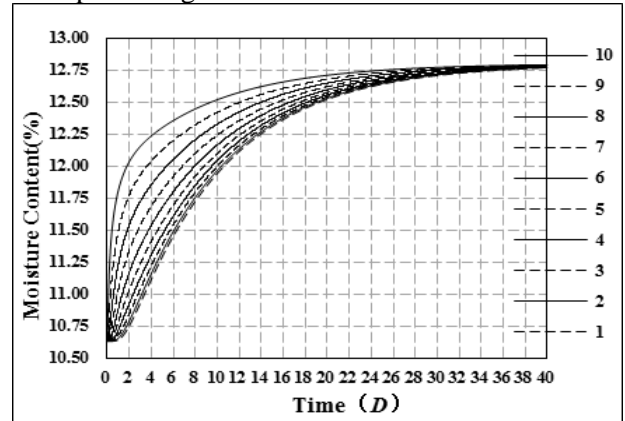


Fig. 9. MC gradients among different layers and time of YNP under RH65-80% environment.

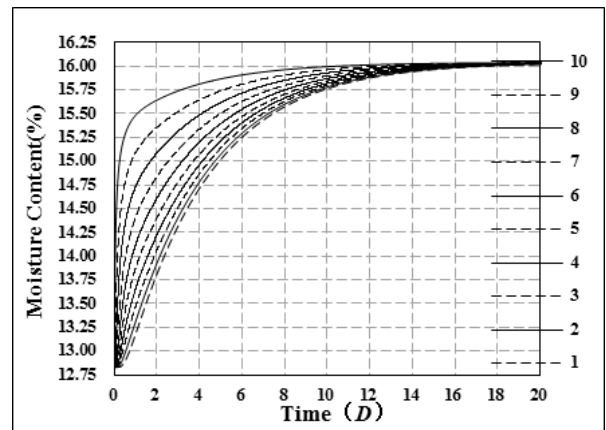


Fig. 10. MC distributions among different layers of YNP along with time under RH80-90% environment.

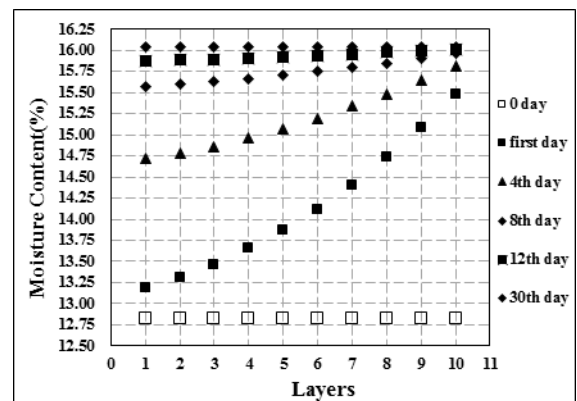


Fig. 11. MC gradients among different layers and time of YNP under RH80-90% environment

It is shown in Figs. 6 and 11 that the larger the change range of wood moisture content is, the faster the moisture content response of each layer especially the surface will be, and thus the greater

Table 1. Relationship between RH of environment and EMC of *Pinus yunnanensis*

Ambient relative humidity	%	42	65	80	90
Actual equilibrium moisture content of <i>Pinus yunnanensis</i>	%	7.95	10.63	12.80	16.04
Maximum theoretical equilibrium moisture content of <i>Pinus yunnanensis</i> calculated by Simpson model	%	8.00	12.00	16.05	20.54

the moisture absorption rate will be, the greater the gradient difference of inter-layer moisture content will be, the faster the rate of moisture content of each layer to achieve EMC will be, and the shorter the time will be.

Therefore, setting up an appropriate change range of wood moisture content and control proper drying rate in wood drying process is an essential way to prevent the excessively large moisture content gradient difference of internal and external wood layer from cracking.

Relationship between wood EMC and surrounding RH

It can be seen from Table 1 that the EMC of *Pinus yunnanensis* under various surrounding RH is not equal to the theoretically calculated EMC [12], and along with the increase of surrounding RH, differences also become greater. Therefore, in the solution of the wood moisture migration model, its environmental boundary W_e should be the actual EMC of wood under this surrounding RH, rather than the theoretical wood EMC calculated by the Simpson model. Otherwise, larger errors occur in the model calculation of required equilibrium time in the setting environment, as well as the size and distribution of moisture content gradient.

CONCLUSIONS

(1) The wood one-dimensional isothermal moisture migration model can accurately predict the wood moisture migration process in each moisture absorption range beneath the fiber saturation point.

(2) The diffusivities of wood bonded water D_{ls} and water vapor D_{vs} increase with greater moisture content, but are considered as constants within a certain moisture content range.

(3) The larger the change range of the gap between initial wood moisture content and surrounding equilibrium moisture content is, the greater the moisture content gradient of wood inter-layer in the dynamic moisture migration process will be, and the shorter the time to reach overall targeted EMC will be.

(4) The environmental boundary W_e should be set as the actual EMC of the wood under this surrounding RH.

Acknowledgments: This research was supported by Special Scientific Research Fund of Foundation of Yunnan Provincial Education Department (No.2015Y291).

Nomenclature

D_{ls} —Diffusivity of liquid water in wood, m^2/s ;
 D_{vs} —Mass diffusivity of vapor in wood, m^2/s ;
 f_p —Inverse function relation of Simpson model;
 h_m^* —Surface mass transfer coefficient, $kg/(m^2 \cdot s)$;
 \dot{m}_v —Volume evaporation rate, $kg/(m^3 \cdot s)$;
 \dot{m}_s —Wood surface evaporation/condensation rate, $kg/(m^2 \cdot s)$;
 p_{sv} —Saturated vapor pressure, Pa ;
 p_v —Unsaturated vapor pressure, Pa ;
 R —Molar gas constant, $J/(mol \cdot K)$;
 t —Temperature, $^{\circ}C$;
 T —Thermodynamic temperature, K ;
 W —Wood moisture content, %, kg/kg or kg/m^3 ;
 W_e —Equilibrium moisture content of wood environment, kg/m^3 .
 W_s —Wood surface moisture content, kg/m^3 ;
 Z —Specimen thickness, mm

Greek symbols

ρ_v —Vapor density, i.e. absolute humidity, kg/m^3 ;
 ρ_d —Absolute dry density of wood, kg/m^3 ;
 τ —Time, s ;
 Φ —Wood void fraction
 φ —Relative air humidity, %;

REFERENCES

1. Y. Ishimaru, K. Oshima, I. Iida, *J. Wood Sci.*, **4**, 47 (2001).
2. M. Fragiaco, S. Fortino, D. Tononi, et al., *Eng. Struct.*, **11**, 33 (2011).
3. Y. X. Huang, C. L. Dong, H. J. Zhang, *China Wood Industry*, **3**, 27 (2013).
4. F. Tariku, K. Kumaran, P. Fazio, *Int. J. Heat Mass Transf.*, **15**, 53 (2010).
5. C. M. Yu, *Tsinghua University Press, Beijing, China* (2011).

6. Z. Y. Cai, *Forest Prod. J.*, **7/8**, 58 (2008).
7. R. Baettig, R. Rémond, P. Perré, *Wood Sci. Tech.*, **4**, 40 (2006).
8. S. G. Harding, D. Wessman, S. Stenström, L. Kennea, *Chem. Eng. Sci.*, **56** (2001).
9. V. P. Dushchenko, K. B. Baidzhanov, *J. Eng. Phys. Thermophysics*, **2**, 9 (1965).
10. V. Möttönen, T. Kärki, O. Martikka, *Eur. J. Wood Prod.*, **2**, 69 (2011).
11. Zhan Jianfeng, Gu Jiyou, Cai Yingchun, *J. Nanjing Forestry Univ. (Nat. Sci. Edit.)*, 4 (2008).
12. USDA, Forest Prod. Lab., *Washington, DC* (1999).

A parametric study on the factors affecting gas turbine combustion using a CFD-based approach

Farhud Shirinzadeh¹, Reza Mohajer Barough², Ali Atashbar Orang^{3*}

¹Department of Mechanical Engineering, Science and Research Branch, Islamic Azad University, Tehran, Iran

²Faculty of Mechanical Engineering, University of Tabriz, Tabriz, Iran

³Young Researchers and Elite Club, Tabriz Branch, Islamic Azad University, Tabriz, Iran

Received June 26, 2015; Revised September 10, 2015

Abstract: In this paper, a numerical simulation was conducted using FLUENT CFD package to investigate injection effects of axial and swirl flow inside the annular combustion chamber with wall jet. The flow was considered as three-dimensional, steady, turbulent, incompressible, viscid, and two-phase and turbulence models including RNG (k- ϵ) and the Reynolds stress model were applied. In order to evaluate the applied numerical method, the results obtained in the reacting combustion chamber were compared with experimental ones. The effects of different parameters inside the combustion chamber including air-fuel ratio, swirl mass flow rate, fuel spray angle and swirl number were studied and optimal values for some of these values were obtained. The results showed that increasing the swirl air flow rate in the inlet area of the combustion chamber stretches the swirl area toward the fuel injection nozzles and causes initiation of combustion near the chamber inlet. The increase of the air-fuel ratio results in increasing the velocities and uniform temperature profiles in the outlet chamber. Increasing swirl number and decreasing fuel spray angle also reduces wall temperature. Optimal values for Sauter mean diameter and fuel spray angle were also determined.

Keywords: gas turbine combustion chamber; air-fuel ratio; fuel spray angle; swirl number

1. INTRODUCTION

Gas turbine combustion chambers need high combustion efficiency, low pollutants emissions and high performance. Turbulent flow field inside the combustion chamber plays a very important role in flame formation. Another important factor is the way in which fuel is injected into the combustion chamber and its mixing with air. Swirl flow has been mostly used to stabilize the flame inside the combustion chamber of gas turbines. Combustion modeling has a fundamental role in accurate simulation of combustion flows. This is, in addition to the amount of species and combustion products, energy release rate resulting from the mixing of the fuel and oxidant is determined by it. An appropriate combustion model should take into account the effect of all these factors. In computational fluid dynamics (CFD), the simulation of processes such as turbulence, combustion and radiation requires mathematical modeling. Simulation of these phenomena can be useful and reliable if the infrastructure model or models are accurate

enough. The extensive applicability, high accuracy, low computational cost and simplicity are four important specifications of mathematical models.

Cameron and Samuelsen [1] studied the characteristics of temperature and velocity profiles inside a combustion chamber with wall jet. The obtained results indicated that velocity and temperature profiles are at isothermal and reactive conditions, respectively. They also investigated the effect of swirl air increasing and fuel droplet atomization. Sue et al. [2] investigated numerically a gas turbine chamber integrated with the diffuser. They used the KIVA-3V code to analyze the flow inside the combustion chamber. Flow fields and temperature distribution were studied along the axial and circumferential directions and the stable behavior of the flow in the combustion-compressor system was evaluated. Zhang et al. [3] studied the thermodynamic conditions inside a combustion chamber considered to be symmetric and two-dimensional. The effects of equivalence ratio, reaction temperature and swirl inside the cylindrical combustion chamber were investigated. The results obtained indicated that the combustion chamber geometry has a trivial effect on pressure fluctuation inside it. Som et al. [4] studied the effect of inlet air swirl and fuel injection angle inside a gas turbine

To whom all correspondence should be sent:
E-mail: Ali.at.orang@gmail.com

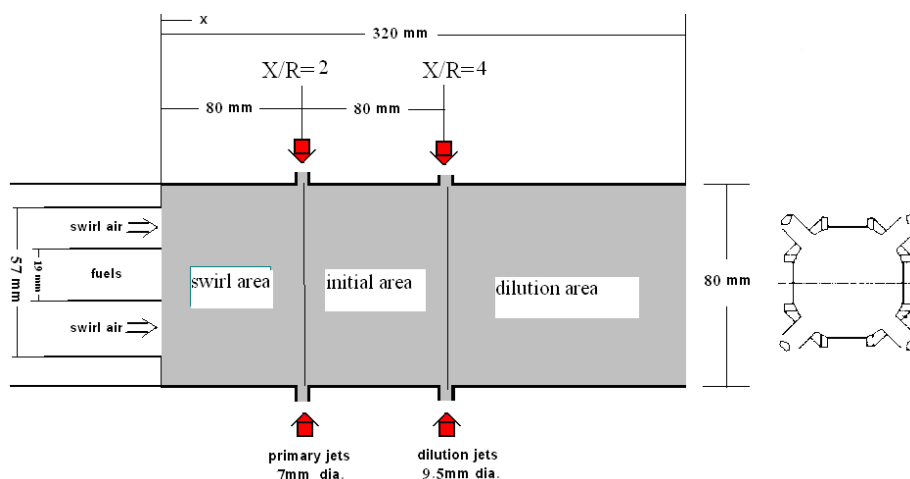


Fig. 1. Schematic of combustion chamber wall jet model

combustion chamber. The results revealed that unlike low swirl numbers, a spiral swirl zone could be seen around the initial central zone at a high swirl numbers. Kurosavwa et al. [5] studied the swirl flame structure inside a gas turbine combustion chamber. They focused on high combustion efficiency, low emissions inside the combustion chamber. Olivani et al. [6] investigated the structure of reactive and non-reactive swirl flows. They found that although the overall mixing process and the main flame structure were handled by the air flow swirl, the fuel injection methods have an important effect on them at the initial zone. Sandararaj et al. [7] studied the effects of jet injection angle, cross-flow Reynolds number and velocity ratio on entrainment and mixing of jet with incompressible cross-flow in venturi-jet mixer.

This paper deals with the effects of axial and swirl air injection and the determination of optimal values for effective parameters including swirl air flow rate, expansion angle of inlet air, diameter of the initial fuel droplets and fuel spray angle. The results of this work can be used for the preliminary design of the aircraft gas turbine combustion chambers and liquid fuel missiles. Furthermore, the optimal values obtained for the average diameter of primary particles and fuel spray angle can be used in design procedures.

2. GEOMETRICAL MODEL AND NUMERICAL METHOD

The wall jet model acts at atmospheric pressure with JP4 fuel. Combustion chamber air is preheated to 600 °C and air flow rate is 163 kg/h. Fuel flow rate and the temperature are 3.27 kg/h and 400 °C, respectively, for an equivalence ratio of 0.3. As shown in Figure 1, air flow is divided into swirl jet, initial jet and diluted air jet. The longitudinal four valves are built around the chamber. Initial jets and diluted air jets have diameter of 7 mm and 9.5 mm,

respectively. A stainless steel channel with radius of 40 cm and length of 32 cm is considered which is blocked from 57 mm onwards. A 60 degree turning is built in the inlet chamber. One of the main needs of gas turbine combustion chambers is that the combustion chamber operates at every working condition. The flow pattern is the first factor of the chamber that affects flame stability. The most common method is recirculation of part of combustion products to the upstream flow and remixing of products with fuel and fresh air. One conventional method involves the use of swirl to create a recirculation. In this design, air nozzles surround the fuel injectors which increase the shear stress and turbulence intensity inside the chamber. The combustion chamber mesh has been built in GAMBIT as shown in Figure 2. It is a 100×80×40 mesh along r, θ, z directions. The FLUNET 6.3 package is used for the simulations. A segregated solver is used to solve the governing equations and an implicit form is used for the linearization of the equations. Convective and diffusion terms are discretized based on power-law and central schemes, respectively. Pressure and velocity fields are coupled through the simple algorithm and Eddy dissipation model is used to model the interactions among them.

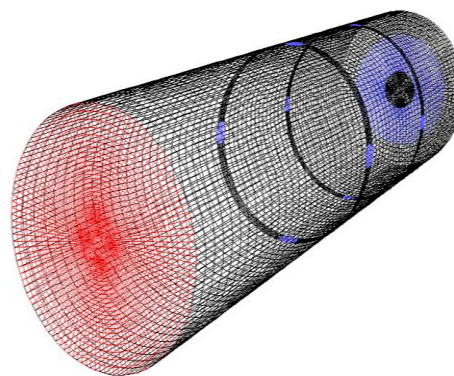


Fig. 2. Combustion chamber mesh

3. GOVERNING EQUATIONS

The Navier-Stokes equations are the fundamental partial-differential equations that describe the flow of fluids. Mass conservation equation or continuity equation, is written as following,

$$\frac{\partial \rho}{\partial t} + \frac{\partial}{\partial X_i} (\rho U_i) = S_m \quad (1)$$

- Momentum conservation equations,

$$\frac{\partial}{\partial t} (\rho U_i) + \frac{\partial}{\partial X_j} (\rho U_i U_j) = -\frac{\partial p}{\partial X_i} + \frac{\partial \tau_{ij}}{\partial X_j} + \rho g_i + \dot{S}_{M_i} \quad (2)$$

- Kinetic energy of turbulence,

$$\rho \frac{Dk}{Dt} = \frac{\partial}{\partial x_i} \left[\left(\mu + \frac{\mu_t}{\sigma_k} \right) \frac{\partial k}{\partial x_i} \right] + G_k + G_b - \rho \varepsilon - Y_m \quad (3)$$

- Dissipation rate of turbulent kinetic energy,

$$\rho \frac{D\varepsilon}{Dt} = \frac{\partial}{\partial x_i} \left[\left(\mu + \frac{\mu_t}{\sigma_\varepsilon} \right) \frac{\partial \varepsilon}{\partial x_i} \right] + C_{1\varepsilon} \frac{\varepsilon}{K} (G_k + C_{3\varepsilon} G_b) - C_{2\varepsilon} \rho \frac{\varepsilon^2}{k} \quad (4)$$

- Energy equation,

$$\frac{\partial}{\partial t} (\rho^s c_p^s T) + \frac{\partial}{\partial x_i} (\rho^s c_p^s U_i T) = \frac{\partial}{\partial x_i} (\rho^s c_p^s \alpha_{eff} \frac{\partial T}{\partial x_i}) - \frac{\partial q_i^r}{\partial x_i} + \dot{S}_E \quad (5)$$

- Discrete phase model: Fuel spray (continuous injection in the combustion chamber), includes a limited number of droplet categories with a range of specific sizes. Initial droplet size distribution of liquid fuel spray is assumed to follow Rosin-Rammler distribution function defined as,

$$G'(d_i) = \frac{\exp(-bd_i^n) - \exp(-bd_{max_i}^n)}{\exp(-bd_{min_i}^n) - \exp(-bd_{max_i}^n)} \quad (6)$$

- Species conservation equation,

$$\frac{\partial}{\partial t} (\rho^s C_j) + \frac{\partial}{\partial x_i} (\rho^s U_i C_j) = \frac{\partial}{\partial x_i} (\rho^s D_{eff} \frac{\partial C_j}{\partial x_i}) + \dot{S}_{C_j} + \dot{S}_{C_j} \quad (7)$$

- Eddy dissipation model is,

$$\overline{\omega_P} = \rho C_{EBU} \frac{\varepsilon}{K} \left(\overline{u^2} \right)^{\frac{1}{2}} \quad (8)$$

The dimensionless number swirl used to determine the swirl applied on the flow, is defined as:

$$S_N = \frac{2G_m}{D_{sw} G_t} \quad (9)$$

where G_m , G_t and D_{sw} are axial flux of angular momentum, axial flux of axial momentum and swirl outer diameter, respectively. These parameters are given in turn by,

$$G_t = \int_0^{\frac{D_{sw}}{2}} 2\pi r \rho U(U) dr + \int_0^{\frac{D_{sw}}{2}} 2\pi r P dr \quad (10)$$

$$G_m = \int_0^{\frac{D_{sw}}{2}} 2\pi r \rho U(Wr) dr \quad (11)$$

where W , U and P are axial velocity, tangential velocity and static pressure, respectively. There is usually no reverse flow for $S_N < 0.4$. The stream lines show considerable divergence for $0.4 < S_N < 0.6$. Reverse flow was observed for $S_N > 0.6$. The following relation is proposed for calculating the swirl number in one-axial swirl with flat blades,

$$S_n = \frac{2}{3} \frac{1 - \left(\frac{D_{hub}}{D_{sw}} \right)^3}{1 - \left(\frac{D_{hub}}{D_{sw}} \right)^2} \tan(\theta) \quad (12)$$

where the model factor is defined as,

$$P.F = \frac{T_{max} - T_{av}}{T_{av} - T_{in}} \quad (13)$$

here T_{max} , T_{av} and T_{in} are the maximum temperature at the outlet section, weighted average temperature in chamber outlet, and weighted average temperature of all chamber inlets, respectively.

4. RESULTS AND DISCUSSION

Referring to Figure 1, swirl air inlet, initial jets and dilution jets are considered as 25, 35 and 40 percent of the total air flow rate, respectively [1]. The results obtained show that the onset of swirl area is in the trap area at $X/R=0.75$ in reactive condition. Figures 3 and 4 illustrate the axial velocity and temperature profiles in different cross-sections, respectively. In order to detect the effects of initial jets on the swirl area, $x/R=1$ has been used. Regarding the total inlet air, 50% for swirl air, 50% for diluted air and 0% for the primary air is utilized. According to Figure 5, temperature is initially high across the swirl area except near the wall because the combustion occurs at this region. Temperature in the downstream of flow is decreased due to increased

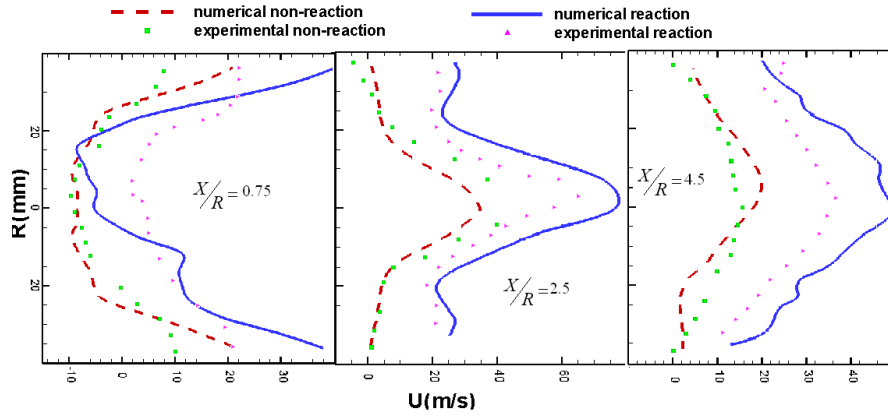


Fig. 3. Axial velocity comparison with reactive and isothermal conditions ($Re=19600$, $S=0.36$, $A/F=1.5$)

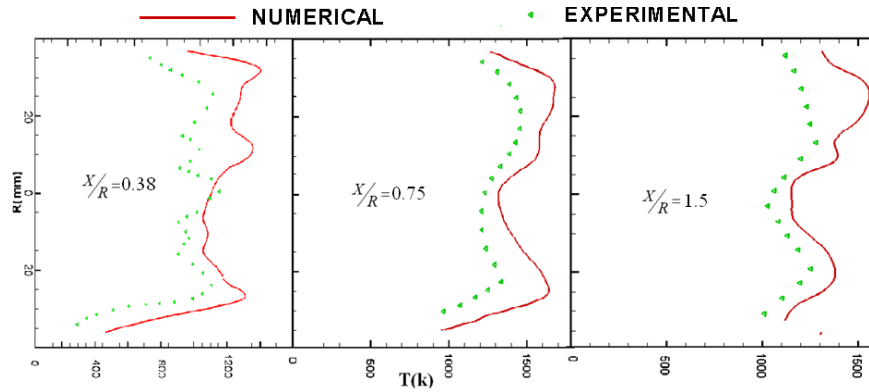


Fig. 4. Total temperature profiles in reactive condition at trap zone ($Re=19600$, $S=0.36$, $A/F=1.5$)

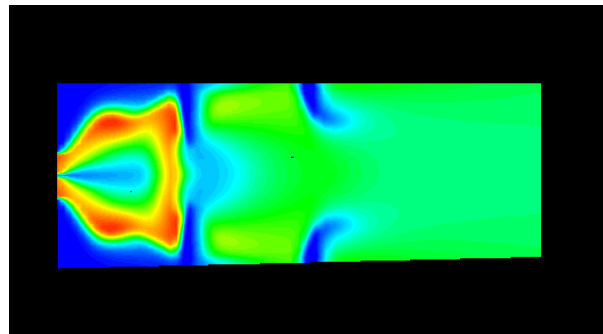


Fig. 5. Temperature profile at reaction case

penetration of the jets and extreme enhancement of the axial velocity in the central line. At outer areas of the combustion chamber due to the penetration of diluted jets, the temperature profile is relatively uniform. Figure 6 shows the variation of radial velocity in the case of swirl air enhancement. A 45 degree expansion is gradually influencing the progress of the swirl flow. The reason for this is that a mechanism was added to the swirl created in the trap area which affected the reverse mixture and, as can be seen in Figure 7, the swirl occurred at $x/R = 0.63$.

The effect of increasing the fuel-air ratio from 1.5 to 3 on the axial velocity and temperature profiles is shown in Figures 8 and 9, respectively. This effect is mostly evident in the trap area at $x/R = 0.38$, 0.75 and 1.13. Although, the velocity profiles are similar

to those obtained in the previous air-fuel ratio ($A/F=1.5$), velocities become much larger. The effect of increasing air-fuel ratio is gradually reduced at $x/R = 2.5$ and 4.5. Asymmetry in the temperature profiles near the nozzle at $x/R = 0.38$ is again evident. Although the hot strip exists in these conditions, its effect is much less. Temperature profiles are relatively symmetric about the central line. The cool core resulting from the jets penetration appears at $x/R = 2.5$ and continues through the flow up to $x/R = 4.5$. The temperature profile is relatively uniform at $x/R = 5$.

The effects of swirl number on the chamber wall temperature and output temperature are shown in Figures 10 and 11, respectively.

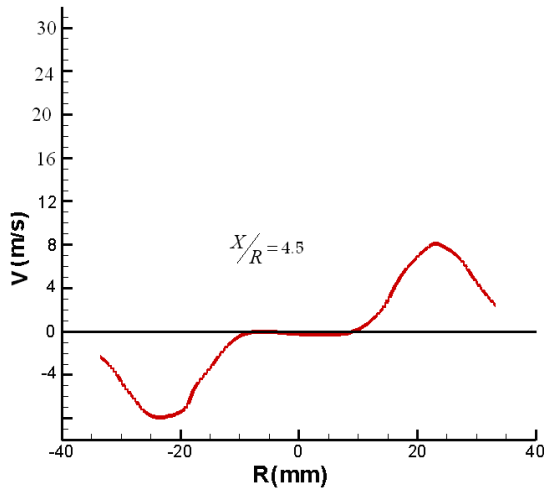


Fig. 6. Variation of radial velocity with swirl air enhancement.

According to Figure 10, the slope of the curve in trap area is caused by chemical interactions. The wall temperature rapidly decreased due to the primary air jet entering to the chamber, and then, because of heat penetration from the core, the temperature near the wall relatively increases. Then, a large drop in wall temperature occurs due to the entering of diluted air followed by an increase in wall temperature up to the outlet. By increasing the swirl number through the increase of the swirl angle, the combustion is prevented from reaching the walls and, as depicted in Figure 13 the temperature near the wall falls. As can be seen in Figure 11, by increasing the swirl number, the outlet temperature reduces near the wall and increases in the central line. The reason for this is that by increasing the swirl number more combustion occurs on the central line and it is not drawn near the wall.

According to Figure 12, by increasing the fuel spray angle, the wall temperature increases due to large radial dispersion of fuel particles and subsequent combustion of the fuel near the wall.

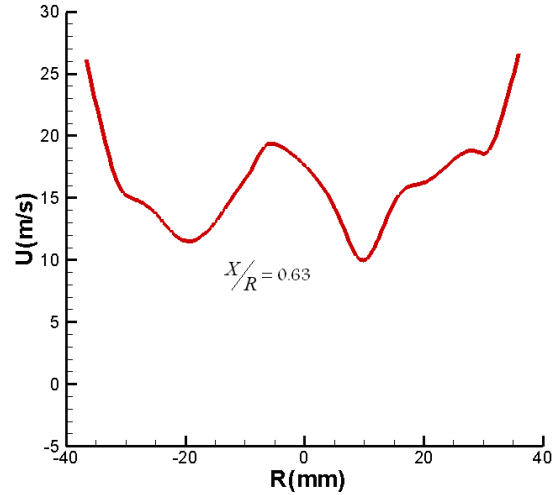


Fig. 7. Velocity profile in the case of 45° gradual increasing.

Outlet temperature variation based on the fuel spray angle is shown in Figure 13. As observed in Figure 13, by increasing the angle of fuel spray, the fuel mixes better with air and most of the reaction process is occurs in the trap area, consequently, the outlet temperature falls.

For issues related to gas turbine combustion, small Sauter mean diameter of the initial fuel droplets increases efficiency and engine performance and reduce pollutants; on the other hand, if the droplet size is too small, they lose the required momentum and force to penetrate into high-pressure gases. Figure 14 depicts the Sauter mean diameter of initial droplets with a constant spray angle of 80°. Combustion efficiency, and P.F. are calculated for several Sauter mean diameters. The mean diameter of initial droplets of 52 μm has more suitable combustion efficiency and P.F. compared to other diameters. As can be seen in Figure 15, the spray angle of 80° results in the highest combustion efficiency and P.F. According to experimental results available in literature, P.F. is between 0.5 and 0.75 [8].

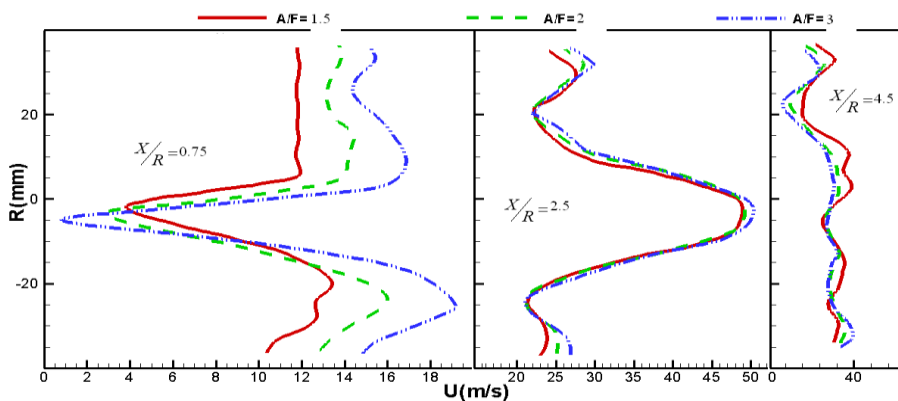


Fig. 8. Axial velocity profiles at three different air-fuel ratios.

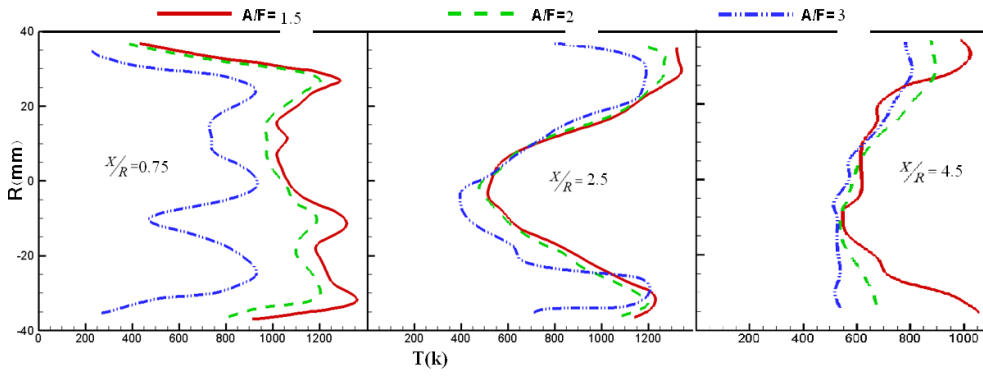


Fig. 9. Temperature profiles at three different air-fuel ratios.

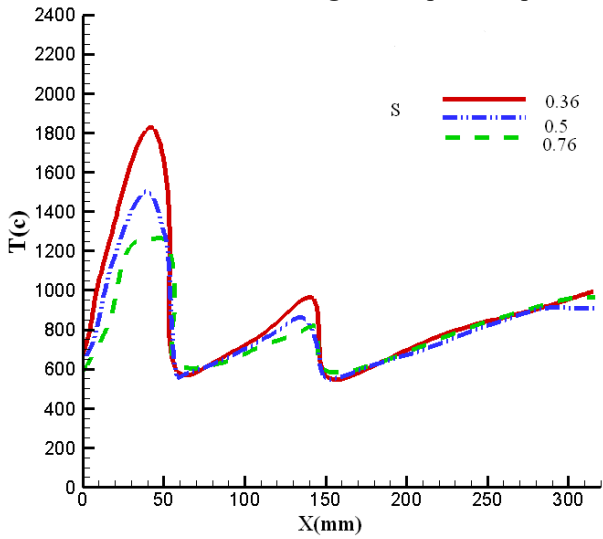


Fig. 10. Effect of swirl number in different cases of wall temperature.

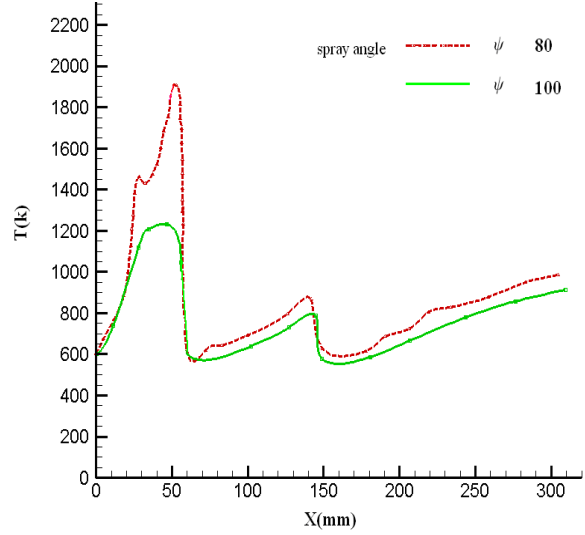


Fig. 12. Effect of fuel spray angle on wall temperature.

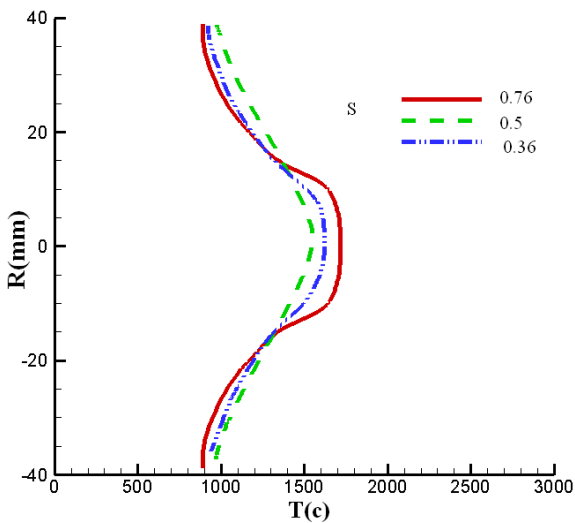


Fig. 11. Effect of swirl number in different cases of outlet temperature.

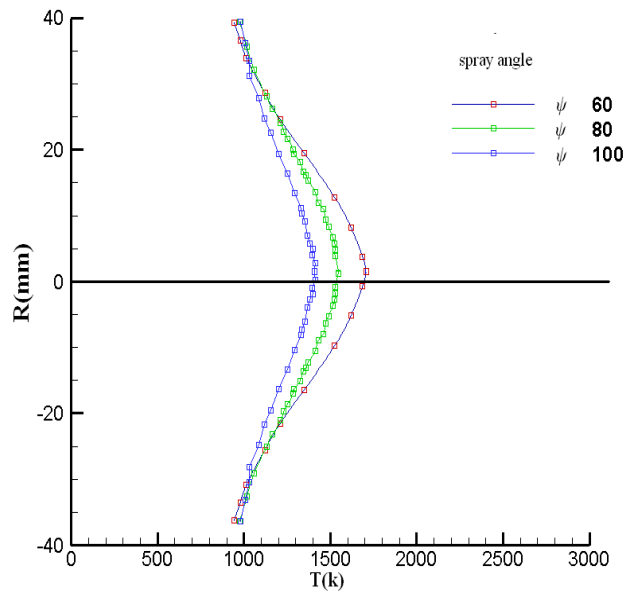


Fig. 13. Effect of fuel spray angle on outlet temperature.

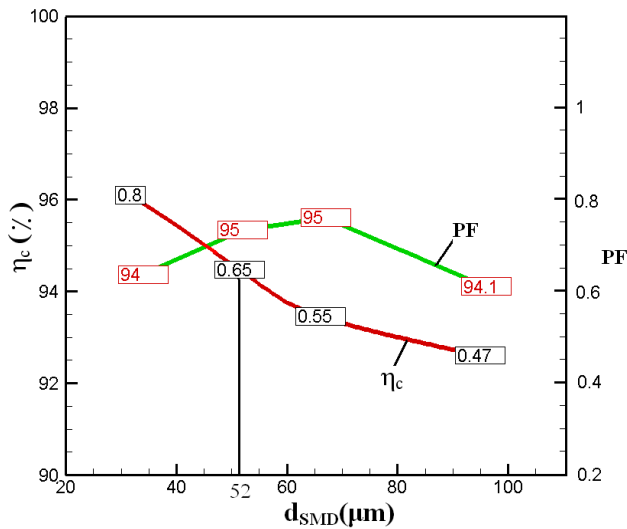


Fig. 14. Optimization of Sauter mean diameter of initial droplets.

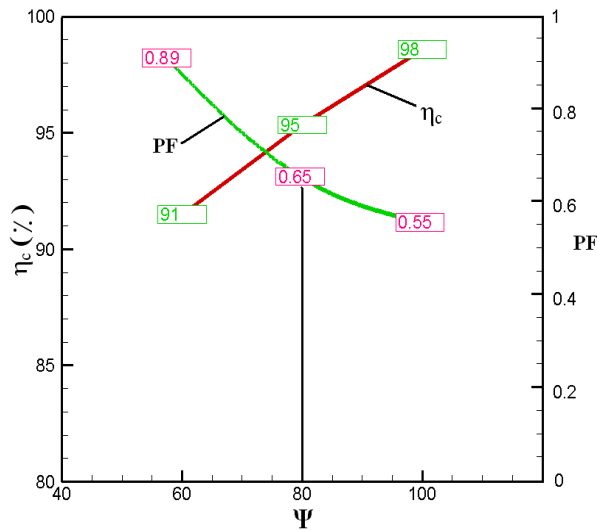


Fig. 15. Optimization of fuel spray angle.

5. CONCLUSIONS

A numerical simulation was performed to investigate the effects of injection of axial and swirl flow inside an annular combustion chamber with wall jet. According to the results, by increasing the flow rate of swirl air entering the combustion chamber it is possible to achieve a rapid and nearly complete mixing mode. An excessive increase in the swirl flow rate at the chamber inlet allows that the combustion reaches the fuel injection nozzles. Thus, an optimum value for the swirl air flow exists. The effect of swirl number and fuel spray angle on wall and outlet temperatures were also investigated. Increasing the swirl air flow rate in the inlet area of the combustion chamber stretches the rotational area toward the fuel

injection nozzles and causes the initiation of combustion near the chamber inlet. A further increase of the swirl flow rate at the chamber entrance makes that the combustion reaches the fuel injection nozzle; hence, an optimal value for swirl flow rate in the chamber entrance needs to be determined. An increase in the air-fuel ratio results in an increase in the velocities and uniform temperature profiles at the outlet chamber. Moreover, increasing swirl number and decreasing fuel spray angle also reduces the wall temperature. According to the results obtained, by enhancing the inlet swirl air flow rate and a sudden 45° expansion through variation in the geometry of the combustion chamber, rapid and quite complete mixing can be achieved. However, due to the proximity of the combustion to the chamber inlet and subsequent damage of the fuel injection nozzle, optimal values need to be obtained for the mentioned parameters.

NOMENCLATURE

S_m	Mass added to the continuous phase of the second diffused phase
p	Static pressure
τ_{ij}	Stress tensor
ρg_i	Gravitational force along i direction
\dot{S}_{M_i}	Momentum term in gas phase equation
G_K	Turbulent kinetic energy
G_b	Kinetic energy of buoyancy
Y_m	Fluctuating expansion in compressible turbulence relative to the overall loss rate
σ_k	Turbulent Prantl number
σ_ϵ	Turbulent Prantl number
\dot{S}_E	energy term
$\dot{G}(d_i)$	Mass fraction of spray
$\frac{\dot{S}_{Cj}}{Y_p}$	Source term
$\frac{\dot{S}_{Cj}}{Y_p^2}$	Variance of product mass fraction

REFERENCES

1. C.D. Cameron, G.S. Samuelsen, *ASME J. Eng. Gas Turbine Power*, **111**, 31 (1989).
2. K. Su, C.Q., Zhou Numerical Modeling of Gas Turbine Combustor Integrated with Diffuser. 34th National Heat Transfer conference Pittsburgh, 2000.
3. C. Zhang, T. Zhao, Parametric Effects on Combustion Instability in a Lean Premixed Dump Combustor. AIAA-02-4014, 2005.

4. S.K. Som, A.K. Ghosh, Effects of Inlet Air Swirl and Spray Cone Angle on Combustion and Emission Performance of a Liquid Fuel Spray in a Gas Turbine Combustor. Dissertation, Wright-Patterson Air Force Base, Dayton, Ohio, July 2000.
5. Y. Kurosavwa, S. Yoshida, T. Yamamoto, K. Shiodira, M. Gomi, K. Suzuki, Structure of Swirler in Gas Turbine Combustor. Technical Report National Aerospace Laboratory of Japan, 2000.
6. A. Olivani, G. Solero, F. Cozzi, A. Coghe, *Exper. Thermal Fluid Sci.*, **31**, 427 (2007).
7. S. Sandararaj, V. Selladurai, *Thermal Sci.*, **16**, 207 (2012).
8. X.R. Duan, W. Meirer, P. Weigand, B. Lehmann, *Lasers and Optics*, **127**, 492 (2005).

The impact of altitude effect on tunnel fire characteristics

D. Yuan, Y. Wang, Y. Zhang, Y. Huang*

Wuhan University of Technology, Wuhan430070, China

Received June 26, 2015, Revised September 10, 2015

Tunnel fire can not only lead to huge damages to economic losses, but also threatens the human safety. Nowadays, more and more tunnels are established on plateau, and there are some differences between tunnel fire in plateau and in plain. Little research has been made about the impact of altitude on tunnel fire, so this paper is concentrated on this topic. CFD (Computational Fluid Dynamics) technology develops rapidly, very many scholars use it in study and the accuracy of the simulation results has been certified. In this background, the technology was applied to study the impact of altitude on tunnel fire. Comparing simulation results at different altitude, some differences were found. Temperature at axle wire of the tunnel is much higher and the high temperature area is bigger at higher altitude than at lower altitude ceiling temperature magnifies with the rising of altitude. Ceiling temperature decays in an exponential model no matter at high or low altitude. The coefficient k increases because of the rising of altitude, meaning that ceiling temperature decays faster at higher altitude. The smoke diffusion length at 100 s told that smoke diffusion velocity is bigger at higher altitude, so the same distance from fire source, the higher altitude will be into danger faster. The smoke diffusion length at 100 s told that smoke diffusion velocity is bigger at higher altitude, so the same distance from fire source, the higher altitude will be into danger faster. All these factors indicate that when HRR is same, the higher altitude, the bigger danger. To some extent, a conclusion can be made that altitude rising can aggravate the consequence of the tunnel fire, and more attention should be paid to high altitude tunnel fire.

Keywords: tunnel fire, altitude, temperature, smoke diffusion, CFD simulation

INTRODUCTION

Tunnel fire can cause disasters. In 1999, a shocking fire accident happened in Mont-Blanc road tunnel, made 39 deaths, 43 cars ruined and traffic interruption for a year and a half [1]; in 2008, DaBao Mountains tunnel fire in China made 2 death, 5 injured, 2 trucks ruined, and traffic interruption for a month.

Tunnel fire safety has attracted many experts' interests, they made lots studies, many literatures have been reported about the maximum smoke temperature under ceiling [2,3], smoke temperature longitudinal distribution in a tunnel fire [4, 5], and ventilation effect on fire development[6]. Almost all these researches only considered standard pressure atmosphere (altitude is about 100 m).

Recently, due to the Western China, many tunnels created for transportation at high altitude places, such as QiLian Mountains tunnel at an altitude of 3700 m, BaLang Mountains tunnel at an altitude of 3800 m, Queer Mountains tunnel at an altitude of 4300 m. Variations in altitude make changes in environment, further greatly influence tunnel fire characteristics. So the study of the impact of altitude to tunnel fire has practical

significance

Nowadays altitude effects on fire have attracted some researchers' attention. Y. Zhang [7-9] carried out a series of comparative laboratory-scale experiments to study on the characteristics of horizontal flame spread on plateau, and found that the flame spread rate on plateau is lower and the altitude difference can change the pyrolysis mechanisms; Niu Yi [10] conducted fire experiments of cardboard boxes filled with shredded office paper to study the difference of solid fuel fire characteristics at different altitudes, found that mass loss and flame axis temperature changed with the pressure changing. F. Tang and L.H. Hu [11] did numerical CFD simulations of CO concentration distributions in a reduced pressure atmosphere with lower air entrainment at high altitude, made the conclusion that longitudinal decay profiles of CO concentration are similar in different pressure and the smoke flow temperature decays faster with distance along the tunnel in the reduced pressure atmosphere

NUMERICAL SIMULATION

CFD brief introduction

CFD is a product of modern hydromechanics, mathematics and computer science. FDS is one of CFD, specialized in fire simulation, based on mass

To whom all correspondence should be sent:
E-mail: 1976968042@qq.com

conservation equation, energy conservation equation, momentum conservation equation and species conservation equation, and it was, is, and will be used to compute the fire behaviors widely. Previous works have already proved the simulation results' accuracy. So this paper will use FDS to simulate tunnel fire under different atmosphere

Simulation model

This paper uses the Chinese typical single hole bi-directional tunnel as the simulation physical model. The simulation section is 300 m long, 10 m wide and 7 m high, seeing as an rectangle, fire source is in the center of the tunnel, simulation model is presented in Fig 1. In this paper, X (0~150) is the direction of the length, Y(0~10) is the direction of the width, Z(0~7) is the direction of the height.

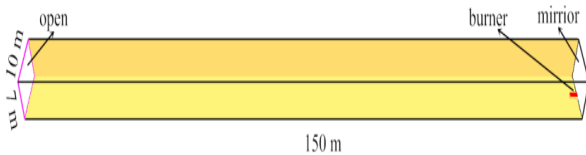


Fig.1. Simulation model.

In order to study the impact of altitude to tunnel fire characters, some parameters are varied in simulation, as Table 1..

Grid is a key issue for the accuracy of simulation results. It is related to the HRR and the environment parameters. The specialists and scholars have found the division of the grid should refer to the formula.

$$D^* = \left(\frac{Q}{\rho_{\infty} c_p T_{\infty} \sqrt{g}} \right)^{\frac{2}{5}} \quad (1)$$

where D^* is fire source characteristic diameter, m; Q is heat release rate, KW; ρ_{∞} is the density of air, kg/m³; C_p is specific heat of environment, kJ/kg•K; T_{∞} is the temperature of environment, K; g is the gravitational acceleration, m/s².

Table 1. The parameters at different altitude

	NO.1	NO.2	NO3	NO.4	NO.5
EGL[m]	0	1000	2000	3000	4000
Pressure[KPa]	101.3	89.6	79.3	70	61
Temperature[K]	298.5	292.5	286.5	280.5	274.5
Air density[kg/m ³]	1.208	40	30	20	10

The cell size should not be larger than 0.1~0.2 D^* , D^* changed with the altitude. A truck's heat release rate is about 30 MW, so consider heat release rate in the simulation as 30 MW. The

largest cell size (Δ) responds to different altitude shows in Table 2.

Table 2. The largest cell size in different altitude

	0	1000	2000	3000	4000
D^* [m]	3.25	3.30	3.51	3.76	4.06
Δ [m]	0.65	0.66	0.702	0.752	0.812

According to table 2, the cell size is designed to be 0.5 m×0.5 m×0.5 m.

Devices and slices

There are some key issues for tunnel fire: temperature and smoke. High temperature not merely damages the tunnel construction but also causes a big harm to people lives. In order to study the temperature distribution, a temperature slice should be set up at the center line (Y=5 m). To learn the ceiling temperature, a series of thermocouples should be installed below the ceiling (Z=6.5 m, Z=6 m respectively) at one section, and every 25 m should be installed one series of thermocouples. Smoke contains a lot of toxic gas, so it can asphyxiate people and make them oxygen-starved, it is the chief reason for human death in a tunnel fire. To analysis smoke characteristics, smoke output must be set as one of the output

RESULTS AND DISCUSSIONS

The altitude effect on smoke diffusion

Smoke diffusion characters is very significant for tunnel fire analysis. Fig.2 demonstrates smoke diffusion length at time of 100 s. It can be seen clearly that smoke diffusion length extends when the altitude rising. This phenomenon shows that the diffusion velocity magnifies along with the increasing of altitude. The main reason is the more smoke is produced at high altitude when HRR is same. Because the area which is at the same distance from fire source will be into danger faster at higher altitude, and the bigger region is influenced by smoke, the tunnel fire in high altitude may result in huger losses.

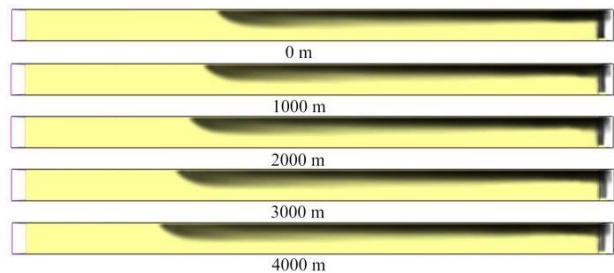


Fig. 2. Smoke diffusion length at T=100s

The altitude effect on temperature

Temperature is another important factor to analysis. Figure.3 shows temperature distribution at Y = 5 m. It's apparent the high temperature area is getting bigger when the altitude gets higher, and so is the maximum temperature increment near the fire source. It is consistent with smoke diffusion, tells that altitude can cause more serious temperature damage when HRR is same.

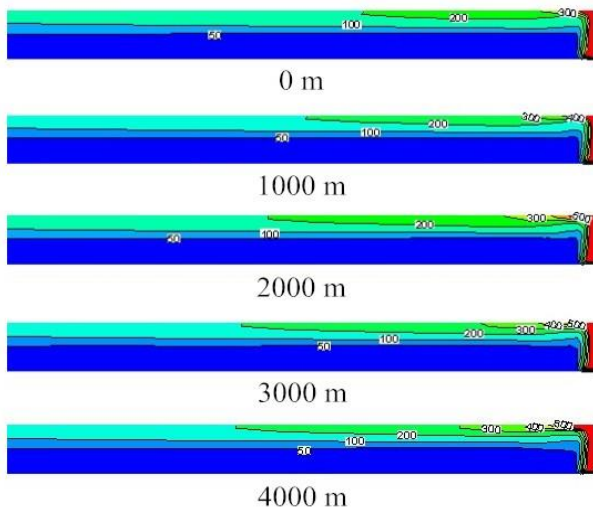


Fig. 3. Ceiling temperature distribution

Hu et al. [2] has found that ceiling temperature decays in an exponential model along the tunnel. The formula is as follows.

$$\frac{\Delta T_x}{\Delta T_0} = e^{-k(x-x_0)}, \quad (2)$$

where ΔT_x is the rising of temperature at the distance x m from fire source, ΔT_0 is the reference rising temperature, meaning the rising temperature at the reference distance, x means the distance form fire, x_0 is the reference distance from fire source

Table 3. Fit coefficient for temperature distribution=

Altitude (m)	0	1000	2000	3000	4000
k	0.0078	0.0085	0.0091	0.0096	0.0103
R	0.9985	0.9958	0.9966	0.9927	0.9946

The ceiling temperature rising at the distance 25 m from fire source as the reference temperature, by using origin software, the fitting formula at different altitude is made respectively, as Fig.4 and Tab.3 represents. The correlation coefficients R at different altitude are all above 0.99, so it certifies that ceiling temperature decays along the tunnel by power exponent no matter at high altitude or at low altitude. And it is seen that k increases as the increasing of altitude, it demonstrates that

altitude rising will lead ceiling temperature decrease faster.

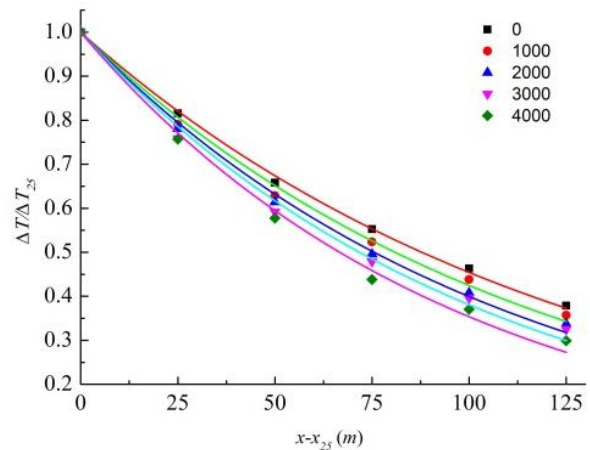


Fig. 4. Ceiling temperature decays fitting model.

CONCLUSION

Altitude effect has great impacts on tunnel fire. Smoke diffusion length is longer when altitude is higher and the diffusion velocity grows with the increase of altitude. The highest temperature under ceiling is bigger too and so is the higher temperature area. Ceiling temperature decays along the tunnel by power exponent no matter at high altitude or at low altitude, the fit coefficient increases with the increasing of altitude.

Both the smoke diffusion characters and the temperature distribution tell that when the altitude is higher, the danger is bigger, the time for people rescuing is less and the loss may be greater.

Acknowledgements: This study has been funded by the National Natural Science Foundation of China (No.51404178), and the National Science & Technology Pillar Program during the 12th Five-year Plan Period (2015BAK40B01).

REFERENCES

1. L. Barbato, F. Cascetta M. Musto, *Tunnelling and Underground Space Technology*, **43**, 253 (2014).
2. L. H. Hu, R. Huo, W. Peng, *Tunnelling and Underground Space Technology*, **21**, 650 (2006)
3. H. Kurioka, Y. Oka, H. Satoh, *Fire Safety*, **38**, 319 (2003).
4. J. P. Kunsch, *Fire Safety Journal*, **37**, 67 (2002)..
5. P. Z. Gao, S.L. Liu, W.K. Chow, *Tunnelling and Underground Space Technology*, **19**, 577 (2004).
6. R.O Carvel, A.N. Beard, P.W. Jowitt, *Tunnelling and Underground Space Technology*, **16**(1), 3 (2006).
7. Y. Zhang, J. Ji, J. Li, *Fire Safety*, **51**, 120 (2012).
8. Y. Zhang, X. Huang, Q. Wang, *J. Hazard.Mater.*, **189**, 34 (2011)..
9. Y. Zhang, J. Ji, X. Huang, *Chinese Sci. Bull.*, **56**, 919 (2011)

10. N. Yi, H. Yaping, H. Xiaokang, *Proc. Combustion Institute*, **34**, 2565 (2013).

11. F. Tang, L. Hu H, L.Z. Yang, *Int. J. Heat Mass Transfer*, **75**, 130 (2014).

Development of network-ranking modeling in planning effective efficiency of multi-stage production industries value chain: A case study of textile industry

A.S. Aboumasoudi, S. Mirzamohammadi, A. Makui

Industrial Engineering Faculty, Iran University of Science and Technology, Tehran, Iran

Received June 26, 2015; Revised September 10, 2015

In order to manage the organization, in n-stage production industries it is important to know whether it is better that, in any of the n-stages of production, a semi-manufactured good is directly sold in the market or it is allowed that completely manufactured good is sent to market at the end of chain. Which of them will have effective efficiency and more profit? Also, it is of great importance for the macro-level planners, in order to strengthen the internal productions against imports and also to gradually create a brand and empower it to gain sustainable competitive advantage in any stage of goods exports. Presented model, formulated through linear programming, can evaluate and assess the strategy of pure profit management by efficiency based on each of production stages work stations (White Box). In fact, a network-ranking model is considered for multi-stage series processes using collective performance analysis to p-stage processes. The ideal decision unit could reach the efficiency of 1 due since it consists of production stations whose efficiencies are 1. With this decision unit, a set of improvement strategies for all 10 understudy production stations can be suggested. It can be claimed that the suggested strategies are based on reality. When two or more networks have the same efficiency, they can be ranked by means of this ideal decision unit.

Keywords: Value chain; Data envelopment analysis (DEA); Ideal decision making unit; Network- Ranking models; Linear Programming

INTRODUCTION

Value chain is usually defined as a network of units that interrelate in different forms. Supplying the demands and organizational sources optimally is among the most important reasons for formation of value chain so that by the management section would be able to guarantee the organization survival, to reach the area of benefit, and gradually create the growth in profits. To achieve this goal, making use of DEA is of paramount importance [14].

In traditional DEA the decision units are taken into consideration as a black box (Charnes et al. [5]) in a way that internal structures of units are often ignored and the performance of a decision unit is determined merely in terms of its inputs and outputs [4].

In many cases it is possible decision units have network structures. Network structures are common in process industries. In the previously conducted studies some attempts have been made to calculate the efficiency based on a network viewpoint. In some of them the relative efficiency of decision unit stages has been calculated by a non-linear model, cf. Liang et al. [15].

A set of examples might be mentioned in terms of production in industry and even services centers in which each system is formed of some sub systems and these sub systems has different inputs and

outputs. During this process it might happen that in the intermediate stages the decision unit enters directly from outside into the intermediate stages or gets out it, cf. Kao&Hwang [13]. The advantage of this view point is, in fact, a meticulous exact look at decision units. It, in fact, makes it possible for the decision maker to make a more appropriate decision because in this type of analysis, the efficiency of decision units and different stages are compared with similar units and stages in other comparable units and their relative efficiency is offered as well. To put it clearly, in this analysis, the Achilles heel of units will be identified [18]. Moreover, by using this type of analysis it will be possible to suggest some strategies to improve the units in a way that by considering their inputs and outputs we can suggest effective strategies to increase their efficiency [19].

In order to reach the intended pattern, in these improvement strategies we can offer the suitable amount of input and output [18]. Another advantage of the model is that the efficiency of each unit is formed from the sum efficiency of stages or its forming sections. Thus, the sum of their efficiency, like the traditional models, will be between $0 \leq E \leq 1$. Different applications can be mentioned for this approach [13].

The models offered after the classic ones made tremendous attempts to remove the weaknesses of the previous models. For example, the Andersen and Petersen efficient units ranking can be mentioned. This model ranks the efficient units. In other words,

by removing the restrictions related to decision unit, it ranks the units whose efficiencies were 1 in the classic models. While this strategy applies in most of cases, in cases where units have a zero input this model encounters an unanswerable question [1].

In a similar vein, different attempts have been made to cover the weaknesses of zero inputs. For example, Chen's articles [3] and Cook et al. research article [9] can be mentioned. Besides, Lee & Zhu [16] offered a new strategy for zero inputs. In their proposed model, titled super-efficiency models tried to rank the efficient units with zero input. Although these approaches could effectively deal with the weakness of classic models in ranking, but other weaknesses and criticisms were still present.

Another approach that tried to cover all the criticisms was the ideal decision making unit. It tries to create an ideal unit to make a pattern for all units ranging from efficient or inefficient ones. This approach especially tried to deal with the inefficiency of efficient units. An important question is available concerning inefficiency of efficient units: why efficient units are good patterns for other units but they themselves lack any improvement pattern? In other words, why should not offer patterns and strategies for patterns and their improvements [2]? In fact, in these models, the efficient units are like machines that merely smooth the path for improvement of other units and move them toward efficiency but no strategy is offered by traditional DEA approaches to improve these efficient units [20]. From another perspective, it sometimes happened in reality that even patterns could not satisfy the managers and shareholders. That is, sometimes the efficient units failed to reach the real determined goals. It means that though efficient units had a relative efficiency 1 in comparison to other units, they could not be regarded as successful patterns that have always achieved the goals and wishes of managers, shareholders, and elites. Thus, in order to take into consideration the opinions of managers and elites about the efficient units, the approach of creating an ideal decision making unit was proposed by Jahanshahloo et al. [11]. Although it was a good response to proposed criticisms about the classic models, but it caused a set of new criticisms. That how and based on what criteria this ideal unit should be created so that it is neither strict nor easy was one of new criticisms. Furthermore, Human interferences were also another weakness and criticism.

On the other hands, in the real world, most of the companies that make use of these types of models for improvement purposes face some problems.

They argue that the strategies offered by ideal virtual units to reach the efficiency frontier are not feasible in reality. That is why; it was a dream for these companies to reach an ideal unit for inefficient units. Given this justification that if these goals, views, and wishes were achievable, the current decision units had achieved them, Jahanshahloo et al. [12].

Stewart [17] in his article examined the ideals using the "Chebyshev scalarizing function". According to the model suggested by him, if these ideals are within the feasible space, they are drawn on the border of feasible space. Some criticisms are made to this model as well. For example, the ideals made by humans for this model are in fact a weak point for it. Moreover, the existence of ideals within the feasible space is meaningless and although it has defined a set of ideals and strategies for current patterns, their being virtual is still open to discussion. Additionally, these models cannot rank the units and only offer improvement strategies and patterns for the units. It should also be pointed out that in the mentioned study some ideals are introduced that are within the recent feasible space meaning that some ideals are sometimes defined for the decision units that those units have reached more achievements than that and now those ideals consider less accomplishments. This is, in itself, a serious criticism to this model in the sense that how could it be that an ideal is within the recent feasible space.

Accordingly, in the present paper a network model was designed in a way that not only has the ranking capability of units, but also offers some improvement strategies for them and patterns which, in turn, makes it possible for the decision unit to reach more achievements than the present ones. This model, in fact, evaluates different scenarios based on duty-oriented management and also the units and stations in each production stage (internal evaluation). It, then, leads to more achievements than present possible space based on separate stages and finally highlights the production for management decision makings at the end of different stages.

MODELING

This model is formulated through linear programming in a way that can evaluate and assess the strategy of pure profit management by efficiency that is based on each of production stages work stations (white box). In fact, network models are taken into account for multi-stage series processes using collective performance analysis to p-stage process.

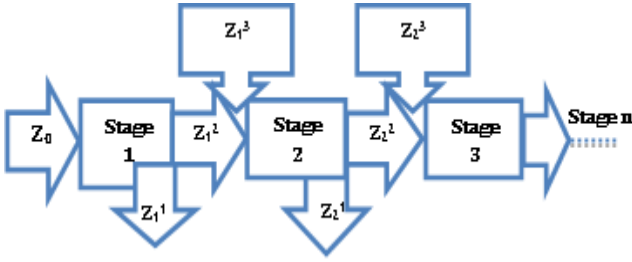


Fig. 1. Network Model.

According to figure 1, the input vector of stage 1 is represented by Z_0 . The output vectors from p stage ($P=1,2,\dots,p$) are of two types: Z_p^1 and Z_p^2 . In figure 1, Z_p^1 indicates the output that has moved out of decision unit in p stage and thus does not entered into next stage as an input. Z_p^2 is the output that has moved out from the p stage and enters into the P+1 stage as an input. The new inputs shown with Z_p^3 are those that directly from the capacitor enter the P+1 stage ($P=2,3,\dots,p$).

MODEL FORMULATION

1. Z_{pr}^{j1} the r component that ($r=1,2,\dots,R_p$) is the output vector of R_p dimension of DMU_j that exits p stage and does not enter the subsequent stage as input.
2. Z_{pk}^{j2} the k component that ($k=1,2,\dots,S_p$) is the output vector of S_p dimension of DMU_j that exits from the p stage and goes into the p+1 stage as input.
3. Z_{pi}^{j3} the i component ($i=0,1,2,\dots,i_p$) of input vector I_p dimension of DMU_j in the p+1 stage that enters into the process.

The following coefficients are taken into account for the above-mentioned factors:

U_{pr} : is the coefficient component of output Z_{pr}^{j1} that exits from stage p.

η_{pk} : is the coefficient component of output Z_{pk}^{j2} in stage p and also the multiple of the same component that goes into stage p+1 as input.

V_{pi} is the coefficient component of input Z_{pi}^{j3} that moves into stage p+1. Thus, when $p=2,3,\dots$, the ratio of DMU_j efficiency is as follow:

$$(1)\theta_p = \frac{(\sum_{r=1}^{R_p} U_{pr} Z_{pr}^{j1} + \sum_{k=1}^{S_p} \eta_{pk} Z_{pk}^{j2})}{(\sum_{k=1}^{S_{p-1}} \eta_{p-1k} Z_{p-1k}^{j2} + \sum_{i=1}^{i_p} V_{p-1i} Z_{p-1i}^{j3})}$$

It should be noted that there is no output that is entered into the first stage. The efficiency for the first stage that is $p=1$ for DMU_j is as follow:

$$(2)\theta_1 = \frac{(\sum_{r=1}^{R_1} U_{1r} Z_{1r}^{j1} + \sum_{k=1}^{S_1} \eta_{1k} Z_{1k}^{j2})}{\sum_{i=1}^{i_0} V_{0i} Z_{0i}^j}$$

Z_{0i} are the only inputs that enter the first stage and the input vector is shown by Z_0 . The claim is that

the whole efficiency of the network is obtained by the component P convex linear combination.

Note that the weights of W_p are offered for showing the relative importance of each stage to the whole network. An approach of determining W_p is the total amount of sources that is allocated to each p stage and reveals that stage relative importance. Specifically, the sum of above-cited fractions denominator indicates the total consumption of network in figure 1 and W_p in it represents the ratio of consumed input in the p stage.

$$W_1 = \frac{\sum_{i=1}^{i_0} V_{0i} Z_{0i}^j}{\sum_{i=1}^{i_0} V_{0i} Z_{0i}^j + \sum_{p=2}^p (\sum_{k=1}^{S_{p-1}} \eta_{p-1k} Z_{p-1k}^{j2} + \sum_{i=1}^{i_p} V_{p-1i} Z_{p-1i}^{j3})}$$

(3)

Therefore, the total efficiency is calculated as follows:

$$W_p = \frac{(\sum_{k=1}^{S_{p-1}} \eta_{p-1k} Z_{p-1k}^{j2} + \sum_{i=1}^{i_p} V_{p-1i} Z_{p-1i}^{j3})}{\sum_{i=1}^{i_0} V_{0i} Z_{0i}^j + \sum_{p=2}^p (\sum_{k=1}^{S_{p-1}} \eta_{p-1k} Z_{p-1k}^{j2} + \sum_{i=1}^{i_p} V_{p-1i} Z_{p-1i}^{j3})}$$

(4)

Also, θ is showing the relative efficiency of each stage.

$$\theta = \frac{\sum_{p=1}^p (\sum_{r=1}^{R_p} U_{pr} Z_{pr}^{j1} + \sum_{k=1}^{S_p} \eta_{pk} Z_{pk}^{j2})}{\sum_{i=1}^{i_0} V_{0i} Z_{0i}^j + \sum_{p=2}^p (\sum_{k=1}^{S_{p-1}} \eta_{p-1k} Z_{p-1k}^{j2} + \sum_{i=1}^{i_p} V_{p-1i} Z_{p-1i}^{j3})}$$

(5)

Now for optimization of the total efficiency of θ - a multi-stage process dependent on restrictions that θ_p should not be more than 1- the non-linear models are changed into linear ones using Charnes & Cooper. Again, it should be noted that W_p is not fixed.

In Charnes and Cooper's model, there are three ways to increase the output/input fraction:

1. While the fraction denominator is fixed, its numerator increases
2. While the fraction numerator is fixed, its denominator decreases
3. While the fraction numerator increases, its denominator decreases.

Charnes et al. [5] consider the fraction denominator of θ a fixed number that is generally 1 and try to increase the fraction numerator in the objective function. That is:

$$\max = \sum_{p=1}^p (\sum_{r=1}^{R_p} U_{pr} Z_{pr}^{01} + \sum_{k=1}^{S_p} \eta_{pk} Z_{pk}^{02}) \quad (6)$$

s. t:

$$\sum_{i=1}^{i_0} V_{0i} Z_{0i}^0 + \sum_{p=2}^p (\sum_{k=1}^{S_{p-1}} \eta_{p-1k} Z_{p-1k}^{02} + \sum_{i=1}^{i_p} V_{p-1i} Z_{p-1i}^{03}) = 1, \quad (7)$$

$$(\sum_{r=1}^{R_1} U_{1r} Z_{1r}^{j1} + \sum_{k=1}^{S_1} \eta_{1k} Z_{1k}^{j2}) \leq \sum_{i=1}^{i_0} V_{0i} Z_{0i}^j \quad (8)$$

$$(\sum_{r=1}^{R_1} U_{pr} Z_{pr}^1 + \sum_{k=1}^{S_p} \eta_{pk} Z_{pk}^2) \leq (\sum_{k=1}^{S_{p-1}} \eta_{p-1k} Z_{p-1k}^2 + \sum_{i=1}^{I_p} V_{p-li} Z_{p-li}^3) \tag{9}$$

$$U_{pr} \cdot \eta_{pk} \cdot V_{pi} \cdot V_{oi} > 0$$

*The first restriction (relation 7) is the inputs in the fraction denominator of θ .

** The second restriction (relation 8) is related to W_1 amount that cannot be more than 1 and for the whole efficiency not to be over 1, the stages' weights are considered less than or equal to 1. That is, by considering the fraction of θ_1 , this restriction is resulted.

*** The third restriction (relation 9) is related to W_p resulted from considering θ_p less than or equal to 1.

CASE STUDY

Due to the fact that the case study is the textile Industry Value Chain, we do the evaluation process of this industry, described by empirical-scientific experts (elites) like figure 2, based on an innovative model of network data envelopment analysis. Furthermore, because the defined value chain

comprises four stages of spinning, weaving, dyeing and finishing, and clothe production (men clothe) and each stage consists of a set of different working stations, we just study the dyeing and finishing unit that, according to figure 3, entails seven different stations with 10 types of production (various production scenarios). The model, in fact, evaluates the different scenarios on the basis of task-oriented management and in terms of the units or working stations within each stage of production process (introvert evaluation).

As it is clear the fabric dyeing and finishing process involves seven working stations in which the output of each station is the input of next station. At the beginning of this network and from outside of the network, serge raw fabric network is injected into the network. This fabric enters the perez fires Station after being **Inspected** and darned. Then after being perez fired, it enters the next station that is crabbing. The output of this station moves into the **cleanup** station and its output would be washed fabric. Then this washed fabric enters into the fifth station that is carbonized station. In the next stage, the carbonized fabric goes into the dyeing station for

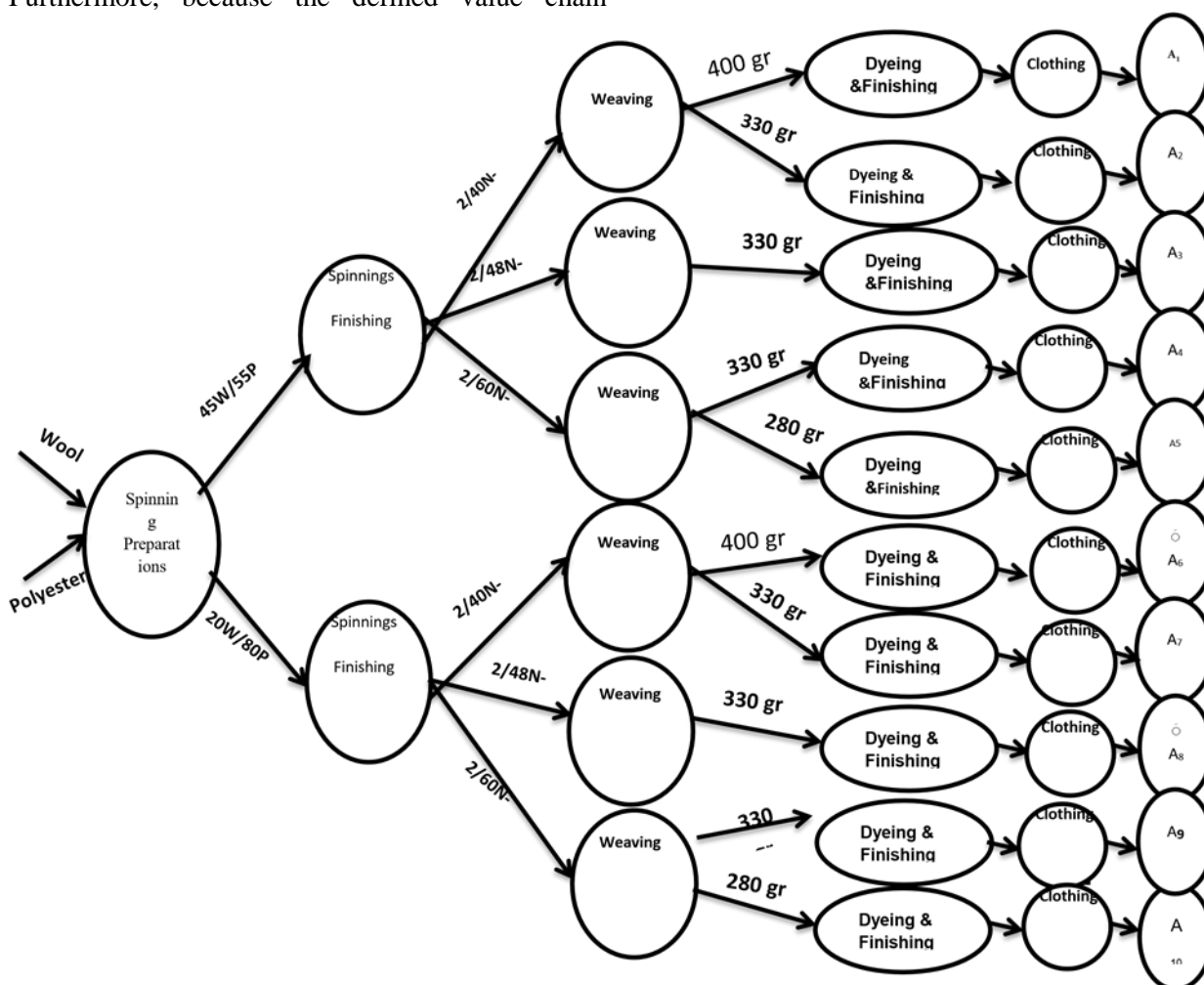


Fig. 2. Multiple scenarios/ Flowchart of production line (From A1 to A10)

the purpose of designing and finally, the fabric enters into the seventh stage for the purpose of ironing and **packaging**. At the end of this network the finished fabric gets out of network. Table 1 shows this network figures for the 10 stations.

Now given the figures in Table 1 and also with regard to model 1, we deal with the evaluation of the 10 production stations. Table 2 represents the efficiency of each of these production stations and the weight of each station in the whole efficiency evaluation is also determined. In this table, θ_i represents the efficiency of each station that because this network consists of seven stations, i is between 1 to 7 ($i= 1,2,\dots,7$). Moreover, W_i indicates the weight of each of the stations efficiency. It should be noted that θ represents the whole efficiency of each of 10 working stations resulted from multiplying the

efficiency weight of each station to the efficiency of the same station.

As Table 2 reveals, none of the dyeing and finishing production line could reach efficiency 1 and the reason is that there was no network that could reach efficiency 1 in all production stations. Though the number 2 production line could reach efficiency 1 in six of working stations, its whole efficiency was not 1 because it could not reach this efficiency in the sixth station.

This section deals with the ideal decision unit creation. Although this unit is virtual meaning that such a network did not really exist in the evaluation process, it is however real too in that it consists of real units. In the following section the way these units were created are described by Tables 3 and 4.

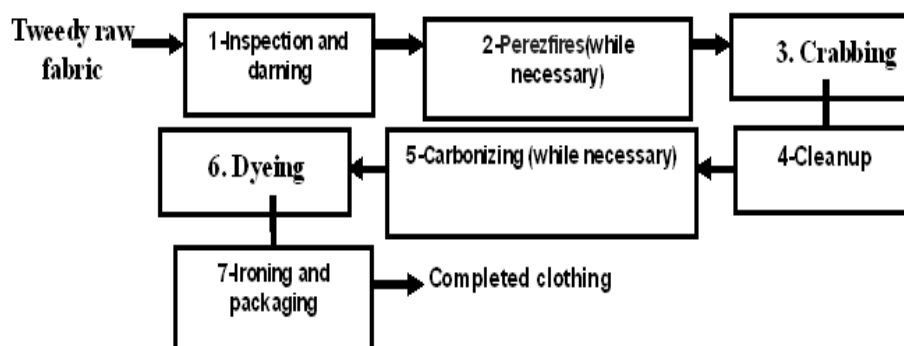


Fig. 3. Working stations of dyeing and finishing stage of fabric production (Men clothes).

Table 1. Input and output figures for the third production stage (Finishing and Dyeing)

Scenarios	1-Inspection and darning		2-Perez firing		3-crabbing		4-Washing		5-Carbonizing		6-Dyeing		7-Ironing and packaging	
	Input Serge Raw Fabric	Output Controlled Fabric	Input Controlled Fabric	Output Perez fired Fabric	Input Perez fired Fabric	Output Crabbed Fabric	Input Crabbed Fabric	Output Washed Fabric	Input Washed Fabric	Output Carbo-nized Fabric	Input Carboniz ed Fabric	Output Washed Fabric	Input Dyed Fabric	Output Finished Fabric
A ₁	10.5	10.725	10.725	10.95	10.95	11.355	11.355	11.715	11.715	12.075	12.075	14.775	14.775	15
A ₂	8.6	8.785	8.785	8.97	8.97	9.303	9.303	9.599	9.599	9.895	9.895	12.115	12.115	12.3
A ₃	11.2	11.44	11.44	11.68	11.68	12.112	12.112	12.496	12.496	12.88	12.88	15.76	15.76	16
A ₄	12.2	12.46	12.46	12.72	12.72	13.188	13.188	13.604	13.604	14.02	14.02	17.14	17.14	17.4
A ₅	10.5	10.72	10.72	10.94	10.94	11.336	11.336	11.688	11.688	12.04	12.04	14.68	14.68	14.9
A ₆	3.8	3.88	3.88	3.96	3.96	4.104	4.104	4.232	4.232	4.36	4.36	5.32	5.32	5.4
A ₇	3.1	3.165	3.165	3.23	3.23	3.347	3.347	3.451	3.451	3.555	3.555	4.335	4.335	4.4
A ₈	4	4.08	4.08	4.16	4.16	4.304	4.304	4.432	4.432	4.56	4.56	5.52	5.52	5.6
A ₉	4.4	4.49	4.49	4.58	4.58	4.742	4.742	4.886	4.886	5.03	5.03	6.11	6.11	6.2
A ₁₀	3.8	3.88	3.88	3.96	3.96	4.104	4.104	4.232	4.232	4.36	4.36	5.32	5.32	5.4

Table 2. The efficiency of production network stations in dyeing and finishing stage of value chain production

	θ_1	θ_2	θ_3	θ_4	θ_5	θ_6	θ_7	w_1	w_2	w_3	w_4	w_5	w_6	w_7
A_1	0.9999187	0.999220	0.9998675	0.9998899	0.9998905	0.807057	0.9999587	0.149	0.131	0.14	0.191	0.113	0.098	0.178
A_2	1	1	1	1	1	0.8075588	1	0.138	0.168	0.138	0.127	0.164	0.142	0.133
A_3	0.9999187	0.999220	0.9998675	0.9998899	0.9998905	0.807057	0.9999587	0.118	0.17	0.134	0.119	0.148	0.168	0.143
A_4	0.9998044	0.999812	0.9996806	0.997346	0.9997504	0.8063557	0.9999004	0.14	0.21	0.137	0.084	0.133	0.134	0.162
A_5	0.9994525	0.999474	0.9991069	0.9992575	0.9993014	0.8041988	0.99997203	0.076	0.193	0.148	0.134	0.175	0.142	0.132
A_6	0.9995507	0.999569	0.9992671	0.9993908	0.9994269	0.8048019	0.9997708	0.13	0.138	0.146	0.176	0.129	0.134	0.147
A_7	0.9994676	0.999489	0.9991314	0.9992779	0.9993206	0.8042912	0.9997281	0.142	0.138	0.159	0.1	0.167	0.145	0.149
A_8	0.9077456	0.998579	0.9975814	0.9979862	0.9981028	0.8352576	0.9992341	0.139	0.159	0.137	0.127	0.142	0.159	0.137
A_9	0.989652	0.999006	0.9983102	0.998594	0.9986762	1	0.9994678	0.108	0.176	0.143	0.133	0.155	0.148	0.137
A_{10}	0.9995507	0.999569	0.9992671	0.9993908	0.9994269	0.8048019	0.9997708	0.13	0.138	0.146	0.176	0.129	0.134	0.147

Table 3.

Scenarios	1-Inspection and darning		2-Perez firing		3-crabbing		4-Washing		5-Carbonizing		6-Dyeing		7-Ironing and packaging	
	Input	Output	Input	Output	Input	Output	Input	Output	Input	Output	Input	Output	Input	Output
	Serge Raw Fabric	Control led Fabric	Control led Fabric	Perez fired Fabric	Perez fired Fabric	Crabbed Fabric	Crabbed Fabric	Washed Fabric	Washed Fabric	Carbonized Fabric	Carbonized Fabric	Washed Fabric	Dyed Fabric	Finished Fabric
A_9											5.03	6.11		
A_2	8.6	8.785	8.785	8.97	8.97	9.303	9.303	9.599	9.599	9.895			12.115	12.3

Table 4.

Scenarios	1-Inspection and darning		2-Perez firing		3-crabbing		4-Washing		5-Carbonizing		6-Dyeing		7-Ironing and packaging	
	Input	Output	Input	Output	Input	Output	Input	Output	Input	Output	Input	Output	Input	Output
	Serge Raw Fabric	Control led Fabric	Control led Fabric	Perez fired Fabric	Perez fired Fabric	Crabbed Fabric	Crabbed Fabric	Washed Fabric	Washed Fabric	Carbonized Fabric	Carbonized Fabric	Washed Fabric	Dyed Fabric	Finished Fabric
Ideal DMU	8.6	8.785	8.785	8.97	8.97	9.303	9.303	9.599	9.599	9.895	5.03	6.11	12.115	12.3

CONCLUSION

Based on the information in Table 2 obtained from Lingo software, the ideal scenario is created from combination of two A_2 and A_9 in Table 4 (More achievements from the present possible space) and as it is obvious, the ideal decision unit could reach the efficiency of 1 due to the fact that it consists of production stations whose efficiencies are 1. Additionally, by means of this decision unit it would be possible to suggest a set of improvement strategies for all 10 understudy production stations. These strategies are on the basis of this ideal decision unit. Thus, it can be claimed that the suggested strategies are based on reality. Furthermore, in the case where there of two or more networks having the same efficiency, they can be ranked by means of this ideal decision unit. This conclusion indicates a set of differences compared to other value chain models as follows:

1. Achievements more than the institution present possible space

2. This model was designed based on DEA model (network-ranking) to reach pure benefit management strategy through effective efficiency

3. This model designs the pure benefit management strategy in stage and integrative ways. Therefore, In the analysis and managerial decisions it will be possible to determine whether a part of produced items up to a specific stage should be sold directly as a Semi manufactured item or let the remaining stages be done to make more added value.

4. In designing this model, n types of factory (in the case study, four types of weaving, spinning, finishing, dyeing, and clothing production) which often work separately, are taken into consideration both separately and integrated.

5. It has the capability of evaluation and measurement in meticulous ways (different working stations of each stage) and also evaluation and measurement of efficiency between different production stages (process-based perspective).

SUGGESTIONS FOR FURTHER RESEARCH

1. The same process can also be carried out in ideal decision unit production of parallel network models.

2. Experts and elites' standpoints in the form of goal programming can be used while creating an ideal decision unit.

REFERENCES

1. P. Andersen, N. C. Petersen, *Management Sci.*, **39**, 1261 (1993).
2. I. Chamodrakas, I. Leftheriotis, D. Martakos, *Appl. Soft Computing*, **11**, 900 (2011).
3. C. Chen, H. Yan, *Eur. J. Oper. Res.*, **213**, 147 (2011).
4. A. Charnes, W. W. Cooper, A. Y. Lewin, L. M. Seiford, *Data envelopment analysis: theory, methodology and application*. Boston, Dordrecht, London: Kluwer Academic Publishers, 1994.
5. A. Charnes, W. W. Cooper, E. Rhodes, *Eur. J. Oper. Res.*, **23**, 429 (1978).
6. Y. Chen, *Eur. J. Oper. Res.*, **161**, 545 (2005).
7. Chin-Nung Liao, Hsing-Pei Kao, *Expert Systems with Applications*, **38**, 10803 (2011).
8. M. Chun Tsai , S. Ping Lin, C. Chan Cheng , Y. Ping Lin, *Expert Systems with Applications* , **36**, 11682 (2009).
9. D. Cook, J. Zhu, G. Bi, F. Yang, *Eur. J. Oper. Res.*, **207**, 1122 (2010).
10. W.D. Cook, L. Liang, J. Zhu, *J. Oper. Res. Soc.*, **60**, 276 (2011).
11. G. R. Jahanshahloo, F. Hosseinzadeh Lotfi, M. Khanmohammadi, M. Kazemimanesh, V. Rezaie, *Expert Systems with Applications*, **37**, 7483 (2010).
12. G. R. Jahanshahloo, F. Hosseinzadeh Lotfi, V. Rezaie, M. Khanmohammadi, *Appl. Math. Model.*, **35**, 218 (2011).
13. C. Kao, S.N. Hwang, *Decision Support Systems*, **48**, 437 (2010).
14. H. F. Lewis, K. A. Lock, T. R. Sexton, *Eur. J. Oper. Res.*, **197**, 731(2009).
15. L. Liang, F. Yang, W. D. Cook, J. Zhu, *Annals Oper. Res.*, **145**, 35 (2006).
16. H. S. Lee, J. Zhu, *Eur. J. Oper. Res.*, **216**, 429 (2012).
17. T.J. Stewart, *Omega*, **38**, 534 (2010).
18. K. Tone, M. Tsutsui, *Eur. J. Oper. Res.*, **197**, 243 (2009).
19. Y-M. Wang, K-S. Chin, Y. Luo, *Expert Systems with Applications*, **38** (8), 10312 (2011).
20. NgAn. Wan Lung, *Eur. J. Oper. Res.*, **186**, 1059 (2008).

Emergency response management native model to reduce environmental impacts using by analytic hierarchy process (AHP)

A. Narimannejad^{1*}, Gh.N. Bidhendi², H. Hoveidi³,

¹Alborz Campus, University of Tehran

²University of Tehran, Graduate Faculty of Environment, Department of Environmental Engineering

³University of Tehran, Faculty Member, Department of Environmental Planning

Received June 26, 2015; Revised September 10, 2015

Oil&petrochemical industry normally uses the large storage tanks, which contain considerable volumes of flammable and hazardous chemicals. Thus, the occurrence of a tank accident is possible and usually leads to fire and explosions. Major industrial accidents can have very dangerous environmental and health consequences. One of the mitigation accident effects implication of Emergency Response Management in the Industries.

Emergency Response Management (ERM) enables and supports emergency response operations across organizational, jurisdictional, and geographical boundaries. Emergency response management guidelines which mostly consist of four parts include prevention, preparedness, response, and recovery.

The paper reviews the existing emergency management patterns (ISO 15544, CCPS, NFPA 1600, DEP, and OSHA 3022) to find an emphasis on identifying and reducing environmental impacts was examined based on five international guidelines.

The common elements of these five international guidelines were determined. A questionnaire containing the information was designed and distributed between experts to give their answers as the best native model. The information gathered through questionnaires was analyzed by Expert choose software and the results was priorities with Analytical Hierarchy Process Method (AHP), in four phases of prevention, preparedness, response, and recovery. The results shows that the CCPS guideline is a best models and suitable for Emergency management in Iran Oil & Petrochemical Plants with an approach to environment priorities

Key words: Native model, Emergency response management, Analytic Hierarchy Process (AHP), Environment Effect

INTRODUCTION

The petrochemical industry normally uses large storage tanks, which contain considerable volumes of flammable and hazardous chemicals. Thus, the occurrence of a tank accident is possible and usually leads to fire and explosions. A thorough analysis of tank accidents with a classification of causes and contributing failures is presented by Chang and Lin [1]. The most common consequence of a tank accident is fire.

Although large-scale tank fires are very rare, they pose a severe challenge to employs & stockholders, oil companies and the environment, due to the multiplicity of the physical processes involved. According to the study of Persson and Lonnermark [2], there are two ways of dealing with a tank fire, either to let it burn-out fully and thereby self-extinguish or, alternatively, to extinguish the fire actively, using firefighting foams. One of the mitigation accident effects implication of emergency response management in the industries.

Tank fires produce large quantities of combustion products, such as Sulphur dioxide (SO₂), carbon monoxide (CO), hydrogen sulfide (H₂S), and lead to soot and particulates formation. More specifically, the transport of combustion products by a wind-blown smoke plume can distribute potentially hazardous materials over a large area and may lead to serious consequences for the health of people and for the environment

Cascading disruptions and failures product of natural, industrial and man-made disasters can be avoided or minimized if the concept of Crisis Lifecycle is included and understood into emergency management. Research studies by Turner and also by Vaughan have shown that crisis often have long incubation times. There are numerous precursors or warnings that are ignored or not detected.

Strategic aspects of emergency management have to include the whole lifecycle of crises [3] to minimize cascading disruptions and failures due to the dynamism of crises as a consequence of variable's evolution over time. To achieve this lifecycle perspective, a bird's eye view in temporal, spatial and configuration space is necessary.

To whom all correspondence should be sent:
E-mail: Narimannejad@nipc.ir

Therefore, it can be argued that effective crisis management starts well in advance of the actual physical manifestation of the crisis. Ideally, crises could be avoided if perfect early warning systems were in place, if managers understand how to solve them and if the evolution of crises is perceived beforehand.

EMERGENCY MANAGEMENT LIFE CYCLE

A life-cycle approach provides a broad and systematic view of the activities relating to emergency response management [4]. Therefore, the framework we suggest is adapted to each of the stages in the life cycle. The management of emergency response can be visualized in terms of three distinct sets of activities on the time line continuum [5]. These include actions taken (a) prior to an incident (typically deals with preparedness issues such as planning and training), (b) during the incident (mitigation), and (c) after the incident (a.k.a. the response and recovery stage).

Disaster operations life cycle and disaster types Tufekci and Wallace [6] suggest that emergency response efforts consist of two stages; prevent and post-event response. Pre-event tasks include predicting and analyzing potential dangers and developing necessary action plans for mitigation. Post-event response starts while the disaster is still in progress. At this stage the challenge is locating, allocating, coordinating, and managing available resources. Tufekci and Wallace also suggest that an effective emergency response plan should integrate both of these stages within its objective. They add that separating pre- and post-loss objectives may lead to suboptimal solutions to the overall problem. In the United States comprehensive emergency

Management is commonly described in terms of four programmatic phases: mitigation, preparedness, response, and recovery [7,8,9]. The four-phase approach covers all of the actions described in Tufekci and Wallace's classification while providing a more focused view of emergency management actions. Moreover, the four-phase classification is based on the Comprehensive Emergency Management concept introduced in the 1978 report of the National Governors Association Emergency Preparedness Project [10].

These terms have been widely used by policy makers, practitioners, trainers, educators, and researchers. As illustrated in Figure 1 the four phases are often described as part of a continuous process.

Mitigation is the application of measures that will either prevent the onset of a disaster or reduce the impacts should one occur. Preparedness activities prepare the community to respond when a disaster



Fig. 1. Four Phases of Emergency Management [11].

occurs. Response is the employment of resources and emergency procedures as guided by plans to preserve life, property, the environment, and the social, economic, and political structure of the community. Recovery involves the actions taken in the long term after the immediate impact of the disaster has passed to stabilize the community and to restore some semblance of normalcy

Industrial and commercial installations which have the potential for causing accidental pollution of air, land or water, or the endangerment of public health and safety are required to develop and implement Prevention/Mitigation, Preparedness, Response and Recovery which encompass the other Departmental program requirements.

ANALYTIC HIERARCHY PROCESS (AHP)

AHP is a decision-making tool that can help describe the general decision operation by decomposing a complex problem into a multi-level hierarchical structure of objectives, criteria, sub criteria and alternatives [12]. Applications of AHP have been reported in numerous fields such as conflict resolution, project selection, budget allocation, transportation, health care, and manufacturing, Environment challenges (Harker, 1989). More and more researchers are realizing that AHP is an important generic method and are applying it to various manufacturing areas [14], [15], [16], [17], [18]. In addition to the wide application of AHP in manufacturing areas, recent research and industrial activities of applying AHP on other selection problems are also quite active [19],[20],[21],[22].

AHP's hierarchic structures reflect the natural tendency of human mind to sort elements of a system into different levels and to group like elements in each level [12]. From a human factor point of view, AHP can be a very effective tool to assist human decision making. A study conducted by [23] show that when a human being and an intelligent machine

cooperate to solve problems, but where each employs different problem-solving procedures, the user must have an accurate model of how that machine operates. This is because when people deal with complex, interactive systems, they usually build up their own conceptual mental model of the system. The model guides their actions and helps them interpret the system's behavior. Such a model, when appropriate, can be very helpful or even necessary for dealing successfully with the system. However, if inappropriate or inadequate, it can lead to serious misconceptions or errors [24]. Therefore, it is very important for decision makers to be able to understand the decision-making model structure, while AHP just provides such a simple, easily understood, and flexible model structure.

Dagdeviren and colleagues [25] have expressed first by AHP method, complex multi-criteria decision making problem turns into a hierarchy of decision elements means purpose, criteria and decision options related to that problem. The method of AHP makes objectives, criteria or options to the hierarchical structure like a family tree. Hierarchy has at least three levels: the total purpose of the first level is, placing multiple criteria that evaluate options in the middle and decision options under this part. View of decision-making hierarchy that has four levels has been drawn in the Figure 2

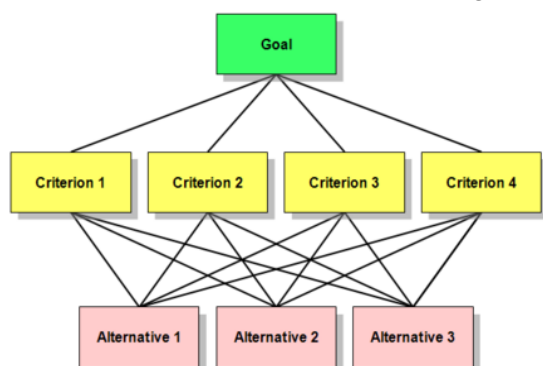


Fig. 2. Grossly Simplified Structure Of an Exemplary AHP Hierarchy.

The next step is the comparison of options and criteria. When the problem breaks down and its hierarchy is made, prioritization procedures start for determining the relative importance of criteria for each level. Pair judgments start from the second level (criteria) and in the last level end. In each level, criteria as pair and according to their effect levels and based on specified criteria are compared at a higher level.

Bogdanovic and colleagues [26] asserted paired comparing should be conducted by the question from decision maker. For example, be asked, according to the purpose of decision which scale of 1 to 9, as

shown in Table 1 should be allocated as the importance level of criteria to each other. Also Vidal and colleagues [27] concluded 8, 6, 4, 2 middle numbers should be used for comparison correction.

Table 1. Scale of paired comparison in AHP method.

Intensity of Importance	Definition	Explanation
1	Equal Importance	Two activities contribute equally to the objective
2	Weak or Slight	
3	Moderate Importance	Experience and judgment slightly favor one activity over another
4	Moderate Plus	
5	Strong Importance	Experience and judgment strongly favor one activity over another
6	Strong Plus	
7	Very strong or demonstrated importance	An activity is favored very strongly over another, its dominance demonstrated in practice.
8	Very very Strong	
9	Extreme Importance	The evidence favoring one activity over another is of the highest possible order of affirmation

GUIDELINES STRUCTURE

The Center for Chemical Process Safety (CCPS)

Technical planning for on-site emergencies

The Center for Chemical Process Safety (CCPS) was established in 1985 by the American Institute of Chemical Engineers (AIChE) for the express purpose of assisting industry in avoiding or mitigating catastrophic chemical accidents. To achieve this goal, CCPS has focused its work on four areas [28], [29]:

- Establishing and publishing the latest scientific, engineering, and management practices for prevention and mitigation of incidents involving toxic, flammable, and/or reactive material.

- Encouraging the use of such information by dissemination through publications, seminars, symposia, and continuing education programs for engineers.
- Advancing the state-of-the-art in engineering practices and technical management through research in prevention and mitigation of catastrophic events.
- Developing and encouraging the use of undergraduate engineering curricula that will improve the safety knowledge, and consciousness of engineers.

This Guideline is a Technical Planning for On-Site Emergencies and Include of four phases Prevention, Preparedness, response and Recovery. Table 2 shows the important elements.

Table 2. Elements of CCPS pattern about Emergency Management.

CCPS
1. Principles of Prevention
2. Principles of Mitigation
3. Identification of Credible Incidents
4. Conceptual Approach to Emergency Response
5. Developing Response Tactics
6. Physical Facilities and Systems
7. Response Equipment and Supplies
8. Developing a Workable Plan
9. Training
10. Response Functions
11. Support Functions, Systems, and Facilities
12. Recovery Functions
13. Cleanup of Facilities

ISO 15544 (Petroleum and natural gas industries Offshore production installations — Requirements and guidelines for emergency response)

ISO (the International Organization for Standardization) is a worldwide federation of national standards bodies [30]. The work of preparing International Standards is normally carried out through ISO technical committees. The successful development of the arrangements required promoting safety and environmental protection during the recovery of hydrocarbon resources requires a structured approach to be applied to the identification and assessment of the hazards which may be present during the various phases in the lifecycle of an offshore installation.

These principles also apply to the development of the strategy, arrangements and procedures required to respond to emergencies.

The content in this International Standard is consistent in table 3.

Table 3. Elements of ISO pattern about Emergency Management.

ISO 15544
1. Emergency response strategy (ERS)
2. Emergency response plan (ERP)
3. Command and control
4. Detection of the need for emergency response
5. Competence
6. Maintenance of emergency response equipment
7. Communications
8. Escape, refuge, evacuation and rescue
9. Environmental emergency response
10. Medical emergency response

This International Standard is based on an approach where the selection of measures for emergency response is determined by an evaluation of hazards on the shore installation. The methodologies employed in this assessment and the resultant recommendations will differ depending on the complexity of the production process and facilities, type of facility (i.e. open or enclosed), manning levels, and the environmental conditions associated with the area of operation.

DEP (Guidelines for the development and implementation of environmental emergency response plans)

Department of Environmental Protection (DEP) has developed and implemented of environmental emergency response plans with this guideline. The policy of this to plan and provide effective and efficient response to emergencies and accidents for any situation dealing with the public health, safety and the environment [31]. A wide variety of industrial activities, both manufacturing and commercial, exist in the world. Many of these activities have the potential for causing environmental degradation or endangerment of public health and safety through accidental releases of toxic, hazardous, or other pollution materials. In recognition of this fact, several State and Federal regulatory programs have been developed to encourage the use of preventive approaches to deal with unwarranted releases of toxic, hazardous, or other pollutants to the environment.

The Department’s objective is to consolidate the similarities of the State and Federal pollution incident prevention and emergency response

programs into one overall program. Industrial and commercial installations which have the potential for causing accidental pollution of air, land or water, or the endangerment of public health and safety are required to develop and implement Preparedness, Prevention and Contingency (PPC) Plans which encompass the other Departmental program requirements. Key elements of this guideline show in table 4.

Table 4. Elements of DEP pattern about Emergency Management.

DEP
Description of Facility
Organization Structure & Duties and Responsibilities
Chain of Command
Emergency Response Plans
Spill Leak Prevention
Housekeeping
Security
Employee Training
Countermeasures
Communications and Alarms
Evacuation Plan
Emergency Response Equipment
Emergency Spill Control Network

National Fire Protection Association (NFPA 1600) Standard on Disaster/Emergency management and business continuity programs

NFPA® codes, standards, recommended practices, and guides (“NFPA Documents”), of which the document contained herein is one, are developed through a consensus standards development process approved by the American National Standards Institute. This process brings together volunteers representing varied viewpoints and interests to achieve consensus on fire and other safety issues. While the NFPA administers the process and establishes rules to promote fairness in the development of consensus, it does not independently test, evaluate, or verify the accuracy of any information or the soundness of any judgments contained in NFPA Documents. [32] The NFPA disclaims liability for any personal injury, property or other damages of any nature whatsoever, whether special, indirect, consequential or compensatory, directly or indirectly resulting from the publication, use of, or reliance on NFPA Documents. . Key elements of this guideline show in table 5.

Table 5. Elements of NFPA pattern about Emergency Management.

NFPA 1600
1. Laws and Authorities
2. Risk Assessment
3. Incident Prevention
4. Mitigation
5. Resource Management and Logistics
6. Mutual Aid/Assistance
7. Incident Management
8. Planning
9. Communications and Warning
10. Operational Procedures
11. Facilities
12. Training
13. Exercises, Evaluations, and Corrective Actions
14. Crisis Communication and Public Information
15. Finance and Administration

OSHA 3022

(Principal emergency response and preparedness requirements and guidance)

The importance of an effective workplace safety and health program cannot be overemphasized. There are many benefits from such a program, including increased productivity, improved Employee morale, reduced absenteeism and illness, and reduced workers’ compensation rates.

Unfortunately, workplace accidents and illnesses still occur in spite of efforts to prevent them, and proper planning is necessary to effectively respond to emergencies. Several Occupational Safety and Health Administration (OSHA) standards explicitly require Employers to have emergency action plans for their workplaces [33]. Emergency preparedness is a Well-known concept in protecting workers’ safety and health. To help employers, safety and Health professionals, training directors, and others, the OSHA requirements for emergencies are compiled and summarized in this booklet.

This publication provides a generic, non-exhaustive overview of OSHA standards for emergencies. It is not intended to alter or determine compliance responsibilities in OSHA standards or the Occupational Safety and Health Act of 1970. Please review the current OSHA standards applicable to your work operations to ensure your compliance. Key elements of this guideline show in table 6.

RESEARCH-METHOD

As previously stated, the aim of this study is the ranking of current international pattern and providing local pattern of Emergency Management. The ranking of crisis management pattern is done

Table 6. Elements of OSHA pattern about Emergency Management.

OSHA 3022	
1.	Medical services and first aid
2.	Prevention through Process Safety Management (PSM)
3.	Design, construction requirements and Maintenance, safeguards and operational features for exit routes
4.	Emergency and fire action plans
5.	emergency response equipment
6.	Additional Requirements for Specific Workplaces / Operations
7.	Personal Protective Equipment
8.	communication

using Analytical Hierarchy Process (AHP) and data analysis is performed by using Expert Choice software.

To ranking is required to define the main criteria and sub-criteria and patterns are rated based on it. Given the importance of the life cycle of any system, phases of the cycle (prevention, preparedness, response and recovery) are considered as the main criteria and the requirements of studied patterns were classified into four groups. In table7, the way of categorizing requirements of studied patterns is shown in four categories: prevention, preparedness, response, and recovery.

By placing each of the criteria, sub-criteria and options to get her and drawing the connection between them, hierarchy pattern is defined as figuer3.

According to the created hierarchical model, a questionnaire to gather experts' opinions in this field were developed and provided them. At the end completed questionnaire in formation was analyzed and investigated using the software.

Among the four main criteria for prevention, readiness, response and recovery prevention phase with a score of 0.662 achieved the higher starting, after it phases of preparation, recovery and response respectively ranked in second to four the respectively. (Figure 4).

Among the studied sub criteria in the prevention group of requirements Principles & method of Prevention, in the preparedness set of sub criteria Emergency response strategy & plan (ERS & ERP), sub-criteria of Communications in Response group and sub-criteria of Cleanup of Facilities in the recovery group achieved the highest score.

Among the studied crisis management patterns that were defined as investigated options in the analysis of hierarchical, models CCPS, NFPA, DEP, OSHA and ISO respectively placed in the first to fifth positions. (Figure 5).

Table 7. How to categorize the requirements of studied patterns

		ISO	CCPS	NFPA	DEP	OSHA
Prevention	1. Principles & method of Prevention					
	2. Principles & method of Mitigation					
Preparedness	1. Emergency response strategy & plan (ERS & ERP)					
	2. Emergency response equipment					
	3. Physical Facilities and Systems					
	4. Competence & Training					
	5. Identification of Credible Incidents					
	6. Exercises, Evaluations, and Corrective Actions					
	7. Laws, Requirements and Authorities					
	8. Mutual Aid/Assistance & Countermeasures					
Response	1. Finance and Administration					
	2. Command and control					
	3. Communications					
	4. Medical emergency response					
	5. Environmental emergency response					
	6. Security					
	7. Detection of the need for emergency response					
Recovery	1. Recovery Functions					
	2. Cleanup of Facilities					

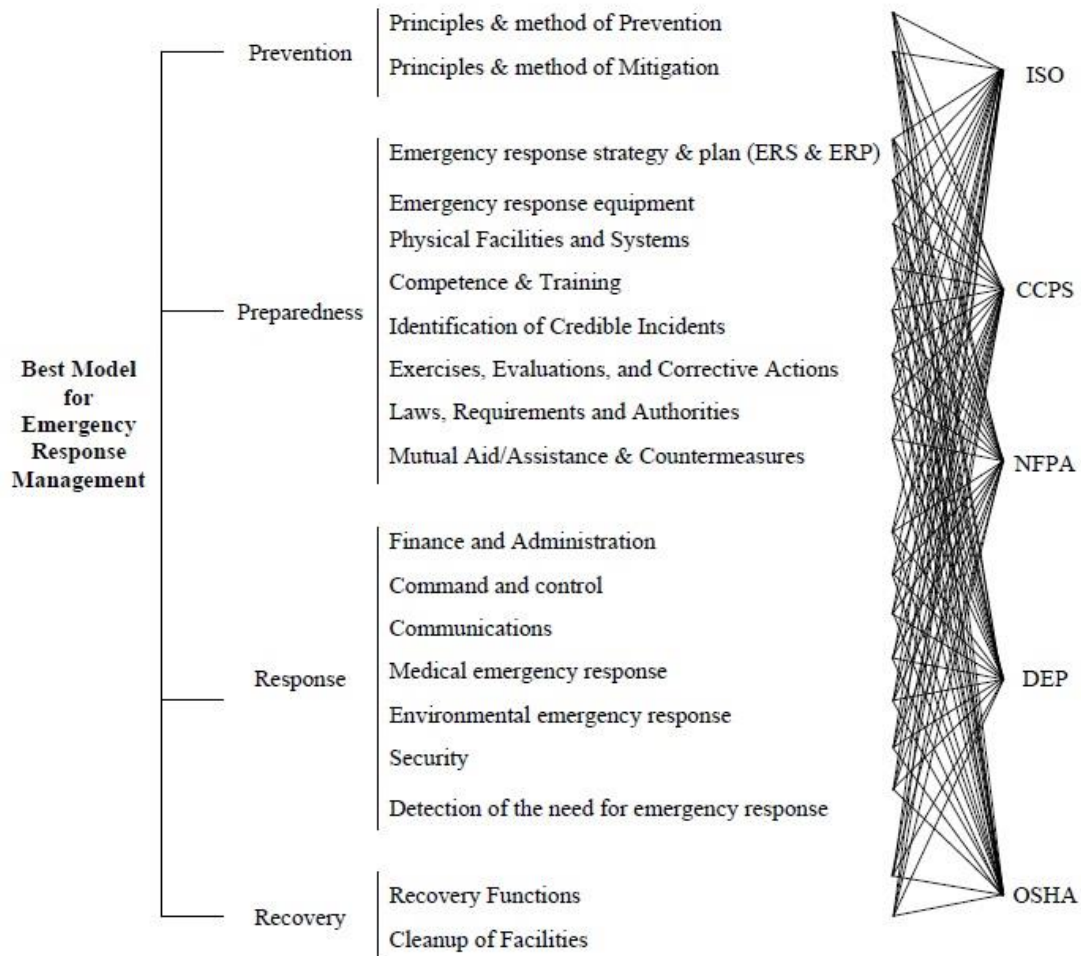


Fig. 3 Pattern of hierarchy.

Priorities with respect to:
Goal: best model



Fig. 4. The results of ranking the main criteria

ISO	.067
CCPS	.375
NFPA	.247
DEP	.178
OSHA	.133

Fig. 5. The results of ranking the main criteria

Table 8. Native model of emergency management.

	Elements	Requirements according with
Prevention	1. Principles & method of Prevention	CCPS ERP Model
	2. Principles & method of Mitigation	CCPS ERP Model
Preparedness	1. Emergency response strategy & plan (ERS & ERP)	DEP ERP Model
	2. Emergency response equipment	NFPA ERP Model
	3. Physical Facilities and Systems	CCPS ERP Model
	4. Competence & Training	CCPS ERP Model
	5. Identification of Credible Incidents	CCPS ERP Model
	6. Exercises, Evaluations, and Corrective Actions	NFPA ERP Model
	7. Laws, Requirements and Authorities	OSHA ERP Model
	8. Mutual Aid/Assistance & Countermeasures	DEP ERP Model
Response	1. Finance and Administration	CCPS ERP Model
	2. Command and control	DEP ERP Model
	3. Communications	NFPA ERP Model
	4. Medical emergency response	CCPS ERP Model
	5. Environmental emergency response	DEP ERP Model
	6. Security	DEP ERP Model
	7. Detection of the need for emergency response	ISO ERP Model
Recovery	1. Recovery Functions	CCPS ERP Model
	2. Cleanup of Facilities	CCPS ERP Model

CONCLUSION

To develop indigamous pattern of crisis management in the petrochemical industry to reduce the environmental consequences of accidents, five international model CCPS, NFPA, DEP, OSHA and ISO are analyzed and ranked, that the presented model by the Center for Chemical Process Safety America (CCPS) with a score of 0.375 achieved the highest rating. But by studying the achieved scores about all the requirements of the 5 models, dealing with the requirements that despite achieving high points in their group, not placed in the pattern CCPS (as Laws, Requirements and Authorities in the defined pattern by OSHA) and or have higher score than the same pattern in CCPS model. For example, it can be pointed to the elements of Emergency response strategy in the presented model of ISO that has achieved a higher rating from the same pattern in the CCPS, namely developing a Workable Plan. Thus, to define the indigenous pattern, these requirements were investigated and placed in the native model. So, indigenous pattern of crisis management with approach of reducing

environmental consequences of accidents were defined as follow.

REFERENCE

- 1.J.I. Chang, C.C. Lin, *J. Loss Prevention Process Industries*, **19**, 51 (2006).
- 2.H. Persson, A. Lonnermark, Tank fires, review of fire incidents 1951e2003. Brandforsk Project 513-021. SP Swedish National Testing and Research Institute. SP Report 14, 2004.
- 3.W.T. Coombs, "Ongoing Crisis Communication: Planning, Managing and Responding" 2nd ed. Los Angeles, London, New Delhi and Singapore, Sage, 2007
4. Y. Yuan, B. Detlor, *Intell. Mobile Crisis Response Syst. Commun. ACM*, **48**, 95 (2005)
- 5.U.S. Department of Homeland Security, National Incident Management System, 2004
- 6.S. Tufekci, W.A. Wallace, *IEEE Trans.Eng. Manag.*, **45**, 103 (1998).
- 7.<http://www.richmond.edu/~wgreen/encyclopedia.htm>
- 8.W.L. Waugh, R.J. Hy, *Handbook of Emergency Management: Programs and Policies Dealing with Major Hazards and Disasters*. Greenwood Press, New York,NY, (1990).
- 9.D.R. Godschalk, Disaster mitigation and hazard management.In: Thomas, E.D., Hoetmer, G.J. (Eds.),

- Emergency Management: Principles and Practice for Local Government. International City Management Association, Washington, DC, 1991, p. 131.
10. National Governors' Association Center for Policy Research Washington, D.C. National Governors' Association Emergency Preparedness Project, 1979.
 11. <http://training.fema.gov/EMIWeb/Earthquake/NEH0101220.htm> (November 1, 2009).
 12. T.L. Saaty, The Analytic Hierarchy Process. McGraw-Hill, New York, 1980.
 13. P.T. Harker, The art and science of decision making: The analytic hierarchy process. In: Golden, B.L., Wasil, E.A., Harker, P.T. (Eds.), The Analytic Hierarchy Process: Applications and Studies. Springer, Berlin, 1989, p. 3.
 14. A.A. Andijani, M. Anwarul, *J. Production Econ.*, **51**, 155 (1997).
 15. F.T.S. Chan, B. Jiang, N.K.H. Tang, *Int. J. Production Econ.*, **65**, 73 (2000).
 16. D. Liu, G. Duan, N. Lei, J.S. Wang, *International J. Adv. Manufact. Technol.*, **15**, 26 (1999).
 17. K. Jiang, E.M. Wicks, *J. Eng. Valuation Cost Anal.*, **2**, 271 (1999).
 18. Z.C. Lin, C.B. Yang, *J. Mater. Process. Technol.*, **57**, 253 (1996).
 19. M.C.Y. Tam, V.M.R. Tummala, *Omega*, **29**, 171 (2001).
 20. V.S. Lai, R.P. Trueblood, B.K. Wong, *Information and Management*, **36**, 221 (1999).
 21. W.A. El-Wahed, H. Al-Hindi, *Adv. Model. Anal.*, **40**, 45 (1998).
 22. M.J. Schniederjans, T. Garvin, *Eur. J. Oper. Res.*, **100**, 72 (1997).
 23. P.E. Lehner, D.A. Zirk, *Human Factors*, **29**, 97 (1987).
 24. R.M. Young, *Int. J. Man-Machine Study*, **15**, 51 (1981).
 25. M. Dagdeviren, S. Yavuz, N. Kılınc, *Exp. Syst. Appl.*, **36**, 8143 (2009).
 26. D. Bogdanovic, D. Nikolic, I. Ilic, *Anais Academ. Brasil. Cien.*, **84**, 219 (2012).
 27. L.A. Vidal, E. Sahin, N. Martelli, M. Berhoune, B. Bonan, *Exp. Syst. Appl.*, **37**, 1528 (2010).
 28. CCPS, Guidelines for Technical Planning for On-Site Emergencies, (1995).
 29. American Institute of Chemical Engineers, AIChE Guidelines for engineering design for process safety Center for Chemical Process Safety. New York, USA, 1993.
 30. ISO 15544:2000(E)
 31. PA 17105-2063, (2001).
 32. NFPA 1600, (2013).
 33. OSHA 3122-06R-2004.

Green strategy management framework towards sustainable development

A. Padash^{1*}, Gh.N. Bidhendi², H. Hoveidi³, M. Ardestani⁴

¹PhD Candidate of Environmental Planning, Alborz Campus, University of Tehran

²University of Tehran, Graduate Faculty of Environment, Department of Environmental Engineering

³University of Tehran, Faculty Member, Department of Environmental Planning

⁴University of Tehran, Faculty of Environment Manager

Received June 26, 2015, Revised September 10, 2015

A green strategy for an enterprise – public or private, government or commercial – is one that complements the business, operations, and asset strategies that are already well understood and often well-articulated by the enterprise. In this paper, an attempt has been made to discuss various issues related to Green Management (GSM). The concept of GSM, the functional Model of an organizational supply chain with an environmental impact, differences between conventional management and GSM and models for the implementation of GSM registered in the literature have been discussed. Various approaches of GSM, implementation of a Green Management and key factors affecting GSM have been also described. The objective of this paper is to identify major works on green strategic management research integrating Environmental, Health and Safety (EHS) toward sustainable developing thinking into all instruments and procedure management, and thereafter, to classify them so as to identify gaps, issues and opportunities for further study and research. Therefore, in order to implement this right and fundamental conceptual model relying on literature review of GSM on the one hand and the key elements of sustainable development other hand, the conceptual model has been proposed. We were determined 20 criteria classify the existing GSM probing into five broad categories based on the problem context in GSM; strategic management, environmental performance, green manufacturing, process management, management system,

Keywords: green strategy management, environmental health and safety, sustainable development, analytic hierarchy process

INTRODUCTION

Economic globalization, increasing resource scarcity and environmental degradation have caused green strategic management (GSM) to become an important competitive approach for organizations involved in international trade.

The story of environmental management can be traced to the Industrial Revolutions of 18th and 19th centuries, the lack of standards for industrial products and processes in the early 20th century, the creation of environmental laws and regulations beginning in the 1970s, the emergence of voluntary codes of corporate conduct and environmental management practices over the past 30 years, international developments related to the environment management and the more recent development of international environmental management standards and guidelines to facilitate global trade. Widespread concern for environmental protection emerged dramatically with the advent of the Industrial Revolution. Public outcries over smoke pouring from the stacks of coal

burning factories, along with the eventual expansion of the petroleum industry, led to an early foothold for the “Environmental Movement” [1].

Perusal of the literature shows that a broad frame of reference for Green Strategic Management (GSM) is not adequately developed.

In early environmental management frameworks, operating managers were involved only at arm's length. Separate organizational units had responsibility for ensuring environmental excellence in product development, process design, operations, logistics, marketing, regulatory compliance and waste management. Today, this has changed. As in the quality revolution of the 1980s and the supply-chain revolution of the 1990s, it has become clear that the best practices call for integration of environmental management with ongoing operations. In 1988 and the Strategies for Today's Environmental Partnership (STEP) program adopted by the American Petroleum Institute in 1990 [2].

Environmental practices have been accepted and adopted in the world of business [3]. The numbers of organizations are contemplating to integrate environmental practices into their strategic plans and daily operations [4].

To whom all correspondence should be sent:

E-mail: apadash@ut.ac.ir

Increasing government regulations and stronger public mandates for environmental accountability have brought the green issues high on the strategic planning agenda of manufacturing firms [5].

Green strategic management (GSM) adds 'green' component to the conventional procedures by including practices like green operations, green design, green manufacturing, reverse logistics and waste management [6].

Strategic planning in GSM context means the identification of relevant goals and specification of long term plans for managing those goals [7].

DIFFERENCE BETWEEN CONVENTIONAL STRATEGIC MANAGEMENT, ENVIRONMENTAL MANAGEMENT SYSTEM AND GREEN STRATEGIC MANAGEMENT

Strategic management involves the formulation and implementation of the major goals and initiatives taken by a company's top management on behalf of owners, based on consideration of resources and an assessment of the internal and external environments in which the organization competes [8]. Conventional Strategic Management usually concentrated on economy and control of the final product but seldom considers its ecological effects [3].

Environmental management system (EMS) refers to the management of an organization's environmental programs in a comprehensive, systematic, planned and documented manner. It includes the organizational structure, planning and resources for developing, implementing and maintaining policy for environmental protection. More formally, EMS is "a system and database which integrates procedures and processes for training of personnel, monitoring, summarizing, and reporting of specialized environmental performance information to internal and external stakeholders of a firm." [9].

Green strategic management is an experimental tool, which can be used to evaluate alternative long term strategies ("what-if" analysis) using total supply chain profit as measure of strategy effectiveness [10].

Green Strategy Management Defined

A green strategy for an enterprise – public or private, government or commercial – is one that complements the business, operations, and asset strategies that are already well understood and often well-articulated by the enterprise. A green strategy fundamentally helps an enterprise make decisions that have a positive impact on the environment. The

principles that form the basis of a green strategy should lead a business to make decisions based on solid business logic and make good business sense [11].

For the purpose of this paper, GSM is defined as 'integrating environmental, health and safety (EHS) toward sustainable developing [12] thinking into all instruments and procedure management, including product design, material sourcing and selection, manufacturing processes, delivery of the final product to the consumers as well as end-of-life management of the product after its useful life'. We specifically focus on key performance indicators (KPI) and mathematical modelling aspects in order to facilitate further study and research.

RESEARCH METHODOLOGY

The objective of this paper is to identify major works on green strategic management research integrating Environmental, Health and Safety (EHS) toward sustainable developing [12] thinking into all instruments and procedure management, and thereafter, to classify them so as to identify gaps, issues and opportunities for further study and research. A literature review seems to be a valid approach, as it is a necessary step in structuring a research field and forms an integral part of any research conducted [13]. This helps to identify the conceptual content of the field [14] and guides towards theory development. Therefore, in order to implement this right and fundamental conceptual model relying on literature review of GSM on the one hand and the key elements of sustainable development other hand, the conceptual model has been proposed.

The compulsory requirement for GSM conceptual selection model should be structure in a way which could be handle it with MCDM appropriately in future.

There are several MCDM methods which have been developed, such as the Elimination and Choice Translating Reality (ELECTRE), the Technique for Order Preference by Similarity to Ideal Solution (TOPSIS), Analytic Network Process (ANP) and the Analytic Hierarchy Process (AHP). But these methods do not deal with the interdependences among elements. For dealing with the interdependences among elements, the ANP as a new MCDM method was proposed by Saaty (1996) [15]. Therefore, from the viewpoint of Kinoshita [16], the ANP may simply be differentiated into two practical kinds of models: the Feedback System model and the Series System model (similar to the AHP model). In the Feedback System model, clusters link one by one in turn as a

network system. This kind of model can capture effectively the complex effects of interplay in human society, especially when risk and uncertainty are involved [17].

However, it is usually hard to obviate the possibility of interactions within the criteria cluster. Thus, this paper suggests a modified Feedback System model (Fig. 1) that allows interdependences within the criteria cluster, in which the looped are signifies the inner dependences.

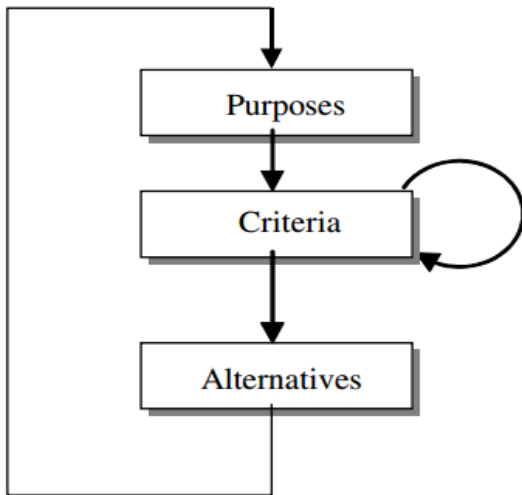


Fig. 1. Modified feedback system model (Proposed Model).

DISCUSSION

Models of Sustainable Development in literature

Model 1: Sustainable Development Basic Model: The man is the main pivot in the sustainable development. Possibility, Planning and implementation of any project should consider many aspects. Sustainable development has been described in terms of three dimensions (Fig.2), domains or pillars. In the three-dimension model, these are seen as "economic, environmental and social" or "ecology, economy and equity" [18] this has been expanded by some authors to include a fourth pillar of culture, [19-20] institutions or governance [19].

Thus, the national and international standards ought to be generated [12].

Model 2: Sustainable Development Extended Model: Working with a different emphasis, some researchers and institutions have pointed out that a fourth dimension should be added to the dimensions of sustainable development, since the triple-bottom-line dimensions of economic, environmental and social do not seem to be enough to reflect the complexity of contemporary society.

The Circles of Sustainability approach distinguishes the four domains (Fig.3.) of economic, ecological, political and cultural sustainability [19].

Other organizations have also supported the idea of a fourth domain of sustainable development. The Network of Excellence "Sustainable Development in a Diverse World" [21] sponsored by the European Union, integrates multidisciplinary capacities and interprets cultural diversity as a key element of a new strategy for sustainable development.

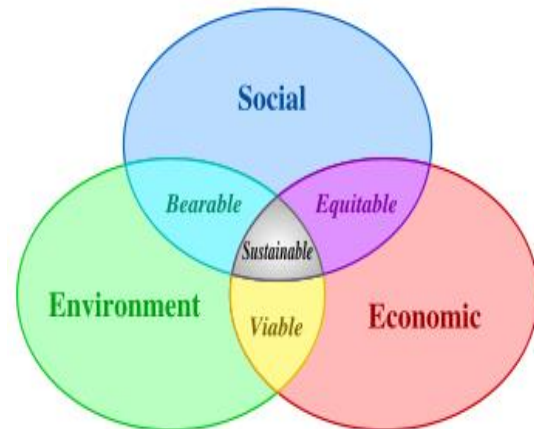


Fig. 2. Scheme of sustainable development: at the confluence of three constituent parts [22].

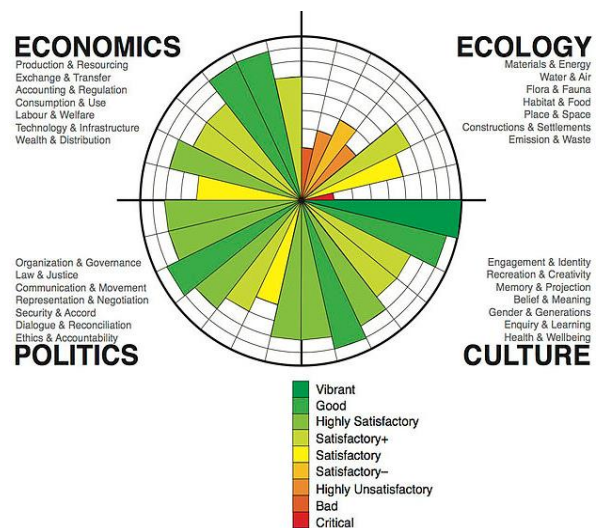


Fig. 3. Circles of sustainability [23]

The growing importance of GSM is driven mainly by the escalating deterioration of the environment, e.g. diminishing raw material resources, overflowing waste sites and increasing levels of pollution. However, it is not just about being environment friendly; it is about good business sense and higher profits. In fact, it is a business value driver and not a cost centre [24].

Sufficient literature exists about various aspects and facets of GSM. Comprehensive reviews on green design [25], issues in green manufacturing and product recovery [26-27], supply management capabilities [28], industrial ecology and industrial ecosystems [29-30-31-32-33] have been published. In addition, Arimura [34] indicate that facilities with environmental management systems (EMS) certified to ISO 14001 are 40% more likely to assess their suppliers' environmental performance and 50% more likely to require that their suppliers undertake specific environmental practices and Babiak and Trendafilova [35] discuss on corporate social responsibility and environmental management as a key elements of GSM.

Models of implementation of green strategic management in literature

Different concepts and models related to environmental issues have been suggested by different researchers. Some of them are briefly described hereunder:

Model 1: Environmental management system (EMS) Model

An EMS follows a Plan-Do-Check-Act, or PDCA, Cycle (Fig. 4). The diagram shows the process of first developing an environmental policy, planning the EMS, and then implementing it. The process also includes checking the system and acting on it. The model is continuous because an EMS is a process of continual improvement in which an organization is constantly reviewing and revising the system [36].

This is a model that can be used by a wide range of organizations — from manufacturing facilities to service industries to government agencies. An EMS can also be classified as:

- A system which monitors, tracks and reports emissions information, particularly with respect to the oil and gas industry. EMSs are becoming web-based in response to the EPA's mandated greenhouse gas (GHG) reporting rule, which allows for reporting GHG emissions information via the internet.

- A centrally controlled and often automated network of devices (now frequently wireless using z-wave and zigbee technologies) used to control the internal environment of a building. Such a system namely acts as an interface between end user and energy (gas/electricity) consumption.

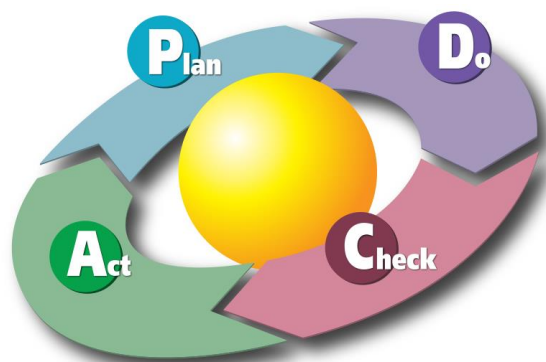


Fig. 4. PDCA Cycle [37].

Model 2: ISO 14001

ISO 14001 sets out the criteria for an Environmental Management System (EMS). It does not state requirements for environmental performance, but maps out a framework that a company or organization can follow to set up an effective EMS. It can be used by any organization that wants to improve resource efficiency, reduce waste, and drive down costs. Using ISO 14001 can provide assurance to company management and employees as well as external stakeholders that environmental impact is being measured and improved [38].

Model 3: Eco-management and audit scheme

The Eco-Management and Audit Scheme (EMAS) is a voluntary environmental management instrument, which was developed in 1993 by the European Commission. It enables organizations to assess, manage and continuously improve their environmental performance. The scheme is globally applicable and open to all types of private and public organizations. In order to register with EMAS, organizations must meet the requirements of the EU EMAS-Regulation [39]. Currently, more than 4,600 organizations and more than 7,900 sites are EMAS registered [39].

EMAS Key Performance Indicators (KPI): The EU Eco-Management and Audit Scheme provides core indicators or Performance Indicator (KPIs) with which registered organizations can measure their environmental performance and monitor their continual environmental improvement against set targets. Energy efficiency, Material efficiency, Water, Waste, Biodiversity and Emissions are the EMAS KPI.

Model 4: Life cycle assessment (LCA)

Life Cycle Assessment is a process to evaluate the environmental burdens associated with a product, process, or activity by identifying and

quantifying energy and materials used and wastes released to the environment; to assess the impact of those energy and materials used and releases to the environment; and to identify and evaluate opportunities to affect environmental improvements. The assessment includes the entire life cycle of the product, process or activity, encompassing, extracting and processing raw materials; manufacturing, transportation and distribution; use, re-use, maintenance; recycling, and final disposal [40].

According to the ISO 14040 [41] and 14044 [41] standards, a Life Cycle Assessment is carried out in four distinct phases as illustrated in the figure shown to the right. The phases are often interdependent in that the results of one phase will inform how other phases are completed (Fig. 5. Phases of Life Cycle Analysis).

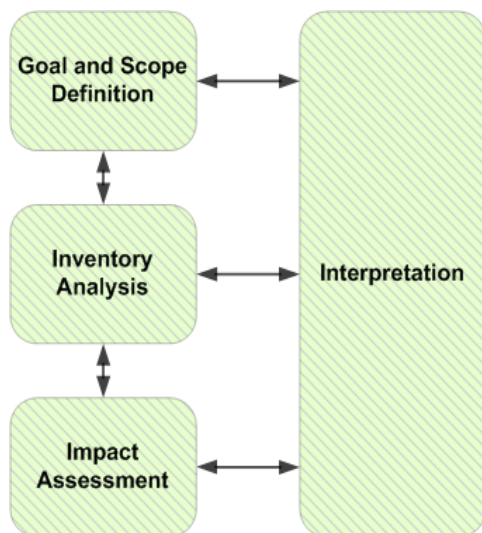


Fig. 5. Phases of life cycle analysis [41]

Model 5: Health, Safety and Environmental-Management System (HSE-MS)

A Health, Safety and Environmental Management System (HSE-MS) monitors health, safety and environmental performance, similar to the way a financial management system monitor's expenditure and income and enables regular checks of a company's financial performance. An HSE integrates health and safety requirements with environmental management into a company's daily operations, long term planning and other quality management systems (Fig.6) [42].

An HSE-MS can assist a company in the following ways:

- Minimize environmental liabilities;
- Maximize the efficient use of resources;

- Minimize the hazard risk in company;
- Maximize the safety in procedure and structure of company;
- Reduce waste;
- Demonstrate a good corporate image;
- Build awareness of environmental concern among employees;
- Gain a better understanding of the environmental impacts of business activities; and
- Increase profit, improving environmental performance, through more efficient operations.

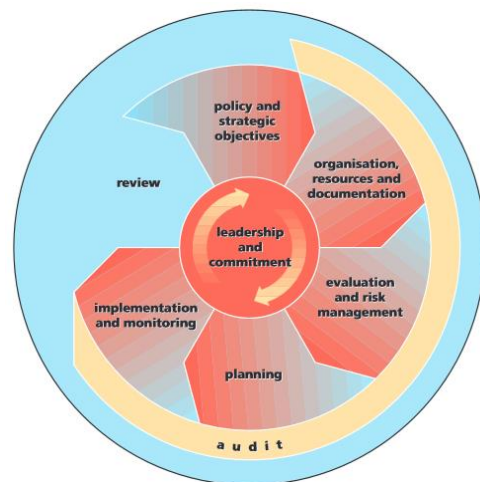


Fig. 6. The model of health, safety and environmental management system (HSE-MS) [43]

RESULTS

Based on integrating the categories and criteria identified from the literature sources, a green strategic management framework was designed for incorporating environmental criteria regarding the competency of green strategy into supplier selection in GSM. The 20 criteria were determined and categorized into five main clusters as follows (see Table 1).

CONCLUSION

We classify the existing GSM probing into five broad categories based on the problem context in GSM; strategic management, environmental performance, green manufacturing, process management, management system, as shown in Fig. 7.

Table 1. Criteria of supplier dimension to GSM (team study).

Dimension (Purpose)	Criteria	SD Models		GSM Models				References	
		1	2	EMS	14001	EMAS	LCA		HSE
Strategic Management (D1)	Environmental Based Strategy							✓	Padash [12]
	Green Supply Network						✓		Vafadarnikjoo [53]
	Design/Operation Requirement of Green Purchasing Social Responsibility	✓	✓					✓	Wu & Chang [47]; Wu & Low [48] Beheshti&Padash [44]
Environmental Performance (D2)	Environmental Regulation (Domestic and International Agreements)			✓	✓	✓			Mathiyazhagan & Haq [55]
	Environmental Policy and Measures and Monitoring Control and Reduction of Emission	✓	✓	✓	✓	✓	✓	✓	Turner et al. [46]; Wu et al.[49]
	Waste Disposal System (WDS)			✓	✓		✓	✓	Wu et al.[49]
	Green Recycling/Reducing				✓	✓	✓		Dawei et al. [50]
Green Manufacturing (D3)	Inventory Management Life Cycle Assessment (LCA)							✓	Xiao et al. [51]
	Environmental Conscious Design (ECD)	✓	✓					✓	UNEP/SETAC [40]
	Management of Failure Mode and Effect Analysis Risk based Inspection (RBI) Process Auditing	✓	✓					✓	Kuo & Chu [56]
Process Management (D4)								✓	Kuo & Chu [56]
								✓	Hsiao et al. [57]
								✓	Hu & Kaabouch [58]
Management System (D5)	Management of Hazardous material			✓	✓			✓	Jabbour et al. [59]
	Environmental Management System and Eco- Management Auditing System(EMAS) OHSAS 18001			✓	✓	✓			Iraldo et al. [39] Lam et al. [69]
	Safety Management System(SMS)							✓	Padash & Darabi [45]
	Energy Management System (ISO 50001)	✓	✓	✓	✓	✓		✓	Padash & Darabi [45], Kumar & Bhimasingu [3]

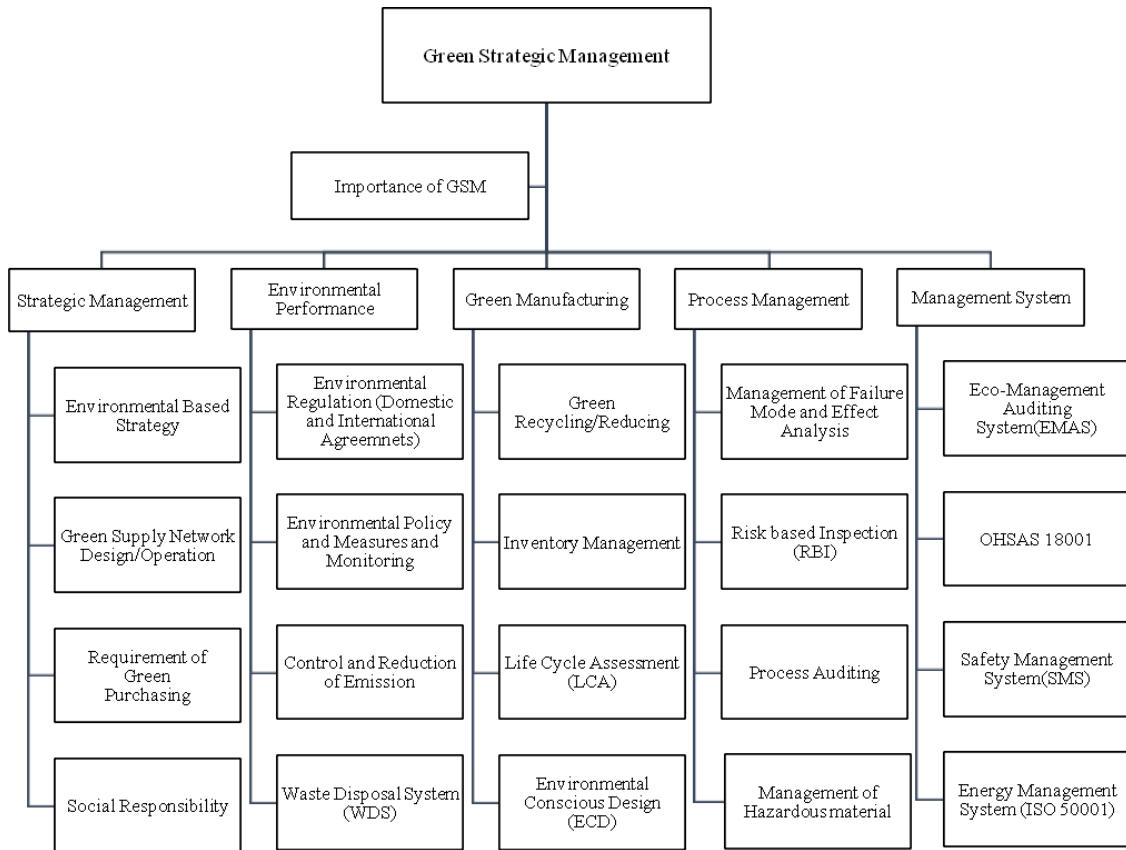


Fig. 7. GSM model for selecting strategies based AHP (team study).

In order to select the appropriate strategy, the basic elements and main activities of environmental strategic management can be determined with three type of strategies. These based on Johnson, Scholes and Whittington’s [64] internationally-recognized book are the following:

- the strategic positioning of the company
- creating environmentally-conscious strategic alternatives
- the implementation of environmentally-conscious strategies

The conceptual model of the elements of strategies to supply GSM is illustrated in Fig.8.

The elements and activities illustrated in the model can be easily understood in environmental terms. In addition, they have a mostly positive influence on achieving the desired results. Naturally, the individual elements do not appear separately in the companies but interact simultaneously. However, in order to aid the readers’ understanding and to integrate additional factors more easily, these elements are discussed as separate points below.

GSM can reduce the ecological impact of industrial activity without sacrificing quality, cost, reliability, performance or energy utilization efficiency. It involves a paradigm shift, going from end-of-pipe control to meet environmental regulations to the situation of not only minimizing ecological

damage, but also leading to overall economic profit. The area throws various challenges to practitioners, academicians and researchers.



Fig. 8. The conceptual model of the elements of strategies to supply GSM (Team Study).

SUGGESTIONS

This proposed framework must address the needs of various executives in developing and implementing green strategies in company along with best business. So, the strategies can start as a project which can be joined to form a cross-organizational program managing Environmental,

Health, Safety and Energy (EHSE) issues in company. However, for effectiveness successfully of building and starting the frame work, as the learnt lessons, there is some special suggestions for the company who would like to start for the best green strategic management practice. Addressing any of those ten key components of a green strategy synchronous business can tangibly lower a company's energy usage and reduce its environmental impact. Addressing them in combination, however, can dramatically amplify those effects in making a company more competitive, successful and social responsible.

1. EHSE strategy

The creation of an enterprise-wide EHSE strategy as part of an overarching corporate social responsibility plan can help companies address "green" issues, resulting in improved financial and EHSE outcomes. Issues to be considered include the alignment of a company's EHSE strategy into an overall business strategy and how EHSE values may be translated into an improved brand image.

2. Define Sustainability

Be sure everyone is working from the same definition of sustainability. When the company use the word sustainability, many customers have a very different interpretation of what the means. It's important to specifically define sustainability from the stakeholders involved.

3. People

The impact of employee behaviors and policies on the environment is significant. Commute time and business travel form a large part of an individual's carbon footprint. The use of online collaboration tools and policies that support reduction in commuting and traveling can also have an impact on costs. Companies also are discovering that their EHSE policies and practices can impact their ability to attract and retain top talent.

4. Make Your Goals Green

For each of your company existing goals, be sure to add realistic and doable actions, with outcomes that lead to sustainable outcomes. Look at company priorities through the lens of sustainability: financial, community and EHSE achievement. Perform a gap analysis to better understand where company land now, and what types of measures the company would like to achieve in the future - then set a timeline with specific and actionable steps to get there.

5. Property

Companies need to reduce the cost and greenhouse gas emissions of their physical assets- from office buildings to truck fleets. The process starts with determining and managing the

environmental impact of physical assets and properly maintaining all property for energy-efficient operations and reduced environmental impact. Through improved maintenance and through improved tracking, deployment, location, and management of facilities and properties, reductions in environmental impact can be achieved.

6. Use measurable targets

To help monitor company's green strategic plan, company will want to keep score of its progress. Third party certifications are now numbered in the hundreds. Be it a green cleaning designation such as Green Seal, a corporate sustainability program such as B Corp certification (B-Corp), or a green building rating like Leadership in Energy and Environmental Design (LEED), using a third party verification is the best key.

7. Product

As companies begin to understand the EHSE impact of their products or services across the entire product lifecycle, they can design products in a manner that has a lower EHSE impact. Streamlining product development and manufacturing also means less material used, less waste created and less energy consumed. Concurrently, an examination of the product or service lifecycle often helps businesses find and exploit market opportunities. Finally, the need to reduce energy consumption is driving an increase in the energy-management intelligence built into certain products.

8. Communicate and educate

A great green plan, poorly communicated, will go nowhere, so it is very important for every company to devise a plan to communicate the goals set in the strategic plan. Obtain feedback and get buy-in from employees early on in the process - don't wait until the plan is complete to start talking about it. Make an announcement and conduct education and feedback sessions to ensure that everyone knows what's in the works - be it employees, investors, partners or vendors. On an ongoing basis, be sure to have monthly e-mail messages, announcements in newsletters, through your organizations blog, and posted on the wall in common areas. Share all or highlights of the plan and keep it forefront and center.

9. Information

With data compounding between 35 percent and 70 percent annually in some industries, it's critical for companies to better manage their data infrastructures. Optimized collection, analysis, tiering and storage of key information helps companies comply with reporting mandates while

minimizing their data footprints. These same information strategies improve business operations by improving information access and system response. They help reduce storage needs through sharing, elimination of redundancies and compression.

10. Business operations

Green strategy need to transform business processes to reduce EHSE impact for operations end-to-end. Consider energy or water consumption, as a start. Through the use of “smart” systems, dramatic efficiency improvement can take place. Any transformation plan put into place must be communicated to key stakeholders.

REFERENCES

1. W.C. Culley, Environmental and Quality Systems Integration. CRC Press, USA, 1998.
2. M. Watson, A.R.T. Emery, *Manag. Audit. J.*, **19**, 760 (2004).
3. B.T. Nones, S. Morques, R. Evgenio, ‘A Theoretical Approach for Green Supply Chain Management, Federal University, Industrial Engineering Program, NATAL-BRAZIL, 2004.
4. J. Sarkis, *J. Cleaner Product.*, **11**, 397 (2003).
5. S. V. Walton, R.B. Handfield, S.T. Melnyk, *Int. J. Purchas. Mater. Manag.*, **34**, 2 (1998).
6. S. Srivastava, *Int. J. Manag. Review*, **9**, 53 (2007).
7. R.K. Mudgal, R. Shankar, P. Talib, T. Raj, *Int. J. Logistics Systems Manag.*, **7**, 81 (2010).
8. R. Nag, D.C. Hambrick, M.J. Chen, *Strategic Manag. J.*, **28**, 935 (2007).
9. R. Sroufe, *Product. Oper.Manag.*, **12**, 416 (2003).
10. Y. Su, Z. Jin, L. Yang, Web-Based Green Products Life Cycle Management Systems: Reverse Supply Chain Utilization, IGI Global, 2008, p. 301.
11. E.G. Olson, *J. Business Strategy*, **29**, 22 (2008).
12. A. Padash, in: World Renewable Energy Congress. Sweden: (2011), p.3034.
13. M. Easterby-Smith, R. Thorpe, A. Lowe, Management Research – An Introduction, London, SAGE Publications. 2002.
14. J. Meredith, *Int. J. Operations&Production Manag.*, **13**, 3 (1993).
15. T. L. Saaty, The analytic network process-decision making with dependence and feedback. Pittsburgh, PA: RWS Publications, 1996, p.82.
16. E. Kinoshita, *Operations Research of Japan*, **48**(9), 677 (2003).
17. T. L. Saaty, Multiple criteria decision analysis: state of the art surveys, Springer, 2005, p.345.
18. J. Korhonen, *J. Cleaner Product.*, **12**, 809 (2004).
19. P. James, Urban Sustainability in Theory and Practice: Circles of Sustainability. London: Routledge, 2014, p.8.
20. A. Scerri, P. James, *Int. J. Soc. Res. Methodol.*, **13**, 41 (2010).
21. C. C. Williams, A.C. Millington, *The Geograph. J.*, **170**, 99 (2004).
22. W. M. Adams, in Report of the IUCN renowned thinkers meeting. UK: (2006), p. 31.
23. P. James, A. Scerri, Auditing Cities through Circles of Sustainability. Ashgate Publishing Ltd, 2011, p. 110.
24. T. Wilkerson, Can One Green Deliver Another?. Harvard Business School Publishing Corporation, 2005, p.4.
25. H.C. Zhang, T.C. Kuo, H. Lu, S.H. Huang, *J. Manufact. Systems*, **16**, 352 (1997).
26. V. D. R. Guide, V. Jayaraman, J.D. Linton, *J. Operat. Manag.*, **21**, 259 (2003).
27. A. Gungor, S.M. Gupta, *Computers & Ind. Eng.*, **36**, 811 (1999).
28. F.E. Bowen, P.D. Cousins, R.C. Lamming, A.C. Farukt, *Product. Operat. Manag.*, **10**, 174 (2001).
29. T.E. Graedel, *Resources, Conserv. Recyc.*, **34**, 107 (2002).
30. I. K. Hui, A.H.S. Chan, K.F. Pun, *J. Cleaner Product.*, **9**, 269 (2001).
31. B. Kaiser, P.D. Eagan, H. Shaner, *Environ. Health Perspect.*, **109**, 205 (2001).
32. J. Sarkis, J.J. Cordeiro, *Eur. J. Operat. Res.*, **135**, 102 (2001).
33. Q. Zhu, J. Sarkis, *J. Operat. Manag.*, **22**, 265 (2004).
34. T. H. Arimura, N. Darnall, H. Katayama, *J. Environ. Econ. Manag.*, **61**, 170 (2011).
35. K. Babiak, S. Trendafilova, *Corporate Soc. Respons. Environ. Manag.*, **18**, 11 (2011).
36. G. E. Fryxell, C. W-H. Lo, S.S. Chung, *Environ. Manag.*, **33**, 239 (2004).
37. H.A. Hahn, in: Conference on Systemics, Cybernetics and Informatics. United States: (2012), p. LA-UR-12-23818.
38. P. Bansal, T. Hunter, *J. Business Ethics*, **46**, 289 (2003).
39. F. Iraldo, F. Testa, M. Frey, *J. Cleaner Product.*, **17**, 1444 (2009).
40. UNEP/SETAC, Guidelines for Life-Cycle Assessment: A 'Code of Practice', Brussels, 2005, p.104.
41. M. Finkbeiner, A. Inaba, R. Tan, K. Christiansen, H-J. Klüppel, *The Int. J. Life Cycle Assess.*, **11**, 80 (2006).
42. A. Padash, M. Khodaparast, A. K. Nejadian, Sustainable development through matching requirement of energy management in HSE-MS, Renewable Energy 2010, Pacifico Yokohama, Japan, 2010.
43. E&P Forum, Guidelines for the Development and Application of Health, Safety and Environmental Management Systems, IOGP Press, 1994, p.4.
44. A. Beheshti, A. Padash, Successful Sustainability by Matching of Environmental, Health, Safety and Social Responsibility Strategy in Project, 25th European Conference on Operational Research Vilnius 2012 Volume 23 Euro Working Group Methodology of Societal Complexity. Vilnius, 2012.
45. A. Padash, H. Darabi, Green Sustainable Island by Implementation of Environmental, Health, Safety and Energy Strategy in QESHM Island -IRAN, 5th

- International Conference on Integrated Natural Disaster Management. Tehran, Iran, 2014.
46. R.K. Turner, R. Salmons, J. Powell, A. Craighill, *J. Environ. Manag.*, **53**, 121 (1998).
 47. H.H. Wu, S.Y. Chang, *Appl. Math. Comput.*, **256**, 394 (2015).
 48. P. Wu, S.P. Low, *J. Prof. Issues Eng. Educ. Practice*, **136**, 64 (2010).
 49. C. Wu, J. Liu, L. Yan, H. Chen, H. Shao, T. Meng, *Atmosph. Environ.*, **103**, 231 (2015).
 50. Z. Dawei, A.B.A. Hamid, T.A. Chin, K.C. Leng, *Sains Humanika*, **5**(2), 15 (2015).
 51. G. Xiao, N. Yang, R. Zhang, *Manufact. & Service Operat. Manag.*, **17**, 321 (2015).
 52. C.N. Madu, C. Kuei, I.E. Madu, *J. Environ. Manag.*, **64**, 261 (2002).
 53. A. Vafadarnikjoo, *J. Cleaner Product.*, **40**, 32 (2013).
 54. P. Wu, S.P. Low, *Int. J. Construc. Manag.*, **14**, 78 (2014).
 55. K. Mathiyazhagan, A. N. Haq, *Int. J. Adv. Manufact. Technol.*, **68**, 817 (2013).
 56. T.C. Kuo, C.H. Chu, *J. Precision Eng. Manufact.*, **14**, 1057 (2013).
 57. T.Y. Hsiao, C.M. Chuang, N.W. Kuo, S.M.F. Yu, *Int. J. Hospitality Manag.*, **36**, 197 (2014).
 58. W. C. Hu, N. Kaabouch, Sustainable ICTs and management systems for green computing, IGI Global, USA, 2012.
 59. A.B.L. de Sousa Jabbour, F.C. de Oliveira Frascareli, C.J.C. Jabbour, *Resources, Conserv. Recycl.*, **104**, 366 (2015).
 60. P.T.I. Lam, E.H.W. Chan, C.K. Chau, C.S. Poon, K.P. Chun, *J. Environ. Manag.*, **92**, 788 (2011).
 61. J. Nanyunja, L. Jacxsens, K. Kirezieva, A.N. Kaaya, M. Uyttendaele, P.A. Luning, *J. Food Protect.*, **78**, 1081 (2015).
 62. Y.V.P. Kumar, R. Bhimasingu, *J. Modern Power Syst. Clean Energy*, **3**, 1 (2015).
 63. G. Johnson, K. Scholes, R. Whittington, Exploring Corporate Strategy. Texts and Cases. Prentice Hall, London, 2006.

Attitude and practice of pharmacist towards oral healthcare and oral hygiene products: An exploratory study

Jalaleddin H Hamissi^{1*}, Hesameddin Hamissi²

¹Associate Professor in Department of Periodontics, College of Dentistry, Qazvin University Medical Sciences, Qazvin, Iran.

²Dentist

Received June 26, 2015, Revised September 10, 2015

The aim of this study was to assess Knowledge, attitude and practice of pharmacists regarding oral healthcare and oral hygiene products in Qazvin, Iran. This is a cross-sectional descriptive and analytical study conducted in Qazvin, Iran. The study group was included of 147 pharmacists who recruited to participate in this study. A self-administered structured validated closed-ended questionnaire was developed for this purpose. Statistic analysis were done using SPSS version 22. Of the total study group, 100 pharmacists responded to the questionnaire and participated in the study. 35% of the respondents had not met the dentists practicing close to their pharmacies, nor were they aware of the opening times of the practice. Most of the pharmacists stocked oral health-related products, which comprised of less than 15% of their total stock. Toothpaste was the most common among the oral healthcare products stocked, followed by toothbrushes and mouth rinses. A total of 38% pharmacists expressed an interest in further developing their oral healthcare knowledge through course attendance or oral health programs. Toothache or mouth ulcers were the most common dental problem for which patients approached the pharmacists for advice. Pharmacists advised patients complaining of dental pain to consult a dentist in 55% of cases, dispensed painkiller in 2% of cases, and in 5% of cases dispensed an antibiotic. The community pharmacists in Qazvin are under-used in the promotion of oral health. There is a need for training of pharmacists and providing them with access to information on available dental service and oral health products.

Keywords: Community pharmacies, Oral health advice, Oral hygiene products, Pharmacists

INTRODUCTION

Oral health is a part of general health and so it affects the entire well-being of individuals [1]. It is the cumulative result of both the progressive and relatively disease-free periods during a lifetime. Recently in public health aspect of medical sciences, the importance of general hygiene has been highlighted. One of the most important fundamentals of general health is oral hygiene. Personal knowledge combined with professional tooth brushing can reduce the progression of dental caries and periodontal disease [2, 3].

Dentists as well as other health professionals realize that oral health cannot be divorced from the general health of the hospitalized patient. Many oral conditions are intimately related to systemic diseases. Optimally, total health care requires the combined efforts of the medical and dental professions [4, 5]. Pharmacy is one of active profession which is growing and changing every minute. Pharmacists have very long helped as the medication experts in health care team and due to their knowledge, accessibility are usually consulted by the public and other specialists to response

health-related questions [6-8].

The role of the pharmacist in oral healthcare has increased importance in view of delivering primary dental care services from the professionals to the public. The pharmacists are in a unique position to disseminate information on oral health, since they are in the frontline of primary source of information to many patients in developing countries [7, 9]. They can emphasize the nature of dental disease, its prevention, and importance of regular dental checkups and medications. Community pharmacist can play an active role in oral disease prevention, identification, assessment, and referral. Even though they cannot take over the role of dental professional, they can endorse the advice given by them [10-11].

Based on the outcome of the several studies, also stressed the importance of training for the pharmacists to access information on available dental services [11-14]. In Iran, its common practice for some people to visit pharmacists for assistances regarding ordinary medical and dental problems and counsels for oral health and dental products due to lack of time and difficulty in getting an appointment with the physician or dentist. Till date, there are no self-reported studies on knowledge, attitude, and behaviors of pharmacists on oral

To whom all correspondence should be sent:

health care products in Iran. Therefore, the present study was undertaken to assess the level of information and attitude of pharmacists on oral health care products in Qazvin, Iran.

METHODOLOGY

Study design, settings and study subjects

This is a cross-sectional survey conducted among pharmacist in Qazvin, Iran. The study commenced in July-2012 and continued for two weeks. A list of all the registered private and community pharmacies in Qazvin region was obtained from the food and drug department of Qazvin University of Medical Sciences was prepared. The pharmacies' could be broadly divided into two types: those owned by individual pharmacist; those pharmacists that were attached to hospitals from the list. Out of one hundred forty seven, one hundred pharmacists (community hospital and private pharmacists) were included in the study with a response rate of 68%. Each pharmacist was asked to fill a validated structured questionnaire delivered by hand. The participated pharmacists (community & hospital and private pharmacists) were from independent and as well as from different hospitals (public and private hospitals). Two hospitals in Qazvin were covered, while the community pharmacies coverage represented about 2 % of the total number of pharmacies in Qazvin.

Questionnaire

We used a Priya S questionnaire that designed with an 18-item self-administered assessing [12]. Content validity was assessed by distributing the questionnaire to 10 pharmacists recruited to complete the validation process. The initial draft of questionnaire was hand delivered to those pharmacists to help review the structured questionnaire and perform any alterations needed. The questionnaire comprised 18 closed-ended questions that had been earlier pre-tested on a group of pharmacists. One pharmacist from each selected pharmacy participated in this study. Each pharmacist took around 15 min to complete the questionnaire. The questionnaire was divided into four sections: section I dealt with details regarding the vicinity of the dentist to the pharmacy, their appointment details, and the frequency with which the pharmacist met the dentist. Section II focused on the range of dental products stocked in the pharmacy. Section III dealt with the advice given by the pharmacist to customers regarding oral hygiene products and oral health, while section IV

dealt with the pharmacist's source of information regarding oral health and oral hygiene, the barriers faced by them, and also methods to improve their knowledge and attitudes regarding oral health. Data was collected by a single investigator, who personally met the pharmacists and explained to them the purpose of the study. The completed questionnaire was collected by the same investigator.

STATISTICAL ANALYSIS

Data were analyzed using statistical package for social science version 22 (SPSS, Inc., Chicago, IL, USA). The descriptive analysis was done using mean and SD for continuous variables and percentage for qualitative variables. Pearson Chi-Square was used to calculate p-values for categorical variables.

RESULTS

Among the 147 pharmacies approached, 100 pharmacists participated in the study and completed the questionnaire. Among them, 96 pharmacies were owned by persons, and the rest were attached to hospitals and else. The mean number of years of practice of the pharmacies was around 22.2 years. Fifty eight (58%) pharmacists who participated in the present study said that there were less than four dentists practicing within 5 km of their pharmacies and 14% felt that there were five to nine dentists practicing near (within a 5 km distance) their pharmacy. When asked whether they had met the dentists practicing close to their pharmacies, only 66 (66%) pharmacists gave a positive answer. Among them 62% had met the dentist less than six times in the past one year on a regular basis. 32 percent of the pharmacists said they did not meet the dentist at any fixed time interval. Nearly 54 pharmacists (54%) who participated in this study gave a negative answer when asked whether they had tried to interact with the dentist regarding oral health. Similarly, 84 (84%) of the participating pharmacists were not even aware of the appointment arrangements of the local dentist. Less than 15% of the total stock was related to oral health in 54% of the pharmacies. 27% of the pharmacist had oral health-related products in the range of 15-25% of the total stock. Toothpaste was the most common (68%) among the oral health care products stocked, followed by mouth rinses (10%). Toothbrushes contributed to around 20% of the total stock. Forty-five pharmacists (45%) said that around ten patients with dental problems visit their pharmacies every day. Among them, nearly 67%

ask the pharmacist for oral health-related advice. Toothache is the most common dental problem (81%) for which patients approach the pharmacist for advice; this is followed by gum problems like bleeding gums and/or bad breath and mouth ulcers. Patients seldom seek advice regarding toothbrushes, toothpastes, whitening of teeth, etc.

Though 22 (22%) of the participating pharmacists ask the patient to consult a nearby dentist after dispensing medications, 7 (7%) dispensed antibiotics and painkillers without any referral to a nearby physician or dentist. 53 (53%) pharmacists said that they just ask the patient to consult a nearby dentist, without dispensing drugs. 39 percent of the pharmacists feel that financial constraints are the reason for patients approaching a pharmacist (instead of a dentist) for oral health care advice. A few (24%) feel that patients approach them for advice because of the difficulty in getting appointments with the nearby doctor/dentist.

Twenty-three percent of the pharmacists give advice based on their comprehensive knowledge of the products available. An equal number give advice based on the suggestions/instructions from the local dentists/doctors. When asked whether fluoride in toothpaste is beneficial, nearly 14 (14%) pharmacists were unaware of the benefits. 86% were aware of the benefits, while 14% felt that there was no benefit in the presence of fluorides in toothpastes. ninety percent of the pharmacists were aware of the different types of toothbrushes present in the market.

The majority of the participating pharmacists, i.e., 85(85 %) in number, expressed interest in giving oral health care advice to patients. However, some of them (8%) feel that lack of proper knowledge is a barrier to providing oral health care advice. 33% feel that oral health care and details regarding oral hygiene products should be made a part of their curriculum. Information disseminated through leaflets/pamphlets/posters was the preferred choice of many pharmacists for improving their knowledge regarding oral health. However, 39% also feel that their knowledge could be improved by oral health care courses, meetings, and training programs.

Demographics

The demographic details of the pharmacists included. The mean age of pharmacist was approximately 22.2 years, and the average year of experience was 22.8years and their mean age was 50 ± 9 years. In this study, 96% of pharmacists were community pharmacists while 4 % were

hospital and else pharmacists. Females accounted for 31.6% of pharmacists.

DISCUSSION

Teamwork is now predictable as a key idea in the delivery of oral health care. Although this is most often discussed in the context of members of the 'dental team,' this role played by pharmacists and has expanded significantly in recent decades from distributor of medication to known member of the health care team. Rather than consult a dentist or physician, many individuals with oral problems seek help from their pharmacists [15]. Therefore, this investigation was done to find out their knowledge and attitudes regarding oral health and oral hygiene products. To the best of our knowledge, this cross-sectional survey is the first study to evaluate this issue in Qazvin.

The role of the pharmacist in the delivery of oral health care has not been taken into consideration for many years. From a mere dispenser of medications prescribed by the doctors, their role has expanded to providing basic oral health care advices to the patients. In many studies have been reported that pharmacists has the second most used source for advice on general health matters and therefore, can and should also be used in an oral health capacity [16, 17]. According to this current study, 90% of community pharmacies had more than one dental clinic nearby, 34.7% of pharmacists never met the dentists practicing close to their pharmacies. Similar observations were reported in other studies [18, 12]. Assessment of the stocks of oral healthcare products in pharmacies revealed that toothpastes were the most common product stocked which was similar to previous studies. The recommendations of oral health products also depended mainly on the limited knowledge of the pharmacist about the product and their personal experience [18, 12].

Most of the pharmacists specified that the greatest common oral health complaints raised by the patients stayed mouth ulcers and toothache, and greatest of them were able to be managed by medications given by pharmacists. Only a small percentage of patients remained referred to the practitioners. This was similar with study by Maunder and Landes [18]. However, it is interesting to take note that 5% of the pharmacists distributed antibiotics for toothache without prescription from a dentist. At top of the list for dental problems of the patients were toothaches or painful teeth, which may seek advice from the pharmacist. This is similar to the findings of the study [18]. Most of the pharmacists referred the

patients to the nearby dentist after dispensing medications for short-term pain relief. However, it is interesting to note that nearly 7% of the pharmacists dispense antibiotics and analgesic and do not refer the patient to a dentist or physician. This is a matter of concern since short-term pain relief might mean that the patient will postpone consulting a dentist or physician and, thereby, an opportunity to diagnose a disease in its early stage may be lost.

Our study showed that most of the respondents felt that financial constraints were the main reason for patients approaching the pharmacist for advice. The results of the present investigation firstly demonstrated that the majority of pharmacists have inadequate knowledge and lack of awareness. This study explored the urgent need for educational programs to emphasize the role and responsibility of pharmacists in oral health. Most probably, all these perceptions, attitude and behaviors could be changed significantly by proper educational programs. Nevertheless, we are aware of some methodological weaknesses of our study; as the questionnaire relied on pharmacists' self-rated assessment of their own practice and attitudes, pharmacists might have felt stressed into completing the questionnaire or might have been unwilling to reveal their practice deficiencies. Also the research has been conducted over a short period of time, which might shed doubt on the objectivity of the responses and introducing some over estimation in both pharmacist's knowledge and attitudes.

CONCLUSION

Pharmacists already provide some amount of oral health advice and they are keen to expand their knowledge. Patients regularly ask for their advice on both general and oral health care issues. They are presently an underused resource, and it is only now that they are beginning to get the recognition they deserve. There is a definitive need for training of pharmacists and providing them with access to information on available dental services.

These results suggest that Iranian pharmacists have little knowledge about the concept and process of oral health. However the pharmacists had positive attitudes toward oral health, but educational programs are needed to increase pharmacists' role and their knowledge about it.

RECOMMENDATIONS

Pharmacists have long served as the medication experts of the health care team and, due to their knowledge and accessibility, are frequently

approached by the general public and other professionals to answer health-related questions. In this context, the recommendations by Maunder and Landes (18) need to be considered for improving the oral healthcare provision by pharmacists; these recommendations are:

1. Setting up of regular multidisciplinary and primary care team meetings.
2. Funding for more opportunities for continuing professional development, such as oral health courses.
3. Funding for information leaflets, especially during national oral health campaigns.
4. A list of key contacts within the area of practice to be provided to pharmacists for advice regarding tobacco cessation, clarifications regarding oral health, etc.
5. Support for window displays, especially about targeting health issues, including oral health.

The above recommendations would enable the pharmacist to follow the correct procedures agreed upon at the local multidisciplinary meetings. They would however have to be validated to meet national standards.

Limitations of the study

This study is a self-reported questionnaire based study. Therefore, in the present study, the subjective self-reported information should be carefully evaluated.

Assessment of practice by direct observation could add insight and reflect adherence to national infection control guidelines

Conflict of interest: None.

Acknowledgments: *The authors wish to thank Mrs. Ghodousi for her valuable help in the statistical analysis and Dr. Farzad Pyroviyan for his advice in undertaking this study and assistance in data collection and to all the pharmacists who gave their time to complete and discuss the questionnaires.*

REFERENCES

1. J. Hamissi, G.H. Ramezani, A. Ghodousi, *Iran. J Indian Soc Pedod Prev Dent*; **26**(S2), 53 2008.
2. J. Hamissi, P. BakianianVaziri, A. Davaloo, *Iranian J Publ Health*, **39**(1), 28 (2010).
3. A. Choo, D.M. Delac, L.B. Messer, *Aust Dent J*, **46**(3), 166 (2001).
4. N.O. Harris, F.G. Godoy, in: Godoy FG, editor. *Primary preventive dentistry*. 6 Ed. New Jersey: Julie Levin Alexander publisher; 2004. p. 605.

5. S. Usman, S.S. Bhat, S.S. Sargod. *J Oral Health Comm Dent*, **1**, 46 (2009).
6. S.L. Iwanowicz, M.W. Marciniak, M.M. Zeolla, *Am J Pharm Educ.*, **70**(3), 57 (2006).
7. Maunder P.E., D.P. Landes, *Br Dent J.*, **199**(4), 219 (2005).
8. M.C. Watson, C.M. Bond, J.M. Grimshaw, J. Mollison, A. Ludbrook, A.E. Walker, *A cluster randomized controlled trial (RCT) Fam Pract.*, **19**(5), 529 (2002).
9. O.A. Bawazir, *Saudi Arabia.J Int Oral Health*, **6**(6), 10 (2014).
10. R.J. Harman, *Handbook of Pharmacy Health Education*, London: Pharmaceutical Press; 2001.
11. C. Anderson, *Br J Community Nurs*, **3**(1), 41 (1998).
12. S. Priya, P.D.M. Kumar, S. Ramachandran, *Indian J Dent Res.*, **19**(2), 104 (2008).
13. I.G. Chestnutt, M.M. Taylor, E.J. Mallinson, *Br Dent J.*, **184**(11), 532 (1998).
14. M.I. Al-Hassan, *Res J Med Sci.*, **3**(3), 111 (2009).
15. <https://www.secure.pharmacytimes.com/lessons/200406-04.asp>.
16. H.H. Ghalamkari, A. Saltrese-Taylor, M. Ramsden, *Pharm J.*, **258**, 138 (1997).
17. P. Goel, *Soc Sci Med.*, **42**(8), 1155 (1996).
18. P.E. Maunder, D.P. Landes, *Br Dent J.*, **199**(4), 219 (2005).

Development of environmental management strategies for thermal power plant wastes in Iran through strategic analysis method (SWOT)

R. Samadi¹, J. Nouri*¹, A.R. Karbassi¹, R. Arjomandi²

¹ Department of Environmental Management, Science and Research Branch, Islamic Azad University, Tehran, Iran

² Graduate Faculty of Environment, University of Tehran, Tehran, Iran

Received June 26, 2016, Revised September 10, 2016

Thermal power plant is one of the most important and fundamental industries in Iran that provides required power for industry, household and commercial sectors through consuming different kinds of fossil fuels. During the process of generating electricity, power plants emission different kinds of environmental pollutants which one of them is solid waste. Generally power plant wastes can be divided into three categories of ordinary, industrial and hazardous waste. The goal of this research is finding suitable strategies with Iran's conditions in order to plant's waste management. Different methods such as library, website of the electrical industry and power plants and completing questionnaire have been used in this paper to collect data and interviewing with chemistry and environmental experts have been also done. For determining power plants' waste management strategies, SWOT has been used. So that using subject's literature in managing plants' waste and questionnaire survey which is done by 40 experts, strengths, weakness, opportunities and threats are extracted and related strategies are determined. Considering environmental situation of country's power plants, establishing an appropriate management system for organizing industrial waste and preventing environmental pollution seem necessary. One of the most important functional strategies for Iran's electricity industry is planning integrated solid waste management and also programming in order to building power plants with high efficiency using natural gas fuel.

Key words: solid waste, management strategy, SWOT, thermal power plant, environmental pollution

INTRODUCTION

Electricity industry as a fundamental and main industry is considered as the most important required infrastructures for developing economical activities. Many power plants are working in the process of generating electrical energy, one of these plants which are used in our country and other ones that have cheap fossil resources is thermal power plant. Fossil fuels are considered as the most important sources of plants' fuel production in order to generating electrical energy which under the influence of combustion publish different kinds of pollutants and dangerous industrial waste [6-8].

In our country Iran also about 90% of whole generated electricity (263 billion kWh in 2013) is provided by different kinds of thermal power plants (steam, gas and combined cycle) [2,3]. Power generation process and combustion of different kinds of fossil fuels in plants units cause producing and publishing a variety pollution of air, water and even sound to the environment which has been always paid attention by environmental and energy experts and even general public [4,9].

The subject which is less paid attention among these is producing solid and semi-solid waste which is produced directly or indirectly as the result of

combustion, water supply system and wastewater treatment plant. Quality and quantity of solid wastes depend on various factors such as the kind of power plant and the kind of consuming fuel [10].

Steam thermal power plants, considering the kind of consuming fuel (mainly oil furnace) and the process of generating electricity, have the most amount of producing solid wastes [11,12]. Then there are combined cycle power plants that considering gasoline consumption or natural gas and having higher efficiency, produce less and low risk wastes. Finally, gas power plants with natural gas consumption and less share of these power plants in country's electricity production don't have considerable environmental problems in solid wastes' production point of view.

Plants' wastes include sludge, ash and health & administrative trashes. There has been administrative trash in all power plants and most of the time there are recyclable, the other wastes of industrial processes such as wastewater treatment, often are delivered to contractors. Reusing plants' wastes in industries which are close to these plants will reduce pollutants' publishing to environment as well as minimizing the volume of waste [13-15].

Hazardous wastes of power plants considering hazardous waste management regulations EPA and definition of hazardous waste are:

- Sludge from waste water treatment of washings outer surfaces of the boiler and air pre-heaters

To whom all correspondence should be sent.

E-mail: nourijafar@gmail.com

- Sludge from waste water treatment of chemical washing of boiler
- A variety of waste and ash into the furnace and combustion chamber

These wastes' being dangerous is because of high concentrations of heavy metals and the possibility of their leakage, cf. Saeidi et al. [1].

Non-hazardous waste of power plants are also:

- Clarifiers' sludge and sediments and dehydrated wastes of these sludges
- Human waste and human waste sludge.

Organizations and institutes which have to compete and try for survival in highly turbulent, non-stable and developing environments, face with two main management approaches for dealing effective environmental events and factors. One is school of adaptation depiction which has reactive and requirements attitude with these developments and the other is the school of pre-contraption which prescribes an active attitude with environmental factors.

Strategic analysis method (SWOT) is used as the recommendation of pre-contraption school and for identifying and codification optimal strategies for organizations that its result is 4 categories of strategy: opportunity-strengths, opportunity-weakness, threat-strengths and threat-weakness.

In these schools, strategy means decision making process, which during that, organization's internal factors (weaknesses and strengths) are related with external factors (opportunities and threats) in a way that the value of each one is clarified well in realizing organization's goals.

Investigating SWOT matrix is considered as effective factor in advancing the goals of an organization. Providing existing weaknesses and strengths in organization as internal factors and opportunities and threats as external factors helps determining chosen strategy in order to achieving an organization's goals in competitive environment and general attitude toward this issue in different

conditions can play an important role in an organization's success in various conditions [5].

MATERIALS AND METHODS

As first phase, general situation of 68 existing thermal power plant in the country and environmental conditions of them were investigated through library studies and interviewing environmental correspondent expert of power plants. In Table 1 some technical information and the amount of consuming fuel in plants affiliated to the power ministry are proposed to separation of a variety of thermal power plants for 2013 [2].

Then we interviewed some experts of electricity industry in environmental issues and based on that SWOT matrix questionnaire was designed for effective internal factor evaluation (IFE) and external factor evaluation (EFE) in environmental management of power plant's waste and was sent for 40 related experts (statistic population) for poll. Internal factors must include existing strengths and weakness in country's thermal power plant waste management. Providing this matrix includes below phases:

1- First strengths and then weaknesses are written.

2- These factors are given coefficient. From one (very unimportant) to five (very important) given coefficient represent the relative importance of each factor in success. Regardless of whether the mentioned factor is considered as internal strengths and weakness, the factor which has had the highest effect in performance, is given the highest coefficient.

Then each one of these factors is given scores from 1 to 4. Score 1 represents the lack of strengths or weakness, score 2 represents usual strengths or weakness, score 3 shows high strengths and weakness and score 4 shows very high strengths or weaknesses of mentioned factor. Scores are based on status of area and coefficients (which are given in second phase) and the kind of activity.

Table 1: Information of thermal power plants affiliated to the ministry of Energy in 2013.

Type of Power plant	Number of Power plant	Nominal capacity (MW)	Annual production (Million KWH)	The average efficiency (Percentage)	Fuel Consumption		
					Furnace Oil Million) (liters)	Gas oil Million) (liters)	Natural Gas (MCM)
Steam	19	14951	87205	37	15308	261	7119
Gas	34	11860	35412	30	-	377	8054
Combined Cycle	15	15913	83986	45	-	5262	13315

3- For determining final score of each factor, each factor's coefficient is multiplied in its score.

4- The sum of final scores of each factor is calculated and the final score is determined.

All phases are true for external factors' matrix as well. In this matrix just instead of strengths and weakness (internal factors), external factors mean threats and opportunities of expanding and developing country's thermal power plant wastes are listed.

Following that obtained results of analyzing SWOT questionnaire which are gathered using the ideas of 31 experts are proposed in results section.

SWOT analysis has been used for identifying and investigating effective internal factors (strengths and weaknesses) and area's effective external factors (opportunities and threats) for investigating effective factors on creating wastes in Iran's thermal power plants. In fact this method is used as a tool for identifying strategic problems and proposing appropriate functions and strategies. First using region's internal and external environment, strengths, weaknesses, opportunities and threats are identified and a list of them is provided and then with asking experts for their ideas and weighting, calculating and analyzing each one of these problems, priorities are clarified and for removing or minimizing weaknesses and threats and improving strengths and existing opportunities in plants' wastes in Iran, appropriate strategies are proposed.

Considering SWOT matrix outputs, another questionnaire named "quantitative strategic planning matrix (QSPM)" was designed in order to determining appropriate strategies for environmental management of plants' wastes and was surveyed. Using quantitative strategic planning matrix (QSPM) designed strategies are optimized prioritized and finally the best and most attractive ones are chosen for organization. QSPM is used for evaluating possibility and stability of proposed strategies in facing environmental conditions and current situation of organization. In this evaluation if one strategy cannot face inside or outside conditions of organization, must be removed from the list of prioritized strategies.

RESULTS AND FINDINGS

SWOT analysis is considered as an important part in process of strategy formation. Analyzing external opportunities and threats is mainly used for investigating this problem that if organization can use opportunities and minimize threats and this analysis also is important for analyzing weaknesses for investigating company's internal performance is very important. The quantitative analysis method of

SWOT provides more detailed data for SWOT analysis. Data analysis is also done through obtained results of internal factors evaluation matrix and external factors evaluation matrix and SWOT matrix.

The goal of analytical method is determining strengths, weaknesses, opportunities and threats in environment. For determining basic information and providing required matrixes for SWOT analysis, questionnaire is used in this research and matrix evaluation of external factors, internal factors analysis, opportunities, threats, strengths and weaknesses' matrix and quantitative strategy planning matrix (QSPM) country's thermal power plant wastes environmental management are provided.

The obtained results of analyzing experts' ideas and completed questionnaires by them are proposed for identifying strengths in Table 2, weaknesses in Table 3, opportunities in Table 4 and threats in Table 5.

For proposing strategies and policies in order to investigating effective factors on creation of waste in Iran's thermal power plant, identifying quartet factors are unavoidable case for removing weaknesses and threats and improving strengths and opportunities. In fact it has been tried to investigate these factors with questionnaire as main advantages and limitations in Iran's power plants for prioritizing options from experts' point of view to be able to quantitative result and obtain more logic and fundamental results. There for considering experts' ideas and performed calculations on these ideas for prioritizing them, below tables were provided that the mean of given weights and the average rank of each of the strengths, weaknesses, opportunities and threats from experts' attitude are shown in tables 6, 7, 8 and 9 respectively.

Then factors which weighted less than 20% were removed from the rest of studies. These factors which are highlighted with gray color are: S4, S5, W7, O5, T6, and T7. So based on summing of obtained results from experts' ideas and prioritizing internal factors including strength and weakness and external factors including opportunity and threat, SWOT matrix based on obtained priorities in each one of. internal or external factors that are effective in thermal power plants of Iran will be according to Figure 1.

PROVIDING SWOT MATRIX

After evaluating internal or external factors which is called input phase, required data for developing strategies are clarified. In second phase

Table 2: IEF matrix- strengths

Row	Factor (Strengths)	Importance degrees(weight) of factor					Weight calculation				Current actual factor points				Calculate the points				Overall points (Weight * points)	
		Very unim- portant	Unim- portant	Moderate importance	Important	Very Important	Count	Sum	Average	Weighted average	Not strength	Normal strength	High strength	Very high strength	Count	Sum	Average	Weighted average	Coefficient	Weighted points
1	The ability of using natural gas in most thermal power plant of country	0	1	7	13	10	31	125	4.03	0.76	1	10	15	5	31	86	2.77	0.40	11.19	0.68
2	Existing strong internal experts	0	6	11	8	6	31	107	3.45	0.32	1	12	13	5	31	84	2.71	0.00	9.35	0.18
3	Existing vast areas for waste management projects	3	8	7	11	2	31	94	3.03	0.00	1	10	12	8	31	89	2.87	1.00	8.71	0.00
4	Existing vast resources for waste management(there are history)	0	4	9	10	9	31	120	3.87	0.63	1	11	12	7	31	87	2.81	0.60	10.86	0.59
5	Existing environmental rules and standards	0	0	5	10	16	31	135	4.35	1.00	0	10	16	5	31	88	2.84	0.80	12.36	1.00

Table 3: IEF matrix- weaknesses

Row	Factor (Weaknesses)	Importance degrees(weight) of factor					Weight calculation				Current actual factor points				Calculate the points				Overall points (Weight * points)	
		Very unim- portant	Unim- portant	Moderate importance	Important	Very Important	Count	Sum	Average	Weighted average	Not strength	Normal strength	High strength	Very high strength	Count	Sum	Average	Weighted average	Coefficient	Weighted points
1	The low quality of fuel	1	2	3	4	5	31	107	3.45	0.54	3	8	13	7	31	86	2.77	0.59	9.58	0.52
2	Lack of natural gas, especially in winter	0	4	9	11	7	31	114	3.68	0.71	0	8	13	10	31	95	3.06	1.00	11.27	0.80
3	The low efficiency of the power industry	1	3	9	11	7	31	113	3.65	0.68	0	11	14	6	31	88	2.84	0.68	10.35	0.65
4	Low water quality in some areas of the country	6	7	9	7	2	31	85	2.74	0.00	4	14	11	2	31	73	2.35	0.00	6.46	0.00
5	Lack of awareness and attention of executives to environmental issues of power industry	0	1	6	14	10	31	126	4.06	1.00	0	7	15	9	31	95	3.06	1.00	12.46	1.00
6	Lack of sufficient resources in the environmental	0	0	3	13	13	31	126	4.06	1.00	2	6	11	10	31	87	2.81	0.64	11.41	0.83
7	Lack of appropriate infrastructure for waste plant management	1	2	9	11	6	31	106	3.42	0.51	0	12	11	6	31	81	2.61	0.36	8.93	0.41

Table 4: EFE matrix- opportunities

Row	Factor (((Opportunities))	Importance degrees(weight) of factor					Weight calculation				Current actual factor points				Calculate the points				Overall points (Weight * points)	
		Very unim- portant	Unim- portant	Moderate importance	Important	Very Important	Count	Sum	Average	Weighted average	Not strength	Normal strength	High strength	Very high strength	Count	Sum	Average	Weighted average	Coefficient	Weighted points
1	The strategic location of the country	10	10	5	5	1	31	70	2.26	0.00	9	14	7	1	31	62	2.00	0.00	4.52	0.00
2	The beginning privatization of the electricity industry (Delegating power plants to the private sector)	0	2	9	13	7	31	118	3.81	0.80	0	10	14	7	31	90	2.90	0.68	11.05	0.69
3	The low cost of energy in the country	1	4	8	13	5	31	110	3.55	0.67	10	9	9	3	31	67	2.16	0.12	7.67	0.33
4	Existing huge reserves of natural gas in the country	0	0	7	13	11	31	128	4.13	0.97	0	8	12	11	31	96	3.10	0.83	12.79	0.88
5	The importance and necessity of environmental issues in national and international communities	0	2	3	13	13	31	130	4.19	1.00	0	5	11	15	31	103	3.32	1.00	13.93	1.00

Table 5: EFE matrix- threats

Row	Factor (Threats)	Importance degrees(weight) of factor					Weight calculation				Current actual factor points				Calculate the points				Overall points (Weight * points)	
		Very unim- portant	Unim- portant	Moderate importance	Important	Very Important	Count	Sum	Average	Weighted average	Not strength	Normal strength	High strength	Very high strength	Count	Sum	Average	Weighted average	Coefficient	Weighted points
1	Government structure in the power industry	0	0	7	14	10	31	127	4.10	1.00	0	6	13	12	31	99	3.19	1.00	13.08	1.00
2	Lack of access to innovative technologies and advanced of power generation and power Plant	0	3	11	10	7	31	114	3.68	0.68	4	14	11	2	31	73	2.35	0.00	8.66	0.32
3	The impossibility of import high-quality fuel	7	6	9	5	4	31	86	2.77	0.00	6	10	13	2	31	73	2.35	0.00	6.53	0.00
4	Iran is one the arid and dry country	3	8	9	8	3	31	93	3.00	0.17	3	11	13	3	31	76	2.45	0.12	7.35	0.13
5	The lack of prioritize in environmental issues	0	2	5	14	10	31	125	4.03	0.95	0	8	12	11	31	96	3.10	0.88	12.49	0.91
6	Low electricity costs (Not being real price of electricity)	0	5	12	9	5	31	107	3.45	0.51	2	11	12	6	31	84	2.71	0.42	9.35	0.43
7	weakness of administrative in the Environmental Protection Agency	0	3	5	12	9	31	114	3.68	0.68	4	4	15	8	31	89	2.87	0.62	10.56	0.61

Table 6: Effective internal factors on waste management in country’s thermal power plant – **Strengths**

Row	(Strengths)	Weighted Points	Priority
5	Existing environmental rules and standards	1.00	1
1	The ability of using natural gas in most thermal power plant of country	0.68	2
4	Existing vast resources for waste management(there are history)	0.59	3
2	Existing strong internal experts	0.18	4
3	Existing vast areas for waste management projects	0.00	5

Table 7: Effective internal factors on waste management in country’s thermal power plant – **Weaknesses**

Row	(weaknesses)	Weighted Points	Priority
5	Lack of awareness and attention of executives to environmental issues of power industry	1.00	1
6	Lack of sufficient resources in the environmental	0.83	2
2	Lack of natural gas, especially in winter	0.80	3
3	The low efficiency of the power industry	0.65	4
1	The low quality of fuel	0.52	5
7	Lack of appropriate infrastructure for waste plant management	0.41	6
4	Low water quality in some areas of the country	0.00	7

Table 8: Effective external factors on waste management in country’s thermal power plant – **Opportunities**

Row	(Opportunities)	Weighted Points	Priority
5	The importance and necessity of environmental issues in national and international communities	1.00	1
1	Existing huge reserves of natural gas in the country	0.88	2
2	The beginning privatization of the electricity industry (Delegating power plants to the private sector)	0.69	3
3	The low cost of energy in the country	0.33	4
4	The strategic location of the country	0.00	5

Table 9: Effective external factors on waste management in country’s thermal power plant – **Threats**

Row	(Threats)	Weighted Points	Priority
7	Government structure in the power industry	1.00	1
1	The lack of prioritize in environmental issues	0.91	2
2	weakness of administrative in the Environmental Protection Agency	0.61	3
3	Low electricity costs (Not being real price of electricity)	0.43	4
4	Lack of access to innovative technologies and advanced of power generation and power Plant	0.32	5
5	Iran is one the arid and dry country	0.13	6
6	The impossibility of import high-quality fuel	0.00	7

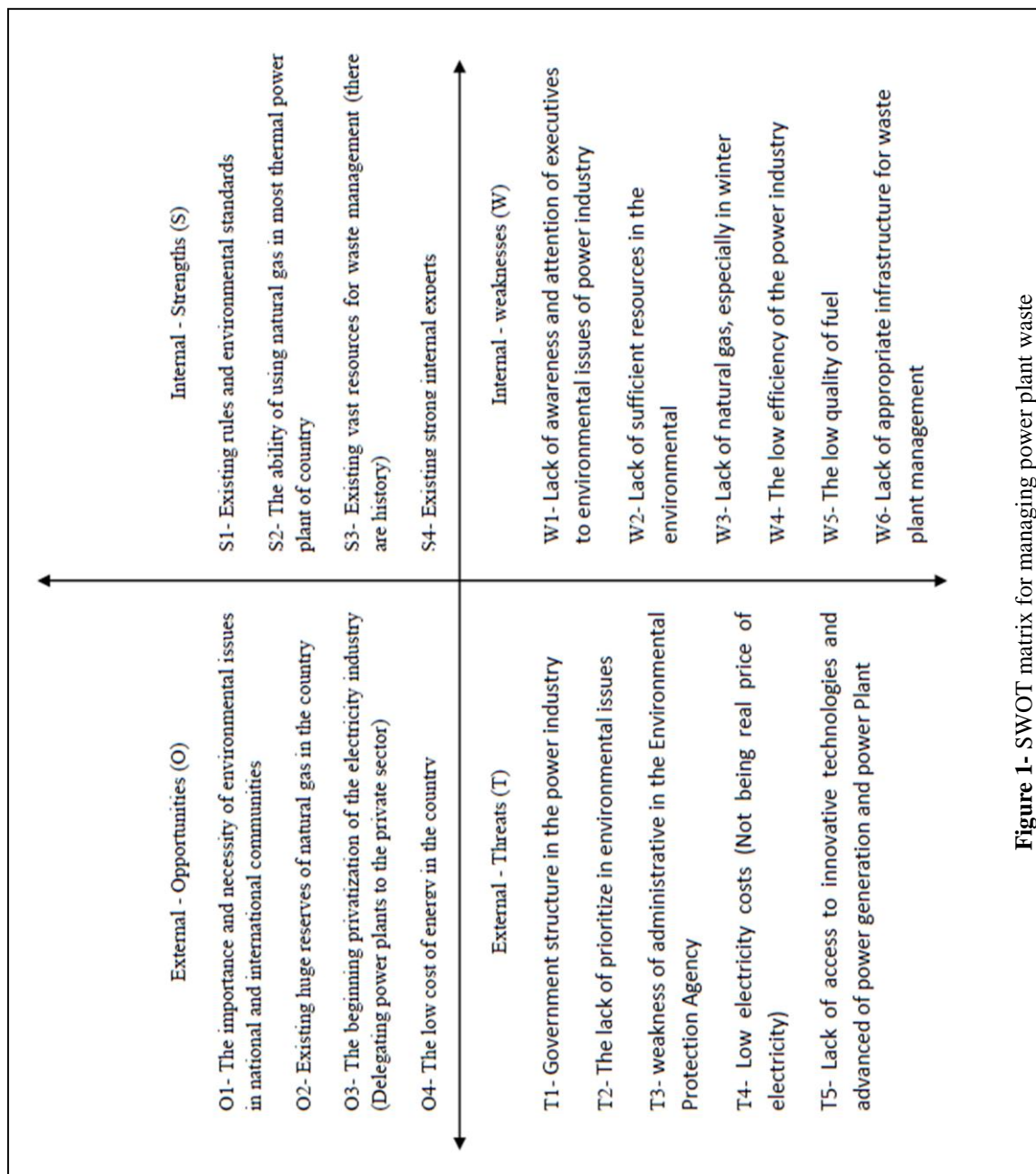


Figure 1- SWOT matrix for managing power plant waste

which is comparison one, variety of possible strategies are, paid attention through providing SWOT matrix. In SWOT matrix a kind of balance is established between main internal and external factors. Strategists can propose four strategies using this matrix: strategies SO, strategies WO, strategies ST and strategies WT.

In performing strategies SO using internal strengths, it is tried to take advantage of external opportunities. The goal of strategies WO is that with exploitation of existing opportunities in outdoor, internal weaknesses can be improved. In performing strategies ST, using its strengths minimize the effects of existing threats outdoor or remove them. Performing strategies WT is in defensive mode and its goal is minimizing internal weaknesses and avoiding threats of outdoor. The obtained result of experts' survey for determining power plant waste management in the country is proposed in table 10.

QUANTITATIVE STRATEGIC PLANNING MATRIX (QSPM)

In next phase, using quantitative strategic planning matrix (QSPM) designed strategies are optimized prioritized and finally choosing the best and most attractive ones are for thermal power plants of Iran. Choosing appropriate strategy is a comprehensive and broad subject because strategy has complex and different aspects that being familiar with that is required to have service and economic development. QSPM is used for

prioritizing strategies. If in this evaluation a strategy isn't able to face internal or external conditions of thermal power plant must be removed from the list of prioritized strategies. According to obtained strategies from SWOT which is shown in table 11, QSPM is used for evaluating strategic items and relative attractiveness of used strategies in decision making phase. This method decides that which one of these items is possible to prioritize them. Of course this method requires good judgment and expertise combined with knowledge which is appropriate for evaluating the possibility and stability of proposed strategies in facing environmental situations and current condition of organization.

Proposed coefficient in second column of table 12 is provided based on weighting the coefficients of matrixes IFE and EFE. Scores are given as no attractiveness (1), somewhat attractive (2), reasonable attractiveness (3) and very attractive (4) for determining the score of attractiveness with investigating internal and external factors of this question that if this factor has an important role in the process of choosing or selecting strategies then score of attractiveness in each factor compared to each of the strategies is determined and the sum of scores is obtained for each strategy from multiplying coefficient in Score of attractiveness. The way of scoring to 15 strategies by one of experts which is close to statistical population and related calculations are proposed in Table 12.

Table 10- SWOT matrix strategies

SWOT	Strengths (S) S1, S2, S3	Weaknesses (W) W1, W2, W3, W4, W5, W6
Opportunities (O) O1 O2 O3 O4	<ul style="list-style-type: none"> * Planning for using natural gas as a clean fuel in thermal power plants * Develop operating procedures to build power plants with high efficiency and compliance with environmental standards (Prohibition of creating low-efficiency and pollutants power plants) * Developing a comprehensive program of environmental management of waste 	<ul style="list-style-type: none"> * Planning power exchange with neighboring countries for peak shaving * Allocation of identified and approved funds to environmental activities * Planning to develop the country's gas refineries and solve its shortage * Use of international opportunities and facilities for environmental education the personnel of power industry
Threats (T) T1 T2 T3 T4 T5	<ul style="list-style-type: none"> * planning in order to accelerate the privatization * Implementation of environmental awareness and sensitization at various levels of expertise and managers * Planning for using new and clean technologies of power generation in the country 	<ul style="list-style-type: none"> • * Creating and strengthening environmental sector in power plants and electricity industry • * Specialized environmental training at various levels of electricity industry • * Realize price of electricity by considering the social costs • * Planning and policy for the development of international relations in power plant industry • * Doing applied research on high-efficiency and clean fuels production

Table 11: obtained strategies of SWOT method

Strategy No.	Strategy name	Strategy title
1	SO1	Planning for using natural gas as a clean fuel in thermal power plants
2	SO2	Develop operating procedures to build power plants with high efficiency and compliance with environmental standards
3	SO3	Developing a comprehensive program of environmental management of waste
4	ST1	planning in order to accelerate the privatization
5	ST2	Implementation of environmental awareness and sensitization at various levels of expertise and managers
6	ST3	Planning for using new and clean technologies of power generation in the country
7	WO1	Planning power exchange with neighboring countries for peak shaving
8	WO2	Allocation of identified and approved funds to environmental activities
9	WO3	Planning to develop the country's gas refineries and solve its shortage
10	WO4	Use of international opportunities and facilities for environmental education the personnel of power industry
11	WT1	Creating and strengthening environmental sector in power plants and electricity industry
12	WT2	Specialized environmental training at various levels of electricity industry
13	WT3	Realize price of electricity by considering the social costs
14	WT4	<ul style="list-style-type: none"> • Planning and policymaking for the development of international relations in power plant industry
15	WT5	Doing applied research on high-efficiency and clean fuels production

Table 12: the sample matrix of QSPM (the way of scoring strategies)

Determining factors	Coefficient	Strategy SO1		Strategy SO2		Strategy SO3		Strategy ST1		Strategy ST2	
		Point	Attraction								
Strengths	S1	2	12.4	4	24.8	3	18.6	3	18.6	3	18.6
	S2	4	22.8	3	17.1	1	5.7	1	5.7	1	5.7
	S3	1	5.5	2	11	4	22	2	11	2	11
weaknesses	W1	2	12.6	3	18.9	3	18.9	1	6.3	2	12.6
	W2	3	17.4	2	11.6	4	23.2	2	11.6	4	23.2
	W3	4	22.8	3	17.1	2	11.4	1	5.7	1	5.7
	W4	3	14.4	4	19.2	4	19.2	2	9.6	1	4.8
	W5	4	20.8	2	10.4	3	15.6	1	5.2	1	5.2
	W6	4	18	2	9	4	18	3	13.5	3	13.5
Opportunities	O1	2	14	3	21	3	21	2	14	3	28
	O2	4	25.6	4	25.6	3	19.2	1	6.4	1	6.4
	O3	2	11.2	4	22.4	3	16.8	3	22.4	2	11.2
	O4	3	11.7	3	11.7	2	7.8	1	3.9	1	3.9
Threats	T1	2	13.2	3	19.8	3	19.8	4	26.4	2	13.2
	T2	2	12.6	3	18.9	4	25.2	2	12.6	4	25.2
	T3	3	16.2	3	16.2	3	16.2	2	10.8	2	10.8
	T4	3	14.1	2	9.4	2	9.4	1	4.7	1	4.7
	T5	2	8.8	4	17.6	2	8.8	2	8.8	1	4.4
total	100	274.1	301.7	296.8	197.2	208.1					

DISCUSSION AND CONCLUSION

Generally solid waste management includes phases of reduction in source, collecting, storing in place, process, recycle and reusing, transportation, excretion and care after excretion. Methods of solid waste management considering the regulation of wastes' management divided into three categories of hazardous, industrial and normal.

Based on mentioned information, the most important solid and semi-solid waste of power plants can be divided into four main categories:

- wastes associated with combustion
- wastes associated with circulation system and water treatment
- wastes associated with human waste
- wastes of sludge from sanitary wastewater treatment

The third and fourth categories have been known in terms of nature, quantity and quality and there are the methods of their management and excretion in country. Especially human waste of power plants that their trustee are municipals of power plants' nearby cities. The wastes of first and second categories have had heavy and poisonous metals and are considered as hazardous industrial wastes and require its special management (DOE, 2011). Generally speaking, solid waste management includes phases of reduction in source, collecting,

storing in place, process, recycle and reusing, transportation, excretion and care after excretion.

Strategies of waste management in country's thermal power plant after analyzing internal and external environment of power plants and obtained results of using SWOT method attractiveness scores were determined as it is shown in table 13. For calculating final attractiveness of strategies the fifteen, obtained attractiveness for each strategy has been averaged in 31 completed questionnaires.

Final prioritizing of these strategies which is has been done based on experts' ideas and using QSPM matrix is proposed in table 13. Then strategies' scores were taken to diagram and four strategies of WT5, WT4, WT3 and WO4 were eliminated from proposed strategies because of having fewer score than other strategies.

In the end, it is concluded that based on electricity industry's experts' ideas, planning in order to establishing power plants with high efficiency, using low polluting fuels such as natural gas, integrated solid waste management program with the operating instructions and also strengthening the body of expertise the section of power plant environment in terms of technical and financial are the most important and effective factors in improving power plants' environmental management.

Table 13: Waste management strategies in thermal power plant in order of preference (attractiveness)

Priority	Strategy	Strategy title	Attraction
1	SO2	Develop operating procedures to build power plants with high efficiency and compliance with environmental standards	301.3
2	SO3	Developing a comprehensive program of environmental management of waste	295.6
3	SO1	Planning for using natural gas as a clean fuel in thermal power plants	261.0
4	WT1	Creating and strengthening environmental sector in power plants and electricity industry	223.1
5	ST3	Planning for using new and clean technologies of power generation in the country	215.4
6	WO3	Planning to develop the country's gas refineries and solve its shortage	201.8
7	ST2	Implementation of environmental awareness and sensitization at various levels of expertise and managers	196.4
8	WO2	Allocation of identified and approved funds to environmental activities	192.5
9	ST1	Planning in order to accelerate the privatization	191.1
10	WT2	Specialized environmental training at various levels of electricity industry	182.8
11	WT5	Doing applied research on high-efficiency and clean fuels production	179.2
12	WO4	Use of international opportunities and facilities for environmental education the personnel of power industry	168.5
13	WT3	Realize price of electricity by considering the social costs	164.9
14	WT4	Planning and policy making for the development of international relations in power plant industry	159.1
15	WT5	Planning power exchange with neighboring countries for peak shaving	150.3

REFERENCES

1. M. Saeedi, A. Karbasi, T. Sohrab, R. Samadi. Environmental management of power plants, Ministry of Energy, Iran Energy Efficiency Organization (2005). ISBN:964-6553-25.
2. Tavanir, Detailed stats of Iran's electricity industry for managers at 2013 ", Company of production, distribution and transfer of electric power of Iran (2014).
3. MOE, Energy balance 1391, planning office, Department of Electrical Energy, Ministry of Energy (2013).
4. M. Khalili Araghi, G.H. Sharzehi, S. Barkhordari, *Journal of Ecology*, **38**, 93 (2012).
5. N. Moharram, "Environmental management and planning", ISBN: 964-06-9353-7 (2006).
6. A. Ataei, Z. Iranmanesh, *Int. J. Environment.Res.*, **6**, 3 (2012).
7. A.R. Karbassi, M.A. Abduli, E. Abdollahzadeh, *Energy Policy*, **35**, 5171 (2007).
8. M.M. Shafipour, M. M. Farsiabi, *Int. J. Environ. Res.*, **1**, 150 (2007).
9. IL&FS. Technical EIA guidance manual for thermal power plants. IL&FS Ecosmart Limited, Hyderabad, India, 2010.
10. WEC., 2008. "Implementation of an effective Waste Management System Into The Thermal Power Plants". WEC Regional Energy Forum.
11. A. Choban, I. Winkler, Analysis of influence of the thermal power plant waste waters discharge on natural water objects. Water treatment technologies for the removal of high-toxicity pollutants. NATO Science for Peace and Security Series C: Environmental Security 2010, pp 225-234
12. WB. 1998." Thermal Power: Guidelines for New Plants. Pollution prevention and abatement handbook", World Bank Group.
13. Zh. Rashidi, A.R. Karbassi, A. Ataei, P. Ifaei, R. Samiee-Zafarghandi, M.J. Mohammadizadeh, *Int. J. Environ. Res.*, **6**, 875 (2012).
14. M.A. Abduli, A.R. Karbassi, R. Samiee-Zafarghandi, Zh. Rashidi, S. Gitipour, M. Pazoki, *Int. J. Environ. Res.*, **6**, 493 (2012).
15. PSC. WI., 2010." Environmental Impacts of Power Plants". Public Service Commission of Wisconsin.
16. M.R. Senapati, *Current science*, **100**, 1791 (2011).
17. Iran DOE. 2011. "Laws and executive regulations in waste management. Iran department of environment", ISBN: 9789641741510 (in Persian).

BULGARIAN CHEMICAL COMMUNICATIONS

Instructions about Preparation of Manuscripts

General remarks: Manuscripts are submitted in English by e-mail or by mail (in duplicate). The text must be typed double-spaced, on A4 format paper using Times New Roman font size 12, normal character spacing. The manuscript should not exceed 15 pages (about 3500 words), including photographs, tables, drawings, formulae, etc. Authors are requested to use margins of 3 cm on all sides. For mail submission hard copies, made by a clearly legible duplication process, are requested. Manuscripts should be subdivided into labelled sections, e.g. **Introduction, Experimental, Results and Discussion, etc.**

The title page comprises headline, author's names and affiliations, abstract and key words.

Attention is drawn to the following:

a) **The title** of the manuscript should reflect concisely the purpose and findings of the work. Abbreviations, symbols, chemical formulas, references and footnotes should be avoided. If indispensable, abbreviations and formulas should be given in parentheses immediately after the respective full form.

b) **The author's** first and middle name initials, and family name in full should be given, followed by the address (or addresses) of the contributing laboratory (laboratories). **The affiliation** of the author(s) should be listed in detail (no abbreviations!). The author to whom correspondence and/or inquiries should be sent should be indicated by asterisk (*).

The abstract should be self-explanatory and intelligible without any references to the text and containing not more than 250 words. It should be followed by key words (not more than six).

References should be numbered sequentially in the order, in which they are cited in the text. The numbers in the text should be enclosed in brackets [2], [5, 6], [9–12], etc., set on the text line. References, typed with double spacing, are to be listed in numerical order on a separate sheet. All references are to be given in Latin letters. The names of the authors are given without inversion. Titles of journals must be abbreviated according to Chemical Abstracts and given in italics, the volume is typed in bold, the initial page is given and the

year in parentheses. Attention is drawn to the following conventions:

a) The names of all authors of a certain publications should be given. The use of “*et al.*” in the list of references is not acceptable.

b) Only the initials of the first and middle names should be given.

In the manuscripts, the reference to author(s) of cited works should be made without giving initials, e.g. “Bush and Smith [7] pioneered...”. If the reference carries the names of three or more authors it should be quoted as “Bush *et al.* [7]”, if Bush is the first author, or as “Bush and co-workers [7]”, if Bush is the senior author.

Footnotes should be reduced to a minimum. Each footnote should be typed double-spaced at the bottom of the page, on which its subject is first mentioned.

Tables are numbered with Arabic numerals on the left-hand top. Each table should be referred to in the text. Column headings should be as short as possible but they must define units unambiguously. The units are to be separated from the preceding symbols by a comma or brackets.

Note: The following format should be used when figures, equations, *etc.* are referred to the text (followed by the respective numbers): Fig., Eqns., Table, Scheme.

Schemes and figures. Each manuscript (hard copy) should contain or be accompanied by the respective illustrative material as well as by the respective figure captions in a separate file (sheet). As far as presentation of units is concerned, SI units are to be used. However, some non-SI units are also acceptable, such as °C, ml, l, etc.

The author(s) name(s), the title of the manuscript, the number of drawings, photographs, diagrams, etc., should be written in black pencil on the back of the illustrative material (hard copies) in accordance with the list enclosed. Avoid using more than 6 (12 for reviews, respectively) figures in the manuscript. Since most of the illustrative materials are to be presented as 8-cm wide pictures, attention should be paid that all axis titles, numerals, legend(s) and texts are legible.

The authors are asked to submit **the final text** (after the manuscript has been accepted for

publication) in electronic form either by e-mail or mail on a 3.5" diskette (CD) using a PC Word-processor. The main text, list of references, tables and figure captions should be saved in separate files (as *.rtf or *.doc) with clearly identifiable file names. It is essential that the name and version of the word-processing program and the format of the text files is clearly indicated. It is recommended that the pictures are presented in *.tif, *.jpg, *.cdr or *.bmp format, the equations are written using "Equation Editor" and chemical reaction schemes

are written using ISIS Draw or ChemDraw programme.

The authors are required to submit the final text with a list of three individuals and their e-mail addresses that can be considered by the Editors as potential reviewers. Please, note that the reviewers should be outside the authors' own institution or organization. The Editorial Board of the journal is not obliged to accept these proposals.

EXAMPLES FOR PRESENTATION OF REFERENCES

REFERENCES

1. D. S. Newsome, *Catal. Rev.–Sci. Eng.*, **21**, 275 (1980).
2. C.-H. Lin, C.-Y. Hsu, *J. Chem. Soc. Chem. Commun.*, 1479 (1992).
3. R. G. Parr, W. Yang, *Density Functional Theory of Atoms and Molecules*, Oxford Univ. Press, New York, 1989.
4. V. Ponec, G. C. Bond, *Catalysis by Metals and Alloys (Stud. Surf. Sci. Catal., vol. 95)*, Elsevier, Amsterdam, 1995.
5. G. Kadinov, S. Todorova, A. Palazov, in: *New Frontiers in Catalysis (Proc. 10th Int. Congr. Catal., Budapest, 1992)*, L. Guzzi, F. Solymosi, P. Tetenyi (eds.), Akademiai Kiado, Budapest, 1993, Part C, p. 2817.
6. G. L. C. Maire, F. Garin, in: *Catalysis. Science and Technology*, J. R. Anderson, M. Boudart (eds), vol. 6, Springer-Verlag, Berlin, 1984, p. 161.
7. D. Pocknell, *GB Patent 2 207 355* (1949).
8. G. Angelov, PhD Thesis, UCTM, Sofia, 2001.
9. JCPDS International Center for Diffraction Data, Power Diffraction File, Swarthmore, PA, 1991.
10. *CA* **127**, 184 762q (1998).
11. P. Hou, H. Wise, *J. Catal.*, in press.
12. M. Sinev, private communication.
13. <http://www.chemweb.com/alchem/articles/1051611477211.html>.

CONTENTS

Nanomaterials & Nanotechnologies

Wu Zhi-fang, Liu Chao, Wu Runong, Coarsening behaviour of Pb particles in a Al-5wt%Pb nanocomposite alloy produced by mechanical alloying.....	5
A. H. Shahbazi Kootenaei, S. Maghsoodi, Effect of calcination and chromium doping on the structural characteristics of titanate nanotubes.....	10
D.J. Naghan, M.D. Motevalli, N. Mirzaei, A. Velayati, F.M. Moghadam, H.R. Ghaffari, K. Sharafi, Parameters effecting on photocatalytic degradation of the phenol from aqueous solutions in the presence of ZnO nanocatalyst under irradiation of UV-C light.....	14
A. Ghadami, J. Ghadam, Influence of CaCO ₃ Micro- and nano-particles on the structure and properties of Nylon-66.....	19
S. Fotoohi, S. Haji-Nasiri, Nichols stability analysis in multiwall carbon nanotube based interconnects.....	35

Physicochemistry

B. Kazeminasab, S. Rowshanzamir, H. Ghadamian, Multi-objective multivariable optimization of agglomerated cathode catalyst layer of a proton exchange membrane fuel cell.....	38
A. Azimi, M. Mirzaei, S.M.T. Ghomshe, Determination of methane hydrate interfacial tension from measurement of induction time in methane hydrate crystallization.....	49
A.H. Fani, A. Pourafshar, The effects of anionic surfactants on the strength and environmental impacts of foamed concrete.....	56
H. Hossini, P. Makhdoumi, S.O. Rastegar, F.M. Moghadam, H.R. Ghaffari, A. Javid, N. Mirzaei, Optimization of the electrocoagulation process for sulfate removal using response surface methodology	63
E. Farahmand, B. Rezai, F.D. Ardejani, S.Z.S. Tonekaboni, Kinetics, equilibrium, and thermodynamic studies of sulphate adsorption from aqueous solution using activated carbon derived from rice straw.....	72
L. Amirkhani, J. Moghaddas, H. Jafarizadeh, Effect of surface modification agent and calcination process on the preparation of the hydrophobic magnetic silica aerogels by ambient pressure drying method.....	82
Tao Wei, Da Zhang, Liang Chen, The kinetics study and reaction mechanism of acrylate grouting materials.....	89
Lan-xin Wang, Shan Yao, Bin Wen, First-principles calculation of stacking fault energies and mechanical properties for high entropy solid solution Al _x CoCrCuFeNi with different mole fraction of Al.....	93
Xiao Yang, Yi-min Zhang, Shen-xu Bao, Extraction of vanadium from sulfuric acid leaching solution of stone coal by ion exchange.....	99
A. Gholami, H. Noorizade, Statistical optimization of surfactant assisted dispersive liquid-liquid microextraction for trace mercury determination by GF-AAS.....	105

Organic & Pharmaceutical Chemistry

S.M. Kazemeini, B.Gh. Tarzi, H. Bakhoda, K. Larijani, P. Damanafshan, Evaluation of the minerals content and fatty acids profiles in <i>Descurainia sophia</i> and <i>Sisymbrium irio</i>	112
Qingzhi Ma, Zhao Li, Zhongfeng Zhang, Hai Hou, Y. Furuta, M. Ohkoshi, Molecular characteristics of drug activities in <i>Vitex negundo</i> woody extractives.....	119
Yabin Li, Jintian Huang, Performance of NaClO in selective oxidation of salix microcrystalline cellulose.....	124
Qing-zhi Ma, Dang-quan Zhang, Y. Furuta, He-ping Deng, Molecular characteristics of immune activities in <i>Cercis chinensis</i> stem extractives for physical anthropology.....	130
N. Montazeri, V. Vahabi, Highly efficient and easy synthesis of biscoumarin catalyzed by pentafluoropropionic acid (PFPA) as a new catalyst in aqueous medium.....	136
N. Rahimi, M. Shiva, S.A. Mortazavi, A.H. Elhamirad, A.M. Maskooki, G. Rajabzadeh, Kinetic study of superheated water extraction of berberine from <i>Berberis vulgaris</i> root.....	140
D. Ahmadi, A. Akbarzadeh, M. Arjmand, A. Heidarinasab, Preparation of pegylated nanoliposomal oxaliplatin and investigation of its efficacy on breast cancer cell lines	

MCF-7 and MDA-MB-231.....	147
Environmental Pollution & Remediation	
G. Bahmannia, A.H. Javid, A.M. Moradi, S.A. Mirbagheri, Dispersion model for assessing oily components of produced water discharges from South Pars Gas offshore.....	152
S.H. Fatemi, A.H. Javid, P. Nasiri, M. Mirilavasani, Chemical characterization and statistical analysis of heavy metals produced discharges from South Pars Gas offshore for dispersion modeling.....	158
Saman H. Mohammadi, Sohrab H. Mohammadi, Studying changes amount of useful chemical elements for pistachio trees in vermicompost animal manure than initial animal manure...	163
Fu-qiang Wang, Yu-juan Li, Qian Zhang, Jiao Qu, Phytoremediation of cadmium, lead and zinc by <i>Medicago sativa</i> L.(alfalfa): A study of different period.....	167
Changlong Pang, Ang Li, Shan Qiu, Li Wang, Jixian Yang, Fang Ma, Nanqi Ren, A novel subsurface flow constructed wetland used in advanced wastewater treatment for nutrient removal in the cold area.....	173
G. Kashi, N. Jaberzadee, Optimization electrophotocatalytic removal of acid red 18 from drinking water by Taguchi model.....	179
G. Kashi, A. Mehree, M. Zaeimdar, F. Khoshab, A.M. Madaree, Removal of fluoride from urbane drinking water by eggshell powder.....	187
Yong Liu, Zhulei Chen, Lie Yang, Zhuwei Liao, Tian-tian Sun, Jia Wang, Huabin Wang, Short-term remediation of soil contaminated with landfill leachate using natural and microwave modified zeolite of the clinoptilolite type.....	193
E. Rouhi-Moghaddam, F. Azarian-Moghaddam, A. Rashki, R. Karami, Effects of forest plantations on soil carbon sequestration in Chah Nimeh Region of Sistan, Iran.....	199
D.J. Naghan, M.D. Motevalli, N. Mirzaei, A. Javid, H.R. Ghaffari, M. Ahmadpour, M. Moradi, K. Sharafi, Efficiency comparison of alum and ferric chloride coagulants in removal of dye and organic material from industrial wastewater-a case study.....	206
M.R. Sadeghi Benis, A.H. Hassani, J. Nouri, I. Mehregan, F. Moattar, The effect of soil properties and plant species on the absorption of heavy metals in industrial sewage contaminated soil: A case study of Eshtehard Industrial Park.....	211
E. Sadeghi, M. Mohammadi, K. Sharafi, S. Bohlouli, Determination and assessment of 3 heavy metal content (Cd, Pb and Zn) in <i>Scomberomorus commerson</i> fish caught from the Persian Gulf.....	220
Engineering Sciences	
Zheng Shaojiang, Song Kuiyan, Dong Chunlei, A study on one-dimensional isothermal moisture migration in <i>Pinus yunnanensis</i>	224
F. Shirinzadeh, R.M. Barough, A.A. Orang, A parametric study on the factors affecting gas turbine combustion using a CFD-based approach.....	231
Dachao Yuan, Yang Huang, The impact of altitude effect on tunnel fire characteristics.....	239
Process Engineering	
A.S. Aboumasoudi, S. Mirzamohammadi, A. Makui, Development of network-ranking modeling in planning effective efficiency of multi-stage production industries value chain: a case study of textile industry.....	243
A. Narimannejad, Gh.N. Bidhendi, H. Hoveidi, Emergency response management native model to reduce environmental impacts using by analytic hierarchy process (AHP).....	250
A.Padash, Gh.N. Bidhendi, H. Hoveidi, M. Ardestani, Green strategy management framework towards sustainable development.....	259
Miscellaneous	
J.H. Hamissi, H. Hamissi, Attitude and practice of pharmacist towards oral healthcare and oral hygiene products: An exploratory study.....	269
R. Samadi, J. Nouri, A.R. Karbassi, R. Arjomandi, Development of environmental management strategies for thermal power plant wastes in Iran through strategic analysis method (SWOT).....	274
Instructions to authors.....	289